THE
PHYSICAL REVIEW

A journal of experimental and theoretical physics established by E. L. Nichols in 1893

SECOND SERIES, VOL. 80, No. 4 NOVEMBER 15, 1950

Neutron Deficient Radioactive Isotopes of Tantalum and Wolfram*

GEOFFREY WILKINSON**
Radiation Laboratory and Department of Chemistry, University of California, Berkeley, California
(Received June 12, 1950)

Neutron deficient radioactive isotopes of tantalum have been produced by bombardment of lutetium with α-particles, of hafnium with 10 Mev protons, and of tantalum with fast neutrons and protons from 10 to 70 Mev energy. In addition, wolfram isotopes produced by 10 to 70 Mev proton bombardments of tantalum, together with their respective tantalum daughter activities were studied. The radiation characteristics of the new activities of tantalum and wolfram are described.

I. EXPERIMENTAL

USING the 60-inch Crocker Laboratory cyclotron, bombardments were made of lutetium with 38, 30 and 20 Mev α-particles, of hafnium with 10 Mev protons, and of tantalum with fast neutrons from bombardment of beryllium with 19 Mev deuterons. Tantalum metal foil was bombarded with different energies of protons from the 184-inch cyclotron and the linear accelerator. The techniques of bombardments and of measurement of radiation characteristics by absorption methods, together with assumptions involved in the interpretation of data, have been described previously.[1,2]

The lutetium oxide targets were dissolved in nitric acid, hafnium oxide and tantalum targets in the minimum of a mixture of nitric and hydrofluoric acids. Where appropriate, carrier solutions of hafnium nitrate, sodium wolframate and tantalum in hydrofluoric acid were added, together with holdback carriers for contaminating activities likely to be formed from target materials; e.g., copper, platinum, etc. Radiochemical exchange of hafnium, tantalum, and wolfram activities with added carriers, was ensured by boiling the target solutions in hydrofluoric acid.

Lutetium and rare earth carriers added for scavenging, were removed by precipitation of the fluorides from hot solutions $3N$ in both nitric and hydrofluoric acids. Wolfram was separated using the following procedure. To the hot hydrofluoric acid solution of the tantalum target, hydrazine sulfate was first added to reduce any nitric acid present. Sufficient strong hydrochloric acid to give a $6N$ solution was added followed by stannous chloride solution, then ammonium thiocyanate solution followed by excess boric acid to complex the fluoride; the green thiocyanate complex of IV valent wolfram formed, was then extracted into ethyl acetate. The washed solvent layer was evaporated, holdback carriers for various elements were added and wolfram VI oxide precipitated by boiling with strong nitric acid. The oxide was dissolved in ammonium hydroxide, thiocyanate added to the solution and the reduction-extraction process repeated after acidification.

Hafnium and tantalum were precipitated as phosphates from boiling $3N$ nitric acid solution after complexing the fluoride ion with boric acid. The phosphates were metathesized with sodium hydroxide.

Hafnium and tantalum were separated by several methods. The mixed hydroxides were fused with sodium hydroxide and the cold melt extracted with water to give an insoluble residue of hafnium oxide and a solution of sodium tantalate, from which tantalum was recovered by acidification and precipitation of the phosphate; hafnium was extracted from $>8N$ hydrochloric acid solutions by tributylphosphate in butanol or from perchloric acid solutions by thenoyltrifluoracetone in benzene—the latter extraction was used in the search for hafnium daughters of tantalum activities where no hafnium carrier was added and the benzene extracts evaporated and ignited on trays for counting. When hafnium was not the target, carrier quantities were separated from tantalum solutions $3N$ in [illegible] from

* This work was performed under the auspices of the AEC.
** Present address: Chemistry Department, Massachusetts Institute of Technology, Cambridge, Mass.
[1] G. Wilkinson, Phys. Rev. 75, 1019 (1949).
[2] G. Wilkinson and H. G. Hicks, Phys. Rev. 75, 1370 (1949).

nitric and hydrofluoric acids by precipitation of barium hafnium fluoride.

After removal of hafnium, tantalum was recovered as the phosphate which was dissolved in the minimum of hydrofluoric acid. Niobium carrier was added and the tantalum separated by precipitation of potassium tantalum fluoride. This precipitate was heated to fuming with strong sulphuric acid to remove the fluoride and the phosphate precipitated from $2N$ acid solution.

A simple separation of tantalum and wolfram used in studying tantalum daughter activities was found to be quantitative, and, further to give a decontamination factor of greater than 10^6. The tantalum daughter activity was separated by scavenging the boiling strongly alkaline wolframate solution with nickel hydroxide. The washed hydroxide was dissolved in acid, excess wolframate solution added and the boiling solution again made alkaline. After three cycles, the active tantalum was finally collected on a small amount of zirconium hydroxide by precipitation from hydrochloric acid solution by addition of ammonium hydroxide; the large amounts of nickel used as a scavenger remain in solution.

In all cases the tantalum and wolfram oxides were prepared for counting and estimation of chemical yields by ignition of the hydrated oxides or phosphates.

In Table I are summarized the production and radiation characteristics of tantalum and wolfram isotopes. The energy of gamma-radiation is obtained from lead and aluminum absorption measurements while the energy of positive and negative electrons were obtained from both aluminum absorption measurements and from a simple magnetic spectrometer. The contribution of soft electromagnetic radiations in aluminum absorption measurements was obtained by removal of electrons by beryllium absorbers.

All the radioactive isotopes of tantalum and wolfram studied decay with the emission of electromagnetic radiations of half thicknesses 16 to 18 mg/cm^2 aluminum and 115 to 130 mg/cm^2 lead, which correspond to the average energies of L and K x-radiation of hafnium and tantalum respectively.

In the bombardment of lutetium with α-particles of 38, 30 and 19 Mev energy isotopes of half-lives 8.0 hours, 53 hours, 2.1 hours, and about 600 days were observed, the latter being in very low yield. The magnitude, and variation in yield of the first three isotopes at the various energies, agree with those observed previously for the production of thulium and rhenium activities by α-particle bombardment of holmium and tantalum respectively, and allow fairly certain mass allocation as in Table I. The long-lived activity is presumably formed from the 2.5 percent abundant Lu^{176} isotope. In the 10 Mev proton bombardment of hafnium, the 2.1 hour, 53 hour and long-lived activities were formed in approximately equal yields; the 8-hour component, which must be a complex of the 8.0-hour Ta^{180} unequivocally assigned by fast neutron bombardment of tantalum and the 8.0-hour Ta^{176}, was in a somewhat higher yield; these yields agree with the present allocations. The 8.0-hour Ta^{176} and 53-hour Ta^{177} have been shown to grow from wolfram parent activities and a further tantalum isotope of half-life 9.35 minutes was found to be the daughter of a 21.5-day wolfram isotope. The wolfram activities were assigned from the yields at various bombarding energies and agree with the above allocations of their daughter activities. The 9.35-min. tantalum must be allocated to Ta^{178} and is thus probably an independent isomer of the 2.1-hour activity; the latter has not been observed to grow from a wolfram parent.

The possibility of a long-lived isomer of Ta^{180} exists, but no evidence for such an isotope has been obtained in fast neutron bombardments where the long-lived background was only the 117-day Ta^{181} formed by neutron capture. No difference in the absorptions or decays of the long-lived activities from Lu+α, Hf+p, or Ta+p bombardments has been observed and all appear to be identical.

No hafnium daughter activities, which would be isomers of stable hafnium isotopes, with half-lives greater than five minutes have been observed.

II. TANTALUM ISOTOPES

16±2-min. Ta^{182}

This activity was known previously and the cross section for production in thermal neutron capture in tantalum has been measured.[3] The aluminum absorption has been remeasured. The approximate ratio of the radiations, 0.12 Mev ϵ^-: 0.6 Mev β^-: K+γ rays $=\sim 0.2:\sim 0.05:1$ suggests that the isotope decays by isomeric transition with a few percent branching by beta particle emission.

8.00±0.05-hour Ta^{180}

This previously known[4] activity, which is produced by fast neutron bombardment of tantalum has been restudied; the isotope was also produced by bombardment of tantalum with protons by the p, pn reaction.

The decays were followed through eleven half-lives. The aluminum and lead absorption curves of the activity show the radiations to consist of beta-particles, range 210 mg/cm^2 aluminum (0.6 Mev), Feather range 238 mg/cm^2 (0.7 Mev) L and K x-radiation and 1.3 Mev gamma-radiation. On the magnetic spectrometer the distribution of the electrons was that of a beta-particle of maximum energy 0.7 Mev. From the measurements, with usual corrections and assumptions counting efficiencies, the following ratios were obtained: 0.7 Mev β^-: L x ray: K x-ray: 1.3 Mev γ-ray$=0.13:\sim 1:1:\sim 0.01$.

---

[3] Seren, Friedlander, and Turkel, Phys. Rev. **72**, 163 (1947).
[4] G. T. Seaborg and I. Perlman, Rev. Mod. Phys. **20**, 585 (1948).

TABLE I. Production and characteristics of tantalum and wolfram isotopes.

Isotope	Type of radiation	Half-life	Energy of radiation in Mev: Particles	Energy of radiation in Mev: γ-rays	Produced by
Ta^{176}	K, ϵ^-, γ	8.0±0.1 hr.	0.12, 0.18, ~1	~2	Lu-α-3n
					W^{176} K decay
Ta^{177}	K, ϵ^-, γ	53±2 hr.	0.11	~1.4 (weak)	Lu-α-2n, 3n
					Hf-p-n
Ta^{178}					W^{177} K decay
	K, ϵ^-, β^+(~3%), γ	2.1±0.1 hr.	~0.1 ϵ^-~1 β^+	1.3–1.5	Lu-α-n
					Hf-p-n
					Ta-p-p3n
Ta^{178}	K, ϵ^-, β^+(~6%)γ	9.35±0.05 min.	0.08 ϵ^-1.06 β^+	~1.5	Hf-p-n
					W^{178} K decay
Ta^{179}	K, ϵ^-, γ	~600 days	~0.1	~0.7 (weak)	Lu-α-n
					Hf-p-n
					W^{179} K decay?
Ta^{180}	K, ϵ^-, β^-(~15%)γ	8.00±0.05 hr.	0.7 β^-		Ta-p-p2n
				1.3	Ta-n-2n
Ta^{182}	I.T. ϵ^-, γ, β^-(<5%)	16±2 min.	0.12 ϵ^-0.6 β^-		Ta-p-pn
					Ta-n-γ
W^{176}	K, ϵ^-, β^+(~0.5%)γ	80±5 min.	~0.1, ~0.2, ϵ^-~2β^+	~1.3	Ta-p-6n
W^{177}	K, ϵ^-, γ	130±3 min.	0.13 ϵ^-~0.4 ϵ^-	~0.45, 1.2	Ta-p-5n
W^{178}	K, γ	21.5±0.1 days		~0.27 (weak)	Ta-p-4n
W^{179}	K	30±1 min.	No ϵ^-		Ta-p-3n
W^{179}	K or I.T.	5.2±0.2 min.			Ta-p-3n

The isotope thus appears to decay predominantly by orbital electron capture with about 15 percent branching by negative beta-particle emission.

~600-day Ta^{179}

After decay of shorter-lived activities the tantalum fractions from Lu+α bombardments show a very weak long lived activity. This activity was also found 10 Mev proton bombardments of hafnium and in tantalum bombarded with high energy protons. The isotope is not formed by decay of wolfram parents of half-life greater than one hour, and since no short-lived tantalum daughters of the 30-min. wolfram activity definitely allocated to mass 179 have been found, it is most likely that the 600-day activity has mass 179. This allocation is consistent with the yields in α-particle bombardments of lutetium and in proton bombardments of tantalum.

The radiation characteristics were measured on samples from 10 Mev proton bombardments of hafnium and from 40–50 Mev proton bombardments of tantalum. The approximate ratio of the various radiations were: 0.1 Mev e^-: L x-rays: K x-rays: ~0.7 Mev γ-ray =~0.03: 1:1: ~0.03. The isotope thus appears to decay predominantly by orbital electron capture.

9.35±0.03-min. Ta^{178}

The decay of this activity separated from its 21.5-day wolfram parent was followed through 13 half-lives; aluminum, beryllium and lead absorptions of the radiations were made, corrections for decay during time of measurement being required. Study on a simple magnetic spectrometer showed conversion electrons of energy ~80 kev together with positrons of maximum energy 1.06 Mev; the energies agree with those obtained from the aluminum absorption.

The ratios of the various radiations, necessarily approximate in view of the various assumptions made, are ϵ^-: β^+: L x-ray: K x-ray: 1.5 Mev γ-ray=~0.5: 0.03: ~1:1: 0.03.

As discussed below, L and K x-radiation arise from both orbital electron capture in tantalum and from conversion in γ-ray transitions in the hafnium product, and it is reasonable to assume that ~0.5 of the K x-radiation results from orbital electron capture. On this basis, the 9.3-min. activity shows approximately 6 percent positron branching decay.

The 9.3-min. activity has been observed directly in the bombardment of hafnium with 10 Mev protons. Allocation of the 21.5-day wolfram parent is made to mass 178 on the basis of reaction yields; since a longer-lived tantalum has been allocated to mass 178 from Lu+α bombardments the 9.35 min. activity must be an isomer decaying independently. Since no long-lived activity has been observed to form from high intensities of the 9.3-min. activity, an upper limit for decay by isomeric transition can be set as 10^{-4} that for decay by orbital electron capture.

2.1±0.1-hour Ta^{178}

This activity was produced in 19 Mev α-particle bombardments of lutetium and also in proton bombardments of hafnium when it was formed in high yields corresponding to its allocation to mass 178. The radiation characteristics obtained from resolution of absorption curves gave approximate ratios of ~0.1 Mev ϵ^-: ~1 Mev β^+: L x-ray: K x-ray: ~1.4 Mev γ-ray=~0.3: ~0.02: ~1:1: ~0.5 showing decay by orbital electron capture with about 3 percent positron branching.

53±2 hours Ta^{177}

This activity has been observed after decay of the shorter-lived isotopes in the tantalum fraction from

Lu+α and Hf+p bombardments. An activity, identical in all respects was shown to be the daughter of the 134-min. wolfram activity by successive chemical separations at fixed time intervals. The decays of samples from the three sources were followed through over nine half lives. The approximate ratios of the various radiations are 0.11 Mev ϵ^-: L x-ray: K x-ray: 1.4 Mev γ-ray = $\sim$0.3: $\sim$0.5: 1: 0.005.

8.0±0.1 hour Ta^{176}

This isotope was formed in high yield in bombardment of lutetium with 38 Mev α-particles, and has also been found to grow from a wolfram parent of half-life 80 min. formed by bombardment of tantalum with protons of energy greater than $\sim$50 Mev. The decays of the several components of the radiation were separately followed through about eight half-lives. The ratios of the various radiations are, approximately 120 kev ϵ^-: 180 kev ϵ^-: $\sim$1 Mev ϵ^-: L x-ray: K x-ray: 1.2 Mev γ-ray = $\sim$0.7: $\sim$0.02: $\sim$0.5: 1: $\sim$0.6.

III. WOLFRAM ISOTOPES

The bombardment of tantalum with protons of energy 10 to 70 Mev has led to the characterization of five new radioactive isotopes of wolfram. The 140-day W^{181} activity produced by p, n and $d, 2n$ reaction in tantalum has been described previously.[5]

30±0.1-min., 5.2±0.2-min., W^{179}

These activities were found in the wolfram fraction from 40–60 Mev proton bombardments of tantalum on the 184-inch cyclotron and, in bombardments with 20 to 30 Mev protons from the linear accelerator in yields corresponding to $p, 3n$ reaction. Chemical separation of tantalum after decay of the wolfram activity showed a very weak long-lived activity which is probably due to the long-lived Ta^{179} discussed previously. No short-lived tantalum daughter activities were found. The decay of the 30-min. activity was followed through seven half-lives. No electrons or hard gamma-rays were observed, and the isotope appears to decay with the emission of L and K x-rays only. The ratio of L to K x-radiation in the 30-min. activity corrected for counting efficiencies, fluorescence yield, etc. was about 0.7: 1 suggesting simple electron capture decay.

The 5.2-min. activity whose decay was followed through six half-lives emits L and K x-rays and soft electrons; the ratio of the activities of the 5.2- and 30-min. activities in various bombardments appeared to be the same, and the activities are most likely isomeric.

21.5±0.1-day W^{178}

This activity was shown to be formed by bombardment of tantalum with protons of energy greater than $\sim$25 Mev in yields corresponding to a $p, 4n$ reaction. The decay of the isotope in equilibrium with the 9.35-min. tantalum daughter activity, has been followed through ten half-lives.

In order to obtain the radiation characteristics of the wolfram activity, the aluminum, beryllium, and lead absorption curves of the gross parent-daughter equilibrium mixture were measured. The daughter activity was then quantitatively separated and its activity measured. The equilibrium contribution of the 9.3-min. tantalum to the absorption curves of the gross activity were estimated, and the absorption of radiations of the wolfram parent obtained by subtraction.

The 21.5-day activity appears to decay by emission of L and K x-rays and a weak gamma-ray only. No electrons were observed. The ratios of the various radiations corrected for counting efficiencies, Auger effect, etc., are: ϵ^-: L x-ray: K x-ray: 0.27 Mev γ-ray = $<$0.05: $\sim$0.8: 1: $\sim$0.02.

From the measurements, the ratios of the L and K x-radiations for the 21.5-day and 9.3-min. activities can be obtained. The ratio of quanta emitted by the tantalum activity to quanta emitted by the wolfram parent activity was 1.7 for K x-radiation and 2.0 for L x-radiation. Thus, if it is assumed that one K x-ray quantum emitted by the wolfram activity represents one disintegration by orbital electron capture (only 0.75 L x-ray quanta are emitted per K electron captured due to direct transitions from M and lower shells), then it is clear that 0.4 of the L and K x-rays of the 9.3-min. tantalum daughter must arise following K shell conversion in γ-ray transitions following orbital electron capture. This figure agrees roughly with the number of electrons per K x-ray observed in the tantalum activity.

No daughter activity other than the 9.3-min. tantalum activity has been found to grow from the 21.5-day wolfram isotope.

130±3-min. W^{177}

This isotope was observed in bombardments of tantalum with protons of about 40 to 65 Mev from the 184-inch cyclotron. The decays of electron and electromagnetic radiations followed separately through seven half-lives.

The ratios of the various radiations, corrected for counting efficiencies, etc. are: 0.13 Mev ϵ^-: 0.4 Mev ϵ^-: L x-ray: K x-ray: 0.4 Mev γ-ray: 1.2 Mev γ-ray = $\sim$0.1: $\sim$0.02: $\sim$0.3: 1: $\sim$0.5: 0.2.

In order to characterize daughter activities of this isotope, the wolfram fraction containing the 130-min. activity was "milked" for tantalum activities. The tantalum fraction was found to contain only a pure 53-hour activity whose decay was followed through seven half-lives and whose radiations are identical with those of the 53-hour Ta^{177} described above. The yield of the tantalum activity in successive separations shows it to be the daughter of the 130-min. wolfram activity. No evidence for shorter- or longer-lived

[5] G. Wilkinson, Nature 160, 864 (1947).

daughter activities was obtained. Allocation of the 130-min. activity to mass 177 is made on the basis of recognition of the 53-hour Ta^{177} daughter activity and also from considerations of yield in bombardments at various energies which agree with formation by a $p, 5n$ reaction.

80±5-min. W^{176}

This activity was formed in bombardments of tantalum with protons of energy greater than about 50 Mev, and was obtained in a relatively pure yield in short bombardments of 0.2-mil tantalum foil with 70 Mev protons. The radiation characteristics were obtained from absorption measurements carried out immediately after chemical separation. The approximate ratios of the various radiations were ~0.1 Mev e^-: ~0.2 Mev e^-: ~2 Mev β^+: L x-ray: K x-ray: γ-ray = ~0.1: ~0.02: ~0.005: ~1: ~1: ~0.1.

The activity was shown to be the parent of the 8.0-hour Ta^{176} activity by chemical separations at successive time intervals. The half-life of the wolfram activity was obtained by measurement of the activity of aliquots of a stock solution taken at fifteen minute intervals and counted immediately after removal of the tantalum daughter activity. The decay through five half-lives was obtained after correction from the 130-min. W^{177} activity initially present to the extent of about five percent. The 53-hour Ta^{177} activity was found in small yield in the decays of the 8-hour daughter of the 80-min. wolfram as would be expected.

Thanks are due Dr. H. G. Hicks for assistance in part of the experimental work, T. Putnam, B. Rossi and the crew of the 60-inch Crocker Laboratory cyclotron, R. Watt and the crew of the linear accelerator, and J. Vale and the crew of the 184-inch cyclotron for their cooperation in bombardments. The advice and interest of Professors G. T. Seaborg and I. Perlman are gratefully acknowledged.

PHYSICAL REVIEW VOLUME 80, NUMBER 4 NOVEMBER 15, 1950

Resonance Capture of Neutrons by Uranium*

HERBERT L. ANDERSON†
Columbia University, New York, New York

(Received April 27, 1940)

The resonance capture of slow neutrons by U^{238} has been studied by absorption methods with "good" geometry and thin detectors using the cyclotron as an intense source of neutrons. The experimental cross section for self-absorption for slow neutrons transmitted by cadmium was measured with thin absorbers and found to be 4600×10^{-24} cm²/atom±40 percent. Evidence is given for the existence of more than one level. The predominant level has an energy somewhat under 11 ev, a total natural width somewhat less than 0.20 ev and a neutron width somewhat less than 0.0086 ev. The value $\int\sigma dE/E$ in the resonance region was found to be 290×10^{-24} cm²/atom±40 percent.

I. INTRODUCTION

IT is known that when neutrons are captured by uranium, either a fission of the uranium nucleus may take place, or the neutron may be captured in a typical resonance process, resulting in a radioactive isotope of uranium, U^{239}, which decays by β-emission of 24-minute half-life.[1] Since the latter process absorbs but does not produce neutrons, its investigation is of interest in relation to the problem of obtaining a self-propagating fission process with uranium.[2]

The process of resonance capture is characterized by a large capture cross section for neutrons of energy close to a certain value. According to the theory as given by Breit and Wigner[3] and extended by Bethe and Placzek,[4] the possibility of resonance arises whenever the compound nucleus, which is formed when a neutron falls upon a nucleus, has an energy level corresponding to positive kinetic energy of the neutron. A neutron of energy close to this value may be captured in the level and the subsequent emission of a γ-ray will leave the neutron bound in the nucleus. The width of the level is determined by the probability of γ-ray emission and by the probability of neutron re-emission.

If only one level predominates, the variation of the capture cross section with energy is given by the dispersion formula of Breit and Wigner,[3]

$$\sigma(E)=\pi\lambda^2\frac{2J+1}{(2s+1)(2i+1)}\frac{\Gamma_n\Gamma_\gamma}{(E-E_R)^2+(\Gamma/2)^2}$$

$$=\left(\frac{E_R}{E}\right)^{\frac{1}{2}}\frac{\sigma_R(\Gamma/2)^2}{(E-E_R)^2+(\Gamma/2)^2}, \quad (1)$$

* This article was originally received for publication on April 27, 1940, but was withheld voluntarily for reasons of national security. It was declassified by the Atomic Energy Commission on June 22, 1950, and submitted for publication in revised form on July 12, 1950. Publication assisted by the Ernest Kempton Adams Fund for Physical Research of Columbia University.

† University Fellow, Columbia University. Present address: Institute for Nuclear Studies, The University of Chicago, Chicago, Illinois.

[1] Meitner, Hahn, and Strassmann, Zeits. f. Physik **106**, 249 (1937). These authors give 23 min. as the half-life.

[2] Anderson, Fermi, and Szilard, Phys. Rev. **56**, 284 (1939).

[3] G. Breit and E. Wigner, Phys. Rev. **49**, 519 (1936).

[4] H. A. Bethe and G. Placzek, Phys. Rev. **51**, 450 (1937).

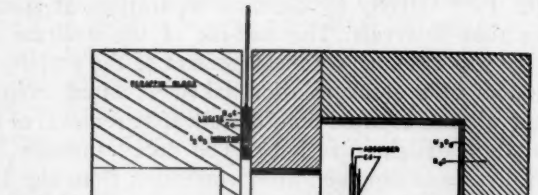

FIG. 1. Arrangement for investigating the resonance capture of neutrons by uranium.

where E is the energy of the neutron; E_R is the energy of the resonance level; σ_R is the capture cross section at exact resonance; $2\pi\lambda$ is the neutron wave-length; i and J are the nuclear spins of the original and compound nucleus, respectively; s is the neutron spin and has the value $\frac{1}{2}$; Γ_n and Γ_r are the neutron and radiation widths, respectively; while $\Gamma=\Gamma_n+\Gamma_r$ is the total natural width of the resonance level at half-maximum. It is to be observed that Γ_n is proportional to the neutron velocity.

Measurements have been carried out on (1) self-absorption, (2) boron absorption, and (3) resonance activation. The first gives information on the capture cross section at resonance; the second, on the resonance energy; and the third, on the area under the resonance curve above the thermal region. These measurements are sufficient to describe completely the resonance process, insofar as the Breit-Wigner formula applies. The capture cross section for thermal neutrons which has already been measured[5] may be used as a test of the assumption that only one level predominates. A unique interpretation of the present experiments is no longer possible when more than one level is effective. The values which result for the resonance energy and the cross section at resonance must then be interpreted as a sort of average over the several levels. Bethe and Placzek[4] have shown that interference effects among the levels may arise as a further complication. However, as they point out, the activation of a given level by neutrons which have been slowed down by paraffin may be expected to have an average dependence on the position of the level as E_R^{-1}. For this reason, levels which lie low in energy are favored in experiments of this kind. In addition, a boron filter technique has been employed which permits the activity due to the activation of levels above about 100 ev to be deducted.

[5] H. L. Anderson and E. Fermi, Phys. Rev. **55**, 1106 (1939); Halban, Kowarski, and Savitch, Comptes rendus **208**, 1396 (1939); L. Meitner, Nature **145**, 422 (1940).

II. ABSORPTION EXPERIMENTS

Absorption experiments were performed on boron and and uranium by measuring the activity induced in a uranium detector with and without the absorber in the path of the neutrons. A uranium detector, which is covered by cadmium to remove thermal neutrons, is sensitive mainly to what will be termed uranium resonance neutrons.[6] Hence, any measurement made with such a detector will be a measurement on uranium resonance neutrons. A small part of the activity induced in a uranium detector covered with cadmium is due to the fission process, but can be accounted for. Ideally, in such experiments, a parallel beam of neutrons should be used and the detectors should be thin enough to avoid the effects of self-absorption. In the previous work[1] on the uranium resonance process, measurements were made under geometrical conditions for which a large correction for obliquity had to be made. In the present experiments a cyclotron was available as an intense source of neutrons. Accordingly, a geometrical arrangement was used for which the correction for obliquity was only 1.5 percent. This arrangement is shown in Fig. 1.

III. EXPERIMENTAL ARRANGEMENT

Neutrons were produced in the cyclotron by bombarding beryllium with 6-Mev protons and were slowed down by means of a paraffin block. The detector was a thin layer of uranyl nitrate deposited on a lead dish and enclosed in cadmium. Lead was used because it is not made radioactive by neutrons from the cyclotron. The detector was surrounded by a thick cylinder of boron carbide which served to shield the detector from stray slow neutrons and to collimate the neutron beam emerging from the paraffin block. The interior of the cylinder was lined with uranium oxide to improve the shielding and to reduce the scattering of those neutrons which are most effective in activating the detector. To monitor the neutron beam, three disks of iodine pentoxide were placed between the paraffin and the boron shield and symmetrically disposed around the opening. They were covered with cadmium so that they would respond to epithermal[6] rather than to thermal neutrons. The radioactivity induced in iodine by slow neutrons has a half-life of 25 minutes. The difference between the half-lives of the detector and monitor is not sufficient to produce an appreciable error in monitoring due to possible variations in neutron intensity which may occur during irradiation.

[6] Cadmium is known to absorb strongly all neutrons below about 0.3-ev energy. In this paper neutrons strongly absorbed by cadmium will be referred to as thermal neutrons. Slow neutrons transmitted by cadmium but absorbed by thick boron will be termed epi-thermal; epi-thermal neutrons strongly captured by uranium, resonance neutrons; while all others will be called fast neutrons. On an energy scale, thermal neutrons are below about 0.3 ev, epi-thermal neutrons are between 0.3 and about 100 ev, while in the present case, fast neutrons have an energy not exceeding 3×10^6 ev.

IV. DETECTORS

The use of uranium as a detector is complicated by the fact that uranium itself is naturally radioactive. The β-activity of one of its daughter products, uranium X_2, was sufficiently intense partially to obscure a measurement of the induced activity. For this reason it was necessary to prepare, for each experiment, a new detector from which the uranium X had been removed. In order to compare the detectors with one another, the UX activity which builds up after the U^{239} activity has decayed was taken as an index. This is preferable to the use of the weight as an index since it minimizes errors due to non-uniformity of the uranium layer. The difference between the absorption coefficients of the β-rays must, however, be taken into account. The mass absorption coefficients in aluminum were measured and found to be 5.8 cm²/g and 13.5 cm²/g for UX_2 and U^{239}, respectively, for the particular geometry used in the measurement of the activity. Furthermore, the absorption was found to follow an exponential law for not too large absorber thicknesses. For $UO_2(NO_3)_2$, these values should be multiplied by a factor 1.5, obtained by assuming that the absorption increases as the cube-root of the atomic number. Since the detectors were quite thin (about 7 mg/cm²) the correction for the difference in the β-ray absorptions in the detector amounted only to about 5 percent.

V. ABSORBERS

Uranium absorbers were prepared by thoroughly mixing U_3O_8 powder with sulphur flowers. The mixture was then uniformly packed in an aluminum dish over which a second aluminum dish was crimped by means of a press, to form a sealed disk 8 cm in diameter and 0.3 cm thick. The U_3O_8 was prepared by ignition of a solution of uranyl nitrate. Boron absorbers were prepared in the same way with 800-mesh B_4C obtained from the Norton Company. I am indebted to Dr. R. R. Ridgeway of that company for an analysis of this boron carbide. He found that it contained 78.13 percent boron, 21.23 percent carbon, 0.14 percent iron, and 0.50 percent oxygen. Data on the absorbers are given in Table I.

VI. PROCEDURE

The experimental procedure was as follows: (1) Purification of uranium from uranium X. Uranyl nitrate was dissolved in ether, a little water added and after shaking removed again with the aid of a separating funnel. UX and other impurities are removed with the water while most of the uranium remains in ether solution. By repeating this several times the activity due to UX_2 can be reduced by a factor of 1000. The detector was prepared by evaporating, out of ether solution, from 150 to 250 milligrams of $UO_2(NO_3)_2$ on a lead dish of 28 cm² area. (2) Measurement of the residual UX activity. All measurements of uranium activities were made by means of a Geiger-Müller counter connected to a scale-of-four recorder. The counter was of the thin-walled silvered glass type[7] filled with a 9-cm argon, 1-cm alcohol mixture. Such a counter has a plateau of several hundred volts and in the several months during which these experiments were being carried out, natural background and sensitivity were frequently checked and found to vary inappreciably. (3) Irradiation by means of the cyclotron for 30 minutes. (4) Measurement of the ment of the U^{239} activity for 27 minutes starting three minutes after the end of the irradiation. (5) Measurement of the monitor activity against a uranium standard by means of an ionization chamber connected to an FP-54 amplifier. The combined activity of the three I_2O_5 disks was measured. (6) Measurement of the build-up of the UX activity for four days after the end of the irradiation. Care was taken to reproduce the disposition of the detector with respect to the counter in all measurements. From these data the initial slope of the UX build-up could be computed in counts per minute per hour.

TABLE I. Scattering data for the absorbers. The amount of each substance contained in the absorber is expressed in g/cm². The assumed cross sections for scattering are expressed in units of 10^{-24} cm². The scattering correction is estimated on the assumption that ½ of the neutrons which are scattered reach the detector.

Substance	Al	B	C	O	S	U	
Scattering cross section[a]	2.0	2.5	4.8	3.0	2.5	13.0	
Absorber	g/cm²						Scattering correction %
0.0191 U	0.12				0.19	0.0191	0.7
0.0342 U	0.12			0.01	0.21	0.0342	0.7
0.123 U	0.13			0.02	0.24	0.123	0.8
0.203 U	0.13			0.04	0.24	0.203	1.5
0.0312 B	0.12	0.0312	0.01		0.21		1.0
0.078 B	0.12	0.078	0.03		0.12		1.6
0.235 B	0.12	0.235	0.08				2.8
0.470 B	0.12	0.470	0.16				5.8
1.96 B	0.24	1.96	0.56				24.3
2.20 B	0.36	2.20	0.64				29.6

[a] The scattering cross sections for C and U are those for indium resonance neutrons reported by H. B. Hanstein and J. R. Dunning, Phys. Rev. **57**, 565 (1940). The others were estimated by comparing the cross sections for fast neutrons reported by Zinn, Seely, and Cohen, Phys. Rev. **56**, 260 (1939), with those for thermal neutrons reported by Dunning, Pegram, Fink, and Mitchell, Phys. Rev. **48**, 265 (1935).

VII. RESULTS

In a typical experiment, a detector with 203 mg of UX-free $UO_2(NO_3)_2$ was irradiated with cadmium only as absorber. The total number of counts in 27 minutes was 39,500, from which was subtracted 2870 counts due to natural background (18 counts per minute) and UX activity. From this, the initial activity immediately after the end of the irradiation was computed to be 2130 counts per minute. The initial slope of the UX build-up was found to be 16.8 counts per minute per hour while the monitor activity was 0.744 referred to a 5-gram uranium standard. Thus, the initial activity, A, of U^{239} per unit monitor and per unit UX slope was 170. The fraction f of uranium atoms activated per second

[7] Made by Eck and Krebs, New York City.

TABLE II. Fraction f of uranium atoms activated per second by a neutron beam having unit intensity, in terms of the iodine monitor, f is given in units of 10^{-18} sec.$^{-1}$.

Absorber thickness g/cm²	Observed	Background	Scattering correction %	Fission	Corrected
O	3.26	0.21	0	1.06	1.99
Cd (0.45 g/cm²)	2.39	0.21	0	0.22	1.96
Cd+0.0191 U	2.02	0.21	0.7	0.22	1.60
Cd+0.0342 U	1.81	0.21	0.7	0.22	1.39
Cd+0.123 U	1.19	0.21	0.8	0.22	0.71
Cd+0.203 U	1.03	0.21	1.5	0.22	0.61
Cd+0.078 B	2.14	0.21	1.6	0.21	1.75
Cd+0.235 B	1.71	0.21	2.8	0.19	1.35
Cd+0.470 B	1.27	0.21	5.8	0.19	0.93
Cd+1.96 B	0.52	0.21	24.3	0.17	0.21
Cd+2.20 B	0.48	0.21	29.6	0.17	0.18
Cd+0.235 B+0.203 U	0.88	0.21	4.3	0.19	0.51
Cd+0.470 B+0.203 U	0.74	0.21	7.4	0.19	0.38
Cd+1.96 B+0.0342 U	0.48	0.21	25.0	0.17	0.17
Cd+1.96 B+0.123 U	0.45	0.21	25.1	0.17	0.13
Cd+1.96 B+0.203 U	0.44	0.21	26.1	0.17	0.12

by a neutron beam of intensity corresponding to unit monitor activity may be calculated from this result by means of the formula,

$$f = A\lambda\eta/\tau_1(1-e^{-t/\tau_2}), \qquad (2)$$

where, $\lambda = 4.87\times10^{-18}$ sec.$^{-1}$ is the disintegration constant of uranium, $\tau_1 = 852$ hours is the average life of UX, η is the factor which takes into account corrections for the absorptions of the neutrons and the β-rays, while $t = 30$ minutes is the irradiation time and $\tau_2 = 34.7$ minutes is the average life of U^{239}. The contribution to η due to the β-ray absorption in the walls of the counter was determined by slipping over the counter a cylinder of aluminum having about the same thickness as the counter wall (0.029 g/cm²). Its transmission for the β-rays of U^{239} was found to be 67.7 percent and for UX, 85.0 percent; this yields a factor 1.25. The correction for the absorption of the β-rays in the detector itself was estimated from the observed value of the UX slope and the measured values of the absorption coefficients, the average weight of uranyl nitrate per unit of UX slope being 48 mg/28 cm². In the present example, this correction raised the result by 4.2 percent. The correction for the self-absorption of neutrons in the detector was estimated from the experimental self-absorption curve and in this case increased the result by 3.0 percent to a final value of 2.31×10^{-18} sec.$^{-1}$; possible differences in the *scattering* of the β-rays were neglected. Individual results obtained in this way had an average deviation from their mean of less than 4 percent. The values of f for different absorbers listed in Table II depend on at least two measurements of this kind and the precision measure of a result stated there may be taken to be 3 percent. On the other hand, the absolute measure of f is subject to considerable error due principally to the uncertainty in estimating η. The *relative* values, which are used in determining the transmissions of absorbers, are not subject to this limitation.

A considerable uncertainty in measurements of this type is due to the scattering in the absorbers and to the activities produced by fast neutrons. If there were no scattering, the residual activity with a thick boron absorber placed in front of the detector could be deducted and the difference properly ascribed to neutrons absorbed by thick boron. However, this is not the case; scattering does take place, and moreover, scattering cross sections, especially for boron, are not well known. In Table I data on the absorbers have been compiled, together with values of the scattering cross sections which were assumed. In computing the scattering correction it was assumed that the scattering was spherically symmetrical and that, therefore, $\frac{1}{2}$ of the scattered neutrons did not reach the detector.

The background due to neutrons striking the detector from behind was estimated to be 0.19 (in units of f) and the scattering correction was not applied to this part of the activity. A part of the observed activity was due to fission of uranium nuclei. To estimate the contribution due to fission, experiments were performed in which uranyl nitrate was irradiated with and without a cadmium absorber, and the U^{239} activity separated from all other activities *after* the irradiation, by a second ether separation. The activity with no absorber was only slightly larger than the activity with a cadmium absorber, wherefore, almost all the activity due to thermal neutrons could be ascribed to the fission process. The ratio of the number of fissions due to thermal neutrons, to the number due to epi-thermal and fast neutrons, was determined by placing, in the detector position, a uranium-lined ionization chamber connected to a linear amplifier. The number of fissions was then recorded with the different absorbers in place. A small boron-trifluoride counter was used as a monitor in these experiments. The activity which remained with the thickest absorber after this fission activity had been subtracted was probably due to the fast neutrons.

VIII. FILTER TECHNIQUE

In studying the resonance process, several filters have been employed in order to distinguish the effects of different neutron groups. A cadmium filter was placed in front of the detector to remove thermal neutrons. A second filter, sometimes of boron and sometimes of uranium, could be interposed or taken out of the beam. Differences of activities observed with and without this second filter represent the action of a neutron band that does not contain the thermal neutrons and is absorbed by the second filter. Thus, whenever the second filter is a thick boron layer the corresponding band includes only the epi-thermal neutrons. With a uranium layer of moderate absorption as second filter, the effect is that of neutrons strongly absorbed by uranium near the center of resonance band.

The columns of Table III give the transmission observed with several second filters. They are calculated

from the data of Table II with the formula,

$$T=(f_A-f_{A+F})/(f_0+f_F), \quad (3)$$

where the subscripts A and F refer to the absorber and the filter, respectively, it being understood that the detector is always covered with cadmium. The transmission value computed in this way is that fraction of the resonance neutrons which is absorbed in the filter but transmitted by the absorber.

IX. SELF-ABSORPTION

If the resonance curve were rectangular in shape the transmission of uranium resonance neutrons by uranium absorbers would decrease, with increasing thickness, according to an exponential law. Usually, the curve has a well-defined maximum and neutrons of energy corresponding to this maximum are absorbed more strongly than the others, giving rise to the phenomenon of self-reversal.[8]

When the resonance curve is sharp enough so that the number of neutrons per unit energy interval does not vary appreciably over the resonance region, then for a parallel beam of neutrons the transmission for self-absorption may be written,

$$T=\int \sigma(E)e^{-\sigma(E)N}dE \Big/ \int \sigma(E)dE, \quad (4)$$

where $\sigma(E)$ is the capture cross section for neutrons of energy E, N is the number of atoms per cm² and the integrals are extended over the resonance region. With the single level formula (1) and neglecting the Doppler effect, the integrals may be evaluated provided that the resonance maximum is very sharp. The expression for the transmission which results is,[9]

$$T=e^{-\sigma_R N/2}I_0(\sigma_R N/2), \quad (5)$$

where I_0 is the Bessel function of zero order and imaginary argument and σ_R is the capture cross section at exact resonance. For very thin absorbers (5) is equivalent to an exponential law with an effective cross section $\sigma_0=\sigma_R/2$, termed the experimental cross section for self-absorption.

The experimental points for the self-absorption of resonance neutrons, obtained with a 1.96-g/cm² boron filter, fit fairly well the theoretical curve (5) plotted in Fig. 2 with $\sigma_0=4600\times10^{-24}$ cm². The result, $\sigma_0=4600\times10^{-24}$ cm²/atom±15 percent, is considerably higher than the value $\sigma_0=1200\times10^{-24}$ cm², obtained by Meitner, Hahn, and Strassmann.[1] It is in good agreement with the result $\sigma_0=5000\times10^{-24}$ cm²/atom reported more recently by Sauerwein.[10]

[8] H. von Halban and P. Preiswerk, Nature **138**, 163 (1936); J. de phys. et rad. **8**, 29 (1937).

[9] Tables for this function are to be found in Watson, *Theory of Bessel Functions* (Cambridge University Press, 1922), p. 698.

[10] K. Sauerwein, Zeits. f. Naturforshg. **2a**, 73 (1947).

TABLE III. Absorber transmissions for uranium resonance neutrons. Transmission values refer to those neutrons which are absorbed by the filter noted. Cadmium (0.45 g/cm²) always covers the detector to remove thermal neutrons.

Absorber	Transmissions for neutrons absorbed by filter 1.96 B	0.470 B	0.203 U
0	1.000	1.000	1.000
0.0191 U	0.806		
0.0342 U	0.697		
0.123 U	0.365		
0.203 U	0.280	0.224	
0.078 B	0.881		
0.235 B	0.660		0.622
0.470 B	0.440		0.407

If there were just one level the transmission values would not be altered by using a thinner boron filter. The existence of higher resonance levels is indicated by the fact that, with a thinner boron filter, the 0.203-g/cm² uranium absorber has a lower transmission.

X. BORON ABSORPTION

The data of Table III for the boron absorbers are plotted on a logarithmic scale in Fig. 3. The experimental points for uranium resonance neutrons absorbed by a 1.96-g/cm² boron filter lie along a curve corresponding to an absorption coefficient in boron $\mu_B=1.68$ cm²/g. The resonance energy may be obtained from this result and a knowledge of the absorption coefficient μ_T of boron for thermal neutrons, by making use of the $1/v$ (v is the neutron velocity) law for the absorption of slow neutrons by boron. Thus, the resonance energy is given by the formula,

$$E_R=E_T(\mu_T/\mu_B)^2. \quad (6)$$

The slow neutron absorption coefficient of boron has been measured in a reliable way with neutron velocity

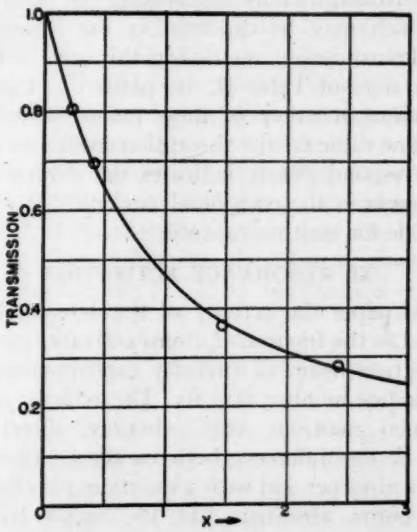

FIG. 2. Self-absorption curve for uranium: The curve is the function $e^{-x}I_0(x)$; the experimental points for various absorber thicknesses N, in atoms/cm², are plotted assuming $x=4600\times10^{-24}N$.

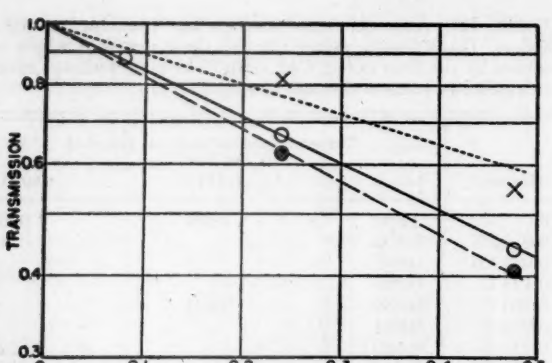

FIG. 3. Boron absorption of uranium resonance neutrons. The empty circles refer to the experimental transmissions for neutrons absorbed by a 1.96 g/cm² boron filter, while the shaded circles and the crosses refer to the transmissions for neutrons absorbed by and transmitted through a 0.203 g/cm² uranium filter, respectively. The three straight lines are drawn to fit as well as possible the three sets of points.

selectors[11] with the result $\mu_T = 39.4$ cm²/g at $E_T = 0.025$ ev.

The value of E_R which is obtained from these data is 13.7 ev. Measurements were also made with a uranium filter. The data given in Table III indicates a somewhat higher boron absorption coefficient, 1.85 cm²/g, which corresponds to a resonance energy of 11.3 ev. If there are several resonance levels, μ_B and E_R represent average properties of these levels. When a uranium filter is used the strongest levels are emphasized, which may account for the difference between this result and that obtained with the boron filter. A more sensitive test for the existence of higher levels is a measurement of the boron absorption coefficient for those resonance neutrons *transmitted* by a uranium filter. The uranium filter removes a large fraction of the low energy resonance neutrons, thereby augmenting the percentage of those which may be captured in the higher energy levels. Transmission values for this case, calculated from the data of Table II, are plotted in Fig. 3. The experimental accuracy of these points is quite poor, but the low value for the absorption coefficient to which they correspond clearly indicates the existence of the higher levels in the compound nucleus U^{239} which are responsible for neutron capture.

XI. RESONANCE ACTIVATION

In this paper the activity of the detector has been expressed as the fraction of atoms activated per second, by a neutron beam of intensity corresponding to one unit of iodine monitor activity. The activity f_R due to epi-thermal neutrons only, obtained directly from Table I as the difference between the f values with a cadmium absorber and with a cadmium plus thick (2.20 g/cm²) boron absorber, has the value 1.78×10^{-18} sec.$^{-1}$. A probable error of about 30 percent might reasonably be assigned to this result due principally to the uncertainty in the value for the correction factor which takes into account the differences between the β-rays of U^{239} and of UX.

It is possible to obtain an estimate of the area of the resonance curve from a knowledge of f_R and the intensity and energy distribution, $N(E)dE$, of the neutron beam corresponding to unit monitor activity. For energies above 1 ev the energy distribution of neutrons emerging from paraffin may be approximately represented by the law,[12]

$$N(E)dE = QdE/E. \tag{7}$$

Below one ev deviations from this law arise due to the thermal motion and the binding of the protons in the paraffin. The lower limit of the energy distribution is determined by the cut-off energy of the cadmium absorber used to shield the detector. Recent experiments by Baker and Bacher[13] using the modulated beam technique for obtaining mono-energic neutrons, indicate that a cadmium absorber of 0.45 g/cm² thickness transmits about 5 percent at 0.2 ev and 50 percent at 0.5 ev. For this reason, it is difficult to speak of a sharp cut-off energy for cadmium.

A measure of a "practical" cut-off energy for cadmium, which will be consistent with the assumptions which have been made, may be obtained by determining, with a boron-lined ionization chamber connected to a linear amplifier as detector, the boron absorption of neutrons transmitted by the cadmium absorber. Under the assumption that boron absorbs according to the $1/v$ law and that (7) holds for the energy distribution of neutrons emerging from paraffin, the transmission of a boron absorber of thickness x g/cm², in terms of the boron absorption coefficient μ_c at the "practical" cut-off energy of cadmium, may be written,

$$T = (1/\mu_c x)(1 - e^{-\mu_c x}). \tag{8}$$

An experiment was performed with the arrangement of Fig. 1 with a boron-lined ionization chamber in place of the detector. The results, corrected for scattering and obliquity in the manner previously described, are plotted in Fig. 4. They are compared with the theoretical transmission curves (8) plotted for several values of the cut-off energy. μ_c is obtained from the cut-off energy E_c by applying the $1/v$ law,

$$\mu_c = \mu_T (E_T/E_c)^{\frac{1}{2}}, \tag{9}$$

and using the values $\mu_T = 39.4$ cm²/g and $E_T = 0.025$ ev. It is seen that the data fit quite well the curve for $E_c = 0.34$ ev. The main uncertainty arises in estimating the magnitude of the background. This result is in good agreement with the value 0.4 ev obtained by Hoffman and Livingston[14] in a similar experiment.

[11] Bacher, Baker, and McDaniel, Phys. Rev. **69**, 443 (1946); Manley, Haworth, and Luebke, Phys. Rev. **69**, 504 (1946); Fermi, Marshall, and Marshall, Phys. Rev. **72**, 193 (1947).

[12] E. Fermi, Ricerca Scient. **7**, 13 (1936); see also Bethe, reference 4, p. 122.

[13] C. P. Baker and R. F. Bacher, Phys. Rev. **57**, 1076A (1940).

[14] J. E. Hoffman and M. S. Livingston, Phys. Rev. **52**, 1228 (1937).

The coefficient Q was determined by depositing a small amount of boron (0.47 milligram of the same boron carbide as was used in the absorbers) on one electrode of an argon-filled ionization chamber connected to a linear amplifier. The ionization chamber was placed in the detector position of Fig. 1. The gain of the linear amplifier was set so as to record all of the α-particles but none of the Li ions from the boron reaction.[15] Account was taken of the fact that one-half of the α-particles entered the electrode on which the boron carbide was deposited, and hence were not recorded.

By monitoring the output of the cyclotron simultaneously with both a BF_3 counter and the iodine monitors it was possible to obtain the number of boron disintegrations per unit iodine monitor activity corresponding to a 30-minute irradiation of constant intensity. The number of boron disintegrations per second, per unit iodine activity and per gram of boron, after subtracting the background, due mostly to gas recoils in the ionization chamber, was found to be 18.78×10^5. Of these, 17.47×10^5 were due to thermal neutrons while 1.31×10^5 were due to epi-thermal neutrons. The number of boron disintegrations per second and per gram due to epithermal neutrons may be obtained by applying (7) and the $1/v$ law, to be,

$$A_B = \int_{E_c}^{\infty} Q \frac{dE}{E} \mu_c \left(\frac{E_c}{E}\right)^{\frac{1}{2}} = 2Q\mu_c, \tag{10}$$

in which a negligible error is incurred by extending the limit of integration to infinity. Thus, taking $\mu_c = 10.7$ cm^2/g (corresponding to $E_c = 0.34$ ev), the result for Q is 6120 per cm^2-second. The activity f_R is given by the expression,

$$f_R = Q \int \sigma(E) dE/E. \tag{11}$$

The integral, which has to be taken over the resonance region, will be called the *resonance activation*. It is

$$\alpha_R = \int \sigma(E) dE/E = f_R/Q = 290 \times 10^{-24} \text{ cm}^2/\text{atom}. \tag{12}$$

If an error of about 30 percent be assigned to the value for Q, due principally to the uncertainty in the value of μ_c, then the error to be assigned to α_R should be about 40 percent.

[15] It is assumed that the boron absorption process always leads to the emission of α-particles which would be detected in the present experiment. Some doubt on this point may be thrown by the work of W. Maurer and J. B. Fisk, Zeits. f. Physik **112**, 436 (1939), who reported a group of low energy protons which would escape detection. However, a cloud chamber study by C. W. Gilbert, Proc. Camb. Phil. Soc. **44**, 447 (1948) is in support of the view adopted here. A low energy proton group is made improbable by the smallness of the Gamow factor.

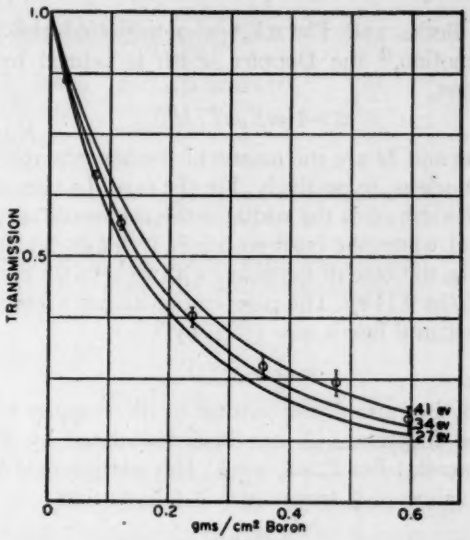

FIG. 4. Determination of the cut-off energy of cadmium. Experimental points for the self-absorption in boron of neutrons transmitted by cadmium, are compared with theoretical curves for several values of the cut-off energy of cadmium.

XII. ANALYSIS OF THE RESONANCE PROCESS

In the experiments described above, the errors were due more to the effects of scattering of the neutrons and the β-rays involved and to the presence of stray neutrons, than to any lack of self-consistency in the individual measurements themselves. The interpretation of the experiments is hampered not only by the somewhat uncertain validity of the theoretical assumptions which have been used, but also by the existence of more than one level which is responsible for neutron capture. The difficulty is fundamental in the method itself because of the lack of the necessary selective elements. In what follows the analysis of the resonance process will be carried through as though only one level were effective and no attempt will be made to correct the results so obtained for the effect of other levels.

For convenience, the experimental results which have bearing on the following analysis are collected below, together with an approximate estimate of the error. $\sigma_0 = 4600 \times 10^{-24}$ cm^2/atom$\pm$15 percent. $E_R = 11$ ev$\pm$30 percent. $\alpha_R = 290 \times 10^{-24}$ cm^2/atom$\pm$40 percent.

In the case where the resonance curve is not broadened to the Doppler effect, its shape is given by the Breit-Wigner formula (1). If the resonance is very sharp

$$\alpha_R = \frac{\sigma_R \Gamma}{2E_R} \int_{-\infty}^{\infty} \frac{dx}{1+x^2} = \frac{\pi}{2} \frac{\sigma_R \Gamma}{E_R}, \tag{13}$$

where $\sigma_R = 2\sigma_0$ is the cross section at exact resonance and Γ is the total natural width of the curve at half-maximum. From this relation and the above data Γ may be computed to be 0.22 ev and the cross section at exact resonance σ_R, to be 9200×10^{24} cm^2.

The above value for the total width indicates that the effect of Doppler broadening is not negligible. Fol-

owing Bethe and Placzek,[4] who neglected the zero-point motion,[16] the Doppler width is defined by the expression,

$$\Delta=4(mE_RkT/M)^{\frac{1}{2}}, \tag{14}$$

where m and M are the masses of the neutron and capturing nucleus, respectively. For the case of a very small natural width, Δ is the width of the resonance curve at the point where the cross section is $1/e$ of its maximum value. In the case of uranium, with $kT=0.026$ ev, Δ is found to be 0.14 ev. The cross section at exact resonance of the natural line is now given by

$$\sigma_R=\sigma_0/\chi(\xi), \tag{15}$$

where ξ the ratio of the natural to the Doppler width, and the function $\chi(\xi)$ has been calculated by Bethe and Placzek.[4] For $\Gamma\gg\Delta$, $\chi=\frac{1}{2}$. The relation (13) holds for all values of ξ, from which it follows that

$$\xi=-\frac{2}{\pi}\frac{E_R\alpha_R}{\sigma_0\Delta}\chi(\xi). \tag{16}$$

From (13), (14), (15), (16) and the graph of the function $\chi(\xi)$ given by Bethe and Placzek,[4] may be found the values: $\xi=1.4$, $\sigma_R=10{,}000\times10^{-24}$ cm^2, and $\Gamma=0.20$ ev.

Wayland and Placzek have kindly communicated to me the results of some calculations of the self-absorption curves with different values of ξ. However, the experimental accuracy is not sufficient to distinguish between the slight differences in shape of the curve of Fig. 2 ($\xi=\infty$) and that corresponding to $\xi=1.4$.

The neutron width at resonance may be calculated by applying Eqs. (1) and (13). Assuming that the spin change in the process $U^{238}\rightarrow U^{239}$ is from $i=0$ to $J=\frac{1}{2}$, it follows that

$$\Gamma_n=\frac{\alpha_RE_R}{2\pi^2\lambda_R^2}=0.0086 \text{ ev}. \tag{17}$$

[16] The effect of chemical binding on the Doppler width has been studied by W. E. Lamb, Phys. Rev. 55, 190 (1939).

If the above values are inserted in the Breit-Wigner formula (1), the capture cross section at thermal energies turns out to be about ten times higher than that obtained[5] by direct measurement. This indicates the presence of more than one level, possibly even of negative energy levels, which, by interference, may give rise to the low thermal cross section observed. It is to be pointed out that in the preceding paragraphs the Breit-Wigner formula was made use of only in the immediate vicinity of resonance, in which use the influence of the other levels is not as marked as when the formula is extrapolated to the thermal energy region.

The neutron and total widths obtained above must be regarded as upper limits for the lowest level for U^{238} above the cadmium cut-off. This is because the value obtained for E_R is certainly higher than the resonance energy of this level, while α_R contains contributions from all the levels above the cadmium cut-off. The indications are, however, that the higher levels contribute in only a minor way to the values obtained here.

Recently, Sauerwein[10] has reported some measurements on the resonance capture of neutrons by uranium, and has given evidence for the existence of an absorption band in the region of several hundred ev. The value $\Gamma=0.0075$ ev given by him is very much smaller than that given here. His method of deducing Γ from the shape of the self-absorption curve is questionable, however, in view of the existence of higher levels.

In conclusion I wish to express my indebtedness to Professors E. Fermi and J. R. Dunning who followed the course of the work with constant interest and much helpful guidance, and to Mr. H. Glassford of the cyclotron staff for his aid in carrying out the experiments. The aid of the Research Corporation has been very helpful. Acknowledgment is made to the United States Work Projects Administration of New York City for assistance rendered under project No. 24.

Small Angle Scattering of Thermal Neutrons

H. H. A. KRUEGER,* D. MENEGHETTI,† G. R. RINGO, AND L. WINSBERG**
Argonne National Laboratory, Chicago, Illinois
(Received July 3, 1950)

Experiments on the small angle scattering of thermal neutrons by powders are compared with theory. The available theories, which closely resemble those for small angle scattering of x-rays, are found to give a satisfactory account of the results. In general, the neutrons are scattered into a Gaussian distribution in angle whose width is directly proportional to the wave-length of the neutrons, the coherent scattering amplitude of the nuclei in the powder and the square root of the number of particles traversed in the powder by any one neutron.

I. INTRODUCTION

SMALL-ANGLE scattering of x-rays has been observed for many years and is, in fact, today widely used in studies of the size and shape of submicroscopic particles.[1] From the similarities in the behavior of thermal neutrons and x-rays, an analogous phenomena would be expected with neutron beams. This was found in studies of neutron polarization[2] and in the transmission of neutrons with energies less than 0.003 ev through powdered materials.[3,4] The first theoretical treatment which concerns itself explicitly with neutrons is that of Halpern and Gerjuoy.[5]

In addition to the obvious possibility of using small angle scattering of neutrons in the same general field of application as that of x-rays, the phenomenon is of some interest for its bearing on purely nuclear studies. It must be considered in many measurements using thermal neutrons and it has been suggested independently by Goldhaber[6] and Beeman[6] that it offers a way of measuring the coherent neutron scattering amplitude of the nuclei of most materials.

Both small angle scattering of x-rays and small angle scattering of neutrons are associated with inhomogeneities in a material of the order of 100 to 10,000 wave-lengths in dimensions. Since intense beams of nearly monoenergetic and well-collimated x-rays are relatively easy to get and the penetration of the convenient x-ray wave-lengths is low in many materials, single small angle scattering is ordinarily studied. In the case of neutrons, however, it is more convenient to observe highly multiple small angle scattering, for the intensities available in a given collimation and energy band are much lower than x-ray intensities while the penetration in many materials is considerably greater than that of x-rays of the same wave-length.

II. DIFFRACTION THEORY

Halpern and Gerjuoy[5] have treated the case of a plane wave incident on a cubical microcrystal randomly oriented. They assumed that the incident wave is not appreciably attenuated in traversing this crystal. From the Laue expression for the diffraction by a three-dimensional lattice they were able to obtain the angular distribution of the scattered radiation and the total cross section for small angle scattering. They give for this cross section for one particle (or microcrystal)

$$\sigma_p = 3\pi N^2 l^6 a^2 (\lambda/\pi l)^2, \tag{1}$$

where N is the number of atoms per cc of crystal, l is the length of an edge of the cubical microcrystal, a is the coherent scattering amplitude of the atoms of the crystal, and λ is the wave-length. If there are n such particles per sq. cm of a sample traversed by the beam, each neutron will be scattered $n\sigma_p$ times on the average. If $n\sigma_p \gg 1$, the distribution in angle of the beam emerging from the sample can be obtained with reasonable accuracy from the theory of random flights.[7] The fluctuations of the direction of the scattered beam correspond to random flights in a plane normal to the direction of the beam. From this we get that

$$I(\theta) = I_0 \exp[-\theta^2/n\sigma_p\langle\theta_p^2\rangle]. \tag{2}$$

Here $I(\theta)$ is the intensity of the beam per steradian at θ radians away from the direction of the incident beam, I_0 is the intensity at $\theta=0$, and $\langle\theta_p^2\rangle$ is the average square of the angle of scattering after one scattering. $\langle\theta_p^2\rangle$ can be obtained from the angular distribution of the scattered neutrons given by Halpern and Gerjuoy. It turns out to be about $13.1(\lambda/\pi l)^2$. From this and Eq. (1) the width of the Gaussian distribution in (2) can be calculated.

In applying this theory to a real powder, there are a number of approximations involved in addition to the assumption that the incident beam is not appreciably scattered in one particle of the powder but is scattered many times in the sample. These are: (1) the particles are assumed to be cubes, (2) interference between adjacent particles is neglected, (3) the particles are

* Now at the University of Wisconsin.
† Now at the University of Pittsburgh.
** Now at the Weizmann Institute of Science, Rehovot, Israel.
[1] D. L. Dexter and W. W. Beeman, Phys. Rev. **76**, 1782 (1949), and references therein.
[2] Hughes, Burgy, Heller, and Wallace, Phys. Rev. **75**, 565 (1949).
[3] Winsberg, Meneghetti, and Sidhu, Phys. Rev. **75**, 975 (1949).
[4] Krueger, Meneghetti, Ringo, and Winsberg, Phys. Rev. **75**, 1098 (1949).
[5] O. Halpern and E. Gerjuoy, Phys. Rev. **76**, 1117 (1949).
[6] M. Goldhaber and W. W. Beeman, private communications.
[7] S. Chandrasekhar, Rev. Mod. Phys. **15**, 1 (1943), Eqs. 103 and 104.

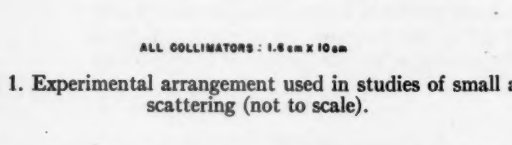

FIG. 1. Experimental arrangement used in studies of small angle scattering (not to scale).

assumed to be the same size. Halpern and Gerjuoy have considered the validity and limits of these assumptions. In the case of the first assumption, they find that other simple shapes give results not appreciably different from those for cubes. The second assumption they say is reasonable if the space between the particles is comparable to or greater than the volume occupied by them. The failure of the third assumption can be taken care of by an integration over the size distribution of the particles in the powder.

III. REFRACTION THEORY

The most serious limitation on the diffraction theory comes from the assumption that the incident beam is not appreciably attenuated by one particle. There are many cases of physical interest in which the scattering cross section as calculated from (1) is much greater than the geometrical cross section of the particles. To treat these cases another approach, in which the particles are regarded as homogeneous spheres characterized by a certain index of refraction, seems useful. The scattering of a plane electromagnetic wave incident on a dielectric sphere has been given formally in a classical paper of Mie's.[8] More recently, H. C. Van de Hulst[9] has developed some manageable approximations to Mie's solutions. On the basis of these, he has worked out a number of graphs for the angular distribution and cross section for small angle scattering in the region of

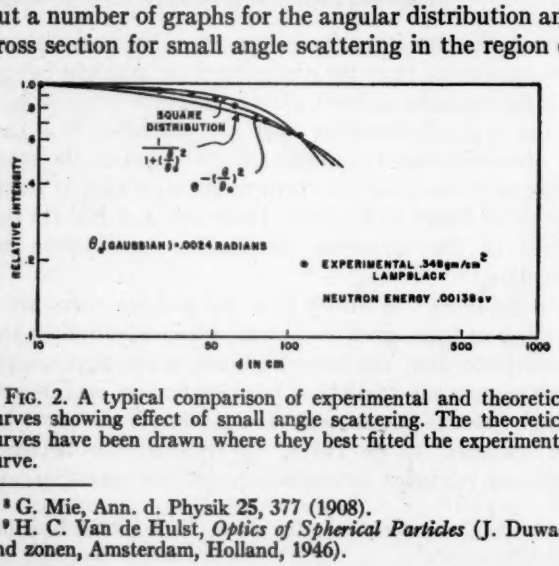

FIG. 2. A typical comparison of experimental and theoretical curves showing effect of small angle scattering. The theoretical curves have been drawn where they best fitted the experimental curve.

[8] G. Mie, Ann. d. Physik 25, 377 (1908).
[9] H. C. Van de Hulst, *Optics of Spherical Particles* (J. Duwaer und zonen, Amsterdam, Holland, 1946).

values of λ, index of refraction, and particle diameter of interest in the present work. These results can be applied to neutron scattering by replacing the optical index of refraction by that for neutrons ($=1-N a\lambda^2/2\pi$).

In calculating the spread of the transmitted beam, Eq. (2) can be used and σ_p and $\langle\theta_p^2\rangle$ calculated from Van de Hulst's graphs. In the calculation of $\langle\theta_p^2\rangle$, it is necessary to extend the angular distribution beyond that given by Van de Hulst's graph, by means of the approximation to the angular distribution of scattered radiation from a single particle at larger angles

$$I_p(\theta)\approx\left[\frac{2\delta r}{\lambda\theta}j_{\frac{3}{2}}\left(\frac{2\pi r\theta}{\lambda}\right)\right]^2\approx\left[\frac{2\delta r}{\lambda\theta}\cos\left(\frac{2\pi r\theta}{\lambda}\right)\right]^2. \quad (3)$$

r is the radius of the spherical particle, $j_{\frac{3}{2}}(x)$ is the spherical Bessel function of order $\frac{3}{2}$, and δ is the index of refraction minus one.

A very simple approximation to this refraction treatment can be found by ignoring diffraction effects altogether, as was done by von Nardroff[10] in an early treatment of small angle scattering of x-rays. In this case, σ_p is taken as the projected area of the particle. From his treatment and Eq. (2), we derive

$$\langle\theta_p^2\rangle=4\delta^2[\ln(2/|\delta|)+1]. \quad (4)$$

The application of Van de Hulst's or von Nardroff's formulas to measurements on a powdered sample involves a set of approximations which are equivalent to those involved in applying Halpern and Gerjuoy's formula, except the assumption that the incident beam is not attenuated appreciably in one particle. In general, the remarks concerning these approximations made earlier should apply here. In any event, the best test of their reasonableness will come from comparison with experiment.

IV. EVALUATION OF DATA

We have measured the small angle scattering of a number of different materials using neutrons from the thermal column of the Argonne heavy water moderated reactor. The measurements were made with neutrons of various energies selected by the thermal neutron time-of-flight selector[11] using the arrangement sketched in Fig. 1. As is indicated in reference 4, it was found qualitatively that small angle scattering was appreciable in powders and porous materials (such as graphite), but not in metals and large crystals. Owing to the low intensity of neutrons of a wave-length long enough to show marked small angle scattering, an indirect approach to the measurement of the angular distribution was used.

The neutron intensity was measured for the six wavelength groups furnished by the velocity selector at various values of d (Fig. 1). The experimental curves

[10] R. von Nardroff, Phys. Rev. 28, 240 (1926).
[11] T. Brill and H. V. Lichtenberger, Phys. Rev. 72, 585 (1947).

of intensity *vs.* d were then compared with theoretical ones for various distributions, since it was not *a priori* certain that the observed scattering would have the Gaussian distribution in angle predicted by Eq. (2). Two distributions were assumed besides the Gaussian. The first was a square distribution taken as representative of those distributions having a lower relative intensity at large angles than the Gaussian. The second was the distribution

$$I(\theta)=I_0/[1+(\theta/\theta_0)^2],$$

taken as representative of those distributions having a higher relative intensity at large angles than the Gaussian. θ_0 is a parameter characterizing the width of the distribution. θ_0 is taken as one-fourth the width of the square distribution and one-half the width of the Gaussian between the points of intensity $=1/e\times$ the intensity of the center.

In the comparison of the calculated curves of intensity *vs.* d with the experimental, it was necessary to use a method which was independent of the width of the assumed distribution. This can be done readily. In fact, from the following argument it can be seen that the best width of the theoretical distribution can be found from this comparison. Let $\theta'=\theta/\theta_0$, then the function $I(\theta')d\theta'$, giving the number of neutrons scattered between θ/θ_0 and $(\theta+d\theta)/\theta_0$, depends only on the type of distribution and not on its width. Now the fraction of the neutrons scattered at an angle θ entering the counter is equal to the fraction of the unscattered beam which would enter the counter if it were moved a distance θd normal to the beam. More exactly, the average fraction entering the counter when it is moved θd cm in a random direction in the plane normal to the beam is needed. Call this $f(\theta d)$, since $\theta=\theta_0\theta'$ we get for the total intensity of the scattered beam

$$I_d=\int_{\theta'} f(\theta'\theta_0 d)I(\theta')d\theta'.$$

The intensity corresponding to a given value of d and of θ_0 then depends only on the product $\theta_0 d$. Thus, the calculated curves of intensity *vs.* d for different values of θ_0 as plotted on a log log graph will all have the same shape but will be shifted along the d-axis with varying values of θ_0 (and along the y axis with varying values of assumed incident intensity). From this it can be seen that it is possible to compare the various types of distribution with the experimental by sliding the calculated log intensity *vs.* $\ln(\theta_0 d)$ curves along the axes of the experimental curve to obtain the best fit.

A typical comparison of the experimental data and the assumed distribution is shown in Fig. 2 which indicates that the distribution is Gaussian, as predicted. From a comparison of the values of the abscissa of the theoretical and experimental curves at any point when they are in the position giving the best fit, the corresponding value of θ_0 can be found from the relation $\theta_0=(\theta_0 d)_{\text{theoretical}}/d_{\text{experimental}}$.

This procedure is roundabout to describe as compared with the more customary scheme of moving the counter in a line normal to the beam and correcting for the finite collimation, but it was more convenient to use experimentally and has the advantage that most of the scattered beam is used in the measurements. When the counter is moved in a line normal to the beam, the fraction of the scattered beam entering the counter decreases with angle. Since the number of neutrons scattered at a given angle also decreases with angle, this method of measuring the scattering is insensitive to the tail of the distribution.

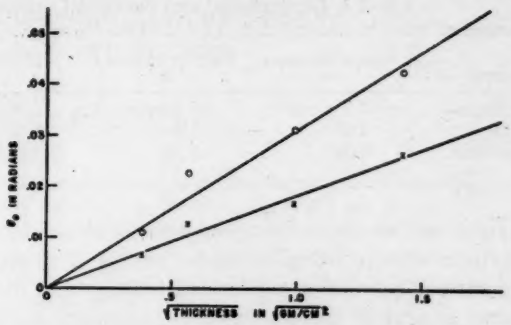

FIG. 3. Dependence of the width of the scattered beam on sample thickness for lampblack.

V. RESULTS OF THE MEASUREMENTS

By use of the method of analysis described in the preceding section, the angular distribution of the scattered neutrons was studied as a function of sample thickness and energy of the neutrons. Typical results are shown in Figs. 3 and 4. Since all of the theories discussed in Sections 2 and 3 agree in predicting substantially the observed dependence of the width of the distribution on $\lambda^2(\sim 1/\text{energy})$ and the square root of the sample thickness, these results do not serve to discriminate among them.

In order to check the theoretical predictions of the absolute value of the angular width of the scattering, it was necessary to measure the particle sizes of the powders. This was originally done by microscopic examination. It was found, however, that there was a rather large range of particle sizes in the powders used and an intolerably long time would have been needed to get reasonably accurate statistics. It was decided, therefore, to determine the sizes by a sedimentation analysis.[12] This method has the advantage of having

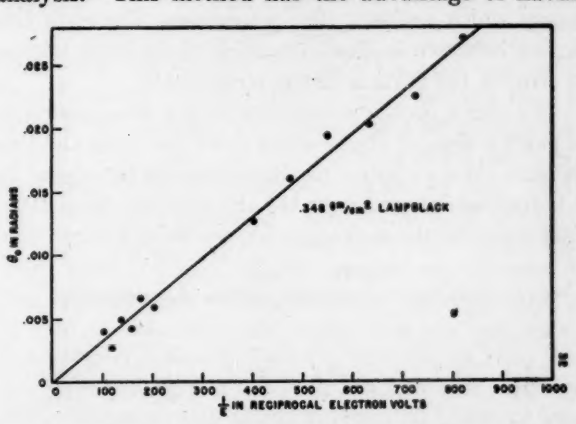

FIG. 4. Dependence of the width of the scattered beam on energy, $E(\sim 1/\lambda^2)$ of the neutrons for lampblack.

[12] W. C. Krumbein and F. J. Pettijohn, *Manual of Sedimentary Petrology* (D. Appleton-Century Company, Inc., New York, 1938).

TABLE I. Experimental and theoretical values for the spread of small angle scattering of 8.25A neutrons.

Material	Sample thickness ρ_s	Particle diameter $2r$	Experimental θ_0	Halpern and Gerjuoy θ_0	Van de Hulst θ_0	von Nardroff θ_0
Aluminum	17.3 g/cm^2	16 microns	0.014 radians	0.0123 radians	0.0114 radians	0.012 radians
$CaCO_3$	4.19	5.6	0.035	0.0232	0.0208	0.024
Lampblack	0.348	0.72	0.027	0.025	0.0245	0.036

the right sort of dependence on particle shape in that a particle with a complex shape having a relatively large surface to volume ratio settles slowly and thus is counted as several smaller particles, as indeed it might appear to a neutron passing through it.

The results obtained from this analysis and the neutron measurements are shown in Table I. The particle diameter was obtained by a weighted average of the sedimentation analysis weighting each fraction as the inverse of the corresponding diameter as this function of the diameter is involved in the determination of $\theta_0^2=n\sigma_p\langle\theta_p^2\rangle$ [from Eq. (2)]. This can be seen in the von Nardroff theory, for instance, for $n=3\rho_s/4_\rho\pi r^3$, and $\sigma_p=\pi r^2$ where ρ_s is the sample thickness in g/cm^2 and ρ is the crystalline density of the material involved. The estimated accuracy of the values of θ_0 is ± 25 percent and of r is ± 40 percent on the basis of a consideration of all the known sources of error. The values of a, the coherent neutron scattering amplitude, were obtained from the diffraction work of Shull and Wollan.[13]

The agreement between the theories and the experiment is very reasonable in view of the approximations involved in applying the theories to particles which are not spheres or cubes, are not all the same size, and are not isolated from each other. It is notable that the theories derived on such different assumptions are in fairly close agreement as to the value of θ_0 in the range of values of a, r, and λ covered by this study.

There is a discrepancy involved in the use of results from the sedimentation analysis, which assumes the particles are spheres, with the Halpern and Gerjuoy theory which assumed they were cubes. The error this causes, however, is small compared to the other sources of error in the particle size determination.

As a check on the importance of the non-uniformity of particle sizes of the powders used, the θ_0 for the Van de Hust theory applied to aluminum was calculated by a numerical integral over the distribution of particles sizes given by the sedimentation analysis. It was found to differ from the θ_0 for the average particle size by considerably less than the experimental error in θ_0.

[13] C. G. Shull and E. O. Wollan, private communication.

VI. DISCUSSION

The present experiments do not serve to discriminate among the three theories considered, as the theories are in substantial agreement numerically on the spreading of the beam by multiple scattering. This is even true of the theories when used beyond the limits of their assumptions as was the Halpern and Gerjuoy theory when applied to the aluminum powder. However, in other experiments it might be advisable not to employ the theories beyond these limits. Thus, the Halpern and Gerjuoy theory should not be applied where the incident beam is significantly attenuated in one particle, say where $\sigma_p \geq l^2$. The von Nardroff theory should not be applied where $2\pi r\delta/\lambda \leq 2$. This can be seen from consideration of the discrepancies between it and the Van de Hulst theory (see Table I) which should be more accurate since it includes diffraction effects. The Van de Hulst theory itself should be applicable to particles containing more than 1000 atoms. In the range of parameters where the Halpern and Gerjuoy and the Van de Hulst theories should both be valid, they do agree and either may be used.

In principle, the differences between these three theories which show up in the angular distribution of a single scattering could be brought out experimentally by using samples only one or two particles thick. However, this would necessitate a very narrow collimation to study the small angles involved and this, in turn, requires higher intensities of monoenergetic neutrons than are presently available. Until this is done, from the foregoing work and the general analogies between x-ray and thermal neutron beams, there is considerable reason for trusting the available theories of small angle scattering of electromagnetic waves as applied to neutrons, with the limitations just mentioned and the modifications discussed in Sections II and III.

It is a pleasure to acknowledge the considerable help of Professor George Vineyard of the University of Missouri and Dr. Morton Hamermesh of this Laboratory in interpretation of our results.

Pressure Broadening of the Ammonia Inversion Line by Foreign Gases: Quadrupole-Induced Dipole Interactions

P. W. ANDERSON
Bell Telephone Laboratories, Murray Hill, New Jersey
(Received July 5, 1950)

The broadening of the 3,3 line of the inversion spectrum of ammonia by foreign gases which are not expected to have dipole or quadrupole moments has been measured accurately by Smith and Howard. This broadening is greater than that previously computed by the author using the interaction of the molecule's dipole moment with the induced dipole on the foreign gas atom. In this paper the broadening is explained quantitatively using the interaction of the induced dipole on the foreign gas atom with the quadrupole moment of ammonia. It is concluded that a model of the ammonia molecule using bond dipoles of the appriate size to give the known dipole moment, or a model with point charges at the atoms, again adjusted to give the correct dipole moment, both give quadrupole moments which explain the broadening cross sections with good accuracy.

I. INTRODUCTION

THE pressure-broadening cross sections of many foreign gas atoms and molecules for the NH_3 inversion lines have been observed to be anomalously high.[1-3] In several cases, in which these cross sections are considerably greater than kinetic theory cross sections, Smith and Howard[2] have successfully ascribed this broadening to the interaction between the NH_3 dipole moment and the quadrupole moment of the foreign gas molecule.

In other cases, usually of atoms or molecules which could be expected to have little or no quadrupole moment, such as argon, Smith and Howard[2] found that the broadening cross section, although comparable with the kinetic theory cross section, showed little correlation with the latter and was instead well correlated with the polarizability of the foreign gas. The relationship between broadening cross section and polarizability is the same as that predicted by the dipole-induced dipole broadening theory of the author.[3] However, the cross sections are considerably greater in magnitude than those predicted by this theory.

The reason why the author's theory[3] gives such low cross sections for this broadening is that the interaction potential between a polarizable atom and a dipolar molecule is

$$H=(\alpha\mu^2/r^6)(1+3\cos^2\theta). \quad (1)$$

θ is the angle between the dipole μ of NH_3 and the interatomic distance r; α is the polarizability of the perturber. This expression contains only even powers of $\cos\theta$. $\cos\theta$ has matrix elements only of the form $(+|\cos\theta|-)$, where the $+$ and $-$ designate the two states connected by the inversion transition. Thus $\cos^2\theta$ can have only diagonal matrix elements in the inversion coordinate, of the form $(+|\cos^2\theta|+)$, and the interaction (1) cannot cause the inversion, and, because of the wide spacing of the NH_3 rotational levels, cannot cause any transition among quantum states other than the spacially degenerate states of different M quantum number.

It has been shown[3,4] that in this case the broadening cross section is greatly reduced from that one obtains in case non-adiabatic transitions between non-degenerate quantum states can be caused by the collision interaction. Transitions among quantum states which are not degenerate were shown to have the effect of breaking off the radiation completely; transitions merely among degenerate quantum states have a considerably smaller effect on the radiation, which can be thought of as a minor phase or amplitude change.

The reduction, due to this fact, in the quantity S_2 of reference 3 is of the order $(4J^2)^{-1}$, where J is the total angular momentum quantum number. Thus one can see that, since S_2 is proportional to the squared "transition probability" a_{jk} of reference 2, and

$$a_{jk}\sim\text{const}/b^5=\tfrac{1}{2}$$

is the rough condition on the broadening diameter b, that b is reduced by a factor $(2J)^{-1/5}$, which is considerable for the $J=3$ line measured by Smith and Howard.

However, at the close distances of approach which enter into the particular broadening under consideration ($\sim$3.5A) the dipole-dipole forces are not the only ones which need to be considered. For instance, one would expect that the NH_3 molecule has a quadrupole moment which corresponds roughly to that of the known dipole moment at a distance at least $h/2\simeq$0.2A (h is the height of the pyramid) from the center of rotation. Then the ratio of the potential (1) between the two configurations in which this dipole is pointed toward the perturber and away from the perturber is $[(3.5+0.2)/(3.5-0.2)]^6=1.97$. This means that there is a potential, odd in the angle function $\cos\theta$, of practically the magnitude of the potential (1), due to interaction between the induced dipole on the perturber and the quadrupole on NH_3. It is this potential which turns

[1] B. Bleaney and R. P. Penrose, Proc. Phys. Soc. London 59, 424 (1948).
[2] W. V. Smith and R. Howard, Phys. Rev. 79, 132 (1950).
[3] P. W. Anderson, Phys. Rev. 76, 647 (1949).
[4] P. W. Anderson, thesis, Harvard, 1948, unpublished.

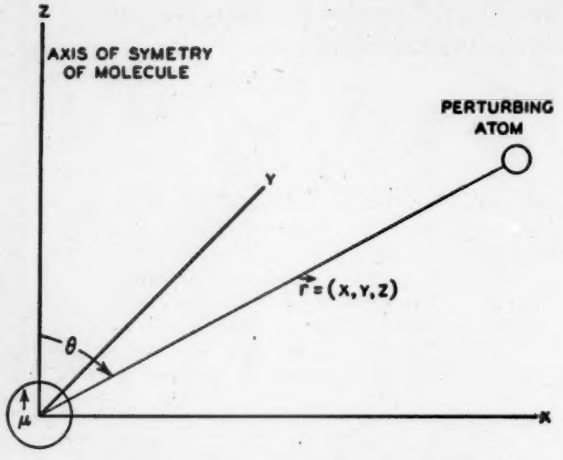

FIG. 1. Coordinates for computation of H.

out to give good agreement with the experimental broadening.

II. COMPUTATION OF THE INTERACTION ENERGY

First let us compute the interaction energy between a molecule, having both a dipole and a quadrupole moment, and a polarizable isotropic atom at a distance r from this molecule. The electrostatic potential at the polarizable atom (the coordinates are shown in Fig. 1.) is

$$V=-\frac{\mu z}{r^3}+\frac{1}{2}\left(\frac{3z^2-r^2}{r^5}\right)(Q_{zz}-Q_{xx}) \tag{2}$$

where the quadrupole moments (assuming that the molecule has an axis of symmetry) are defined by

$$\begin{aligned} Q_{xx}&=\textstyle\sum_{\text{mole}}\rho_i x_i^2=Q_{yy},\\ Q_{zz}&=\textstyle\sum_{\text{mole}}\rho_i z_i^2. \end{aligned} \tag{3}$$

Since the molecule has a dipole moment these quadrupoles are not independent of the choice of origin; we must use as origin the center of rotation of the molecule; i.e., the center of mass. Let

$$Q=Q_{zz}-Q_{xx}. \tag{4}$$

Then the field at the polarizable atom is

$$E=\nabla V \tag{5}$$

of which a typical component is

$$E_z=-\frac{\mu}{r^3}\left(1-\frac{3z^2}{r^2}\right)+\frac{1}{2}\frac{Q}{r^4}\left[\frac{9z}{r}-\frac{15z^3}{r^3}\right]. \tag{5a}$$

The interaction energy is, most simply

$$H=\tfrac{1}{2}\alpha(E_x^2+E_y^2+E_z^2), \tag{6}$$

α is the polarizability of the perturbing atom. H can be easily computed and is

$$H=-(6\alpha\mu Q/r^7)\cos^3\theta, \tag{7}$$

where

$$\cos\theta=z/r.$$

We have included here only the μQ cross term, since the other two terms are both even in $\cos\theta$, and can have

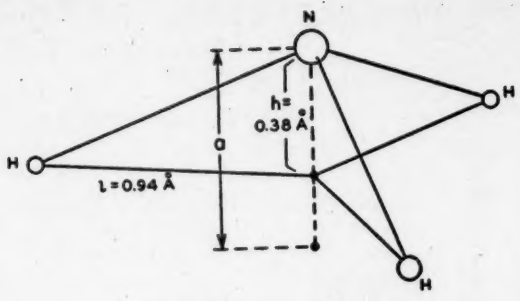

FIG. 2. The NH_3 molecule.

little effect, even though in actual magnitude they must be greater than (7).

III. THE QUADRUPOLE MOMENT OF NH_3

The quadrupole moments of NH_3 about the center of mass can be computed using two models, one with charges on each of the atoms sufficient to give the observed dipole moment, or one with dipoles aligned along the three bonds, again just sufficiently large to give the observed dipole moment. Both models give the same quadrupole moment. Figure 2 shows the model of NH_3 we are using.[5] We choose our origin at a distance a from the nitrogen atom (where a will later be chosen to be 0.07A, or the position of the center of mass). Then, if $-q$ is the charge on the hydrogen,

$$\begin{aligned} Q_{zz}&=3q(a^2)-3q(a-h)^2\\ &=-3q(h^2-2ah). \end{aligned}$$

Since

$$\begin{aligned} \mu&=3qh,\\ Q_{zz}&=\mu(2a-h). \end{aligned} \tag{8a}$$

On the other hand,

$$Q_{zz}=-q[l^2+2(\tfrac{1}{2}l)^2],$$

$$Q_{zz}=-\mu\left(\frac{l^2}{2h}\right). \tag{8b}$$

Then

$$\begin{aligned} Q&=\mu\left[2a-h+\frac{l^2}{2h}\right]\\ &=0.92\times10^{-8}\mu\\ &=1.325\times10^{-26}\text{e.s.u.-cm}^2. \end{aligned} \tag{8c}$$

We shall find that the value (8c) for Q gives good results for the broadening, which fact seems to confirm sig-

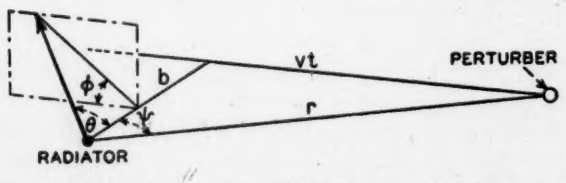

FIG. 3. Coordinates for computation of the transition matrix P.

[5] The interatomic distances are from G. Herzberg, *Infrared and Raman Spectra* (D. Van Nostrand Company, Inc., New York, 1945), p. 439.

nificantly that the charge distribution on NH_3 is not greatly different from that which we have assumed.

IV. THEORY OF THE BROADENING

As has been shown in references 2 and 3, the broadening depends on the "transition and phase-shift" matrix P, where

$$P=\int H dt/\hbar. \tag{9}$$

The integral is taken over the collision path; no energy factors need be considered, since at these distances, and with only the small energy of the inversion transition involved, the energy for the transition comes easily from the kinetic energy of translation. The coordinate system is shown in Fig. 3.

$$P=\frac{6\alpha\mu Q}{\hbar}\int\frac{dt}{r^7}[\cos\theta\cos\psi+\sin\theta\sin\psi\cos\varphi]^3$$

$$=\left(\frac{6\alpha\mu Q}{\hbar}\right)\frac{5\pi}{128b^6v}\left[\frac{3}{2}\cos\theta+\frac{11}{2}\cos^3\theta+\frac{3}{2}\sin^2\theta\cos\theta\cos 2\varphi\right]. \tag{10}$$

The matrix elements of P are easily derived, using, for instance

$$(JKM,+|\cos\theta|JKM,-)=KM/J(J+1). \tag{11}$$

It turns out that the contribution to the broadening of the last term in (10) is quite negligible; then we can give the only matrix element of P which is of importance:

$$(JKM,+|P|JKM,-)=\left(\frac{6\alpha\mu Q}{\hbar}\right)\frac{5\pi}{128b^6v}\left[\frac{3}{2}\frac{KM}{J(J+1)}+\frac{11}{2}\frac{K^3M^3}{J^3(J+1)^3}\right]. \tag{12}$$

The next step in computing broadening cross sections is to compute the quantity S_2, which in the case occurring here is merely a mean square of the matrix elements of P

$$S_2=\tfrac{1}{2}(1/2J+1)\sum_{l,M}\times[|(i,M|P|l)|^2+(f,M|P|l)|^2] \tag{13}$$

where l are all the possible final states for the transition caused by the collision (here only the one state $(J,K,M\pm)$) and i and f designate the initial and final states of the radiative transition. Here this reduces simply to

$$S_2=(1/2J+1)\sum_M|(JKM+|P|JKM-)|^2. \tag{13a}$$

This has been computed. It is

$$S_2=\left(\frac{5\pi}{128b^6v}\right)^2\left(\frac{6\alpha\mu Q}{\hbar}\right)^2\frac{3}{4}\frac{K^2}{J(J+1)}\times\left[1+\frac{22}{5}\frac{K^2}{J(J+1)}+\frac{121}{21}\frac{K^4}{J^2(J+1)^2}-\frac{K^2}{3J^2(J+1)^2}\times\left(\frac{22}{5}+\frac{121}{7}\frac{K^2}{J(J+1)}\right)+\frac{K^4}{J^4(J+1)^4}\frac{121}{63}\right]. \tag{14}$$

In the case $K=3$, $J=3$ this is

$$S_2=(5\pi/128b^6v)^2(6\alpha\mu Q/\hbar)^2(4.05). \tag{14a}$$

The quantity which is equivalent to the phase-shift of normal impact theories,[6] or to the transition probability a_{jk} of Smith's simplified version[2] of the author's theory is

$$P_{\text{r.m.s.}}=(2S_2)^{\frac{1}{2}}. \tag{15}$$

Smith's criterion for the broadening diameter b is

$$P_{\text{r.m.s.}}=A/b^6=\tfrac{1}{2}.$$

Where this equation defines A. Then the broadening diameter is

$$b=2^{1/6}A^{1/6}=1.12A^{1/6} \tag{16a}$$

our own criterion[3] gives

$$\sigma=\pi b^2=1.1\pi A^{\frac{1}{3}},\qquad b=(1.1)^{\frac{1}{2}}A^{1/6}=1.05A^{1/6}. \tag{16b}$$

These two criteria give slightly different answers; since the second is a lower limit, we shall increase it slightly to give a somewhat better answer, and take ±5 percent as the rough theoretical error. Thus we choose

$$b=1.08A^{1/6}=1.08[b^6(2S_2)^{\frac{1}{2}}]^{1/6}\pm 5\text{ percent}, \tag{17}$$

where S_2 is given by (14a). Table I shows the results given by formula (17) for several gases broadening the NH_3 3,3 line, compared with Smith's experimental results.[2] N_2 is included in order to show that certainly some extra source of broadening must be coming in here, even using our present theory. Thus Smith's computation of the quadrupole moment of N_2 is certainly sound. O_2 also shows a slight hint of having a quadrupole moment. The A value is a little disturbing, since the experimental error is probably considerably less than 0.1A. However, the general agreement seems to be excellent, and to indicate that our estimate for the quadrupole moment of NH_3 is not off by more than 20 to 30 percent.

TABLE I. Broadening of the NH_3 3,3 line by several foreign gases.

Foreign gases	b(Theoretical)	b(Experimental)
H_2	2.57±0.1	2.71
He	2.15±0.1	2.00
A	3.42±0.2	3.73
O_2	3.35±0.2	3.86
(N_2)	(3.39±0.2)	(5.54)

I should like to express my thanks to Dr. W. V. Smith for the correspondence which led to the work of this paper.

[6] See, for instance, H. Margenau and W. W. Watson, Rev. Mod. Phys. 8, 22 (1936).

On the Interactions of Birkhoff's Gravitational Field with the Electromagnetic and Pair Fields

MARCOS MOSHINSKY
Institutos de Fisica y Geofisica, Universidad de México, México, D. F.

(Received April 13, 1950)

The flat space-time theory of gravitation proposed by G. D. Birkhoff is discussed from the standpoint of a field theory and, in particular, the interaction of Birkhoff's field with other fields is developed. This interaction is shown to take place through the interaction Lagrangian function $h_{\mu\nu}\theta_{\mu\nu}$, and when applied to the electromagnetic and pair fields, it leads to a modification of the Maxwell and Dirac equations. These modified equations determine a change in the index of refraction and a shift of the energy levels of the atom, which account for the bending of light and the red shift in gravitational phenomena. Furthermore, they predict a gravitational correction to the magnetic moment associated with the spin and orbital motion of the electron.

I. INTRODUCTION

At the present time there is a wide interest in relativistic field theories in connection with the interactions between meson, electromagnetic, and pair fields. The effect of the gravitational field on these interactions has been mainly neglected, partly because of the smallness of the gravitational interactions, and partly because of the special position given to the gravitational field in the general theory of relativity.

It seems therefore, worthwhile to examine descriptions of gravitation in flat space-time, from the standpoint of field theory. The theory of gravitation that we propose to discuss from this viewpoint was introduced by G. D. Birkhoff,[1–5] and in it, the gravitational field is described in flat space-time by a symmetric tensor potential $h_{\alpha\beta}$, $\alpha, \beta = 0, 1, 2, 3$. The equation of motion for a particle of rest mass m is given by the usual relation of special relativity, $m(d^2x_\alpha/ds^2) = f_\alpha$, where f_α the ponderomotive force for the gravitational field, has the form:

$$f_\alpha = m(\partial h_{\alpha\beta}/\partial x^\gamma - \partial h_{\beta\gamma}/\partial x^\alpha) dx^\beta/ds\, dx^\gamma/ds. \quad (1)$$

The motion is therefore independent of the mass of the particle.

The field caused by a distribution of matter represented by the energy momentum tensor $T_{\alpha\beta}$ is given by the field equation:[6]

$$\Box h_{\alpha\beta} = 4\pi G/c^4 T_{\alpha\beta}, \quad (2)$$

where $\Box \equiv \nabla^2 - 1/c^2\, \partial^2/\partial t^2$, and G is the gravitational constant.

It can be shown from (2) and other assumptions that the field outside of an homogeneous sphere of mass M at a distance r from its center, is given by:[2]

$$h_{\alpha\beta} = MG/c^2 r \delta_{\alpha\beta}, \quad \text{where} \quad \delta_{\alpha\beta} = \begin{cases} 0 & \text{if } \alpha \neq \beta \\ 1 & \text{if } \alpha = \beta \end{cases} \quad (3)$$

and that this is also the field of a point particle. With the field (3) introduced in the equation of motion (1), one obtains an advance for the perihelion of a planet in the field of a star, which has the same value as in the general theory of relativity.[1–4]

While the bending of light rays and the red shift could be discussed in Birkhoff's theory with the help of the equation of motion (1) and the photon concept,[1–4] it is more proper to view them as due to the action of the gravitational field on the electromagnetic field and on the process of emission of light. For this purpose, the procedure for setting the interaction of Birkhoff's field with other fields, must be developed.

The Lagrangian function[7] from which the field equations (2) could be derived, is given by:

$$L = -\frac{c^4}{8\pi G} g^{\alpha\beta} \frac{\partial h^{\gamma\delta}}{\partial x^\alpha} \frac{\partial h_{\gamma\delta}}{\partial x^\beta} + h^{\gamma\delta} T_{\gamma\delta} \equiv L_B + h^{\gamma\delta} T_{\gamma\delta}, \quad (4)$$

as $\delta \int L d^4x = 0$ leads to (2). The first part of this Lagrangian function, L_B, corresponds to a free gravitational field, as the variational procedure applied to it leads to $\Box h_{\gamma\delta} = 0$. The second part, $h^{\gamma\delta} T_{\gamma\delta}$, in which $T_{\gamma\delta}$ is the energy momentum tensor of the external field, gives rise to the interaction between the gravitational and external fields. This term is somewhat similar to the corresponding interaction Lagrangian function $j_\alpha A^\alpha/c$ between the electromagnetic and matter fields.

When we introduce the Lagrangian function L_B for Birkhoff's free field, we obtain from the general formalism of field theory[7,8] an energy momentum tensor for this field, and this energy momentum tensor of gravitational origin, will affect the field equations (2). It is clear therefore, that an interaction term of the form $h^{\gamma\delta} T_{\gamma\delta}$, in which $T_{\gamma\delta}$ corresponds to the external field,

[1] G. D. Birkhoff, Proc. Nat. Acad. Sci. **29**, 231 (1943).
[2] G. D. Birkhoff, Proc. Nat. Acad. Sci. **30**, 324 (1944).
[3] Barajas, Birkhoff, Graef, and Vallarta, Phys. Rev. **66**, 138 (1944).
[4] A. Barajas, Proc. Nat. Acad. Sci. **30**, 54 (1944).
[5] G. D. Birkhoff, Bol. Soc. Mat. Mexicana **1** (No. 4, 5) 1 (1944).
[6] In Birkhoff's papers (references 1, 2) the field equations take the form $\Box h_{\alpha\beta} = 8\pi G/c^4 T_{\alpha\beta}$ where $h_{\alpha\beta}$ is dimensionless and $T_{\alpha\beta}$ has dimensions of energy density. The difference of a factor of 2 from the above expression (2), stems from the special form taken by Birkhoff for the tensor of a perfect fluid. When the usual form of this tensor is introduced, the factor 8π must be changed to 4π (reference 10, p. 71).
[7] W. Pauli, Rev. Mod. Phys. **13**, 203 (1941).
[8] G. Wentzel, *Quantum Theory of Fields* (Interscience Publishers, Inc., New York, 1949) Chap. 1.

will only be valid for weak gravitational fields ($h_{\gamma\delta} \ll 1$), to which we shall restrict ourselves in this article.

The Lagrangian function from which the interaction of Birkhoff's field with any other field can be derived is then given by:

$$L = L_B + h^{\alpha\beta}\theta_{\alpha\beta} + L', \tag{5}$$

where L' is the Lagrangian function of the other field and $\theta_{\alpha\beta}$ its corresponding symmetric energy-momentum tensor.

The modified field equations will be derived from the usual variational principle:

$$\delta \int L d^4x = 0. \tag{6}$$

We will apply this analysis to the interaction of Birkhoff's field with the electromagnetic and pair fields, for which we need the following notation:

$x^\alpha = (ct, \mathbf{r})$ the indices $\alpha, \beta, \gamma, \delta$ take the values 0, 1, 2, 3 with repeated indices summed from 0 to 3.
$x^\mu = (\mathbf{r}, ict)$ the indices μ, ν, ρ, σ take the values 1, 2, 3, 4 with repeated indices summed from 1 to 4.
$g^{\alpha\beta} = 0$ if $\alpha \neq \beta$ and $g^{00} = -g^{11} = -g^{22} = -g^{33} = 1$.
$g_{\mu\nu} = 0$ if $\mu \neq \nu$ and $-g_{11} = -g_{22} = -g_{33} = g_{44} = 1$.
$\delta_{\mu\nu} = 0$ if $\mu \neq \nu$, $\delta_{\mu\nu} = 1$ if $\mu = \nu$.
$ds^2 = g_{\alpha\beta} dx^\alpha dx^\beta = -\delta_{\mu\nu} dx^\mu dx^\nu$.
$dl^2 = (dx^1)^2 + (dx^2)^2 + (dx^3)^2$.
$A_\mu = (\mathbf{A}, i\phi)$ electromagnetic potentials.
$E_{\mu\nu} = \partial A_\mu / \partial x^\nu - \partial A_\nu / \partial x^\mu$ electromagnetic field strengths.
$\mathbf{E} = -i(E_{14}, E_{24}, E_{34})$, $\mathbf{B} = (E_{32}, E_{13}, E_{21})$.
ϵ = dielectric constant.
μ = magnetic permeability.
n = index of refraction.
ψ = four component wave function of Dirac's equation.
ψ^+ = the adjoint Dirac wave function.
m, e = mass and charge of the electron.
$\gamma_\mu, \alpha_i, \beta, \sigma_i$ = Dirac matrices defined as in Pauli's book.[9]
j_μ = 4-vector current density.
$L_B = c^4/8\pi G \cdot \partial h_{\rho\sigma}/\partial x^\mu \, \partial h_{\rho\sigma}/\partial x^\mu$ the Lagrange function of the Birkhoff field.
$\delta L/\delta q = -\partial/\partial x^\mu [\partial L/\partial(\partial q/\partial x^\mu)] + \partial L/\partial q)$ the variational derivative of L with respect to the variable q.
$T_{\mu\nu}$ = the energy momentum tensor defined from the Lagrangian of the field as in Wentzel's book.[8]
$\theta_{\mu\nu}$ = the symmetric energy momentum tensor.
$P_\mu = \hbar/i \, \partial/\partial x^\mu$.
M = mass of the body originating the gravitational field.
G = gravitational constant.
$\hbar$ = Planck constant.
c = velocity of light.
r, θ, φ = spherical coordinates.
$u = 1/r$.
$M' = MG/c^2$; $f \equiv MG/c^2 r$.
ν = frequency, $\lambda = c/\nu$ wave-length.

We will use from now on the coordinates x^μ, so that we must transform the tensors defined with respect to the coordinates x^α to the coordinate system x^μ by the usual rules. For example $h_{\alpha\beta}$ goes into $h_{\mu\nu}$ whose components are:

$$h_{\mu\nu} = \begin{pmatrix} h_{ij} & -ih_{i0} \\ -ih_{0j} & -h_{00} \end{pmatrix}.$$

In the system of coordinates x^μ the gravitational field (3) becomes then:

$$h_{\mu\nu} = -MG/c^2 r g_{\mu\nu} \equiv -f g_{\mu\nu}. \tag{7}$$

The metric tensor of the coordinate system x^μ is $-\delta_{\mu\nu}$ and this imples $A^\mu = -A_\mu$, $h^{\mu\nu} = h_{\mu\nu}$. The interaction part of the Lagrangian function becomes $h_{\mu\nu}\theta_{\mu\nu}$.

II. INTERACTION WITH THE ELECTROMAGNETIC FIELD

The Lagrangian function for the electromagnetic field is given by:

$$L_{em} = -1/16\pi E_{\mu\nu} E_{\mu\nu} \equiv 1/8\pi(\mathbf{E}^2 - \mathbf{B}^2) \tag{8a}$$

and the corresponding symmetric energy-momentum tensor is:

$$\theta_{\mu\nu}{}^{em} = 1/4\pi[E_{\mu\rho}E_{\nu\rho} - \tfrac{1}{4}E_{\rho\sigma}E_{\rho\sigma}\delta_{\mu\nu}]. \tag{8b}$$

The Lagrangian function for the interacting gravitational and electromagnetic fields takes the form:

$$L = L_B + \theta_{\mu\nu}{}^{em} h_{\mu\nu} + L_{em}. \tag{8c}$$

The field equations are derived from it with the help of the variational principle (6), where $h_{\mu\nu}$, A_μ are the field variables, so that:

$$\delta \int L d^4x = \int \left(\frac{\delta L}{\delta h_{\mu\nu}} \delta h_{\mu\nu} + \frac{\delta L}{\delta A_\mu} \delta A_\mu \right) d^4x = 0. \tag{9}$$

This variational relation leads to the equations $\delta L/\delta h_{\mu\nu} = 0$ and $\delta L/\delta A_\mu = 0$. The first is the Eq. (2) of the gravitational field with $T_{\mu\nu} = \theta_{\mu\nu}{}^{em}$. The second gives the electromagnetic field equations in the presence of a gravitational field, which take the form:

$$\partial/\partial x^\nu [E_{\mu\nu} - 2h_{\mu\rho}E_{\rho\nu} - 2E_{\mu\rho}h_{\rho\nu} + E_{\mu\nu}h_{\rho\rho}] = 0. \tag{10a}$$

To these equations we must add the field equations which are obtained from the definition[10] of $E_{\mu\nu}$, i.e.:

$$\partial E_{\mu\nu}/\partial x^\rho + \partial E_{\rho\mu}/\partial x^\nu + \partial E_{\nu\rho}/\partial x^\mu = 0. \tag{10b}$$

Equations (10) reduce to the ordinary Maxwell equations if there is no gravitational field, i.e., if $h_{\mu\nu} = 0$.

We are particularly interested in the electromagnetic field equations in the gravitational field outside of a spherical distribution of matter, such as a star. For that purpose we only need to substitute the corresponding field $h_{\mu\nu} = -MG/c^2 r g_{\mu\nu}$ in (10). We write the resulting equations in terms of the vectors $\mathbf{E}$, $\mathbf{B}$ and we obtain:

$$\nabla \cdot (1+2f)\mathbf{E} = 0, \quad \nabla \times (1-2f)\mathbf{B} = 1/c \, \partial/\partial t (1+2f)\mathbf{E} \tag{11a}$$

$$\nabla \cdot \mathbf{B} = 0, \quad \nabla \times \mathbf{E} = -1/c \, \partial/\partial t \mathbf{B} \tag{11b}$$

$$f \equiv MG/c^2 r.$$

We compare these equations with the electromagnetic equations in an inhomogeneous material medium in the

[9] W. Pauli, Handb. der Physik. 2 Aufl., Band 24, (Springer, Berlin, 1933) p. 219–220.

[10] R. C. Tolman, *Relativity, Thermodynamics, and Cosmology* (Oxford University Press, London, 1934) p. 97.

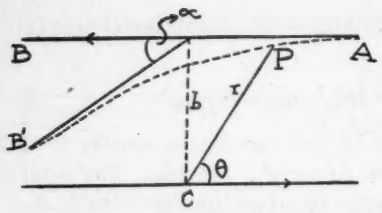

FIG. 1. Bending of a light ray in a gravitational field.

absence of currents and free charges,[11] which are:

$$\nabla\cdot\mathbf{D}=0, \quad \nabla\times\mathbf{H}=1/c\,\partial/\partial t\mathbf{D} \tag{12a}$$

$$\nabla\cdot\mathbf{B}=0, \quad \nabla\times\mathbf{E}=-1/c\,\partial/\partial t\mathbf{B} \tag{12b}$$

$$\mathbf{D}=\epsilon\mathbf{E}, \quad \mathbf{B}=\mu\mathbf{H}. \tag{12c}$$

From (11) and (12), it is clear that the gravitational field of the star makes the space surrounding it behave, from an electromagnetic standpoint, as an inhomogeneous material medium. In fact, (11) and (12) become identical if we set:

$$\epsilon=1+2M'/r, \quad \mu=1/(1-2M'/r). \tag{13}$$

As the dielectric constant and magnetic permeability are functions of the distance from the star, the index of refraction in the space surrouning the star, which is given by[11]

$$n=(\epsilon\mu)^{\frac{1}{2}}=\left(\frac{1+2M'/r}{1-2M'/r}\right)^{\frac{1}{2}} \tag{14}$$

is also a function of the distance from the star. Light that passes in the neighborhood of a star will therefore be bent by its gravitational field.

III. THE BENDING OF LIGHT RAYS

We can use Fermat's principle to calculate the bending of light rays in the gravitational field of a star, as this principle is a consequence of the electromagnetic field equations[12] in flat space-time.

Let us take a light ray coming from infinity which, in the absence of a gravitational field, would travel along the straight line $[AB]$. Let C be the point at which the gravitating mass is situated, and b the length of the perpendicular from C to $[AB]$ as in Fig. 1. We introduce spherical coordinates with origin at C and polar axis parallel to $[AB]$. The plane CAB is taken as $\varphi=0$.

Fermat's principle states that the path taken by the light ray is given by:

$$\delta\int ndl=0. \tag{15a}$$

As the index of refraction $n=n(r)$ is only a function of the distance from C, the problem has spherical symmetry and a light ray starting in the plane $\varphi=0$ will continue its motion in it. The variational principle (15a) becomes:

$$\delta\int n(r)(dr^2+r^2d\theta^2)^{\frac{1}{2}}$$

$$=\delta\int n(r)(1+r^2\theta'^2)^{\frac{1}{2}}dr\equiv\delta\int \mathfrak{L}dr \tag{15b}$$

and the corresponding Euler equation is:

$$\frac{d}{dr}\frac{\partial\mathfrak{L}}{\partial\theta'}-\frac{\partial\mathfrak{L}}{\partial\theta}=\frac{d}{dr}\frac{n(r)r^2\theta'}{(1+r^2\theta'^2)^{\frac{1}{2}}}=0 \tag{15c}$$

or

$$n(r)r^2\theta'(1+r^2\theta'^2)^{-\frac{1}{2}}=\text{const}=a. \tag{15d}$$

Introducing $u=1/r$, the Eq. (15d) becomes:

$$n(u)[(du/d\theta)^2+u^2]^{-\frac{1}{2}}=-a \tag{16a}$$

where from (14) $n^2(u)=1+2M'u/1-2M'u\simeq 1+4M'\mu$. This last approximation is valid because r must be larger than the radius R of the star so that $M'u<M'/R$ and for all stars M'/R is small, e.g., for the sun it is $\simeq 10^{-6}$. With this value of $n^2(u)$ the equation (16a) can be immediately integrated, giving:

$$u=1/a[2M'/a+(1+4M'^2/a^2)^{\frac{1}{2}}\sin(\theta+\delta)]. \tag{16b}$$

The path described by the light ray is then a hyperbola, and the two integration constants a, δ are determined by the condition that the hyperbola tends asymptotically to the line $[AB]$ whose equation is $u=b^{-1}\sin\theta$. When $\theta\to 0$ we must have then $u\to 0$ and $du/d\theta\to b^{-1}$, and assuming that $(2M'/b)^2$ can be disregarded as compared with unity, we have the relations:

$$a=b \quad \text{and} \quad \sin\delta=-2M'/b \quad \text{or} \quad \delta\simeq-2M'/b \tag{16c}$$

as again $M'/b<M/R\ll 1$. The equation for the hyperbola becomes:

$$u=1/b[2M'/b+\sin(\theta-2M'/b)] \tag{16d}$$

and the second asymptote is given by $\theta=\pi+4M'/b$ as $u\simeq 0$ for this value. The angle α between the asymptotes, shown in Fig. 1, is given then by:

$$\alpha=4M'/b \tag{17}$$

which is the same value of the general theory of relativity.

IV. INTERACTION WITH THE PAIR FIELD

The Lagrangian function for the pair field is given by:[7]

$$L_D=-\hbar c/2i(\psi^+\gamma_\mu\partial\psi/\partial x^\mu-\partial\psi^+/\partial x^\mu\gamma_\mu\psi)+imc^2\psi^+\psi \tag{18a}$$

and the corresponding energy momentum tensor is:

$$T_{\mu\nu}{}^D=\hbar c/2i(\psi^+\gamma_\mu\partial\psi/\partial x^\nu-\partial\psi^+/\partial x^\nu\gamma_\mu\psi). \tag{18b}$$

This tensor is not symmetric, but it is known[7] that the symmetric energy momentum tensor has the form: $\theta_{\mu\nu}{}^D=\frac{1}{2}(T_{\mu\nu}{}^D+T_{\nu\mu}{}^D)$. The interaction with the gravita-

[11] J. H. Van Vleck, *The Theory of Electric and Magnetic Susceptibilities* (Oxford University Press, London, 1932), pp. 1, 13.

[12] J. A. Stratton, *Electromagnetic Theory* (McGraw-Hill Book Company, Inc., New York, 1941), First Edition, p. 343.

tional field is given by $\theta_{\mu\nu}{}^{D}h_{\mu\nu}$ and as $h_{\mu\nu}$ is symmetric, this is equivalent to $T_{\mu\nu}{}^{D}h_{\mu\nu}$.

The Lagrangian function for the interacting gravitational and pair fields takes the form:

$$L=L_B+T_{\mu\nu}{}^{D}h_{\mu\nu}+L_D. \tag{18c}$$

The field equations are derived from it by means of the variational principle (6), where $h_{\mu\nu}$, ψ, ψ^+ are the field variables, so that:

$$\delta\int Ld^4x=\int\left[\frac{\delta L}{\delta h_{\mu\nu}}\delta h_{\mu\nu}+\delta\psi^+\frac{\delta L}{\delta\psi^+}+\frac{\delta L}{\delta\psi}\delta\psi\right]d^4x=0. \tag{19}$$

This variational relation leads to the equations $\delta L/\delta h_{\mu\nu}=0$, $\delta L/\delta\psi^+=0$, $\delta L/\delta\psi=0$, the first of which is Eq. (2) with $T_{\mu\nu}=\theta_{\mu\nu}{}^{D}$ and the others are the pair field equations in the presence of a gravitational field, that take the form:

$$\gamma_\mu\partial\psi/\partial x^\mu+mc/\hbar\psi-\tfrac{1}{2}h_{\mu\nu}\gamma_\mu\partial\psi/\partial x^\nu -\tfrac{1}{2}\gamma_\mu\partial h_{\mu\nu}\psi/\partial x^\nu=0, \tag{20a}$$

$$-\partial\psi^+/\partial x^\mu\gamma_\mu+mc/\hbar\psi^++\tfrac{1}{2}\partial\psi^+h_{\mu\nu}/\partial x^\nu\gamma_\mu +\tfrac{1}{2}\partial\psi^+/\partial x^\nu\gamma_\mu h_{\mu\nu}=0. \tag{20b}$$

Introducing the operators $P_\mu=\hbar/i\,\partial/\partial x^\mu$, we see that Eq. (20a) could be derived from the free particle Dirac equation by the substitution:

$$P_\mu\rightarrow P_\mu-\tfrac{1}{2}h_{\mu\nu}P_\nu-\tfrac{1}{2}P_\nu h_{\mu\nu}. \tag{21}$$

In the classical picture, where the energy-momentum vector P_μ and $h_{\mu\nu}$ commute, (21) implies that P_μ must be substituted by $P_\mu-h_{\mu\nu}P_\nu$, which is somewhat similar to what happens in the electromagnetic case where $P_\mu\rightarrow P_\mu+e/cA_\mu$. This result could not be derived directly from the equations of motion (1) as they do not admit in general, a Hamiltonian formulation.

We are interested in the form of the charge-current density 4-vector in the presence of a gravitational field. For that purpose we multiply (20a) by ψ^+ to the left and (20b) by ψ to the right and subtract, and making use of the symmetric form of $h_{\mu\nu}$ we obtain:

$$\partial/\partial x^\mu(\psi^+\gamma_\mu\psi-h_{\mu\nu}\psi^+\gamma_\nu\psi)=0. \tag{22a}$$

It is clear that the charge-current 4-vector for an electron field becomes:

$$j_\mu=ec(\psi^+\gamma_\mu\psi-h_{\mu\nu}\psi^+\gamma_\nu\psi) \tag{22b}$$

as it satisfies the continuity equation (22a), and in the absence of the gravitational field, i.e., $h_{\nu\tau}=0$, it reduces to usual form for the charge-current 4-vector.

The problems which interest us are those in which the electron moves in a combined gravitational and electromagnetic field. For that purpose we must add to the free pair field Lagrangian besides the term $T_{\mu\nu}{}^{D}h_{\mu\nu}$, a term of the form $j_\mu A^\mu/c=-j_\mu A_\mu/c$ which gives the interaction with the electromagnetic field. In this term, we should take the current j_μ as modified by the presence of the gravitational field as in (22b). The Lagrangian function for the pair field with these interactions, becomes:

$$L=L_D+T_{\mu\nu}{}^{D}h_{\mu\nu}-e(\psi^+\gamma_\mu\psi-h_{\mu\nu}\psi^+\gamma_\nu\psi)A_\mu. \tag{22c}$$

The field equations are derived as usual, from the variational principle (6), where ψ, ψ^+ are taken as the variables, and we obtain for ψ the equation:

$$\gamma_\mu[(\hbar/i\,\partial/\partial x^\mu+e/cA_\mu)\psi-(\hbar/2i\,h_{\mu\nu}\,\partial\psi/\partial x^\nu +\hbar/2i\,\partial h_{\mu\nu}\,\psi/\partial x_\nu+e/cA_\nu h_{\mu\nu}\psi)]-imc\psi=0. \tag{23}$$

Equation (23) is then the Dirac wave equation for an electron moving in a combined gravitational and electromagnetic field. This equation can be obtained from the Dirac free particle equation if we replace P_μ by $(P_\mu+e/cA_\mu)-h_{\mu\nu}(P_\nu+e/cA_\nu)$ and symmetrize the expression to allow for lack of commutability between P_μ and $h_{\mu\nu}$ in the quantum picture. It can also be obtained from (20a) if we replace P_μ by the form $P_\mu+e/cA_\mu$ it takes in the presence of an electromagnetic field.

With the help of (23) we can study the effect of a gravitational field on atoms and electrons. The gravitational interaction between the elementary particles themselves, is of the order of $m^2G/e^2\simeq10^{-40}$ times smaller than the electromagnetic interaction, and therefore, is not observable. On the other hand, the effect of an external gravitational field, such as that of a star, on atoms and electrons does give rise to observable phenomena which merit discussion.

V. THE HYDROGEN ATOM IN A GRAVITATIONAL FIELD

Let us consider a hydrogen atom near the surface of a gravitating mass M (such as a star) of radius R. The hydrogen atom will then be acted on by a constant gravitational field $h_{\mu\nu}=-MG/c^2Rg_{\mu\nu}\equiv-fg_{\mu\nu}$ and f is small for all gravitating bodies; i.e., $f\ll1$. We assume furthermore, that the hydrogen atom is acted by an external electromagnetic field represented by the vector potential **A**.

From (23) we see that the wave equation for the electron of this hydrogen atom becomes:

$$\gamma_\mu(\delta_{\mu\nu}+fg_{\mu\nu})(\hbar/i\,\partial/\partial x^\nu+e/cA_\nu)\psi-imc\psi=0 \tag{24}$$

where $(A_i)=\mathbf{A}$ and $A_4=i\phi$ where ϕ is the electrostatic field of the proton. In the absence of the gravitational field, the electrostatic field of the proton takes the usual form $\phi=e/r$ where r is the distance from the proton. When a gravitating mass is present, we recall that it changes the dielectric constant of the space surrounding it, so that ϵ takes the value (13), i.e., $\epsilon=1+2f$. The electrostatic field of the proton takes then the form:

$$\phi=e/\epsilon r=e/(1+2f)r. \tag{25}$$

Multiplying Eq. (24) by $i\gamma_4/1+f$ and using the relations[9] $i\gamma_4\gamma_i=\alpha_i$, $\gamma_4=\beta$, we obtain:

$$(i\hbar/c\,\partial/\partial t+e/c\phi)\psi =(1-f)/(1+f)\boldsymbol{\alpha}\cdot(\hbar/i\nabla+e/c\mathbf{A})\psi+mc/1+f\beta\psi. \tag{26}$$

In the case $\mathbf{A}=0$ we can solve this equation and show that it leads to a shift of the spectral lines toward the red. Our physical picture would be simpler though, if we work in the Heisenberg representation. As the Hamiltonian is $\mathcal{H}=i\hbar\partial/\partial t$, Eq. (26) determines it by the relation:

$$\mathcal{H}/c+e/c\phi=(1-f)/(1+f)\alpha\cdot(-i\hbar\nabla+e/c\mathbf{A}) +(mc/1+f)\beta. \quad (27)$$

Squaring both sides of (27) and using the anticommuting properties of α_i, β we obtain by a procedure similar to that of Dirac:[13]

$$(\mathcal{H}/c+e/c\phi)^2=\frac{(1-f)^2}{(1+f)^2} \times[(\mathbf{P}+e/c\mathbf{A})^2+e\hbar/c(\boldsymbol{\sigma}\cdot\mathbf{B})]+\frac{m^2c^2}{(1+f)^2}, \quad (28)$$

where $\mathbf{B}=\nabla\times\mathbf{A}$, and σ_i are the spin matrices.

Assuming now that the energy of the first term on the right of (28) is small compared with the rest energy, which is actually the case for the hydrogen atom, we can take square root of both sides and obtain:

$$\mathcal{H}/c+e/c\phi=\frac{mc}{1+f}+\frac{(1-f)^2}{2mc(1+f)} \times[(\mathbf{P}+e/c\mathbf{A})^2+e\hbar/c\boldsymbol{\sigma}\cdot\mathbf{B}]. \quad (29)$$

The non-relativistic Hamiltonian is given by (29), when we disregard the modified rest energy term $mc/1+f$. Introducing (25) in (29) and making use of $f\ll 1$, so that $(1-f)^2/(1+f)\simeq 1/1+3f$ we obtain:

$$\mathcal{H}=-e^2/(1+2f)r+1/2m(1+3f) \times[(\mathbf{P}+e/c\mathbf{A})^2+e\hbar/c\boldsymbol{\sigma}\cdot\mathbf{B}]. \quad (30)$$

With the help of this Hamiltonian we can discuss the effect of an external gravitational field on the hydrogen atom. Let us first assume that there is no external magnetic field; i.e., $\mathbf{A}=0$,

$$\mathcal{H}=-e'^2/r+1/2m'\mathbf{P}^2, \quad (31)$$

where $e'^2=e^2/1+2f$, $m'=m(1+3f)$. The Schroedinger equation with this Hamiltonian gives for sth energy level E_s' the value[14]

$$E_s'=-m'e'^4/2\hbar^2s^2 =-(1+3f)me^4/2(1+2f)^2\hbar^2s^2\simeq(1-f)E_s \quad (32a)$$

where E_s is the corresponding energy level in the absence of a gravitational field. We see, therefore, that there is a shift in the energy levels which gives a corresponding shift in frequencies:

$$\nu_{sp}'=h^{-1}(E_s'-E_p')=(1-f)h^{-1}(E_s-E_p)=(1-f)\nu_{sp} \quad (32b)$$

which leads to: $(\nu'-\nu)/\nu=\delta\nu/\nu=-f$. The corresponding shift in wave-lengths, observed at large distances from the gravitating mass, so that the relation $\lambda\nu=c$ holds, is given then by:

$$\delta\lambda/\lambda=f=M'/R. \quad (33)$$

We seen then, that the gravitational field leads to shift of the wave-length of the emitted light toward the red, which has the same value as that predicted by the general theory of relativity.

VI. GRAVITATIONAL CORRECTION TO THE MAGNETIC MOMENT OF THE ELECTRON

In the Hamiltonian expression (30), the last term corresponds to the additional potential energy of the spin of the electron. We can replace in this term $\mathbf{B}$ by $\mu\mathbf{H}$, and because of the presence of the gravitational field, μ takes the form (13), i.e., $\mu=1/1+2f$. As $f\ll 1$, we can write the last term of (30) in the form $(1-f)e\hbar/2mc\boldsymbol{\sigma}\cdot\mathbf{H}$. This potential energy may be interpreted as arising from the electron having a magnetic moment:

$$-(1-f)e\hbar/2mc\boldsymbol{\sigma}, \quad (34)$$

which reduces to the usual magnetic moment[13] when the gravitational field disappears, i.e., $f=0$.

The gravitational correction to the magnetic moment of the electron is very small, as on the surface of the earth, where we could attempt to detect it, f is only $\simeq 10^{-9}$. This gravitational effect is therefore, masked by the correction of quantum electrodynamical origin,[15] which is of the order of 10^{-3}. It would be of interest though, to study the effect on the magnetic moment of the electron of the gravitational field of rotating bodies, in connection with the recent suggestion of Blackett[16] concerning the magnetic moment of rotating masses.

The gravitational correction affects the orbital as well as the spin magnetic moment of the electron in the hydrogen atom. In fact, if we assume a constant magnetic field $\mathbf{B}_0=\mu\mathbf{H}_0$ we can write as usual $\mathbf{A}=\frac{1}{2}(\mu\mathbf{H}_0\times\mathbf{r})$, and introducing this in the Hamiltonian (30), we have $\mathcal{H}=\mathcal{H}_1+\mathcal{H}_2$ where $\mathcal{H}_1$ is given by (31) and $\mathcal{H}_2$ becomes:

$$\mathcal{H}_2=(1-f)e/2mc[(\mathbf{r}\times\mathbf{P})+\hbar\boldsymbol{\sigma}]\cdot\mathbf{H}_0 +e^2/8mc^2(1+f)(\mathbf{r}\times\mathbf{H}_0)^2. \quad (35)$$

The magnetic moment associated with the orbital motion of the electron is $-(1-f)(e/2mc)(\mathbf{r}\times\mathbf{P})$ and it is affected by the same gravitational correction as is the spin magnetic moment.

From the form of $\mathcal{H}_2$ we see that there will be a gravitational correction to the Zeeman effect, though again, it is very small, and it will be masked by the second term in (35) as well as by the quantum electrodynamical corrections.

[13] P. A. M. Dirac, *Quantum Mechanics* (Oxford University Press, London, 1947), Third Edition, p. 264.
[14] Reference 13, p. 158.
[15] J. Schwinger, Phys. Rev. **73**, 416 (1948).
[16] P. M. S. Blackett, Nature **159**, 658 (1947).

The observed gravitational effects can be explained quite simply in terms of the interaction of Birkhoff's gravitational field with other fields. The mathematical simplicity of flat space-time gravitational theories, suggest that they could be used with profit in the study of the classical and quantum aspects of field theories.

I am indebted to Professors A. Barajas and C. Graef of the University of Mexico for a presentation of G. D. Birkhoff's theory of gravitation, and to Professors G. Birkhoff and W. H. Furry of Harvard University for discussion of the manuscript.

It is a pleasure to acknowledge the support given to the present research by the Comisión Impulsora y Coordinadora de la Investigación Científica, and the interest taken in it by its Physics Chairman, Prof. M. S. Vallarta.

PHYSICAL REVIEW VOLUME 80, NUMBER 4 NOVEMBER 15, 1950

Three New Delayed Alpha-Emitters of Low Mass*

LUIS W. ALVAREZ
Radiation Laboratory, Department of Physics, University of California, Berkeley, California
(Received July 24, 1950)

Two new positron active isotopes, B^8 and Na^{20}, have been found to decay to excited states of Be^8 and Ne^{20}, which in turn decay "instantaneously" by alpha-emission. Their half-lives are 0.65 ± 0.1 sec. and $\frac{1}{4}$ sec., respectively. N^{12} is also found to have a low energy positron group which leads to an α-unstable excited state in C^{12}. The masses of B^8 and Na^{20} are 8.027 and 20.015, respectively. B^8 decays by a 13.7 ± 0.3-Mev positron, through the same excited state of Be^8 as does Li^8. Estimates of the energies of the excited state in C^{12} and Ne^{20} are made.

I. INTRODUCTION

UNTIL the present time, the only known light, delayed alpha-emitter,[1] was Li^8. In the terminology of classical radioactivity, "delayed alpha-particles," such as those from Li^8, are called "long-range alpha-particles." They arise from excited states of a daughter nucleus, following a beta-decay, and their real lifetimes are too short to be measured directly. Their apparent lifetimes are those of their parents, with which they are in equilibrium. The expression "delayed neutron emitter," is used for the same reason, to indicate that the observed neutron activity of nuclei such as[2] N^{17}, is not a true neutron radioactivity, but rather the "instantaneous" disintegration of an excited beta-decay daughter nucleus. In both neutron and alpha-decays of the delayed variety, it is possible to determine the lifetime of the actual heavy particle reaction, not by time measurements, but indirectly, from the uncertainty principle, using a measurement of the energy spread of the emitted particles.

Li^8 has been investigated by a number of nuclear physicists,[3–6] and its decay scheme is well understood. The beta-transition is first forbidden, and leaves the Be^8 daughter in a broad excited state about 3.1 Mev above the ground state. The width of the state is 0.8 Mev.

II. DESCRIPTION OF EXPERIMENTS

The present experiments were started in an attempt to observe an example of delayed proton emission. Although this process has not yet been reported, it would be expected from nuclei such as Ne^{17}, O^{13}, and C^9. In the case of Ne^{17}, the reactions would be

$$_{10}Ne^{17}\rightarrow{}_9F^{17*}+e^+$$
$$_9F^{17*}\rightarrow{}_8O^{16}+{}_1H^1.$$

This pair of reactions is similar to the pair describing the delayed neutron activity of N^{17}:

$$_7N^{17}\rightarrow{}_8O^{17*}+e^-$$
$$_8O^{17*}\rightarrow{}_8O^{16}+n.$$

The 32-Mev proton beam from the Berkeley linear accelerator was used to bombard a proportional counter filled with $B^{10}F_3$. (Protons plus B^{10} could give C^9, and protons plus F^{19} could give Ne^{17}.) The linear accelerator is pulsed 15 times per second, for 300 μsec., and the proportional counter "cleans up" in a few milliseconds from the huge burst of ions formed during the 300-μsec. pulse. It is therefore very convenient to count delayed heavy particles through a gate circuit which eliminates all pulses during the time the counter is paralyzed. Activities may be followed in this manner, through buildup to equilibrium, and after the accelerator is turned off, through decay. A delayed heavy particle activity was observed in BF_3, with a half-life of about $\frac{3}{4}$ sec.

Before giving the reasons for the assignment of this activity to B^8, it will be well to describe other experimental techniques which were used in these investigations. Gaseous targets of CH_4 and Ne were also bom-

* This work was supported by the AEC.
[1] Crane, Delsasso, Fowler, and Lauritsen, Phys. Rev. 47, 971 (1935).
[2] L. W. Alvarez, Phys. Rev. 75, 1127 (1949).
[3] D. S. Bayley and H. R. Crane, Phys. Rev. 52, 604 (1937).
[4] Bonner, Evans, Malide, and Risser, Phys. Rev. 73, 885 (1948).
[5] F. L. Hereford, Phys. Rev. 73, 574 (1948).
[6] W. F. Hornyak and T. Lauritsen, Phys. Rev. 77, 160 (1950).

barded, and heavy particle activities were again observed in the manner just described. In the case of BF_3, coincidences between the heavy particles and the positrons were detected. Actually, triple coincidence techniques were used to reduce the background. The positrons were observed with a pair of trays of proportional counters; an absorber was placed between the trays to eliminate coincidences from secondary electrons of gamma-ray origin. The alpha-particles were detected in the bombarded counter. The energy of the B^8 positrons was measured by absorption techniques, using the triple coincidence circuit, and finally comparing the B^8 curve with that[7] of N^{12}, in the Feather comparison method. The N^{12} absorption curve was taken in the same geometry, immediately after the B^8 curve.

Excitation curves for all of the observed reactions were determined, and the values of the thresholds were measured relative to the $C^{12}(p, n)N^{12}$ threshold, which was investigated very carefully in this laboratory last year.[7] The linear accelerator beam is very monoenergetic at a given time, but the value of the energy may change by a few hundred kilovolts from day to day, depending upon the adjustment of the final accelerating gap. It is therefore important to have an easily reproducible energy standard in the region under investigation. The sharp (p, n) threshold for the production of N^{12} serves this purpose.

Solid targets of Be^9, B^{10}, and B^{11} were bombarded on a number of occasions, and both alpha-particles and beta-rays of short half-lives were observed. Alpha-particle range distributions were measured from solid targets, using calibrated mica absorbers and a proportional counter equipped with a thin mica window. Beta-radiation from solid targets was detected by a pair of proportional counters in coincidence, and in some experiments, a magnetic field was used to separate the effects of positrons and electrons. This technique was essential in the study of the activities from Be^9, where Li^8 and B^8 are made at the same time. They have similar excitation curves, nearly equal half-lives, almost identical beta-ray upper limits, and identical alpha-particle spectra.

III. BORON 8

The delayed heavy particles from $B^{10}F_3$ were observed to have a half-life of 0.65 ± 0.1 sec. Since Li^8 has a half-life of 0.88 sec., and since it can be produced by the reaction

$$B^{10}(p, 3p)Li^8,$$

it was first necessary to show that the observed activity was not due to Li^8. The energetic threshold for the $(p, 3p)$ reaction is 25.8 Mev, but the observed threshold for the delayed heavy particles was found to be 21.2 Mev. If one does not believe that the tri-proton is a stable nucleus with a binding energy of at least 4.6 Mev, these energy data indicate that the activity cannot be due to Li^8, and must be from some unknown isotope. One would then assign the activity tentatively either to B^8 or C^9. Assuming the reactions to be

$$B^{10}(p, 2n)C^9 \quad \text{or} \quad B^{10}(p, p, 2n)B^8$$

one calculates the masses to be

$$C^9=9.0270 \quad \text{or} \quad B^8=8.0189.$$

Barkas'[8] estimate of the mass of C^9 is 9.036. Although his mass estimates have proved to be very reliable, there are known nuclei with three more protons than neutrons, so that there is no way to evaluate the accuracy of his estimates so far from the region of stability. It was hard to believe that the mass of B^8 would be 5.7 Mev lighter than that of Li^8, (8.02502) in view of its greater Coulomb energy. For this reason, it was at first felt that the activity was probably C^9. But if one assumes the reaction to be

$$B^{10}(p, H^3)B^8,$$

the mass of B^8 would be 8.0279. This is a more reasonable value from simple energetic arguments, but it is higher than is allowed by the proton stability of the active nucleus. B^8 must be lighter than the sum of Be^7 plus a proton, which is 8.0273 mass units. The discrepancy between this upper limit and the mass calculated from the threshold energy can be attributed to the barrier effect. In other words, the observed threshold for a (p, H^3) reaction must be greater than the energetic threshold. This effect was observed by Panofsky and Phillips in the $C^{12}(p, d)C^{11}$ reaction, where the masses of all the reacting atoms are known. They found that the observed threshold was about 0.5 Mev higher than the calculated energetic threshold. Since it would take only a 0.6-Mev shift in the experimental threshold for the $B^{10}(p, T)B^8$ reaction, to make B^8 stable against proton loss, it will be assumed from now on, that the mass of B^8 is almost equal to its maximum stable value of 8.0273. In view of the uncertainties of the actual threshold and the strong evidence that the new activity is B^8, no other view could be taken seriously. (Barkas' estimate of the mass of B^8 is 8.027.)

There are several ways of eliminating C^9 from consideration. In the first place, the maximum possible positron energy it could have (if its mass were 9.027) is about 7 Mev; in the second place, it could not be produced from Be^9, while B^8 could be so produced. Both of these lines of attack were followed, and C^9 was shown to be ruled out by both of them.

The positrons in coincidence with the heavy particles were found by the Feather comparison method to have an upper limit of 13.7 ± 0.3 Mev, thereby ruling out C^9 with certainty. This upper limit energy checks closely with the value calculated from the mass of B^8, if one assumes that the alpha-particles come from the same state of Be^8 as those following the decay of Li^8. The calculated upper limit is 14.0 Mev. The absorption

[7] L. W. Alvarez, Phys. Rev. 75, 1815 (1949).

[8] W. Barkas, Phys. Rev. 55, 691 (1939).

curve of the alpha-particles, as measured from a solid, thick target of B^{10}, was in agreement with that calculated from the known Li^8 spectrum. This confirms the view that the same excited state of Be^8 is responsible for the delayed alpha-particles from both Li^8 and B^8. The measured energy of the positrons is another indication that the observed heavy particles are alpha-particles with the same energy distribution as those following the Li^8 beta-transition.

There is experimental evidence to support the theoretical view that the ground states of pairs of "mirror nuclei" have the same spectroscopic character. Since Li^8 and B^8 have the same forbidden value of ft for their beta-decays, it would be very surprising if they did not decay to the same state in Be^8. The two measurements of the B^8 alpha-particle energy (direct, and by subtraction of the beta-energy from the mass difference) support this view.

The first attempts to produce the 0.65-sec. activity by proton bombardment of Be^9 were unsuccessful in that the measured half-life of the observed beta-particles was always close to the 0.88-sec. half-life of Li^8. Since it was felt that the cross sections for producing a $(p, 2n)$ reaction should be much greater than that leading to a $(p, 2p)$ reaction near the threshold, this observation was the best evidence that the new activity was C^9. But later work with magnetic analysis of the beta-rays showed that the shorter-lived positrons were present, and with the calculated threshold. The smallness of the cross section is still an unexplained fact, although it might be related to the almost negligible binding energy of the last proton in B^8. Figure 1 shows the yield curves of positrons and electrons from Be^9 bombarded with protons. It is apparent from the curves why the B^8 half-life could not be seen without magnetic analysis. The mass of B^8, as calculated from the Be^9 threshold is 8.0264. This is not so reliable a mass value as that from the B^{10} experiment, since no calibration relative to the N^{12} threshold was made, and no background runs were made. The purpose of the experiment was primarily to see if the 0.65-sec. activity could be made from Be^9 by proton bombardment, thereby ruling out C^9. The threshold value, and its related B^8 mass are merely inaccurate by products of a qualitative experiment to check the isotope assignment.

An additional method of producing B^8 was found. A proportional counter filled with CH_4 was bombarded with protons, and two delayed alpha-emitters were observed. One of these was N^{12}, as will be described in the next section. The other had a lifetime of about $\frac{1}{2}$ sec., but the activity was too weak to give an accurate decay curve. (It is an interesting experimental fact that with the techniques used in this laboratory a half-life in this range of times is about the most difficult to measure accurately. If it is 10 times shorter, the "movable gate" technique can be employed, with 15 new samples being made every second. Thousands of counts may be taken at each setting of the gate, so that an accurate decay

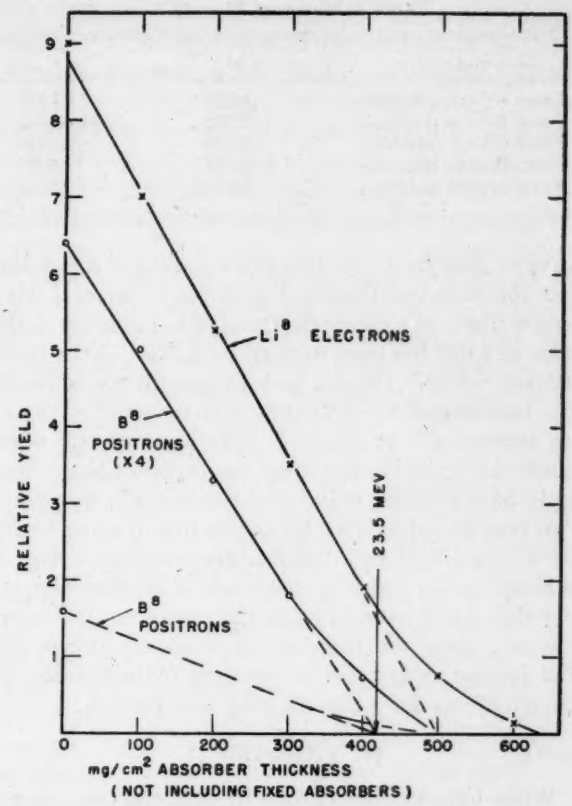

FIG. 1. Excitation curves protons on Be^9.

curve can be made, as was done in the case of N^{12}. If the lifetime is several seconds, a pen recorder can be used to exhibit the output pulses of a scaler, and the scaling ratio can be changed several times during the course of the decay. But with a half-life of $\frac{1}{2}$ sec., the time consumed in changing the scaling factor is appreciable compared with the half-life. The counting rate then changes too rapidly from a value that "jams" the pen recorder to one that is too slow to give more than one count per half-life. This, of course, is not a fundamental difficulty, but is one which depends upon the available techniques.) The evidence that the activity from CH_4 was also B^8 was so strong that it could not have been altered by anything less than a very extensive program of half-life measurement. In addition to the approximate half-life (which could not be off by 50 percent) the threshold for the reaction, which was assumed to be $C^{12}(p, n\alpha)B^8$, agreed closely with that calculated from the previously measured value of B^8. The observed threshold was about 30 Mev. A simple calculation using this threshold shows the mass of B^8 to be 8.029. The increase in apparent threshold due to barrier effect will be greater in this reaction than in the (p, T) reaction on B^{10}, since an alpha-particle must come out. In addition it has been found that observed thresholds are higher than true thresholds when the activities are weak. Since the threshold is almost at the maximum energy of the linear accelerator, it was impossible to extrapolate the yield

TABLE I. Masses of B^8 and C^9.

Calculated mass of	B^8	C^9
From $B^{10}+p$ threshold	8.027	9.027
From Be^9+p threshold	8.026	Impossible
From $C^{12}+p$ threshold	~8.027	~9.014
From Barkas (theory)	8.027	9.036
From proton stability	8.0273	9.035

curve to zero yield. For those two reasons it is believed that the observed threshold is of the order of 2 Mev greater than the energetic threshold. In Table I the value of 8.029 has been reduced by 2 Mev, so the value listed is ~8.027. The energetic arguments for believing that the assignment of the new activity to B^8 is correct are summarized in Table I. Additional energy arguments can be used to show that no other possible nucleus could have the alpha- and positron energies measured. This may be appreciated by noting that if other heavy particles are emitted in the primary reactions, energy is required (of the order of magnitude of binding energy), and this would have to be at the expense of the decay energies, since the threshold is fixed experimentally. The isotope assignment is therefore quite definite, although no chemical identification was possible.

IV. NITROGEN 12

When CH_4 was bombarded by protons, two delayed heavy particle emitters were observed. One of these was shown in the last section to be B^8. The second group of heavily ionizing particles had a measured half-life of 0.013 ± 0.001 sec. The half-life of the positrons from N^{12}, as measured by the same "delayed gate" equipment, was 0.0125 sec. The threshold for the production of heavy particles was the same as that previously found for the N^{12} positrons. The coincidence of half-life and threshold makes it quite certain that N^{12} can decay in either of the following two ways:

$$N^{12}\rightarrow C^{12}+e^+ \quad (1)$$
$$N^{12}\rightarrow C^{12*}+e^+ \quad (2)$$
$$C^{12*}\rightarrow Be^8+\alpha$$
$$Be^8\rightarrow 2\alpha.$$

Shortly after the low energy positron branching of N^{12} was observed, a paper on B^{12} by Hornyak and Lauritsen[9] appeared. These investigators show that a Kurie plot of the B^{12} beta-ray spectrum can be resolved into three components, with end points at 13.4, 6.3, and 2 Mev. Within the accuracy of the Kurie plot resolution the excited state of C^{12} to which the 6.3-Mev beta-ray leads has the same mass as Be^8+He^4. This state therefore cannot be responsible for the heavily ionizing particles observed in the N^{12} branching, as it must decay by emitting either gamma-rays or very low energy alpha-particles. It is tempting to identify the alpha-particles seen in the N^{12} branching as arising from the decay of the higher excited state of C^{12} postulated by Hornyak and Lauritsen to explain the lowest energy component of the B^{12}. This state should lead to three alpha-particles with a total energy of about 4 Mev. This is consistent with the pulse height observed in the CH_4-filled proportional counters. Alpha-particles from the lower excited state of C^{12} could not have been detected above the gamma-ray background. In the discussion so far it has been tacitly assumed that the observed heavy particles are alpha-particles. It can easily be shown from the measured mass of N^{12} that there is insufficient energy available for any other known particle, such as a proton or an He^3 nucleus to be emitted. It is therefore considered as established that the delayed heavy particles are alphas.

It would be interesting to make an accurate determination of the shape of the N^{12} beta-spectrum to see if three components exist. (So far only the upper limit of the highest energy group is known.) According to present ideas, the same groups should be observed from B^{12} and N^{12}. Both of the groups which could be detected by the methods employed have shown up, so the results so far are in agreement with the theory that the mirror nuclei are identical insofar as their ground states are concerned.

Lauritsen's table of nuclear energy states[10] shows no excited state of C^{12} at the energy required to explain the lowest energy group of B^{12} beta-rays, and presumably the N^{12} delayed alpha-particles. In fact, the lowest tabulated excited state of C^{12} which leads to α-emission is at 16.1 Mev. This is not too unexpected, since the excited state of Be^8 which gives the delayed α's from Li^8 and B^8 is observed in no other reactions. There must be many highly excited states of the simple nuclei which have not yet been observed, since the density of observed states does not increase markedly with energy, as the Bohr theory requires.

V. SODIUM 20

A proportional counter filled with neon was bombarded with protons, and a new delayed heavy particle activity was found. The half-life is approximately $\frac{1}{4}$ sec., and the cross section for the production of the heavily ionizing particles is at least a hundred times greater than that for the two previously described activities. The obvious assignment of this activity is to Na^{20}, since it is a member of the series $Z=2n+1$, $A=4n$. In this series, we have: for $n=1$, Li^4, which is almost certainly unstable; for $n=2$, B^8, a delayed α-emitter; for $n=3$, N^{12}, a delayed α-emitter; for $n=4$, F^{16}, a nucleus which is almost certainly proton unstable (high energy proton bombardment of O^{16} yields no short-lived, high energy positrons). It is therefore reasonable to assume that the $\frac{1}{4}$-sec. activity is Na^{20} ($n=5$ in the series), produced in a (p, n) reaction on Ne^{20}. The threshold for the reaction is 16.9 Mev. The mass of Na^{20}, assuming that the assignment is correct, is 20.0152. Barkas predicts a value of

[9] W. F. Hornyak and T. Lauritsen, Phys. Rev. 77, 160 (1950).

[10] T. Lauritsen, National Research Council Preliminary Report No. 5 (1949).

20.0160, and the highest mass which a Na^{20} atom could have and be stable against proton emission is 20.01593. The predictions of Barkas on the masses of the series $Z=2n+1$, $A=4n$ are all so close to the limit of proton stability that Barkas could not say whether or not they would be stable. It appears experimentally that B^8, N^{12}, and Na^{20} are just stable, while F^{16} is just unstable.

After noting that Na^{20} is a reasonable assignment of the activity, it is necessary to inquire whether any other isotope could equally well fill the bill. Na^{19}, produced in a $(p, 2n)$ reaction with the observed threshold, would be lighter than Ne^{19}, and so it and all lighter isotopes of Na are ruled out. Ne^{19} is known to have a half-life of 23 sec. All lighter Ne isotopes produced at the observed threshold would be lighter than the known isotopes into which they would have to decay, and are therefore ruled out. The same is true for all unknown isotopes of elements with Z less than 10. These energetic arguments complete the identification of the $\frac{1}{4}$-sec. activity as Na^{20}.

By the energy arguments used in the case of N^{12}, it is possible to show that the observed heavy particles from Na^{20} are alpha-particles. It is then possible to set limits on the height of the excited state in Ne^{20}, which decays into an alpha-particle plus an O^{16} nucleus. The combined mass of He^4 and O^{16} is 20.0039, and the mass of Ne^{20} is 19.99877. The lowest excited state of Ne^{20} which could give rise to an alpha-particle, is then 4.8 Mev above the ground state. The highest state of Ne^{20} which could be reached from Na^{20} (by a positron of zero energy), is 14.3 Mev above the ground state. The limits can be pushed together from both directions by the following arguments. The heights of the alpha-particle pulses indicated that the energy release was greater than 2 Mev. This is qualitative, in view of the fact that the windows of the proportional counter were too thick to allow calibrating alpha-particles to be introduced. We will therefore raise the lower limit on the excited state to 6.8 Mev. The intensity of the alpha-particles was so great that it is very improbable that the positron branching ratio to the excited state of Ne^{20} is less than five percent. This would make the effective half-life for the transition less than 5 sec., or the positron energy greater than 3.5 Mev. These considerations lower the maximum height of the excited state of Ne^{20} to 10.8 Mev. It seems relatively safe, then, to conclude that the excited state of Ne^{20} is between 6.8 and 10.8 Mev above the ground state.

It should be possible to measure the heights of the excited levels in both C^{12} and Ne^{20} in either of two ways. An absorption curve of the positrons in coincidence with the alpha-particles would give the necessary information, and so would a pulse-height analysis of the alpha-particles. The energy distribution of the alpha-particles was observed to be broad, by inspection of the cathode-ray tube display, but no accurate measurements were possible in the absence of a good calibration. A search was made for positrons in coincidence with the N^{12} and Na^{20} alpha-particles. A low intensity of relatively soft positrons was found from N^{12}, but in the case of Na^{20}, no convincing proof of the existence of positrons was found. This shows that most of the Na^{20} positrons to Ne^{20*} were not energetic enough to penetrate the brass walls of the counter, and would indicate that the excited level is somewhat higher than the lower limit of 6.8 Mev quoted in the last paragraph.

It is interesting to note that F^{20}, the mirror image of Ne^{20}, does not combine in a beta-transition with the ground state of Ne^{20}. From the magnitude of the branching ratio in Ne^{20} it is apparent that the transition between the ground states of Na^{20} and Ne^{20} is also not an allowed one.

The latest isotope chart issued by the General Electric company shows a 3-sec. positron activity assigned to Na^{20}. The classification is "C" (element certain; one of several possible mass numbers). Dr. J. R. Stehn, who prepared the chart, has told the author that the 3-sec. assignment is unwarranted, and that the present identification will replace it in his next edition.

VI. INTERPRETATION OF "HAMMER TRACKS"

Cosmic-ray observers have found many examples of "stars" in photographic emulsions, which have "hammer prongs." A heavily ionizing track is observed to leave the exploding nucleus, and at the end of the track appear a pair of heavy prongs of equal range, but opposite directions. It has always been assumed that such hammer tracks are Li^8 nuclei, and that the heads of the hammers are formed by the resulting pairs of alpha-particles. The lengths of the hammer heads are in agreement with this assumption. But now that it has been found that B^8 gives delayed alpha-particles with the same range distribution, this strict interpretation of hammer tracks can no longer be made. But it is probably true that most of the observed hammer tracks are actually due to Li^8 and not to B^8, since their lower charge would allow them to escape more easily.

The author wishes to thank the linear accelerator crew and its chief operator, Mr. Robert Watt, for valuable assistance in the course of the experiments.

Proton-Neutron Reactions and Thresholds*

H. T. RICHARDS, R. V. SMITH,** AND C. P. BROWNE
University of Wisconsin, Madison, Wisconsin
(Received July 10, 1950)

Threshold proton energies for neutron emission have been determined carefully for Be^9, B^{11}, C^{13}, O^{18}, Cl^{37}, K^{41}, V^{51}, Mn^{55}. Thin target yield data up to about 4 Mev proton energy are reported for Be^9, B^{11}, O^{18}, and K^{41}. A summary of all reported p-n thresholds for $Z \leq 25$ is included. Isobaric mass differences from p-n measurements and from beta-ray end points are compared. Data concerning the suitability of various p-n reactions as controlled energy neutron sources are included.

I. INTRODUCTION

THE general type reaction

$$Z^A + H \rightarrow (Z+1)^A + n + Q$$

is always endoergic if one starts with a stable nucleus Z^A. The threshold proton energy for neutron emission will therefore always be greater than 782 kev, the $n-H$ mass difference. Since the outgoing neutron has no coulomb barrier to penetrate, the neutron yield near threshold need not be vanishingly small. Hence such thresholds can often be located to a precision comparable with the resolution in energy of the incident proton beam. The threshold energy and the $n-H$ mass difference then permit accurate determination of the mass difference between the two isobaric nuclei involved.

Such (p, n) reactions are also of practical interest as possible laboratory sources of neutrons whose energy can be varied by control of the proton energy. Furthermore, the sharp thresholds of these reactions provide useful calibration points on the high voltage scale.

The present paper summarizes work on (p, n) thresholds and yields investigated at Wisconsin over the last several years.

II. EXPERIMENTAL ARRANGEMENTS AND RESULTS

Protons of energy up to 4 Mev and monoergic to 0.1 percent were available from the Wisconsin electrostatic generator and high resolution cylindrical electrostatic analyzer. Target arrangement and preparation are discussed separately for each element. Neutrons were detected by a shielded energy insensitive BF_3 (plus paraffin) counter placed in front of the target and subtending about π-steradians. All targets were kept heated to 200°C to minimize surface contamination. A liquid air cooled trap was also located between the targets and the diffusion pumps.

The voltage scale was checked several times during the measurements by sliding lithium targets in place and observing the $Li^7(p, n)Be^7$ threshold. Calibration curves for different lithium targets are shown in Fig. 1.

Beryllium

One thick and two thin Be targets were used. The thick target was metallic beryllium and the thin targets ($\frac{1}{2}$ kev and 2 kev stopping power) were prepared by evaporation onto tantalum. Figure 2 shows the thick and thin target yields near threshold. The thick target yield below threshold is believed to result from secondary $(p, d; d, n)$ reactions in the thick Be target. Such thick target effects for Be have been discussed by Jennings, Sun, and Leiter.[1] Thin target yield below threshold shows no effect above background. Hence the yield from $Be^9(p, pn)Be^8$ reaction (threshold $E_p = 1.84$ Mev) appears to be negligible at these bombarding energies. The maximum in yield near threshold is an effect associated with the forward bunching of the low energy neutrons which bunching results from the center of mass motion. Figure 3 shows the yield curve from

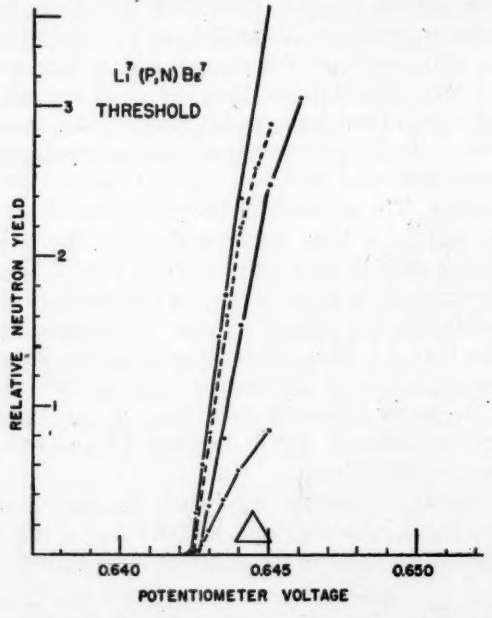

FIG. 1. Calibration measurements on the $Li^7(p, n)Be^7$ threshold taken with different lithium targets and at different times. The potentiometer setting of 0.6426 was taken to correspond to the lithium threshold, 1.882±0.002 Mev. The triangle is the proton energy spread calculated from the slit settings of the electrostatic analyzer.

* Work supported by the AEC and the Wisconsin Alumni Research Foundation.
** Now at Westinghouse Research Laboratories, East Pittsburgh, Pennsylvania.

[1] Jennings, Sun, and Leiter, Phys. Rev. 80, 109 (1950).

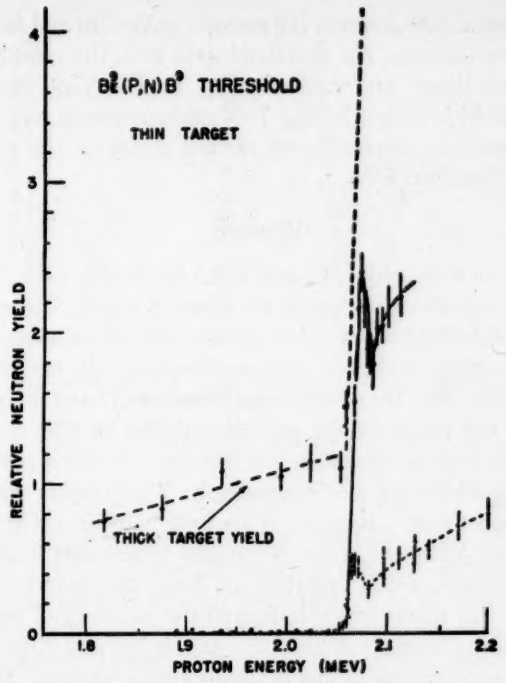

FIG. 2. Threshold data from thin and thick beryllium targets. See text for discussion of thick target yield.

threshold to 4.0 Mev proton energy. Only one resonance (previously reported by Hushley)[2] at $E_p = 2.56$ Mev was observed. Neutron spectrum studies[3] and differential cross section measurements[4] have also been completed in this laboratory and are being reported separately.

Boron

Thin targets of ordinary boron on tantalum were formed by running a high voltage discharge between a tantalum cathode and an aluminum anode in BF_3 at a few cm pressure. The targets so prepared were only a few kev thick for 3 Mev protons. Threshold runs on two different targets are shown in Fig. 4. The change in slope at $E_p = 3.03$ Mev is again the effect associated with the opening cone of neutrons. Yield data at higher energy have been taken but with no indication of resonances. The (p, n) reaction is with the B^{11} isotope, not B^{10}, since C^{11} is observed to be formed and mass values put the $B^{10}(p, n)C^{10}$ threshold above 5 Mev.

Carbon

A thick target of spectroscopic carbon was used. The neutron yield is low even from a thick target, since the

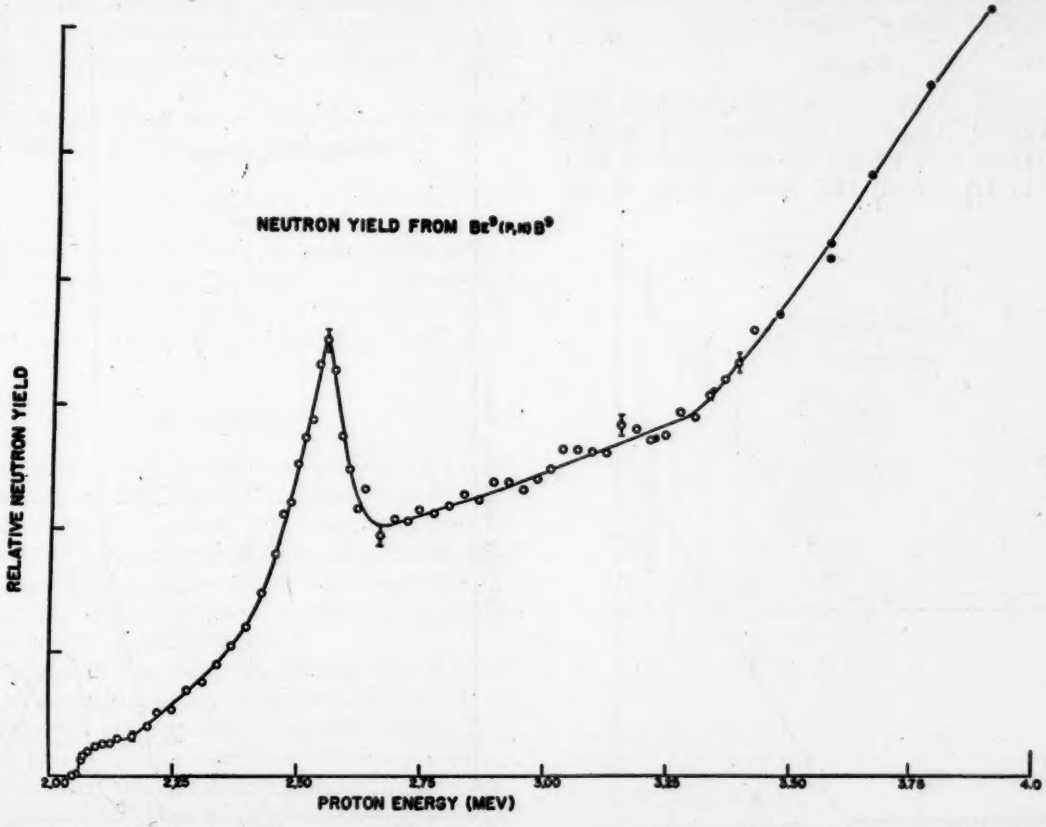

FIG. 3. Forward direction neutron yield from beryllium. The solid circles are data taken at a later time with a thicker target and normalized at 2.23 Mev.

[2] W. J. Hushley, Phys. Rev. **67**, 34 (1945).
[3] Johnson, Ajzenberg, and Wilson-Laubenstein, Phys. Rev. **79**, 187 (1950).
[4] Richards, Wilson-Laubenstein, Johnson, and Ajzenberg (report in preparation).

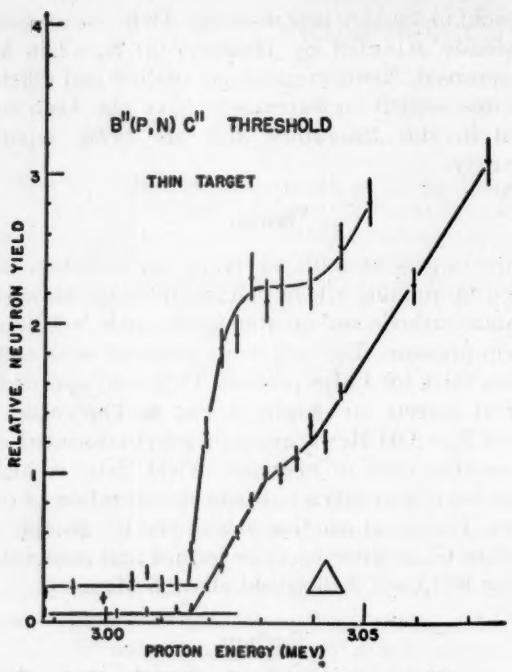

FIG. 4. Threshold data for two thin targets of boron.

reaction is with C^{13} whose abundance is only 1.1 percent. Results for two targets are shown in Fig. 5.

Oxygen

O^{18} is the only oxygen isotope with a threshold below 4 Mev. Thin O^{18} targets on aluminum and tantalum anode backings were formed by electrolysis of water enriched[5] to 1.5 percent O^{18}. Several hours of electrolysis at low currents (10 mamp.) gave thin and fairly uniform targets. The threshold data with the tantalum backed target are shown in Fig. 6. The yield above threshold is shown in Fig. 7. Numerous resonances are observed corresponding to excited states of the compound nucleus F^{19}.

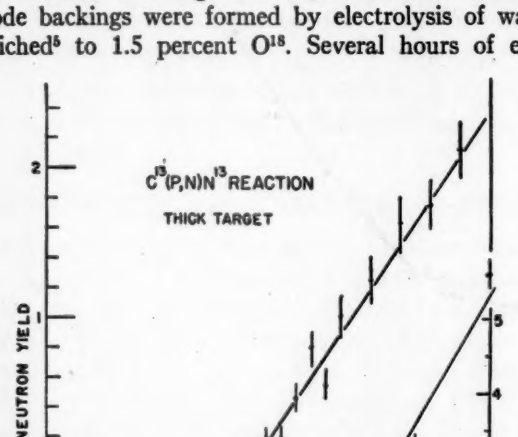

FIG. 5. Threshold data from thick targets of spectroscopic carbon.

[5] This water was obtained from Stuart Oxygen Company on allocation from the AEC.

Chlorine

Thick targets of LiCl and NaCl have been used. The results on the NaCl target are given in Fig. 8. The yield near threshold is low. Mass values necessitate assigning the reaction to the Cl^{37} isotope. However, the threshold is higher than that predicted theoretically[6] and is probably the result of the special stability of Cl^{37} which results from its closed shell of 20 neutrons. The observed threshold energy also confirms the K capturing classification for A^{37}. Because of its long half life (34 days) and its gaseous nature, A^{37} might have some interest for neutrino recoil experiments. Some thin target yield data was taken which indicated the presence of many resonance levels in A^{38} but the yield is low and difficulty was experienced in maintaining stable targets. More work on Cl^{37} is planned.

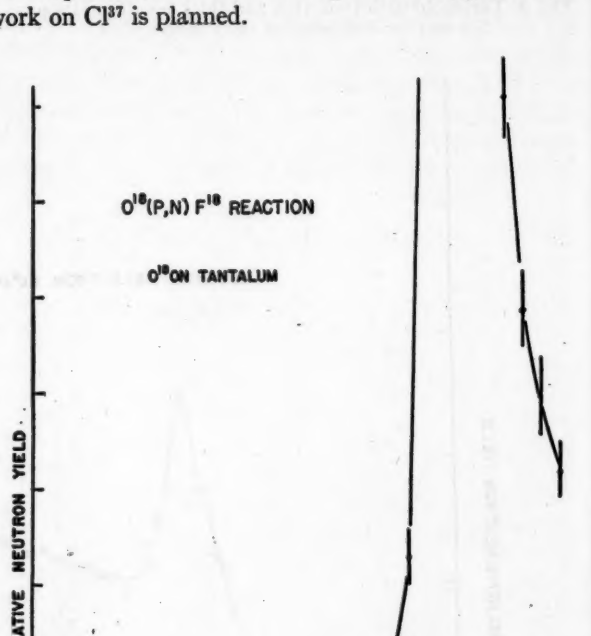

FIG. 6. Thin target threshold data from an enriched O^{18} target.

[6] H. A. Bethe, *Elementary Nuclear Theory* (John Wiley & Sons, Inc., New York, 1947), p. 126.

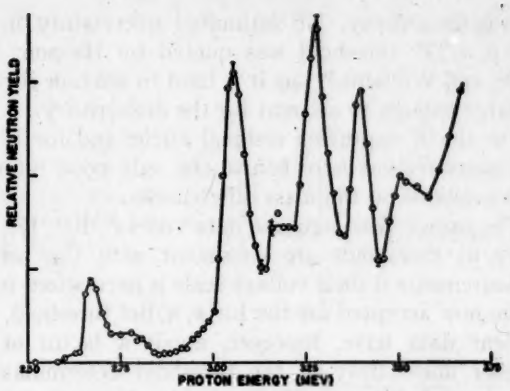

FIG. 7. Forward direction neutron yield from O^{18}.

Potassium

Thin evaporated targets of potassium metal were used. The yield near threshold is small (Fig. 9). The observed neutron reaction is attributed to K^{41} since K^{40} is of too low abundance to account for the observed yield and the reaction with the K^{39} isotope should be endoergic by several Mev according to theoretical arguments[7] and according to the 1.06-sec. activity[8] attributed to Ca^{39}. The $Ca^{41}-K^{41}$ mass difference as computed from our threshold excludes the possibility of a 1.1 Mev gamma-ray previously attributed to Ca^{41} K-capture.[9]

A thin target yield curve (Fig. 10) shows many excited states of the compound nucleus, Ca^{42}.

Vanadium

Thick targets were prepared by melting V_2O_5 onto a tantalum backing. A large probable error is assigned to the threshold because the yield near threshold (Fig. 11) was only slightly above the neutron background of the counter.

Manganese

Thick metallic manganese was used for a target. Definite neutron yield above background was detected (Fig. 12) down to $E_p=1.19$ Mev and reasonable extrapolation of the yield would indicate a threshold of $E_p=1.18\pm0.01$ Mev. This value is our lowest observed proton energy capable of giving neutrons from proton bombardment of a stable nucleus.

It is of interest that both the K^{41} and $Mn^{55}(p, n)$ reactions form residual nuclei which are actually of lower energy than the target nuclei. Thus, our present (p, n) data together with the n-p mass difference $(=n-H+mc^2)$ show that the K^{41} nucleus is 70 kev heavier than the Ca^{41} nucleus and that the Mn^{55} nucleus is about 130 kev heavier than the Fe^{55} nucleus. The reason that the

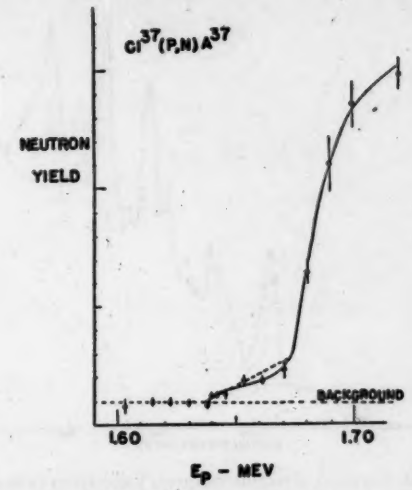

FIG. 8. Threshold data from a thick target of NaCl.

"heavier" nucleus is actually the stable nucleus is, of course, that the "lighter" nucleus can capture its K electron and thereby becomes the "heavier."

III. DISCUSSION

Table I summarizes the data on observed p-n thresholds in elements up to $Z=25$. The Q of each reaction[10] $[Q=-E_{th}M_2/(M_1+M_2)]$ is calculated from the observed thresholds and is recorded in column three. The energy difference ΔE between the two isobars is given in the fourth column assuming 782 kev for the $n-H$

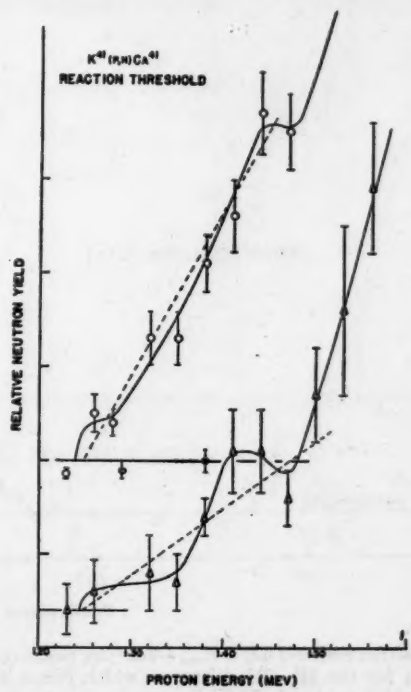

FIG. 9. Threshold data from two thin potassium targets.

[7] E. P. Wigner, quoted by H. Walke, Phys. Rev. 57, 183 (1940).
[8] Huber, Leinhard, Scherrer, and Waffler, Helv. Phys. Acta 16, 33 (1943).
[9] H. Walke, Phys. Rev. 57, 179 (1940).
[10] Hanson, Taschek, and Williams, Rev. Mod. Phys. 21, 635 (1949).

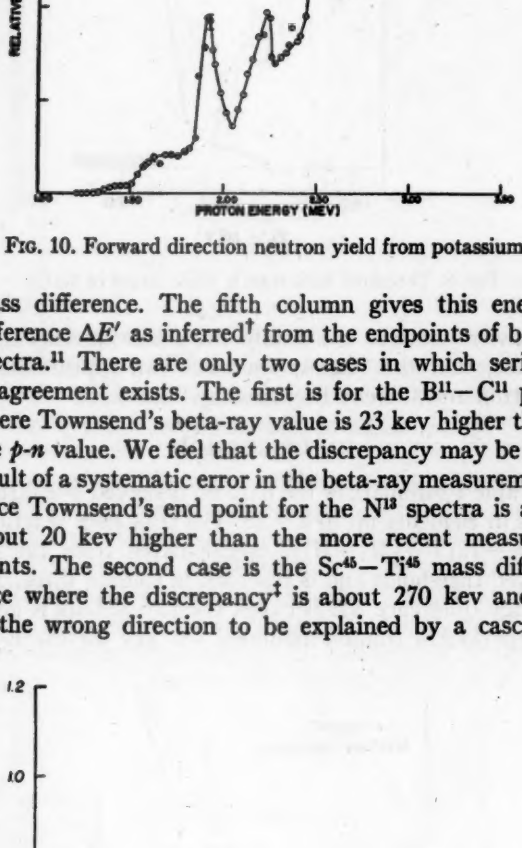

FIG. 10. Forward direction neutron yield from potassium.

mass difference. The fifth column gives this energy difference $\Delta E'$ as inferred† from the endpoints of beta-spectra.[11] There are only two cases in which serious disagreement exists. The first is for the $B^{11}-C^{11}$ pair where Townsend's beta-ray value is 23 kev higher than the p-n value. We feel that the discrepancy may be the result of a systematic error in the beta-ray measurement since Townsend's end point for the N^{13} spectra is also about 20 kev higher than the more recent measurements. The second case is the $Sc^{45}-Ti^{45}$ mass difference where the discrepancy‡ is about 270 kev and is in the wrong direction to be explained by a cascade beta-gamma-decay. No estimated uncertainty in the $Sc^{45}(p, n)Ti^{45}$ threshold was quoted by Hanson, Taschek, and Williams,[10] but it is hard to see how it could be large enough to account for the discrepancy.

For the K capturing residual nuclei and for B^9 the p-n measurement is of course the only good information available on the mass differences.

The earlier Westinghouse data[12] on Li^7, Be^9, B^{11}, and $C^{13}(p, n)$ thresholds are consistent with the present measurements if their voltage scale is normalized to the value now accepted for the $Li^7(p, n)Be^7$ threshold. The present data have, however, about a factor of ten smaller uncertainty in the threshold determinations. For the Be^9, B^{11}, and C^{13} thresholds, the error assigned (0.1 percent) is that of the absolute voltage scale. The comparison of these thresholds to the $Li^7(p, n)Be^7$ threshold as a standard can be made more precise than the absolute voltage scale is known. For all the other reactions, the yield near threshold is small enough that the selection of the extrapolated threshold is somewhat uncertain. Those assigned errors represent, therefore, a somewhat subjective estimate of this uncertainty.

Two earlier measurements of the O^{18} threshold have been reported.[13,14] Both used stacked foils technique and cyclotron accelerated protons. These measurements are unsuited for precise threshold determination.

For the vanadium reaction, Hanson, Taschek, and Williams[10] quote a threshold some 36 kev less than our observation. They do not estimate the uncertainty in

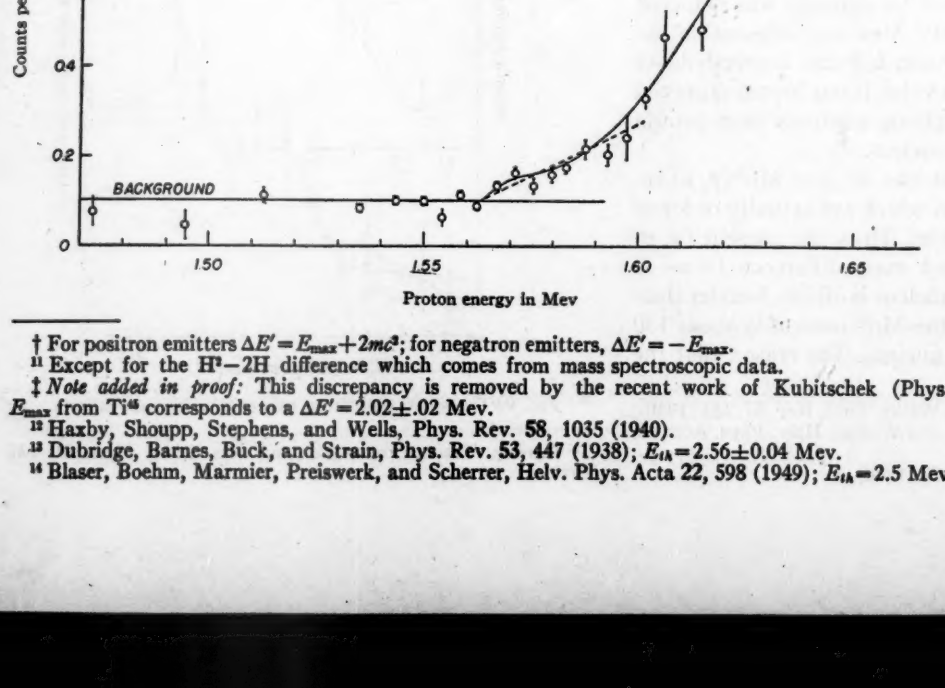

FIG. 11. Threshold data from a thick V_2O_5 target.

† For positron emitters $\Delta E' = E_{max} + 2mc^2$; for negatron emitters, $\Delta E' = -E_{max}$.

[11] Except for the H^3-2H difference which comes from mass spectroscopic data.

‡ *Note added in proof:* This discrepancy is removed by the recent work of Kubitschek (Phys. Rev. **79**, 23 (1950)) whose E_{max} from Ti^{45} corresponds to a $\Delta E' = 2.02 \pm .02$ Mev.

[12] Haxby, Shoupp, Stephens, and Wells, Phys. Rev. **58**, 1035 (1940).

[13] Dubridge, Barnes, Buck, and Strain, Phys. Rev. **53**, 447 (1938); $E_{th} = 2.56 \pm 0.04$ Mev.

[14] Blaser, Boehm, Marmier, Preiswerk, and Scherrer, Helv. Phys. Acta **22**, 598 (1949); $E_{th} = 2.5$ Mev.

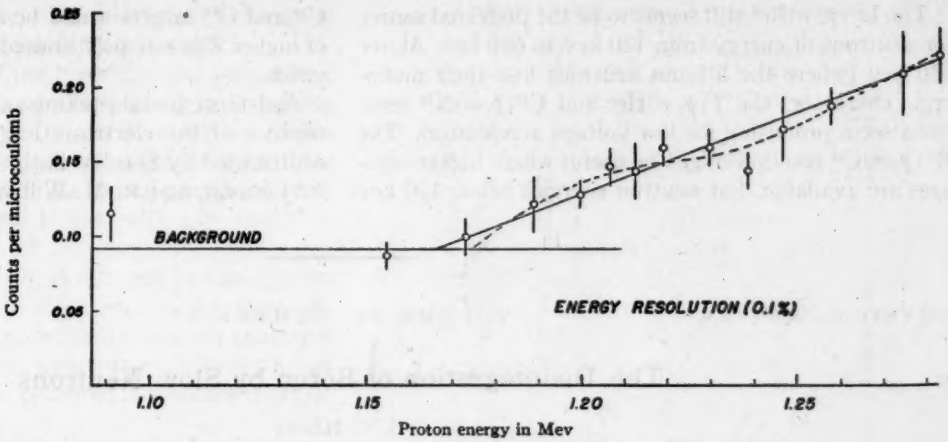

FIG. 12. Threshold data from a thick manganese target.

the result, but the published yield curve (Fig. 21, reference 10) would not appear to be in serious disagreement with our result.

The last three columns contain information useful to those contemplating these reactions as neutron sources. The neutron energy at threshold[10] (from center of mass motion) is $E_{th}/(M_1+M_2)^2$. The minimum energy monochromatic neutrons in the forward direction occur after the forward cone fills the forward hemisphere. This minimum energy is calculated in the next to the last column by setting $A_3=B_3$ (McKibben diagram notation)[10] and noting that $E_3=A_3^2+B_3^2+2A_3B_3\cos\phi=4A_3^2$ for $A_3=B_3$ and $\phi=0$.

The last column gives information which permits a calculation of the maximum neutron energy available from the reaction before the monoergic character of the neutrons is lost by possible excitation of the first excited state of the residual nucleus.

TABLE I. Summary of observed *P-N* thresholds for $Z\leq 25$.

Target and Product nuclei		Observed E_{th} (Mev)	$-Q$ (Mev)	ΔE (Mev)	$\Delta E'$ (Mev)	Threshold E_n (kev)	Min. E_n at 0° (kev)	Lowest excited level in Mev
H^2	2H	3.339±0.015[a]	2.225	1.442±0.010	1.442 ±0.00?[h]	371	1979	
H^3	He^3	1.019±0.001[b]	0.764	(used for $n-H$ diff.)	−0.0189±0.0005[i]	63.7	286.5	>2.5[m]
Li^7	Be^7	1.882±0.002[c]	1.646	+0.864±0.002	ϵ_k^-	29.4	120.1	0.435[n]
Be^9	B^9	2.059±0.002	1.852	1.070±0.002	P	20.6	83.4	>1.5[o]
B^{11}	C^{11}	3.015±0.003	2.762	1.980±0.003	2.003 ±0.005[j]	20.9	84.5	2.02[p]
C^{12}	N^{12}	20.0±0.1[u]	18.5	17.7 ±0.1	17.6[u]	118	477	—
C^{13}	N^{13}	3.236±0.003	3.003	2.221±0.003	2.222 ±0.003[k]	16.5	66.4	2.383[q]
C^{14}	N^{14}	0.664±0.009[d]	0.620	−0.161±0.009	−0.156 ±0.001[k]	2.9	11.8	2.3[k]
O^{18}	F^{18}	2.590±0.004	2.453	+1.671±0.004	+1.657 ±0.015[v]	7.2	28.8	
F^{19}	Ne^{19}	4.18 ±0.25[e]	3.97	3.09 ±0.25	3.22[e]	10.5	42	
Na^{23}	Mg^{23}	4.78 ±0.3[e]	4.58	3.80 ±0.30	3.84[e]	8.3	33	
Cl^{37}	A^{37}	1.640±0.004	1.598	0.816±0.004	ϵ_k^-	1.1	4.6	1.4[r]
A^{40}	K^{40}	≤2.4(?)[f]	2.3(?)	≤1.5(?) also see ref. s	ϵ_k^-	1.6	5.7	0.81[s]
K^{41}	Ca^{41}	1.25 ±0.02	1.22	0.44 ±0.02	ϵ_k^-	0.7	2.8	1.95[t]
Sc^{45}	Ti^{45}	~2.85[g]	2.79	2.01	2.28[l,w]	1.35	5.4	
V^{51}	Cr^{51}	1.562±0.006	1.532	0.750±0.006	ϵ_k^-	0.58	2.3	
Mn^{55}	Fe^{55}	1.18 ±0.01	1.16	0.38 ±0.01	ϵ_k^-	0.38	1.5	

[a] R. V. Smith, Ph.D. thesis, Univ. of Wisconsin, 1950 and unpublished work.
[b] Taschek, Argo, Hemmendinger, and Jarvis, Phys. Rev. 76, 325 (1949).
[c] Herb, Snowdon, and Sala, Phys. Rev. 75, 246 (1949); also Shoupp, Jennings, and Jones, Phys. Rev. 76, 502 (1949).
[d] Shoupp, Jennings, and Sun, Phys. Rev. 75, 1 (1949).
[e] White, Delsasso, Fox, and Creutz, Phys. Rev. 56, 512 (1939).
[f] H. T. Richards and R. V. Smith, Phys. Rev. 74, 1870 (1948).
[g] Hanson, Taschek, and Williams, Rev. Mod. Phys. 21, 635 (1949).
[h] T. R. Roberts and A. O. Nier, Phys. Rev. 77, 746A (1950).
[i] G. C. Hanna and B. Pontecorvo, Phys. Rev. 75, 983 (1949).
[j] A. A. Townsend, Proc. Roy. Soc. A177, 357 (1940–1941).
[k] NRC Nuclear Science Series No. 5.
[l] Allen, Pool, Kurbatov, and Quill, Phys. Rev. 60, 425 (1941).
[m] H. T. Richards and E. Hudspeth, Phys. Rev. 58, 382 (1940).
[n] Johnson, Wilson-Laubenstein, and Richards, Phys. Rev. 77, 413 (1950).
[o] Johnson, Ajzenberg, and Wilson-Laubenstein, Phys. Rev. 79, 187 (1950).
[p] W. M. Gibson, Proc. Phys. Soc. Lond. A62, 586 (1949).
[q] D. M. Van Patter, Phys. Rev. 76, 1264 (1949).
[r] J. C. Grosskreutz and K. B. Mather, Phys. Rev. 77, 580 (1950).
[s] V. L. Sailor, Phys. Rev. 77, 794 (1950).
[t] V. L. Sailor, Phys. Rev. 75, 1836 (1949).
[u] L. W. Alvarez, Phys. Rev. 75, 1815 (1949).
[v] Blaser, Boehm, and Marmier, Phys. Rev. 75, 1953 (1949).
[w] *Note added in proof:* This discrepancy is removed by the recent work of Kubitschek (Phys. Rev. 79, 23 (1950)) whose E_{max} from Ti^{45} corresponds to a $\Delta E'=2.02\pm.02$ Mev.

The $Li^7(p, n)Be^7$ still seems to be the preferred source for neutrons of energy from 120 kev to 640 kev. Above 640 kev (where the lithium neutrons lose their monoergic character) the $T(p, n)He^3$ and $C^{14}(p, n)N^{14}$ reactions seem promising for low voltage accelerators. The $B^{11}(p, n)C^{11}$ reaction might be useful where higher voltages are available. For neutron energies below 120 kev C^{14} and O^{18} targets would be attractive. Use of targets of higher Z is seriously limited by the very low neutron yields.

Assistance in data taking and in operation and maintenance of the electrostatic generator was generously contributed by Stanley Bashkin, Gerson Goldhaber, V. R. Johnson, and R. M. Williamson.

PHYSICAL REVIEW VOLUME 80, NUMBER 4 NOVEMBER 15, 1950

The Disintegration of Boron by Slow Neutrons

G. C. HANNA
Atomic Energy Project, National Research Council of Canada, Chalk River, Ontario, Canada

(Received July 13, 1950)

The total ionization produced by the Li^7 and α-particles from the $B^{10}(n, \alpha)Li^7$ reaction has been measured in an argon-boron trifluoride gas mixture, and that produced by the two particles separately with a thin boron film. Electron collection has been employed, using a fast amplifier feeding a 30-channel pulse-analyzer. The results indicate a departure from linearity in the relation between ionization and energy. Using the formula suggested by Cranshaw and Harvey in their work on natural α-emitters, values of the Q of the boron reaction have been obtained. They are 2.793 ± 0.027 Mev and 2.320 ± 0.020 Mev for the ground state and excited state transitions, in agreement with the recently published values of Tollestrup, Fowler, and Lauritsen. The branching ratio, that is the probability of the reaction going to the ground state, has been measured as 5.8 ± 0.1 percent.

I. INTRODUCTION

THIS investigation was undertaken primarily to measure the relative probabilities of the two reactions $B^{10}(n, \alpha)Li^7$ and $B^{10}(n, \alpha)Li^{7*}$. At that time (1947) the best value 1:15, due to Bøggild,[1] appeared to be limited in statistical accuracy. Moreover, the measurements on the energy release, which were summarized by Bøggild, were not in good agreement. It therefore seemed worth while to extend the scope of the experiment and make an accurate comparison of the ionizations produced by the boron reactions with that of Pu^{239} α-particles.

At first the total ionization of the Li^7 and α-particles was measured relative to that of the Pu^{239} α-particle in an ionization chamber containing boron trifluoride and argon. Later a thin boron film was used and the ionizations of the Li^7 and α-particles were measured separately, thus permitting a more reliable estimate to be made of the ionization-energy relation.

II. DESCRIPTION OF APPARATUS

The Ionization Chamber

The ionization chamber contained two plane parallel electrodes, 10 cm square and 6.6 cm apart, with a grid of parallel wires placed 1.5 cm in front of the electron collecting electrode. The wires in the grid were 0.12 mm in diameter and were spaced 0.95 mm apart. Such a grid is adequate for shielding the collector from the induced effect of the slowly moving positive ion component of the ionization.[2,3] The calibration source of Pu^{239}, deposited on a 1-cm diameter platinum disk, was mounted in the center of the negative electrode and covered with a simple collimator, a sheet of $\frac{1}{2}$-mm brass drilled with 1-mm holes. The electrodes were supported on glass insulators.

The chamber was sealed with a lead gasket so that it could be baked out (at about 200°C) in preparation for a boron trifluoride filling. The gasket was made of lead containing 1 percent of tin, an alloy which creeps much less than pure lead. High tensile steel bolts, $3\frac{1}{2}$ inches long and $\frac{1}{4}$ inch in diameter, were used to compress the gasket between heavy flanges. If short thick bolts were used the extension of the bolt for a given force on the gasket would be less, and any creep of the lead would quickly result in a loss of gasket compression.[4] A leak would then be likely to develop, particularly during the baking out procedure.

Chamber Fillings

The chamber was filled with argon (99.8 percent pure) containing 2 percent of boron trifluoride to a pressure of one atmosphere. The boron trifluoride was prepared from calcium fluoroborate by J. F. Steljes. No deteriora-

[1] J. K. Bøggild, Kgl. Danske Vid. Sels. Math.-Fys. Medd. 23, No. 4 (1945).

[2] Bunemann, Cranshaw, and Harvey, Can. J. Research A27, 191 (1949).

[3] T. E. Cranshaw and J. A. Harvey, Can. J. Research A26, 243 (1948).

[4] H. Carmichael, "Design of the Chalk River Ion Chambers" C.R. Tec-276 (1946).

tion in the gas filling could be detected, by change in pulse size, after standing for several months.

In the second stage of the investigation, using a thin boron film, the chamber was filled with argon containing 2 percent of carbon dioxide, again to a pressure of one atmosphere. The chamber was not baked out for these measurements, simple flushing being considered adequate. No change of pulse size with age could be detected.

Measurements were made at different operating voltages up to -2.5 kv on the high tension electrode (cathode) to check that saturation had been achieved. The grid was maintained at a negative potential of about half the cathode potential to ensure that it collected no electrons.

The Boron Source

The thin boron film was deposited on the cathode. A dilute aqueous solution of boric acid was sprayed on to the highly polished front surface of the electrode using a De Vilbiss No. 40 "Nebulizer". This device produces an exceedingly fine spray, but to avoid any coagulation of the droplets the electrode was kept heated (to about 120°C) during the spraying so that evaporation of the water was almost instantaneous. It is not possible with this technique to predict how much boric acid will be deposited, and the operation is accordingly a matter of trial and error. Finally the electrode was heated to about 200°C to convert the boric acid to boric anhydride (B_2O_3). This change can be observed as a return of the electrode to an apparently more highly polished state after the slight dullness caused by the initial boric acid deposition. (If it is necessary to keep the prepared film for any time before using it should be kept in a desiccator.) Boron of natural isotopic composition was used.

With the neutron flux available an adequate counting rate was an important consideration. Accordingly the film was not covered with a collimator. The thickness of the film was estimated, from the neutron flux and the observed counting rate, to be about 2 μg of B_2O_3 per square centimeter.

The Amplifier

To ensure a good signal-to-noise ratio the head amplifier was mounted directly onto the chamber. The head amplifier employed a ring-of-three feedback circuit to give high stability of gain. Its output was fed to the main amplifier via a cathode follower. The main amplifier consisted of two further rings separated by a condenser-resistance network determining the pulse shape. The ring-of-three circuit is a slightly modified version of that used by Cranshaw and Harvey.[3]

The amplifier was normally operated with a differentiating time constant of 4 μsec. and a smoothing time constant (to limit the band width) of about 1 μsec. That the use of such short time constants was permissible was demonstrated in subsidiary experiments with lower chamber operating voltages using the same band width, and with slower amplifier responses using the same operating voltages.

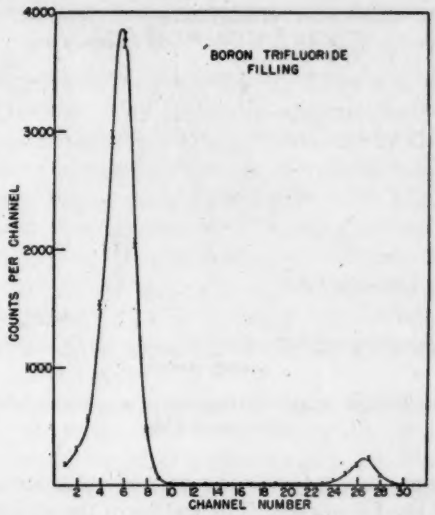

FIG. 1. Pulse height distribution from boron trifluoride showing the transitions to the ground state and excited state of the Li^7 nucleus.

Pulse Height Measurements

The spread in amplitude of the pulses was only a few percent. To obtain an accurate value for the most probable pulse height it is clearly desirable to extend this spread over several channels of the pulse-analyzer. This was accomplished by feeding the output of the main amplifier through a biased amplifier unit similar to the one described by Cranshaw and Harvey.[3]

The 30-channel pulse analyzer has been described by Westcott and Hanna.[5]

All pulse height measurements were made in terms of the output of a pulse signal generator which fed standard pulses, of adjustable amplitude, to the collecting electrode through a small (5 $\mu\mu$F) condenser.[6]

The Neutron Source

The measurements on boron trifluoride were made using a small polonium-beryllium source and a paraffin moderator. The slow neutron flux was about 10^2 neutrons/cm^2-sec. For the thin boron film work a stronger source was used to give a flux about 100 times larger. It will be noticed that the curves shown in Figs. 2 and 3 show a considerable background level at low energy. This background was due almost entirely to fast neutrons.

III. RESULTS

A typical pulse height distribution obtained with the boron trifluoride filling is shown in Fig. 1. The two peaks

[5] C. H. Westcott and G. C. Hanna, Rev. Sci. Inst. 20, 181 (1949).
[6] D. C. Brunton and G. C. Hanna, Can. J. Research A28, 190 (1950).

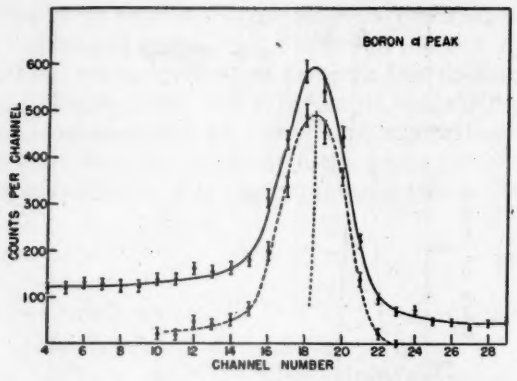

FIG. 2. Pulse height distribution of α-particles from a thin boron film.

arise from transitions to the excited state and ground state of the Li^7 nucleus. The widths of the distributions at half-maximum is 60 kev, almost all of which is due to amplifier noise, measured using the signal generator pulses.

The separate peaks due to Li^{7*} and the associated α-particle are shown in Figs. 2 and 3. The high fast-neutron background prevented measurements being made on the less probable transition to the ground state. The figures also show the peaks after the subtraction of the interpolated background level. The widths here are larger, about 80 kev, with a noticeable low energy asymmetry of the Li peak. The increase in width is due to a deterioration in the signal-to-noise ratio of the amplifier compared with the earlier runs. The asymmetry is probably due to the use of an uncollimated source. Self absorption of the oblique tracks in the source material would be more noticeable with the Li fragments because of their greater rate of loss of energy with distance penetrated. The recoil of the γ-ray, which is emitted during flight,[7] produces a total spread in energy of only 15 kev, which is not sufficient to affect the width appreciably.

Following Cranshaw and Harvey,[3] the position of the peaks was fixed by the method of drawing the central

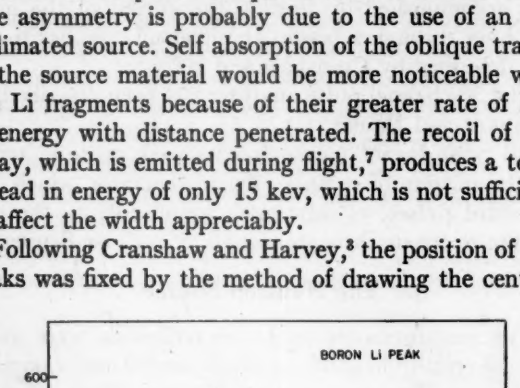

FIG. 3. Pulse height distribution of Li-particles from a thin boron film.

[7] L. G. Elliott and R. E. Bell, Phys. Rev. **74**, 1869 (1948).

line of the distribution. The agreement between the results from boron trifluoride and the thin boron film suggest that the asymmetry does not introduce an appreciable error if the most probable pulse height is taken as the measure of the ionization.

The results are summarized in Table I. I_1 and I_2 denote the ionizations produced by the α-particle and Li^{7*} ion respectively, when the reaction proceeds to the excited state, and I_1' and I_2' when the ground state is formed. I_3 denotes the ionization produced by the Pu^{239} α-particle.

The errors quoted are an attempt to give reasonable limits of error, the reproducibility of the measurements is considerably better.

From Table I we take a mean value of 0.431 ± 0.003 for $(I_1+I_2)/I_3$, and consequently adjust (I_1/I_3) to 0.279 ± 0.0025 and (I_2/I_3) to 0.152 ± 0.0015.

The experiments using boron trifluoride fillings gave a value of 5.8 ± 0.1 percent for the probability of the reaction going to the ground state of Li^7.

IV. EVALUATION OF ENERGIES

It will be noticed immediately that the ratio of ionizations I_2/I_1 is not equal to the energy ratio E_2/E_1, which by conservation of momentum $=4.0039/7.0182$ $=0.5705$. This is here ascribed to a difference in W, the mean energy (in electron volts) per ion pair produced, for the two particles. In fact, since $I_2/I_1=0.544\pm0.007$, $W_2/W_1=1.049\pm0.013$.

This result is in conflict with the measurements in air by Fünfer,[8] and in helium by Bower, Bretscher, and Gilbert,[9] who obtained respectively values of 0.77 and 0.82 for W_2/W_1. It may be remarked that such a large change as this in W is most unexpected in view of its relative constancy, pointed out for example by Gray,[10] for all other particles. If W increases as the velocity of the ionizing particle decreases one would expect a larger value of W for the more slowly moving Li-particle, that is $W_2/W_1>1$.

Cranshaw and Harvey[3] from their measurements on the natural α-emitters proposed a formula $W=27.5+1.9E^{-\frac{1}{2}}$ for α-particles in argon, where W is in electron volts/ion pair and E in Mev. Accepting this formula, then

$$W_1=27.5+1.9E_1^{-\frac{1}{2}}$$

and $$W_3=27.5+1.9E_3^{-\frac{1}{2}}=28.34 \text{ ev/ion pair.}$$

The ionization measurements give

$$I_1/I_3=(W_3/W_1)(E_1/E_3)=0.279\pm0.002_5.$$

Solving these equations by successive approximations we have, taking[3] $E_3=5.159$ Mev,

$$E_1=1.477\pm0.013 \text{ Mev, with } W_1=29.06.$$

[8] E. Fünfer, Ann. Phys. Leipzig **29**, 1 (1937).

[9] Bower, Bretscher, and Gilbert, Proc. Camb. Phil. Soc. **34**, 290 (1938).

[10] L. H. Gray, Proc. Camb. Phil. Soc. **40**, 72 (1944).

TABLE I. Ionization of the Li^7 and α-particles from the $B^{10}(n, \alpha)Li^7$ reaction.

Experiment	$(I_1'+I_2')/(I_1+I_2)$	$(I_1+I_2)/I_3$	I_1/I_3	I_2/I_3	I_2/I_1
BF_3	1.211±0.006	0.433±0.004	—	—	—
Thin B film	—	0.429±0.004	0.278 ±0.0025	0.151 ±0.0015	0.544 ±0.007

Now $E_2/E_1=0.5705$ (conservation of momentum) and we have immediately

$$E_2=0.843\pm0.007 \text{ Mev},$$
and $$Q=E_1+E_2=2.320\pm0.020 \text{ Mev}.$$

In order to analyze the ionization data in the case in which the boron reaction proceeds to the ground state it is necessary to make some assumptions about W for the Li-particle, since the ionization of the α-particle alone was not measured. We shall assume, somewhat arbitrarily but plausibly enough, that a Li-particle has the same value of W as an α-particle of the same velocity. If we evaluate E_2 from I_2/I_3 on this basis we obtain $E_2=0.837\pm0.008$ Mev, with $W_2=30.24$ (which is the value for an α-particle of energy 0.57×0.837 Mev). The agreement between this value of E_2 and that obtained from E_1 above is not to be taken as a complete justification of our assumption regarding W_2, and clearly the experimental errors permit some latitude. However it seems reasonable to make the same assumption in the analysis of the disintegration to the ground state.

Using the Q value $E_1+E_2=2.320\pm0.020$ Mev above, we obtain from $(I_1'+I_2')/(I_1+I_2)=1.211\pm0.006$, $Q'=E_1'+E_2'=2.793\pm0.027$ Mev, with $E_1'=1.778$ Mev, $W_1'=28.92$, $E_2'=1.015$ Mev, and $W_2'=30.00$.

If, on the other hand, W were assumed to be the same for all the particles involved (including the Pu^{239} α-particle) we should obtain $Q=2.224\pm0.019$ and $Q'=2.693\pm0.024$ Mev.

These values for Q and Q' should be compared with those obtained by Chao, Lauritsen, and Tollestrup[11] in magnetic deflection experiments: 2.316 ± 0.006 and 2.794 ± 0.006 Mev. In a later publication Tollestrup, Fowler, and Lauritsen[12] give "adopted" values of 2.313 and 2.791 Mev.

Our results are based on a value of 5.159 Mev for the Pu^{239} α-particle energy. Actually the collimator covering the Pu^{239} source was somewhat thicker than desirable; it consisted of 1-mm diameter holes in a plate $\frac{1}{2}$-mm thick. The collecting field will be weakened inside the collimator holes, and some loss of ionization by recombination will result. The correction is not easy to determine but it is estimated to be not more than 0.5 percent. If applied—which has not been done—the correction would reduce the energies given above by 0.5 percent—a difference less than the experimental error.

The results derived above are summarized in Tables II and III.

[11] Chao, Lauritsen, and Tollestrup, Phys. Rev. **76**, 586 (1949).
[12] Tollestrup, Fowler, and Lauritsen, Phys. Rev. **78**, 372 (1950).

V. THE RELATIONSHIP BETWEEN IONIZATION AND ENERGY

The agreement between our Q values and those of Chao, Lauritsen, and Tollestrup suggests that the empirical relation between W and E obtained by Cranshaw and Harvey from data at higher energies is valid in the low energy region also, and further that Li-particles spend much the same energy in creating one ion pair as do α-particles of the same velocity. Our data however are not sufficiently accurate to establish this relation uniquely. What is clear is that W is not constant in our experiments. This point will be further emphasized in this section in a more direct way.

In the previous section we were concerned with $W=E/I$, the mean value of the energy loss per ion pair over the whole range of a particle of initial energy E. Here we consider $W^*=dE/dI$, its instantaneous value at the energy E.

The theory (see for example Bohr's monograph[13]) indicates that the relative probability of excitation and of lightly-ionizing collisions (in which the energy losses are of the order of the ionization potential) is practically independent of the nature and velocity of the ionizing particle, provided its velocity is comfortably greater than that of the atomic electrons. Williams[14] has pointed out that although the number of violent collisions does depend on the velocity of the primary particle this is not important because nearly all of the energy is ultimately dissipated in subsequent lightly-ionizing collisions. This theoretical constancy of W^* at high energy is confirmed by the work of Cranshaw and Harvey and others, on α-particles, who found that the differences of the ionization produced are very closely proportional to the differences in energy.

At high energy then, greater than 4 Mev say, $W^*=dE/dI$ is constant. That is, $E=W^*I+\epsilon_0$, where ϵ_0

TABLE II. Final Q-values for the reaction $B^{10}(n, \alpha)Li^7$.

Particle		Energy, Mev	W, ev/ion pair
α	E_1	1.477±0.013, from I_1	29.06
Li*	E_2	0.843±0.007, from E_1 0.837±0.008, from I_2	30.24
α+Li*	$Q=E_1+E_2$	2.320±0.020, from E_1	(29.48)
α	E_1'	1.778±0.017	28.92
Li	E_2'	1.015±0.010 from Q'	30.00
α+Li	$Q'=E_1'+E_2'$	2.793±0.027, from Q and $(I_1'+I_2')/(I_1+I_2)$	(29.31)

TABLE III. Comparison of results for the energy values.

Experiment		Q	Q'	E_γ
Chao, Lauritsen, and Tollestrup		(2.316±0.006)	2.794±0.006	(0.478±0.001)
This work	W as above	2.320±0.020	2.793±0.027	0.473±0.013
	W constant	2.224±0.019	2.693±0.023	0.469±0.013

[13] N. Bohr, Kgl. Danske Vid. Sels. Math.-Fys. Medd. **18**, No. 8 (1948).
[14] E. J. Williams, Proc. Roy. Soc. **A135**, 108 (1932).

is a constant of integration. At intermediate energies, where W^* is not constant, we can still write $E=W^*I+\epsilon_\alpha$, where ϵ_α is a small energy (less than 100 kev) which diminishes as E gets less. This has a physical interpretation. Below a certain minimum energy the α-particle will produce no ionization, expending its energy in elastic collisions, so that $I=0$ and $\epsilon_\alpha=E$. At higher energies ionization becomes a progressively more probable event (ϵ_α increasing with, but not as fast as, E) until finally, at a sufficiently high energy which is here taken as 4 Mev, the fraction of energy absorbed in ionization attains a constant value, and ϵ_α also reaches its maximum and constant value ϵ_0.

The interpretation of experimental results in terms of this ϵ_α, which appears as a slowly varying correction term, has much to recommend it. In a number of published researches conclusions have been based on the assumption of a constant W with neglect of ϵ_α. With a knowledge of the magnitude of the latter the energy error introduced by this procedure can be appreciated immediately. Data from which the magnitude of ϵ_α (and the corresponding correction energies ϵ_A for ions of character A) can be evaluated are at present scarce and not very continuous. It therefore seems worth while to present the experimental results reported above in terms of ϵ_α and ϵ_{Li}, which can be done if it is assumed that the energies determined by Chao, Lauritsen, and Tollestrup by a quite independent method are correct. (Actually we shall take here the "adopted" Q value of $2.791-0.478=2.313$ Mev.)

We write then for the Pu α-particle, and the α-particle and Li-particle from the excited-state disintegration, respectively,

$$\left.\begin{aligned} W^*I_3&=E_3-\epsilon_\alpha-\Delta\epsilon_\alpha \\ W^*I_1&=E_1-\epsilon_\alpha \end{aligned}\right\}$$

and

$$W^*I_2=E_2-\epsilon_{\mathrm{Li}}$$

As explained above, we expect $\Delta\epsilon_\alpha$, which is here indeterminate but positive, to be considerably smaller than ϵ_α.

The solution of these equations, using Tollestrup, Fowler, and Lauritsen's values of $E_1=1.473$ Mev, $E_2=0.840$ Mev, and Cranshaw and Harvey's value of $E_3=5.159$ Mev, with $I_1/I_3=0.279\pm0.002_5$ and $I_2/I_3=0.152\pm0.001_5$, gives

$$\epsilon_\alpha=47+0.39\Delta\epsilon_\alpha\pm17 \text{ kev}$$

and

$$\epsilon_{\mathrm{Li}}=65+0.20\Delta\epsilon_\alpha\pm10 \text{ kev}.$$

While it is possible to derive a further value for $(\epsilon_\alpha+\epsilon_{\mathrm{Li}})$ from the measured value of $(I_1'+I_2')/(I_1+I_2)$ the experimental errors deprive it of any significance. (The points are too close together to give adequate information on the slope of the $I:E$ curve.)

Since $\Delta\epsilon_\alpha$ is positive, ϵ_α and ϵ_{Li} cannot be zero, that is W is not constant. If $\Delta\epsilon_\alpha$ is set equal to zero, we have $\epsilon_{\mathrm{Li}}/\epsilon_\alpha=65/47=1.4\pm0.5$. On simple theory we would expect $\epsilon_{\mathrm{Li}}/\epsilon_\alpha\approx M_{\mathrm{Li}}/M_\alpha=1.75$.

The results of these ionization measurements are significantly different from those obtained by Jesse, Forstat, and Sadauskis[15] in argon containing 0.1 percent of boron trifluoride, and our conclusions regarding the relationship between ionization and energy are in conflict with their general thesis of constancy of W in pure argon.

An explanation of this discrepancy may lie of course in the purity of the gases used. The argon used by Cranshaw and Harvey, whose results we confirm, was not of spectroscopic purity; it was cylinder argon nominally 99.8 percent pure. But then, if this were an important factor, the argon containing 0.1 percent of boron trifluoride used by Jesse, Forstat, and Sadauskis would be expected to behave differently.

Along with Cranshaw and Harvey we are measuring only the immediately available electronic component of the ionization. Jesse, Forstat, and Sadauskis, using a slow recorder, measure the total ionization. It is possible that in pure argon atoms in metastable states of excitation can release delayed secondary electrons from the electrodes of the ionization chamber, an effect which might not unreasonably be expected to increase in relative importance for slower ionizing particles. Such secondaries would be missed if fast electron collection were employed. The magnitude of such an effect would however seem to be too small.

The author wishes to thank Mr. J. F. Steljes for his help with boron trifluoride and Mr. N. Moss who made the plutonium source. He is especially grateful to Mr. J. Emerson for the initial construction of the ionization chamber and much assistance in the early stages, and to Drs. W. B. Lewis, B. W. Sargent and W. N. English for helpful discussions.

[15] Jesse, Forstat, and Sadauskis, Phys. Rev. 77, 782 (1950).

N-Component in Extensive Air Showers†

K. GREISEN, W. D. WALKER,* AND S. P. WALKER*
Cornell University, Ithaca, New York

(Received July 6, 1950)

The high energy *N*-component, capable of producing penetrating showers, has been found to have an intensity near the cores of air showers about 60 percent as great as that of the non-interacting penetrating particles, and about ½ percent as great as that of the electrons. The ratio of charged to neutral *N*-component is about 1.5. Large penetrating showers are more frequently observed to be associated with air showers than are small penetrating showers. It is suggested that all of the *N*-component in the lower atmosphere belongs to extensive showers and contributes to the shower development. Near the core, the lateral density distribution of the *N*-component is found to be as strong as that of the electrons. It is shown that this results from purely geometric considerations, provided one accepts the concept of a core containing *N*-component of great energy, continually feeding out lower energy particles to the side.

I. INTRODUCTION

THAT particles with strong nuclear interaction, or *N*-component, exist in the extensive air showers has already been shown by cloud chamber photographs,[1–3] by Geiger counter experiments on penetrating showers[4,5] and on penetrating particles in air showers,[6–8] and by detection of groups of low energy neutrons produced by penetrating particles in the air showers.[9,10]

The experiment described below was undertaken to add to the quantitative information concerning the *N*-component of high energy in extensive air showers. The experiment was carried out at Mt. Evans, Colorado; elevation about 4260 meters, mean pressure about 616 g/cm².

The *N*-component and μ-meson detector consisted of the heavily shielded array of 85 counters shown in Fig. 1. We refer to this below as the *PP* (penetrating particle) detector. The absorber thickness above trays A_1 and A_2 of the *PP* detector was varied from 13 inches of lead to zero. In most of the measurements, this absorber was thick enough to prevent electrons of the air showers from reaching tray *A*. The lower trays were further protected from incident electrons by the other layers of lead and iron.

To detect the air showers, there were two trays of unshielded counters, one situated at 7 meters from the shielded array, and one at 26 meters. In each tray were 5 large counters (usually of area 560 cm² each) and 3 small counters (each of area 29 cm²). For brevity we shall henceforth call the unshielded trays *ED* (electron density) detectors.

Mixing circuits allowed the selection of events in which at least one of the unshielded counters was struck simultaneously with a preselected minimum number of counters, n, in each of the trays *B*, *C*, *D* of the *PP* detector. Such a coincidence is called *AS* (air shower) $+B^nC^nD^n$. The resolving time for this coincidence was about 5 μsec. Thereupon a master pulse was generated, which was put in coincidence with each of the 101 individual counters, with a resolving time of about 30 μsec. An array of neon bulbs was photographed to show which counters had been struck.

During most of the running time, the trigger requirement was $AS+B^2C^2D^2$. For comparatively short times, the requirement was reduced to $AS+B^1C^1D^1$, or to $B^2C^2D^2$ (at least two penetrating particles, but without the requirement that an unshielded counter be struck). The coincidence rate $B^2C^2D^2$ was continually recorded with a mechanical register.

The observation of which counters had been struck in the *ED* detectors permitted a grouping of the showers according to the electron density at 7 m and at 26 m from the *PP* detector. The simultaneous use of counters of two sizes provided a rather wide range over which the density could be roughly determined.[11]

II. EXAMPLES AND INTERPRETATION OF COMMON EVENTS

Figures 2A to 2D show illustrations of some of the types of events recorded with the trigger $AS+B^2C^2D^2$. In these drawings we have blackened the circles representing the counters struck in the *PP* detector.

In general, we interpret a coincidence of the type $AS+B^2C^2D^2$ as a penetrating shower associated with an air shower, unless the counters struck in the *PP* detector are so located as to indicate parallel particles arriving from the air, or a single particle strongly inclined rela-

† Some of the apparatus used in this experiment was made available through a contract with ONR.

* Now at Rice Institute, Houston, Texas.

[1] W. B. Fretter, Phys. Rev. **76**, 511 (1949).
[2] J. Ise, Jr., and W. B. Fretter, Phys. Rev. **76**, 933 (1949).
[3] W. W. Brown and A. S. McKay, Phys. Rev. **76**, 1034 (1949).
[4] J. Tinlot and B. Gregory, Phys. Rev. **75**, 520 (1949).
[5] K. Sitte, Phys. Rev. **78**, 721 (1950).
[6] Cocconi, Tongiorgi, and Greisen, Phys. Rev. **76**, 1020 (1949).
[7] B. Chowdhuri, Proc. Phys. Soc. **A63**, 165 (1950).
[8] G. T. Zatsepin and L. E. Sarycheva, Dokl. Akad. Nauk. SSSR **69**, 635 (1949).
[9] V. Cocconi Tongiorgi, Phys. Rev. **74**, 226 (1948); **75**, 1532 (1949).
[10] G. Cocconi and V. C. Tongiorgi, Phys. Rev. **79**, 730 (1950).

[11] During the experiment, the larger counters in the *ED* were changed from 560 to 196 cm² each, which necessitates an extra subdivision of the data given below. The reason for the change was a rapid deterioration of the large counters which finally made it impossible to continue their use. We do not believe these troubles introduce significant unreliability in our data, since we tested the counters frequently, replaced bad ones, and discarded all data taken with questionable counters.

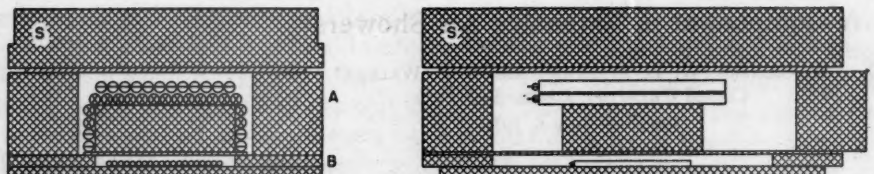

FIG. 1. Cross sections of the *PP* detector. The thickness of the absorber above the top tray, *A*, was varied from 13 inches of lead to zero.

tive to the zenith. The first question we must decide is whether or not a large fraction of these events could be due to other phenomena.

A. Electrons and Photons Penetrating through the Lead

We shall give primary emphasis to the data taken with 5 to 13 inches of lead (plus $\frac{3}{8}$ inch iron) above tray *A*. Between trays *A* and *B* was another 4 inches of lead (and $\frac{1}{4}$ inch iron). As shown in Fig. 1, the 4-inch absorber between *A* and *B* did not completely cover the ends of trays *C* and *D*, which were wider than *B*. However, between tray *B* and the lower trays were two broad layers of absorber, so that even the ends of tray *C* were covered in the vertical direction with 7 to 15 inches of lead plus an inch of iron. With the maximum absorber in place (i.e., for about half of our data), the lowest tray, *D*, was covered with 57 cm of absorber over most of its area, and 47 cm over the ends.

The side and end shielding was about 6 inches of lead. Since only badly scattered particles (i.e., those of low energy) travel horizontally, the effective thickness for particles from the side was considerably more than 6 inches. Moreover, showers from the side could be recognized in the hodoscope records.

It is essential that it be accepted that electron showers incident from the air could not penetrate to all the counter trays except with negligible frequency, and that even the penetration to trays *B* and *C* be rare. According to our previous experiments and calculations,[12,13] we believe the absorber thicknesses were more than sufficient to assure this.

Indeed, even when no lead was above tray *A*, the bottom tray was protected in the vertical direction over most of its area by 8 inches of lead plus an inch of iron, and over the edges by 4 inches of lead plus an inch of iron. Therefore, even in this case, the background effects due to penetration of electrons and photons are expected to be small compared with the rates of the penetrating showers that were recorded.

Further guarantee that electrons and photons penetrating the lead were unimportant is given by the dependence of the rate $AS+B^2C^2D^2$ on the thickness of lead above the top tray (Table I).

B. Cascade Showers Generated by Single Mesons

The knock-on and radiation processes of mesons could produce a serious background if the mesons were as abundant, compared with the *N*-component, as in the cosmic rays not associated with dense air showers (see the following paper). However, associated with extensive air showers we observe the penetrating showers to be almost as frequent as the single penetrating particles. Therefore the small probabilities of mesons to produce multiple knock-ons or high energy cascade showers are negligible.

C. Inclined Mesons

A single meson travelling in a strongly inclined direction could strike two counters in each of the trays *B*, *C*, *D*. It would then either miss tray *A* or strike one of the side counters of the tray. Some events of this sort did occur, but they were easy to recognize and eliminate (see Fig. 2D). In almost every case only one of the unshielded counters was struck, indicating that these were chance coincidences of single mesons with unassociated particles striking an unshielded counter.

D. Chance Coincidences

Because of the high counting rate in the unshielded counters (430/sec. in each *ED* detector), there was a significant probability that a penetrating shower should be coincident by chance with an unassociated discharge of a single counter in one of the two unshielded sets. This probability was approximately 0.003 per *ED* detector or 0.006 for both trays when the larger counters were used, and 0.0025 for both trays when the smaller counters were used. The chance coincidence rate was about 20 percent of the coincidence rate observed for penetrating showers and single unshielded counters. The chance coincidences with showers striking more than one counter in an *ED* detector were negligible.

These facts are verified by the observation (see Figs. 4 and 6) that the frequency of coincidences between penetrating showers and particles in the *ED* at 7 meters was much greater than that of coincidences with the *ED* at 26 meters.

[12] Cocconi, Tongiorgi, and Greisen, Phys. Rev. **75**, 1063 (1949).
[13] K. Greisen, Phys. Rev. **75**, 1071 (1949).

In addition to the background effects listed above, there are other sources of error which affect our conclusions concerning the point in the absorber at which the penetrating shower begins, whether the penetrating shower is initiated by a charged or neutral particle, or whether non-interacting particles are present in addition to one or more penetrating showers. These uncertainties arise mainly from the ejection of secondary particles backwards or to the side, and from successive interactions occurring in a single penetrating shower. However, these errors do not lead to false indication that a penetrating shower has occurred.

III. ANALYSIS OF EVENTS RECORDED WITH THE TRIGGER $AS+B^2C^2D^2$

The pictures showing air showers plus two or more penetrating particles were examined and subdivided into the following classes:

(1) Side showers: penetrating showers or mesons coming from the side, so as to strike the side counters of tray A or miss tray A altogether. These events are excluded as being outside the solid angle in which particles are accepted.

(2) Parallel tracks of penetrating particles: we list the number of events of this type, not the number of tracks.

(3) Penetrating showers starting in the absorber above tray A.

(4) Penetrating showers starting in the "producing layer" between trays A and B. Type 4 was further subdivided according to whether the primary particle initiating the shower appeared to be neutral or charged.

Table II presents this subdivision of the data for three thicknesses of absorber above tray A.

One cannot deduce "mean free path" values from the data of Table II, for the following reasons: (a) when the absorber was 5 inches Pb, electrons could penetrate as far as the counters of tray A, and make showers appear to start above this tray when in reality they started below it; and (b) layers of absorber added on top are not as efficient in producing detectable showers[14] as the layers below tray A, because of the absorption of the secondaries and because of the smaller solid angle subtended by the lower trays at the point of origin of the shower. Both of these effects tend to reduce the variation of the ratio of PS produced below A to PS produced above A, as the absorber is increased.

Nevertheless, the observed decrease of the ratio PS produced below A to PS produced above A, as the absorber is increased, helps to verify that most of the apparent penetrating showers were not caused by μ-mesons, because mesons that can produce penetrating cascades or multiple knock-ons should not be appreciably absorbed in 8 inches of lead.

One can derive an approximate ratio of mesons to N-component in the air showers from the frequency of parallel tracks compared with that of penetrating showers. Let M and N represent the numbers of mesons and N component relative to the total number of charged particles in the showers, and let Δ represent the shower density. Then, assuming that the mesons and nucleons are distributed in constant proportion to the electrons, the frequency of observation of pairs of mesons is given by:

$$K\int_0^\infty \tfrac{1}{2}(MS\Delta)^2 e^{-MS\Delta}\cdot e^{-NS\Delta}(1-e^{-S'\Delta})\Delta^{-\gamma}d\Delta.$$

Here S is the area of the shielded counters and S' the area of the unshielded counters. The term $\exp(-NS\Delta)$ enters because two parallel tracks could not be observed in the presence of a penetrating shower. The term $[1-\exp(-S'\Delta)]$ is the probability that the unshielded tray be struck.

TABLE I. Dependence of the rate $AS+B^2C^2D^2$ on the lead absorber above the top tray.

Absorber above tray A	Rate (min.$^{-1}$) $AS+B^2C^2D^2$
5″ Pb, 148 g/cm^2	0.155±0.010
9″ Pb, 260 g/cm^2	0.130±0.005
13″ Pb, 370 g/cm^2	0.114±0.004

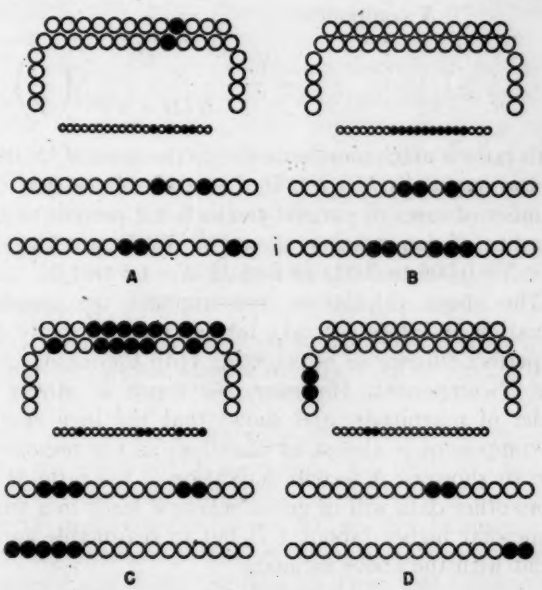

FIG. 2. A. Small penetrating shower initiated in the "producing layer" beneath tray A by a single ionizing particle. Two unshielded counters were struck at 7 meters distance, and none of 26 meters. The lead above tray A was 13″ thick. B. Penetrating shower initiated in "producing layer," under 13″ Pb, by a neutral particle. Two unshielded counters were struck at 7 m and one at 26 m. C. Penetrating shower of a kind seen more frequently than the types in Figs. 2A and 2B. It was initiated in the 13″ Pb above tray A, but further multiplication apparently occurred beneath tray A. One cannot trace the paths of individual particles. D. Most frequent spurious event, caused by single meson from the side. In practically all cases of this sort, only one of the unshielded counters was struck. These events are probably chance coincidences of mesons with unassociated particles in the air, rather than real associations of mesons with air showers.

[14] E. P. George and A. C. Jason (1950). We are grateful to the authors for communicating their results prior to publication.

TABLE II. Subdivision of events with trigger requirement $AS+B^2C^2D^2$.

Absorber above tray A	Side showers	Parallel tracks	PS starting above A	PS in producing layer: Neutral primaries	PS in producing layer: Charged primaries	Ratio: $\frac{PS \text{ below } A}{PS \text{ above } A}$
5″ Pb 148 g/cm²	62	5	181	19	29	0.265±0.043
9″ Pb 260 g/cm²	109	3	386	27	53	0.207±0.025
13″ Pb 370 g/cm²	227	10	716	34	78	0.156±0.016
Totals	398	18	1263	80	160	

With the same notation, the frequency of observed N-component is

$$K\int_0^\infty (1-e^{-NS\Delta})(1-e^{-S'\Delta})\Delta^{-\gamma}d\Delta.$$

By using the approximation that S' is large compared with MS and NS, one can reduce the ratio of the above integrals to:

$$\frac{\text{Double mesons without } N \text{ component}}{N \text{ component}} = \frac{\gamma-2}{2}\frac{M^2}{N(M+N)^{3-\gamma}}\left(\frac{S}{S'}\right)^{\gamma-2}.$$

This ratio is much more sensitive to the ratio M/N than to the quantity $(M+N)$. In Table II we see that the number of cases of parallel tracks is 1.2 percent of the number of penetrating showers. With[15] $\gamma=2.4$ and $M+N=0.005$ to 0.02, we find $M/N=1.5$ to 1.0.

The above calculation oversimplifies the physical situation and does not take into account correctly the imperfect efficiencies of detecting both the mesons and the N-component. However, the result is correct in order of magnitude, and shows that the high energy N-component is almost as abundant as the mesons in the air showers. A second derivation of the ratio M/N from other data will be given below; it leads to a value somewhat higher (about 1.7) but in reasonable agreement with the above estimate.

IV. RELATIVE NUMBERS OF NEUTRAL AND CHARGED PARTICLES

Only the showers beginning below tray A can be separated according to the sign of the initiating particle. The total number of apparently neutral-primary events is 80, and of charged-primary events is 160, so that it appears at first glance that the neutral N-component is $\frac{1}{3}$ of the total.

However, it is known from other experiments[16] that when a neutron produces a penetrating shower, a back projected particle frequently makes it appear that the primary was charged. Also, in a small percentage of the events the neutral particle that produces a penetrating shower will be accompanied in the air shower by an independent charged particle. Similarly, a fraction of the showers produced by charged particles will be missed because back projected secondaries or accompanying particles make it appear that the shower began above tray A instead of below. The net result of these effects is to increase the apparent ratio of charged to neutral primaries.

From the recognizable cases in the hodoscope records, and from the data of Walker[16] and other unpublished information, we have estimated the corrections, with the result that the ratio of charged to neutral particles is 1.5±0.3. The error listed includes an estimate of the uncertainties in the corrections, as well as the statistical error.

V. RELATIVE NUMBERS OF μ-MESONS AND N-COMPONENT

A better evaluation of the relative numbers of μ-mesons and N-component can be made from the pictures taken under the trigger requirement of $AS+B^1C^1D^1$, when single penetrating particles as well as penetrating showers could be seen.

In order to reduce the effects of chance coincidences we consider only the events in which two or more of the unshielded counters were struck. Even with this restriction of the data, a large fraction (about 40 percent) of the cases of "single mesons plus air showers" are casuals.

The use of the criteria for discriminating between mesons and N-component is illustrated by the data of Table III, where the pictures have been classified according to the thickness of lead above tray A and the multiplicity of counters struck in rows B, C, and D.

In examining Table III, we see that class 5 (penetrating showers) is about half of class 1 (mostly mesons) independently of the thickness of lead. This independence can be explained by the long range of the energetic penetrating showers.

Class 2 is 25 percent of the sum of classes 1 and 2. If both of these classes represent single penetrating particles, a knock-on probability of 8 percent per layer of absorber is indicated. This is in close agreement with the value of 7 percent reported by Brown, McKay, and Palmatier,[17] and indicates that almost all the events of class 2 should be considered as single penetrating particles that generate knock-on electrons, and not as nuclear disintegrations.

Classes 3 and 4 contain too many events (9 percent of the penetrating particles) to be entirely due to double knock-ons and the small fraction of the knock-on secondaries that can penetrate 2″ Pb plus ⅜″ Fe. Some of them must represent penetrating showers either of

[15] J. Treat and K. Greisen, Phys. Rev. 74, 414 (1948).
[16] W. D. Walker, Phys. Rev. 77, 686 (1950).
[17] Brown, McKay, and Palmatier, Phys. Rev. 76, 506 (1949).

small size or starting below tray *B*. These events are few enough so that precision is not needed in the assignment. We estimate that $\frac{1}{3}$ of them are due to electronic secondaries of single penetrating particles, and $\frac{2}{3}$ are due to energetic nuclear disintegrations.

Thus, we have a total of 96 recognized arrivals of *N*-component and 220 single penetrating particles. To these numbers the following corrections must be applied:

(1) Chance coincidences account for about 85 of the cases of single penetrating particles plus air showers.

(2) Failure of the *N*-component to interact in the absorber above tray *B* makes 7 percent of the charged *N*-component appear as single penetrating particles, and 7 percent of the neutral *N*-component fail to be recorded at all.

(3) Single mesons are apt to be missed in the presence of a penetrating shower. By using the approximate meson and *N*-component intensities relative to the electrons, and integrating over the density spectrum of showers that strike the *ED* detectors, we find that 9 percent of the mesons were probably accompanied by *N*-component and therefore escaped observation.

(4) Although strongly inclined penetrating showers were eliminated by examination of the hodoscope records, the effective area for detection of the *N*-component was nevertheless greater than the effective area for single mesons, because of the spread of penetrating showers and because the "producing layer" between trays *A* and *B* was larger in area than tray *B* (144 sq. in. as compared with 100 sq. in. for tray *B*). We estimate the correction as 20 percent plus or minus 10 percent.

After applying these corrections, we have for the ratio of *N*-component (including both charged and neutral *N*-component) to mesons in the air showers,

$$N/M = 0.60 \pm 0.15.$$

The uncertainty we have listed includes both the statistical standard error and the estimates of uncertainties in the corrections. Sitte[5] has obtained a considerably lower value for the ratio N/M, 0.26 ± 0.03, which seems inconsistent with the data analyzed in the present section, and with the data analyzed above in Section III, where we found $N/M = 0.8 \pm 0.2$. His measurements were made at an altitude 1000 meters lower than the present ones, but the chief cause of the discrepancy probably lies in a difference in the energy and geometric requirements imposed on the recorded nuclear interactions.

VI. COMPARISON OF PENETRATING SHOWERS ASSOCIATED AND NOT ASSOCIATED WITH AIR SHOWERS

The penetrating showers observed both associated and not associated with air showers have been classified according to size, as indicated by the number of counters struck in the lowest row, *D*. The relative frequencies are shown in Fig. 3, with the associated and non-associated events normalized to be equal in number for the smallest

TABLE III. Classification of events seen with trigger $AS^2+B^1C^1D^1$.

Pb above tray *A*	5″	9″	13″	Totals
Class 1: Single particles with no secondaries observed in either of the rows *B*, *C*, *D*	25	76	59	160
Class 2: Single particles with secondary observed in one row only	8	26	20	54
Class 3: Secondary observed in row *B* and row *D* but not in row *C*	0	5	2	7
Class 4: Secondary observed in two adjacent rows	1	3	8	12
Class 5: Penetrating showers, recognized by multiplicity in all 3 rows, or by high multiplicity (4 or more) in 2 rows	13	43	27	83

showers, that struck only two counters in row *D*. The total number of counters in row *D* was 16.

The difference between the two histograms shows that the large penetrating showers are more often associated with dense air showers than are the small penetrating showers.

This is also illustrated by the data presented in Table IV, where we compare the fractions of the penetrating showers that are associated with observed air showers, for all penetrating showers that strike two or more counters in row *D*, and for the showers that strike seven or more counters in row *D*. It may be seen that a comparatively large fraction of the big penetrating showers are associated with observable air showers.

Occasionally, huge penetrating showers or groups of such showers occurred that discharged all or almost all of the 85 counters of the *PP* detector. In every such case, an accompanying air shower was detected.

These results support the view that all of the *N*-component is associated with extensive air showers, but that the particles of higher energy are more apt to be found near the core or in a shower of great density, than are the particles of lower energy.

VII. DISTRIBUTION OF DENSITIES OF RECORDED AIR SHOWERS ACCOMPANYING PENETRATING SHOWERS

For each event of the type $AS+B^2C^2D^2$ an approximate shower density measurement was made at 7 m and at 26 m from the *PP* detector, on the basis of the number of unshielded counters struck. By following an analysis similar to that of Cocconi, Tongiorgi, and Greisen,[6] and using the data of Treat and Greisen on Mt. Evans[15] for the *a priori* probabilities of showers of different densities, most probable and median densities were calculated for the different counter combinations, which were then grouped into density classes as listed in Table V. For the extreme classes the probability distributions are not very steep so that individual events may differ from the most probable or median density by a rather large factor, but for the other classes the error in an individual density assignment should seldom be more than a factor three.

The experimental results did not seem to be sensitive

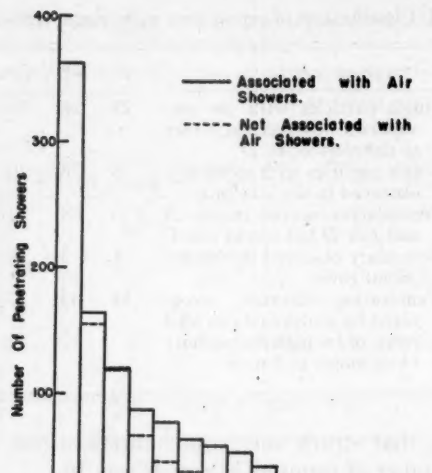
Associated with Air Showers.
Not Associated with Air Showers.
Number Of Penetrating Showers
Number Of Counters Struck In Row D
0
100
200
300
400
2 3 4 5 6 7 8 9 10 11 12 13 14 15 16

FIG. 3. Distribution of penetrating shower sizes as indicated by number of counters struck in the lowest counter tray, D. The non-associated showers, represented by the dashed line, have been normalized to the associated showers at $D=2$, by multiplying the observed number of local events by a factor 1.36. Both histograms include showers beginning above tray A as well as below tray A.

to the amount of absorber used; therefore in Fig. 4 we have put together the data obtained with 5″, 9″, and 13″ Pb above tray A. Figure 4 lists the numbers of cases falling into the various density classes at the two *ED* detectors. For all of these data the unshielded counters in each *ED* detector consisted of 5 counters of 560 cm² each, and 3 of 29 cm² each.

Chance coincidences and showers or mesons coming from the side were not removed from the tabulation in Fig. 4, but occur almost entirely in the groups 0—I and I—0; i.e., coincident with only a single counter pulse in one of the *ED* detectors. It may be noted that such coincidences were more than twice as frequent with the *ED* at 7 m as with the *ED* at 26 m, showing that only a small fraction of the showers detected at 7 m were casuals. On the other hand, we know from the resolving time of the circuit that a large fraction (about 200 cases in Fig. 4) of the events in which no counter was struck at 7 m and only one was struck at 26 m were chance coincidences. Of the more dense showers, a negligible number were casuals.

From the data of Fig. 4, the integral density distributions were derived that are shown in Fig. 5. In drawing these curves it was assumed that half of the showers in each density class had densities above the calculated median density for that class, and that the remainder had densities above the median density of the next lower class. This should be true in first approximation for all the classes appearing in the graph. Class 0 and half of class I are not included; and class I has been corrected for the chance coincidences.

The curves represent the frequencies of extensive showers that (a) are associated with a recorded penetrating shower, (b) strike the *ED* detector with at least one particle, and (c) have a density greater than the corresponding abscissa. As the density decreases below 10 particles/m², an increasing fraction of the associated air showers miss the *ED* detectors entirely. If this did not occur, the curves would continue to rise with decreasing density, as shown by the dashed extension of the "calculated distribution."

For comparison with the data, a theoretical curve has been included in Fig. 5, representing the *a priori* probability distribution of recorded showers of density greater than Δ. This is given by:

$$F(\Delta)=243\int_{\Delta}^{\infty}\delta^{-2.4}d\delta[1-\exp(-S'\delta)]\times[1-\exp(-NS\delta)]\text{ per min.}$$

Here the first term in brackets represents the probability that an unshielded counter be struck, and the second term in brackets is the probability that N-component hits the *PP* detector. The coefficient 243 (per minute) was taken from the counting rates of Treat and Greisen;[15] the areas S and S' were taken as 0.065 and 0.27 meter respectively; and for N, the number of penetrating shower producers per electron, the value 1/200 was assumed.

The assumption of perfect correlation between N-component and electron densities, which is implicit in this equation, means that the curve should be most nearly correct for an *ED* detector at zero meters from the *PP* detector.

The agreement in shape between the calculated and experimental curves is satisfactory. The absolute values on the calculated curve are higher than the measured values, but there are several reasons for this to be so, even if our estimate of the ratio between N component and electron density is correct. First, there is the 7-meter separation between the N-component detector and the nearer *ED* detector, which accounts for about 30 percent loss in counting rate, if the N-component is distributed similarly to the electrons.[12] Secondly, there is the inefficiency of the N-component in causing coincidences of the type $B^2C^2D^2$ (see Section V above). This is accentuated by the fact that most of the data in Figs. 4 and 5 were taken with 9″ or 13″ Pb above tray A, and the average rate was 22 percent lower than the rate under 5″ Pb. Therefore one should expect the experimental data to fall lower than the calculated curve by a factor of 0.4 to 0.5, about as observed.

Hence we conclude that the amount of high energy N-component relative to the electrons is about 0.005, as assumed in the calculations. We believe this to be correct within 40 percent. The uncertainty in the lower energy limit of the detected N-component makes higher precision scarcely meaningful. It must be emphasized that this relative intensity was determined only near the cores of the air showers, and may be quite different from the relative intensity of nucleons and electrons far from

TABLE IV. Penetrating showers associated and not associated with observed air showers. Rates corrected for casuals and events from the side.

$B^2C^2D^2$	3.23 ±0.15 min.$^{-1}$
$AS+B^2C^2D^2$	0.102±0.005 min.$^{-1}$
Ratio	3.2 percent
$B^2C^2D^7$	0.34 ±0.04 min.$^{-1}$
$AS+B^2C^2D^7$	0.031±0.002 min.$^{-1}$
Ratio	9 percent

the core. Moreover, it applies to both charged and neutral *N*-component.

In Section V we found that the *N*-component was about 60 percent as numerous as the μ-mesons. This would indicate that the meson intensity relative to the electrons is about 0.008 near the shower core, and the total penetrating component (detectable by its own charge or by producing charged secondaries) amounts to 1.3 percent of the electrons. This is in agreement with other measurements at a slightly lower elevation.[6,12] The measurement of Treat and Greisen[15] gives a higher number, partly because they used insufficient absorbers and partly because of a difference in distance from the cores of the showers (see discussion by Ise and Fretter[2]).

Data similar to those of Figs. 4 and 5 were also taken with zero absorber above the counter tray *A*, and with 10″ or 17″ of graphite. For these data, another change was a reduction in area of the larger counters from 560 to 196 cm^2. Therefore a smaller number of low density showers were detected and there were also less chance coincidences. The densities corresponding to the various counter combinations are listed in Table V, and the data are collected in Fig. 6. Graphs of the density distributions are in Fig. 7, where the dashed curve represents a distribution calculated in the same way as the one in Fig. 5.

The experimental ordinates in Fig. 7 are higher than in Fig. 5, agreeing more closely with the calculated curve. This is due partly to increased efficiency and smaller absorption in the detector, and partly to the inclusion of some events caused by high energy electrons and photons.

When the absorber above tray *A* was entirely removed the upper row of 12 counters in tray *A* could be

TABLE V. Median densities for the density classes in Figs. 4, 6, and 8.

Density class	Median density; classes in Fig. 4	Fig. 6 and classes at 7 m in Fig. 8	Classes at 0 m in Fig. 8
0 (no counter struck)	0	0	2 m^{-2}
I (one counter struck)	1.25 m^{-2}	3 m^{-2}	8
II	6	16	18
III	14	36	35
IV	25	66	75
V	50	120	150
VI	100	250	250
VII	250	1100	600
VIII	1000	—	—

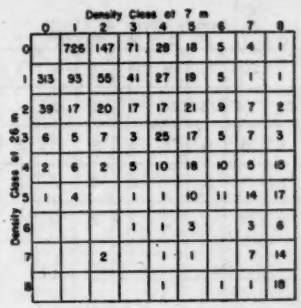

FIG. 4. Density distribution of air showers at 7 m and at 26 m from the *PP* detector, for 1974 events of type $AS+B^2C^2D^2$. Absorber above tray *A* in *PP* detector = 5″, 9″ or 13″ Pb. The median densities for the different classes are listed in Table V.

used for the density measurement. Always one of the counters struck was discounted, as being due to the primary particle initiating the penetrating shower. This could be sometimes an overcorrection, if the penetrating shower was initiated by a neutral particle, and sometimes an undercorrection, when back-projected particles of the penetrating shower strike the upper counters. The back scattering of electrons from the absorber underneath the counters also tends to increase the apparent shower density. However, we believe that such events in general only change the number of counters struck by plus or minus one, and do not change the order of magnitude of the measured density.

The density classes corresponding to different numbers of counters struck in the top row of tray *A* are listed in Table V, and the results of the density measurements are collected in Figs. 8 and 9, where the densities at zero and 7 meters are compared. The density class 0 at 7 m had to be blank because the master pulse only occurred when one counter was struck in either the *ED*

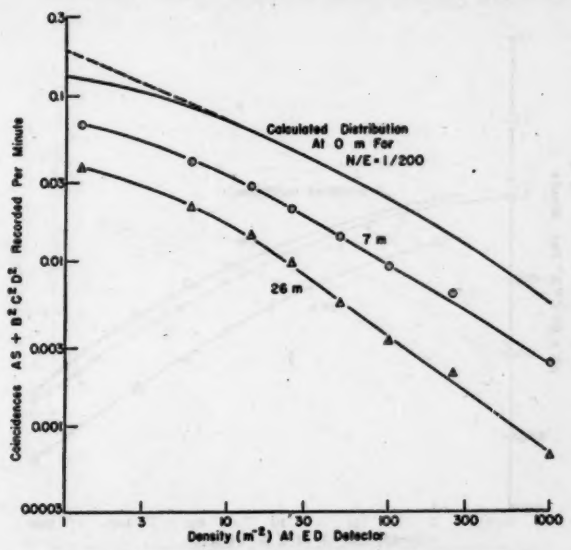

FIG. 5. Integral density distribution of the air showers detected at 7 m and 26 m from the *PP* detector, in association with penetrating showers. Lead above tray *A* in *PP* detector = 5″, 9″ or 13″. The calculated curve is explained in the text.

Density Class at 26 m \ Density Class at 7 m	0	1	2	3	4	5	6	7
0		203	55	19	14	7	6	
1	63	24	13	20	8	5	12	1
2	7	5	6	7	5	8	13	2
3	2		3		2	8	3	2
4	2	1			1	2	14	7
5							5	6
6	1						4	10
7						1	2	15

FIG. 6. Density distribution at 7 m and 26 m, for 594 events of type $AS+B^2C^2D^2$, observed with zero absorber, or 10″ or 17″ graphite, above tray A in the PP detector. The density classes are explained in Table V.

detector at 7 m or the one at 26 m. The few instances in which a counter was struck at 26 m and none at 7 m were mostly chance coincidences.

The requirement for each recorded event, of a particle at 7 m as well as a penetrating shower at the PP detector, increases the *a priori* probabilities of the low density showers so much that even when no counters were struck in tray A the probable air shower density was finite at the PP detector. Except for the groups 0 and I, however, the density classes at zero and 7 m are approximately equivalent (see Table V).

For the data in Figs. 8 and 9, like those in Figs. 6 and 7, the rates probably include some showers due to incident electrons and photons, and are therefore slightly too high.

VIII. SPATIAL DISTRIBUTION

Figures 4 to 9 contain information on the spatial distribution of the N-component in extensive air showers.

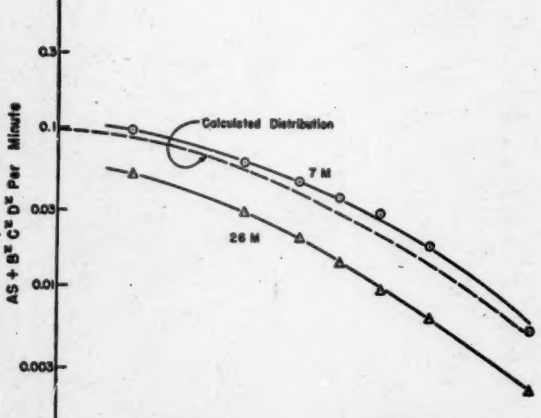

FIG. 7. Integral density distribution of air showers detected at 7 m and 26 m from the PP detector, in association with penetrating showers. Absorber above tray A in PP detector = zero, 10″ or 17″ graphite.

In Figs. 4, 6, and 8, where the data are presented in tabular form, one can see evidence of a correlation between the shower densities measured at the two different distances. The spread of the data, or lack of perfect correlation, is due in part to the errors in the density measurements (which are only expected to be accurate within a factor of 3, or $\pm 1\frac{1}{2}$ density classes), and in part to the cores of the air showers striking at different distances from the apparatus. In the great majority of the events, however, the showers are more dense at 7 m than at 26 m from the PP detector, and more dense at 0 m than at 7 m.

In Figs. 4 and 6 together (excluding the cases in which all of the counters were struck at both ED detectors, and correcting for chance coincidences in classes 0—I and I—0), we find that there are 1629 events (78 percent) in which the density at 7 m seems to be greater than at 26 m, 178 events (9 percent) in which the densities seem about equal, and only 288 cases (14 percent) in which the density at 26 m seems greater than at 7 m. In Fig. 8 (excluding class 0 at each detector and the cases when all the counters were struck at both detectors), we find that there are 115 cases (74 percent) in which the density at the PP detector seems to be greater than at 7 m, 22 events (14 percent) in which the densities are about equal, and only 18 events (12 percent) in which the density at 7 m seems to be greater than at the PP detector.

The average differences in shower density at the two ED detectors can be obtained from the horizontal separations of the frequency-density curves in Figs. 5, 7, and 9. In Figs. 5 and 7, the horizontal separation is found to be a factor varying from about 4 to 6. Because the statistical accuracy and the conditions of measurement were better for Fig. 5 than for Fig. 7, we estimate that the showers were on the average $4\frac{1}{2}$ times as dense at 7 m as at 26 m. From Fig. 9 we conclude that the showers were on the average $3\frac{1}{2}$ times as dense at the PP detector as at 7 m.

According to the Molière theory of the lateral distribution of the electrons,[18] the electron densities at 7 m and 26 m from the cores of air showers at Mt. Evans (where the characteristic scattering length is 130 m) should be in the ratio 5.6 to 1, not much more than the ratio $4\frac{1}{2}$ deduced above. A ratio of 3.5 should exist between the densities at 2.5 m and at 7 m from the core. We conclude therefore that when a penetrating shower *and* an associated air shower were recorded, the core of the air shower was usually very close to (within 5 to 10 meters of) the N-component detector.

Another way of looking at the data is as follows. Air showers of any given density strike both of the ED detectors (in either of the pairs considered above) with the same frequency, and they strike with the core nearer to the detector at 26 m just as frequently as with the core nearer to the other ED detector. But a much larger

[18] G. Molière, in *Cosmic Radiation*, edited by W. Heisenberg (Dover Publications, Inc., New York, 1946).

fraction (by a factor of about 6) of the showers that strike nearer the 7-m *ED* detector exhibit *N*-component at the *PP* detector, than of the showers that strike nearer to the 26 m *ED*. And a much larger fraction (again by a factor 6) of the showers that strike closer to the *PP* detector than to the *ED* at 7 m exhibit *N*-component, than of the showers that strike closer to the 7 m *ED*.

This is illustrated by the diagram in Fig. 10. The two circles enclose the areas in which the cores may strike, with the electron density more than about twice as great at one *ED* detector as at the other. The showers falling in one of the circles have *N*-component detected about 6 times as frequently as the showers falling in the other circle. The average distances (obtained by averaging r^{-1}) of points in the two circles from the *PP* detector are about 6 meters for the nearer, more efficient circle, and 30 meters for the other. Thus, the mean density of the *N*-component at 6 m from the core is about 6 times as great as at 30 m from the core of an air shower.

A similar treatment of the data of Fig. 8, with *ED* detectors at the *PP* detector and at 7 m, indicates that the *N*-component density at about $3\frac{1}{2}$ meters from the core is roughly 6 times as great as at about 10 meters. This factor may be slightly exaggerated because of the back scattering effects discussed above.

It is clear that the number of *N*-component particles per unit area decreases very rapidly with increasing distance from the cores of the air showers: about as rapidly as r^{-1}, or perhaps a little faster. This means that the *N*-component is concentrated near the shower cores about as strongly as are the electrons.

Cocconi and Tongiorgi, in further studies of neutrons in air showers[10] find that the neutron producers are concentrated near the core about as strongly as the electrons. Presumably the neutron producers are mostly neutrons of higher energy, identical with star producers, and have a mean energy of a few hundred Mev. Thus our conclusion concerning the spatial distribution of the high energy *N*-component (penetrating shower producers) applies also to the *N*-component of lower energy.

Cocconi, Tongiorgi, and Greisen[6] have used a group of shielded counters and an unshielded counter as a "core selector" in a study of air showers. The sharp decoherence curves of the core selectors, and the fact that the electron density decreased with distance from the core selector according to the Molière function, and without showing inversions, indicate that the core selectors were much more selective of the cores of showers than were the groups of unshielded counters (*ED* detectors) used in the same experiment. Thus, whatever the particles were that triggered the core selectors, they must have been concentrated in the shower cores more strongly than the low energy electrons. From our present experiment, we must conclude that a large fraction (25 to 50 percent) of the coincidences in the core selectors were due to stars and penetrating showers produced by particles of the *N*-component in air showers. Hence that experiment also gives evidence for a strong concentration of the *N*-component near the core. The energy requirement was less than in the present experiment, since the secondary particles did not need to be very penetrating.

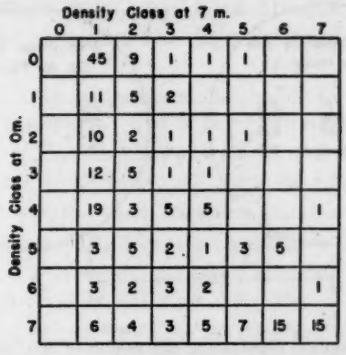

FIG. 8. Density distribution of air showers at 0 m and 7 m, for 227 events of type $AS+B^2C^2D^2$, observed with zero absorber above tray *A*. The upper row of counters, A_1, was used for the density measurement. The density classes are explained in Table V.

One should remember that, both for electrons and for other particles in the showers, the mean distance of the particles from the core is much larger than the mean distance between shower *detectors* and the core, when the detectors require more than one particle; but is equal to the mean distance between detector and core if single particles of the showers are counted. For instance, the mean distance of electrons from the cores of air showers is theoretically about 80 meters (at 3000 m elevation), but the same theory, as applied by Ise and Fretter,[2] shows that showers in which electrons discharge 3 neighboring counters strike mostly within 10 meters of the counters.

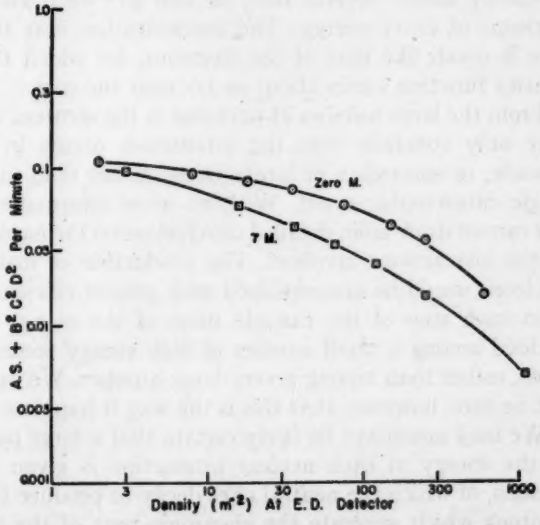

FIG. 9. Integral density distribution of air showers detected at 0 m and 7 m from the *PP* detector, in association with penetrating showers. Absorber above tray *A* in *PP* detector = zero.

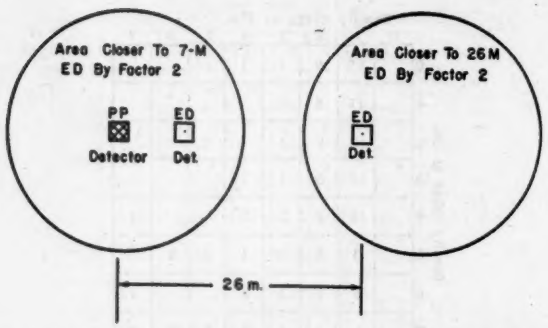

FIG. 10. Diagram illustrating discussion of spatial distribution of the penetrating particles in air showers. The showers with cores falling in one of the circular areas will have densities more than about twice as great at one *ED* detector as at the other. Those falling in the circle nearer the *PP* detector register penetrating showers six times as frequently as those falling in the other circle.

In the present experiment the requirement for all events is the detection of an N-component particle *and* one or more electrons. The mean distance to the cores of the showers is found to be about 5 to 10 meters. However, the mean distance of all nucleons from the shower cores may be 50–100 meters or more. In experiments where the detector only requires the presence of a single nucleon (as in almost all experiments on local penetrating showers), the associated shower cores will strike at an average distance so large that the associated air shower will usually not be detected. This can account for the usual observation[4,5,14–16] that N-component particles in the air occur without associated showers.

IX. IMPLICATIONS OF THE EXPERIMENTAL RESULTS

We have two properties to account for in the extensive air showers: (a) the existence of a large number of high energy nucleons, and (b) the concentration of the nucleons near the core of the shower. In showers that contain 10^7 electrons, there are about 50,000 nucleons of energy above several Bev, as well as[10] even more nucleons of lower energy. The concentration near the core is much like that of the electrons, for which the density function varies about as $1/r$ near the core.

From the large number of nucleons in the showers we may only conclude that the production occurs in a cascade, or succession of interactions, rather than in a single catastrophic event. Without more information, one cannot draw more detailed conclusions on the nature of the interactions involved. The production of many nucleons would be accomplished with greater efficiency if in each step of the cascade most of the energy is divided among a small number of high energy secondaries, rather than among a very large number. We cannot be sure, however, that this is the way it happens.

We may nowadays be fairly certain that a large part of the energy in each nuclear interaction is given to mesons, of which the neutral ones decay to produce the photons which generate the electronic part of the air showers. If the charged mesons have large cross sections for producing further nuclear interactions with further meson production, one can arrive at a consistent picture in which most of the energy, after 5 to 10 mean free paths, is transferred irreversibly to the electronic component, while 10 to 20 percent of the energy is distributed about equally between μ-mesons and nucleons. But if the charged mesons are supposed not to interact strongly with nuclei of the air such a consistent picture cannot be formed. In that case very few high energy nucleons would be produced and most of the energy of the shower would be retained by a rather small number of high energy mesons. Therefore we think it necessary to believe that the high energy charged mesons that are directly produced in nuclear interactions have a large cross section for nuclear interaction with further meson and nucleon production.

A direct inference that can be made from the spatial distribution is that a large fraction of the observed N-component originates locally in the core of the shower, within distances of the order of 200 meters of air (15 g/cm²) above the apparatus.

For those particles which originate at a height greater than x above the apparatus, the spatial distribution about the core must be approximately flat within a distance of the order of $x\bar{\theta}$, where $\bar{\theta}$ is the average angle of divergence in the production process. For secondary nucleons of energy around 10 Bev, $\bar{\theta}$ must be at least as large as about 0.1 radian, hence the secondaries originating more than 200 meters above the apparatus must be expected to have a spatial distribution which is flat for lateral distances up to 20 meters, contrary to our observations. If the particles are π-mesons of about the same energy, the distance in which they must originate is limited to a few hundred meters by the decay probability. However, we suspect from the abundance of neutral particles in the N-component that most of the particles are nucleons.

Thus the N-component cascade in the extensive air showers must still be active in reproduction near the height of observation of the showers. The local activity, however, does not need to be as great as at higher altitudes.

Let x be the height above the level of observation of a shower, and $\rho(r)$ be the density of the N-component at a distance r from the core. Let $I(x)$ be the intensity of N-component production (per g/cm²) in the core, and $f(\theta)$ be the angular distribution (per unit solid angle) of the secondaries. Then one can write

$$\rho(r)=K\int_{x=0}^{\infty} dx\left[\frac{x}{(x^2+r^2)^{\frac{3}{2}}}\right]f(\theta)I(x)\exp\left(-\frac{x}{x_0}-\frac{x}{\lambda}\right).$$

The term in brackets is just the solid angle subtended by a unit horizontal area at a height x. The term $\exp(-x/x_0)$ represents the decrease in density of the air, with $x_0\approx 7000$ m, while $\exp(-x/\lambda)$ represents absorption of the secondaries. Strictly, λ (in meters) should vary with the density of the air, but this is not impor-

tant here. λ, like x_0, is rather long—about 1700 meters for an absorption length of 130 g/cm². The equation neglects the production of high energy N-component by particles which are not in the core of the shower.

If the variation of the terms outside of the brackets is ignored, the purely geometric factor integrates to give $\rho(r) \propto r^{-1}$. This result is unchanged if the factor $f(\theta)$ is included, under the approximation

$$f(\theta)=\begin{cases}0, & \theta>K,\\ \text{const.}, & \theta<K.\end{cases}$$

The main contribution to the particles at distance r from the axis is found to come from a height r/K to $2r/K$. Thus if $K=0.1$ (particles in a cone of 6° half-angle), the particles found at 10 m from the core originate in the core mostly at heights of 100 to 200 meters.

The variation of $\rho(r)$ as r^{-1} is approximately the sort of variation that is necessary to account for our experimental data; a weaker dependence on r would not suffice.

The exponential terms in the above equation do not change much in distances of a few hundred meters, and therefore do not affect the dependence of ρ on r near the core.

Thus the only requirement needed to obtain the sort of lateral distribution which has been observed is that the intensity function $I(x)$ be finite and not vary too strongly with x. That is, one must be able to use the concept of a core that contains particles of enough energy to generate locally some particles of the N-component with secondary energies greater than 5 Bev. The number of such particles generated in the showers at mountain elevations must not be negligible compared with the numbers generated near the top of the atmosphere. However, an exponential increase of $I(x)$ with decreasing pressure, with a mean free path of the order of 100 g/cm², would be permissible.

The authors are grateful to the Research Corporation for a grant which covered the expense of performing the experiment described above. The facilities of the Inter-University High Altitude Laboratories were used in the performance of the experiment. We also wish to thank Professor Cocconi and Dr. Tongiorgi for helpful discussions of the experiment.

Mean Free Path of Penetrating Shower Producers†

W. D. WALKER,* S. P. WALKER,* AND K. GREISEN
Cornell University, Ithaca, New York

(Received July 6, 1950)

The collision mean free path has been measured in carbon and in lead for both neutral and charged particles capable of producing penetrating showers. The results are practically equal for the neutral and charged particles, and average 160±10 g/cm² in lead, and 81±5 g/cm² in carbon. The indicated cross section in carbon is significantly less than the geometric cross section. The ratio of neutral to charged primaries was found, after correction, to be 0.84±0.13.

I. INTRODUCTION

SEVERAL experiments have previously been carried out to determine the "collision mean free path" of the penetrating shower producers. The results of most of the experiments in which the absorber was lead[1–7] are in good agreement, and give cross sections close to the geometric cross section of the lead nucleus, at least for the most energetic primaries. For light elements, however, the different results do not agree very well.[1,5–7]

It is of particular interest to find the mean free path for interaction of high energy nucleons in light elements because the mean free path for interaction with light nuclei is more sensitive to the value of the nucleon-nucleon cross section than is the mean free path for interaction with heavy nuclei.

Measurements of the mean free path for shower production by neutral primaries have been made by Rossi and Regener[8] and by Jánossy and Rochester.[9] However, the statistics were rather poor in both cases. Consequently it was thought to be worth while to find separate mean free paths for the charged and neutral primaries of penetrating showers.

II. MEASUREMENTS

The penetrating shower detector is shown in Fig. 1 of the preceding paper, and was used in the present experiment with the following triggering coincidence required for photographing the hodoscope arrangement. It was required that no more than one counter be struck in A_1 and no more than one in A_2, in coincidence with at least two counters in each of rows B, C and D, and in anticoincidence with the unshielded air shower counters (not shown in the figure). Part of the time it was required that no counter be struck in either row A_1 or row A_2. The apparatus was run with absorber S, above trays A_1 and A_2, equal to zero, 5″ Pb, 9″ Pb, 13″ Pb, 10″ C, and 17″ C.

The apparatus was designed primarily to have a high efficiency for the study of the penetrating showers associated with extensive air showers. The hard component of the extensive air showers is relatively much richer in N-component particles than is the unassociated hard component. Therefore mu mesons which produce showers of photons and electrons by electromagnetic processes cause very little uncertainty in the identification of the N component in the air showers, but produce a large background in the study of the unassociated penetrating showers. Also, in order to determine a mean free path, we must eliminate all showers whose primaries do not traverse S.

Thus the triggering coincidences described above gave a very loose selection of events including the phenomena we wished to record, but the more stringent selection was made by examining the hodoscope pictures and picking out these events representing penetrating showers produced beneath tray A by charged or neutral primaries that had traversed the absorber S.

The events discarded (in the order of decreasing frequency) were of the following types:

(1) Coincidences apparently caused by a single charged meson arriving with such great inclination as to strike two adjacent counters in each of rows B, C and D, and possibly one or two of the side counters in trays A_1 and A_2. Such events were very easily recognized.

(2) Showers of more than one particle, with axes so inclined that the primaries did not need to traverse the absorber S. In many of these cases it was obvious that the shower had been initiated in the shielding at the side of the counters. Selection was facilitated in numerous instances by observing that the side counters of trays A_1 and A_2 were discharged but not the top counters. Showers which entered from the ends gave rise to pictures in which the counters struck in rows B, C and D were badly out of line.

(3) Very narrow or "collimated" showers, involving only two or three adjacent counters in each of rows B, C and D, and no more than eight counters total. This category overlaps type (1) and is characteristic of events caused by electronic secondaries of mu mesons.

Because the selection depended on the geometry of

† Some of the apparatus used in this experiment was made available through contract with the ONR.

* Now at Rice Institute, Houston, Texas.

[1] G. Cocconi, Phys. Rev. 75, 1074 (1949).
[2] W. D. Walker, Phys. Rev. 77, 686 (1950).
[3] K. Sitte, Phys. Rev. 78, 714 (1950).
[4] J. Tinlot and B. P. Gregory, Phys. Rev. 75, 519 (1949).
[5] E. P. George and A. C. Jason (1950). We are grateful to the authors for communicating their results prior to publication.
[6] R. H. Rediker and H. S. Bridge, Phys. Rev. 79, 206 (1950).
[7] G. Cocconi, Phys. Rev. 76, 984 (1949).
[8] B. Rossi and V. H. Regener, Phys. Rev. 58, 837 (1940).
[9] L. Jánossy and G. D. Rochester, Nature 150, 633 (1942); Proc. Roy. Soc. A181, 399 (1943).

TABLE I. Classification of hodoscope records.

Absorber	Penetrating showers with charged primaries	Penetrating showers with neutral primaries	Total rate of discarded events
Zero	0.723±0.033 min.$^{-1}$	0.473±0.017 min.$^{-1}$	2.95±0.10 min.$^{-1}$
42 g/cm^2 C	0.438±0.022	0.266±0.015	2.76±0.05
71 g/cm^2 C	0.315±0.020	0.212±0.012	2.52±0.06
140 g/cm^2 Pb+7 g/cm^2 Fe	0.286±0.019	0.191±0.013	2.33±0.06
252 g/cm^2 Pb+7 g/cm^2 Fe	0.157±0.014	0.125±0.010	2.26±0.05
364 g/cm^2 Pb+7 g/cm^2 Fe	0.105±0.010	0.075±0.007	2.27±0.05

the showers, it was essential that the part of the apparatus in which the showers were initiated and developed remain constant throughout the experiment. The only change in the course of the experiment was in absorber S, and all the showers selected were required to begin beneath this absorber.

In the selection there is no doubt but that some penetrating showers initiated by primaries which had traversed S were excluded along with the background. However, the fraction excluded should be independent of the thickness of absorber S. To avoid a systematic error, rigid selection rules were used, and the order of examination of the films was so adjusted that the films with any given amount of absorber were interspersed with films taken with other thicknesses. All doubtful events were transcribed onto cards which were then mixed so that the decisions were made at random with respect to absorber thickness. The consistency of selection was checked by repeating the examination of some of the films after a few weeks lapse of time, and the agreement was found to be practically perfect.

The rate of the discarded events (Table I) was found to decrease by 20 to 25 percent in the first five inches of lead, and thereafter to remain constant. This independence of absorber thickness was found to apply not only to the total background rate, but to the frequencies of each of the types of discarded events, and it verifies that the large majority of the events were properly interpreted as background. The small decrease in the first five inches of lead was probably due to narrow showers caused by electrons and photons entering near the ends of the counters, where (in the absence of absorber S) the shielding of trays C and D was insufficient.

III. RESULTS

Table I presents a summary of the classification of the films. In Figs. 1 and 2 the rates of the penetrating showers beginning under tray A have been plotted against the thickness of the absorber S. The data for lead absorbers extend to large enough thicknesses to show clearly a departure from exponential shape. From the work of Cocconi,[7] we know that this is not due to a real variation of the cross sections, but to an incomplete elimination of the background events. Since the residual background showers were probably either knock-on showers more extensive than those we discarded, or penetrating showers whose primaries missed S, their rate should be practically independent of the absorber thickness. A correction was made by subtracting a constant rate from each of the four points. The rate subtracted was the one which made the corrected points

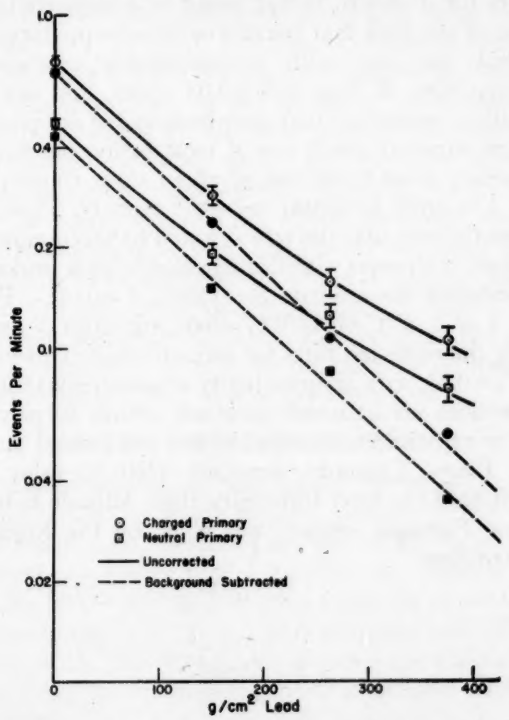

FIG. 1. Frequency of local penetrating showers initiated beneath tray A, as a function of the vertical thickness of lead above tray A. An iron supporting plate of 7 g/cm^2 was counted as equivalent to 10 g/cm^2 of lead.

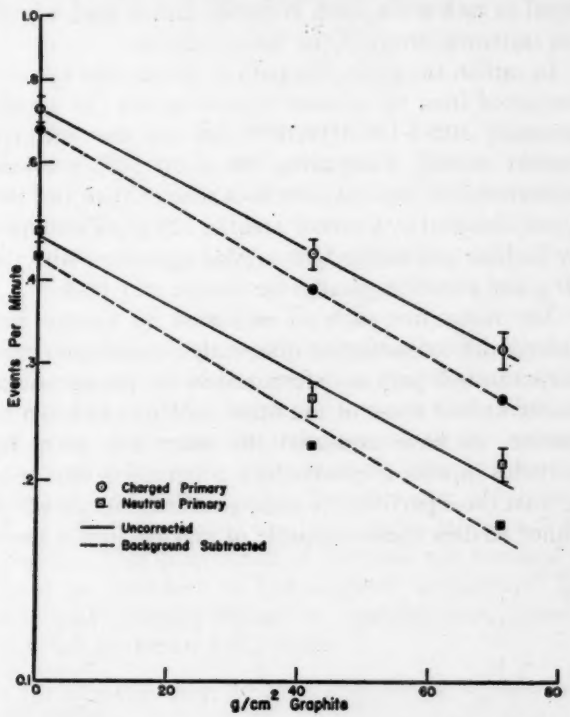

FIG. 2. Frequency of local penetrating showers initiated beneath tray A, as a function of the vertical thickness of graphite above tray A.

fall most nearly on a straight line, in the sense of least squares. The background rates so determined were 0.05/min. for the charged primaries and 0.04/min. for the neutral primaries, about 7 percent and 8 percent respectively of the rates with zero absorber.

The corrections were assumed to be independent of the absorber S and so to apply also to the data taken with carbon absorbers. The corrected points are plotted in Figs. 1 and 2 and are connected by the dashed straight lines.

Because of the shape of the apparatus it was possible for primaries coming in at a considerable inclination from the vertical to produce recorded showers. This makes the effective absorber thickness greater than the vertical depth by a factor of 1.08, which we have calculated with a zenith angle dependence of $\cos^6\theta$ for the incident particles.[2]

The mean free paths, taken from the lines fitted to the corrected points by the method of least squares, and using the effective absorber thicknesses, are as follows:

Neutral primaries in Pb:	164 ± 15 g/cm^2
Charged primaries in Pb:	157 ± 12
Neutral primaries in C:	80 ± 7
Charged primaries in C:	82 ± 8.

The errors indicated are the standard deviations, including the statistical errors and an estimate of ±0.01/min. as the standard error in the background correction.

The results obtained for lead are in agreement with most of the previous measurements, cited above. The mean free paths for charged and neutral primaries are equal to each other, both in carbon and in lead, within the statistical errors of the measurements.

In carbon the mean free path is longer than the one computed from the geometric cross section [48 g/cm^2, assuming $(0.5+1.37A^{\frac{1}{3}})\times10^{-13}$ cm for the effective nuclear radius]. Comparing our result with previous measurements, we find that it is shorter than the 100 g/cm^2 obtained by Cocconi[1] and the 120 g/cm^2 obtained by Rediker and Bridge,[6] but in good agreement with the 80 g/cm^2 found in paraffin by George and Jason.[5]

The mean free path as measured by George and Jason is defined somewhat differently (in principle) from the mean free path as determined in the present measurements and those of the other authors cited. To be precise, we have measured the mean free path, for particles capable of producing a penetrating shower of at least three particles, to undergo an interaction which either renders them incapable of making such a penetrating shower, or gives rise to one or more penetrating secondaries.

IV. RELATIVE NUMBER OF CHARGED AND NEUTRAL PRIMARIES

It is possible to get some information concerning the relative number of charged and neutral primaries from the data of Table I. However, it is necessary to consider the fact that the shower detector was biased in favor of recording showers produced by charged primaries. The following two kinds of showers were both counted as having charged primaries, while there are no similar events that were counted as having neutral primaries: (*a*) showers produced by charged primaries with one or more secondaries going back through the same counters in rows A_1 and A_2 that were struck by the primary; and (*b*) showers produced by neutral primaries with a back projected secondary that appears to be the primary. If N = recorded rate of showers with neutral primaries, C = recorded rate of showers with charged primaries, A = rate of coincidences of type (a), and B = rate of coincidences of type (b), then the unbiased rate, C_0, comparable to N for charged primaries, is

$$C_0=C-A-B$$

and the unbiased ratio of neutral to charged primaries is N/C_0.

Lack of information about the range and number of back projected secondaries which are produced in penetrating showers makes it impossible to give precise values for A and B. It was found by a separate tabulation of the films that the rate of showers produced by neutral particles, with distinguishable secondaries striking row A, was 0.28 ± 0.03 times the rate N. Usually a secondary that goes back in the direction of the primary can reach row A most easily, but such a secondary must strike one of about three counters in row A in order to appear to be the primary. Therefore it was thought that the rate B would be about equal to the rate of showers with distinguishable back projected secondaries. We estimate $B=0.28N$; $A=0.07C_0$. From Fig. 1 or 2, $N/C=0.43/0.67=0.64$, the rates N and C being the corrected rates for zero absorber. This yields $N/C_0=0.84$, with an uncertainty of about ±0.13 if the corrections are assumed uncertain within 50 percent.

The experiment described above was carried out at Mt. Evans, Colorado, elevation 4260 m, using the facilities of the Inter University High Altitude Laboratories. Financial support was given by the Research Corporation.

Hyperfine Structure of Zeeman Levels in Nitric Oxide

ALLAN F. HENRY
Sloane Physics Laboratory, Yale University, New Haven, Connecticut*
(Received July 17, 1950)

This paper contains a calculation of the energy arising from the magnetic interaction of the extranuclear electrons with the magnetic moment of the nitrogen nucleus in $N^{14}O^{16}$. An operator is derived for the interaction, which is more fundamental than the one, proportional to $\mathbf{I}\cdot\mathbf{J}$, which is commonly used. This operator is employed, together with previously calculated state functions, to compute the hyperfine structure of the $^2\Pi_{\frac{1}{2}}$ state of $N^{14}O^{16}$. The formula which results from this procedure accounts for the experimental data, which cannot be explained completely if the interaction operator is taken to be proportional to $\mathbf{I}\cdot\mathbf{J}$.

I. INTRODUCTION

IN a paper by Margenau and Henry[1] the magnetic fine structure and hyperfine structure of the $^2\Pi_{\frac{1}{2}}$ state of $N^{14}O^{16}$ were investigated. NO in this state corresponds closely to Hund's case (a), in which both the orbital and spin angular momenta of the electrons are quantized along the internuclear axis, the quantum numbers associated with these projections being Λ and Σ. For the $^2\Pi_{\frac{1}{2}}$ state $\Lambda=1$ and $\Sigma=\frac{1}{2}$. The quantum number J has the value $\frac{3}{2}$. In an external magnetic field, $\mathbf{H}$, the energy level in question is separated into four sublevels in accordance with the four possible values of M_J. The N^{14} nucleus has a spin $\mathbf{I}$ of value 1; hence each magnetic sublevel is divided into $2I+1=3$ hyperfine levels.

The interaction between the nuclear magnetic moment and the magnetic fields caused by the extranuclear electrons is the main cause of this hyperfine structure. Commonly, this interaction is taken to be being proportional to $\mathbf{I}\cdot\mathbf{J}$, where $\mathbf{I}$ is the operator representing nuclear spin and $\mathbf{J}$ is the operator representing the total angular momentum of the electrons; this assumption was made in (MH). However, careful examination of the experimental data shows that the form $A\mathbf{I}\cdot\mathbf{J}$ (A being a proportionality constant) leads to an expression for the energy which is not wholly consistent with the measurements of Beringer and Castle.[2] Data which they estimate to be accurate to within 1 percent lead to values of the proportionality constant, A, which differ from one another by as much as 7 percent. In this paper we attempt to overcome the difficulty by returning to a more fundamental view of the interaction.

II. THE INTERACTION OPERATOR

It is convenient to describe the $N^{14}O^{16}$ molecule in terms of the coordinate systems pictured in Fig. 1. In this figure there are three Cartesian axis systems. XYZ is fixed in space with its center at C, the center of mass of the $N^{14}O^{16}$ nuclei; $X'Y'Z'$ is a system imbedded in the molecule; $X''Y''Z''$ is a system parallel to XYZ with origin at N, the N^{14} nucleus. θ and ψ are Euler-angles specifying the orientation of $X'Y'Z'$ relative to XYZ; these angles are such that the coordinates of a point, xyz, in XYZ are related to the coordinates $x'y'z'$, of that same point in $X'Y'Z'$ by the equations

$$\begin{aligned} x&=x'\cos\psi-y'\cos\theta\sin\psi+z'\sin\theta\sin\psi,\\ y&=x'\sin\psi+y'\cos\theta\cos\psi-z'\sin\theta\cos\psi,\\ z&=y'\sin\theta+z'\cos\theta. \end{aligned} \tag{1}$$

The X' axis lies in the XY plane. In Fig. (1) the line $[NO]=\rho$ represents the internuclear distance. We let $[NP]\equiv r$, $[CP]\equiv r'$, $[PD]\equiv\rho'$, and $[NC]\equiv\xi\equiv\rho M_0/(M_N+M_0)$; M_0 and M_N are masses of O^{16} and N^{14} nuclei. In the top view $[C''N]$, the projection of $[CN]$ on the $X''Y''$ plane, equals $\xi\sin\theta$. The following relations appear from an examination of the figure.

$$\begin{aligned} x''&=x+\xi\sin\theta\sin\psi,\\ y''&=y-\xi\sin\theta\cos\psi,\\ z''&=z+\xi\cos\theta,\\ z'&=r\cos\chi-\xi=r'\cos\theta',\\ \rho'&=r\sin\chi=r'\sin\theta',\\ r'^2&=r^2+\xi^2-2r\xi\cos\chi,\\ r^2&=r'^2+\xi^2+2r'\xi\cos\theta'. \end{aligned} \tag{2}$$

In atomic spectra [see Hargraves,[3] Fermi,[4] Breit and Doermann[5]] the magnetic interaction of an electron in a P state with the nucleus can be described in terms of the operator

$$\mathcal{H}_I=-\frac{eh}{2mc}\left[\frac{\boldsymbol{\mu}_I\cdot\mathbf{L}}{r^3}+\frac{3(\mathbf{S}\cdot\mathbf{r})(\boldsymbol{\mu}_I\cdot\mathbf{r})}{r^5}-\frac{\boldsymbol{\mu}_I\cdot\mathbf{S}}{r^3}\right], \tag{3}$$

$\mathbf{r}$=position of the electron relative to the nucleus, $\boldsymbol{\mu}_I$=magnetic moment of the nucleus, $\mathbf{S}$=spin of the electron, $\mathbf{L}$=orbital angular momentum of the electron. This comes directly from the non-relativistic approximation for the energy of interaction between a moving electron and a field arising from a vector potential $\mathbf{A}$, $\mathbf{A}$ in turn being caused by the magnetic moment of the nucleus. The inner shells of electrons are assumed to have no net effect on this magnetic interaction. The non-relativistic approximation is suitable here, although it is not legitimate for S states.

* Supported by the ONR.
[1] H. Margenau and A. F. Henry, Phys. Rev. 78, 587 (1950); henceforth this paper will be referred to as (MH).
[2] R. Beringer and J. G. Castle, Jr., Phys. Rev. 78, 581 (1950).
[3] J. Hargraves, Proc. Roy. Soc. A124, 568 (1929); A127, 141, 407 (1930).
[4] E. Fermi, Zeits. f. Physik 60, 320 (1930).
[5] G. Breit and F. W. Doermann, Phys. Rev. 36, 1262, 1732 (1930).

We assume that (3) can be applied to $N^{14}O^{16}$ without any fundamental change. This is equivalent to regarding the magnetic interaction as taking place between the N^{14} nucleus and an electron outside a cylindrically symmetric cloud of inner electrons. The effect of the inner cloud of electrons is then assumed to be independent of M_J and M_I, the quantum number representing the component of $\mathbf{I}$ in a direction fixed in space.

In applying (3) to NO, the components, $L_{x'}$ and $L_{y'}$, of the operator $\mathbf{L}$ in the X' and Y' directions (perpendicular to the internuclear axis) are ignored. The matrix elements of these components connect neighboring electronic states; as in (MH) we neglect the effect of such states, since the perturbation arising from them is very small. The third component of $\mathbf{L}$ is $L_{z'}$ or Λ whose quantum number is 1 for the $^2\Pi_{\frac{1}{2}}$ state. We then obtain

$$\begin{aligned}\mathcal{H}_I=4\mu_0\mu_I\Big\{&\frac{\mathbf{I}\cdot\boldsymbol{\Lambda}}{r^3}+\frac{3}{r^5}[S_xI_xx''^2+(S_xI_y+S_yI_x)x''y''\\&+(S_xI_z+S_zI_x)x''z''+S_yI_yy''^2\\&+(S_yI_z+S_zI_y)y''z''+S_zI_zz''^2]\\&-\frac{S_xI_x+S_yI_y+S_zI_z}{r^3}\Big\}.\end{aligned}\tag{4}$$

r is the position of the $^2\Pi$ electron relative to the N^{14} nucleus (the line $[PN]$ in Fig. (1)); we have written out $\mathbf{S}\cdot\mathbf{r}=S_xx''+S_yy''+S_zz''$ and $\mathbf{I}\cdot\mathbf{r}=I_xx''+I_yy''+I_zz''$ and have used the abbreviations: $\mu_0\equiv-e\hbar/2mc$ and $\boldsymbol{\mu}_I=2\mu_I\mathbf{I}=2g_I\mu_0\mathbf{I}/1840$, g_I being the number of nuclear magnetons for one unit ($\hbar$) of nuclear spin in N^{14}.

III. THE STATE FUNCTION FOR THE $^2\Pi_{3/2}$ LEVEL

In (MH), a state function for the $^2\Pi_{\frac{3}{2}}$ level in the absence of nuclear spin was computed. This expression is a linear combination of four eigenfunctions $\psi(K, J)$ corresponding to Hund's case (b) and having different values of the rotational quantum number, K, and the total angular momentum quantum number, J. Explicitly, it has the form

$$\Psi=a\psi(1,\tfrac{3}{2})+b\psi(2,\tfrac{3}{2})+c\psi(2,\tfrac{5}{2})+d\psi(3,\tfrac{5}{2}).\tag{5}$$

The coefficients in the linear expansion are given by

$$\begin{aligned}a&\equiv-S_{ab}(1+S_{ab}^2)^{-\frac{1}{2}}(1+S_{12}^2)^{-\frac{1}{2}},\\b&\equiv-S_{ab}(1+S_{ab}^2)^{-\frac{1}{2}}(1+S_{12}^2)^{-\frac{1}{2}}S_{12},\\c&\equiv(1+S_{ab}^2)^{-\frac{1}{2}}(1+S_{34}^2)^{-\frac{1}{2}},\\d&\equiv(1+S_{ab}^2)^{-\frac{1}{2}}(1+S_{34}^2)^{-\frac{1}{2}}S_{34},\end{aligned}\tag{6}$$

the quantities S being defined in (MH). The case (b) eigenfunctions, $\psi(K, J)$, are also eigenfunctions of the operators $\mathbf{\Lambda}$, $\mathbf{S}$, and $\mathbf{M}_J$. Dependence on vibrational and electronic quantum numbers (other than Λ) will be ignored. It follows as a result of the cylindrical symmetry of the potential energy in the Hamiltonian of the molecule that $\psi(K, J)$ depends on Λ through the factor $\exp(i\Lambda\phi')$, ϕ' being the azimuthal angle of the set of cylindrical coordinates, r', z', ϕ', in Fig. 1.

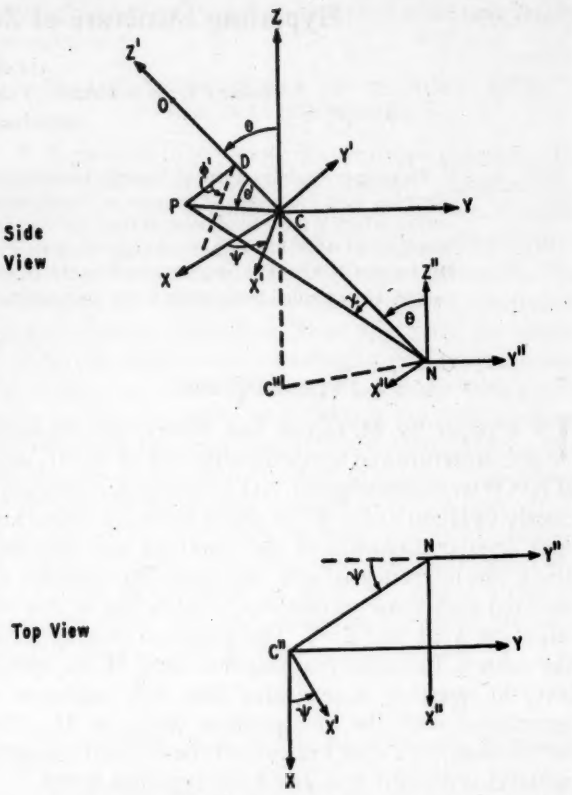

FIG. 1. Axis systems convenient for describing nuclear magnetic interaction in $N^{14}O^{16}$.

To account for the presence of nuclear spin in $N^{14}O^{16}$, we use as state function for the $^2\Pi_{\frac{1}{2}}$ levels a product function, $\Psi\Phi(IM_I)\equiv\Psi(M_J, M_I)$, in which $\Phi(IM_I)$ represents an eigenfunction for the nuclear spin, $\mathbf{I}$, and its component, M_I, in the direction of the external field; Ψ is given by (5). We use the notation $|JKSIM_JM_I)$ for the individual products $\psi(KJ)\Phi(IM_I)$ in the sum $\Psi\Phi(IM_I)$. The different values of M_J and M_I determine the nine sublevels within the $^2\Pi_{\frac{1}{2}}$ state.

IV. THE CALCULATION

The magnetic interaction of the nucleus with the electrons is computed by treating the operator (4) as a perturbation on the state functions, $\Psi(M_JM_I)$. The procedure is greatly simplified by the fact that the dependence of the $\psi(K, J)$ on the quantum number, Λ, has the form, $\exp(i\Lambda\phi')$. Since we neglect the small perturbation of neighboring electronic states, all eigenfunctions employed in the calculation are associated with the same value of Λ. Thus, when matrix elements of $\mathcal{H}_I$ are computed, the integration over ϕ' is a simple average. we can perform that average at the start and the resulting operator will still be perfectly general. The advantage of this procedure is that it separates the dependence of $\mathcal{H}_I$ on the rotational coordinates from its dependence on the electronic coordinates. The last of relations (2) shows that the scalar, r is a function of the electronic and vibrational coordinates only. The vector,

$\mathbf{r}$, depends also on the rotational coordinates, θ and ψ Thus we need only consider $(\mathbf{S}\cdot\mathbf{r})(\mathbf{I}\cdot\mathbf{r})$ and $\mathbf{I}\cdot\mathbf{S}$ in averaging over ϕ'.

When (1) is substituted in the first three of relations (2) and use is made of the equations: $x'=\rho'\cos\phi' = r\sin\chi\cos\phi'$; $y'=\rho'\sin\phi'=r\sin\chi\sin\phi'$; $z'+\xi=r\cos\chi$, we find

$$\begin{aligned} x''&=r(\sin\chi\cos\psi\cos\phi'-\sin\chi\cos\theta\sin\psi\sin\phi' \\ &\qquad +\cos\chi\sin\theta\sin\psi), \\ y''&=r(\sin\chi\sin\psi\cos\phi'+\sin\chi\cos\theta\cos\psi\sin\phi' \\ &\qquad -\cos\chi\sin\theta\cos\psi), \\ z''&=r(\sin\chi\sin\theta\sin\phi'+\cos\chi\cos\theta). \end{aligned} \tag{7}$$

On introducing this result in Eq. (4), averaging over ϕ', and adopting the notation, $S^{\pm}\equiv S_x\pm iS_y$; $I^{\pm}\equiv I_x\pm iI_y$, we obtain

$$\begin{aligned} \langle\mathcal{H}_I\rangle_{\phi'}=\frac{4\mu_0\mu_I}{r^3}\Big\{&\mathbf{I}\cdot\mathbf{\Lambda}+\left(\frac{3\cos^2\chi-1}{2}\right)[S_zI_z(3\cos^2\theta-1) \\ &+\tfrac{3}{2}I_z\sin\theta\cos\theta(iS^+e^{-i\psi}-iS^-e^{+i\psi}) \\ &+\tfrac{3}{2}S_z\sin\theta\cos\theta(iI^+e^{-i\psi}-iI^-e^{+i\psi}) \\ &-\tfrac{3}{4}\sin^2\theta(S^+I^+e^{-2i\psi}+S^-I^-e^{+2i\psi}) \\ &-\tfrac{1}{4}(3\cos^2\theta-1)(S^+I^-+S^-I^+)]\Big\}. \end{aligned} \tag{8}$$

The last two of relations (2) show that r and χ are functions of electronic and vibrational coordinates(r', θ' and $\rho=\xi(M_N+M_0)/M_0$). Because of this, we may write for the operator representing the effect of the nuclear interaction on rotational states as follows:

$$\begin{aligned} \langle\mathcal{H}_I\rangle_{\phi',\text{elec, vib}}=&A'\mathbf{I}\cdot\mathbf{\Lambda}+B'[S_zI_z(3\cos^2\theta-1) \\ &+\tfrac{3}{2}I_z\sin\theta\cos\theta(iS^+e^{-i\psi}-iS^-e^{+i\psi}) \\ &+\tfrac{3}{2}S_z\sin\theta\cos\theta(iI^+e^{-i\psi}-iI^-e^{+i\psi}) \\ &-\tfrac{3}{4}\sin^2\theta(S^+I^+e^{-2i\psi}+S^-I^-e^{+2i\psi}) \\ &-\tfrac{1}{4}(3\cos^2\theta-1)(S^+I^-+S^-I^+)], \end{aligned} \tag{9}$$

where

$$\begin{aligned} A'&\equiv\langle 4\mu_0\mu_I/r^3\rangle_{\text{elec, vib}}; \\ B'&\equiv\langle 2\mu_0\mu_I(3\cos^2\chi-1)/r^3\rangle_{\text{elec, vib}}. \end{aligned}$$

We are now in a position to compute the nuclear magnetic interaction energy. Its principal part is the diagonal matrix element,

$$\int\Psi(M_JM_I)\mathcal{H}_I\Psi(M_JM_I)d\tau.$$

There is also a contribution from states differing in M_J by ±1 and M_I by ∓1. In computing this, we have used only the term $A'\mathbf{I}\cdot\mathbf{\Lambda}$ assuming that B' is much less than A'; analysis of the experimental data under this assumption leads to a ratio of B' to A' of approximately 0.1.

The matrix elements needed for the calculation can be obtained from the article of Rademacher and Reiche[6] together with the angular momentum addition laws. These are employed along with the relations

$$\begin{aligned} &\mathbf{I}\cdot\mathbf{\Lambda}=\tfrac{1}{2}(I^+\Lambda^-+I^-\Lambda^+)+I_z\Lambda_z, \\ &I_z|JKSIM_JM_I)=M_I|JKSIM_JM_I), \\ &I^{\pm}|JKSIM_JM_I) \\ &\quad=[(I\pm M_I+1)(I\mp M_I]^{\frac{1}{2}}|JKSIM_J,M_I\pm1), \\ &\Lambda_x-i\Lambda_y\equiv\Lambda^-=e^{-i\psi}\sin\theta(\partial/\partial\phi'). \end{aligned} \tag{10}$$

The elements $(J_1K_1SIM_JM_I|I_z\Lambda_z|J_2K_2SIM_JM_I)$ can be obtained from formulas given by Hill.[7] For the elements of the term involving B' we obtain

$$\begin{aligned} &(JKSIM_JM_I|S_m''|JKSIM_JM_I) \\ &\quad=\frac{M_JM_I}{2K+1}\left[\frac{3\Lambda^2}{K(K+1)}-1\right]\frac{2(J-K)(4K-2J+1)}{4J-2K+1} \\ &(JKSIM_JM_I|S_m''|J,K+1,SIM_JM_I) \\ &\quad=\frac{-6\Lambda M_IM_J}{(K+1)(2K+1)(2K+3)}[(K+1)^2-\Lambda^2]^{\frac{1}{2}} \\ &(JKSIM_JM_I|S_m''|J+1,KSIM_JM_I) \\ &\quad=\frac{M_I}{2(2K+1)}\left[\frac{3\Lambda^2}{K(K+1)}-1\right][(J+1)^2-M_J^2]^{\frac{1}{2}} \\ &(JKSIM_JM_I|S_m''|J+1,K+1,SIM_JM_I) \\ &\quad=\frac{3\Lambda M_I(J-K)}{2(K+1)(J+1)(2J-K+1)} \\ &\qquad\times\{[(J+1)^2-M_J^2][(K+1)^2-\Lambda^2]\}^{\frac{1}{2}} \\ &S_m''\equiv B'[S_zI_z(3\cos^2\theta-1) \\ &\qquad+\tfrac{3}{2}I_z\sin\theta\cos\theta(iS^+e^{-i\psi}-iS^-e^{+i\psi})]. \end{aligned} \tag{11}$$

These relations are valid only for the case $S=\frac{1}{2}$.

The principal part of the interaction energy is computed by use of (5), (6), and (11).

The correction for the terms off-diagonal in M_J and M_I is

$$\begin{aligned} \Delta E_I=&\frac{A'^2}{4\nu_0}\left(\frac{a^2}{3}+\frac{2ab\sqrt{3}}{15}+\frac{b^2}{5}\right) \\ &\times\left[2M_J^2M_I+4M_J-\frac{15}{2}M_I-2M_JM_I^2\right]. \end{aligned} \tag{12}$$

In ΔE_I, we approximate the state function, $\Psi(M_JM_I)$, by $[a|\frac{3}{2},1,\frac{1}{2},1,M_JM_I)+b|\frac{3}{2},2,\frac{1}{2},1,M_JM_I)]$ and the energy differences, $E(M_JM_I)-E(M_J-1,M_I+1)$ and $E(M_J+1,M_I-1)-E(M_J,M_I)$ by ν_0. The energy of interaction is then

$$E(M_JM_I)=\int\Psi(M_JM_I)\mathcal{H}_I\Psi(M_JM_I)d\tau+\Delta E_I. \tag{13}$$

[6] H. Rademacher and F. Reiche, Zeits. f. Physik 41, 453 (1927).

[7] E. L. Hill, Phys. Rev. 34, 1507 (1929).

V. COMPARISON WITH EXPERIMENT

The complete theoretical expression for the energy of one of the nine sublevels of the $^2\Pi_{\frac{1}{2}}$ energy level of $N^{14}O^{16}$ is (see MH)[8]

$$W(M_J M_I)=E_{ab}(M_J)+\Delta E_{ab}(M_J)+E_Q(M_J^2, M_I^2) +E_I(M_J M_I)+(\mu_0 g_I M_I H/1840). \quad (14)$$

The first two terms are those belonging to the molecular Zeeman effect; the third term accounts for the interaction of the electric quadrupole moment of the N^{14} nucleus with the field of the extranuclear electrons. The term, $\mu_0 g_I M_I H/1840$, takes account of the interaction of the nuclear spin with the external field.

The experimental data of Beringer and Castle consist of nine values of the external magnetic field strength for which

$$W(M_J M_I)-W(M_J-1, M_I)=\nu_0,$$

ν_0 being the driving frequency of 0.31220 cm^{-1}. We make use of six of these nine numerical data and determine A' and B' from the following equations:

$$\begin{aligned} &W_{H_1}(\tfrac{3}{2}, 1)-W_{H_1}(\tfrac{1}{2}, 1) \\ &\quad =W_{H_3}(\tfrac{3}{2}, -1)-W_{H_3}(\tfrac{1}{2}, -1), \\ &W_{H_4}(\tfrac{1}{2}, 1)-W_{H_4}(-\tfrac{1}{2}, 1) \\ &\quad =W_{H_6}(\tfrac{1}{2}, -1)-W_{H_6}(-\tfrac{1}{2}, -1), \\ &W_{H_7}(-\tfrac{1}{2}, 1)-W_{H_7}(-\tfrac{3}{2}, 1) \\ &\quad =W_{H_9}(-\tfrac{1}{2}, -1)-W_{H_9}(-\tfrac{3}{2}, -1). \end{aligned} \quad (15)$$

[8] The equation defining E_{ab} in (MH) contains a typographical error; the first parenthesis on the right should be multiplied by $\frac{1}{2}$.

The subscripts indicate the different values of the magnetic field strength at which the energy differences are taken. The last term in (14), which is proportional to M_I, and the quadrupole term, which is a function of the squares of M_J and M_I, make no contribution to Eqs. (15).

Solving the first and the last of Eqs. (15) for A' and B' leads to $A'=0.002627$ cm^{-1}; $B'=0.000256$ cm^{-1}. These two values satisfy the second Eq. (16) to within 0.1 percent.

VI. DISCUSSION

The fact that consistent values of A' and B' are found as solutions of the three Eqs. (15) is, of course, not conclusive evidence that the operator (9) is the correct one for describing the interaction. All that can be said is that experiments are not in contradiction with (9) whereas they *are* in contradiction with the results of using $A\mathbf{I}\cdot\mathbf{J}$ as the interaction operator.

It can be shown that (9) is equivalent to $A\mathbf{I}\cdot\mathbf{J}$ if the total spin, $\mathbf{S}$, is zero. The small quantity, B', is a measure of the error made when $A\mathbf{I}\cdot\mathbf{J}$ is used in place of (9) in treating states for which $\mathbf{S}$ is not zero.

I am indebted to Professor Henry Margenau for his valuable suggestions in carrying out and writing up this research.

Mr. J. G. Castle, Jr. suggested the problem by insisting that the interaction $A\mathbf{I}\cdot\mathbf{J}$ is insufficient to account for the experimental data on $N^{14}O^{16}$.

PHYSICAL REVIEW VOLUME 80, NUMBER 4 NOVEMBER 15, 1950

Methods of Calculation of Radial Wave Functions and New Tables of Coulomb Functions

I. Bloch,* M. H. Hull, Jr., A. A. Broyles,† W. G. Bouricius,‡ B. E. Freeman,§ and G. Breit
Yale University,‖ New Haven, Connecticut

(Received July 3, 1950)

In connection with the tabulation of Coulomb wave functions special methods of obtaining numerical results having an accuracy of about one percent have been developed and are reported. Some of the methods are applicable also to other problems. Many of them are concerned with the calculation of the second solution of an ordinary differential equation of second order making use of the first solution. The present paper contains an introduction to the use of new Coulomb Functions tables which cover ranges of parameters required for the calculation of nuclear reactions of protons, deuterons and alpha-particles from hydrogen to oxygen in the energy range of a few Mev. The ranges covered are 0 to 6 for ρ, 0 to 3.98 for η. For alpha-particles the tables suffice for the treatment of reactions up to about 10 Mev for $Z=9$(F) and 5 Mev for $Z=2$(He). For protons the tables cover an energy range of roughly 4 times that for alpha-particles.

I. INTRODUCTION

THE availability of Coulomb functions is of obvious importance for the development of nuclear physics. The computation of these functions was started in 1946 under the auspices of the ONR and approximate values of the functions sufficing for the treatment of nuclear reactions of protons, deuterons, and alpha-particles bombarding elements from hydrogen up to oxygen have been obtained at the close of June 1948. The tables have been tried out in some applications during the last year and a few minor errors have been found. They are now available for distribution.[1]

During the course of the work it has been found possible to employ some short cuts and methods of approximation which should be of help in the calculation of radial wave functions not only in the Coulomb case but also for more general central fields. A summary of these methods is presented below. A characteristic feature of the problem is the fact that one needs two functions for each energy, the regular and the irregular functions. The regular solution can be started as a power series at $r=0$ and its calculation is easier than that of the irregular function. Means of making use of available relations between the two functions have been found. It also proved possible to make use of solutions for the special case of zero charge in the calculation of functions for the case of a non-vanishing charge and the method employed in this connection has considerable generality.

The introduction of high speed computational machines decreases the importance of approximation methods. Nevertheless, there is still a large need for being able to obtain approximate answers without the aid of such machines or of large computational projects. This is especially true for problems in which a systematic tabulation covering large ranges of parameters is not needed. The tables referred to above may be considered to be an extension of those published by Yost, Wheeler and Breit;[2,3] Breit, Condon, and Present;[4] Breit, Thaxton, and Eisenbud;[5] Thaxton and Hoisington;[6] Wicher;[7] Wheeler;[8] and Pavinsky.[9] It is understood that new and much more complete tables will be published soon by the National Bureau of Standards.

Notation

(*a*) Physical quantities

$L\hbar$ = angular momentum.
v = relative velocity of colliding particles.
e = electronic charge.
Λ = wave-length of relative motion.
μ = reduced mass.
$a=\hbar^2/\mu e^2$.
Z, Z' = atomic numbers of colliding particles.
$k/2\pi=1/\Lambda$ = wave number.
$\eta=ZZ'e^2/\hbar v$.
r = distance between particles.
$\rho=kr$.
Q = energy evolved in a reaction.

(*b*) Functional symbols and mathematical abbreviations

$\Gamma(x)$ = gamma-function of argument x.
$\sigma_L=\arg\Gamma(L+1+i\eta)$.
$'=d/d\rho$.
F_L = regular Coulomb function otherwise defined by being a solution of $d^2F_L/d\rho^2+[1-2\eta/\rho-L(L+1)/\rho^2]F_L=0$ and having its asymptotic form $F_L\sim\sin(\rho-L\pi/2-\eta\ln 2\rho+\sigma_L)$ at $\rho=\infty$.

* Now at Vanderbilt University, Nashville, Tennessee.
† Now at University of Florida, Gainesville, Florida.
‡ Now at N.E.P.A., Oak Ridge, Tennessee.
§ Now at Los Alamos, New Mexico.
‖ Assisted by the joint program of the ONR and AEC.
[1] Copies of the tables may be obtained by writing G. Breit, Yale University, New Haven, Connecticut.

[2] Yost, Wheeler, and Breit, Phys. Rev. 49, 174 (1936), referred to hereafter as YWB.
[3] Yost, Wheeler, and Breit, J. Terr. Mag. At. El. 40, 443 (1935).
[4] Breit, Condon, and Present, Phys. Rev. 50, 825 (1936).
[5] Breit, Thaxton, and Eisenbud, Phys. Rev. 55, 1018 (1939), hereafter referred to as BTE.
[6] H. M. Thaxton and L. E. Hoisington, Phys. Rev. 56, 1194 (1939).
[7] E. R. Wicher, J. Terr. Mag. At. El. 41, 389 (1936).
[8] J. A. Wheeler, Phys. Rev. 52, 1123 (1937).
[9] P. P. Pavinsky, J. Exper. Theor. Phys. 9, 411 (1939) (in Russian).

G_L=irregular Coulomb function satisfying the same differential equation as F_L, otherwise defined by its asymptotic form $G_L \sim \cos(\rho - L\pi/2 - \eta \ln 2\rho + \sigma_L)$.

$C_L = \{[1+\eta^2/L^2][1+\eta^2/(L-1)^2]\cdots[1+\eta^2/1^2]\}^{\frac{1}{2}} \times [2\pi\eta/(e^{2\pi\eta}-1)]^{\frac{1}{2}}/[1\cdot 3\cdot 5\cdots(2L+1)]$.

$D_L = 1/[(2L+1)C_L]$.

$y_L = dF_L/F_L d\rho$, $y = dF/Fd\rho$.

$p_L = (2L+1)(e^{2\pi\eta}-1)C_L^2/\pi$.

$$q_L = p_L\left[\Sigma_1^L \frac{s}{s^2+\eta^2} - \Sigma_1^{2L+1}\frac{1}{s} + 2\gamma + \text{R.P.}\frac{\Gamma'(i\eta)}{\Gamma(i\eta)}\right]$$
$$+(-)^{L+1}\frac{2^L}{(2L)!}\text{I.P.}\left\{\frac{2^{-L}}{2L+1}+\frac{2^{1-L}(i\eta-L)}{1!(2L)}+\cdots\right.$$
$$+\frac{2^{s+1-L}(i\eta-L)(i\eta-L+1)\cdots(i\eta-L+s)}{(s+1)!(2L-s)}+\cdots$$
$$\left.+\frac{2(i\eta-L)(i\eta-L+1)\cdots(i\eta+L-1)}{(2L)!}\right\}.^{10}$$

γ=Euler's constant$=0.5772\cdots$.

Φ_L, Θ_L=quantities defined by $F_L = C_L\rho^{L+1}\Phi_L$, $G_L = D_L\rho^{-L}\Theta_L$.

Φ_L^*, Θ_L^*=quantities defined by $F_L' = C_L\rho^L\Phi_L^*$, $G_L' = D_L\rho^{-L-1}\Theta_L^*$.

$\mathfrak{g}_L = 1 - 2\eta/\rho - L(L+1)/\rho^2$.

$$H(\rho) = -F(\rho)\int_{\rho_1}^{\rho} F^{-2}(\rho')d\rho'.$$

$A_L = |F_L^2+G_L^2|^{\frac{1}{2}}$.

φ_L=phase of the phase amplitude method, defined by $F_L = A_L\sin\varphi_L$, $G_L = A_L\cos\varphi_L$ with the additional requirement $\varphi_L = 0$ when $\rho = 0$.

General convention: subscript L will be dropped when no confusion will arise by doing so.

II. RICCATI EQUATION METHOD

The differential equation

$$F'' + \mathfrak{g}F = 0, \tag{1}$$

is equivalent to

$$y' + y^2 + \mathfrak{g} = 0, \tag{2}$$

where

$$y = dF/Fd\rho, \tag{2.1}$$

is the logarithmic derivative of F. A way of expanding y in terms of one or more parameters has been described by Breit, Thaxton, and Eisenbud.[2] By means of their Eqs. (9), (9.1) one can compute successive derivatives of y with respect to parameters $\kappa, \lambda, \mu, \nu, \cdots$ entering linearly in

$$\mathfrak{g} = \kappa + \lambda\mathfrak{g}^{(\lambda)} + \mu\mathfrak{g}^{(\mu)} + \cdots. \tag{2.2}$$

[10] A misprint in Eq. (16) of YWB, the omission of 2γ in the formula for χ_L, is here corrected.

If the boundary conditions are such that F^2y_κ, F^2y_λ, $\cdots$, $F^2y_{\kappa\lambda\mu\cdots}$ vanish at $\rho = 0$ then there result formulas[11]

$$y_\kappa = -F^{-2}\int_0^\rho F^2 d\rho, \quad y_\lambda = -F^{-2}\int_0^\rho F^2\mathfrak{g}^{(\lambda)}d\rho, \cdots$$
$$y_{\lambda\lambda} = -2F^{-2}\int_0^\rho F^2 y_\lambda^2 d\rho,$$
$$y_{\kappa\lambda} = -2F^{-2}\int_0^\rho y_\kappa y_\lambda F^2 d\rho, \cdots \tag{2.3}$$
$$y_{\lambda\lambda\lambda} = -6F^{-2}\int_0^\rho y_\lambda y_{\lambda\lambda}F^2 d\rho,$$
$$y_{\lambda\lambda\mu} = -F^{-2}\int_0^\rho (4y_\lambda y_{\lambda\mu} + 2y_\mu y_{\lambda\lambda})F^2 d\rho, \cdots.$$

A few additional formulas are available in Eq. (9.1) of Breit, Thaxton, and Eisenbud for the calculation of derivatives with respect to four parameters.

By means of these expansions it is possible to calculate y for the regular Coulomb function from y for the corresponding field free function, with the same L. The values tabulated by Yost, Wheeler, and Breit[3] served as a convenient starting point. In a few cases their accuracy had to be improved in order to secure sufficient reliability of the final values.

The application of the BTE expansion is convenient if it is desired to obtain the values of y and F for a number of values of η and if the expansion for y converges sufficiently rapidly. If this is not the case the following procedure works satisfactorily. The equation corresponding to Eq. (1) for which a solution is available is

$$F^{(0)\prime\prime} + \mathfrak{g}^{(0)}F^{(0)} = 0, \tag{3}$$

and the relations corresponding to Eqs. (2), (2.1) are

$$y^{(0)\prime} + y^{(0)2} + \mathfrak{g}^{(0)} = 0, \tag{3.1}$$
$$y^{(0)} = dF^{(0)}/F^{(0)}d\rho. \tag{3.2}$$

Denoting the difference between the two logarithmic derivatives by

$$\delta y = y - y^{(0)}, \tag{3.3}$$

there results

$$\frac{d}{d\rho}[F^{(0)2}\delta y] + [(\delta y)^2 + (\delta\mathfrak{g})]F^{(0)2} = 0, \tag{3.4}$$

where

$$\delta\mathfrak{g} = \mathfrak{g} - \mathfrak{g}^{(0)}. \tag{3.5}$$

If one neglects the term in $(\delta y)^2$ in Eq. (3.4) there results an approximation for δy identical with that obtainable

[11] The formula for $y_{\lambda\lambda\mu}$ in Eq. (9.1) of Breit, Thaxton, and Eisenbud contains a misprint $2y_\lambda^2 y_\mu$ for $2y_\mu y_{\lambda\lambda}$ under the integral sign.

from Eqs. (2.3) by neglecting contributions to δy which arise from derivatives of higher order than the first. It has been found possible to employ Eq. (3.4) for a step by step construction of δy by the following procedure. The range of needed values of ρ is divided into suitably chosen relatively small intervals and the value of δy at one end of an interval is found from the value at the beginning of the same interval. This is accomplished by integrating Eq. (3.4) through the interval. Quantities corresponding to the smaller value of ρ in the interval will be here designated by the subscript 1, those for the larger by 2. For an interval that is not too large one has with sufficient accuracy

$$(\delta y)_2=[F^{(0)2}(\rho_1)/F^{(0)2}(\rho_2)](\delta y)_1 -(\rho_2-\rho_1)[F^{(0)}(\rho_2)]^{-2}\tfrac{1}{2}\{[F^{(0)}(\rho_2)]^2 +[F^{(0)}(\rho_1)]^2\{\tfrac{1}{2}[\delta\mathfrak{g}(2)+\delta\mathfrak{g}(1)] +\tfrac{1}{2}[(\delta y)_1^2+(\delta y)_2^2]\}. \quad (3.6)$$

On the right side, in this equation, there is only one unknown quantity $(\delta y)_2^2$. By employing the value of δy_2 which results from an extrapolation from lower ρ for $(\delta y)_2^2$ on the right side of the equation one obtains a first approximation to $(\delta y)_2$ which can be improved by inserting the first approximation for $(\delta y)_2^2$, and repeating the procedure if necessary. This iteration procedure is simply a convenient way of solving a quadratic equation for δy_2.

In the application to Coulomb functions the initial values are

$$(\delta y)_{\rho=0}=\eta/(L+1), \quad (3.7)$$

and

$$\delta\mathfrak{g}=-2\eta/\rho. \quad (3.8)$$

III. CALCULATION OF THE IRREGULAR FUNCTION FROM THE REGULAR FUNCTION BY QUADRATURE

Omitting the subscript L, one has

$$G(\rho_2)/F(\rho_2)-G(\rho_1)/F(\rho_1)+\int_{\rho_1}^{\rho_2}F^{-2}(\rho)d\rho=0. \quad (4)$$

This formula is closely related to the Wronskian relation

$$F'G-G'F=1, \quad (4.1)$$

and in fact the latter is the differential form of the former. By means of Eq. (4) one can obtain $G(\rho_2)$ if one knows $F(\rho_1)$, $G(\rho_1)$, $F(\rho_2)$ and if there is enough information about $F(\rho)$ between ρ_1 and ρ_2 to enable a numerical quadrature to be made for the integral occurring in Eq. (4). The computation of the regular function F is usually easier than that of the irregular function G and Eq. (4) is, therefore, more frequently applicable than the similar relation

$$F(\rho_2)/G(\rho_2)-F(\rho_1)/G(\rho_1)-\int_{\rho_1}^{\rho_2}G^{-2}(\rho)d\rho=0. \quad (4.2)$$

In applying Eq. (4) special methods recommend themselves whenever the integrand varies rapidly and in such a manner that the accuracy of the numerical quadrature becomes questionable. In particular this is the case whenever a node of F falls in the interval $\rho_1<\rho<\rho_2$. At the node then one of the two terms G/F becomes infinite and so does the integrand. However, the quantity needed is G rather than G/F and in the equation,

$$G(\rho)=[G(\rho_1)/F(\rho_1)]F(\rho)-F(\rho)\int_{\rho_1}^{\rho}F^{-2}(\rho')d\rho', \quad (4.3)$$

the two terms representing $G(\rho)$ remain finite as one goes through a node. The only practical question is, therefore, that of carrying the second term across a small interval surrounding the node. Two general procedures which have been found useful for doing so will now be described. In this discussion the node of F will be referred to as ρ_0, the point to which the quadrature has carried the solution as $\rho_<$ and the point at which the quadrature is resumed as $\rho_>$.

(a) The value of the second term on the right side of Eq. (4.3) is obtained on one side of the node from that on the other by noting that this term, $H(\rho)$, satisfies the original differential equation and that the values of the term and of its first derivative,

$$H'(\rho_<)=\left[-F^{-1}(\rho)-F'(\rho)\int_{\rho_1}^{\rho}F^{-2}(\rho')d\rho'\right]_{\rho=\rho_<}, \quad (4.3')$$

are available from the quadratures. The values of any desired number of successive derivatives are, therefore, also available at $\rho=\rho_<$ from the result of differentiating the original differential equation. Thus H'' can be determined as $-\mathfrak{g}H$, H''' is obtainable from

$$H'''+\mathfrak{g}'H+\mathfrak{g}H'=0, \quad (4.4)$$

and so on. The value of $H(\rho_>)$ is thus obtainable from $H(\rho_<)$ by a Taylor Series expansion around $\rho=\rho_<$. The series is

$$H=\{h-h^3\mathfrak{g}(\rho_<)/6-h^4\mathfrak{g}'(\rho_<) +h^5[\mathfrak{g}^2(\rho_<)-3\mathfrak{g}''(\rho_<)]+\cdots\}/F(\rho_<), \quad (4.5)$$

where

$$h=\rho-\rho_<. \quad (4.6)$$

This series applies on either side of the node. If it is desired to obtain the integral in Eq. (4) for $\rho_1=\rho_<$, $\rho_2=\rho$, the same series may be used on division by $F(\rho)$. The right side of Eq. (4.5) varies smoothly on going through the node. The integral varies rapidly and behaves to a first approximation as $h/F(\rho_<)F(\rho)$.

(b) The Taylor Series expansion just described is used with a small number of terms in the series to calculate the values of $H(\rho)$ at $\rho=\rho_<+h$, $\rho_<+2h$, $\rho_<+3h$. These values of $H(\rho)$ are then used as starting values of a numerical integration of the Hartree type[12] for the

[12] D. R. Hartree, Memoirs and Proc. Man. Lit. Phil. Soc. 77, 91 (1932-33).

differential equation $H''+\mathfrak{g}H=0$. This procedure is superior to (a) if it is desired to have a higher accuracy. A larger interval $\rho_>-\rho_<$ can be handled by this means and the numerical integration of H can be used to check on the accuracy of the numerical quadrature for $\int F^{-2}d\rho$ by arranging for an overlap of the two procedures. The main inaccuracies in the numerical quadrature arise for values of ρ close to $\rho_<$ and $\rho_>$ and an occasional check of the type just described has been found to be a useful precaution.

It is desirable to point out that usual quadrature formulas are not especially suitable for the integration of F^{-2} as one approaches the node. In this region one deals essentially with integrals of the type

$$\int_a^b dx/x^2=(b-a)/ab. \tag{5}$$

This circumstance suggests the approximation,

$$\int_\rho^{\rho+h} F^{-2}(\rho)d\rho\cong h/[F(\rho)F(\rho+h)], \tag{5.1}$$

which is often better than Simpson's rule. A still better approximation is obtainable from Eq. (4.5) by applying it to the intervals $(\rho-h, \rho)$, $(\rho, \rho+h)$ and employing values of $\mathfrak{g}$, $\mathfrak{g}'$, $\mathfrak{g}''$ at ρ. One obtains in this manner

$$\int_{\rho-h}^{\rho+h} F^{-2}(\rho)d\rho\cong[h/F(\rho)]\times[1/F(\rho+h)+1/F(\rho-h)][1-h^2\mathfrak{g}(\rho)/6], \tag{5.2}$$

where all terms in an expansion in powers of h have been kept up to h^3. This equation is often more reliable than the Newton-Cotes five point quadrature formula. It will be noted that the methods just discussed are applicable not only to Coulomb functions and that the numerical procedure for obtaining a second solution of an ordinary differential equation of second order is not made impractical by the presence of a node of the first solution within the desired range of values of the independent variable.

It is desirable to caution against the employment of a value of ρ_1 close to a node of $F(\rho)$ in Eq. (4.3). In such a case $|G(\rho_1)/F(\rho_1)|$ will be greater than the absolute value of the integral in (4.3) through most of the range of values of ρ and the numerical accuracy will be poor. It is desirable to have, therefore, a starting value of $G(\rho_1)$ at a value of ρ reasonably close to a maximum of $|F(\rho)|$ or a node of $G(\rho_1)$. If ρ_1 is made to be a node of G the accuracy close to the node of F suffers because the second term in Eq. (4.3) is then the only one present and the fractional accuracy of the factor multiplying F becomes poor close to its node unless the interval $\rho_>-\rho_<$ is made large enough.

The function F has a node also at $\rho=0$. Here there is no need of carrying G across the node of F. Some convenient approximations can be made, however. They will be listed consecutively with methods (a), (b). The first of these approximations is:

(c) For small ρ and especially for large L the integrand of

$$I_L(\rho)=\int_\rho^\infty d\rho/F_L^2 \tag{6}$$

varies rapidly primarily on account of the factor ρ^{L+1} which is present in F_L. This circumstance suggests the introduction of

$$\chi_L=\Phi_L^{-2}, \tag{6.1}$$

and integration by parts as follows

$$C_L^2I_L(\rho)=\int_\rho^\infty \rho^{-2L-2}\chi_L d\rho$$

$$=\Sigma_n+\frac{(2L+1-n)!}{(2L+1)!}\int_\rho^\infty \rho^{-2L-2+n}\chi_L^{(n)}d\rho, \tag{6.2}$$

where

$$\chi_L^{(n)}=d^n\chi_L/d\rho^n, \tag{6.3}$$

$$\Sigma_n=\Sigma_1^{n-1}\frac{(2L-i)!}{(2L+1)!}\chi_L^{(i)}\rho^{-(2L+1-i)}. \tag{6.4}$$

The sum Σ_n often converges very rapidly for small ρ and large L. Under these circumstances the method is very convenient because two or three terms suffice for high accuracy. Thus, for example, for $\eta=0.1585$, $\rho=1.4$, $L=4$ the second term is of the order of 3 percent and the third of the order of 0.1 percent of the first. In cases of such rapid convergence the calculation of derivatives of χ_L need not be accurate for the higher i. The first term of the series gives

$$C_L^2I_L\cong 1/[(2L+1)\rho^{2L+1}\Phi_L^2], \tag{6.5}$$

so that

$$G_L\cong\rho^{-L}/[(2L+1)C_L\Phi_L], \tag{6.6}$$

and

$$\Phi_L\Theta_L\cong 1. \tag{6.7}$$

This relation corresponds to what one expects from the JWKB approximation, in the $(L+\frac{1}{2})^2$ modification, which is applicable to these conditions and yields[13]

$$F_LG_L\cong\rho/[2(L+\tfrac{1}{2})], \tag{6.8}$$

in agreement with Eq. (6.7). The first derivative of Φ_L has been available in the present work through the calculation of the series Φ_L^*.

(d) A related method applicable under similar circumstances makes use of an effective value of L which will be referred to as L^* and which is defined by

$$L^*+1=\rho F'/F. \tag{7}$$

There are appreciable ranges of values of ρ for fixed η

[13] Equation (38) of YWB.

for which L^* varies nearly linearly with ρ. If it is assumed that the variation of L^* between ρ_1 and ρ_2 is exactly linear then one obtains

$$[2\langle L^*\rangle+1]\int_{\rho_1}^{\rho_2}\frac{d\rho}{F^2}=\frac{\rho_1}{F^2(\rho_1)}-\frac{\rho_2}{F^2(\rho_2)}+\frac{b/\langle L^*\rangle}{2\langle L^*\rangle+1}\left\{\frac{\rho_1^2}{F^2(\rho_1)}-\frac{\rho_2^2}{F^2(\rho_2)}-\langle L^*\rangle(\rho_2-\rho_1)\left[\frac{\rho_1}{F^2(\rho_1)}-\frac{\rho_2}{F^2(\rho_2)}\right]\right\}, \quad (7.1)$$

where

$$b=-[L^*(\rho_2)-L^*(\rho_1)]/(\rho_2-\rho_1), \quad (7.2)$$

and

$$\langle L^*\rangle=[L^*(\rho_1)+L^*(\rho_2)]/2. \quad (7.3)$$

The accuracy obtainable by this method is illustrated in Table I for intervals with $\rho_2-\rho_1=0.4$, $\eta=0$, $L=4$.

(e) A modification of the χ_L procedure for $L=0$.

The procedure described under (c) is not convenient for $L=0$. A modification is possible in this case which makes the numerical quadrature appreciably more manageable than it would be in a direct application of general quadrature formulas. The integral $I(\rho)$ is integrated partially once, yielding

$$C_0^2 I(\rho)=-\rho^{-1}\Phi_0^{-2}(\rho)\Big|_{\rho_1}^{\rho_2}+\int_{\rho_1}^{\rho_2}(1/\rho)(d\Phi_0^{-2}/d\rho)d\rho=C_0^2\int_{\rho_1}^{\rho_2}d\rho/F_0^2.$$

By singling out the dominant term for small ρ under the integral sign, subtracting it from the integrand and integrating it separately there results

$$C_0^2 I(\rho)=\left[-\frac{1}{\rho\Phi_0^2}-2\eta\ln\rho\right]\Big|_{\rho_1}^{\rho_2}+\int_{\rho_1}^{\rho_2}\left\{\frac{2\eta}{\rho}-\frac{2(\Phi_0^*-\Phi_0)}{\rho^2\Phi_0^3}\right\}d\rho. \quad (8)$$

For $\rho>1$, in the range of parameters used, this formula is only slightly better than a direct quadrature. For smaller ρ, however, the transformed form listed above as Eq. (8) gives a considerably higher accuracy than the original.

The special methods (c), (d), (e) described for small ρ have been valuable because the numerical integration of the differential equation has to be used with caution when G varies rapidly. A transformation of the independent variable to

$$\ln\rho$$

makes it feasible[7] to handle this region by the Hartree type of numerical integration. The methods (c), (d), however, have the advantage of representing $G(\rho)$ very simply. In the work for the tabulations use has been made of the logarithmic transformation for occasional checks and some overlap between methods applicable to adjacent ranges of parameters was usually arranged for.

TABLE I. Values of error introduced by approximation of Eq. (7.1) for $\eta=0$, $L=4$, $\rho_2-\rho_1=0.4$.

$\rho_1=0.6$	3	4.6	5.0
Error (percent) 0.03	0.22	1.2	5.7

IV. NUMERICAL CALCULATION BY CONTOUR INTEGRATION

Most of the methods described in the preceding section are applicable only if the value of the irregular function $G(\rho)$ is available in some other way. An exception to the general rule is found for small ρ and large L. In this case the contributions to the integral in Eq. (4) from the region of small ρ outweight everything else and the result is very insensitive to the value of $G(\rho_1)$. In the general case, however, it is necessary to obtain $G(\rho_1)$ by some other means. An obvious way of doing so is to calculate one or a few values by the series listed by YWB. It has also been found practical to calculate the values by means of a numerical quadrature of one of the integral representations of the functions in the complex plane. The general method is similar to that of Hoisington and Breit.[14]

The same integral representation can be used[15] for the establishment of corrections to the expressions obtained by the application of the method of steepest descents. The latter are of special value for heavy elements and can be used for the theory of α-decay. Formulas by means of which one can evaluate corrections to the expressions obtained by the method of steepest descents will be also listed.

The starting point is the definite integral

$$Y_L=F_L+iG_L=\frac{ie^{-i\rho}}{(2L+1)!C_L\rho^L}\int_0^\infty t^{-i\eta+L}(t+2i\rho)^{i\eta+L}e^{-t}dt, \quad (9)$$

where the integral may be terminated in any part of the complex plane for which $Re(t)=+\infty$. The saddle point lies at

$$t_0=\tau_0-i\rho, \quad \tau_0=L+(L^2+2\rho\eta-\rho^2)^{\frac{1}{2}}, \quad (9.1)$$

where the quantity τ_0 is supposed to be real. The path is led from $t=0$ to $t=-i\rho$ and from $t=-i\rho$ along a line parallel to the real axis to $-i\rho+\infty$. Its direction at t_0 is the same as that of the path of steepest descents. The integrand is expressed as an exponential, the integral is first approximated by neglecting all terms in the Taylor

[14] L. E. Hoisington and G. Breit, Phys. Rev. 54, 627 (1938).
[15] A. A. Broyles and J. L. Powell, Phys. Rev. 72, 155A (1947).

TABLE II. Values of $G_0/(G_0)_{SD}$.

$\rho=$	11	14	18	10	30	35
$\eta=$	16	16	16	20	20	20
$G_0/(G_0)_{SD}=$	1.012	1.013	1.016	1.010	1.027	1.099

expansion of the exponent around the saddle point and carrying out the integration from $-\infty$ to $+\infty$ for the variable $\tau=\tau_0-i\rho$. This approximation will be referred to here as the "steepest descents approximation." The difference between Y_L and its steepest descents approximation is evaluated by subtracting the integrands in the two integrals and correcting for the presence in the steepest descents approximation of an extra integral from $\tau=-\infty$ to $\tau=0$ and for the true function from $t=0$ to $t=-i\rho$. It is found in this manner that

$$G_L/(G_L)_{SD}=1+\frac{(\tau_0-L)^{\frac{1}{2}}}{(2\pi\rho\eta)^{\frac{1}{2}}(1+L\tau_0/\rho\eta)^{\frac{1}{2}}}\times\int_0^\infty \exp[g(\tau_0)-g(\tau)]$$
$$-\exp[-(\tau-\tau_0)^2g''(\tau_0)/2]d\tau$$
$$-\frac{1}{2}\left[1-\Phi\left(\frac{\tau_0(\tau_0-L)^{\frac{1}{2}}}{2^{\frac{1}{2}}(L\tau_0+\rho\eta)^{\frac{1}{2}}}\right)\right]$$
$$-\frac{(\tau_0-L)^{\frac{1}{2}}\rho^{2L+1}\exp[-\pi\eta+\tau_0+2\eta\tan^{-1}(\rho/\tau_0)]}{(2\pi)^{\frac{1}{2}}2^L(L\tau_0+\rho\eta)^{L+\frac{1}{2}}}\times\int_0^1(1-z^2)^L\sin\left(\rho z+\eta\ln\frac{1-z}{1+z}\right)dz, \quad (9.2)$$

where

$$\tau_0=L+(L^2+2\rho\eta-\rho^2)^{\frac{1}{2}}, \quad (9.3)$$

$$g(\tau)=\tau+2\eta\tan^{-1}(\rho/\tau)-L\ln(\rho^2+\tau^2), \quad (9.4)$$

$$g''(\tau_0)=(L^2-\rho^2+2\rho\eta)^{\frac{1}{2}}/(L\tau_0+\rho\eta), \quad (9.5)$$

and the value obtained by taking into account only the main term in the steepest descents integral is

$$(G_L)_{SD}=\frac{2^L(2\pi)^{\frac{1}{2}}(L\tau_0+\rho\eta)^{L+\frac{1}{2}}\exp[-\tau_0-2\eta\tan^{-1}(\rho/\tau_0)]}{(2L+1)!C_L\rho^L(\tau_0-L)^{\frac{1}{2}}}. \quad (9.6)$$

Equation (9.2) gives the correction factor which must be applied to $(G_L)_{SD}$ in order to obtain G_L. Values of $G_0/(G_0)_{SD}$ obtained by means of these formulas are reproduced in Table II. This quantity has the value 1.01 for $\eta=23$, $\rho=8$, 10, 13; $\eta=30$, $\rho=7$, 10. Variations in the correction factor occur in the latter cases in the third place after the decimal. Similarly for $\eta=20$, $\rho=10$ the correction factor has values 1.010, 1.0097, 1.0093, 1.0089 for $L=0$, 1, 2, 3 respectively; for $\eta=20$, $\rho=30$ it has the values 1.027, 1.025, 1.022, 1.018, 1.017 for $L=0$, 2, 4, 6, 7 and for $\eta=16$, $\rho=18$ the correction factor is 1.015, 1.014 for $L=0$, 1. The JWKB method yields a very similar approximation

$$(G_L)_{\text{JWKB}}=\frac{\rho^{\frac{1}{2}}(l\mathrm{T}_0+\rho\eta)^l\exp\{\pi\eta-\mathrm{T}_0-2\eta(\rho/\mathrm{T}_0)+l-\eta\tan^{-1}(l/\eta)\}}{\rho^l\{\eta+l^2/[\eta+(l^2+\eta^2)^{\frac{1}{2}}]^l\}(\mathrm{T}_0-l)^{\frac{1}{2}}}, \quad (10)$$

where

$$l=[L(L+1)]^{\frac{1}{2}}, \quad (10.1)$$

$$\mathrm{T}_0=l+(l^2+2\rho\eta-\rho^2)^{\frac{1}{2}}. \quad (10.2)$$

The quantity $(G_L)_{\text{JWKB}}$ behaves similarly to $(G_L)_{SD}$. The correction factor $G_L/(G_L)_{\text{JWKB}}$ has the values 1.010, 1.0096, 1.011, 1.011 for $L=0$, 1, 2, 3 with $\eta=20$, $\rho=10$; 1.027, 1.026, 1.025, 1.023, 1.020 for $L=0$, 2, 4, 6, 7 with $\eta=20$, $\rho=30$. The values of ρ and η referred to above are in the general range needed for the calculation of the escape of alpha-particles from naturally radioactive nuclei. Thus, for example, a nuclear radius of 10^{-12} cm for atomic number $Z=80$ corresponds approximately to $\eta=22$, $\rho=10$.

The contour integral has proved to be useful for the calculation of F_L and G_L at the classical turning point; i.e., for values of ρ and η for which $\mathfrak{g}=0$. For this purpose it proved practical to use

$$F_L=[D_L e^{-\pi\eta}\rho^{L+1}/(2L)!]\int_0^1(1-z^2)^L\cos\xi dz, \quad (10.3)$$

$$G_L=[D_L e^{-\pi\eta}\rho^{L+1}/(2L)!]\int_0^1(1-z^2)^L\sin\xi dz$$
$$+[\rho^{L+1}D_L/(2L)!]\int_0^\infty(1+u^2)^L\times\exp[-u\rho-2\eta\tan^{-1}(1/u)]du, \quad (10.4)$$

where

$$\xi=2\eta\tanh^{-1}z-\rho z. \quad (10.5)$$

This computation has been carried out with the aid of auxiliary tables of $\tanh^{-1}z$, $\tan^{-1}(1/u)$, $(1+u^2)^L$, $(1-z^2)^L$ and for each η of $2\eta\tanh^{-1}z$, $\exp[-2\eta\tan^{-1}(1/u)]$, C_0,

$e^{-\pi\eta}$. In much of the numerical work it proved useful to replace dz in the integrals by $(dz/d\xi)d\xi$. Integration by parts when applied to $\int(\sin\xi)(dz/d\xi)d\xi$ gives outside the integral a result which would be exact if $dz/d\xi$ were constant, a second integration by parts gives a result which would be exact if $d^2z/d\xi^2$ were constant. By repeating this procedure convenient series have been obtained by means of which it has proved practical to evaluate the contributions to the integrals arising from regions within which the integrand has an oscillatory character.

V. RECURRENCE FORMULAS

A set of recurrence formulas developed by Powell[16] has proved to be very useful, especially as a means of checking values obtained by other means. A convenient set of formulas suitable for intercomparison of F_L, G_L for different L is

$$-\beta_{L-1}Y_{L-1}+\alpha_L Y_L+\alpha_{L-1}Y_{L-2}=0, \tag{11}$$

$$(\alpha_L{}^2-\beta_L\beta_{L-1})Y_L+\alpha_{L-1}\alpha_L Y_{L-2}+\beta_{L-1}\alpha_{L+1}Y_{L+1}=0, \tag{11.1}$$

$$(\beta_L\beta_{L-1}\beta_{L-2}-\alpha_{L-1}{}^2\beta_L-\alpha_L{}^2\beta_{L-2})Y_L+(\alpha_{L-1}{}^2\alpha_{L+1}-\alpha_{L+1}\beta_{L-1}\beta_{L-2})Y_{L+1}-\alpha_L\alpha_{L-1}\alpha_{L-2}Y_{L-3}=0, \tag{11.2}$$

$$\alpha_L(F_{L-1}G_L-F_LG_{L-1})=1, \tag{11.3}$$

$$\alpha_L=[1+\eta^2/L^2]^{\frac{1}{2}},$$
$$\beta_L=(2L+1)\{\eta/[L(L+1)]+1/\rho\}. \tag{11.4}$$

Equations (11.1), (11.2) are obtainable from Eq. (11). They are reproduced here so as to provide convenient ways of checking tables. An additional relation due to Powell which was also found to provide useful checks is

$$Y_L'+\alpha_{L+1}Y_{L+1}=\left[\frac{L+1}{\rho}+\frac{\eta}{L+1}\right]Y_L. \tag{11.5}$$

A disadvantage of recurrence formulas as a means of checking is the frequent lack of indication as to which of the values is at fault if agreement is not secured.

VI. ADDITIONAL METHODS

The phase amplitude method has been found convenient as a means of checking. By means of it, values at smaller ρ can be compared with values in the region within which the Coulomb functions become essentially sinusoidal. It has also proved useful to tabulate the phase and the amplitude as a means of detecting slips in calculation. The smooth behavior of phase and amplitude as functions of ρ enable better detection of erroneous values than is readily possible with F_L, G_L. The relation

$$\varphi_L(\rho_2)-\varphi_L(\rho_1)=\int_{\rho_1}^{\rho_2}A_L{}^{-2}(\rho)d\rho$$

provides for an additional check. It is also possible to relate the phase amplitude method to the JWKB approximation for the larger ρ, as will be discussed presently.

The Hartree form of arranging a numerical integration of a differential equation is convenient as a means of extending tabulations to values of ρ not covered by other means. Numerical quadrature of $F''=-\mathfrak{g}F$ or $G''=-\mathfrak{g}G$ to check on F', G' and of these quantities for intercomparison with F, G is practically equivalent to a check by a numerical integration of the differential equation. Being somewhat simpler it has proved very useful in detecting slips. The JWKB method of approximation has been of occasional value in the work reported on. It suffers, however, from the disadvantage of having an accuracy which is difficult to ascertain except under special circumstances such as exist for the high repulsive barriers when alpha-particles react with heavy elements.

VII. VALUES OF PARAMETERS FOR NUCLEAR REACTIONS

In the notation,

M_u = mass of oxygen atom/16,
M_i = mass of incident particle,
M_b = mass of bombarded particle,

and on the assumption that the bombarded particle is at rest one has for the parameters of the first stage of the reaction

$$\eta=0.1574ZZ'E_{\text{Mev}}{}^{-\frac{1}{2}}(M_i/M_u)^{\frac{1}{2}}, \tag{12}$$

where E_{Mev} is the energy of the incident particle measured in Mev.

$$\rho\eta=(ZZ'\mu/M_u)[r/(2.905\times10^{-12}\text{ cm})], \tag{12.1}$$

where

$$\mu=M_iM_b/(M_i+M_b).$$

The set of units used is such that

$$\hbar/[(M_um)^{\frac{1}{2}}c]=0.9043\times10^{-12}\text{ cm}, \tag{12.2}$$

and

$$\rho\eta=0.3113(\mu/M_u)ZZ'[r(M_um)^{\frac{1}{2}}c/\hbar]=0.0969(2)(\mu/M_u)ZZ'(rmc^2/e^2). \tag{12.3}$$

If the reaction gives rise to two outgoing particles of masses M_1 and M_2 with an energy release Q then the value of η for the end products is

$$\eta=0.1574Z_1Z_2(E_{\text{Mev}}')^{-\frac{1}{2}}(\mu'/M_u)^{\frac{1}{2}}, \tag{12.4}$$

where

$$\mu'=M_1M_2/M, \quad M=M_1+M_2, \tag{12.5}$$

is the reduced mass for the second stage of the reaction and

$$E'=(M_b/M)E+Q, \tag{12.6}$$

is the energy available in the rest system after disintegration.

[16] J. L. Powell, Phys. Rev. 72, 626 (1947).

TABLE III. Comparison of coefficients of series for A_L given by J.W.K.B. approximation and asymptotic series.

n	Coefficient of $(1/\rho)^n$ asymptotic series
0	1
1	$\frac{\eta}{2}$.
2	$\frac{5\eta^2}{8}+\frac{L(L+1)}{4}$.
3	$\frac{15\eta^3}{16}+\frac{5\eta L(L+1)}{8}-\frac{\eta}{4}$.
4	$\frac{195\eta^4}{128}+\frac{45\eta^2L(L+1)}{32}-\frac{23\eta^2}{16}+\frac{5L^2(L+1)^2}{32}-\frac{3L(L+1)}{8}$.
5	$\frac{663\eta^5}{256}-\frac{91\eta^3}{16}+\frac{195\eta^3L(L+1)}{64}+\frac{45\eta L^2(L+1)^2}{64}-\frac{23\eta L(L+1)}{8}+\frac{3\eta}{4}$.
6	$\frac{4641\eta^6}{1024}-\frac{2431\eta^4}{128}+\frac{3315\eta^4L(L+1)}{512}+\frac{585\eta^2L^2(L+1)^2}{256}-\frac{455\eta^2L(L+1)}{32}+\frac{281\eta^2}{32}+\frac{15L^3(L+1)^3}{128}-\frac{13L^2(L+1)^2}{32}+\frac{15L(L+1)}{8}$.
	J.W.K.B. *approximation*
0	1
1	$\frac{\eta}{2}$.
2	$\frac{5\eta^2}{8}+\frac{L(L+1)}{4}$.
3	$\frac{15\eta^3}{16}+\frac{5\eta L(L+1}{8}$.
4	$\frac{195\eta^4}{128}+\frac{45\eta^2L(L+1)}{32}+\frac{5L^2(L+1)^2}{32}$.
5	$\frac{663\eta^5}{256}+\frac{195\eta^3L(L+1)}{64}+\frac{45\eta L^2(L+1)^2}{64}$.
6	$\frac{4641\eta^6}{1024}+\frac{3315\eta^4L(L+1)}{512}+\frac{585\eta^2L^2(L+1)^2}{256}+\frac{15L^3(L+1)^3}{128}$.

VIII. QUANTITIES CONVENIENT FOR INTERPOLATION AND SOME RELATIONS USEFUL IN APPLICATIONS

For smaller ρ, especially for the higher L, the Coulomb functions F_L, G_L vary too rapidly for accurate interpolation. Here the quantities Φ_L, $\Phi_L\Theta_L$, Φ_L^*/Φ_L form a convenient set. The latter two have the advantage of giving the combinations which are needed in the calculation of the amplitude of the wave function at the nuclear boundary in a "potential well" picture of the nucleus. The formula for the latter is[17]

$$\mathfrak{F}=F/(1-FG\delta-iF^2\delta), \tag{13}$$

where

$$\delta=F'/F-\mathfrak{F}'/\mathfrak{F}. \tag{13.1}$$

[17] G. Breit and F. L. Yost, Phys. Rev. 48, 204 (1935).

At the nuclear boundary one knows $\mathfrak{F}'/\mathfrak{F}$ from the internal solution and one has it available for substitution into Eq. (13.1). It is convenient to deal with $FG\delta$ as

$$(FG/\rho)(\rho\delta).$$

The quantity $\rho\delta$ contains

$$\rho F'/F=\Phi^*/\Phi. \tag{13.2}$$

The remaining quantity

$$\rho\mathfrak{F}'/\mathfrak{F}=xd\mathfrak{F}/\mathfrak{F}dx, \tag{13.3}$$

where x is length expressed in any unit. The latter circumstance is convenient. The factor multiplying $\rho\delta$ is

$$F_LG_L/\rho=\Phi_L\Theta_L/(2L+1). \tag{13.4}$$

The phase amplitude variables A_L, φ_L defined in the section on notation are very useful in applications and have good interpolation properties. They are connected by

$$A_L{}^2d\varphi_L=d\rho, \tag{13.5}$$

which make it possible to calculate differences in φ_L from values of A_L. In applying the phase amplitude variables it is natural to express results in terms of the phase shift K_L. A formula for the latter has been given by Wheeler.[8] Substituting for φ_L' its value in terms of A_L^{-2} his formula becomes

$$xd\mathfrak{F}/\mathfrak{F}dx-\rho A'/A=(\rho/A^2)\cot(\varphi+K). \tag{14}$$

Having K one can obtain $\mathfrak{F}$ at the nuclear boundary from

$$\mathfrak{F}=e^{iK}(F\cos K+G\sin K). \tag{14.1}$$

Equation (14) is convenient when $\rho dA/Ad\rho$ is readily available. If this is not the case use can be made of

$$\cot(\varphi+K)-\cot\varphi=(\mathfrak{F}'/\mathfrak{F}-F'/F)A^2. \tag{14.2}$$

A knowledge of the behavior of A_L for large ρ is helpful in determining values of the functions in regions not covered by the tables. It also can be used for starting a numerical integration of the differential equation for A_L toward smaller ρ. A list of coefficients of powers of $1/\rho$ in the asymptotic series for A_L is given in Table III. In this table the coefficients are compared with those corresponding to the usual JWKB approximation; *i.e.*, to the approximation $A_L\cong g_L^{-\frac{1}{2}}$.

The authors would like to express their indebtedness to Drs. P. R. Zilsel, J. S. Blair, J. L. Powell, and Mr. J. L. Greenstadt for their help with various phases of the work and to Mrs. Gloria Cole, Mrs. Carolyn Arfken, and Mr. J. F. Bartram for computational assistance. Acknowledgment should also be made to the University of Wisconsin under whose auspices the work has begun.

Asymptotic Expansion of the Irregular Coulomb Function

G. Breit and M. H. Hull, Jr.
Yale University, New Haven, Connecticut*
(Received July 21, 1950)

It is shown that the irregular Coulomb Function G_L can be expanded as an asymptotic power series in the energy, with coefficients which are expressible in terms of the modified Bessel function of the second kind. The form of the coefficients is the same as obtained by Yost, Wheeler, and Breit in an expansion of the regular function F_L with the modified Bessel function of the second kind replacing that of the first kind of the same order.

IT has been shown in a previous note[1] that the expansion of the irregular Coulomb function for angular momentum zero can be made employing a series in powers of the energy, each term of the series being obtainable by replacement of the Bessel function I_ν by the Bessel function K_ν in a series occurring in the representation of the regular function.

In the present note a similar relationship is shown to hold for angular momenta greater than zero. Standard notation, a list of which is given in the previous note, will be used below. This notation is identical with that of Yost, Wheeler, and Breit.[2] The proof, as carried out in [I], depends on the possibility of rearranging the power series in ρ which represents Θ_0. The result of the rearrangement is a power series in $1/\eta^2$, *i.e.*, essentially in the energy. The coefficients are functions of the distance r and are expressed in terms of $K_\nu(x)$ the Bessel function of the second kind of imaginary argument, in the notation of Whittaker and Watson.[3] It will first be shown that for $L\neq 0$ a similar rearrangement of terms can be made.

The series Ψ_L can be rearranged in this manner, as may be seen from the fact that any power of ρ, ρ^s may be expressed as $(\rho\eta)^s/\eta^s$ and that, when the whole solution is substituted into Eq. (27) of YWB, there can be no connection when working in the $(\zeta, 1/\eta^2)$ variables between coefficients connecting powers of η differing by odd numbers. The same may be seen from Eqs. (19), (20) of YWB which give Ψ_L as

$$\Psi_L=\Sigma_{-L}^{\infty}a_j\rho^{j+L};\quad a_{-L}=1,\ a_{L+1}=0,$$
$$a_j=[2\eta a_{j-1}-a_{j-2}-p_L(2j-1)A_j]/[(j+L)(j-L-1)], \quad (1)$$

and here A_j is the coefficient of ρ^{j-L-1} in the series for Φ_L. The latter starts with 1 for $j=L+1$ and, as has been shown in YWB, it can be rearranged in terms of the variable x with the aid of even powers of $1/\eta^2$. The result of this reordering is the series on the right side of Eq. (33). The rearrangement would give also odd powers of $1/\eta$ unless the A_j are even or odd functions of η for even or odd values of $j-L-1$; this fact can be seen directly from the recurrence formula between the A_j which connects A_j with ηA_{j-1} and A_{j-2} by a linear relation. It is seen, on the other hand, that for $j=-L$ the quantity a_j is by definition even in η and that $j-L-1$ is in this case odd. Since p_L is odd in η the recurrence formula for a_j connects quantities of the same parity provided a_j is even or odd in η according as to whether $j-L$ is even or odd. A consideration of how a_{-L+1} follows from a_L shows that the construction of coefficients gives coefficients having a parity in η in accordance with the rule just mentioned. The value zero for a_{L+1} is consistent with a_{L+1} being odd in η as is in agreement with $L+1-(-L)$ being odd. It has thus been shown that only even powers $1/\eta$ occur in the result of rearranging Ψ_L in terms of x.

It will be seen next that the term in $\ln(2\rho)$ which multiplies Φ_L in the formula for Θ_L does not leave a term in $\ln\eta$ if Stirling's series for $\Gamma'(i\eta)/\Gamma(i\eta)$ is employed. The disappearance of $\ln\eta$ occurs because the combination

$$p_L\ln 2\rho+q_L, \quad (1.1)$$

contains $\Gamma'(i\eta)/\Gamma(i\eta)$ only in q_L as

$$p_L\,\text{R.P.}[\Gamma'(i\eta)/\Gamma(i\eta)],$$

so that $\ln(2\rho)$ and Stirling's series combine in the same way independently of the value of L. The remaining part of q_L contributes to Θ_L the following amount

$$\text{I.P.}(-)^{L+1}\frac{2^L}{(2L)!}\left\{\frac{2^{-L}}{2L+1}+\frac{2^{1-L}(i\eta-L)}{1!(2L)}+\cdots\right.$$
$$+\frac{2^{s+1-L}(i\eta-L)\cdots(i\eta-L+s)}{(s+1)!(2L-s)}+\cdots$$
$$\left.+\frac{2^L(i\eta-L)(i\eta-L+1)\cdots(i\eta+L-1)}{(2L)!1}\right\}\rho^{2L+1}\Phi_L. \quad (1.2)$$

The factor $\rho^{2L+1}=(x^2/8)^{2L+1}/\eta^{2L+1}$ is odd in η. The factor Φ_L can be expressed as a power series in $1/\eta^2$. The remaining factor is the imaginary part of a sum of products containing η in the form $i\eta$ only. It introduces therefore odd powers of η only. Taking into account the

* Assisted by the joint program of the ONR and the AEC.
[1] G. Breit and M. H. Hull, Jr., Phys. Rev. 80, 392 (1950), referred to as [I].
[2] Yost, Wheeler, and Breit, Phys. Rev. 49, 174 (1936), referred to as YWB.
[3] E. T. Whittaker and G. N. Watson, *Modern Analysis* (Cambridge University Press, London, 1920), third edition, Chapter XVII.

factor η^{-2L-1} arising from ρ^{2L+1} it is seen that only even powers of η are brought in. The highest power of η in the sum of products is η^{2L} and therefore the imaginary part of the sum of products contributes only terms in η^{2L-1} and lower. The contributions of this part of q_L are seen to be confined to positive powers of $1/\eta^2$. The same holds for terms coming from $\Gamma'(i\eta)/\Gamma(i\eta)$ because the highest power of η in p_L is η^{2L+1} which is absorbed by ρ^{2L+1} to form $(x^2/8)^{2L+1}$ and because Stirling's series contributes terms in positive powers of $1/\eta^2$ only. An examination of the recurrence relation for the series for Ψ_L shows that here also there occur only positive powers of $1/\eta^2$ in the x, η representation. Thus $2\eta a_{j-1}$ can contribute to a_j at most η^{j+L} which is absorbed by ρ^{j+1}, the term $-a_{j-2}$ can contribute at most a power of η less by two than that coming from $2\eta a_{j-1}$. The quantity A_j, which is the coefficient of ρ^{j-L-1} in Φ_L, does not contain η to a power higher than η^{j-L-1}. The powers of η contained in $p_L A_j$ are, therefore, no higher than $\eta^{j-L-1+(2L+1)}=\eta^{j+L}$ and this power of η is absorbed by ρ^{j+L} which is multiplied by a_j in Ψ_L. It may be concluded that all powers of $1/\eta^2$ occurring in the x, η representation with the introduction of the Stirling's series for $\Gamma'(i\eta)/\Gamma(i\eta)$ are positive or zero and that odd powers of $1/\eta$ are absent. The discussion so far is the equivalent of part A of the proof as conducted in [I].

The integral representation

$$Y_L=F_L+iG_L$$

$$=\frac{ie^{-i\rho}}{(2L+1)!C_L\rho^L}\int_0^\infty t^{-i\eta+L}(t+2i\rho)^{i\eta+L}e^{-t}dt \quad (2)$$

gives by the same deformation of the path as in [I]

$$G_L=(\Theta_L{}^{\mathrm{I}}+\Theta_L{}^{\mathrm{II}})/[(2L+1)C_L\rho^L], \quad (2.1)$$

with

$$\Theta_L{}^{\mathrm{I}}=[1/(2L)!]\int_0^\infty (\tau^2+\rho^2)^L \times\exp[-\tau-2\eta\tan^{-1}(\rho/\tau)]d\tau, \quad (2.2)$$

$$\Theta_L{}^{\mathrm{II}}=[e^{-\pi\eta}\rho^{L+1}/(2L)!]\int_0^1 (1-u^2)^L \times\sin\left[-\rho u+\eta\ln\frac{1+u}{1-u}\right]du, \quad (2.3)$$

and

$$\Phi_L=C_L{}^{-2}[e^{-\pi\eta}/(2L+1)!] \times\frac{1}{2}\int_{-1}^{+1}(1-u)^{L-i\eta}(1+u)^{L+i\eta}e^{-i\rho u}du. \quad (2.4)$$

According to the reasoning presented in connection with Eqs. (10), (11), (12), (13) of [I] the result of arranging Θ_0 as a power series in $1/\eta^2$ gives coefficients which can be obtained from $\Theta_0{}^L$ by a symbolic expansion. This part of the proof in [I] applies in the present case without essential change. The form of Eq. (10) is changed but this circumstance is immaterial since it is only the possibility of obtaining the coefficient of η^{-2s} as $(1/s!)[\partial^s\Theta_L/\partial(\eta^{-2})^s]_{\eta=\infty}$ that is essential. It is thus seen that part C of the proof in [I] applies here also and that the series for Θ_L can be obtained by expanding

$$[\Theta_L]_{\mathrm{Symb}}=[1/(2L)!](x/2)^{2L+1}\int_0^\infty [v^2+(x/4\eta)^2]^L \times\exp\left[-\frac{vx}{2}-2\eta\tan^{-1}\frac{x}{4\eta v}\right]dv \quad (3)$$

in powers of $1/\eta^2$ under the integral sign, with the employment of the Taylor expansion for $\tan^{-1}(x/4\eta v)$.

A transformation of the integral representation for Φ_L given by Eq. (2.4) by means of the variable θ used in Eq. (14) of [I] and a consideration of the result as a sum of two parts arising from the presence of $e^{\pi\eta}$ and $e^{-\pi\eta}$ in $C_L{}^{-2}$ by deformation of the path of integration described in connection with Eq. (14′) of [I] yield

$$\Phi_L=(i/\pi x)(C_0{}^2/C_L{}^2)[x^{-2L}/(2L+1)!]\int_C (x^2+16\eta^2\zeta^2)^L \times\exp\left[-\frac{x\zeta}{2}-2\eta\tan^{-1}\frac{x}{4\eta\zeta}\right]d\zeta \quad (4)$$

where C is a contour around $\zeta=0$, taken counterclockwise and where it is understood that $\tan^{-1}(x/4\eta\zeta)$ should be expanded as a Taylor's series.

Comparison of Eq. (4) with Eq. (3) and employment of integral representations for K_ν, I_ν listed as Eqs. (17), (18) in [I] shows that

$$[\Theta_L]_{\mathrm{Symb}} =-(2L+1)(C_L{}^2/C_0{}^2)2^{-6L-1}x^{4L+2}\eta^{-2L}[\Phi_L]_{I\to K}, \quad (5)$$

where $I\to K$ indicates the replacement of all the I_ν by the K_ν. Since the recurrence formulas for the I_ν and the K_ν are the same in form, the replacement may be made in any form obtainable from Eq. (4) by expansion in powers of η^2 and employment of Eq. (18) of [I]. The coefficient,

$$C_L{}^2/C_0{}^2 =\frac{[1+\eta^2/L^2][1+\eta^2/(L-1)^2]\cdots[1+\eta^2/1^2]}{[1\cdot3\cdots(2L+1)]^2}. \quad (5.1)$$

Its limiting value for $\eta\to\infty$ is

$$(2\eta)^{2L}/[(2L+1)!]^2. \quad (5.2)$$

The limiting form of Eq. (5) for $\eta\to\infty$ is, therefore,

$$\mathrm{Lim}[\Theta_L/\Phi_L]=-[2K_{2L+1}(x)/I_{2L+1}(x)](x/2)^{4L+2}/[(2L)!(2L+1)!],$$

in agreement with Eqs. (32), (36) of YWB.

The right side of Eq. (5.1) can be obtained from the expression on the right side of Eq. (5.2) by multiplying the latter by the factor.

$$[1+L^2/\eta^2][1+(L-1)^2/\eta^2]\cdots[1+1^2/\eta^2],$$

whose presence cannot be inferred from the consideration of limiting forms for $\eta\to\infty$. This factor can be checked, however, by collecting all terms in $\ln x$ which are present in the $K_\nu(x)$.

The result of the consideration is that the employment of Stirling's asymptotic expansion for $\Gamma'(i\eta)/\Gamma(i\eta)$ in the formula for Θ_L, ordering of all terms according to powers of $1/\eta^2$ with coefficients expressed as functions of $x=(8\rho\eta)^{\frac{1}{2}}$ gives a series which is identical with the series obtainable by evaluating the right side of Eq. (5). The series in the I_ν may be obtained either by means of Eq. (4) and Eq. (18) of [I] or by means of Eq. (33) of YWB.

The integral representation reproduced as Eq. (2) of the present paper applies also to attractive fields. The quantity Θ_L^{II} may not be disregarded, however, in this case when one evaluates the coefficients of $1/\eta^{2s}$ in Θ_L because $e^{-\pi\eta}$ is infinite. The considerations do not apply, therefore, to attractive Coulomb Fields.

PHYSICAL REVIEW VOLUME 80, NUMBER 4 NOVEMBER 15, 1950

Hartree Computation of the Internal Diamagnetic Field for Atoms*

W. C. Dickinson†
Physics Department, Research Laboratory of Electronics, Massachusetts Institute of Technology, Cambridge, Massachusetts
(Received June 22, 1950)

For an atom or monatomic ion in a magnetic field H there will be an induced shielding field $H'(0)$ at the the nucleus given by $H'(0)=(eH/3mc^2)v(0)$ where $v(0)$ is the electrostatic potential produced at the nucleus by the atomic electrons. Using the Thomas-Fermi model, Lamb put this expression into a calculable form. However, in modern nuclear induction and resonance absorption experiments it is important to have a more precise knowledge of the magnitude of this shielding field. In this paper computed values of $v(0)$ are given for all atoms and singly charged ions which have been treated by the Hartree or Hartree-Fock approximations to the self-consistent field method. By interpolation a list of $H'(0)/H$ values for all neutral atoms is given. Although it is impossible to check the accuracy of these values experimentally it is estimated from other evidence that they can be trusted to within five percent. An exception must be made, however, for the heaviest atoms where the relativity effect becomes appreciable, amounting to an estimated six percent correction to $H'(0)/H$ for $Z=92$. Finally, the usefulness of accurate values of the atomic shielding field in analyzing the total shielding field in molecules is discussed.

I. INTRODUCTION

In the case of an atom or monatomic ion in an external magnetic field H, Larmor's theorem states that the motion of the atomic electrons in the field is the same (neglecting terms in H^2) as the motion before the existence of the field, except for the superposition of the Larmor precession. This creates a shielding field at the nucleus which, although always small compared with the external field, constitutes an important correction in the measurement of nuclear magnetic moments by the resonance method. Lamb[1] derived an expression for this shielding field, showing it to depend directly on the electrostatic potential $v(0)$ produced at the nucleus by the atomic electrons. Evaluating $v(0)$ on the basis of the Thomas-Fermi model he obtained for the ratio of induced to external field

$$H'(0)/H=-0.319\times10^{-4}Z^{4/3}. \quad (1)$$

In the cases $Z=19$, 20, 26, 29, 37, 55, 74, and 80 where $v(0)$ was explicitly available from Hartree wave functions, Lamb showed that Eq. (1) is checked fairly well. This paper extends the computation of $v(0)$ and hence $H'(0)/H$ for all atoms and singly charged ions which have been treated by the Hartree or Hartree-Fock approximations to the self-consistent field method. The project was undertaken originally for a limited number of cases to determine the dependence of the shielding field $H'(0)$ on the state of ionization of an atom. The results indicated the possibility of just detecting a shift in nuclear resonance positions between an atom in a neutral and singly ionized state. However, with the subsequent discovery of larger shifts due to the effect of chemical binding (discussed below) it would be difficult to distinguish this small effect experimentally.

II. THEORY

Consider an atom with a spherically symmetrical charge distribution of radial charge density $\rho(r)$ in an external field H. As an element of volume we take a ring with axis passing through the nucleus and parallel to H, with cross section $rd\theta dr$ and perimeter $2\pi r\sin\theta$, so that its volume is $2\pi r^2\sin\theta d\theta dr$ and it will contain a

* This work has been supported in part by the Signal Corps, the Air Materiel Command, and the ONR.
† Present address: Los Alamos Scientific Laboratory, Los Alamos, New Mexico.
[1] W. E. Lamb, Jr., Phys. Rev. 60, 817 (1941).

charge $\sin\theta d\theta dr\rho(r)/2$. The rotation of this charge ring with the Larmor frequency results in a current

$$di=[\sin\theta d\theta dr\rho(r)/2]eH/4\pi mc \quad (2)$$

and by the Biot-Savart law the field $dH'(0)$ at the nucleus due to this current loop is

$$dH'(0)=(2\pi di\sin^2\theta)/rc. \quad (3)$$

TABLE I. Values of $-v(0)$ for neutral atoms and singly charged ions computed from Hartree and Hartree-Fock wave functions.

Atomic number	$-v(0)$ in atomic units (a) without exchange	(b) with exchange	Reference (a)	(b)
1	1.000	1.000	a	a
2^+	2.000	2.000	a	a
2	3.37		b	
3^+		5.369		c
3	5.463	5.714	d	c
4	8.365	8.410	e	f
5		11.23		g
6	14.51	14.69	h	i
7		18.32		j
7^-		18.70		j
8^+	21.373	21.61	k	l
8	21.944	22.26	k	l
8^-		22.72		l
9		26.12		m
9^-	26.5	26.56	n	m
10		30.811		m
11^+	34.8	35.13	b	j
11		35.43		j
11^-		35.57		o
17^-	63.88	64.67	p	p
18	68.89	69.67	q	q
19^+	73.91	74.67	q	q
19		74.90		o
19^-		75.02		o
20^+		79.95		r
20	79.3	80.20	e	r
26	114.0		s	
29^+	133.5	135.1	t	t
30	139.3		u	
31^+	145.2		u	
31	146.5		u	
32	153.7		v	
33^+	160.0		u	
33	160.3		u	
37^+	187.5		n	
47^+	262		w	
55^+	323		x	
74	490		y	
80	543		e	

[a] Exact wave function.
[b] D. R. Hartree, Camb. Phil. Soc. Proc. **24**, 111 (1927–28).
[c] V. Fock and M. J. Petrashen, Physik. Zeits. Sowjetunion **8**, 547 (1935).
[d] J. Hargreaves, Proc. Camb. Phil. Soc. **25**, 75 (1928–29).
[e] D. R. and W. Hartree, Proc. Roy. Soc. **149A**, 210 (1935).
[f] D. R. and W. Hartree, Proc. Roy. Soc. **150A**, 9 (1935).
[g] Brown, Bartlett, and Dunn, Phys. Rev. **44**, 296 (1933).
[h] C. C. Torrance, Phys. Rev. **46**, 388 (1934).
[i] A. Jucys, Proc. Roy. Soc. **173A**, 59 (1939).
[j] D. R. and W. Hartree, Proc. Roy. Soc. **193A**, 299 (1948).
[k] D. R. Hartree and M. M. Black, Proc. Roy. Soc. **139A**, 311 (1933).
[l] D. R. Hartree and B. Swirles, Phil. Trans. Roy. Soc. **238A**, 229 (1939–40).
[m] F. W. Brown, Phys. Rev. **44**, 214 (1933).
[n] D. R. Hartree, Proc. Roy. Soc. **151A**, 96 (1935).
[o] D. R. and W. Hartree, Proc. Camb. Phil. Soc. **34**, 550 (1938).
[p] D. R. and W. Hartree, Proc. Roy. Soc. **156A**, 45 (1936).
[q] D. R. and W. Hartree, Proc. Roy. Soc. **166A**, 450 (1938).
[r] D. R. and W. Hartree, Proc. Roy. Soc. **164A**, 167 (1938).
[s] M. F. Manning and L. Goldberg, Phys. Rev. **53**, 662 (1938).
[t] D. R. and W. Hartree, Proc. Roy. Soc. **157A**, 490 (1936).
[u] W. and D. R. Hartree and M. F. Manning, Phys. Rev. **59**, 299 (1941).
[v] W. and D. R. Hartree and M. F. Manning, Phys. Rev. **59**, 306 (1941).
[w] M. M. Black, Mem. Manchester Lit. Phil. Soc. **79**, 29 (1935).
[x] D. R. Hartree, Proc. Roy. Soc. **143A**, 506 (1933–34).
[y] M. F. Manning and J. Millman, Phys. Rev. **49**, 848 (1936).

Substitution for di from Eq. (2) gives

$$\frac{H'(0)}{H}=\frac{e}{4mc^2}\int_0^\pi \sin^3\theta d\theta\int_0^\infty\frac{\rho(r)dr}{r}=\frac{e}{3mc^2}v(0). \quad (4)$$

This is just the expression obtained by Lamb. For purposes of computation this may be written as

$$H'(0)/H=\tfrac{1}{3}\alpha^2 v(0), \quad (5)$$

where α is the fine structure constant and $v(0)$ is now understood to be in atomic units and is of course a negative quantity.

In the self-consistent field method the approximation is made of spherical symmetry in the electronic distribution so that $v(0)$ can be computed simply. For carrying out the quadrature of $v(0)$ Simpson's "One-Third" rule was used. Suppose the definite integral of $f(x)$ over an interval of x from a to b is desired. Indicating the values of $f(x)$ at $x=a$ and at $x=b$ by y_0 and y_n and the intermediate values by $y_1, y_2, y_3\cdots$, Simpson's rule gives

$$I=\int_a^b f(x)dx=\tfrac{1}{3}h[y_0+4(y_1+y_3+\cdots+y_{n-1})+2(y_2+y_4+\cdots+y_{n-2})+y_n], \quad (6)$$

where h is the value of the equal intervals between successive values of y. The quantity usually evaluated at successive intervals of r by the self-consistent field method is P or P^2, the latter being just the radial charge density $\rho(r)$ in atomic units if P is suitably normalized. Thus

$$y_m=(P_m^2/r_m)\Big/\left(\int_0^\infty P^2dr\right). \quad (7)$$

Table I gives the computed values of $-v(0)$. Considering the internal consistency of the data it is felt that the numerical integration does not introduce errors larger than 0.5 percent. In the first column a + or − sign after the atomic number signifies a positive or negative ion respectively. The second column lists the values of $-v(0)$ for atoms and ions whose wave functions have been calculated without taking account of exchange terms (Hartree approximation), and the third column lists values in those cases where exchange terms have been included (Hartree-Fock approximation). The fourth and fifth columns give the references for the wave functions used. This list of references should serve incidentally as a useful bibliography of wave functions obtained by the self-consistent field method.

Table II gives values of $H'(0)/H$ for neutral atoms. These values have been obtained using Eq. (5) with[2] $\alpha^2=5.3263\times10^{-5}$ and interpolating from Table I. As is seen from Table I, values of $v(0)$ with exchange for all neutral atoms up to and including Na are available

[2] J. W. M. DuMond and E. R. Cohen, Rev. Mod. Phys. **20**, 82 (1948).

(except for He in which case there are no exchange terms). For higher Z, values of $v(0)$ without exchange or for a singly charged ion often are the only ones available. That this introduces only a small error can be seen from Table I. Thus the values of $v(0)$ with exchange are on the average about one percent greater than the corresponding values without exchange, and the difference in $v(0)$ is 0.8 percent between Na and Na^+ and falls to 0.2 percent between As and As^+.

Figure 1 is a comparison of $H'(0)/H$ values for the light elements computed from Hartree-Fock wave functions and from Eq. (1) based on the Thomas-Fermi model.

III. DISCUSSION

Unfortunately there seems to be no way of determining $H'(0)$ experimentally since there is no way of stripping the atom of all of its electrons. Since the precision to which $H'(0)/H$ is known affects directly the precision to which a nuclear moment ratio can be quoted, an attempt will be made to estimate the accuracy of the values of $H'(0)/H$ listed in Table II.

Concerning the accuracy of wave functions obtained by the self-consistent field method the following evidence is available.

(1) The bulk diamagnetic susceptibility has been measured experimentally for most atoms and ions which have been treated by the self-consistent field method. The theoretical values from wave functions calculated without exchange tend to be lower than the experimental values by from 10 to 25 percent. However, when exchange terms are included the agreement is on the average good to within seven percent. The explanation for this is that the main contribution to the bulk diamagnetic susceptibility comes from the outer atomic electrons,[3] hence its value is quite sensitive to a contraction of the outer charge distribution which is the effect of adding exchange terms. On the other hand the electrostatic potential $v(0)$ of the atomic electrons is relatively insensitive to a change in the outer charge distribution so that its value is little affected by inclusion of exchange.

TABLE II. The internal diamagnetic correction for neutral atoms.

Z	$H'(0)/H$(%)	Z	$H'(0)/H$(%)	Z	$H'(0)/H$(%)
1	0.0018	32	0.273	63	0.693
2	0.0060	33	0.285	64	0.709
3	0.0101	34	0.296	65	0.724
4	0.0149	35	0.308	66	0.740
5	0.0199	36	0.321	67	0.756
6	0.0261	37	0.333	68	0.772
7	0.0325	38	0.345	69	0.788
8	0.0395	39	0.358	70	0.804
9	0.0464	40	0.371	71	0.820
10	0.0547	41	0.384	72	0.837
11	0.0629	42	0.397	73	0.853
12	0.0710	43	0.411	74	0.869
13	0.0795	44	0.425	75	0.885
14	0.0881	45	0.438	76	0.901
15	0.0970	46	0.452	77	0.917
16	0.106	47	0.465	78	0.933
17	0.115	48	0.478	79	0.949
18	0.124	49	0.491	80	0.965
19	0.133	50	0.504	81	0.982
20	0.142	51	0.517	82	0.998
21	0.151	52	0.531	83	1.01
22	0.161	53	0.545	84	1.03
23	0.171	54	0.559	85	1.05
24	0.181	55	0.573	86	1.06
25	0.191	56	0.587	87	1.08
26	0.202	57	0.602	88	1.10
27	0.214	58	0.616	89	1.11
28	0.226	59	0.631	90	1.13
29	0.238	60	0.647	91	1.15
30	0.249	61	0.662	92	1.16
31	0.261	62	0.678		

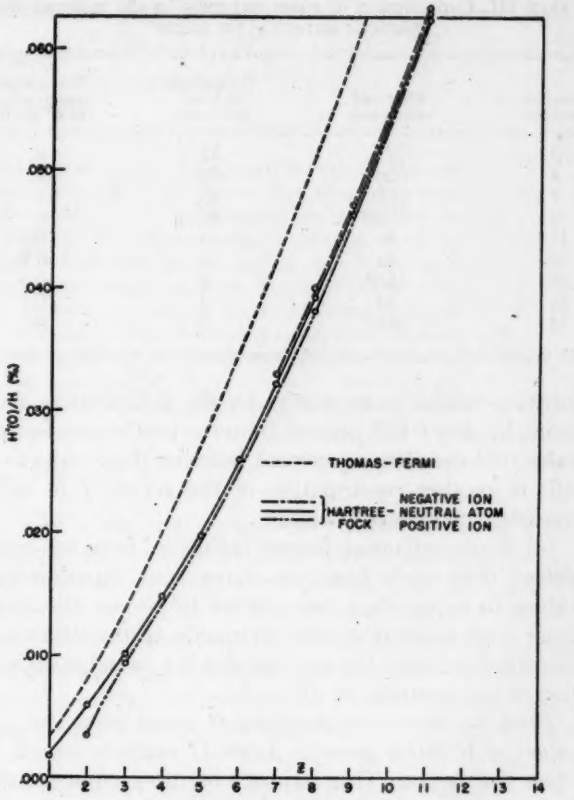

FIG. 1. Comparison of $H'(0)/H$ for the light elements, computed from the Thomas-Fermi model and from the Hartree-Fock model.

(2) X-ray and optical term values given by the self-consistent field method agree on the average to four percent with experimental values. If only the x-ray term values are considered the agreement is even better. Thus the self-consistent field method gives quite accurate energy values, *particularly for the inner electrons.*

(3) Hylleraas has carried out the calculation of $v(0)$ for He using his analytic He wave function. His final value $v(0)=-3.3764\pm0.0002$ is to be compared with $v(0)=-3.37$ from Table I.[4] Since the Hylleraas wave

[3] Because of this fact an average agreement of seven percent is quite good. Diamagnetic susceptibilities are measured in the liquid or solid state where distortion of the outer electronic distribution by other atoms would be expected to be large.

[4] The author is indebted to Dr. H. L. Anderson for making available the results of this calculation by Professor Hylleraas. E. Hylleraas and S. Skavlem, Phys. Rev. 79, 117 (1950).

TABLE III. Contribution of outer electrons to the internal diamagnetic correction for atoms.

Atomic number	Electrons concerned	Percentage of total electrons	Percentage contribution to $H'(0)/H$
3	$2s$	33	6
4	$(2s)^2$	50	12
7	$(2p)^3$	43	14
9	$(2p)^5$	55	16
11	$3s$	9	0.8
19	$4s$	5	0.3
26	$(4s)^2$	8	0.6
31	$4p$	3	0.1
74	$(6s)^2$	3	0.1

function results in an energy for the helium atom differing by only 0.028 percent from the best experimental value, the excellent agreement between these values of $v(0)$ is another confirmation of the accuracy of self-consistent field energy values.

(4) X-ray scattering factors calculated from self-consistent field wave functions agree with experimental values to better than five percent in almost all cases. Since x-ray scattering depends mainly on the electronic distribution nearer the nucleus, this is a valuable indication of the accuracy of $v(0)$.

From the above considerations it would seem that the values of $H'(0)/H$ given in Table II could be trusted to about five percent. This estimate of the accuracy must however be qualified for the heaviest atoms due to the relativity effect which is generally not taken into account in self-consistent field calculations.[5] Since the inner shells are most affected by this correction it cannot be neglected. The heaviest atom for which it has been included[6] is Cu^+ where the value $v(0)=-134.3$ including relativity is to be compared with $v(0)=-133.5$ without relativity. Thus an increase of 0.6 percent occurs for $Z=29$. By approximate considerations it can be shown that the relativistic correction would be expected to go as Z^2 so that for $Z=92$ the correction would amount to about six percent of the computed value of $H'(0)/H$.

In recent nuclear induction and magnetic resonance absorption experiments it has been discovered that the value of the applied magnetic field H_0 for nuclear resonance at a fixed radiofrequency may depend on the chemical compound containing the resonating nucleus.[7-9] Ramsey[10] subsequently obtained a formal expression for the total magnetic shielding field in molecules, showing it to consist of two terms. The first is a simple diamagnetic term identical with the term for atoms except that the integration is extended over all the electrons in the molecule rather than only the one atom containing the resonating nucleus. The second is a second-order paramagnetic term which depends on the wave functions of all the excited states of the molecule. Ramsey gives a method of calculating the contribution of this term for linear molecules.

Accurate knowledge of the atomic diamagnetic correction is of value for two reasons. First, in those experiments in which the nucleus is contained in a free atom or in a monatomic ion rather than in an atom bound in a molecule or ionic complex, the atomic diamagnetic correction can be applied directly. Thus for aqueous solutions of *some* salts and for monatomic gases such as He^3 and $Xe^{129,131}$ this would be the case. Second, the self-consistent field computations give not only the most accurate evaluation now possible for the atomic diamagnetic correction but also information as to the relative contributions of the different electronic shells to this term. From Table III it is seen that the outer or valence electrons give a very small contribution to $H'(0)/H$. This of course would be predicted due to the $1/r$ behavior of $v(0)$.[11] Thus it would be expected, except perhaps for the lightest atoms, that molecular perturbations of the outer electrons would have little effect on $H'(0)/H$ and that contributions to $v(0)$ from electrons belonging to other atoms of the molecule would be relatively small. Hence to a first approximation the diamagnetic term in Ramsey's expression for the molecular shielding can be replaced by the value of $H'(0)/H$ from Table II for the atom concerned. This simplifies matters considerably. The observed shifts of nuclear resonances from one molecule to another are often as large as, or greater than, the entire atomic diamagnetic correction for the atom concerned.[12] The diamagnetic field at the nucleus for both molecules would be closely the same and hence the shift must be attributed chiefly to a *difference* in the second-order paramagnetic field in the two molecules. In particular, when a difference of resonance position is measured between a nucleus in an ion or atom and the same nucleus in a polyatomic molecule, the field difference would be entirely attributed to a second order paramagnetism in the molecule. Of course when an observed shift between two molecules is *small* compared to the atomic internal diamagnetic field for the atom containing the resonating nucleus, it could well be due to a difference in the diamagnetic term, the second-order paramagnetism being essentially the same for both molecules.

The writer wishes to express his thanks to Dr. L. C. Biedenharn, Jr. for several valuable discussions about this work.

[5] The spin-orbit coupling correction which is also not taken into account would alter the wave functions of the outer electrons slightly, but would be expected to have a negligible effect on $v(0)$.
[6] A. O. Williams, Jr., Phys. Rev. 58, 723 (1940).
[7] W. D. Knight, Phys. Rev. 76, 1259 (1949). The bulk of this letter is concerned with the nuclear magnetic resonance shift in metals. However, a brief mention is made of the observation of shifts among some phosphorous compounds.
[8] W. G. Proctor and F. C. Yu, Phys. Rev. 77, 717 (1950).
[9] W. C. Dickinson, Phys. Rev. 77, 736 (1950).
[10] N. F. Ramsey, Phys. Rev. 78, 699 (1950).
[11] For comparison, the contribution of the $(1s)^2$ shell to $v(0)$ varies from 44 percent for $Z=26$ to 30 percent for $Z=74$.
[12] Experimental data on second-order paramagnetic shifts for several elements will be given in a forthcoming paper.

Wave Functions for Superconducting Electrons

JOHN BARDEEN
Bell Telephone Laboratories, Murray Hill, New Jersey
(Received July 17, 1950)

The observed variation of the transition temperature of mercury with isotopic mass is evidence that the superconducting state arises from interaction of electrons with lattice vibrations. The interaction term which gives scattering of electrons at high temperatures contributes at low temperatures a term to the energy of the system of electrons plus normal modes. Fröhlich has calculated the interaction energy at $T=0°K$ by second-order perturbation theory. The energy is calculated here by taking wave functions of superconducting electrons, which have energies near the Fermi surface, as linear combinations of Bloch functions whose coefficients are functions of coordinates of the normal modes. In an equivalent approximation, Fröhlich's expression for the interaction energy is obtained. When the energy is calculated directly rather than by perturbation theory, modified expressions are obtained for the energy and distribution of electrons in the superconducting state. The criterion for superconductivity is $\hbar/\tau > \sim 2\pi\kappa T$, where τ is the relaxation time for electrons at some high temperature T where τT is constant. It is shown that superconducting electrons have small effective mass.

I. INTRODUCTION

THE isotope effect observed by Reynolds, Serin, Wright, and Nesbitt[1] and by Maxwell[2] is evidence that the superconducting state arises from the interaction of electrons with lattice vibrations rather than from electrostatic interactions between electrons. They found a shift in the transition temperature, T_c, of mercury with isotopic mass, M, such that $M^{\frac{1}{2}}T_c$ is approximately constant, or such that T_c varies directly with the Debye temperature.[3]

The interaction term in the Hamiltonian which gives rise to scattering of electrons and resistance at high temperatures contributes at low temperatures a term to the energy of the system of electrons plus normal modes of vibration. It is possible to make an approximate calculation of the interaction energy on the basis of Bloch theory of metals in which correlations between the positions of electrons which arise from Coulomb forces are neglected. That the Bloch theory works as well as it does in view of the large magnitude of the Coulomb energy is surprising. The theory has a firm empirical foundation in explaining in a qualitative or quantitative way a wide variety of experimental results. An explanation of superconductivity in terms of the Bloch theory would extend its scope to cover nearly all conduction phenomena.

Fröhlich has made a calculation of the interaction energy at $T=0°K$ by an application of perturbation theory.[4] Except for interactions with lattice vibrations, the electrons are treated as free. The interaction terms give no first-order contribution to the energy. Fröhlich calculated the second-order energy. As the energy denominators vanish over part of the range of summation or integration of the second-order energy, it is necessary to take principal values in integrating over the singular regions.

The interaction energy can be interpreted as a self-energy which arises from the virtual emission and absorption of phonons. The operation of the exclusion principle is such as to give a contribution to the self-energy which acts formally like an interaction between electrons in momentum or k-space. The interaction is repulsive when the energies of the electrons are nearly equal and is attractive when the energy difference is larger than the energy of the phonon which connects the two states in the Bloch theory of conductivity.

Fröhlich finds that if the interaction terms are sufficiently large for superconductivity, there exists a state of lower energy than the usual one in which states inside a sphere of radius $k=k_0$ in k-space are occupied and those outside unoccupied. The lower energy state is obtained by taking electrons in a thin outer shell of the usual Fermi distribution and displacing them outward in k-space so as to leave a small gap between an occupied sphere and an occupied concentric spherical shell. This modified distribution has a lower interaction energy and is stable if the energy gained in this way more than compensates for the increase in Fermi energy. This condition gives a criterion for superconductivity.

An approach which appears to be formally quite different from that of Fröhlich has been suggested independently by the author.[5] We shall show here that these two different treatments lead to nearly the same results. They represent different ways of approximating the energy of the same basic Hamiltonian. We have suggested that in the superconducting state the wave functions of electrons which have energies near the Fermi surface, $E=E_0$, are modified by interaction with the normal modes.[5] Wave functions of the superconducting electrons are linear combinations of Bloch functions with energies near $E=E_0$. The coefficients, which are functions of the displacement coordinates of the normal modes, are determined by a modification of the adiabatic theory. The net effect is to lower the energies of those electrons having energies near the

[1] Reynolds, Serin, Wright, and Nesbitt, Phys. Rev. 78, 487 (1950).
[2] E. Maxwell, Phys. Rev. 78, 477 (1950); 79, 173 (1950).
[3] Serin, Reynolds, and Nesbitt, Phys. Rev. 78, 813 (1950).
[4] H. Fröhlich Phys. Rev. 79, 845 (1950).
[5] J. Bardeen, Phys. Rev. 79, 167 (1950).

Fermi surface. This energy gain is a consequence of the zero-point motion of the ions, and can be interpreted as a lowering of zero-point energy as a result of the interaction between electrons and lattice vibrations.

The mean-square amplitude of a mode with zero-point energy is inversely proportional to the volume over which it extends. It was suggested that as a consequence the lowest energy would be obtained if the modes extended over a distance of the order of 10^{-6} cm, which is about the minimum distance over which the electrons can be localized. However, we shall show here that as a result of the increase in the number of normal modes involved with increase in volume, the interaction energy is independent of the volumes occupied by the normal modes. The distance of $\sim 10^{-6}$ cm thus represents a minimum rather than an optimum value.

The way in which the typical superconducting properties follow from the model is not yet completely clear and our explanation differs from that of Fröhlich.[4] In our picture, the superconducting electrons with energies near the Fermi surface have a small effective mass, of the order of kT_c/E_0, and this leads to a perfect diamagnetism according to the theories of Landau and of Peierls.[5] A model of a gas of non-interactinge lectrons of small effective mass leads to a theory of the London type.[5a] Fröhlich's explanation is based more on a persistent current idea. He finds current carrying states that are metastable in that it requires energy to remove a single electron or group of electrons in such a way as to reduce the current, although the lowest state, which is the one described above, has zero net current.[5b]

Whether or not a metal becomes superconducting depends on the magnitude of the electron-lattice interaction terms. As the same interaction terms enter into the theory of high temperature resistivity, the criterion for superconductivity can be expressed in terms of the resistivity or in terms of the relaxation time associated with the resistivity. The approximate criterion which we obtain below is similar to but somewhat more restrictive than the one derived earlier by Fröhlich.[4] It may be expressed in either of the following ways: A metal is superconducting if

$$\rho n > 10^6,$$

where ρ is the room temperature resistivity expressed in e.s.u. and n is the number of valence electrons per cc, or what amounts to the same thing, if

$$\hbar/\tau > \sim 2\pi\kappa T,$$

where τ is the relaxation time for the conduction electrons at the high temperature T. As τT is constant at high temperatures, the criterion is really independent of T. It should be noted that the superconducting metals are just those for which the electron-lattice interaction is so strong that the usual perturbation theory treatment for calculating high temperature resistivity begins to break down. The above criterion holds in nearly all cases except for the transition metals which are not expected to be superconducting in any case.

This paper is concerned primarily with the energy of the lowest state of pure metals and so should give the energy difference at $T=0$. We shall not be concerned with the thermodynamics of the superconducting state nor with the nature of the transition from the normal state. Except for some estimates of effective mass, we shall not attempt to show here how the typical superconducting properties follow from the model.

II. THE HAMILTONIAN

We consider a metal of volume V in which there are N_A atoms and $n=\nu N_A$ conduction electrons. The Hamiltonian is the sum of three terms corresponding to the electrons, the lattice displacements, and the interaction between them:

$$H=H_e+H_L+H_I. \tag{2.1}$$

The first term, H_e, is the Hamiltonian for the electrons with ions in their equilibrium positions. We shall neglect correlation effects and assume that each electron moves in the periodic field $U(x)$ of the lattice. Then

$$H_e=\Sigma_i H_{ei} \quad i=1, 2, \cdots n, \tag{2.2}$$

where

$$H=-(\hbar^2/2m)\Delta_i+U(x_i) \tag{2.2a}$$

and x_i represents the coordinates of the ith electron. The wave functions of H_{ei} are the Bloch functions $\psi_k(x_i)$ with energy ϵ_k:

$$H_{ei}\psi_k(x_i)=\epsilon_k\psi_k(x_i). \tag{2.3}$$

The wave functions of H_e are products of Bloch functions.

The Hamiltonian for the lattice, H_L, can be expressed in the form:

$$H_L=\Sigma_r\left\{-\frac{\hbar^2}{2\mu}\frac{\partial^2}{\partial q_r^2}+\tfrac{1}{2}K_r q_r^2\right\}, \quad r=1, 2, \cdots 3N_A, \tag{2.4}$$

where μ is proportional to the mass of the atoms, the exact value depending on how the displacement coordinate, q_r, is defined. The force constant, K_r, can be expressed in terms of the angular frequency, ω_r, of the mode:

$$K_r=\mu\omega_r^2. \tag{2.5}$$

We shall be concerned only with the N_A longitudinal modes which interact with the electrons.

The interaction terms are linear in the displacements, and we shall indicate this explicitly by taking

$$H_I=\Sigma_{i,r}V_r(x_i)q_r. \tag{2.6}$$

[5a] *Added in proof.* In a paper submitted for publication in the Physical Review we show that the London phenomenological equations for superconductivity follow as a limiting case when the effective mass is so small that the Landau-Peierls theory yields a diamagnetic susceptibility $<-\frac{1}{4}\pi$, and also that the method of effective mass may be applied to wave functions for superconducting electrons as derived in the present paper.

[5b] *Added in proof.* Fröhlich has abandoned this explanation. See the comments added in proof to his paper (reference 4).

The interaction terms give the matrix elements

$$\mathfrak{M}_{kk'}=\int \psi_k^* V_r(x)\psi_{k'}d\tau \tag{2.7}$$

which vanish except for a normal mode with wave vector κ_r such that

$$k'=k\pm\kappa_r+K_n, \tag{2.8}$$

where K_n is a lattice vector of the reciprocal lattice space. This selection rule is well known from the theory of metals.[6] Since we have indicated q_r explicitly, $\mathfrak{M}_{kk'}$ differs from the usual $M_{kk'}$ by a factor q_r. We shall define:

$$|M_{kk'}|^2=(q_{kk'}^2)_{Av}|\mathfrak{M}_{kk'}|^2, \tag{2.9}$$

where $q_{kk'}$ is the coordinate of the normal mode which connects k and k'. The average is over the zero-point wave function of the normal mode.

III. WAVE FUNCTIONS FOR THE SYSTEM OF ELECTRONS PLUS NORMAL MODES

An approximate wave function for the system may be constructed as follows. The wave function for the electrons is taken to be a product of functions $\varphi_i(x_i, q_r)$ each of which depends on the coordinates of a single electron, x_i, and which depends parametrically on the coordinates of the normal modes, q_r. This product is multiplied by a product of functions $Q_r(q_r)$ for the normal modes:

$$\Psi=\Pi_i\varphi_i(x_i, q_r)\cdot\Pi_r Q_r(q_r). \tag{3.1}$$

In the lowest energy state the functions Q_r are the harmonic oscillator functions for zero-point energy, $\frac{1}{2}\hbar\omega_r$.

Each φ_i is assumed to be normalized so that

$$\int \varphi_i^*\varphi_i d\tau=1 \tag{3.2}$$

for all values of the q_r. This relation, when differentiated with respect to q_r, gives the real part of

$$\int \varphi_i^*(\partial\varphi_i/\partial q_r)d\tau=0, \tag{3.3}$$

and by a second differentiation:

$$-\int \varphi_i^*(\partial^2\varphi_i/\partial q_r^2)d\tau=\int|\partial\varphi_i/\partial q_r|^2 d\tau. \tag{3.4}$$

These well-known relations are useful in calculating the contribution of the terms $(-\hbar^2/2\mu)(\partial^2/\partial q_r^2)$ to the energy. Equation (3.3) implies that cross terms of the form

$$\varphi_i^*\varphi_j^*(\partial\varphi_i/\partial q_r)(\partial\varphi_j/\partial q_r)$$

vanish on integration. Equation (3.4) is used in calculation the contribution of φ_i to the kinetic energy of the ions.[7]

The functions φ_i can be expressed as a linear combination of Bloch functions in which the coefficients are functions of the q's:

$$\varphi_i=\Sigma_k a_k(q)\psi_k. \tag{3.5}$$

The normalization condition requires that

$$\Sigma_k|a_k|^2=1. \tag{3.6}$$

The wave function, φ_i, makes the following contribution to the energy:

$$E_i=\{\Sigma_k\epsilon_k|a_k|^2+\Sigma_{kk'}a_k^* q_{kk'}\mathfrak{M}_{kk'}a_{k'}$$
$$+\Sigma_{kk'}a_{k'}^* q_{kk'}\mathfrak{M}_{k'k}a_k+(\hbar^2/2\mu)\Sigma_{k,r}|\partial a_k/\partial q_r|^2\}_{Av}, \tag{3.7}$$

where the first term comes from H_e, the second and third from the interaction terms, and the last from the kinetic energy of the ions after making use of (3.3). The whole expression is averaged over the normal modes.

The total energy is obtained by summing (3.7) over all occupied states of the electrons and adding the energies of the normal modes. It is, of course, necessary to take the exclusion principle into account in calculating the energy of the electrons. If the φ_i are orthogonal, each such state can be occupied by two electrons of opposite spin.

To get a non-vanishing contribution from the interaction terms, a_k and $a_{k'}$ must have opposite parity. Thus if a_k is an even function of $q_{kk'}$, $a_{k'}$ must be an odd function or at least have an odd part. This suggests taking φ_i of the form

$$\varphi_i=N(\psi_k+\Sigma_{k'}b_{k'}q_{kk'}\psi_{k'}) \tag{3.8}$$

where N is a normalization factor chosen to satisfy (3.2):

$$N=(1+\Sigma b_{k'}^2 q_{kk'}^2)^{-\frac{1}{2}}, \tag{3.9}$$

and the $b_{k'}$ are constant factors to be chosen to make the energy a minimum. The normal coordinate $q_{kk'}$ is that for the mode which connects the states k and k'.

The calculation of the energy by using (3.8) for φ_i in (3.7) is straightforward. The only term which requires discussion is that involving $|\partial a_k/\partial q_r|^2$. We shall show that terms arising from derivatives of the normalization factor give a negligible contribution. We have

$$\Sigma_{k'}\int|\partial\varphi_i/\partial q_{kk'}|^2 d\tau$$
$$=\Sigma_{k'}\{N^{-2}|\partial N/\partial q_{kk'}|^2+N^2 b_{k'}^2\}$$
$$=\Sigma_{k'}(q_{kk'})^{-2}\{(N^2 b_{k'}^2 q_{kk'}^2)^2+N^2 b_{k'}^2 q_{kk'}^2\}. \tag{3.10}$$

[6] See, for example, N. F. Mott and H. Jones, *Properties of Metals and Alloys* (Oxford University Press, Oxford, 1936), or F. Seitz, *Modern Theory of Solids* (McGraw-Hill Book Company, Inc., New York, 1940).

[7] A simpler treatment, which leads to the same final results, could be made if it were assumed that each q_r is contained in no more than one φ_i. This would allow an immediate separation of the equation into parts which depend only on the coordinates of a single electron and the normal modes with which it interacts.

Since

$$\Sigma N^2 b_{k'}{}^2 q_{kk'}{}^2 < 1, \tag{3.11}$$

and since the sum is over a large number of positive terms,

$$\Sigma (q_{kk'})^{-2} (N^2 b_{k'}{}^2 q_{kk'}{}^2)^2 \ll \Sigma (q_{kk'})^{-2} (N^2 b_{k'}{}^2 q_{kk'}{}^2), \tag{3.12}$$

and we shall neglect it in comparison.

The last term of (3.7) then reduces to

$$(\hbar^2/2\mu)\Sigma_{k'} N^2 b_{k'}{}^2. \tag{3.13}$$

The mean square amplitude of a mode with zero-point energy is such that the mean potential energy is one-half the total energy, $\frac{1}{2}\hbar\omega_r$, or

$$\tfrac{1}{2} K_r (q_r{}^2)_{Av} = \tfrac{1}{4}\hbar\omega_r. \tag{3.14}$$

Thus

$$[\hbar^2/2\mu(q_r{}^2)]_{Av} = (\hbar K_r/\mu\omega_r) = \hbar\omega_r, \tag{3.15}$$

since $K_r/\mu = \omega_r{}^2$. With use of (3.15), (3.13) becomes:

$$\Sigma \hbar\omega_{kk'} N^2 b_{k'}{}^2 (q_{kk'}{}^2)_{Av}. \tag{3.16}$$

The expression for the energy obtained by using (3.8) in (3.7) can be simplified considerably by setting:

$$c_k{}^2 = (N^2)_{Av}, \quad c_{k'}{}^2 = (N^2 q_{kk'}{}^2)_{Av} b_{k'}{}^2. \tag{3.17}$$

With use (3.16) for the last term, Eq. (3.7) becomes (with neglect of the small difference between $(N^2)_{Av} \times (q_{kk'}{}^2)_{Av}$ and $(N^2 q_{kk'}{}^2)_{Av}$):

$$E_k = c_k{}^2 \epsilon_k + \Sigma c_{k'}{}^2 (\epsilon_{k'} + \hbar\omega_{kk'}) + \Sigma c_k M_{kk'} c_{k'} + \Sigma c_{k'} M_{k'k} c_k. \tag{3.18}$$

We have replaced $(q_{kk'}{}^2)_{Av}{}^{\frac{1}{2}} \mathfrak{M}_{kk'}$ by $M_{kk'}$ (see Eq. (2.9)). The c's are subject to the normalization condition

$$c_k{}^2 + \Sigma_{k'} c_{k'}{}^2 = 1. \tag{3.19}$$

The variational problem gives the following set of equations for the c's

$$c_k \epsilon_k + \Sigma c_{k'} M_{k'k} = E_k c_k, \tag{3.20a}$$

$$c_{k'}(\epsilon_{k'} + \hbar\omega_{kk'}) + c_k M_{kk'} = E_k c_{k'}. \tag{3.20b}$$

If the $c_{k'}$ are determined by second-order perturbation theory, we have

$$c_{k'} = c_k M_{kk'}/(\epsilon_k - \epsilon_{k'} - \hbar\omega_{kk'}), \tag{3.21}$$

and the second-order contribution to the energy is

$$\Delta E_k = \Sigma_{k'} |M_{kk'}|^2/(\epsilon_k - \epsilon_{k'} - \hbar\omega_{kk'}). \tag{3.22}$$

If this contribution is summed over all k for the occupied states, the total change is

$$\Delta W = 2\Sigma_k \Sigma_{k'} |M_{kk'}|^2/(\epsilon_k - \epsilon_{k'} - \hbar\omega_{kk'}). \tag{3.23}$$

The factor 2 accounts for the fact that each state can be occupied by two electrons. Because of the exclusion principle, the states k' must be normally unoccupied. Thus if f_k is the probability that a state k is occupied and $(1-f_{k'})$ the probability that k' is unoccupied, the energy becomes

$$\Delta W = 2\Sigma_k \Sigma_{k'} \frac{|M_{kk'}|^2 f_k (1-f_{k'})}{\epsilon_k - \epsilon_{k'} - \hbar\omega_{kk'}}, \tag{3.24}$$

where the sum is now over *all* values of k and k'.

This expression can be obtained directly from the original Hamiltonian (2.1), and is the one which Fröhlich[4] used to calculate the self-energy of the electrons as a result of interaction with the phonon field.

It will be noted that the energy denominators are small and the perturbation procedure breaks down when

$$|\epsilon_k - \epsilon_{k'} - \hbar\omega_{kk'}| <\sim |M_{kk'}|. \tag{3.25}$$

Fröhlich integrated over these singular regions by taking principal parts. We shall follow a different method which we believe gives a better insight into the superconducting states.

IV. WAVE FUNCTIONS FOR SUPERCONDUCTING ELECTRONS

The exclusion principle imposes severe restrictions on the wave functions. For each linear combination of the type (3.8) which yields a low energy state there is an orthogonal state using the same Bloch functions which has higher than normal energy. In order to get a net decrease in energy of the electrons, it is necessary to include twice as many Bloch states as there are electrons to be accommodated so that only the low energy states need be occupied. This is possibly only if the initial states have energies within the order of Δ of the Fermi surface, where Δ is the decrease in energy resulting from the electron-lattice interaction terms.

We shall construct wave functions for the superconducting electrons for the state corresponding to $T=0°\text{K}$ by taking k-values which lie in the energy range between E_0 and $E_0+\epsilon_1$ and k' values which lie between $E_0-\epsilon_1$ and E_0. The wave functions for $\epsilon_k < E_0-\epsilon_1$ are taken to be the usual Bloch functions. The energy ϵ_1 will be determined below to make the total energy a minimum and is approximately equal to Δ for the superconducting wave functions. This configuration is similar to that which Fröhlich obtained by displacing a spherical shell of electrons outward from the boundary of the Fermi distribution. Our calculation of the energy differs from his in that we do not use perturbation theory and the questionable procedure of an integration over singularities by taking principal parts is avoided.

In the superconducting state, the interaction is so large that (3.25) is satisfied for k' such that $E_0-\epsilon_1 < \epsilon_{k'} < E_0$. There are terms in the energies of both the normal and superconducting states which come from ϵ_1 interaction with unoccupied states of higher energy and which contribute terms proportional to M^2 to the self-energy. Since these latter terms do not differ much between the normal and superconducting states we shall omit them from calculations of the energy difference.

If we assume that $\epsilon_k \simeq \epsilon_{k'} + \hbar\omega_{kk'}$, Eq. (3.20b) gives

$$c_{k'} = c_k M_{kk'}/\Delta, \tag{4.1}$$

where Δ is the energy difference $E_k - \epsilon_k$. Substitution of this value into (3.20a) gives

$$\Delta^2 = \Sigma_{k'} |M_{kk'}|^2, \tag{4.2}$$

or

$$\Delta = (\Sigma_{k'} |M_{kk'}|^2)^{\frac{1}{2}}. \tag{4.3}$$

The wave function of the superconducting state is then

$$\varphi_k = N(\psi_k \pm \Delta^{-1} \Sigma_{k'} \mathfrak{M}_{kk'} q_{kk'} \psi_{k'}). \tag{4.4}$$

Normalization requires that the average value of N^2 be $\frac{1}{2}$. The negative signs apply to the low energy state and the positive to the high energy state; the energies being

$$E_k = \epsilon_k \pm \Delta. \tag{4.5}$$

The number of states k' in the sum depends on the spread of the energies $\epsilon_{k'} + \hbar\omega_{kk'}$ about ϵ_k. It is reasonable to take an energy spread of the order of Δ and we shall include only those k' which satisfy:

$$\epsilon_k - \epsilon_{k'} - \Delta < \hbar\omega_{kk'} < \epsilon_k - \epsilon_{k'} + \Delta. \tag{4.6}$$

Criterion for Superconductivity

The criterion for superconducivity is obtained from the condition that (4.6) be satisfied for most k' in the gap between the occupied sphere and the occupied spherical shell.[7a] One can then use (4.3) and (4.5) for the energies and Δ is proportional to the first power of $M_{kk'}$. Since the average value of $\epsilon_k - \epsilon_{k'}$ is ϵ_1, and since ϵ_1 is approximately equal to Δ, the k' which satisfy (4.6) are such that

$$\hbar\omega_{kk'} < 2\Delta. \tag{4.7}$$

The value of $\omega_{kk'}$ is proportional to $|k - k'|$ which in turn depends on the angle, θ, between k and k'. If ω_m is the maximum value[8] corresponding to $\theta = 180°$,

$$\hbar\omega_{kk'} = \hbar\omega_m \sin\tfrac{1}{2}\theta. \tag{4.8}$$

It is convenient to use

$$x = \sin\tfrac{1}{2}\theta \tag{4.9}$$

as a measure of the angle between k and k'. According to (4.7), the limiting value of x is

$$x_1 = 2\Delta/\hbar\omega_m. \tag{4.10}$$

We shall now evaluate Δ from (4.2), taking those k' in the sum which satisfy (4.7) and assuming that $|M_{kk'}|^2$ depends on the angle between k and k' and thus on x. The total number of k' states in volume V in the energy range, ϵ_1 is

$$\epsilon_1 V N(E_0), \tag{4.11}$$

where $N(E_0)dE$ is the number of states per unit volume in the range dE at the Fermi surface. In integrating over angles the factor $\sin\theta d\theta$ becomes $4xdx$. The sum (4.2) is given approximately by an integration over x between 0 and x_1:

$$\Delta^2 = 2\epsilon_1 V N(E_0) \int_0^{x_1} [M(x)]^2 x dx. \tag{4.12}$$

Since $\epsilon_1 \simeq \Delta$, this equation can be simplified to:

$$\Delta = 2VN(E_0) \int_0^{x_1} [M(x)]^2 x dx. \tag{4.13}$$

This is an implicit equation for Δ. The upper limit x_1 is $2\Delta/\hbar\omega_m$ or unity, whichever is the smaller.

The criterion for the existence of the superconducting state is that (4.13) have a solution other than $\Delta = 0$. With reasonable assumptions regarding the dependence of M on x, the right-hand side has an upward curvature until x_1 is almost equal to its maximum value of unity. If there is a solution, it must occur for x_1 close to unity. Thus we must have (see Eq. (4.7)):

$$a = 2VN(E_0) \int_0^1 [M(x)]^2 x dx > \tfrac{1}{2}\hbar\omega_m. \tag{4.14}$$

As in the previous work,[4,5] an estimate of the average value of the matrix element can be obtained from the resistivity at high temperatures. When this is done, (4.14) gives a criterion similar to, but more restrictive than that of Fröhlich.[4]

The criterion may be expressed most simply in terms of the relaxation time associated with high temperature conductivity. The expression for the relaxation time, τ, in terms of the matrix element $(M_{kk'})_T$ for high temperatures is given by[9]

$$\hbar/\tau = \pi V N(E_0) \int_0^{\pi} [M_T(\theta)]^2 (1 - \cos\theta) \sin\theta d\theta. \tag{4.15}$$

The high temperature matrix element corresponds to an

[7a] *Added in proof.* The criterion may be derived in a simple way as follows. The energy corresponding to (4.4) is:

$$E_k = \tfrac{1}{2}\epsilon_k + \tfrac{1}{2}(\epsilon_{k'} + \hbar\omega_{kk'}) - \Delta.$$

In order to have a net decrease in energy it is necessary that the superconducting states have a lower energy than the Bloch states they replace. The energy difference is on the average:

$$(E_k - \epsilon_{k'})_{Av} = \tfrac{1}{2}(\epsilon_k - \epsilon_{k'})_{Av} + \tfrac{1}{2}(\hbar\omega_{kk'})_{Av} - \Delta$$
$$= \tfrac{1}{2}\epsilon_1 + \tfrac{1}{2}(\hbar\omega_{kk'})_{Av} - (a\epsilon_1)^{\frac{1}{2}}.$$

It follows from (4.3) that Δ^2 is proportional to the number of states k' and thus to ϵ_1. The factor a is given by (4.14). The right-hand side is lowest for $\epsilon_1 = a$ and is negative only if

$$a > (\hbar\omega_{kk'})_{Av}.$$

This criterion is equivalent to (4.17) which was derived from the condition (4.6).

[8] Assuming that "Umklapp" processes of Peierls are not involved. Transitions through large angles may result from such processes (see J. Bardeen, Phys. Rev. 52, 688 (1937)). The values of $\hbar\omega_{kk'}$ for large angles would then be smaller than those given by (4.8), and the criterion for superconductivity somewhat less restrictive.

[9] N. F. Mott and H. Jones reference 6, Eq. (48), p. 262.

energy κT in a vibrational mode while the low temperature matrix element corresponds to zero-point energy $\frac{1}{2}\hbar\omega_{kk'}$. Thus

$$M_T^2=(2\kappa T/\hbar\omega_{kk'})M^2=(2\kappa T/\hbar\omega_m)(M^2/x)$$

with change of the variable of integration from θ to x, (4.15) becomes:

$$\hbar/\tau=16\pi(\kappa T/\hbar\omega_m)VN(E_0)\int_0^1[M(x)]^2x^2dx. \quad (4.16)$$

Except for an extra factor of x, the integral in (4.16) is the same as that in (4.14), so that we can express a in terms of τ. We shall assume for simplicity that the angular dependence is such that the extra factor of x gives an extra factor of $\frac{1}{2}$ on integration. We may then write (4.14) in the form

$$a=(\hbar\omega_m/4\pi\kappa T)(\hbar/\tau)>\tfrac{1}{2}\hbar\omega_m \quad (4.17)$$

The criterion for superconductivity is then:

$$\hbar/\tau>\sim 2\pi\kappa T. \quad (4.18)$$

As $1/\tau$ is proportional to T at high temperatures, relation (4.18) is independent of T. It indicates that a large interaction between electrons and lattice vibrations is required for superconductivity. The interaction must be so large, in fact, that the usual theory of conductivity based on perturbation theory and variation of constants begins to break down. The assumption that the wave functions are Bloch functions only weakly coupled to the vibrations is not a good approximation even for the normal state of the superconducting metals.

TABLE I. Test of the approximate criterion for superconductivity: $10^{-6}\rho n>1$.

Normal	ν	$10^{16}\rho$(e.s.u.) 293°K	$10^{-22}n$/cm³	$10^{-6}\rho n$
Li	1	0.10	4.7	0.47
Na	1	0.054	2.56	0.14
K	1	0.079	1.33	0.105
Rb	1	0.15	1.1	0.165
Cs	1	0.22	0.85	0.185
Cu	1	0.018	8.5	0.15
Ag	1	0.018	5.9	0.11
Au	1	0.025	6.3	0.16
Be	2	0.04	24.5	0.97
Mg	2	0.045	8.6	0.39
Ca	2	0.05	4.7	0.24
Sr	2	0.35	3.6	1.25
Ba	2	0.72	3.2	2.3
Superconducting				
La	3	0.68	8.1	5.5
Ti	4	0.50	23	11.5
Zr	4	0.48	17	8.5
Hf	4	0.39	17	6.6
Th	4	0.12	12	1.44
V	5	0.20	34	6.8
Nb	5	0.28	27.5	7.7
Ta	5	0.17	27	4.6
Zn	2	0.065	13.2	0.86
Cd	2	0.09	10	0.90
Hg	2	0.30	8.5	2.5
Al	3	0.03	18	0.54
Ga	3	0.45	15	6.8
In	3	0.10	11.5	1.15
Tl	3	0.18	10.5	1.9
Sn	4	0.13	15	1.95
Pb	4	0.24	13	3.1

The criterion (4.18) can be expressed in terms of the room-temperature resistivity, ρ, if we use the free-electron formula:[6]

$$\sigma=1/\rho=ne^2\tau/m, \quad (4.19)$$

where n is the number of valence electrons per unit volume. For $T=20°C=293°K$, (4.18) becomes

$$n\rho>2\pi m\kappa T/\hbar e^2\sim 10^6 \text{ (e.s.u.)}, \quad (4.20)$$

The value 10^6 applies if ρ is expressed in e.s.u. and would be about 10^{18} if ρ is in practical units.[10] Except for the transition metals, (4.20) is valid for practically all cases (Table I). None of the monovalent metals satisfy (4.20). Since the transition metals have narrow energy bands, one would not expect to get much energy gain by taking linear combinations corresponding to the superconducting states. A large effective mass should be used in (4.20). Thus they are not expected to be superconducting.

Energy of the Superconducting State

We shall suppose that the criterion for superconductivity is satisfied so that practically all k' in the energy range ϵ_1 satisfy (4.6) and may be included in the sum (4.2). The energy Δ^2 is then given by (4.12) with $x_1=1$. Using the definition of a in (4.14), we have

$$\Delta^2=\epsilon_1 a. \quad (4.21)$$

The difference in energy between the superconducting and normal states is

$$W_s-W_n=2N(E_0)\epsilon_1(\epsilon_1-\Delta). \quad (4.22)$$

The factor $2N(E_0)\epsilon_1$ is the number of superconducting electrons, counting both spin states, and $\epsilon_1-\Delta$ is the average energy difference per electron.

We shall find the value of ϵ_1 which makes W_s a minimum. With use of (4.21), we have

$$W_s-W_n=2N(E_0)(\epsilon_1^2-a^{\frac{1}{2}}\epsilon_1^{\frac{1}{2}}). \quad (4.23)$$

Setting

$$\partial(W_s-W_n)/\partial\epsilon_1\sim 2\epsilon_1-3/2a^{\frac{1}{2}}\epsilon_1^{\frac{1}{2}}=0,$$

we find

$$\epsilon_1=(9/16)a, \quad (4.24)$$

and

$$\Delta=(3/4)a. \quad (4.25)$$

The minimum value of W_s-W_n is then

$$W_s-W_n=-(27/128)N(E_0)a^2$$
$$=-(27/128)N(E_0)(\hbar\omega_m/4\pi\kappa T)^2(\hbar/\tau)^2. \quad (4.26)$$

[10] Fröhlich's criterion is approximately $\rho n\nu^{\frac{1}{2}}>0.2\times 10^6$, where ν is the valency. This criterion is less restrictive than ours and is not in as good agreement with observation. Compare Table I with the corresponding table in reference 4.

The second expression is obtained by using (4.17) for a. A very similar expression would have been found if we had used (4.4) for the wave functions and calculated the energy from the Hamiltonian instead of using (4.2).[10a]

The energy difference is usually determined from the critical field, H_c, at $T=0$:

$$W_s-W_n=-H_c^2/8\pi. \tag{4.27}$$

From (4.26) and (4.27), we find

$$H_c=(27\pi N(E_0)/16)^{\frac{1}{2}}(\hbar^2\omega_m/4\pi\kappa T\tau). \tag{4.28}$$

The free-electron model gives[6]

$$N(E_0)=mk_0/2\pi^2\hbar^2, \tag{4.29}$$

where k_0 is the maximum value of k in the Fermi distribution:

$$k_0=(3\pi^2n)^{\frac{1}{3}}. \tag{4.30}$$

Equation (4.28) gives values for H_c which are too large, as does the corresponding expression of Fröhlich.[4] For example, approximate values for lead, taking 3 valence electrons per atom, are:

$$\rho=2.2\times10^{-17}\text{ e.s.u. at }273°\text{K},$$
$$n=1.3\times10^{23}\text{ electrons/cm}^3,$$
$$\hbar\omega_m\sim10^{-14}\text{ ergs},\quad 1/\tau\sim ne^2\rho/m\sim7\times10^{14}\text{ sec.}^{-1},$$
$$k_0\sim1.6\times10^8\text{ cm}^{-1},\quad N(E_0)\sim8\times10^{33},$$

which give $H_c\sim3000$ oersteds as compared with the observed value of 800. Values are even higher for lighter elements with larger values of $\hbar\omega_m$.

Our calculations undoubtedly overestimate the energy, and the free-electron approximation is probably poor for most of the superconducting metals. Even when these factors are taken into consideration, the theoretical values of H_c appear to be too large. It is believed that the difficulty is not so much in the calculations and model for the superconducting state as for the normal state. The criterion (4.18) indicates that the Bloch functions are probably not sufficiently good wave functions for the normal states of superconducting metals. A theory of transition phenomena would require a good model for both superconducting and normal states.

The expression for a (Eq. (4.14)) is similar to the expression for the energy change, ΔE, estimated in the earlier publication[5] from the adiabatic approximation and is what would have been obtained there if account had been taken of the increase in the number of interactions with increase in volume. The number of interactions is equal to p as there defined, and the expression for ΔE (Eq. (4)) should be multiplied by p. This makes ΔE independent of the volume, V, but the expression then gives values which are about an order of magnitude larger than most values of κT_c.

[10a] *Added in proof.* It probably would have been better to have used this method which involves replacing $\epsilon_1-\Delta$ in (4.22) with $\frac{1}{2}\epsilon_1+\frac{1}{2}(\hbar\omega_{kk'})_{Av}-\Delta$. This procedure leads to a larger value for the energy difference, W_s-W_n when a is larger compared with $(\hbar\omega_{kk'})_{Av}$.

The calculation given in the present paper shows that the pure adiabatic approximation is not valid. Terms coming from $\int|\partial\varphi_i/\partial q_\tau|^2d\tau$ give an increase in Fermi energy which reduces the average energy change per superconducting electron, but it still appears to be larger than κT_c for most elements.

The expressions for the energy change are consistent with the isotope effect. Since $\hbar\omega_m$ varies as $M^{-\frac{1}{2}}$ and τ is independent of isotopic mass, H_c, and thus T_c should vary as $M^{-\frac{1}{2}}$, in agreement with experiment.[3]

Non-Symmetric Distributions; Effective Mass

According to Eqs. (4.24) and (4.25) the average energy difference, $\Delta-\epsilon_1$, between the normal and superconducting states per superconducting electron is $\Delta/4$. The energy difference is large only for a symmetric distribution in k-space corresponding to zero net current. Let us imagine a distribution displaced in k-space by a small vector k_1 corresponding to an average momentum $\hbar k_1$ per electron. If the displacement k_1 changes the Fermi energy of electrons near the Fermi surface by an amount of the order of Δ, the condition (4.6) for the linear combinations will be valid only for a small number of the k' states and the energy difference between the superconducting and normal states will be small. From this we can estimate the change in superconducting energy with k_1 and thus estimate the effective mass of electrons in the superconducting state.

The displacement k_1 which gives a change in Fermi energy Δ is such that

$$\Delta\sim\hbar^2k_0k_1/m,$$

or

$$k_1\sim m\Delta/\hbar^2k_0. \tag{4.31}$$

The effective mass, m_e, in the superconducting state can be estimated by equating $\hbar^2k_e^2/2m_e$ to the energy difference $\Delta/4$. This gives

$$\Delta/4\sim\hbar^2k_1^2/2m_e=(\hbar^2/2m_e)(m\Delta/\hbar^2k_0)^2, \tag{4.32}$$

from which we get

$$m_e\sim(2\Delta m/\hbar^2k_0^2)m\sim(\Delta/E_0)m, \tag{4.33}$$

which is of the order of 10^{-4} or 10^{-3} m.

As the diamagnetic susceptibility varies as $(m/m_e)^2$ according to Peierls' modification[11] of the Landau theory, a value of $m_e\sim10^{-3}$m is sufficiently small to make $\chi<-1/4\pi$, which suggests that when this condition is fulfilled the "superconducting state" is a

[11] R. Peierls, Zeits. f. Physik **80**, 763 (1933). Peierls' formula may be expressed in the following way. The contribution to the susceptibility of electrons in a given Brillouin zone which contains n_z electrons and is filled to an energy E_z, measured from the bottom of the zone, is $\chi_z=-(m/m_e)^2n_z\mu^2/2E_z$, where $\mu=e\hbar/2mc$. The number of Brillouin zones required to accomodate all electrons with energies within $\sim E_z$ of the Fermi surface, E_0, is the order of (nE_z/n_zE_0), where n is the total number of electrons per unit volume. The total susceptibility is thus of the order $\chi_s=-(m/m_e)^2n\mu^2/2E_0$, or the order of $(m/m_e)^2$ times Landau's expression. As Landau's expression gives values of the order of 10^{-7}, it is necessary to have $m/m_e>\sim10^{-3}$ to have a perfect diamagnetic.

perfect diamagnetic. To get a complete theory of the superconducting properties it would be necessary to re-examine the problem for the situation in which the magnetic field is confined to a thin surface layer corresponding to the penetration depth of the London theory.[5a]

The author is indebted to H. Fröhlich for an opportunity to discuss his work with him and to read his manuscript in advance of publication. The author is also indebted to P. Debye and to a number of coworkers at the Bell Telephone Laboratories for stimulating discussions and suggestions.

PHYSICAL REVIEW VOLUME 80, NUMBER 4 NOVEMBER 15, 1950

Angular Distribution of the $Al^{27}(d, \alpha)Mg^{25}$ Reaction and Energy Levels in Mg^{25}†

A. D. SCHELBERG, M. B. SAMPSON, AND R. G. COCHRAN
Department of Physics, Indiana University, Bloomington, Indiana

(Received July 19, 1950)

The energy distribution and angular dependence of the alpha-particle groups from the nuclear reaction $Al^{27}(d, \alpha)Mg^{25}$ have been investigated. A magnetically analyzed beam of 11.1 Mev deuterons was used. Eleven alpha-particle groups were measured, corresponding to ten excited levels in Mg^{25} at 0.57, 0.96, 1.63, 1.97, 2.74, 3.36, 4.01, 4.81, 5.48, and 5.95 Mev. The ground state Q-value for the reaction was found to be 6.58 ± 0.03 Mev, giving a value for the mass difference Al^{27}–Mg^{25} of 1.99626 ± 0.00003 mass units. The intensities of all the groups, with the exception of Q_2, show marked dependence on the angle of measurement. The average spacing of the levels in Mg^{25} is 0.6 Mev, and is nearly constant over the range studied.

I. INTRODUCTION

An excited level in Mg^{25} was first observed by McMillan and Lawrence,[1] from the $Al^{27}(d, \alpha)Mg^{25}$ reaction. Two groups of alpha-particles were found with an energy difference corresponding to an excited level at 0.7 Mev. Pollard, Sailor, and Wyly,[2] using 3.79 Mev deuterons, observed two additional groups showing three excited levels in the Mg^{25} nucleus. French and Treacy[3] repeated these measurements with 0.93 Mev deuterons, using an ionization chamber to count the alpha-particles and found five groups.

The present investigation of the $Al^{27}(d, \alpha)Mg^{25}$ reaction was undertaken to measure the angular distribution of the alpha-particle groups and to search for groups corresponding to states of higher excitation made feasible by the use of the 11-Mev deuteron beam of the Indiana University Cyclotron.

II. METHOD AND APPARATUS

The deuteron beam was led through a four-inch diameter, evacuated tube from the target chamber of the cyclotron to a magnetic analyzer situated outside the water shielding tanks; a distance of fifteen feet.

The analyzer magnet was constructed using a rectangular yoke with a cross section sixteen inches square. The pole pieces were made in the form of a truncated wedge with a gap of 2.0 inches. The lids of the magnet vacuum chamber are of one-half inch iron, leaving a net gap of one inch. The magnet coils require about one kilowatt of power to produce a maximum field of 12,000 Gauss. A field of 10,635 gauss was sufficient to deflect the 11-Mev deuteron beam through 56°. The current in the coils is supplied by a motor generator, and the use of an electronic stabilizer enables the current to be held constant within 0.2 percent. The magnetic field is measured with a flip coil and ballistic galvanometer, calibrated against a standard mutual inductance.

Scattering of the beam in the analyzer chamber is prevented by the use of suitable diaphragms to define the beam. Adjustable slits are placed at the entrance to the analyzer chamber and in the tube leading to the reaction chamber to define the beam to the target.

The magnetic analyzer was calibrated with alpha-particles of polonium and thorium active deposit. The source was placed on the axis of the beam tube, ten feet from the analyzer. A proportional counter located behind the focal slit was then used to count the alpha-particles as the magnetic field was varied. Alpha-particles from Po, ThC and ThC′ were used to give three points on the energy *versus* magnetic field curve at energies of 5.3, 6.05, and 8.78 Mev respectively. A linear relation was obtained between the alpha-particle energy and the square of the magnetic field. The energy of the deuteron beam striking the target could then be determined by using the relation:

$$E_D = (He\rho)^2/2mc^2,$$

where m is the deuteron mass, e is the charge, c is the velocity of light, and H is the magnetic field required to focus the deuteron beam of energy E_D on the target slit. ρ is the effective radius of curvature in the analyzer and was found equal to 64.1 cm from the alpha-particle

† This work was assisted by the joint program of the ONR and AEC.

[1] E. McMillan and E. O. Lawrence, Phys. Rev. **47**, 343 (1935).
[2] Pollard, Sailor, and Wyly, Phys. Rev. **75**, 725 (1949).
[3] A. P. French and P. B. Treacy, Proc. Phys. Soc. London **63**, 665 (1950).

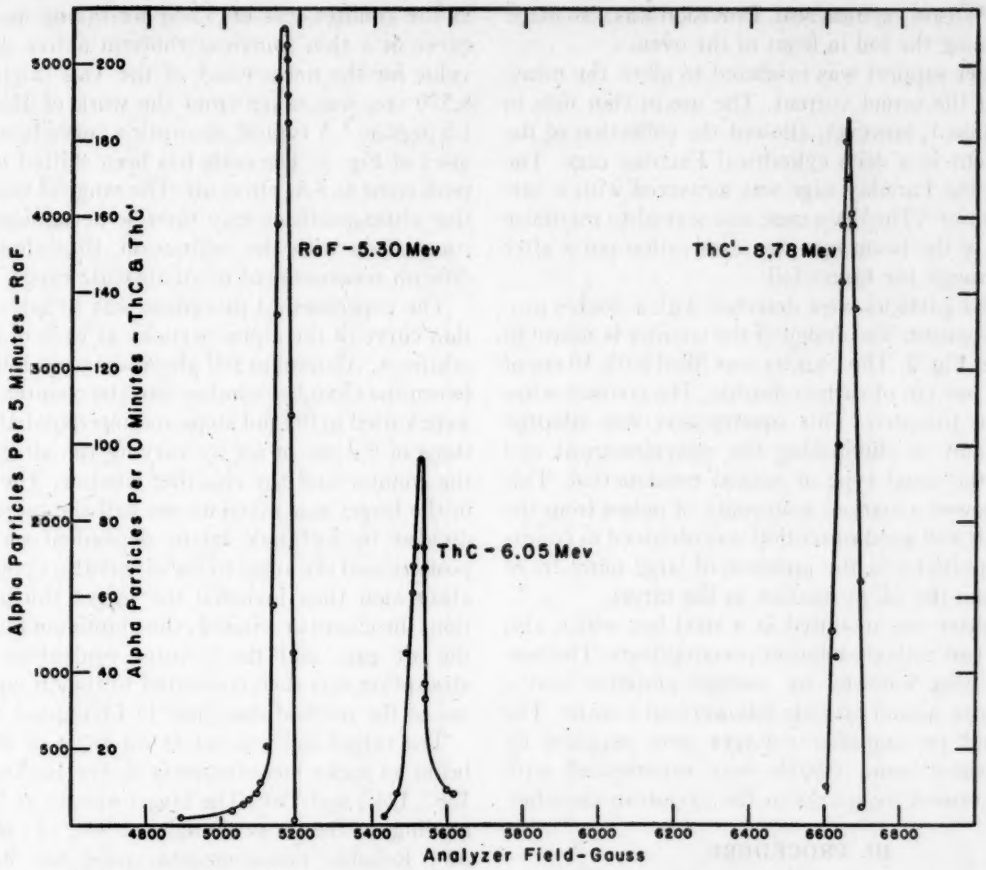
Alpha Particles Per 5 Minutes - RaF
Alpha Particles Per 10 Minutes - ThC & ThC'
RaF - 5.30 Mev
ThC - 6.05 Mev
ThC' - 8.78 Mev
Analyzer Field - Gauss

FIG. 1. Curves obtained in calibrating the beam analyzer. The value of the magnetic field at the position of each peak was used together with the corresponding mean energy to determine the effective radius of curvature $\rho = 64.1$ cm.

calibration. Figure 1 shows the three calibration curves obtained.

The beam is spread out into an energy spectrum across the target slit by the analyzer magnet. The adjustment of this slit then allows the selection of the energy spread in the beam striking the target. With a beam current of about 0.05 μamp. on the target the energy spread was found to be ± 70 kev at a beam energy of 11.1 Mev, for a slit width of 0.2 inch.

The evacuated tube and analyzer were adjusted to align the beam path with the center of the target. The following method was found convenient in aligning the beam and determining the position and size of the beam in the reaction chamber. An ordinary lantern slide plate is placed in the tube where it is desired to know the position and size of the beam, and bombarded for a few seconds. Upon removal from the vacuum the plate is blackened and shows clearly the location and intensity distribution of the beam. It is quite unnecessary to shield the plate from light either before or during the bombardment.

The target chamber, shown schematically in Fig. 2, was adjusted to make the ion beam incident on the target at the center of the chamber. The slits were adjusted to confine the region of the target foil hit by the beam to an area 0.2 inch wide by 0.6 inch high. The angular spread of the emergent particles was then determined by the chamber ports which were 0.5 inches in diameter and located on a radius of 5.5 inches from the chamber center. This arrangement sufficed to provide "good geometry" according to the criterion of Livingston and Bethe.[4]

Nine windows situated on one side of the target chamber permitted the measurement of the angular distribution of the alpha-particles emitted in the reaction. The oven shown in the drawing of the chamber was incorporated to provide for the evaporation of other target materials in future experiments.

The target was an aluminum foil of 0.5 mg/cm^2 surface density. The use of a thinner foil was found to give inadequate counting rates with the beam currents used in this experiment. The foil was mounted on a one-inch diameter brass ring which insured that the beam hit only the target foil. The foil mount was so arranged that the angle with the incident beam could be changed

[4] M. S. Livingston and H. A. Bethe, Rev. Mod. Phys. 9, 278 (1937).

through a Wilson vacuum seal. Provision was also made for positioning the foil in front of the oven.

The target support was insulated to allow the measurement of the target current. The use of thin foils in this experiment, however, allowed the collection of the beam current in a deep cylindrical Faraday cage. The current to the Faraday cage was measured with a current integrator.[5] The deep cage also served to minimize scattering of the beam into the observation ports after passing through the target foil.

The alpha-particles were detected with a double proportional counter. The design of the counter is shown in the inset in Fig. 2. The counter was filled with 10 cm of argon and one cm of carbon dioxide. The counter wires were 3 mil tungsten. This construction was adopted with the aim of eliminating the unsymmetrical end effects in the usual type of coaxial construction. This counter showed a marked uniformity of pulses from the two seconds and good resolution was obtained in counting alpha-particles in the presence of large numbers of protons from the (d, p) reaction in the target.

The counter was mounted in a steel box which also contained two cathode-follower pre-amplifiers. The pre-amplifiers were followed by another amplifier and a mixer stage, a second cathode-follower and a scaler. The counter and pre-amplifier voltages were supplied by batteries since some trouble was experienced with transients caused by sparks in the cyclotron chamber.

III. PROCEDURE

The counter was adjusted to give a good differential range curve by setting the discriminator bias on the scaler so that only those alpha-particles which passed through the first section and ended their range in the second section were recorded. The effective absorption in the counter was obtained by taking an absorption curve of a thin source of thorium active deposit. The value for the mean range of the ThC′ alpha-particles, 8.570 cm, was taken from the work of Holloway and Livingston.[6] A typical absorption curve is shown in the inset of Fig. 3. The scale has been shifted to make the peak come at 8.57 cm of air. The range of the disintegration alpha-particles may then be determined by direct comparison with the calibration, thus eliminating the difficult measurement of an absolute range.

The experimental procedure was to take an absorption curve of the alpha-particles at each of the angular positions. Aluminum foil absorbers were interposed between the chamber window and the counter. These foils were varied in 0.5-mil steps and interpolated between in steps of 0.2 cm of air by varying the air gap between the counter and the chamber window. The absorption in the target was taken as one half the target thickness divided by an angle factor dependent on the target position and the angle to the observation port. The total absorption then included the target thickness correction, the chamber window, the aluminum foil absorbers, the air gap, and the counter equivalent. The total absorption was then converted to the air equivalent by use of the method described in Livingston and Bethe.[4]

The target foil was set at an angle of 45° with the beam to make measurements at the backward angles, 138°, 124°, and 110°. The target was set at 135° to take readings at the forward angles of 90°, 74°, 60°, 46°, and 32°. Reliable measurements could not be made at angles less than 32° because of the larger number of scattered deuterons at these angles.

The effective thickness of the foil presented to the beam was calculated from the measured surface density to be 35 kev for the 11.1 Mev deuterons.

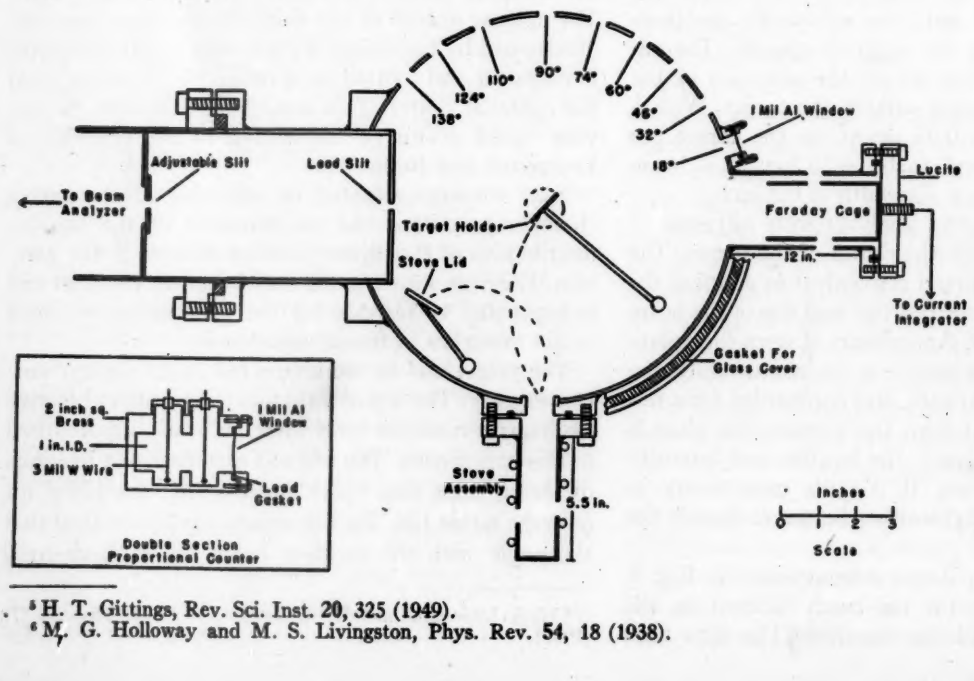

FIG. 2. Schematic of the 10-inch O.D. reaction chamber with 1 of the 9 window assemblies shown in detail at 18°. The inset shows the counter which was used to detect the alpha particles emerging at the various angles.

[5] H. T. Gittings, Rev. Sci. Inst. 20, 325 (1949).
[6] M. G. Holloway and M. S. Livingston, Phys. Rev. 54, 18 (1938).

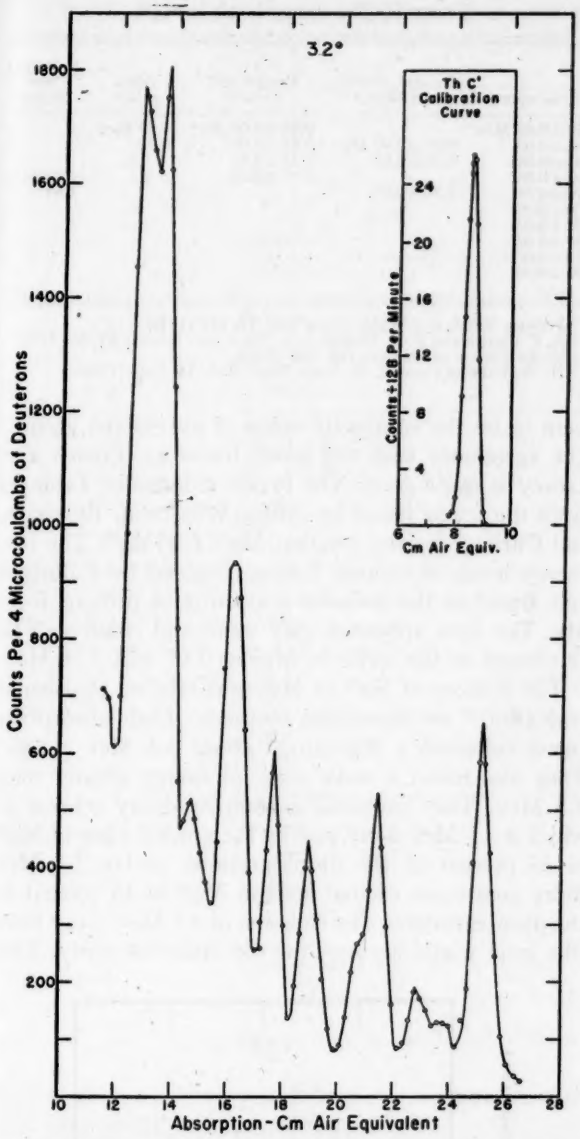
32°
Th C' Calibration Curve
Counts ± 1√8 Per Minute
Cm Air Equiv.
Counts Per 4 Microcoulombs of Deuterons
Absorption - Cm Air Equivalent

FIG. 3. Energy spectra of the alpha-particles from the reaction $Al^{27}(d,\alpha)Mg^{25}$ at 32°. The inset shows the counter calibration curve obtained using the alpha-particles from ThC'.

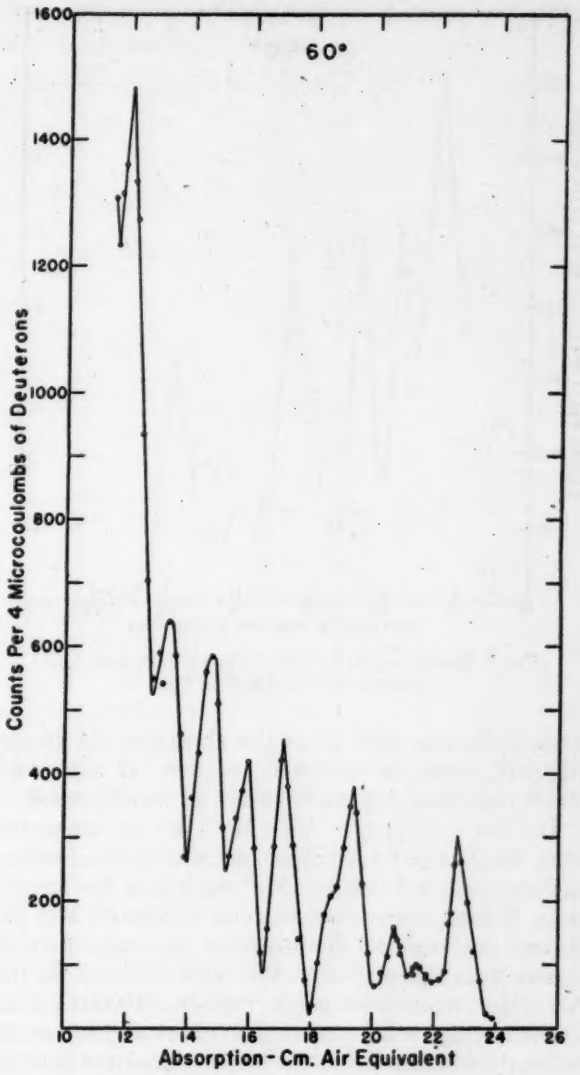

FIG. 4. Energy spectra of the alpha-particles from the reaction $Al^{27}(d,\alpha)Mg^{25}$ at 60°.

The absorption curves were obtained by taking the alpha-particle counts recorded while a given amount of charge was collected by the beam current integrator. The counts at each point were thus normalized even when the beam current varied during a run.

IV. RESULTS AND DISCUSSION

The absorption curves obtained from measurements made at four representative angles with the deuteron beam are shown in Figs. 3–6. More alpha-particle groups are observed at the forward angles because of the greater momentum contribution from the beam. The counter and reaction chamber windows plus the minimum air gap limited the counting of alpha-particles from the target to those with a range greater than 11.5 cm of air. The curve taken at 32° shows nine of the groups well resolved with definite evidence of two additional groups, Q_1 and Q_4, that are not completely resolved. The width of the groups agrees well with the straggling in the absorbers to be expected at these energies. A calibration curve of ThC′ alpha-particles is shown in the inset of Fig. 3 for comparison.

The mean ranges of the alpha-particle groups were obtained by locating the position of the ThC′ alpha-particle peak on the absorption curve and then adding the differences to the mean range of the ThC′ alpha-particles. The conversion of the range to energy was then made from the range-energy curves of Livingston and Bethe.[4]

The Q-values were calculated for the alpha-particle groups from the data taken at each of the eight angles and are presented in tabular form in Table I. The agreement at the different angles is well within the probable

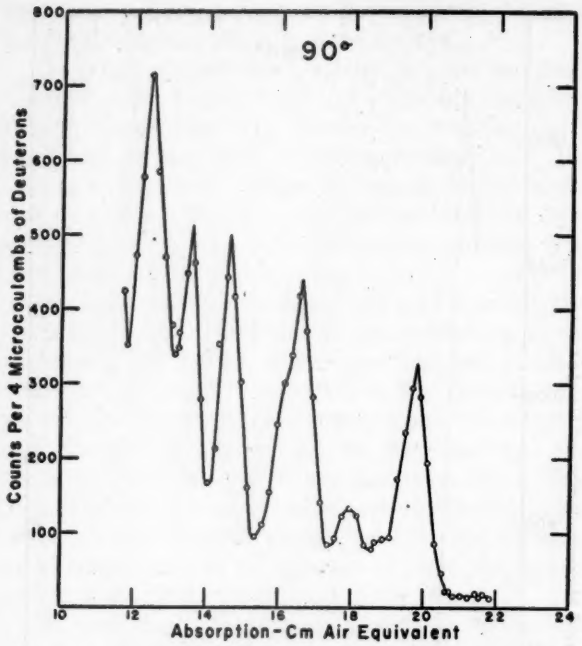

FIG. 5. Energy spectra of the alpha-particles from the reaction $Al^{27}(d, \alpha)Mg^{25}$ at 90°.

error, indicating that all of the alpha-particle groups originate from the deuteron reaction on aluminum rather than from any contaminant on the target foil.

The mass difference $Al^{27}-Mg^{25}$ can be calculated from the Q value for the most energetic group of alpha-particles, which leaves the Mg^{25} nucleus in the ground state. Taking the average value of 6.58±0.03 Mev for Q_0 and the value for the deuteron and alpha-particle masses from Bethe's[7] table, the value obtained for the $Al^{27}-Mg^{25}$ mass difference is 1.99626±0.00003 a.m.u.

The average level spacing is 0.6 Mev and is seen to be nearly constant up to the highest measured level at 5.95 Mev. The general trend may be noted for the higher values of the relative intensities, of the alpha-particle groups which leave the residual nucleus in a higher state of excitation.

The energy levels in Mg^{25} are tabulated in Table II, together with the values for the levels given by other authors for comparison. The values of Pollard, Sailor, and Wyly lie between the values given in this paper and

TABLE I. Q-values of $Al^{27}(d, \alpha)Mg^{25}$ (values are in Mev).

	32°	46°	60°	74°	90°	110°	124°	138°	Average
Q_0	6.55	6.61	6.55	6.58	6.60	6.58	6.61	6.58	6.58±0.03
Q_1	5.92	6.04	5.96	6.04	6.05	6.07	5.99	6.03	6.01±0.08
Q_2	5.54	5.65	5.61	5.64	5.66	5.69	5.62	5.56	5.62±0.07
Q_3	4.92	4.96	4.96	5.00	4.95	4.95	4.98	4.92	4.95±0.03
Q_4	4.59	4.61	4.55	4.73	4.58				4.61±0.06
Q_5	3.78	3.88	3.80	3.87	3.85	3.85	3.84		3.84±0.04
Q_6	3.19	3.19	3.25	3.23	3.27	3.19			3.22±0.04
Q_7	2.45	2.60	2.60	2.62	2.57				2.57±0.05
Q_8	1.68	1.81	1.83						1.77±0.08
Q_9	1.11	1.10	1.08						1.10±0.04
Q_{10}	0.61	0.65							0.63±0.04

[7] H. A. Bethe, *Elementary Nuclear Theory* (John Wiley & Sons, Inc., New York, 1947).

TABLE II. The energy levels in Mg^{25}.

This report	Pollard, Sailor, and Wyly[a]	French and Treacy[b]	Allan *et al.*[c]	Fulbright and Bush[d]
0.57±0.05 Mev		0.58±0.05 Mev	0.58 Mev	
0.96±0.05	0.81±0.07 Mev	0.94±0.05	0.98	
1.63±0.04	1.58±0.07	1.54±0.05		
1.97±0.05		1.87±0.05		1.98 Mev
2.74±0.04	2.54±0.07			2.64
3.36±0.04				
4.01±0.05				
4.81±0.05				
5.48±0.05				
5.95±0.05				

[a] Pollard, Sailor, and Wyly, Phys. Rev. **75**, 725 (1949).
[b] A. P. French and P. B. Treacy, Proc. Phys. Soc. London **63**, 665 (1950).
[c] H. R. Allan *et al.*, Nature **163**, 210 (1949).
[d] H. W. Fulbright and R. R. Bush, Phys. Rev. **74**, 1323 (1948).

seem to be the composite value of unresolved groups. The agreement with the levels found by French and Treacy is quite good. The fourth column in Table II gives the levels found by Allan, Wilkinson, Burcham, and Curling[8] for the reaction $Mg^{24}(d, p)Mg^{25}$. The two energy levels in column 5 were obtained by Fulbright and Bush[9] in the inelastic scattering of protons from Mg. The lines appeared very weak and could well be attributed to the levels in Mg^{25} at 1.97 and 2.74 Mev.

The β-decay of Na^{25} to Mg^{25} was studied by Bleuler and Zünti[10] by absorption methods. Their absorption curve indicated a β-group of about 3.4 Mev energy. They also found a weak γ-ray of energy greater than 0.5 Mev. They proposed a complex decay scheme in which a 3.7 Mev β-ray goes to the ground state of Mg^{25} in 55 percent of the disintegrations, and a 2.7 Mev β-ray goes to an excited level in Mg^{25} in 45 percent of the disintegrations. The emission of a 1 Mev γ-ray from this level would account for the observed γ-ray. This

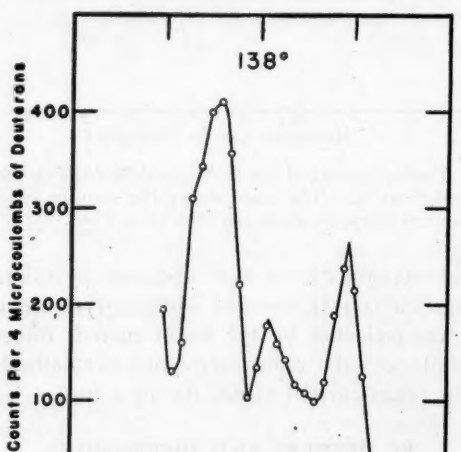

FIG. 6. Energy spectra of the alpha-particles from the reaction $Al^{27}(d, \alpha)Mg^{25}$ at 138°.

[8] Allan, Wilkinson, Burcham, and Curling, Nature **163**, 210 (1949).
[9] H. W. Fulbright and R. R. Bush, Phys. Rev. **74**, 1323 (1948).
[10] E. Bleuler and W. Zünti, Helv. Phys. Acta **20**, 195 (1947).

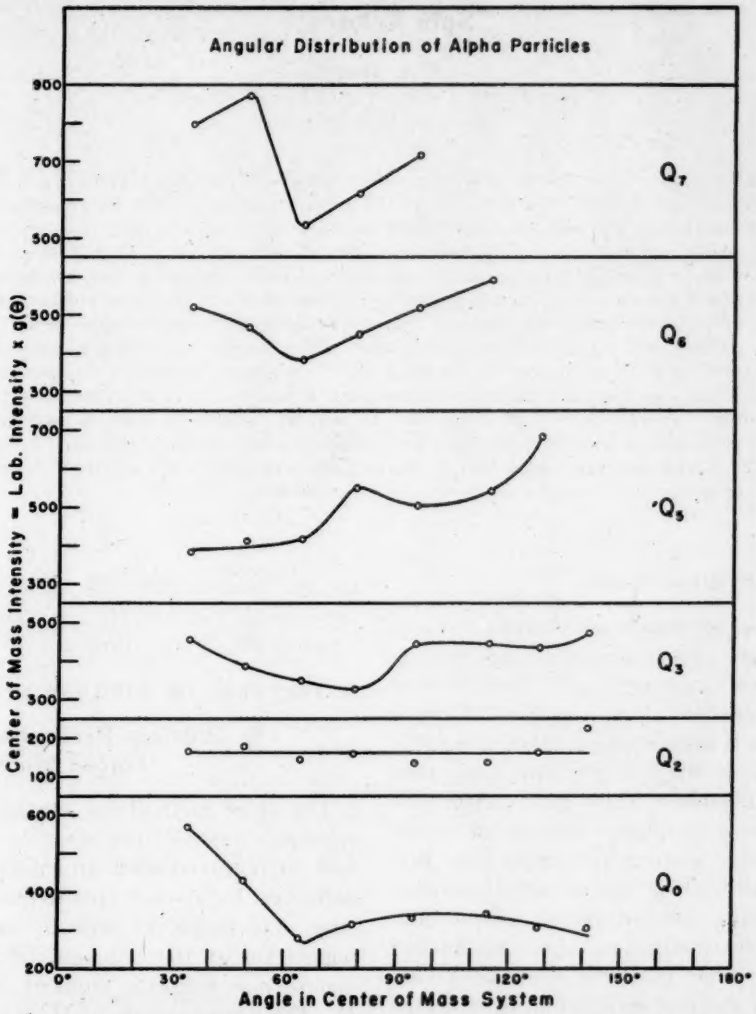

FIG. 7. Angular distribution of alpha-particles from the reaction $Al^{27}(d, \alpha)Mg^{25}$.

excited state could very well be the same one found at 0.96 Mev in the reaction $Al^{27}(d, \alpha)Mg^{25}$.

The angular dependences of the intensities of the alpha-particle groups are shown in Fig. 7 for each of the angles measured. The angles in the laboratory system were converted to the center of mass system by the relation:

$$\sin^2(\theta_r-\theta)/\sin^2\theta = m_1m_2E_1/m_3(m_0E_1+MQ).$$

The subscripts 0, 1, 2, 3 refer to the target nucleus, the incident particle, the product particle and the residual nucleus respectively, and M is the total mass in the reaction; θ and θ_r are the laboratory and center of mass angles respectively.

The observed intensity in the laboratory system must then be converted to the true intensity in the center of mass system since the solid angle defined by the detector aperature is different in the two systems. This conversion factor is:

$$g(\theta) = (\sin^2\theta/\sin^2\theta_r)\cos(\theta_r-\theta).$$

It may be remarked that the curves in Fig. 7 show a marked dependence of the alpha-particle yield on the angle for all the groups except Q_2. This group is isotropic within the probable error of the measurements.

The authors wish to thank Professor Allan C. G. Mitchell for his interest in this work. They would also like to acknowledge the help given by the Indiana University cyclotron crew and in particular the assistance of Mr. E. Toops in plotting some of the graphs.

Spin Echoes*†

E. L. HAHN‡
Physics Department, University of Illinois, Urbana, Illinois
(Received May 22, 1950)

Intense radiofrequency power in the form of pulses is applied to an ensemble of spins in a liquid placed in a large static magnetic field H_0. The frequency of the pulsed r-f power satisfies the condition for nuclear magnetic resonance, and the pulses last for times which are short compared with the time in which the nutating macroscopic magnetic moment of the entire spin ensemble can decay. After removal of the pulses a non-equilibrium configuration of isochromatic macroscopic moments remains in which the moment vectors precess freely. Each moment vector has a magnitude at a given precession frequency which is determined by the distribution of Larmor frequencies imposed upon the ensemble by inhomogeneities in H_0. At times determined by pulse sequences applied in the past the constructive interference of these moment vectors gives rise to observable spontaneous nuclear induction signals. The properties and underlying principles of these spin echo signals are discussed with use of the Bloch theory. Relaxation times are measured directly and accurately from the measurement of echo amplitudes. An analysis includes the effect on relaxation measurements of the self-diffusion of liquid molecules which contain resonant nuclei. Preliminary studies are made of several effects associated with spin echoes, including the observed shifts in magnetic resonance frequency of spins due to magnetic shielding of nuclei contained in molecules.

I. INTRODUCTION

In nuclear magnetic resonance phenomena the nuclear spin systems have relaxation times varying from a few microseconds to times greater than this by several orders of magnitude. Any continuous Larmor precession of the spin ensemble which takes place in a static magnetic field is finally interrupted by field perturbations due to neighbors in the lattice. The time for which this precession maintains phase memory has been called the spin-spin or total relaxation time, and is denoted by T_2. Since T_2 is in general large compared with the short response time of radiofrequency and pulse techniques, a new method for obtaining nuclear induction becomes possible. If, at the resonance condition, the ensemble at thermal equilibrium is subjected to an intense r-f pulse which is short compared to T_2, the macroscopic magnetic moment due to the ensemble acquires a non-equilibrium orientation after the driving pulse is removed. On this basis Bloch[1] has pointed out that a transient nuclear induction signal should be observed immediately following the pulse as the macroscopic magnetic moment precesses freely in the applied static magnetic field. This effect has already been reported[2] and is closely related to another effect, given the name of "spin echoes," which is under consideration in this investigation. These echoes refer to spontaneous nuclear induction signals which are observed to appear due to the constructive interference of precessing macroscopic moment vectors after more than one r-f pulse has been applied. It is the purpose of this paper to describe and analyze these effects due to free Larmor precession in order to show that they can be applied for the measurement of nuclear magnetic resonance phenomena, particularly relaxation times, in a manner which is simple and direct.

II. FEATURES OF NUCLEAR INDUCTION METHODS

(A) Previous Resonance Techniques (Forced Motion)

The chief method for obtaining nuclear magnetic resonance has been one whereby nuclear induction signals are observed while an ensemble of nuclear spins is perturbed by a small radiofrequency magnetic field. A large d.c. magnetic field $\bar{H}_0$ establishes a net spin population at thermal equilibrium which provides a macroscopic magnetic moment $\bar{M}_0$ oriented parallel to $\bar{H}_0$. The forced motion of $\bar{M}_0$ is brought about by subjecting the spin ensemble to a rotating radiofrequency field $\bar{H}_1$ normal to $\bar{H}_0$ at the resonance condition $\omega=\omega_0=\gamma H_0$, where γ is the gyromagnetic ratio, ω is the angular radiofrequency, and ω_0 is the Larmor frequency. The techniques which obtain resonance under this condition provide for the application of a driving r-f voltage to an LC circuit tuned to the Larmor frequency. The sample containing the nuclear spins is placed in a coil which is the inductance of the tuned circuit. At resonance a small nuclear signal is induced in the coil and is superimposed upon an existing r-f carrier signal of relatively high intensity. In order to detect this small nuclear signal the r-f carrier voltage is reduced to a low level by a balancing method if the LC circuit is driven by an external oscillator,[1,3] or the LC circuit may be the tuned circuit of an oscillator which is designed to change its level of operation when nuclear resonance absorption occurs.[4,5] In general, a condition exists whereby transitions induced by H_1, which tend

* This research was supported in part by the ONR.
† Reported at the Chicago Meeting of the American Physical Society, November, 1949; Phys. Rev. 77, 746 (1950).
‡ Present address: Physics Dept. Stanford University, Stanford, California.
[1] F. Bloch, Phys. Rev. 70, 460 (1946).
[2] E. L. Hahn, Phys. Rev. 77, 297 (1950).
[3] Bloembergen, Purcell, and Pound, Phys. Rev. 73, 679 (1948).
[4] R. V. Pound, Phys. Rev. 72, 527 (1947); R. V. Pound and W. D. Knight, Rev. Sci. Inst. 21, 219 (1950).
[5] A. Roberts, Rev. Sci. Inst. 18, 845 (1947).

to upset the thermal equilibrium of the spins, are in competition with processes of emission due to lattice perturbations which tend to restore equilibrium. Spin relaxation phenomena, which are measured in terms of the relaxation times T_2 and T_1 (spin-lattice), must be distinguished simultaneously from effects due to the influence of r-f absorption. Consequently the study of resonance absorption line shapes, intensities, and transients must carefully take into account the intensity of H_1 and the manner in which resonance is obtained.

In practice, resonance takes place over a range of frequencies determined by the inhomogeneity of H_0 throughout the sample. For resonances concerning nuclei in liquids it is generally found that the natural line width given by $1/T_2$ on a frequency scale is much narrower than the spread in Larmor frequencies caused by external field inhomogeneities, whereas the converse is true in solids. Therefore steady state resonance lines due to nuclei in liquids are artificially broadened; transient signals are modified in shape and have decay times which are shorter than would otherwise be determined by T_1 and T_2.

(B) Nuclear Induction Due to Free Larmor Precession

The observation of transient nuclear induction signals due to free Larmor precession becomes possible at the resonance condition described above if the r-f power is now applied in the form of intense, short pulses. The r-f inductive coil which surrounds the sample is first excited by the applied pulses and thereafter receives spontaneous r-f signals at the Larmor frequency due to the precessing nuclei. In particular, the echo effect is brought about by subjecting the sample to two r-f pulses in succession (the simplest case) at pulse width $t_w < \tau < T_1, T_2$, where τ is the time interval between pulses. At time τ after the leading edge of the second pulse the echo signal appears. Since H_1 is absent while these signals are observed, no particular attention need be given to elaborate procedures for eliminating receiver saturation effects (as must be done in the forced motion technique) providing that T_2 is large enough to permit observation of echoes at times when the receiver has recovered from saturation due to the pulses. Because the T_2 of nuclei in liquids is generally large enough to favor this condition, the technique for obtaining echoes in this work has been largely confined to the magnetic resonance of nuclei in liquid compounds. Preliminary observations of free induction signals in solids, where T_2 becomes of the order of microseconds, indicate again, however, that procedures must be undertaken for preventing receiver saturation due to intense pulses.

For spin ensembles in liquids it will be shown that the analysis of observed echo signals yields direct information about T_1 and T_2 without requiring consideration of the effect of H_1 on the measured decay of the signal. Because of the inhomogeneity in H_0, the self diffusion of "spin-containing liquid molecules" brings about an attenuation of observed transient signals in addition to the decay due to T_1 and T_2. However, this is only serious for liquids of rather low viscosity which also have a large T_2 for the resonant nuclei concerned, whereas in conventional resonance methods (forced motion), field inhomogeneities obscure a direct measurement of T_2 in liquids over a much wider range of viscosities. The free motion technique, which will hereafter be denoted by the method of spin echoes or free nuclear induction, also reveals in a unique manner differences in resonant frequency between nuclear spins of the same species located in different parts of a single molecule or in different molecules. Such differences have been observed by previous resonance methods,[6,7] and the echo technique gives at least as good a resolution in the measurement of small shifts.

In this investigation the in-phase condition of a precessing spin ensemble is considered to be eventually destroyed because of lattice perturbations which limit the phase memory time of Larmor precession. The precession of an individual spin may be interrupted either because its energy of precession is transferred to neighboring spins in a time $\sim T_2''$ (mutual spin-spin flipping), or because this energy is transferred to the lattice as thermal energy in a time $\sim T_1$. The spread in Larmor frequencies, due to local "z magnetic field" fluctuations at the position of the nucleus caused by neighboring spins and paramagnetic ions, also serves to disturb phase memory (H_0 is in the z direction). In a formal treatment[8] this effect is considered in conjunction with the interaction giving rise to T_2'', and a general relaxation time T_2' is formulated. The inverse of the total relaxation time, $1/T_2 \sim 1/T_2' + 1/T_1$, therefore becomes the uncertainty in frequency of a precessing spin, which can then acquire an uncertainty in phase of the order of one radian in time T_2.

It will be convenient to describe the formation of free induction signals by considering the free precession of individual macroscopic moment vectors $\bar{M}_0(\omega_0)$. Each of these vectors has a magnitude at a given ω_0 which is determined by a z magnetic field distribution imposed upon the ensemble by inhomogeneities in H_0. In this spectral distribution $\bar{M}_0(\omega_0)$ can be defined as an isochromatic macroscopic moment which consists of an ensemble of nuclear moments precessing in phase at the assigned frequency ω_0. The precessional motion of any $\bar{M}_0(\omega_0)$ vector about the total magnetic field (with or without r-f pulses) can be followed regardless of what phases the individual isochromatic moments have with respect to one another throughout the entire spectrum. At the time a short r-f pulse initiates the free precession of $\bar{M}_0(\omega_0)$ from a classically non-precessing initial condition at thermal equilibrium, relaxation and possibly diffusion processes begin to diminish the magnitude of

[6] W. G. Proctor and F. C. Yu, Phys. Rev. 77, 717 (1950).
[7] W. C. Dickinson, Phys. Rev. 77, 736 (1950).

UNIVERSITY OF MICHIGAN LIBRARIES

the precessing vector $\bar{M}_0(\omega_0)$ as the individual nuclear spins get out of phase with one another or return to thermal equilibrium.

The actual H_0 field which persists at the position of a precessing spin accounts for a given ω_0 and hence for a given $\bar{M}_0(\omega_0)$. In liquids this persisting field and the way it is distributed over the sample is taken to be entirely due to the magnet; any contributions to the local field at the nucleus by neighbors in the lattice average out in a time short compared to a Larmor period. Free induction signals from nuclei in solids, however, indicate that a broad distribution in H_0 exists (compared to a relatively homogeneous external field) which is determined by fixed lattice neighbors, and now this local field distribution does not average out.

The description of free induction effects is simplified by transforming to a coordinate system in which the $x'y'$ plane (Fig. 1) is rotating at some convenient reference angular frequency ω'. This frequency is usually chosen to be the center frequency of a given distribution of isochromatic moments, where the distribution is typically described by a Gaussian or Lorentz (damped oscillator) function. In the next section definite properties of the rotating coordinate representation are presented. The precessional motion as viewed in the rotating system is conveniently followed when (1) $\bar{M}_0(\Delta\omega)$ undergoes forced transient motion during the driving pulse, and (2) when the $\bar{M}_0(\Delta\omega)$ vectors precess freely, where $\Delta\omega=\omega_0-\omega'$ and $\bar{M}_0(\omega_0)=\bar{M}_0(\Delta\omega)$. The condition in (1) has already been analyzed theoretically and experimentally.[8,9,10] Although it is strictly a condition in which $\bar{M}_0(\Delta\omega)$ precesses about the total field $\bar{H}_0+\bar{H}_1$, as viewed in the laboratory system, it has been characterized by the fact that not only does $\bar{M}_0(\Delta\omega)$ appear to precess about the z axis at a high Larmor frequency, but also it appears to nutate with respect to the z axis at a much lower frequency.[11]

III. THEORY AND APPLICATIONS

(A) The Moving Coordinate Representation

Consider the torque equation, with no damping, which describes the precession of $\bar{M}$ as seen in the laboratory system:

$$d\bar{M}/dt=\gamma(\bar{M}\times\bar{H}), \tag{1}$$

where $\bar{H}$ is the total magnetic field. During the application of r-f pulses, $\bar{H}=\bar{H}_0+\bar{H}_1$; and during the free precession of $\bar{M}$ in the absence of pulses, $\bar{H}=\bar{H}_0$. During a pulse it is convenient to transform to a moving coordinate system in which $\omega'=\omega$, and $\bar{H}_1$ is chosen to lie along the x' axis. It will be pointed out, however, that, regardless of the choice of direction of $\bar{H}_1$ in the $x'y'$ plane, the description of the spin echo model presented later is not affected, except under a very special condition. If $D\bar{M}/dt$ is the observed torque in the moving coordinate system, then by a well-known transformation,

$$d\bar{M}/dt=D\bar{M}/dt+\bar{\omega}\times\bar{M}, \tag{2}$$

where $\bar{M}\equiv M(u, v, M_z)$ and $\bar{H}\equiv H(H_1, 0, H_0)$. Combining (1) and (2) we obtain

$$D\bar{M}/dt=\bar{M}\times(\Delta\bar{\omega}+\bar{\omega}_1) \tag{3}$$

as the torque in the moving system during a pulse. The vector $\bar{M}$ is identified with the isochromatic moment $\bar{M}_0(\Delta\omega)$ which appears to precess about the effective field vector $(\Delta\bar{\omega}+\bar{\omega}_1)/\gamma$. Let $(\Delta\omega)_{\frac{1}{2}}$ be the width at half-maximum of an assumed function which describes the distribution of $\bar{M}_0(\Delta\omega)$ over the inhomogeneous external field, and let ω' be the center frequency of this distribution. If, during a pulse, the inequality $1/t_w$, $\omega_1\gg(\Delta\omega)_{\frac{1}{2}}$ applies at resonance ($\omega\approx\omega'$), then the precession of any $\bar{M}_0(\Delta\omega)$ vector will appear to take place practically about the $\bar{\omega}_1$ vector in the moving system. This precessional frequency is given by $\omega_1=\gamma H_1$ (of the order of kilocycles) which appears in the laboratory system as a frequency of nutation superimposed upon a high Larmor precession frequency ($\sim$30 Mc). In the rotating system any $\bar{M}_0(\Delta\omega)$ vector will precess in a cone whose axis is in the direction of $\bar{H}_1$ and whose angle is determined by the angle between $\bar{M}_0(\Delta\omega)$ and $\bar{H}_1$ at the time $\bar{H}_1$ is suddenly applied. When $\bar{H}_1$ is suddenly removed, the vector $\bar{M}_0(\Delta\omega)$ is oriented at a fixed angle θ with respect to the z axis, and precesses freely at angular frequency $\Delta\omega$ about the effective magnetic field $\Delta\bar{\omega}/\gamma$ along the z axis. The angle θ will be determined by $\omega_1 t_w$ and the initial conditions established by successive pulses applied in the past.

(B) Simple Vector Model of the Spin Echo

For spin ensembles in liquids a simple vector model will account for the manner in which two applied r-f pulses establish a given spectral distribution of moment components in the $x'y'$ plane, where the axis of the inductive coil is oriented. This distribution then freely precesses to form, by constructive interference, a resultant "echo" in the $x'y'$ plane. This is formulated by integrating a general expression for the $x'y'$ component of the isochromatic moment over all frequencies $\Delta\omega$ imposed by H_0 field inhomogeneities. Purcell[12] has suggested a three-dimensional model of the echo, Fig. 1, which arises in a special case. At $t=0$, when $\bar{H}_1$ is suddenly applied, $\bar{M}_0(\Delta\omega)$ is at thermal equilibrium, aligned parallel to $\bar{H}_0$ along the z axis. During time t_w

[8] N. Bloembergen, *Nuclear Magnetic Relaxation* (Martinus Nijhoff, The Hague, 1948).
[9] H. C. Torrey, Phys. Rev. 76, 1059 (1949).
[10] E. L. Hahn, Phys. Rev. 76, 461 (1949).
[11] This is observed to come about in the laboratory system as the resonance absorption mode becomes modulated at the low nutation frequency. Classically speaking, the term nutation is applied only to the physical top, in which the presence of angular momentum about an axis other than the spin axis is responsible for the nutation. Although a nuclear spin possesses extremely negligible angular momentum about any axis other than its spin axis, the term nutation is convenient to retain here in order to refer to the tipping motion of $\bar{M}_0(\Delta\omega)$ with respect to the z axis.
[12] Private communication.

of the first pulse, let $\bar{M}_0(\Delta\omega)$ precess an angle $\omega_1 t_w=\pi/2$ about $\bar{H}_1$, so that all moment vectors in the spectrum will have nutated into the $x'y'$ plane. Let $\tau\gg 1/(\Delta\omega)_{\frac{1}{2}}$, $T_1=T_2=\infty$, and assume a rectangular spectrum over $\Delta\omega$, i.e., $g(\Delta\omega)=$const., where $g[(\Delta\omega)_{\frac{1}{2}}]=0$. During time $t_w\leqslant t\leqslant\tau$, the various isochromatic moment pairs $M_0(+|\Delta\omega|)$, $M_0(-|\Delta\omega|)$, will precess at frequency $\Delta\omega$, maintaining a symmetry about the y' axis but rotating in opposite directions. These precessing moments will attain an isotropic distribution in a time $\gtrsim 2\pi/(\Delta\omega)_{\frac{1}{2}}$ prior to which a free induction decay is observed.[2] At time τ the second r-f pulse, identical with the first one, will rotate the moment pairs from angular positions $\varphi=3\pi/2\pm|\Delta\omega|\tau$, $\theta=\pi/2$ to $\varphi=(0,\pi)$, $\theta=\pi-|\Delta\omega|\tau$ in spherical coordinates. During the time interval $\tau+t_w\leqslant t<2\tau$ all moment vectors interfere destructively with one another and distribute themselves isotropically over a unit sphere until the time $t\approx 2\tau$ when they interfere constructively. At time 2τ all of the moment vectors will have again precessed angles $\Delta\omega\tau$ respectively from their positions at $t=\tau+t_w$ so that they terminate in a figure eight pattern whose equation is $\theta=\varphi$. Free induction for $t\geqslant\tau+t_w$ will be obtained from the linearly polarized component of magnetization

$$v(\Delta\omega,t)=M_0\sin\Delta\omega\tau\sin\Delta\omega(t-\tau) \tag{4}$$

along the y' axis. The observed induction voltage will be due to the integrated precessing moment

$$V(t)=\int_{-(\Delta\omega)_{\frac{1}{2}}}^{(\Delta\omega)_{\frac{1}{2}}} g(\Delta\omega)v(\Delta\omega,t)d(\Delta\omega), \tag{5}$$

where

$$\int_{-(\Delta\omega)_{\frac{1}{2}}}^{(\Delta\omega)_{\frac{1}{2}}} g(\Delta\omega)d(\Delta\omega)=1.$$

Therefore, from (4) and (5) we obtain

$$V(t)=\frac{M_0}{2}\left[\frac{\sin(\Delta\omega)_{\frac{1}{2}}(t-2\tau)}{(\Delta\omega)_{\frac{1}{2}}(t-2\tau)}-\frac{\sin(\Delta\omega)_{\frac{1}{2}}t}{(\Delta\omega)_{\frac{1}{2}}t}\right]. \tag{6}$$

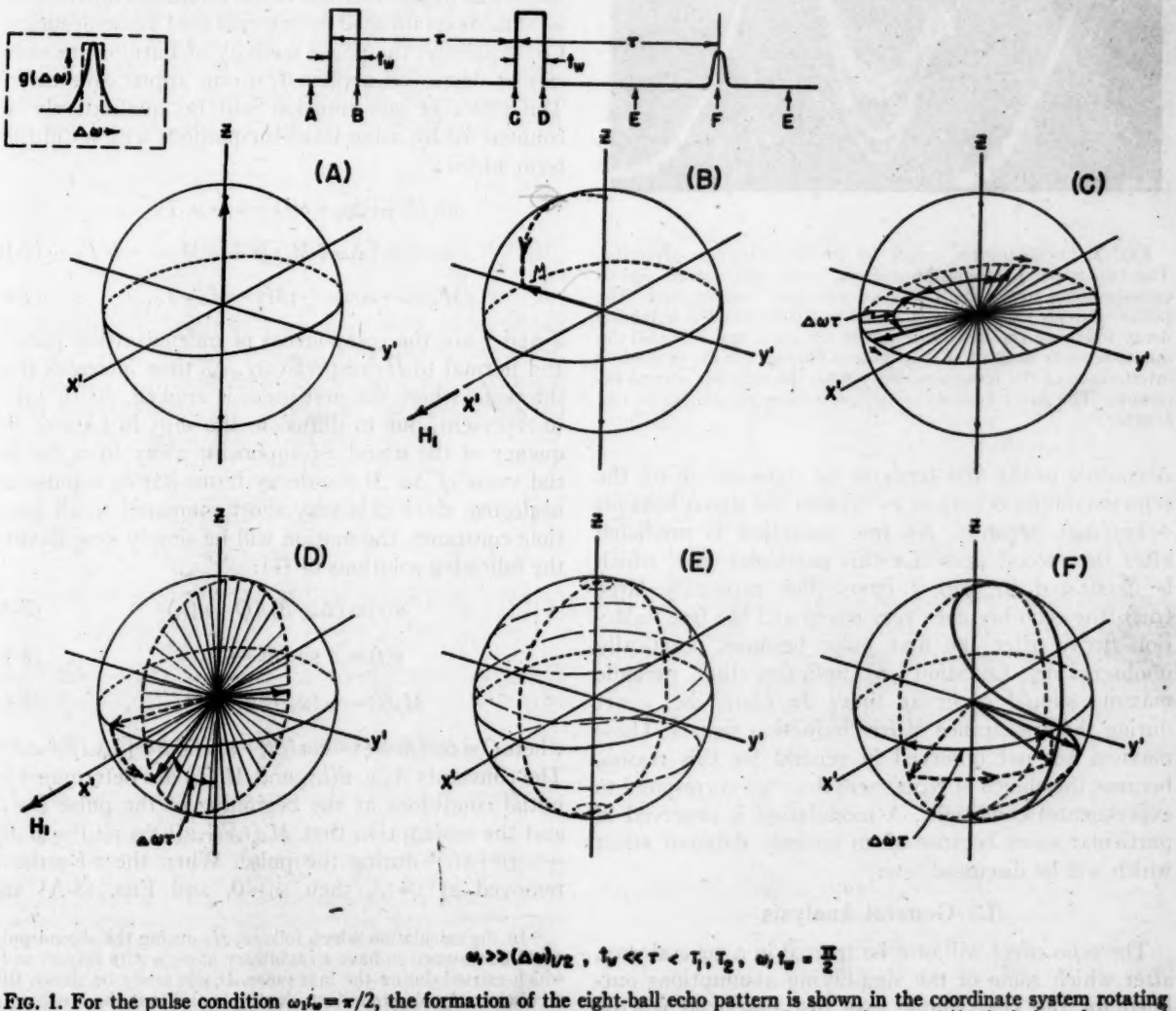

FIG. 1. For the pulse condition $\omega_1 t_w=\pi/2$, the formation of the eight-ball echo pattern is shown in the coordinate system rotating at angular frequency ω. The moment vector monochromats are allowed to ravel completely in a time $\tau\gg 1/(\Delta\omega)_{\frac{1}{2}}$ before the second pulse is applied. The echo gives maximum available amplitude at $\omega_1 t_w=2\pi/3$.

UNIVERSITY OF MICHIGAN LIBRARIES

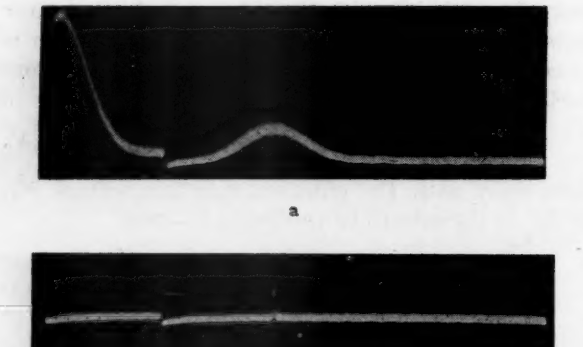

a

b

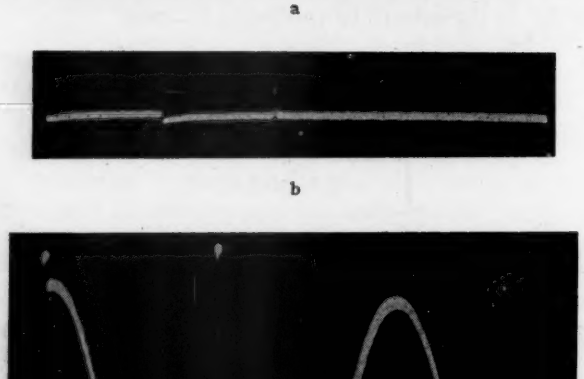

c

FIG. 2. Oscillographic traces for proton echoes in glycerine. The two upper photographs indicate broad and narrow signals corresponding to H_0 fields of good and poor homogeneity. The pulses, scarcely visible, are separated by 0.0005 sec. The induction decay following the first pulse in the top trace has an initial dip due to receiver saturation. The bottom photograph shows random interference of the induction decay with the echo for several exposures. The two r-f pulses are phase incoherent relative to one another.

According to the first term on the right side of (6) the echo maximum occurs at $t=2\tau$, and the signal lasts for $\sim 4\pi/(\Delta\omega)_{\frac{1}{2}}$ seconds. No free induction is predicted after the second pulse for this particular case, which is illustrated in Fig. 2 (top). For extremely large $(\Delta\omega)_{\frac{1}{2}}$ the echo becomes very sharp and the free induction decay after the first pulse becomes practically unobservable. Equation (6) indicates that periodic maxima should occur at times $2\pi/(\Delta\omega)_{\frac{1}{2}}$ sec. apart during the appearance of free induction signals. These maxima are not observed in general for this reason, because the choice of $g(\Delta\omega)$ here does not correspond to experimental conditions. A modulation is observed in particular cases because of an entirely different effect which will be discussed later.

(C) General Analysis

The echo effect will now be treated in a general way, after which some of the simplifying assumptions outlined for the very simple case just described will be applied. By making use of Bloch's equations[1] and choosing $g(\Delta\omega)$ to approximate the actual distribution of spins over H_0, the decay of echo signals due to T_1, T_2, and self-diffusion (in the case of some liquids) can be accounted for. As in the case illustrated above, $\bar{H}_1$ will be chosen to lie along the x' axis in the rotating system for both pulses. Actually $\bar{H}_1$ may appear in any possible position in the $x'y'$ plane during the second pulse since the r-f is not necessarily coherent for both pulses. However, free induction signals will be independent of this random condition as long as $\tau \gg 1/(\Delta\omega)_{\frac{1}{2}}$.[13] This signifies that free induction decay following a single pulse does not interfere with the echo (see Fig. 2, bottom, where this interference effect is shown). Ordinarily the scalar differential equations obtained from (3) are written to include additional torque terms due to relaxation according to Bloch. In the case of echo phenomena it is found that nuclear signals due to precessing nuclear moments contained in liquid molecules (particularly of low viscosity) are not only attenuated by the influence of T_1 and T_2, but also suffer a decay due to self-diffusion of the molecules into differing local fields established by external field inhomogeneities. Consequently, the phase memory of Larmor precession can be destroyed artificially to an appreciable extent. The effect of self-diffusion will be qualitatively accounted for by using Bloch's equations with a diffusion term added:

$$du/dt+[\Delta\omega+\delta(t)]v=-u/T_2 \tag{7-A}$$

$$dv/dt-[\Delta\omega+\delta(t)]u+\omega_1 M_z=-v/T_2 \tag{7-B}$$

$$dM_z/dt-\omega_1 v=-(M_z-M_0)/T_1. \tag{7-C}$$

u and v are the components of magnetization parallel and normal to $\bar{H}_1$ respectively. As time increases from the point where the first pulse is applied, $\delta(t)$ is taken to represent, due to diffusion, the shift in Larmor frequency of the u and v components away from the initial value of $\Delta\omega$. If the decay terms during a pulse are neglected, since t_w is very short compared to all decay time constants, the motion will be simply described by the following solutions of (7):

$$u(t)=(\Delta\omega/\beta)AQ+u(t_i) \tag{8-A}$$

$$v(t)=A\sin(\beta t+\xi) \tag{8-B}$$

$$M_z(t)=-(\omega_1 A/\beta)Q+M_z(t_i), \tag{8-C}$$

where $Q=\cos(\beta t+\xi)-\cos(\beta t_i+\xi)$ and $\beta=[(\Delta\omega)^2+\omega_1^2]^{\frac{1}{2}}$. The constants A, ξ, $u(t_i)$, and $M_z(t_i)$ are determined by initial conditions at the beginning of the pulse ($t=t_i$) and the assumption that $M_z(t_i)^2+u(t_i)^2+v(t_i)^2=M_z(t)^2+u(t)^2+v(t)^2$ during the pulse. When the r-f pulse is removed at $t=t_i'$, then $\omega_1=0$, and Eqs. (8-A) and

[13] In the calculation which follows, $\bar{H}_1$ during the second pulse could be assumed to have an arbitrary angle α with respect to $\bar{H}_1$ which existed during the first pulse. It can easily be shown that all nuclear signals are independent of α and that the direction of the echo resultant will be at an angle $\alpha+\pi/2$ with respect to the direction of $\bar{H}_1$ which was applied during the second pulse.

(8-B) combine to give a solution

$$F(t)=F(t_i')\exp\{-(t-t_i')/T_2 + i[\Delta\omega(t-t_i')+\int_{t_i'}^{t}\delta(t'')dt'']\}, \quad (9)$$

where $F=u+iv$ and $t\geqslant t_i'$.

A constant field gradient, $(dH_0/gl)_{hw}=G$, shall be assumed to exist throughout the sample, where l is any direction in which the field gradient has the given average value G. The actual direction of $\bar{H}_0$ must vary in the sample. Any precessing moment which experiences a change in the magnitude of $\bar{H}_0$ due to diffusion will adiabatically follow a corresponding change in Larmor frequency of precession which will take place about the new direction of $\bar{H}_0$. Therefore $\bar{H}_1$ will not have the same magnitude during both pulses for a particular spin because the component of the applied r-f field perpendicular to the different directions of $\bar{H}_0$ will differ. Free induction signals will suffer negligible distortion because of this as compared to the distortion caused by variation in direction and magnitude of $\bar{H}_1$ throughout the sample due to coil geometry. For purposes of simplicity, the analysis will not attempt to take into account any sort of inhomogeneity of the $\bar{H}_1$ field.

In (9) let $\delta(t'')=\gamma Gl(t'')$ and

$$\int_{t_i'}^{t}\delta(t'')dt''=\Phi(t)-\Phi(t_i'), \quad (10)$$

where $\Phi(t)-\Phi(t_i')$ is the total phase shift accumulated in a time $t-t_i'$ by a precessing spin due to diffusion. The solution (9) must be averaged over all Φ, using a phase probability function $P(\Phi, t)$, by considering in particular the integral

$$\int_{-\infty}^{\infty}\{\exp i[\Phi(t)-\Phi(t_i')]\}P(\Phi, t)d\Phi = \exp\left[-\frac{kt^3}{3}-i\Phi(t_i')\right], \quad (11\text{-A})$$

where $k=(\gamma G)^2D$, and D is the self-diffusion coefficient of the spin-containing molecule. It can be shown[14] that

$$P(\Phi, t)=(4\pi kt^3/3)^{-\frac{1}{2}}\exp[-\Phi^2/(4\pi kt^3/3)]. \quad (11\text{-B})$$

[14] First one must take into account all possible paths (essentially all possible areas expressed by the integral in (10)) which the diffusing molecule may take in the l, t plane so that the total phase shift accumulated by the precessing spin which the molecule carries with it has a given value which is the same regardless of path length and final position of the molecule. The ordinary diffusion law is assumed to apply in expressing the probability of a given path under the constraint that a certain $\Phi(t)$ be accumulated. The distribution function (11-B) over all phases then follows by applying a standard deviation theorem (see James V. Uspensky, *Introduction to Mathematical Probability* (McGraw-Hill Book Company Inc., New York, 1937), p. 270). The author is indebted to Dr. C. P. Slichter for this derivation.

From Eq. (7-C) the solution for $M_z[\Delta\omega+\delta(t)]$ must be averaged over the probability that the moment vector corresponding to it is precessing at frequency $\Delta\omega+\delta(t)$ at time t. The ordinary diffusion law will be assumed to apply as regards the distance of diffusion l which corresponds to frequency shift δ. General solutions of (7) representing free motion can therefore be written as follows:

$$F(t)=F(t_i')\exp\{-(t-t_i')/T_2-\tfrac{1}{3}kt^3 + i[\Delta\omega(t-t_i')-\Phi(t_i')]\} \quad (12)$$

$$M_z(t)=M_0\left[1+\frac{M_i-M_0}{M_0}\exp-(t-t_i')/T_1\right], \quad (13)$$

where

$$M_i=\int_{-\infty}^{\infty}M_z(\Delta\omega+\delta, t_i')P(\delta, t)d\delta \quad (14)$$

and[15]

$$P(\delta, t)=\frac{1}{[4\pi k(t-t_i')]^{\frac{1}{2}}}\exp[-\delta^2/4k(t-t_i')].$$

For the case in which twin pulses are applied, we have at $t=0$, $M_z=M_0$ and $u=v=0$. At $t=t_w$ the moments in the rotating system are obtained from (8). At time τ the r-f pulse is again applied and removed at $t=\tau+t_w$. After the second pulse the initial values of the magnetization components which undergo free motion are as follows:

$$u(\tau+t_w)=\frac{\Delta\omega}{\omega_1M_0}[v(\tau)v(t_w)-u(\tau)u(t_w)] + \frac{u(t_w)M_z(\tau)}{M_0}+u(\tau) \quad (15\text{-A})$$

$$v(\tau+t_w)=\frac{v(t_w)}{M_0}\left[M_z(\tau)-\frac{\Delta\omega}{\omega_1}u(\tau)\right]+v(\tau)\cos\beta t_w \quad (15\text{-B})$$

$$M_z(\tau+t_w)=\frac{1}{M_0}[M_z(\tau)M_z(t_w) + u(\tau)u(t_w)-v(\tau)v(t_w)]. \quad (15\text{-C})$$

The v component, which is an even function in $\Delta\omega$, provides the free induction voltage, whereas the u component is an odd function in $\Delta\omega$ and does not contribute to the integral which will be applied in (18). Imposing the condition $\omega_1\gg\Delta\omega$ and $\tau\gg t_w$ we obtain:

(a) $(t\leqslant\tau)$:

$$v(t, \Delta\omega)\approx -M_0\sin\omega_1t_w\cos\Delta\omega t\exp(-t/T_2-\tfrac{1}{3}kt^3) \quad (16)$$

(b) $(t\geqslant\tau)$:

$$v(t, \Delta\omega)\approx M_0\sin\omega_1t_w[\sin^2\tfrac{1}{2}\omega_1t_w\cos\Delta\omega(t-2\tau) - \cos^2\tfrac{1}{2}\omega_1t_w\cos\Delta\omega t]\exp(-t/T_2-\tfrac{1}{3}kt^3) - M_z(\tau)\sin\omega_1t_w\cos\Delta\omega(t-\tau) \exp[-(t-\tau)/T_2-\tfrac{1}{3}k(t-\tau)^3]. \quad (17)$$

[15] E. H. Kennard, *Kinetic Theory of Gases* (McGraw-Hill Book Company, Inc., New York, 1938), p. 283.

UNIVERSITY OF MICHIGAN LIBRARIES

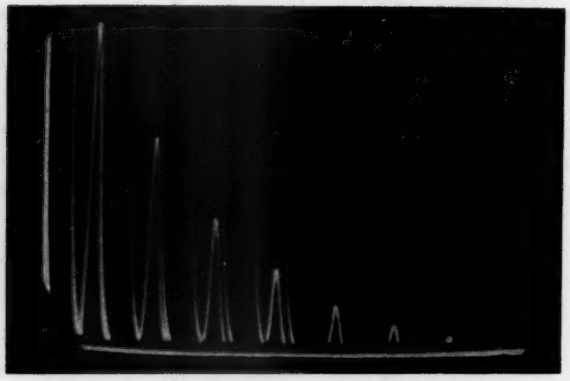

FIG. 3. Multiple exposures of proton echoes in a water solution of $Fe(NO_3)_3$ (2.5×10^{18} Fe^{+++} ions/cc). The faint vertical traces indicate paired pulses which are applied at time intervals $\gg T_2$, with the first pulse of each pair occurring at the same initial position on the sweep. For each pulse pair the interval τ is increased by 1/300 sec. The echoes are spaced 2/300 sec. apart and the measured decay time constant of the echo envelope gives $T_2=0.014$ sec.

The measured signal will be due to the integral

$$V(t)=\int_{-\infty}^{\infty} g(\Delta\omega)v(t,\Delta\omega)d(\Delta\omega). \tag{18}$$

For convenience $g(\Delta\omega)$ is chosen to be a Gaussian distribution:

$$g(\Delta\omega)=(2\pi)^{-\frac{1}{2}}T_2^*\exp[-(\Delta\omega T_2^*)^2/2],$$
$$T_2^*=(2\ln 2)^{\frac{1}{2}}/(\Delta\omega)_{\frac{1}{2}}, \tag{19}$$

where the integral of $g(\Delta\omega)$ over all $\Delta\omega$ is equal to unity. Integration of (16) and (17) according to (18) gives the following:

(a) $(t\leq\tau)$:

$$V(t)\approx -M_0\sin\omega_1 t_w\exp\left[-\left(\frac{t^2}{2T_2^{*2}}+t/T_2+\frac{kt^3}{3}\right)\right], \tag{20}$$

(b) $(t\geq\tau)$:

$$V(t)\approx M_0\sin\omega_1 t_w\left\{\left(\sin^2\frac{\omega_1 t_w}{2}\right)\exp\left[-\frac{(t-2\tau)^2}{2T_2^{*2}}\right]-\left(\cos^2\frac{\omega_1 t_w}{2}\right)\exp\left(-\frac{t^2}{2T_2^{*2}}\right)\right\}$$
$$\times\exp\left(-\frac{kt^3}{3}-t/T_2\right)-M_z(\tau)\sin\omega_1 t_w$$
$$\times\exp-\left[\frac{1}{2}\left(\frac{t-\tau}{T_2^*}\right)^2+\frac{t-\tau}{T_2}+\frac{k}{3}(t-\tau)^3\right]. \tag{21}$$

The echo at $t=2\tau$ is accounted for by the first term in (21) and has a width of $\sim T_2^*$ seconds. The remaining terms in (20) and (21) predict the occurrence of free induction decay signals immediately following the removal of the pulses. Actual shapes of all induction signals are determined mainly by what shape $g(\Delta\omega)$ happens to have due to external field inhomogeneities over the magnet. T_2 will play a significant role in affecting the shape only if $T_2\gtrsim T_2^*$. Signal amplitudes are independent of T_2^* as long as $\omega_1\gg 1/T_2^*$. In practice $g(\Delta\omega)$ is roughly a function which is some compromise between the Gaussian distribution given above and the Lorentz damped oscillator function given by

$$g(\Delta\omega)=\frac{2T_2^*}{1+(\Delta\omega T_2^*)^2}\quad\text{where}\quad T_2^*=\frac{1}{(\Delta\omega)_{\frac{1}{2}}}.$$

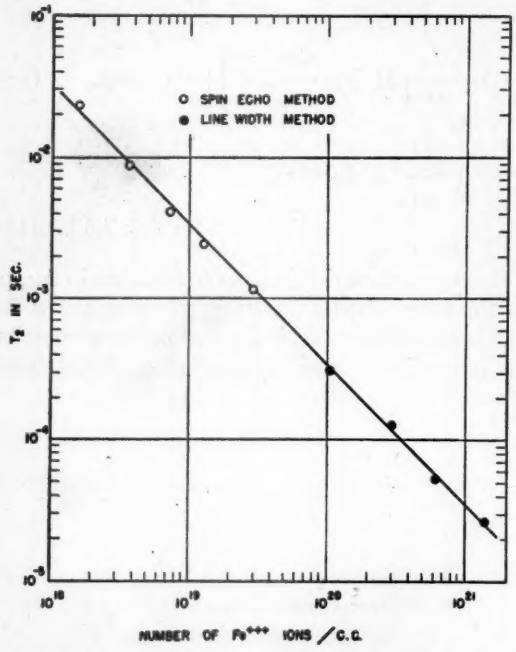

FIG. 4. T_2 measurements from the envelope decay of proton echoes are obtained for given concentrations of $Fe(NO_3)_3$ in H_2O. The plot compares with measurements made by the line width method (see reference 3).

(D) Measurement of T_2

If $\frac{1}{3}kt^3\ll t/T_2$ and $T_2^*\ll\tau<T_2$, T_1, then T_2 can be measured directly by plotting the logarithm of the maximum echo amplitude at $t=2\tau$ *versus* arbitrary values of 2τ. Figure 3 illustrates photographs of echoes on the oscilloscope for protons in a water solution of Fe^{+++} ions under these conditions. Figure 4 indicates how the measured T_2 for various concentrations of Fe^{+++} ions agrees with results obtained by Bloembergen, *et al.*[3] using the line width method. The law $C\propto 1/T_2$ is obeyed where C is the number of Fe^{+++} ions/cc for a given sample.

(E) Secondary Spin Echoes

If a third r-f pulse (identical to pulses producing the primary echo) is applied to the sample at a time T with respect to $t=0$, where $2\tau<T<T_2$, additional echoes occur at the following times: $T+\tau$, $2T-2\tau$, $2T-\tau$, $2T$. For $\tau<T<2\tau$ the signal at $2T-2\tau$ is absent but the others remain (see Fig. 5). These additional echoes can be readily predicted by rewriting Eq. (15) such that $\tau+t_w\rightarrow T+t_w$, $\tau\rightarrow T$, $t_w\rightarrow\tau+t_w$ ($\cos\beta t_w$ remains un-

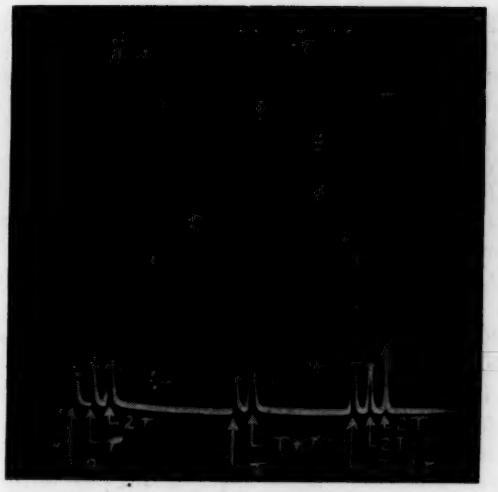

a

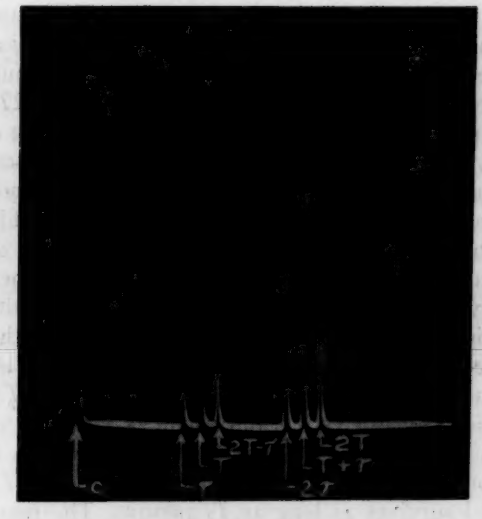

b

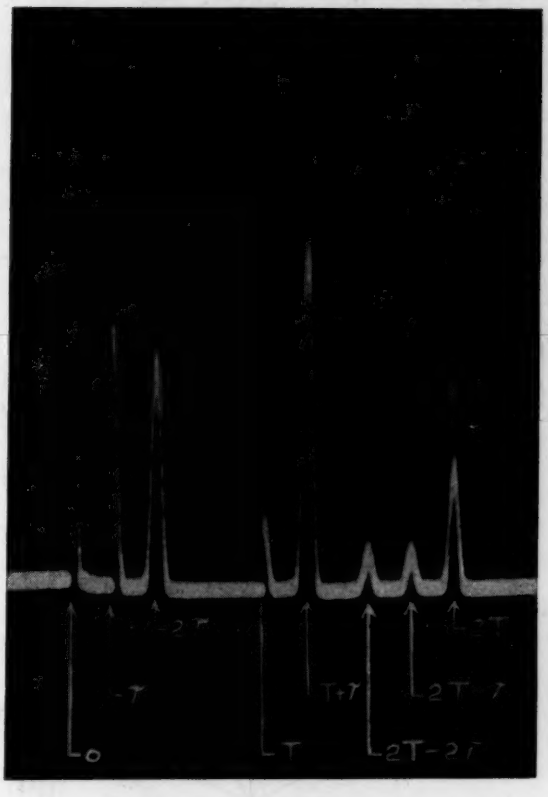

c

FIG. 5. Proton echo patterns in H_2O resulting from three applied r-f pulses. The pulses are visible in the upper two traces, and have a width $t_w \sim 0.5$ msec. In the upper trace $\tau = 0.008$ sec., $T = 0.067$ sec., and for the second trace $\tau = 0.046$ sec. and $T = 0.054$ sec. The bottom photograph shows a similar pattern for the case $T > 2\tau$ where induction decay signals can be seen following very short invisible r-f pulses. Saturation of a narrow band communications receiver, used in the case of the upper two traces, prevents the observation of these signals, whereas a wide band i.f. amplifier makes this observation possible in the bottom photograph.

changed in (15-B)) and applying the resulting expressions as initial conditions in (12), (13), and (14). In this manner, by successive application of accumulating initial conditions, the echo pattern resulting from any number and sequence of r-f pulses can be predicted. After integrating $v(t)$ over $\Delta\omega$ for $t \gtrsim T > 2\tau$, using $g(\Delta\omega)$ according to (19), the following expression for $V(t)$ is obtained (terms due to induction decay directly following the pulse are omitted and assumed not to interfere with the echoes since $\tau \gg T_2^*$):

$$V(t) \approx \frac{M_0}{2}(\sin^3\omega_1 t_w) \times \exp\left\{-(T-\tau)\left(\frac{1}{T_1}-\frac{1}{T_2}\right)-t/T_2 - \frac{k}{3}[\tau^3+(t-T)^3]-k\tau^2(T-\tau) - \frac{[t-(T+\tau)]^2}{2T_2^{*2}}\right\} \quad (22\text{-A})$$

$$-M_0\left(\sin\omega_1 t_w \sin^4\frac{\omega_1 t_w}{2}\right) \times \exp\left\{-\frac{[t-(2T-2\tau)]^2}{2T_2^{*2}}-t/T_2-\frac{kt^3}{3}\right\} \quad (22\text{-B})$$

$$+M_s(\tau)\left(\sin\omega_1 t_w \sin^2\frac{\omega_1 t_w}{2}\right) \times \exp\left\{-\frac{[t-(2T-\tau)]^2}{2T_2^{*2}}-(t-\tau)/T_2 - k(t-\tau)^3/3\right\} \quad (22\text{-C})$$

$$+\frac{M_0}{4}(\sin^3\omega_1 t_w) \times \exp\left\{-\frac{(t-2T)^2}{2T_2^{*2}}-t/T_2-\frac{kt^3}{3}\right\}. \quad (22\text{-D})$$

Term (22-A) provides a "stimulated echo" signal at $T+\tau$. The signal at $2T-2\tau$ (22-B) can be expected qualitatively by considering the "eight ball" alignment

in Fig. 1 as equivalent to an initial orientation of moments in a given direction by an imaginary r-f pulse at 2τ. Therefore, it follows that the stimulating pulse at T causes an "image echo" to occur at $2T-2\tau$. The signals at $2T-\tau$ (22-C) and $2T$ (22-D) are essentially primary echoes corresponding to twin pulses at τ, T and 0, T respectively. The signal at $2T$ is modified by the presence of the second r-f pulse at τ so that it does not have the same trigonometric dependence on $\omega_1 t_w$ as do the primary echoes at τ and $2T-\tau$.[16] Experimentally the various echo signals are observed to go through maxima and minima in general agreement with their respective trigonometric dependences on $\omega_1 t_w$ as this quantity is varied. The stimulated echo at $T+\tau$ is particularly interesting and useful in view of the fact that if τ is sufficiently small so that all terms in the exponent of (22-A) are negligible except T/T_1, the signal survives as long as T_1 permits. The remaining echo signals in liquids of low viscosity have maxima which attenuate in a time much shorter than T_1 as T is arbitrarily increased for a given τ. This is due to the diffusion factor $\frac{1}{3}k\beta^3$ which occurs in the exponents of (22-B), (22-C), and (22-D), but occurs only as $k\tau^2 T$ in (22-A). This property of the stimulated echo is schematically indicated in Fig. 6. The constructive interference at $T+\tau$ is due to moment vectors which previously existed as $M_z(\Delta\omega)$ components distributed in a spectrum approximately as $\cos\Delta\omega\tau$ during the time interval $\tau+t_w \rightarrow T$. This can be seen by noting that $M_z(\tau+t_w)$ has a term $v(\tau)$ proportional to $\cos(\Delta\omega+\delta)\tau$ from (15-C). This cosine distribution becomes smeared due to diffusion and must be averaged over all δ by applying the integral in (14). However, the self-diffusion of spin-containing molecules will not seriously upset this frequency pattern providing $1/\tau \gg \gamma(dH/dl)l(T)$ (let $T \gg \tau$), where $l(T)$ is the effective distance of diffusion in time T over which a shift in Larmor frequency can occur. The attenuation effect of diffusion upon echoes

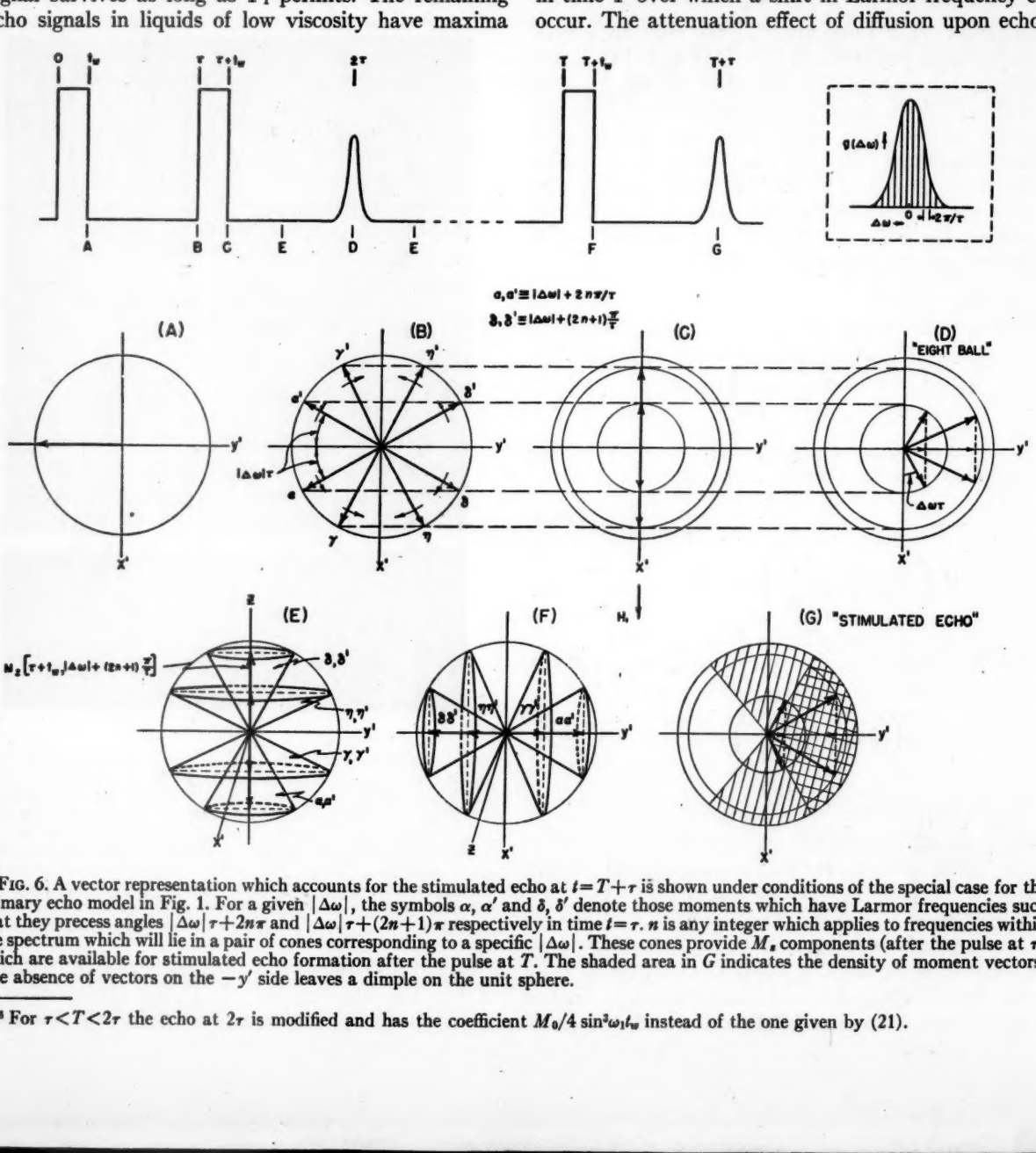

FIG. 6. A vector representation which accounts for the stimulated echo at $t=T+\tau$ is shown under conditions of the special case for the primary echo model in Fig. 1. For a given $|\Delta\omega|$, the symbols α, α' and δ, δ' denote those moments which have Larmor frequencies such that they precess angles $|\Delta\omega|\tau+2n\pi$ and $|\Delta\omega|\tau+(2n+1)\pi$ respectively in time $t=\tau$. n is any integer which applies to frequencies within the spectrum which will lie in a pair of cones corresponding to a specific $|\Delta\omega|$. These cones provide M_z components (after the pulse at τ) which are available for stimulated echo formation after the pulse at T. The shaded area in G indicates the density of moment vectors. The absence of vectors on the $-y'$ side leaves a dimple on the unit sphere.

[16] For $\tau<T<2\tau$ the echo at 2τ is modified and has the coefficient $M_0/4\sin^3\omega_1 t_w$ instead of the one given by (21).

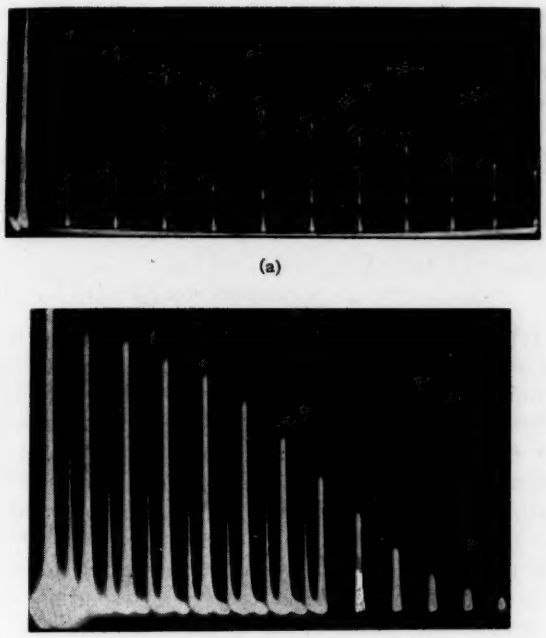

(a)

(b)

FIG. 7. A typical exponential plot of stimulated echo amplitudes is shown in the top photograph for protons in H_2O. This is obtained in a manner described for Fig. 3, except that T for the third pulse here is increased by 16/60 sec. intervals while τ is fixed at 0.0039 sec. The measured decay of the envelope is 1.89 sec. which serves as a point on the graph in Fig. 8. The apparent break in intensity in each of the stimulated echoes (seen as vertical traces because of the slow sweep speed) is due to a condition where the echo follows so soon after the stimulating pulse that it superimposes upon the voltage recovery of the receiver detector RC filter.

The bottom photograph indicates approximately an $\exp(-kt^3/3)$ decay law for the primary echo envelope in H_2O. The separation between echoes is 1/60 sec.

whose configuration depends purely upon phase and not frequency is much greater due to the exponential factor $\frac{1}{3}kt^3$ rather than $k\tau^2T$ which occurs only for the stimulated echo.

(F) Measurement of T_1; Qualitative Confirmation of the Diffusion Effect

If the condition $k\tau^2T \ll T/T_1$ is maintained by choosing τ very small, a plot of the logarithm of the stimulated echo maximum amplitude *versus* arbitrary values of T gives a straight line whose slope provides an approximate measure of T_1. In this manner glycerine is found to have a $T_1=0.034$ sec. The self-diffusion coefficient of glycerine is apparently sufficiently small so that T_1 can be measured directly as well as T_2, according to the discussion in III-D. A measured value of $T_2=0.023$ sec. is obtained, which is in substantial agreement with previous measurements.[3,9] The data for T_1 is obtained from oscillographic traces, an example of which is shown in Fig. 7 (top) for protons in distilled water. All relaxation measurements are made at room temperature, at $\omega=30$ Mc. A better value of T_1 is obtainable by plotting $1/T_m$ against τ^2 where T_m is the measured envelope decay time for the stimulated echo which decays as e^{-T/T_m}. A straight line is obtained which has the equation $1/T_m=1/T_1+k\tau^2$, which is seen from the exponential factor in (22-A) where $t=T+\tau$ and $\tau \ll T$. Such a plot is given in Fig. 8 for protons in distilled water (not in vacuum) where the reciprocal of the ordinate intercept gives $T_1=2.3\pm0.1$ sec., in agreement within experimental error with previous measurements.[3,17] Using the value of $D=2\times10^{-5}$ cm²/sec. for the water molecule,[18] the field gradient, G, calculated from the measured slope is 0.9 gauss/cm, which correlates roughly with the actual gradient over the sample. The gradient is expressed as $G\approx(\Delta H)_{\frac{1}{2}}/d$ where $(\Delta H)_{\frac{1}{2}}$ $\sim$0.2 gauss is measured directly from the resonance absorption line width (or echo width) and $d\sim3$ to 4 mm is the average thickness of the cylindrical sample. In Fig. 7 (bottom) the echo envelope for protons in distilled H_2O is reduced to $1/e$ of its maximum amplitude at $t=(3/k)^{\frac{1}{3}}$, since we neglect the decay due to T_2, which is negligible compared to diffusion. The calculated $(\Delta H)_{\frac{1}{2}}$ here is also in rough agreement with the actual field inhomogeneity present. This agreement with the predicted diffusion law confirms the existence at least of a smooth gradient in H_0 over the sample. If the sample is slightly rotated while r-f pulses are applied to obtain echoes, the echo amplitude is markedly reduced as the spin ensemble rotates into varying field inhomogeneity patterns.

(G) The Echo Beat and Envelope Modulation Effects

It has been found that the exact magnetic resonance frequency of nuclear moments of a given species depends upon the type of molecule in which it is contained. It is apparent that the local magnetic field at the position of the nucleus is shifted from the value of the applied external field by an amount which is too large to be accounted for by the normal diamagnetic correc-

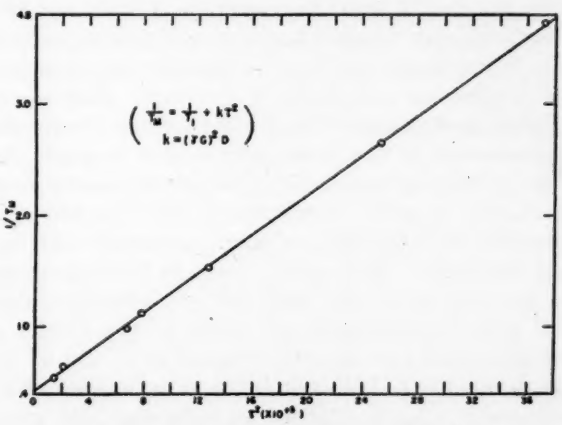

FIG. 8. Stimulated echoe measurement of spin-lattice relaxation time (T_1) of protons in H_2O.

[17] E. L. Hahn, Phys. Rev. **76**, 145 (1949).
[18] W. J. C. Orr and J. A. V. Butler, J. Chem. Soc. 1273 (1935).

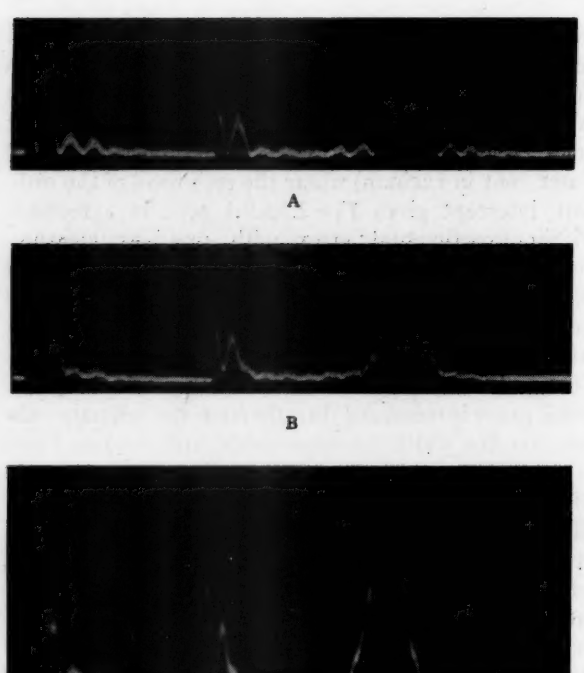

A

B

C

FIG. 9-A-B-C. Heterodyne beat signals for different F^{19} resonance frequencies due to the chemical Larmor shift effect.
(A) $CF_3CCl=CCl_2$ and 1,4 difluoro-benzene ($C_6H_4F_2$) mixture
(B) $CF_3CCl=CCl_2$ and 1,2,4 trifluoro-benzene ($C_6H_3F_3$) mixture
(C) 1, trifluoro-methyl 2,3,6 trifluoro-benzene ($C_6H_2F_3CF_3$)

tion.[19] Ramsey has shown that there exists the possibility of a much stronger field shift[20] due to second-order paramagnetism arising from the type of molecule which contains the nuclear spin. The echo technique reveals simultaneously the presence of two or more groups of resonant nuclei having slightly different Larmor frequencies due to such possible shifts in the local field at the nucleus, providing they are of the order of $(\Delta\omega)_{\frac{1}{2}}/\gamma$ gauss in magnitude. Echoes and free induction decay signals are modulated by beat patterns (Fig. 9) due to the fact that two or more spin groups of one species are contained in the same molecule or different molecules and have non-equivalent molecular environments in the same sample. For example, let ω' and ω'' denote respectively the Larmor frequencies at which the rotating coordinate systems of two spin ensembles may precess, and allow symmetric distribution functions $g'(\Delta\omega')$ and $g''(\Delta\omega'')$ to be a maximum for $\Delta\omega'=\omega_0-\omega'=0$, $\Delta\omega''=\omega_0-\omega''=0$. Therefore, identical echo configurations will result in two frames of reference, each rotating with frequencies ω' and ω'' respectively. The r-f induction is due to the magnetization component $v(\Delta\omega, t)\sin\omega t$ for an individual spin group where $v(\Delta\omega, t)$ is described as in (16) and (17). Integration over all frequencies leading to (20) and (21) provides the following total induction:

$$V(t)=V'(t)\sin\omega'(t-t_1')+V''(t)\sin\omega''(t-t_1'). \quad (23)$$

$V'(t)$ and $V''(t)$ signify the free induction signals due to each of the spin groups alone. The envelope of the echo signal (Fig. 9-A) is given by

$$V(t)_{\max}=[V'(t)^2+V''(t)^2+2V'(t)V''(t)\times\cos(\omega''-\omega')(t-2\tau)]^{\frac{1}{2}}. \quad (24)$$

As typical examples of this effect it has been found that the signals due to F^{19} nuclei in certain organic compounds yield modulation patterns which obey the heterodyne law expressed by (24). In order to observe this effect the condition $2\pi/(\omega''-\omega')\gtrsim T_2^*$ must be attained in order to observe at least one period of the modulation within the lifetime T_2^* of an echo or induction decay signal following a pulse. Consequently, a high degree of homogeneity in the magnetic field must be attained in order to get very good resolution; i.e., to resolve very small shifts in Larmor frequency. It appears that this approach to the determination of very small Larmor shifts has a resolution no better than ordinary magnetic resonance absorption methods[1,3] in which the limitation is also due to external field inhomogeneities. However, the echo method is fast and lends itself more conveniently to search purposes in finding these shifts.[21] Somewhat higher resolution than that available by the normal method can be attained beyond the limitation imposed by field inhomogeneities by introducing into the receiver an r-f signal at a frequency somewhere near the Larmor frequencies present. An audio beat modulation appears having an envelope which is modulated in turn by the Larmor shift beat note. These beats can then be more easily distinguished from noise for the condition $2\pi/(\omega''-\omega')\gtrsim T_2^*$ in favorable cases in which the induction signals are sufficiently intense. Periods of the order of $3, 4T_2^*$ may possibly be observed, in which case Larmor shifts as small as 0.01 gauss, of the order of normal diamagnetic shifts, may be detected, assuming a $(\Delta H)_{\frac{1}{2}}\sim 0.05$ gauss is available out of a total field of 7000 gauss. It can be seen from Fig. 9 that the modulation on the echo and decay signals (following r-f pulses) correlate in pattern. It is significant that the pattern on the echo is always symmetric regardless of the spacing τ between the two r-f pulses. This is understandable in view of the fact that two rotating frames of reference, for example, increase in phase difference by $(\omega''-\omega')\tau$ radians between the pulses. The second pulse produces an initial condition such that the two frames

[19] W. E. Lamb, Phys. Rev. 60, 817 (1941).
[20] This is treated theoretically in a paper in Phys. Rev. 78, 699 (1950), kindly forwarded to the author in advance of publication by Professor N. F. Ramsey.
[21] One must be careful that the observed modulation is not due instead to a condition where the H_0 magnetic field inhomogeneity pattern over the sample has two or more discrete bumps in it. The modulation will again be symmetric on the echo and can only be distinguished from a true beat effect by moving the sample to a different part of the field in the magnet gap and noting whether or not the modulation disappears or varies in frequency.

of reference now rotate into one another by the same amount and coincide at the time 2τ of the echo maximum. This principle is inherent in the echo effect itself: the phase differences of all moment vectors (with respect to the initial orientation established by the first pulse) are effectively cancelled at the time of the echo maximum. This cancellation is made possible by the second pulse. If no further pulses are applied, the echo at 2τ can never repeat itself, as might be expected, because the "eight-ball" configuration is essentially only a single recurrence of the initial in-phase condition of the moment vectors at $t=t_w$, though not quite the same due to a spread in Larmor frequencies.[22]

Fluorine nuclei in the compounds[23] $CF_3CCl=CCl_2$ and $C_6H_4F_2$ (1,4 difluoro-benzene) give induction signals in separate samples in which no significant beat patterns appear. Weak beats may appear due to other fluorine compound impurities used in the synthesis of these compounds. Figure 9-A indicates the beat which results when these two molecules are mixed in liquid form in a single sample such that two fluorine spin groups are in a one-to-one ratio in concentration. The separate molecules contain fluorine atoms located in equivalent positions and therefore cannot give rise to a beat among themselves. A mixture of the two molecules, having fluorine nuclei which are relatively non-equivalent in molecular environment, now reveals a separation of 1.9 kc in Larmor frequency for the two groups in a field of 7500 gauss. According to (24) the modulation pattern goes to a complete null at this frequency since the mixture is adjusted so that $V'(t) = V''(t)$. By observing the normal resonance absorption signal of this mixture on the oscilloscope, using 30 cycle field modulation, two distinct absorption lines are observed, separated by 1.9 kc on a frequency scale. By using a mixture in which the concentration of one molecule exceeds that of the other, the relative difference in intensity of the absorption lines indicates that the fluorine resonance frequency in $C_6H_4F_2$ lies on the high side relative to that in $CF_3CCl=CCl_2$. It is reasonable to expect this if the charge density of the electronic configuration about the fluorine nuclei in $C_6H_4F_2$, being less than that in $CF_3CCl=CCl_2$, can be correlated with a correspondingly smaller negative magnetic shielding correction. This property appears to exist in all mixtures and single molecules so far investigated in which a distinction between spin groups has been made. Within experimental error, the Larmor frequency shifts observed here appear to be proportional to the applied field, based on measurements made at 7070 and 3760 gauss. Figure 9-B shows the beat pattern due to approximately a one-to-one mixture (in terms of fluorine nuclei) of the compounds 1, 2, 4 trifluoro-benzene and $CF_3CCl=CCl_2$. More than one beat modulation frequency is evident, due obviously to the presence of more than two fundamental spin groups. Figure 9-C shows how a similar complexity in beat pattern arises from a sample of 1-trifluoro-methyl 2, 3, 6 trifluoro-benzene. All observable beat frequencies are of the order of a few kilocycles.

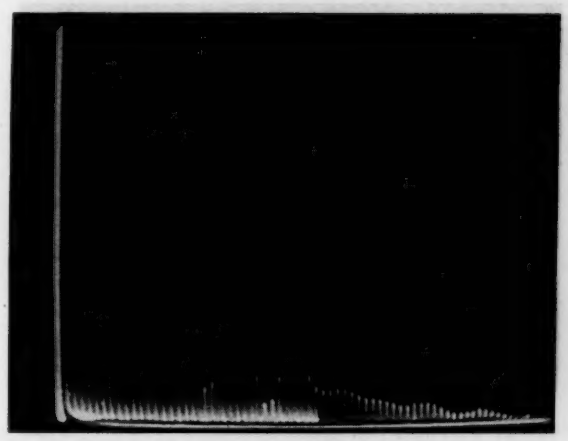

FIG. 10. The echo envelope modulation effect for protons in C_2H_5OH. Paired pulses are applied in the usual manner for obtaining multiple exposures. The echo separation is 1/300 sec. The first echo at the left follows so closely after the r-f pulses that it is not at normal amplitude because of receiver saturation.

Preliminary studies have been made of another effect which is shown in Fig. 10. The envelope of the normal echo maximum envelope plot is modulated by a beat pattern which is in violation of the normal decay due to self-diffusion and T_2. The envelope shown for C_2H_5OH (period$\approx$0.027 sec.) is an example which is typical for protons in various organic compounds. If the effect is present in the particular substance investigated it is readily observable only if the period of the modulation is shorter than the normal decay time of the echo envelope upon which it is superimposed. Several organic compounds studied so far have been observed to have characteristic periods of the order of 0.1 to 0.01 sec. Modulation patterns in many cases do not contain a single frequency but perhaps several as it appears in C_2H_5OH. The period of the modulation is found in general to be greater than T_2^*, the echo lifetime. This modulation effect cannot be attributed to an interference between several spin groups because the observed echo maximum is always due to the sum of the echo maxima contributed by each of the spin groups alone. This is true regardless of the number of different spin groups present, and therefore the beat frequencies due to such Larmor shifts cannot show up in the envelope of the echo maxima. Within experimental error

[22] It is interesting to note that the configuration at $t=t_w$, namely, $M_{xy}=M_0$, can in principle be exactly repeated at $t=2\tau$ by doubling the second r-f pulse width with respect to the first one which is at the pulse condition $\omega_1 t_w=\pi/2$ (see Fig. 1). Actual experiment indicates that the inhomogeneity in H_1 throughout the sample prevents this from exactly taking place, but shows an increase in the available echo amplitude beyond the optimum amplitude at $\omega_1 t_w=2\pi/3$ (Eq. 21). The stimulated echo at $t=T+\tau$ then nearly disappears.

[23] The fluorine compounds used were kindly provided by Dr. G. C. Finger of the Fluorspar Research Section of the Illinois State Geological Survey, where they were synthesized.

FIG. 11. Free induction signals for protons in paraffin. The echo lasts for $\sim 1.4\times 10^{-5}$ sec. The r-f pulses, about 25 μsec. wide, cause some blocking of the i.f. amplifier. The echo envelope decay time is also of the order of the single echo lifetime.

(five to ten percent) the period of the envelope modulation is found to be inversely proportional to the applied magnetic field. It is possible that an interaction between the nuclear spin and the molecule which contains it causes a periodic reduction of the echo amplitude by a modification of the echo constructive interference pattern. This effect will be treated in a later paper in greater detail.

(H) Free Nuclear Induction in Solids

It has been established in the case of liquids that, if one excludes the effect of diffusion, the lifetime of the nuclear induction decay following a pulse is given by $T_m = T_2T_2^*/(T_2+T_2^*)$, and the single echo lifetime is given by T_2^*. Qualitative observations of free nuclear induction signals due to nuclei in solids, however, indicate that the role played by T_2^* is no longer significant. The ensemble instead precesses in a magnetic field distribution described by a function $G(\delta\omega)$, where $\delta\omega = \omega_0' - \omega'$ and $\omega_0' = \gamma(H_{\text{local}} + H_{\text{magnet}})$. The local field H_{local}, due to lattice neighbors, is superimposed on the externally applied field at the positions of the precessing nuclei. This local field is spread over a width much greater than the width due to the magnet. In one case echoes have been observed for protons in paraffin (Fig. 11) where it appears that the echo and induction decay lifetimes are now given by $\sim 1/(\delta\omega)_{\frac{1}{2}}$ seconds. Extremely intense r-f power is required in order to excite all of the spins over a broad spectrum of Larmor frequencies in a pulse time $t_w \gtrsim 1/(\delta\omega)_{\frac{1}{2}}$ seconds, and therefore the condition $1/t_w,\ \omega_1 \gg (\delta\omega)_{\frac{1}{2}}$ must apply. A striking indication of the predominance of either T_2^* or $1/(\delta\omega)_{\frac{1}{2}}$ is shown by observing how the broad free induction signals from protons in liquid paraffin become very narrow as the paraffin cools and solidifies. It appears that echoes in solids can be observed in principle in a time $\lesssim T_2 \sim 1/(\delta\omega)_{\frac{1}{2}}$, because a given distribution in H_{local} determined by $G(\delta\omega)$ (which now plays the role of $g(\Delta\omega)$ in the case of liquids) is able to last roughly for a time T_2. The local z magnetic field due to neighboring magnetic moments (nuclear spins, paramagnetic ions and impurities) therefore not only depends upon the particular location of these moments with respect to the precessing nucleus, but also upon a time T_2. This time determines how long a given parallel and antiparallel configuration of these neighboring moments can exist with respect to the externally applied field. It follows, therefore, in the case of paraffin, that the stimulated echo, which depends upon frequency memory of the spin distribution, cannot be observed out to times $T+\tau \sim T_1 = 0.01$ sec., where $T_1 \gg T_2$.

Although the Bloch theory is highly successful in accounting for the echo effect in liquids where T_1 and T_2 are introduced in a phenomenological way, it must be understood in this theory that the predicted natural resonance line shapes will always be described by a damped oscillator resonance function (Lorentz) in the steady state. This corresponds to the observed exponential decay of free induction signal amplitudes in the transient case. This concept does not necessarily apply in general, especially as regards magnetic resonance line shapes in solids in the steady state. It remains to be shown that the properties of free nuclear induction signals in solids are explained by a transient analysis which gives results equivalent to the general steady state treatment formulated by Van Vleck[24] and others.[3,25]

With further refinements in technique for obtaining a sufficiently fast response of the r-f circuits to very short r-f pulses of large intensity (t_w of the order of microseconds at $H_1 \sim 20$ to 100 gauss), it may be possible to obtain informative data from free nuclear induction signals in solids which have a T_2 of the order of 10^{-5} to 10^{-6} seconds. It will be of profit to investigate the induction decay which follows single pulses (already found for protons in powdered crystals of NH_4Cl, $(NH_4)_2SO_4$, $MgSO_4 \cdot 7H_2O$ and for F^{19} in CaF_2) without the attempt to observe echoes.

IV. EXPERIMENTAL TECHNIQUE

The block diagram in Fig. 12 indicates the necessary components for obtaining the echo effect. All features of the sample, inductive coil, and methods of coupling from the oscillator and to the receiver are typical of nuclear induction techniques and have been discussed in detail elsewhere. A great simplification is introduced here because only a single LC tuned circuit is necessary. However, in the case where a narrow band receiver is used ($\sim$8 kc) in place of a very broad band i.f. strip ($\sim$5 Mc) and where r-f pulses are particularly intense, it is convenient to use a bridge balance in order to minimize overloading of the receiver. Two methods have been used to provide r-f power in the form of pulses. A method best suited for r-f amplitude and frequency stability employs a 7.5 Mc crystal-controlled

[24] J. H. Van Vleck, Phys. Rev. 74, 1168 (1948).
[25] G. E. Pake, J. Chem. Phys. 16, 327 (1948).

oscillator whose frequency is quadrupled to 30 Mc and amplified r-f power is then gated through stages whose grids are biased by square wave pulses from a one shot multivibrator controlled in turn by timer pulses. This method is essential for studies of the phases of various echo signals and other effects. The crystal maintains a source of coherent r-f oscillations which can be used to heterodyne weakly with the nuclear signal that has a phase determined initially by these oscillations in the form of intense pulses. The phases of the resulting audio beat frequency oscillations seen superimposed on the echoes then yield certain interesting proofs.

(a) The phase of the audio modulation on all echoes is invariant to any time variation in the spacing between r-f pulses. With respect to a fixed reference in a rotating coordinate system, all echoes form a resultant which is constant in direction due to the fact that the accumulated phase differences before the r-f pulse (at $t=\tau$) are exactly neutralized after it (referring to discussion in III-G).

(b) The negative sign of the "image echo" term (Eq. 22-B) signifies that the resultant of this signal is 180° out of phase relative to the resultants of all other echoes formed before or after it. This is borne out by the fact that the phase of the observed audio modulation on the image echo is exactly 180° out of phase with respect to the modulation pattern on all other echoes. Otherwise, the modulation patterns appear to be identical.

(c) Echoes at $t=2\tau$ are observed not to fluctuate in amplitude when $\tau<T_2^*$ due to the fact that the r-f is coherent for successive pulses, and the phase of the moment configuration prior to the r-f pulse at τ has a definite relationship with respect to the phase of the echo which follows.

With the above method, precautions must be taken to prevent r-f power leakage to the sample during the absence of pulses. The necessity for this precaution is eliminated by turning on and off a high power oscillator (by gating the oscillator grid bias, Fig. 13) which drives the *LC* circuit directly. This method, although not as stable, makes available higher r-f power, and the ability to vary the driving frequency ω is convenient. Although r-f pulses are produced now in random phase, experimental results are the same as long as $\tau\gg T_2^*$. Both

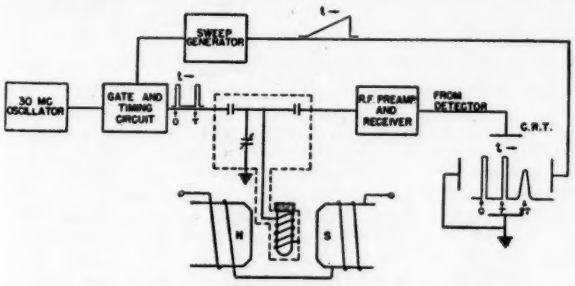

FIG. 12. Arrangement for obtaining spin echoes.

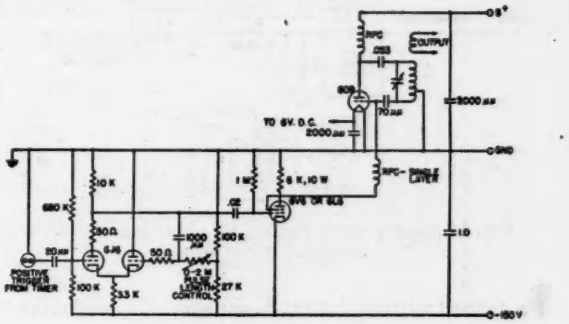

FIG. 13. Gated oscillator.

pulse methods combined provide pulses of $t_w\sim 20$ μsec. to a few milliseconds and $H_1\sim 0.01$ to 50 gauss.

In order to obtain accurate and reproducible data with echoes it is necessary that the dc magnetic field be held constant to at least one part in 10^5 over the length of time during which a set of echo data is being photographed. One might say that some field drift is tolerable within the limits set by the condition $\omega_1\gg(\Delta\omega)_{\frac{1}{2}}$. However, it is advisable even to guard against field drifts less than H_1 gauss because the Fourier amplitudes of all r-f frequency components which resonate with the given Larmor spin frequencies will vary to some degree as the dc field varies. In cases where the decay of echoes is plotted for nuclei in liquids having a long T_1 (several seconds for protons in most organic liquids) and where maximum available signal is desired, the spins must be allowed to return to complete thermal equilibrium between applications of paired pulses. Therefore, if one waits at least five half-lives to obtain a plot such as is shown in Fig. 10, a total time of 17 minutes is required during which the magnetic field must not drift appreciably. In order to minimize the effect of slow field drifts it is convenient to apply paired pulses at a repetition rate whose period is some constant fraction of T_1. During this period the operator has sufficient time to adjust timer switches (reset switches on a conventional scalar unit[17]) in order to provide increasing integers of time between the two pulses. The sample is therefore partially saturated at a level which is practically constant when the pulses are applied, although a small but negligible variation in the level of saturation is introduced as the time τ is systematically increased. The over-all signal to noise ratio of the pattern is reduced but data can be recorded at a convenient speed.

For these experiments the magnetic field is stabilized by means of a separate proton resonance regulator[26] which monitors practically the same magnetic field which is present at the echo sample. The regulator resonance sample is located in the same magnet gap and is subjected to 30 Mc r-f power which is well shielded from the experiment sample. The regulator sample is placed in the inductance of the tuned circuit

[26] To be discussed in a later paper.

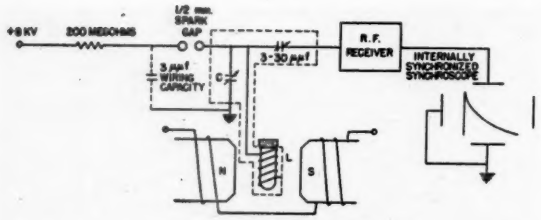

FIG. 14. Simple spark method for obtaining free nuclear induction decay signals.

of a transitron oscillator. A sinusoidally vibrating reed capacitively modulates the frequency of this oscillator within the line width of the regulator proton resonance. When the magnetic field is brought into the resonance value it is locked in and controlled by the regulator. The transitron oscillator r-f voltage level decreases due to resonance absorption and is modulated at the frequency of the vibrating reed. A discriminator circuit utilizes this signal to control a correction current to the magnet in a conventional manner.[27]

In Fig. 14 a sparking technique is noted purely for its novel features of simplicity in demonstrating, qualitatively, free nuclear induction decay signals directly following single random r-f pulses. The spark generated across the gap contains essentially all frequencies and excites for a very short time the tuned circuit in which the sample is located. After the spark extinguishes, the sample in the inductive coil transmits a decaying r-f induction signal to the receiver at the Larmor frequency determined by H_0. Capacitor C needs adjustment such that the tank circuit will resonate approximately in the region of the Larmor frequency (with no spark). Signals can be obtained over a broad range of H_0 without requiring a retuning of C. The observed signal, of course, has random amplitudes since the r-f energy transferred by the sparks is random within a certain range.

[27] M. Packard, Rev. Sci. Inst. 19, 435 (1948).

V. CONCLUDING REMARKS

Simple principles of the free nuclear induction technique have been described and tested, principally with proton and fluorine (F^{19}) signals in liquids. Data which is made available by this technique is to be presented later in more systematic detail. The echo technique appears to be highly suitable as a fast and stable method in searching for unknown resonances. Intense pulses of H_1 provide a broad spectrum of frequencies. This makes possible the observation of free induction signals far from exact resonance. Echo signals have proved useful for the measurement of relaxation times under conditions where interference effects (microphonics, thermal drifts, oscillator noise) encountered in conventional resonance methods are avoided. The self-diffusion effect in liquids of low viscosity offers a means of measuring relative values of the self-diffusion coefficient D, a quantity which is very difficult to measure by ordinary methods. It is of technical interest to consider the possibility of applying echo patterns as a type of memory device.

The formal analysis of the signal-to-noise ratio of the echo method is nearly identical to the treatment already given by Torrey with regard to transient nutations.[9] However, a great practical improvement in eliminating noise is available with the echo technique which cannot be assessed from formal analysis; namely, that H_1 is absent during the observation of nuclear signals, and noise or hum that may be introduced by the oscillator and associated bridge components is avoided.

The author wishes to thank Professor J. H. Bartlett for his counsel in carrying out this research, and is grateful to Dr. C. P. Slichter for the benefit derived from many clarifying discussions with him regarding this work. The author is indebted to H. W. Knoebel for his excellent design and construction work on the electronic apparatus.

Protons from the Deuteron Bombardment of Enriched Silicon and Related Atomic Masses*

H. T. Motz** and R. F. Humphreys***
Sloane Physics Laboratory, Yale University,† New Haven, Connecticut
(Received June 20, 1950)

Enriched samples of silicon have been bombarded with 3.8 Mev deuterons and 17 proton groups have been assigned to the $Si^{28}(d,p)Si^{29}$, $Si^{29}(d,p)Si^{30}$ and $Si^{30}(d,p)Si^{31}$ reactions. The ground state transitions for $Si^{28}(d,p)Si^{29}$ and $Si^{29}(d,p)Si^{30}$ are found to be 6.18 ± 0.09 Mev and 8.36 ± 0.10 Mev. Seven proton groups corresponding to excited states in Si^{29} and three groups leading to excited states in Si^{30} have been observed. Five groups are found to be associated with $Si^{30}(d,p)Si^{31}$, with a sixth in doubt. A method for using extrapolated range measurements to obtain mean ranges is described. The published transition energies of reactions possibly involving ground states of aluminum, silicon and phosphorus isotopes are tabulated. These energies are converted to mass differences which are presented on a diagram. The lack of satisfactory consistency of these mass differences is discussed and the discrepancy of reaction data and mass spectroscopic data between aluminum and sulphur is outlined.

I. INTRODUCTION

THE investigation of the (d,p) reaction for silicon has been complicated by the presence of the three stable isotopes having mass numbers 28, 29, and 30 which occur in the natural abundance ratio of 30:1.5:1. The large percentage of Si^{28} indicates that the prominent proton groups from natural silicon would probably belong to this isotope. The consideration of the trends in binding energies leads one to expect that $Si^{29}(d,p)Si^{30}$ will have the highest Q value of the three reactions. With only these guiding characteristics, an interpretation of the proton spectrum from natural silicon is indefinite. The use of three enriched silicon targets in the present work has removed the ambiguity of assignment and has allowed the identification of 17 observed proton groups from the three isotopes.

Preliminary results obtained with the use of natural silicon targets have been published by Pollard and Humphreys.[1] Allan and Wilkinson[2] have observed four proton groups with the use of a 0.9 Mev deuteron beam. Their arbitrary assignment of these groups to parent isotopes has been confirmed for three of these groups.

II. EXPERIMENTAL ARRANGEMENT

The 3.8 Mev deuteron beam from the Yale cyclotron was used for this experiment. The beam range was determined in two ways. An ion current *versus* absorption curve was obtained by the use of an air range cell and galvanometer as described by Martin.[3] In addition, the range of the deuterons scattered at 90° from gold leaf was found by the use of the same proportional counters used in the proton measurements. These determinations agreed within their experimental errors. During the series of bombardments, adjustments of the cyclotron dee position and oscillator frequency resulted in a beam energy increase of approximately 100 kev. The beam distribution in range was found to be closely Gaussian for both energies. The deuteron beam intensity was monitored by the use of a neon discharge tube current integrator.[4]

The numbers-range curves of the emitted protons were obtained by the use of carefully weighed aluminum absorbers placed between the target and the proportional counters used for detection. Three counting systems were used at different times in the series of bombardments. The argon filled proportional counters described by Martin[3] were used in the initial runs. The circuits described by Martin were also used in this work. In order to obtain a higher yield while searching for low intensity groups, a large single counter discussed by Benson[5] was utilized for several runs. Unfortunately this counter could not be employed in coincidence with a second counter, and an undesirably high background resulted. In order to combine the desirable properties of these two counting systems, two large counters were built and housed in a common vacuum box, as illustrated in Fig. 1. The counter cylinders of $\frac{1}{8}''$ brass were supported in polystyrene blocks and aligned along a common axis. The counter wires were of 5-mil platinum wire supported by rods mounted on Stupakoff seals. The wires were mechanically joined by means of a glass bead. The aluminum window through which particles entered was held between two $\frac{1}{16}''$ thick brass grids which had a transparency of about 70 percent.

The necessary penetration into the counter to produce a recorded count was found by measurements with ThC′ alpha-particles. The minimum penetration was found by properly adjusting the biases and counter voltages. In order to convert the alpha-particle data to the corresponding absorption in cm air equivalent for protons, the specific ionization curves must be taken

* Part of a Dissertation presented by H. Motz to the Faculty of the Graduate School of Yale University in partial fulfillment of the requirements for the Degree of Doctor of Philosophy.
** Now at Brookhaven National Laboratory, Upton, New York.
*** Now at Armour Research Foundation, Chicago, Illinois.
† Assisted by the joint program of the ONR and AEC.
[1] E. Pollard and R. F. Humphreys, Phys. Rev. **59**, 466 (1941).
[2] Allan and Wilkinson, Proc. Roy. Soc. **A194**, 131 (1948).
[3] A. B. Martin, Phys. Rev. **72**, 379 (1947).
[4] B. E. Watt, Rev. Sci. Inst. **12**, 362 (1941).
[5] Bruce B. Benson, Phys. Rev. **73**, 7 (1948).

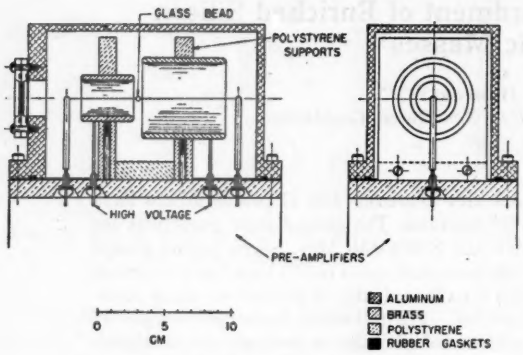

FIG. 1. Coincidence proportional counters.

into account. This correction is of the order of 0.1 mm air equivalent and is discussed by Holloway and Livingston[6] and Holloway and Moore.[7]

The natural targets were prepared from both pure silicon metal†† and quartz. Thin films of these materials were evaporated on masked gold foils so that the area of the deposit was known. The thickness was estimated by weighing the foil before and after evaporation. Because of the high temperature necessary to evaporate the quartz deposit efficiently, an appreciable quantity of tungsten from the filament was also evaporated during the preparation of the targets. Because of the variable amount of tungsten and the unavoidable flaking of the quartz layer during cooling and bombardment, the target thickness as determined by weighing was not considered a sufficiently accurate measurement of silicon deposit as a basis of curve normalization.

Enriched silicon in the form of SiO_2 powder was obtained from the Carbide and Carbon Chemicals Corporation, Y-12 Plant, on allocation from the Isotopes Division of the Atomic Energy Commission. The targets from these samples were prepared in a manner similar to the natural targets. The silicon content of these three samples is given in Table I. Si^{28} is present in all samples to at least 29 percent and the yields were normalized to the 100 cm group of Si^{28} in order to compare curves from different targets. The normalized curves obtained in a few of the more extensive but less detailed runs are shown in Figs. 6–9.

TABLE I. Relative abundance of silicon samples (percent).

	Si^{28} content	Si^{29} content	Si^{30} content
Natural silicon	92.27±0.08	4.68±0.05	3.05±0.03
Enriched 28 sample*	99.4 ±1.0	0.8 ±0.1	0.2 ±0.1
Enriched 29 sample*	29.1 ±0.5	68.6 ±1.0	2.2 ±0.5
Enriched 30 sample*	47.6 ±1.0	2.8 ±0.5	49.6 ±1.0

* Enriched samples were prepared and analyzed by the Carbide and Carbon Chemicals Corporation, Oak Ridge, Tennessee. The following impurities were found in the three samples, each present to less than 0.5 percent: Ag, Mg, B, Cu, Pt, and Na.

[6] M. G. Holloway and M. S. Livingston, Phys. Rev. 54, 18 (1938).

[7] M. G. Holloway and B. L. Moore, Phys. Rev. 58, 847 (1940).

†† The pure silicon used for these targets was kindly furnished by the Bell Telephone Laboratories.

The target plane was aligned at 45° with respect to the incident beam direction for the observation of protons emitted at 90°. For 0° proton observation, the targets were perpendicular to the incident beam. Gold backing sufficiently thick to absorb totally the incident deuterons was used for the 0° runs. The absorption in gold was not necessary for 90° observation, since the counters could detect only particles coming from the target.

III. METHOD OF ENERGY MEASUREMENT

The observed range distribution of a proton group having a constant mean energy is influenced by several factors. In order to calculate the Q value for the group, the mean energy must be known and each of the factors influencing the distribution must therefore be taken into account. Assuming that the natural width of the energy levels is much less than the various inhomogeneities, the major factors are: (1) incident beam distribution, (2) solid angle of the detector, (3) straggling, and (4) detector characteristics. For reasonably thin targets, the target thickness can usually be neglected except for shifting the distribution to lower energies.

As previously stated, the cyclotron beam was found to be closely Gaussian and will be assumed to be Gaussian for convenience in combining this factor with the three others listed. The beam half-width 2Γ, the full width at half-intensity, was found to be approximately 200 kev and results in an appreciable spread in observed ranges compared to the range straggling. As has been shown by Livingston and Bethe,[8] the range spread due to the finite solid angle of the detector may be approximated as Gaussian for reasonably small solid angles for a detector whose axis is located at 90° with the beam. The third factor, range straggling, is well known to be accurately Gaussian and values for this factor are given by Livingston and Bethe.[8] These three Gaussian factors combine to give a Gaussian distribution whose parameter is the square root of the sum of the squares of the individual Gaussian parameters.

The detector characteristics are of primary importance in determining the observed distribution. An ion chamber or proportional counter counts particles whose ranges fall within a finite interval of range between R and $R+\Delta R$. If ΔR is 10 cm or greater as is the case for low recorder bias and a sufficiently sensitive system, an approximately integral numbers-range curve is obtained. As the recorder bias is increased, however, ΔR becomes much smaller and may approach a fraction of a millimeter. In the latter case a "peaked" or nearly differential curve is obtained, since the range spread of a proton group is many times the counting interval ΔR. In order to find the true mean range from such an observed curve, the value of ΔR corresponding to the counter setting used and the position of the maximum

[8] M. S. Livingston and H. A. Bethe, Rev. Mod. Phys. 9, 245 (1937).

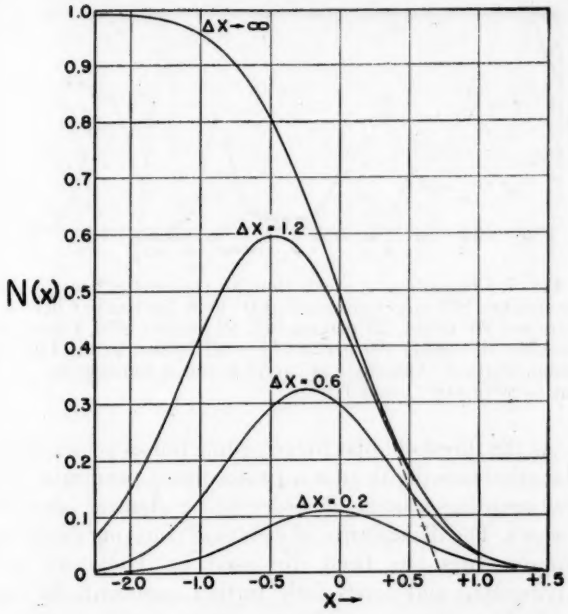

FIG. 2. Numbers-range curves for a Gaussian differential distribution $dN(x)=\pi^{-\frac{1}{2}}\exp(-x^2)dx$ for four values of the counting interval Δx.

yield range (or the extrapolated range) relative to the true mean range must be known for that value of ΔR. Holloway and Moore[7] have treated this subject carefully for an ionization chamber and give the relation between the true mean range and the range corresponding to the observed maximum yield range for various bias settings. Unfortunately the bias level for a proportional counting system cannot always be reset with sufficient reliability to allow its use as an index for the counting interval ΔR. Such is the case with the equipment used in this work. The following analysis shows how the maximum intensity relative to the total number of particles in the group can be used as an index of the counting level or counting interval.

Consider a Gaussian distribution in range for a unit total number of particles. Let R_0 be the mean range of the group, β the parameter of the distribution, and let $x=(R-R_0)/\beta$. Then if dN is the number of particles whose range lies in the interval dR, the differential

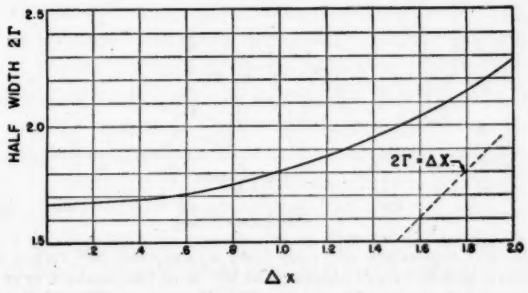

FIG. 3. Half-width (the full width at half-maximum) for number-range curves as a function of the counting interval Δx. The half-width asymptotically approaches the line $2\Gamma=\Delta x$ for $\Delta x \gg 1$. For $\Delta x=0$, $2\Gamma=2(\ln 2)^{\frac{1}{2}}=1.665$.

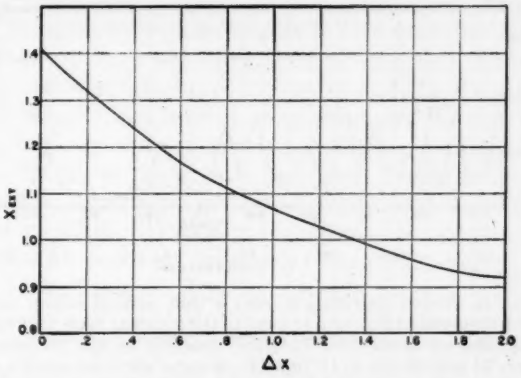

FIG. 4. Extrapolated range of numbers-range curves measured from the mean range ($x=0$) as a function of the counting interval Δx. For $\Delta x=0$, $x_{ext}=2^{\frac{1}{2}}$ and for $x\to\infty$, $x_{ext}\to 2^{-1}\pi^{\frac{1}{2}}=0.886$.

distribution is given by $dN(x)=\pi^{-\frac{1}{2}}\exp(-x^2)dx$. An observed curve will correspond to a finite interval of counting Δx which is equivalent to $\Delta R/\beta$. The observed curve will be

$$N(x)=\pi^{-\frac{1}{2}}\int_x^{x+\Delta x}\exp(-x^2)dx=\tfrac{1}{2}\{\Phi(x+\Delta x)-\Phi(x)\}$$

where Φ is the error integral. With the use of tabulated values for Φ, a family of curves for various values of Δx can be obtained. The maximum of such a curve is displaced to the left of the mean range by $\Delta x/2$. Four such curves are shown in Fig. 2. The manner in which the half-width, extrapolated range, and maximum yield vary is illustrated in Figs. 3, 4, and 5 as obtained from accurately plotted curves for $N(x)$. The maximum yield is given as a fraction of the total number of particles in the group.

Figure 5 illustrates that the maximum yield of an observed curve is an excellent index of the value of Δx for the curve is $\Delta x<1$ or $\Delta R<\beta$. Thus one compares the yield for a given curve with that obtained from a curve corresponding to a very low bias and sufficiently small range so as to count all of the particles in the group, and Δx can then be determined by the use of Fig. 5. Knowing Δx for the curve, one finds the mean range from the range corresponding to the maximum

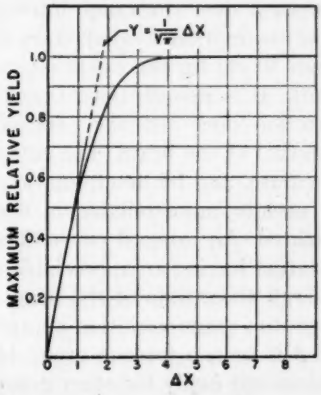

FIG. 5. Maximum relative yield of number-range curves as a function of the counting interval Δx. As $\Delta x\to 0$, $N(x)_{max}\to\pi^{-1/2}\Delta x$.

UNIVERSITY OF MICHIGAN LIBRARIES

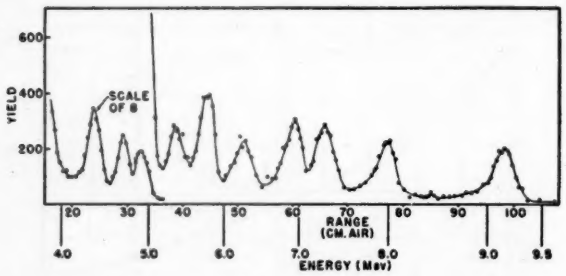

FIG. 6. Proton distribution from a thin natural silicon metal target observed at 90° with respect to the incident deuteron beam. All groups are from the $Si^{28}(d,p)Si^{29}$ reaction except the two at ranges 24 and 32 due to $O^{16}(d,p)O^{17}$. Ranges are approximate and are calculated assuming 1.52 mg/cm² of aluminum is equivalent to 1 cm air.

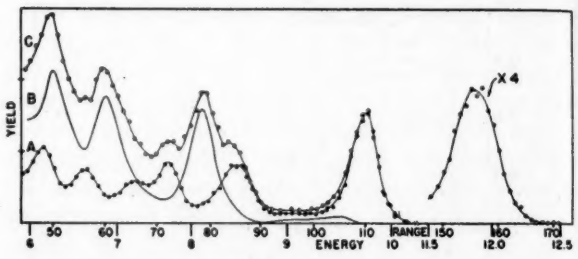

FIG. 7. Comparison of yields from an enriched Si^{29} target and an enriched Si^{28} target observed at 0° with the beam. Curve C: Enriched Si^{29} target (29 percent Si^{29}, 69 percent Si^{28}). Curve A: Enriched Si^{28} target (99 percent Si^{28}) normalized to the 110 cm group. Curve B: Difference of curves C and A showing the yield due to $Si^{29}(d,p)Si^{30}$ below 110 cm.

yield by adding $\Delta x/2$. To convert this to cm air equivalent, β, the gaussian parameter, must be known since the range correction is $\beta\cdot\Delta x/2$. Similarly, the mean range can be determined from the extrapolated range by subtracting the value of x_{ext} given by Fig. 2.

The total parameter for the group, β, can be determined directly from an observed integral curve or calculated from the three major parameters of which it is comprised. From an integral curve the difference in the extrapolated and mean ranges, $R_{ext}-R_0$, can be found. Using this, $\beta=2\pi^{-\frac{1}{2}}(R_{ext}-R_0)$. Alternatively, $\beta^2=\beta_s^2+\beta_B^2+\beta_A^2$ where β_s is the range straggling parameter, β_B is the beam spread parameter as "reflected" into the proton spectrum, and β_A is the angular spread parameter. The straggling parameter, β_s, and the angular spread term β_A, are given by Livingston and Bethe.[8] The beam component, β_B, for a Gaussian beam is

$$\beta_B=\left(\frac{M-2}{M+1}\right)\left(\frac{dE}{dR}\right)_{R_0}^{-1}\frac{2\Gamma}{1.665}$$

where M is the mass of the recoil nucleus, dE/dR is the slope of the range energy relation evaluated at the approximate mean range of the group, and 2Γ is the full energy width of the incident deuteron beam. The "reflected" parameter is merely the beam parameter reduced because of the finite recoil mass. This transformation from energy to range assumes that dE/dR is constant over the range interval of the proton group. The assumption is satisfactory for proton ranges greater than 30 cm for the range intervals encountered in this work. It is also assumed that the cross section for the reaction does not vary appreciably over the energy interval of the beam. The calculation of β need not be accurate, and its determination from an integral curve is usually more reliable in cases where the group is isolated. An integral curve determination is better for a target having an appreciable thickness, that is, if the energy absorption of the beam in the target results in a proton range variation appreciable with respect to β. If β is known for one group of a spectrum, it can be calculated easily for other groups.

As the threshold bias for recording pulses is increased, the minimum depth that a proton must penetrate into the counting volume in order to be counted also increases. The dependence of electrical counting depth on counter bias has been discussed by Holloway and Livingston[6] and needs little further comment. By the use of an integrated Bragg curve, the interval of integration being taken as the air equivalent absorption of the detector, the variation of counter depth with ΔR can be determined. The maximum observed change in counter depth for the system used in this work was about 6 mm air equivalent for a counter pressure corresponding to 10 mm total absorption.

It is seen from these considerations that the corrections necessary to determine the mean range from an observed extrapolated range vary with the mean range of the group as well as with the counter setting. The change in the correction from extrapolated to mean range as the bias is altered is small since the shift due to curve shape as given by Fig. 2 and that due to the change in counter depth are of opposite sign. The correction for the range corresponding to the maximum yield is a function of counter setting alone and does not depend on the mean range of the group. The invariance

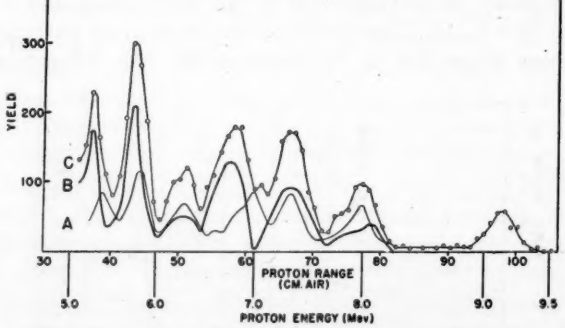

FIG. 8. Comparison of yields from an enriched Si^{30} target and a natural silicon target observed at 90° with the beam. Curve C: Enriched Si^{30} target (50 percent Si^{30}, 48 percent Si^{28}). Curve A: Natural silicon target (93 percent Si^{28}, 3 percent Si^{30}) normalized to the 100 cm group. Curve B: Difference of curves C and A showing the yield due to $Si^{30}(d,p)Si^{31}$. See text for discussion of the 80 cm group.

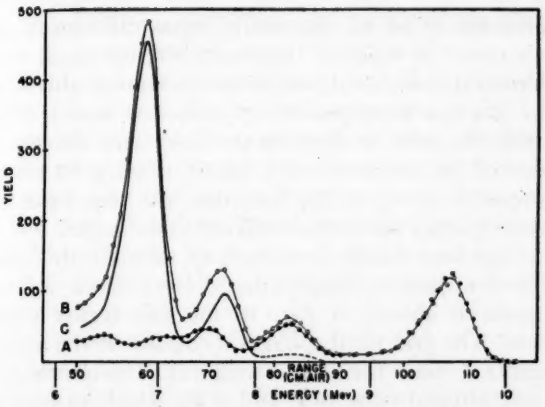

FIG. 9. Comparison of yields from an enriched Si^{30} target and an enriched Si^{28} target observed at 0° with the beam. Curve *B*: Enriched Si^{30} target (50 percent Si^{30}, 48 percent Si^{28}). Curve *A*: Enriched Si^{28} target (99 percent Si^{28}) normalized to the 110 cm group. Curve *C*: Difference of curves *B* and *A* showing the yield due to $Si^{30}(d,p)Si^{31}$. See text for discussion of the 85 cm group.

of the latter correction for a given counter setting gives preference to this method for determining the mean range. In addition, the lack of an exactly Gaussian shape is a more serious limitation on the extrapolated range correction than it is for the maximum yield range correction. The mean range values used in this work were obtained by the use of both methods since the observed numbers range curves were closely Gaussian.

IV. RESULTS

Figure 6 shows the uncorrected proton spectrum from a thin natural silicon metal target observed at 90° to the deuteron beam. Except for the two low range groups of ranges 24 and 32 cm belonging to oxygen contamination, all groups are from the reaction $Si^{28}(d,p)Si^{29}$. The assignment of these groups was verified by the use of a quartz target enriched in Si^{28}, except for the lowest energy group which was masked by the much larger oxygen content of the enriched target. The assignment was also verified by the observation of the protons emitted at 0°. The 100 cm group corresponds to the highest *Q* value assigned to Si^{28} and is assumed to represent the transition to the ground state of Si^{29}. The *Q* value of 6.18±0.09 Mev was obtained from the 90° runs alone, since the gold used in the 0° runs increases the error of those *Q* values considerably. The seven excitation levels listed in Table II were calculated from both the 0° and 90° observations, since for these ranges the uncertain absorption due to the gold does not appreciably alter these energy differences.

The comparison of the spectrum from Si^{28} and that from Si^{28} plus Si^{29} from an enriched Si^{29} target is shown in Fig. 7. The 155 cm group is due to $Si^{29}(d,p)Si^{30}$ and is assumed to give the *Q* for the ground state transition. By normalization of the yields to the 100 cm group from the Si^{28} in the targets, the lower energy part of the spectrum can be compared in detail. Ideally, the difference curve indicated would give the true spectrum of the protons from $Si^{29}(d,p)Si^{30}$. The reliability of the difference curve was checked carefully several times by making consecutive runs with enriched Si^{28} and enriched Si^{29} targets. The general group structure of the difference curve was repeated consistently, though the amplitudes of the groups fluctuated, probably due to drifts in the counter system. The effects of these drifts are amplified by such a subtraction procedure. The excitation levels as determined from this analysis are given in Table II. The first level is uncertain, as the difference curve illustrates. The small excess yield due to the Si^{29} was verified in detail by using a Si^{29} target that was thinner than the comparison Si^{28} target.

There exists some ambiguity in assigning *Q* values to the $Si^{30}(d,p)Si^{31}$ reaction which is illustrated in Figs. 8 and 9. There is an indication of a group at about 80-cm range, the amplitude of which is unusually large for the data shown in Fig. 8. In most runs the amplitude was too small so as to be definitely greater than yield variations caused by counter drift. The residual is nearly symmetrical with the Si^{28} group and this increases the doubt as to its validity. The ground state *Q* value

TABLE II. *Q* values and excitation levels.

	Q values		
This paper		Comparison values and references	
$Si^{28}(d,p)Si^{29}$	6.18±0.09	6.16±0.06[a]	[a]
$Si^{29}(d,p)Si^{30}$	8.36±0.10		
$Si^{30}(d,p)Si^{31}$	(4.93±0.2)		
	4.33±0.15		
	3.60±0.15		
	3.10±0.15		
	2.60±0.15		
	2.00±0.15		
	Excitation levels		
		$Si^{28}(d,p)Si^{29}$	$Al^{29}(\beta)Si^{29}$
Si^{29}	1.29±0.04	1.29 (a)	1.2±0.2[b]
	2.06±0.04	2.02 (a)*	
	2.43±0.04	2.41 (a)	2.35[b]
	3.08±0.05		
	3.60±0.05		
	4.09±0.06		
	4.87±0.10		
		$Al^{27}(\alpha,p)Si^{30}$	
Si^{30}	(2.4 ±0.2)	2.28[e]	
	3.91±0.15	3.58[e]	3.49[d]
	5.00±0.15	4.75[e]	
	5.7 ±0.2	~6[e]	5.44[d]
		$P^{31}(n,p)Si^{31}$	
Si^{31}	0.73±0.15	0.7±0.2[f]	
	1.23±0.15		
	1.73±0.15		
	2.33±0.15		

* The *Q* value of 4.16 Mev published by Allan and Wilkinson has been assigned above to $Si^{28}(d,p)Si^{29}$ rather than to $Si^{30}(d,p)Si^{31}$. Because of the different recoil mass, the *Q* value becomes 4.14 Mev for this assignment. Using these author's value of 6.16 Mev for the ground state transition, an excited level of 2.02 Mev is obtained as listed above.

[a] See reference 2.
[b] Seidlitz, Bleuler and Tendam, Phys. Rev. 76, 861 (1949).
[e] See reference 8.
[d] Brolley, Sampson and Mitchell, Phys. Rev. 76, 624 (1949).
[e] E. Pollard and C. J. Braesefield, Phys. Rev. 50, 890 (1936).
[f] Metzger, Alder and Huber, Helv. Phys. Acta 21, 278 (1948).

UNIVERSITY OF MICHIGAN LIBRARIES

is believed to be given by the 70 cm group for which $Q=4.33\pm0.15$ and the excited levels listed in Table II are based on this assumption. The discussion on isotopic masses from reaction data indicates that this interpretation is more correct.

The accurate Q values recently published by Buechner *et al.*[9] for $O^{16}(d,p)O^{17}$ allow a check on the above silicon Q values by means of the comparison of the oxygen and silicon ranges. The Q values obtained by measuring the energy difference between the oxygen and silicon groups indicate that the Q values should be about 50 kev higher than those listed in Table II. This is within the assigned probable errors.

The values obtained for the ground state Q values and for the excitation levels are compared with other available determinations in Table II. The agreement is satisfactory except for two excited levels of Si^{30} as determined from this work and as determined by the $Al^{27}(\alpha,p)Si^{30}$ reaction, for which the disagreement is two or three times the assigned probable error.

V. ATOMIC MASS VALUES

The Q values corresponding to the ground state transition allows a calculation of the mass difference of the residual and initial target nuclei, since the light particle masses are well known. The combination of mass differences involving adjacent nuclei permits a mass difference chain or mass difference table to be constructed. If the absolute mass of one or more of these nuclei is known, the absolute masses of all of the nuclei in the chain are fixed to an accuracy dependent on the observed mass differences. The correct modification of a mass table to take into account a new, more accurately determined, mass difference requires a knowledge of all of the related mass differences and their errors or weights. Unfortunately, the usual mass tables available do not permit modification readily since they are not accompanied by sufficient source information. In order to compare the three mass differences observed in this work with others relating to silicon isotopes, a survey of the literature has been made for known nuclear reactions involving these nuclei.

It has been found convenient to tabulate this mass difference data in diagrammatic form. Such a mass diagram is shown in Fig. 10 for the region about silicon. The grid for the diagram consists of the atomic number Z *versus* the atomic weight A. The intersection of any integral value of Z and A for which an isotopic mass has been determined is labeled with the symbol for that nucleus. The lines joining a given nucleus with other nuclei represent the reactions for which the isotope is either the initial or the final nucleus. The attached arrow indicates the direction of the observed reaction and aids in identification by means of comparison with the reaction types illustrated. The mass difference associated with each reaction is drawn beside the line joining the initial and residual nuclei. A circled item number is also given for convenience in following the tabulated values and the discussion. The numerical value of the mass difference is given in milli-mass-units, *neglecting* the integral number of mass units.* The sign of the mass difference is based on the convention that the subtrahend is always the isotope having the lower A, or lower Z, or both. The mass difference as defined in this way does not depend on the direction of the reaction on which it is based. The sum of mass differences between any two nuclei, taking into account the arbitrary sign, should agree for any possible paths if

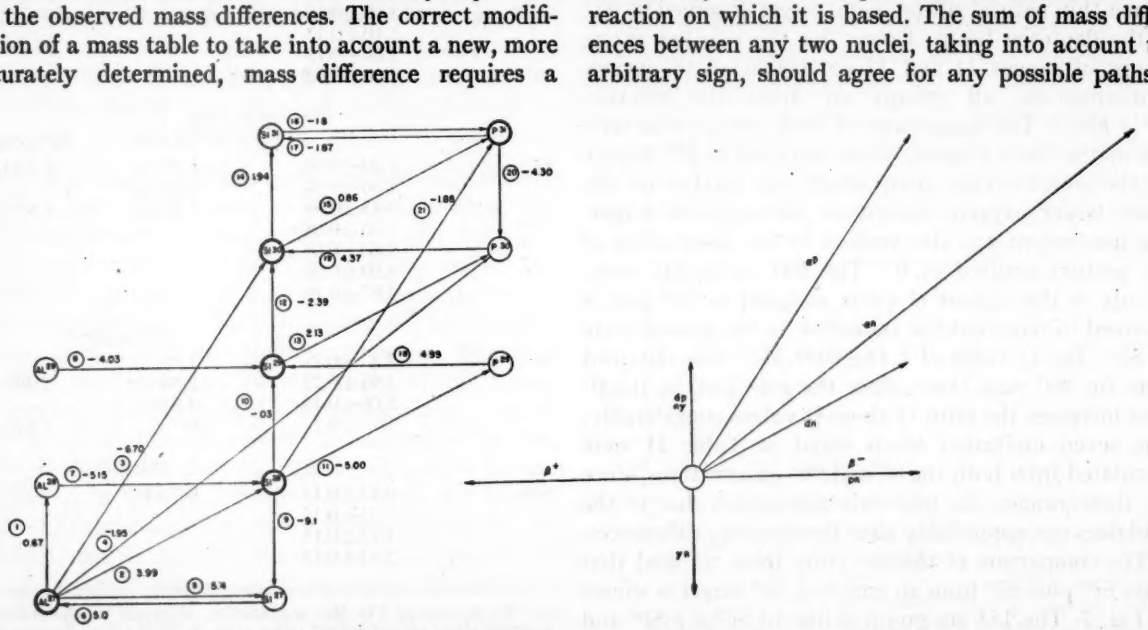

FIG. 10. Mass diagram for aluminum, silicon, and phosphorus isotopes showing mass differences in milli-mass-units between isotopes *neglecting* the whole number of mass units. The mass differences are shown beside the line representing the reaction from which they are determined. See text for sign convention. Closed polygons allow internal consistency checks. The circled numbers are item numbers corresponding to entries in Table III.

[9] Buechner, Strait, Sperduto, and Malm, Phys. Rev. **76**, 1543 (1949).

* The symbol Δ is used throughout to designate a quantity referring to a mass difference in mmu neglecting whole mass units.

the data are consistent. Thus any closed polygon affords a check of the observed mass differences.

The 21 reactions involved in Fig. 10 are listed in Table III along with the energy release, or "Q," for the transitions and the corresponding mass differences. Some values are averaged from the values given by the references cited in order to limit the size of the table.

The mass of Al^{27} has been determined by Mattauch and Ewald[10] from the C_2H_3-Al doublet. Their value for Al^{27} is $(M-A)=-10.20\pm0.08$ mmu. The mass differences given by items 1, 1a, 7, 10, 10a, and 3 allow the determination of the Si^{28}, Si^{29}, and Si^{30} masses relative to Al^{27} with a probable error of about 0.15 mmu for each mass difference. The use of the $Al^{27}(d,n)Si^{28}$ Q value, item 2, does not fit as well as the above reactions. A more accurate analysis of these masses is hardly justified because of the large experimental errors and the lack of agreement of item 2. The mass difference $Si^{28}-Al^{27}$ is also given by items 5, 6, and 9 to about 0.6 mmu. The discrepancy between items 5 and 6 greatly reduces the reliability of the path.

From the Si^{28}, Si^{29}, and Si^{30} masses, the use of linking reactions allows the determination of the Al^{29}, P^{29}, and P^{30} masses. The mass differences involved in the loops containing P^{29} and P^{30} are not sufficiently accurate to cause an alteration of the Si^{28}, Si^{29}, and Si^{30} masses as determined by the chain given above.

The Q values for items 11, 13, and 15 are arbitrarily chosen from the ten neutron groups observed from a natural silicon target by Peck.[11] The Q value assigned to the ground state transition for item 11 does not agree with Peck's assignment, and was chosen here so as to afford better agreement with items 10 and 19.

The mass of P^{31} is not definitely established by the reactions shown on the mass diagram. The values for $\Delta(P^{31}-Si^{30})$ given by eight paths from Si^{30} to P^{31} are listed below:

Path	Items	$\Delta(P^{31}-Si^{30})$
A. $Si^{30}\rightarrow P^{31}$	15	0.86 ± 0.14
B. $Si^{30}\rightarrow Al^{27}\rightarrow Si^{28}\rightarrow P^{31}$	3, 2, 21	0.83 ± 0.33
C. $Si^{30}\rightarrow Al^{27}\rightarrow Al^{28}\rightarrow Si^{28}\rightarrow P^{31}$	3, 1, 7, 21	0.34 ± 0.34
D. $Si^{30}\rightarrow Al^{27}\rightarrow P^{30}\rightarrow P^{31}$	3, 4, 20	0.45 ± 0.36
E. $Si^{30}\rightarrow Si^{29}\rightarrow P^{30}\rightarrow P^{31}$	12, 13, 20	0.22 ± 0.30
F. $Si^{30}\rightarrow P^{30}\rightarrow P^{31}$	19, 20	0.07 ± 0.27
G. $Si^{30}\rightarrow Si^{31}\rightarrow P^{31}$	14, 16, 17	0.09 ± 0.20
H. $Si^{30}\rightarrow Si^{29}\rightarrow Si^{28}\rightarrow P^{31}$	12, 10, Aston	0.3 ± 0.8

A possible explanation for the discrepancy indicated by path *A* is that the observation of the $Si^{30}(d,n)P^{31}$ reaction (22) did not include the ground state transition. A higher Q value would decrease the discrepancy. Similarly, the value for path *B* would be lower if either the $Al^{27}(d,n)Si^{28}$ or $Si^{28}(a,p)P^{31}$ Q values were to an excited state. The last six paths listed indicate that

[10] Mattauch and Ewald, Physik Zeits. 44, 181 (1943).
[11] R. A. Peck, Phys. Rev. 73, 947 (1948).

TABLE III. Published reaction data relating to aluminum, silicon and phosphorus isotopes and the corresponding mass differences of the initial and final isotopes involved in each transition. The mass differences are calculated assuming the following values for $(M-A)$ in milli-mass-units: $n=8.96$, $p=8.131$, $d=14.724$, $\alpha=3.86$.

Item	Transition	Transition energy (Mev)	Δ(mmu)	Reference
1	$Al^{27}(d,p)Al^{28}$	5.45 ± 0.05	0.74 ± 0.06	a, b
1a	$Al^{27}(n,\gamma)Al^{28}$	7.72 ± 0.02	0.67 ± 0.03	c
2	$Al^{27}(d,n)Si^{28}$	9.08 ± 0.13	-3.99 ± 0.15	d
3	$Al^{27}(\alpha,p)Si^{30}$	2.26	$-6.70\pm(0.15)$	e, f, g, h, i, j
4	$Al^{27}(\alpha,n)P^{30}$	-2.93 ± 0.17	-1.95 ± 0.18	k
5	$Al^{27}(p,n)Si^{27}$	-5.8 ± 0.1	5.4 ± 0.12	l, m
6	$Si^{27}(\beta)Al^{27}$	3.6 ± 0.2	5.0 ± 0.2	m, n
7	$Al^{28}(\beta)Si^{28}$	4.8 ± 0.17	-5.15 ± 0.18	o, p, q, r, s, t
8	$Al^{29}(\beta)Si^{29}$	3.75 ± 0.25	-4.03 ± 0.27	u
9	$Si^{28}(\gamma,n)Si^{27}$	-16.8 ± 0.4	-9.1 ± 0.4	v
10	$Si^{28}(d,p)Si^{29}$	6.17 ± 0.06	-0.03 ± 0.07	a
10a	$Si^{28}(n,\gamma)Si^{29}$	8.38 ± 0.10	-0.04 ± 0.11	c
11	$Si^{28}(d,n)P^{29}$	0.71 ± 0.13	5.00 ± 0.14	k
12	$Si^{29}(d,p)Si^{30}$	8.36 ± 0.10	-2.39 ± 0.11	this paper
12a	$Si^{29}(n,\gamma)Si^{30}$	11.00 ± 0.3	-2.85 ± 0.3	c
13	$Si^{29}(d,n)P^{30}$	3.38 ± 0.17	2.13 ± 0.18	k
14	$Si^{30}(d,p)Si^{31}$	4.33 ± 0.15	1.94 ± 0.17	this paper
15	$Si^{30}(d,n)P^{31}$	4.56 ± 0.13	0.86 ± 0.14	k
16	$Si^{31}(\beta)P^{31}$	1.7 ± 0.2	-1.8 ± 0.2	w, x
17	$P^{31}(n,p)Si^{31}$	-0.97 ± 0.13	-1.87 ± 0.15	y
18	$P^{29}(\beta)Si^{29}$	3.63 ± 0.07	4.99 ± 0.07	z
19	$P^{30}(\beta)Si^{30}$	3.05 ± 0.14	4.37 ± 0.15	n, z
20	$P^{31}(\gamma,n)P^{30}$	-12.35 ± 0.2	-4.30 ± 0.22	v
21	$Si^{28}(\alpha,p)P^{31}$	-2.23	$-1.88\pm(0.25)$	e, aa
22	$S^{32}(n,\alpha)Si^{29}$	1.16 ± 0.15	-3.85 ± 0.16	bb

[a] See reference 2.
[b] Pollard, Sailor, and Wyly, Phys. Rev. 75, 725 (1949).
[c] Kinsey, Bartholomew, and Walker, Phys. Rev. 78, 481 (1950).
[d] R. A. Peck, Jr., Phys. Rev. 76, 1279 (1949).
[e] See reference 5.
[f] See reference 8.
[g] J. Chadwick and J. E. R. Constable, Proc. Roy. Soc. 135, 48 (1931).
[h] O. Haxel, Zeits. f. Physik 93, 400 (1935).
[i] Duncanson and Miller, Proc. Roy. Soc. 146, 396 (1934).
[j] Merhaut, Physik Zeits. 41, 528 (1940).
[k] See reference 11.
[l] G. Kuerti and S. N. Van Voorhis, Phys. Rev. 56, 614 (1939).
[m] McCreary, Kuerti, and Van Voorhis, Phys. Rev. 57, 351 (1940).
[n] Barkas, Creutz, Delasso, Sutton, and White, Phys. Rev. 58, 383 (1940).
[o] Junkicki Itoh, Proc. Phys. Math. Soc. Japan 23, 605 (1941).
[p] S. Eklund and N. Hole, Arkiv. Mat. Astr. Fys. 29, No. 26 (1943).
[q] Benes, Hedgran, and Hole, Arkiv. Mat. Astr. Fys. 35, No. 12 (1948).
[r] Bleuler, Scherrer, Walter, and Zunti, Helv. Phys. Acta 20, 195 (1947).
[s] J. V. Dunworth, Nature 159, 436 (1947).
[t] A. Wattenberg, Phys. Rev. 71, 497 (1947).
[u] Seidlitz, Bleuler, and Tendam, Phys. Rev. 76, 861 (1949).
[v] McElhinney, Hanson, Becker, Duffield, and Diven, Phys. Rev. 75, 542 (1949).
[w] Kurie, Richardson, and Paxton, Phys. Rev. 49, 368 (1936).
[x] H. W. Newson, Phys. Rev. 51, 624 (1937).
[y] Metzger, Alder, and Huber, Helv. Phys. Acta 21, 278 (1948).
[z] White, Creutz, Delasso, and Wilson, Phys. Rev. 59, 63 (1941).
[aa] O. Haxel, Zeits. f. Physik 36, 840 (1935).
[bb] Stebler and Huber, Helv. Phys. Acta 21, 59 (1948).

UNIVERSITY OF MICHIGAN LIBRARIES

$\Delta(P^{31}-Si^{30})=0.15\pm0.10$. Aston's value[12] for the mass difference $P^{31}-Si^{28}$ is used for path H.

To determine the P^{31} mass, the reactions linking it to S^{32} must be considered. Stebler and Huber's Q value for $S^{32}(n,\alpha)Si^{29}$, item 22, completes the chain from Al^{27} to S^{32}. The mass difference $\Delta(S^{32}-Al^{27})$ using this reaction is -8.31 ± 0.26 by means of items 1, 7, 10, and 22, or -7.82 ± 0.24 by means of items 2, 10, 22. Using the value S^{32} $(M-A)=-19.11\pm0.07$ obtained by Okuda, Ogata, Aoki, and Sugawara[13] together with Mattauch and Ewald's value Al^{27} $(M-A)=-10.20\pm0.08$,[10] the value $\Delta(S^{32}-Al^{27})=-8.91\pm0.11$ is obtained. If this mass difference is calculated by a chain passing through P^{31}, values of about -7.9 result if $\Delta(P^{31}-Si^{30})=0.15$. Thus an unavoidable discrepancy between the reaction data and the mass spectroscopic data is found in linking Al^{27} and S^{32}. A value $\Delta(S^{32}-Al^{27})=-8.0\pm0.2$ is consistent with most of the nuclear reactions. Aston's values[12] for the mass of Si^{28} and S^{32}, together with reaction data, furnishes an additional value $\Delta(S^{32}-Al^{27})=-8.6\pm0.8$ which overlaps all of the above values.

The discussion of atomic masses between Al and P given here points up the severe difficulties in making a mass table. It is customary to make some sort of judicious choice of those reactions needed to form links in the chain between masses known from mass doublet data. Since this choice is arbitrary and contains weighting factors designed to give some consideration to alternative links, it becomes difficult to make explicitly clear in a mass table the exact method by which the values were derived. Consequently, to take advantage of any new and more accurately measured reaction one must in every case perform his own mass-link calculations, using his own judgment and weighting factors. It therefore seems evident that the more useful means of data presentation is a mass difference table of the sort presented in Fig. 10, allowing the user to select the best path of mass links in the light of any improved data.

[12] F. W. Aston, *Mass Spectra and Isotopes* (Longmans, Green and Co., New York, N. Y.) second edition (1941), pp. 105, 139.
[13] Okuda, Ogata, Aoki, and Sugawara, Phys. Rev. 58, 578 (1940).

Note added in proof: Preliminary results obtained at M.I.T. by P. Endt, W. W. Buechner and D. M. Van Patter on the $P^{31}(d\alpha)$ Si^{29} reaction indicate that the excited levels of Si^{29} are 1.28, 2.05, 2.44, and 3.11 Mev in excellent agreement with the values given in Table II. The masses of Si^{28}, Si^{29}, and Si^{30} have recently been reported by H. Duckworth and R. Preston, Phys. Rev. 79, 402 (1950). The mass spectrograph value $\Delta(Si^{29}-Si^{28})=-0.14\pm0.15$ is in good agreement with the value from reaction data. A small discrepancy exists for $Si^{30}-Si^{29}$, however, and the value $\Delta(Si^{28}-Al^{27})=-3.99\pm0.11$ is obtained by combining Duckworth and Preston's value for Si^{28} with Mattauch and Ewald's Al^{27}. The value $\Delta(Si^{28}-Al^{27})=-4.48$ is given as the preferred value in the text. Recent measurements on the $P^{31}(d\alpha)Si^{29}$ and $S^{32}(\gamma d)P^{30}$ reactions in addition to Duckworth and Preston's masses verify the conclusion that the mass of S^{32} as given by Okuda *et al.* is incorrect. The mass of S^{32} using Si^{28} as a base and items 10 and 22 of Table III is $S^{32}(M-A)=-18.07\pm0.19$ mmu in good agreement with Aston's value of -17.7 ± 0.3 mmu.

Angular Yield of Both Proton Groups from $Li^6(d,p)Li^7$

R. W. KRONE,* S. S. HANNA, AND D. R. INGLIS†
Department of Physics, Johns Hopkins University, Baltimore, Maryland‡

(Received May 9, 1950)

The simultaneous measurement of the intensities of two energy groups of product particles is accomplished by sorting out their proportional-counter pulses in an electronic ten-channel discriminator. The angular yields of protons leading to the ground state and to the 480-kev state of Li^7 in the reaction $Li^6(d,p)Li^7$ have been measured at deuteron energies between 400 and 800 kev. At the higher bombarding energies the angular yields of the two groups are complex and somewhat similar, both containing terms at least as high as $\cos^4\theta$. As the deuteron energy is reduced, the short-range group retains this complexity while the long-range group becomes more nearly spherically symmetric.

I. INTRODUCTION

EVER since its discovery by Rumbaugh and Hafstad[1] in 1936, the interpretation of the 480-kev level of Li^7 in its relation to the ground level has provided a stimulating challenge to theories of nuclear structure. At the time this investigation was undertaken, the only specific proposal that had been made[2] interpreted the ground state as $^2P_{\frac{3}{2}}$ and the excited level as $^2P_{\frac{1}{2}}$, but this was doubted partially because of the lack of a theory to explain so large a spin-orbit coupling. More recently a consideration of the relative yields[3] of the alpha-groups in the $B^{10}(n,\alpha)Li^7$ reaction seems to indicate,[4] although perhaps not conclusively, a value of I as great as 5/2 for the excited state. This investigation was motivated by the hope that detailed comparison of the angular yields of the two groups of protons arising from transitions to these two states would shed further light on their nature.

II. METHOD OF OBSERVATION

The usual methods of observing the intensities of two energy groups involve the use of a shallow counter either with high bias so that two peaks may be plotted as range is varied, or with low bias so that two plateaus may be measured, the difference of which is required for the intensity of the short-range group. The method used in this work was developed to eliminate the uncertainty, as well as the tedium, of making successive intensity measurements at each angle and bombarding energy. It requires instead a single run, during which sufficient data are recorded to give the intensities of both groups of product particles directly.

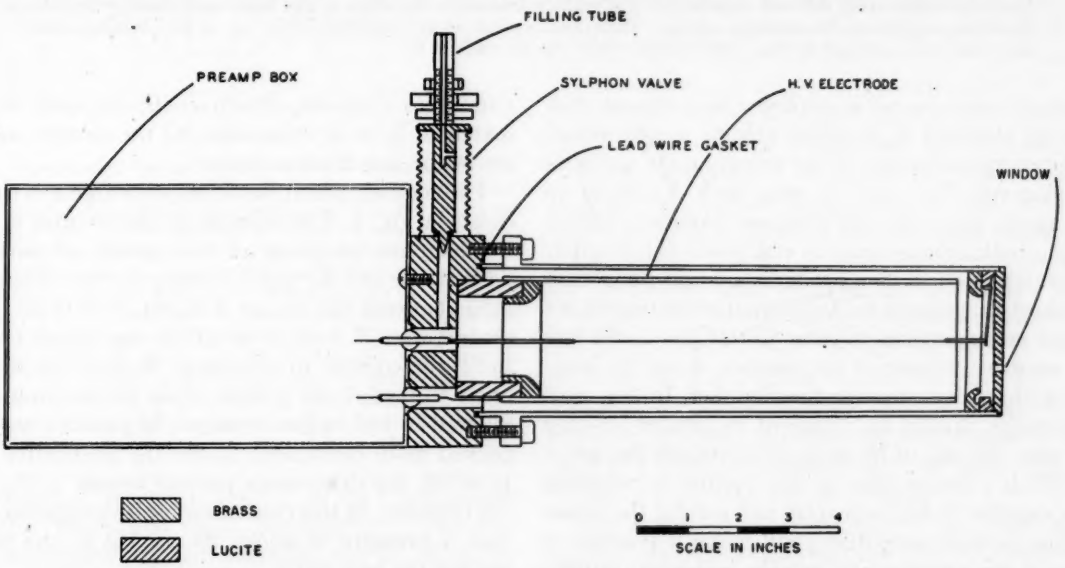

FIG 1. Deep proportional counter used in measuring the intensities of the two ranges of protons from $Li^6(d,p)Li^7$. In the present experiment the central (2-mil tungsten) wire was 4.5 in. long.

* Now at the University of Kansas, Lawrence, Kansas.
† Now at Argonne National Laboratory, Chicago, Illinois.
‡ Assisted by a contract with the AEC.
[1] L. H. Rumbaugh and L. R. Hafstad, Phys. Rev. **50**, 681 (1936).
[2] D. R. Inglis, Phys. Rev. **50**, 783 (1936); G. Breit and J. R. Stehn, Phys. Rev. **53**, 459 (1938).
[3] J. K. Bøggild, Kgl. Danske Vid. Sels. Math-Fys. Medd. **23**, 4, 26 (1945).
[4] D. R. Inglis, Phys. Rev. **74**, 1876 (1948).

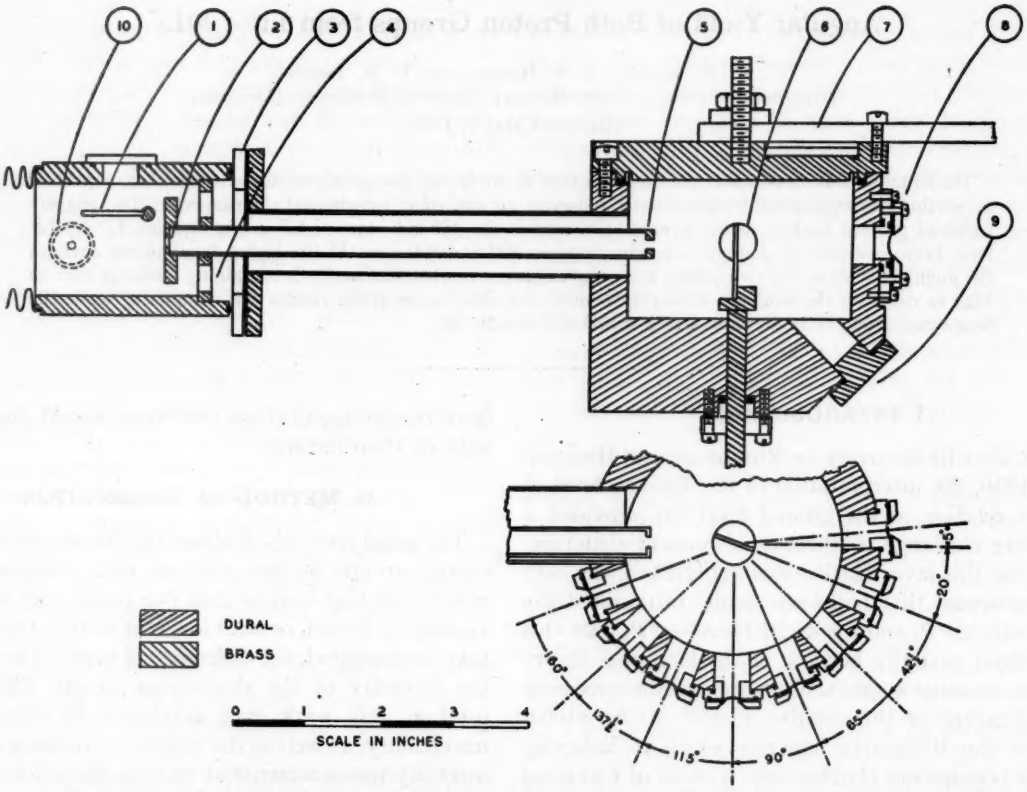

FIG. 2. Target chamber assembly. (1) Quartz plate which can be rotated so as to intercept the beam. (2) Collimating slit. (3) Lucite insulating ring. (4) Openings in flange to provide greater pumping speed. (5) Entrance slit into chamber. (6) 90° window (one on each side of chamber). (7) Rotating arm on which the proportional counter is mounted. (8) 5° window showing assembly detail. (9) Port in which the lithium oven is inserted. (10) Stupakoff insulators supporting the two members of a slit which intercepts the edges of the beam and thereby provides a signal for regulating the statitron voltage. Three Lucite windows are provided in the top of the chamber. The 5° port was later enlarged so that observations could also be made at 0°.

A proportional counter is employed deep enough that the energy absorbed in its active volume is comparable with the energy difference of the two groups of particles being observed. One way of using such a counter to advantage in resolving two groups of particles consists in letting both groups come to rest inside the counter. A long-range particle then produces a larger pulse than does a short-range particle. An alternative setting allows the short-range particles to come to rest just at the end of the sensitive volume of the counter, while the long-range particles pass through the chamber. In this case, a short-range particle by virtue of its greater ionizing power near the end of its range will produce the larger pulse. With either setting of the counter a recording system capable of discriminating and sorting the pulses according to their amplitude, will make it possible to observe in one experimental run the individual intensities of both groups.

III. APPARATUS AND PROCEDURE

In the present experiment the pulses from the deep proportional counter, after suitable amplification, were sorted in a ten-channel electronic discriminator. A "sliding pulser" was provided for calibrating the discriminator channels, which could be made approximately 2, 5, or 10 volts wide. All the circuits employed are of the Los Alamos design.[5]

The counter, which was filled with argon, is shown in detail in Fig. 1. The pressure in the counter is critical if maximum resolution of two groups of particles is desired. In the $Li^6(d,p)Li^7$ reaction the difference in range between the groups is about 4 cm of air. With a central wire 11.5 cm in length it was found necessary to fill the counter to a pressure of about 50 cm Hg in order to resolve the groups, when all the protons were allowed to end in the chamber. In practice however it proved more convenient to use the alternative setting in which the short-range protons passed to the end of the chamber. In this case extensive investigation showed that a pressure of about 20 cm Hg in the chamber yielded the best result.

Preliminary tests also revealed that the resolution depended very critically on the range setting. This was especially true because it was found desirable to obtain at each angle and energy that setting of the counter which would produce a similar distribution of pulses in

[5] W. C. Elmore and M. Sands, *Electronics* (McGraw-Hill Book Company, Inc., New York, 1949).

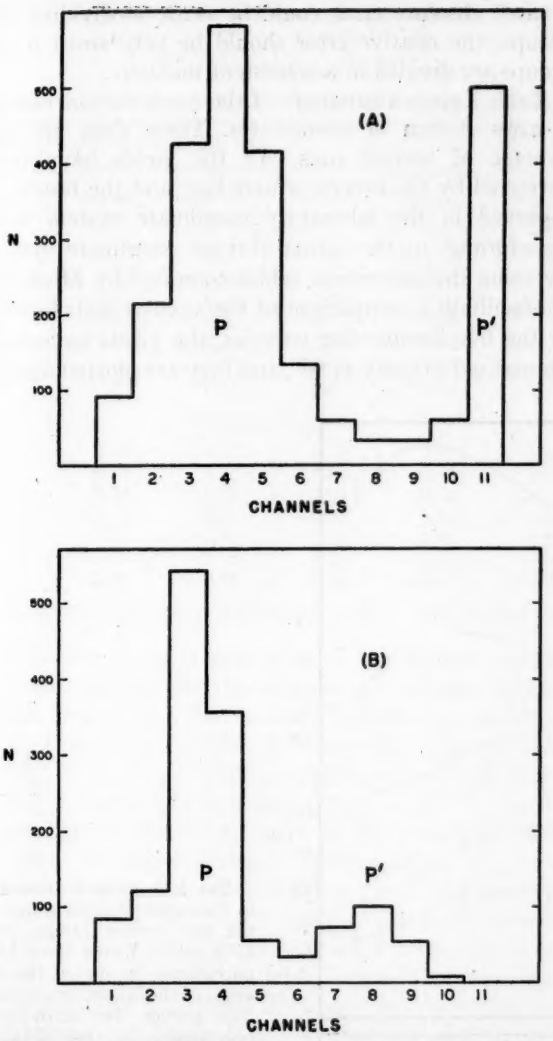

FIG. 3. Typical distributions of proton pulses obtained with the ten-channel discriminator. Pulse height increases with increasing channel number. Channel 11 represents the "overflow," i.e., all pulses larger than those in channel 10. These data were obtained with that setting of the proportional counter for which the short-range protons produced the larger pulses and therefore registered in the higher numbered channels. Distribution (A) was obtained with channels approximately 2 volts wide and most of the short-range protons were recorded in the overflow. The starting bias was approximately 50 volts. In distribution (B) the channels were over twice as wide and both groups were recorded within the ten channels. In these plots the numbers of counts in the various channels have been adjusted to compensate for inequalities in channel widths.

the channels of the discriminator, so that inequalities in channel width and slight overlapping of the two groups would not seriously affect the results. Since the proton energies depend on both bombarding energy and angle of observation, it was necessary to alter the range setting for each observation. This was accomplished by using appropriate aluminum absorbers as a coarse range adjustment, with variation of air path as a fine adjustment.

The counter was mounted on a carriage which provided a screw-driven radial motion, and the carriage in turn was attached to a radial arm which pivoted on the axis of the target chamber so that observation could be made at any one of seven thin windows of the target chamber. The latter was milled from a 4-in. solid aluminum cylinder. The complete assembly is shown in detail in Fig. 2.

TABLE I. Intensities in the center-of-mass system of the two ranges of protons from $Li^6(d,p)Li^7$. For each bombarding energy the yields have been normalized to one at 90° (in the laboratory system).

cosθ	400 kev	430 kev	540 kev	650 kev	780 kev
		Long range			
−0.95	0.88	0.92	0.95	1.04	0.99
−0.77	1.00	1.03	0.99	1.04	1.10
−0.48	0.98	0.98	0.95	1.01	1.05
−0.06	1	1	1	1	1
0.37	1.03	1.00	1.09	1.00	1.20
0.71	1.02	1.00	1.14	1.18	1.47
0.93	1.04	1.02	1.11	1.33	1.42
1.00	1.04	1.01			1.40
		Short range			
−0.95	0.67	0.62	0.72	0.93	0.60
−0.77	0.81	0.86	0.79	1.08	0.91
−0.48	0.98	1.06	1.00	1.08	1.04
−0.06	1	1	1	1	1
0.37	1.19	1.14	1.23	1.16	1.28
0.71	1.19	1.05	1.13	1.38	1.72
0.93	0.97	0.80	0.95	1.17	1.64
1.00	0.97	0.68			1.51

The target used for these measurements was a thin layer of ordinary lithium evaporated onto a thin silver foil by means of an oven introduced into the target chamber through a Wilson seal. Aside from the lowered intensity, the presence of Li^7 offers no difficulty in the present experiment. Observations at the backward angles were made with a target setting of 60° and at the forward angles with a setting of 120°, observation at 90° being included in each case for intercomparison.

Since angular yield measurements are critically dependent on reliable monitoring of the beam, two methods were employed. An electronic current integrator (Sands' design, Los Alamos) was used to measure the total integrated beam intensity during a run. In addition a small proportional counter was employed to observe the products of the reaction at a 90° window provided for this purpose on the free side of the target chamber. By accepting all the charged particles coming from the reaction, including the very numerous alphas from $Li^7(d,n\alpha)\alpha$, the statistical uncertainty introduced by the monitor was kept very small.

The general procedure followed in recording the angular yields was to traverse the windows in one direction and then to repeat the measurements in the reverse order. This precaution revealed the absence of any systematic drifts in the counting rate. Before each run the position of the proportional counter was adjusted so that the short-range protons gave maximum pulses. If this adjustment is made properly the pulse amplitudes are nearly independent of the angle of observation and the bombarding energy. In the course

of the work, several settings of discriminator channel width and starting bias were tried. Results obtained with two different settings are shown in Fig. 3. The deuteron beam was obtained from the small horizontal statitron described elsewhere.[6]

IV. RESULTS

It is evident from Fig. 3 that the two groups of protons are not completely resolved, and it is therefore necessary to use some judgment in making a division between them. As mentioned above, an effort was made to produce similar distributions of pulses in the various channels over an entire angular run, so that, although a small absolute error could be made in dividing the groups, the relative error should be very small if the groups are divided in a consistent manner.

Table I gives a summary of the results in the center-of-mass system of coordinates. These data are the average of several runs. All the yields have been corrected by the inverse square law, and the results as observed in the laboratory coordinate system were transformed to the center-of-mass coordinate system by using the conversion tables compiled by Moskow.[7] To facilitate a comparison of the angular distributions at the five bombarding energies, the yields have been normalized to unity at 90°, and they are plotted against

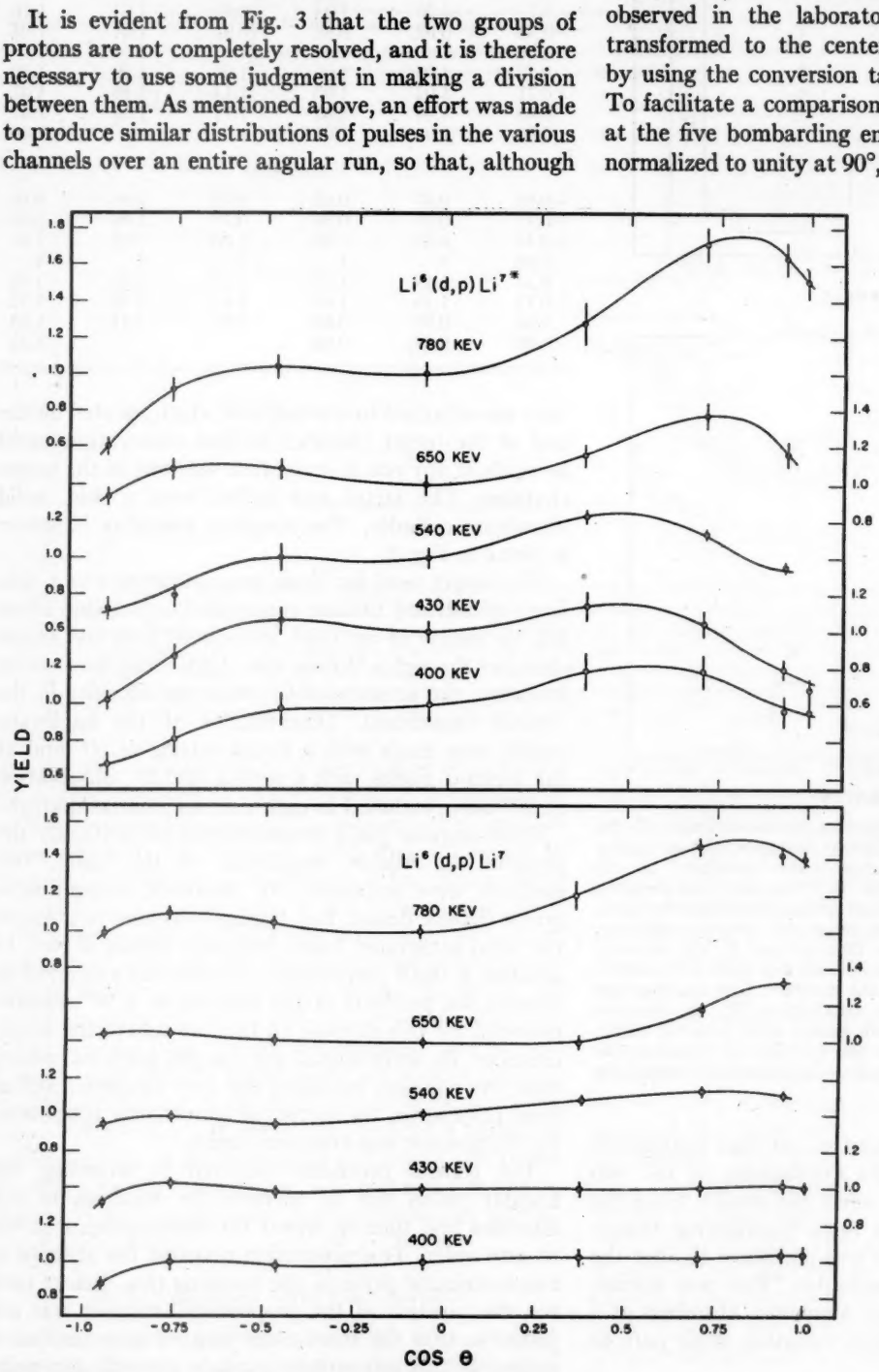

FIG. 4. Angular distributions in the center-of-mass system of the two proton ranges from $Li^6(d,p)Li^7$. Yields have been normalized to one at the 90° angle of the laboratory system. The curves are sixth-power polynomials in $\cos\theta$ obtained from an analysis using the seven points of observation (an average of the two forward measurements was used for the 400-, 430-, and 780-kev runs).

[6] Inglis, Krone, and Hanna, Rev. Sci. Inst. **20**, 834 (1949).
[7] M. Moskow, master's thesis, Johns Hopkins University (1948). (Copies available on request.)

TABLE II. Coefficients in the expansion,

$$Y(\cos\theta)=Y(0)\left(1+\sum_{n=1}^{6}A_n\cos^n\theta\right)$$

for both ranges of protons from $Li^6(d,p)Li^7$. The yields for $\cos\theta=0$ are expressed in arbitrary units which make the yield of long-range protons equal to one at 400 kev.

	400 kev	430 kev	540 kev	650 kev	780 kev
		Long range			
$Y(0)$	1	1.11	1.51	1.80	1.91
A_1	0.13	0.09	0.24	−0.07	0.25
A_2	−0.11	−0.26	−0.03	−0.03	0.78
A_3	−0.46	−0.40	−0.35	0.46	0.12
A_4	0.44	0.94	0.43	0.79	−0.28
A_5	0.46	0.41	0.21	−0.28	−0.13
A_6	−0.42	−0.77	−0.43	−0.61	−0.38
		Short range			
$Y(0)$	0.23	0.29	0.49	0.60	0.66
A_1	0.28	0.15	0.36	0.12	0.26
A_2	0.83	1.05	1.02	0.86	1.23
A_3	−0.12	−0.22	−0.52	0.36	0.88
A_4	−2.21	−2.94	−2.86	−0.65	−0.99
A_5	−0.20	0.15	0.28	−0.38	−0.61
A_6	1.20	1.54	1.63	−0.26	−0.26

$\cos\theta$ in Fig. 4. It is seen that at the highest energy recorded, the angular dependence is somewhat similar for the two groups. At the lower energies, on the other hand, there is a marked difference between the two distributions; the long-range distribution tends fairly rapidly toward spherical symmetry, while the short-range distribution retains most of the complexity displayed at the higher energy.[8] To investigate this more fully the results have been analyzed into polynomials in $\cos\theta$ up to the sixth power and the curves so obtained are plotted in Fig. 4. The analysis was made using seven observation points (a suitable average of the two forward angles was used in those runs in which an observation was made at 0°) so that the sixth power curves pass through all of these points. The coefficients A_n in the expansion:

$$Y(\cos\theta)=Y(0)\left(1+\sum_{n=1}^{6}A_n\cos^n\theta\right)$$

are given in Table II. An inspection of this table shows that all of the coefficients for the long-range distributions are less than unity, while some of those for the short-range group are considerably larger, especially at the lower energies. Because small uncertainties in the measured yields can lead to relatively large uncertainties in the expansion coefficients, it is questionable how much significance can be attached to these large values of the coefficients. In particular it seemed worth while to analyze the data into polynomials including terms only up to the fourth power. With such an analysis using a least-square criterion it is possible to fit the long- and short-range data to within about three and five percent, respectively. In view of the statistical uncertainty of the observations such a fit would seem to be entirely satisfactory were it not that the discrepancies so introduced are in general systematic and certain features of the distributions which seem reasonably well established from the observations are lost in the less complex analysis. Nevertheless, an inspection of the set of coefficients obtained from the less complex analysis given in Table III, shows that in general the coefficients are smaller, and it seems reasonable that at these low bombarding energies the analysis, which utilizes smaller powers of $\cos\theta$ and at the same time leads to smaller values of the coefficients, is more nearly correct.

TABLE III. Coefficients in the expansion,

$$Y(\cos\theta)=Y(0)\left(1+\sum_{n=1}^{4}A_n\cos^n\theta\right)$$

for both ranges of protons from $Li^6(d,p)Li^7$.

	400 kev	430 kev	540 kev	650 kev	780 kev
		Long range			
A_1	−0.00	−0.04	0.18	0.02	0.30
A_2	0.11	0.13	0.26	0.26	1.03
A_3	0.09	0.08	−0.11	0.15	−0.07
A_4	−0.17	−0.16	−0.25	−0.03	−0.87
		Short range			
A_1	0.30	0.09	0.28	0.23	0.43
A_2	0.27	0.30	0.16	1.03	1.43
A_3	−0.13	−0.02	−0.19	−0.12	0.12
A_4	−0.56	−0.77	−0.48	−1.08	−1.45

The angular measurements presented here do not conveniently give the variation of yield with energy. Since excitation curves have recently been obtained elsewhere,[8,9] it was thought advisable to make only a single check run with the present method. Only the relative change in yield with energy was measured and the data at the energies corresponding to the angular runs, included in Table II for completeness, have been normalized to make the yield of long-range protons equal to unity at the lowest energy.

[8] We note that the complexity that we find in the short-range group at the low energies disagrees with the result obtained by Whaling. In his method the intensity of the short-range group is obtained by subtracting the long-range plateau from the total-intensity plateau measured with a shallow counter and low bias. We are indebted to him for making his results available to us before publication. See W. Whaling and T. W. Bonner, Phys. Rev. 79, 258 (1950).

[9] N. P. Heydenburg and D. R. Inglis, private communication.

Evidence from Nuclear Masses on Proposed Closed Shells at 20 Nucleons*

W. Low and C. H. Townes
Physics Department, Columbia University, New York, New York
(Received May 18, 1950)

Combining microwave measurements of sulfur and chlorine masses with mass spectroscopic and nuclear reaction information, the effect of nuclear shell structure on masses in the region of 20 neutrons or protons is investigated. It is found that except for Ca^{40}, nuclei with 20 neutrons or protons do not show any special stability.

THERE are various types of evidence[1–4] that neutron and proton numbers N and Z of 2, 8, 20, 50, 82 and 126 form particularly stable nuclei. These numbers can be associated with the completion of shells of the quantum levels of a single particle in a potential well.[5–7] Such a single particle model has been used with considerable success to correlate nuclear moments, isomerism, and β-decay. However, there has as yet been very little information about nuclear masses at N or Z of 20, 50, or 82. Hence, the most direct test for closed shells having extra stability has not yet been made.

Combining the recent microwave measurements of masses S^{36}, S^{34}, Cl^{36}, and Cl^{37} with mass spectroscopic and nuclear transmutation data, one can determine the masses of a large number of nuclei in the region of $N=20$ or $Z=20$. It is, therefore, feasible to test the expected variation in proton or neutron binding energy near the supposed closed shell at 20 nucleons. This is most conveniently done by comparison of the experimentally determined masses with those calculated from a semi-empirical formula which allows for most of the known sources of mass variation except shell structure. Such a formula has been given by Bohr and Wheeler[8,9] as:

$$M_{AZ}=A-0.00081Z-0.00611A+0.014A^{\frac{1}{3}}+0.083(A/2-Z)^2/A+0.000627Z^2A^{-\frac{1}{3}}+\lambda,$$

where A=mass number, Z=nuclear charge, $\lambda=0$ for A odd, $\lambda=-0.036A^{-\frac{1}{2}}$ for A even, Z even, $\lambda=0.036A^{-\frac{1}{2}}$ for A odd, Z odd.

This equation thus takes into account the normal odd-even fluctuations of masses. Although in general this expression does not agree with the experimentally measured masses to high accuracy, nevertheless the difference between the experimental and calculated masses plotted as a function of N or Z should give a relatively smooth curve. Any marked deviation from this curve, i.e., a sudden change in slope, might indicate the effects of shell structure.

Figures 1 and 2 show a plot of the difference between

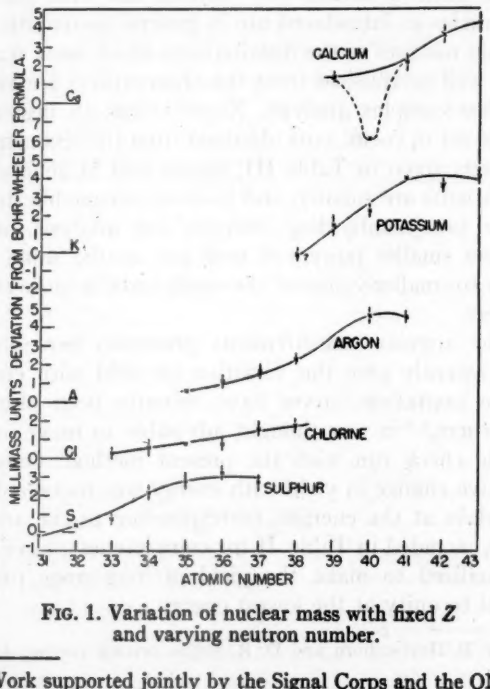

FIG. 1. Variation of nuclear mass with fixed Z and varying neutron number.

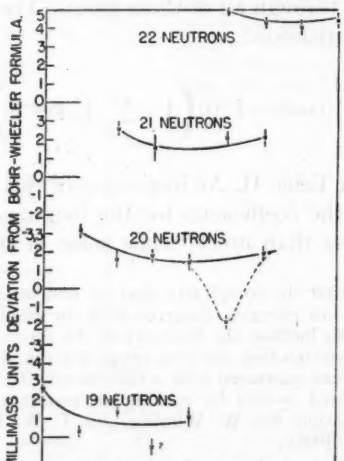

FIG. 2. Variation of nuclear mass with fixed neutron number and varying Z.

* Work supported jointly by the Signal Corps and the ONR.
[1] W. Elsasser, J. de phys. et rad. **5**, 625 (1934).
[2] E. Wigner, Phys. Rev. **51**, 447 (1937).
[3] A. Berthelot, J. de phys. et rad. **3**, 17, 52 (1942).
[4] M. G. Mayer, Phys. Rev. **74**, 235 (1948).
[5] E. Feenberg and K. C. Hammack, Phys. Rev. **75**, 1877 (1949).
[6] L. W. Nordheim, Phys. Rev. **75**, 1894 (1949).
[7] M. G. Mayer, Phys. Rev. **75**, 1969 (1949).
[8] N. Bohr and J. A. Wheeler, Phys. Rev. **56**, 426 (1939).
[9] G. B. von Albada, Astrophys. J. **105**, 393 (1947).

TABLE I. Mass differences calculated from microwave data and nuclear reactions.

$H^1 = 1.008128$, $D^2 = 2.014718$, $n = 1.008938$, $\alpha = 4.003880$ mass units

Nuclei	Calculated mass difference	Reactions used	Reference
$P^{32}-P^{31}$	1.00028±40	dp	a
$S^{31}-P^{31}$	0.00519±17	β^+	b
$P^{32}-S^{32}$	0.00179±20	β^-	c
$S^{34}-P^{31}$	2.99542±40	αp	d
$P^{34}-S^{34}$	0.000547±20	β^-	e
$S^{33}-S^{32}$	0.99965±05	dp	f
	0.99977±30	mic.	g
$S^{33}-S^{34}$	0.99725±05	dp	f
	(0.99709±15)	(mic.)	
$S^{34}-S^{36}$	2.00054±30	mic.	h
$Cl^{35}-S^{32}$	2.99800±40	αp	i
$Cl^{35}-S^{33}$	1.99893±40	$d\alpha$	j
$S^{35}-Cl^{35}$	0.000179±03	β^-	k
$Cl^{33}-S^{33}$	0.00549±07	β^+	b
$Cl^{34}-S^{34}$	0.00656±10	β^+	l
$Cl^{35}-Cl^{37}$	1.99751±14	mic.	m
$Cl^{35}-Cl^{36}$	0.99988±30	dp	n
	1.00017±40	mic.	o
$S^{37}-Cl^{37}$	0.00461±20	β^-	e
$Cl^{38}-Cl^{37}$	1.00228±30	dp	p
$A^{35}-Cl^{35}$	0.00580±30	β^+	b
$Cl^{36}-A^{36}$	0.000768±.000006	β^-	k
$A^{37}-A^{36}$	0.99961±05	dp	q
$A^{38}-Cl^{35}$	2.99443±40	αp	r
$Cl^{38}-A^{38}$	0.00558±20	β^-	s
$K^{38}-A^{38}$	0.00641±20	β^+ ($\gamma+\beta^+$-ray in cascade probably)	t
$A^{41}-A^{40}$	1.00249±05	dp	u
$A^{41}-K^{41}$	0.00274±20	β^-	v
$K^{40}-A^{40}$	0.0017±20	pn	w
	≥0.00167±10	K-capture	x
$K^{40}-K^{39}$	1.00070±07	dp	y
$Ca^{39}-K^{39}$	0.00619±30	theoretical	
$K^{40}-Ca^{40}$	0.00145±05	β^-	aa
	0.00148±03	β^-	bb
$Ca^{41}-Ca^{40}$	0.99997±05	dp	cc
$Ca^{41}-K^{41}$	0.00047±07	pn	dd
$K^{39}-Ca^{42}$	2.99669±40	αp	ee
$K^{42}-Ca^{42}$	0.00383±20	β^-	v
$K^{43}-Ca^{43}$	0.000868±03	β^-	ff
$Sc^{41}-Ca^{41}$	0.00630±20	β^+	b
$Sc^{43}-Ca^{43}$	0.00226±25	β^+	gg
$Ca^{40}-Sc^{43}$	3.00036±40	αp	ee
$K^{41}-K^{41}$	1.00109±10	αp	hh
$Ca^{40}-A^{40}$	0.00032±08	mass-spectros.	ii

[a] E. C. Pollard, Phys. Rev. **57**, 1086 (1940).
[b] D. R. Elliott and L. D. P. King, Phys. Rev. **59**, 403 (1941); White, Creutz, Delasso, and Wilson, Phys. Rev. **59**, 63 (1941).
[c] K. Siegbahn, Phys. Rev. **70**, 127 (1946).
[d] E. C. Pollard and C. J. Brasefield, Phys. Rev. **51**, 8 (1937).
[e] W. Zunti and E. Bleuler, Helv. Phys. Acta **18**, 263 (1945).
[f] P. Davison, Phys. Rev. **74**, 1233 (1948).
[g] C. H. Townes and S. Geschwind, Phys. Rev. **74**, 626 (1948).
[h] W. Low and C. H. Townes, Phys. Rev. **75**, 529 (1949).
[i] C. J. Brasefield and E. C. Pollard, Phys. Rev. **50**, 296 (1936).
[j] See reference 18.
[k] R. T. Overman, *Radio Activities Produced in Neutron Irradiation o Chlorine* AECD 857 (1947). C. S. Wu and L. Feldman, Phys. Rev. **76**, 693 (1949).
[l] Zah Wei Ho, Phys. Rev. **70**, 782 (1946).
[m] See references 15 and 16.
[n] See reference 18.
[o] C. H. Townes and R. Shulman, private communication.
[p] See reference 18.
[q] A. Zucker and W. W. Watson, Phys. Rev. **79**, 241 (1950).
[r] See references 18 and 22.
[s] N. Hole, Arkiv. Mat. Astron. Fysik **32A**, No. 3 (1945).
[t] Ramsey, Meem, and Mitchell, Phys. Rev. **72**, 639 (1947).
[u] E. C. Pollard and P. W. Davison, Phys. Rev. **73**, 1241 (1948).
[v] Bleuler, Bollman, and Zunti, Helv. Phys. Acta **19**, 419 (1946); **20**, 96 (1947).
[w] H. T. Richards and R. V. Smith, Phys. Rev. **74**, 1870 (1948).
[x] O. Hizel and H. Waffler, Helv. Phys. Acta **19**, 216 (1946).
[y] See reference 21a.
[z] See reference 20.
[aa] Dzelepow, Kopjova, and Vorobjov, Phys. Rev. **69**, 538 (1946).
[bb] D. E. Alburger, Phys. Rev. **79**, 236 (1950).
[cc] See reference 21.

the experimental and computed masses against A for various Z and N. Tables I and II summarize data employed for determination of the masses, the mass values, estimates of their probable errors, and the references. Figure 3 indicates the experiments which relate the various nuclear masses.

TABLE II. Atomic masses based on Table I.*

Standard: $S^{32} = 31.98089$, $A^{40} = 39.97516$

Nucleus	Mass, based on Table I	Comment	Masses computed from Bohr-Wheeler formula	Δ difference in m.m.u.
P^{31}	30.98239±40	Average of $P^{31}\alpha pS^{34}$ and $P^{31}dpP^{32}$ reactions	30.98218	0.21
P^{32}	31.98268±20		31.98315	−0.47
P^{34}	33.98326±25		33.98219	0.07
S^{31}	30.98758±50		30.98756	0.02
S^{32}	31.98089	Standard all nuclei from P^{31} to A^{40} calculated with respect to S^{32}	31.98051	0.38
S^{33}	32.98058±10		32.98011	0.47
S^{34}	33.97780±20	Average of microwave and $S^{32}-dp-S^{33}$ reaction	33.97566	2.14
S^{35}	34.97907±45		34.97649	2.58
S^{36}	35.97834±40		35.97510	3.24
S^{37}	36.98111±50		36.97866	2.45
Cl^{33}	32.98607±10		32.98575	0.32
Cl^{34}	33.98436±25		33.98391	0.45
Cl^{35}	34.97889±40	Average of $S^{32}-\alpha p-Cl^{35}$ and $S^{33}-d\alpha-Cl^{35}$	34.97817	0.72
Cl^{36}	35.97892±50	Average of $Cl^{35}dpCl^{36}$ and microwave data	35.97855	+0.37
Cl^{37}	36.97640±50		36.97503	1.37
Cl^{38}	37.97868±55		37.97728	1.40
A^{35}	34.98468±50		34.98406	0.63
A^{36}	35.97822±55		35.97717	1.05
A^{38}	37.97320±60	Average of $Cl^{35}\alpha pA^{38}$ and $Cl^{38}\beta^-A^{38}$ reactions	37.97138	1.82
A^{40}	39.97516±26	Standard, reevaluated using references 10, 11 (Mattauch)	39.97020	4.96
A^{41}	40.97765±05		40.97293	4.72
K^{38}	37.97905±70	Assuming β^+ and γ are in cascade	37.98035	−1.30
K^{39}	38.97613±30		38.97460	+1.53
K^{40}	39.97683±10		39.97446	2.37
K^{41}	40.97491±25		40.97075	4.16
K^{42}	41.97600±30		41.97235	3.65
K^{43}	42.97433±65		42.97038	3.95
A^{37}	36.9783 ±60		35.97634	1.49
Ca^{39}	38.98232±40	Theoretical value using $\beta^+ = 4.8$ Mev.	38.98100	+1.32
Ca^{40}	39.97546±08		39.97701	−1.55
Ca^{41}	40.97543±12		40.97299	2.44
Ca^{42}	41.97217±35		41.96829	3.88
Ca^{43}	42.97346±55		42.96888	4.58
Sc^{41}	40.98173±35		40.97955	2.18
Sc^{43}	42.97572±50		42.97141	4.29

* Note that masses and errors given are not absolute values, but are relative to the masses chosen for S^{32} and A^{40}.

[dd] H. T. Richards and R. V. Smith, Phys. Rev. **74**, 1257 (1948).
[ee] E. C. Pollard and E. J. Brasefield, Phys. Rev. **51**, 8 (1937).
[ff] G. T. Seaborg and I. Perlman, Rev. Mod. Phys. **20**, 589 (1948).
[gg] Hibdon, Pool, and Kurbatov, Phys. Rev. **67**, 289 (1945).
[hh] See reference 21a.
[ii] See reference 20a.

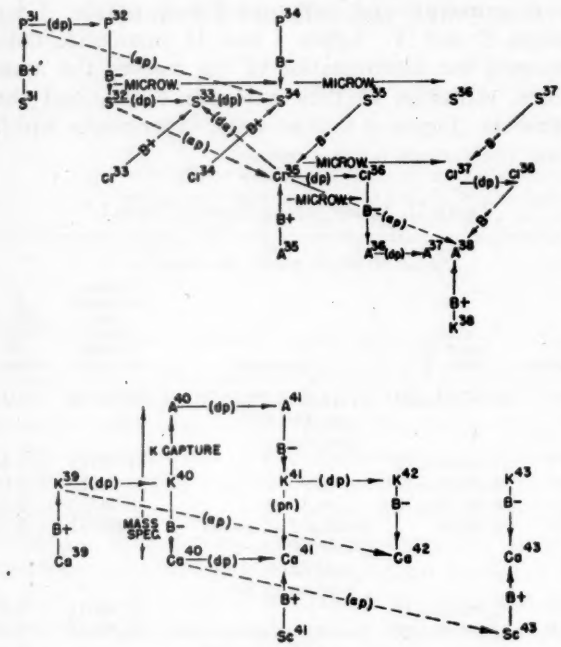

FIG. 3. Known connections between masses of certain nuclei.

II. DISCUSSION OF MASS DETERMINATIONS

All masses from P^{31} to A^{40} have been calculated with respect to the mass of $S^{32}=31.98089$. The masses from argon to scandium have been computed with respect to A^{40}. The mass of A^{40} has been taken as 39.97516 ± 0.00028 determined from the doublet[10] $(Ne-A/2)=111.42\times10^{-4}\pm0.38$ and using[11] $Ne^{20}=19.99872\pm0.00013$. All reactions used for the determination of masses have been recalculated using Bainbridge's values[11] for the masses of H, n, D, and α. The mass values of a few nuclei require further explanations as given below.

S^{31}.—S^{31} is positron active and has been determined with respect to S^{32} through the mass of P^{31}, as is indicated in Fig. 3. The P^{31} mass obtained is 30.98238 ± 45 or 30.98240 ± 40 for the reaction paths involving S^{34} or P^{32} respectively. The S^{31} mass is obtained immediately from P^{31}.

Cl^{35}.—The mass of Cl^{35} can be determined from two different reactions as shown in Fig. 3. From the αp reaction $Cl^{35}=34.97889\pm40$ and from the $d\alpha$-reaction $Cl^{35}=34.97888\pm40$. For the αp reactions Bethe's revised Q values have been used throughout.[12]

Cl^{37}.—The Cl^{37} mass is determined from the mass ratio of Cl^{35}/Cl^{37}. Unfortunately there are different values for this ratio from mass spectroscopy and microwave spectroscopy. A recent mass spectroscopic determination[13] of this ratio gives the value as 0.9459441±65 (Aston[14] had found earlier the ratio as 0.9459806, but his experimental error is stated as ±300). This value disagrees with the values obtained from microwave measurements[15,16] in ICl and FCl which give 0.9459801±50 and 0.9459775±40 respectively. Isotopic frequencies for Cl^{35}, Cl^{36}, and Cl^{37} in the molecule ClCN have also been measured.[16a] With these and a knowledge of the mass difference $Cl^{35}-Cl^{36}$ (obtained from Cl^{35} dp Cl^{34} reaction) one finds this ratio $Cl^{35}/Cl^{37}=0.9459906\pm120$ in agreement with other microwave results. Moreover, an evaluation of this ratio from transmutation data[17,18] leads to a value in essential agreement with microwave results. Hence the most recent mass spectroscopic value must be in error. Table III summarizes these results.

A^{38}.—A^{38} may be determined from Cl^{35} with an α,p reaction and from the beta-decay of Cl^{38}. The values are 37.97332 and 33.97322 ± 60 respectively.

K^{38}.—K^{38} gives off a positron of 2.53 Mev and a γ-ray of 2.15 Mev. We assume that these are in cascade.

Ca^{39}.—Ca^{39} belongs to a class of nuclei with $Z-N=1$ which are positron active. These "mirror" nuclei have been studied extensively; their half-lives and positron energies form a very regular and apparently well-understood series. The half-life of Ca^{39} has been measured recently[19] and is 1.06 sec. in good agreement with expectations from this series. Hence the predicted[20] but still unmeasured† value of 4.8 Mev for the positron energy seems to us very reliable for obtaining the mass difference $K^{39}-Ca^{39}$.

Ca^{40}.—The mass difference $Ca^{40}-A^{40}$ has recently been obtained as $(3.2\pm0.8)\times10^{-4}$ from mass spectroscopy[20a] and as $(2.7\pm2.1)\times10^{-4}$ from nuclear reactions.[21]

K^{43}, $Ca^{42,43}$, Sc^{43}, Ca^{42}.—The Ca^{42} mass has been determined from beta-decay of K^{42}. From the measurement by Sailor[21a] of the mass difference $K^{42}-K^{41}$ one obtains for the mass of Ca^{42} $=41.97217\pm35$. If the K^{39} αp Ca^{42} reaction reported by Pollard and Brasefield[22] is used, a value 41.97293 ± 50 results. This gives support to Bethe's suggestion[12] that the αp reaction measured does not represent a transition to the ground state. Similarly, it is not quite certain whether the observed Ca^{40} αp Sc^{43} reaction represents a transition to the ground state, and therefore, the

TABLE III. Value of Cl^{35}/Cl^{37} ratio.

Name	Method	Value
Aston[a]	Mass spectroscopy	0.9459806±300
Okuda *et al.*[b]	Mass spectroscopy	0.9459452± 65
Townes *et al.*[c]	Microwave (ICl)	0.9459801± 50
Roberts *et al.*[d]	Microwave (FCl)	0.9459775± 40
Townes *et al.*[e]	Microwave (ClCN)	0.9459906±120
Pollard[f]	Nuclear reaction	0.9459893±110

[a] See reference 14.
[b] See reference 13.
[c] See reference 15.
[d] See reference 16.
[e] Townes and Shulman, private communication.
[f] See references 17 and 18.

[10] J. Mattauch, *Nuclear Physics Tables* (Interscience Publishers, Inc., New York, 1942).
[11] K. Bainbridge, *Isotopic Weights of the Fundamental Isotopes, Nuclear Science Series* (Nat. Res. Council, 1949).
[12] M. S. Livingston and H. A. Bethe, Rev. Mod. Phys. **9**, 300 (1937).
[13] Okuda, Ogata, Aoki, and Sugawara, Phys. Rev. **58**, 578 (1940).
[14] F. W. Aston, Proc. Roy. Soc. **162A**, 191 (1937).
[15] Townes, Merritt, and Wright, Phys. Rev. **73**, 1334 (1948).
[16] Gilbert, Roberts, and Griswold, Phys. Rev. **76**, 1721 (1949).
[16a] We are grateful for the help of Dr. R. G. Shulman in measuring the difference in B_0 values for $Cl^{35}CN$ and $Cl^{36}CN$ as 63.51±0.02 Mc. The similar difference for $Cl^{35}CN$ and $Cl^{37}CN$ is 123.56 Mc. [Townes, Holden, and Merritt, Phys. Rev. **74**, 1123 (1948).]
[17] E. C. Pollard, Phys. Rev. **57**, 1086 (1940).
[18] J. H. Shrader and E. C. Pollard, Phys. Rev. **59**, 277 (1941).
[19] Huber, Leinhardt, Scherrer, and Waffler, Helv. Phys. Acta **16**, 33 (1943).
[20] E. Wigner, private communication to Walke, Phys. Rev. **57**, 177 (1940).
† L. Motz has pointed out to us the determination of the (γ, n) threshold for Ca^{40} as 15.9±0.4 Mev by McElhinney, Hanson, Becker, Duffield, and Diven, Phys. Rev. **75**, 542 (1949). This would give Ca^{39} the surprisingly large mass of 38.9362 ± 40, but would not appreciably modify other conclusions presented here.
[20a] T. R. Roberts and A. O. C. Nier, Phys. Rev. **79**, 198 (1950).
[21] V. L. Sailor, Phys. Rev. **75**, 1836 (1949).
[21a] V. L. Sailor, Phys. Rev. **77**, 749 (1950).
[22] E. C. Pollard and C. J. Brasefield, Phys. Rev. **51**, 8, (1937).

masses of Ca^{43}, K^{43}, and Sc^{43} given in Table I may be somewhat too high.

III. DISCUSSION OF RESULTS

Figures 1 and 2 show that although there is considerable deviation of the measured masses from the Bohr-Wheeler formula, all deviations with the exception of the value for Ca^{40} lie on relatively smooth curves. The deviations from the curves are not generally larger than 0.5 Mev. There seems to be no abrupt change of mass or of slope of the curves of mass *versus* neutron number near S^{36}, Cl^{37}, A^{38}, or K^{39}, all of which are atoms with 20 neutrons. Similarly, there is no evidence of shell structure at 20 protons from the curves of mass *versus* proton number, except in the case of Ca^{40} which shows a striking deviation from the smooth curves of about 3.5 Mev. This deviation is far greater than the probable error of mass determinations or than the deviation of any other nucleus plotted.

The absence of any change in slope at 20 nucleons makes it rather questionable whether 20 nucleons should be regarded as the closing point of a major shell. The well-known stability of Ca^{40} seems not to be simply connected with the completion of a shell at 20 nucleons. This case indicates that some large deviations from the stability curve may be encountered for other nuclei which are not attributable to neutron or proton shells alone but depend on the combination of neutron and proton numbers. Perhaps the large mass spread of stable Ca isotopes is due to this exceptional stability of Ca^{40} and to a shell at 28 neutrons which makes Ca^{48} stable rather than to a general stability of 20 protons.

PHYSICAL REVIEW VOLUME 80, NUMBER 4 NOVEMBER 15, 1950

On a Difference Equation Method in Cosmic-Ray Shower Theory*

W. T. Scott
Smith College, Northampton, Massachusetts
and
Brookhaven National Laboratory, Upton, New York
(Received May 29, 1950)

The recent results of Snyder and Bhabha-Chakrabarty for the cascade theory of cosmic-ray showers are shown to be derivable from a general approach involving the use of the Laplace and Mellin transforms, and a general and powerful method, due to Snyder, for solving the resulting difference equations. Boundary conditions are introduced in a natural and automatic way, and the accuracy of the solution is limited by the possible ways of evaluating the resulting triple complex integral.

I. INTRODUCTION

SNYDER[1] has recently obtained numerical results for the cascade theory of electron-photon showers which appear to be considerably more accurate than those of Bhabha and Chakrabarty.[2] It is the object of this paper to present a general method of solving the shower equations which yield both of the above-mentioned solutions, and which should be applicable to a number of other problems.

II. THEORY

Using Snyder's[1] notation, we write the diffusion equation for $P(E,t)$, the mean energy spectrum of electrons at depth t, and $\gamma(E,t)$, the mean energy spectrum of photons:

$$\frac{\partial P(E,t)}{\partial t}=\lim_{\delta\to 0}\left[\int_{E+\delta}^{\infty}P(E',t)R(E',E'-E)\frac{E'-E}{E'^2}dE' - P(E,t)\int_{\delta}^{E}R(E,E')\frac{E'dE'}{E^2}\right]+\beta\frac{\partial P(E,t)}{\partial E} +2\int_{E}^{\infty}\gamma(E',t)R(E,E')\frac{dE'}{E'}, \quad (1)$$

$$\frac{\partial \gamma(E,t)}{\partial t}=\int_{E}^{\infty}P(E',t)R(E',E)\frac{EdE'}{E'^2} -\gamma(E,t)\int_{0}^{E}R(E',E)\frac{dE'}{E}. \quad (2)$$

In these equations $R(E',E)$ is a function which yields the elementary probabilities per unit path length of the pair-production and bremsstrahlung processes. In the case of high energies, the asymptotic form of R is that of a function homogeneous in E/E'; this is the only case dealt with in the present treatment.

* This work was started in 1940 (Ph.D. Thesis, University of Michigan, 1941). It was completed at the Brookhaven National Laboratory, under the auspices of the AEC.

[1] H. S. Snyder, Phys. Rev. **76**, 1563 (1949).

[2] H. J. Bhabha and S. K. Chakrabarty, Phys. Rev. **74**, 1352 (1948).

Here β is the ionization or collision loss per unit path length, and is taken to be a constant. Its inclusion is essential. Solutions of the equations for $\beta=0$ are obtained easily, but are fundamentally different from those for *any* finite value of β, since for $\beta=0$ there is no removal of particles from the showers defined by Eqs. (1) and (2). In what follows, we shall measure energy in units of β by introducing $x=E/\beta$; where an initial energy E_0 is used, we write $x_0=E_0/\beta$. The resulting equations differ from (1) and (2) only by the replacement of E's by x's and the suppression of β.

The method here presented consists in applying both a Laplace transformation in t and a Mellin transformation in E, and then solving the resulting difference equation. Following the usual practice for Laplace transforms, we shall denote by s the transformed variable corresponding to t. The variables referred to by various authors as (λ, μ), (λ_1, λ_2) or (μ, ν) will appear later on after evaluation of the Laplace inversion integral by the calculus of residues. The variable for the Mellin transform we then call p.

Let us, therefore, set

$$g(p,s)=\int_0^\infty e^{-st}dt\int_0^\infty x^p dx P(x,t),$$
$$\theta(p,s)=\int_0^\infty e^{-st}dt\int_0^\infty x^p dx \gamma(x,t). \tag{3}$$

Multiply Eqs. (1) and (2) by $e^{-st}dtx^pdx$ and integrate over x and t. We find

$$\begin{aligned} sg(p,s)-\varphi_P(p)&=-A(p)g(p,s)\\ &\quad +B(p)\theta(p,s)-pg(p-1,s), \qquad (4)\\ s\theta(p,s)-\varphi_\gamma(p)&=C(p)g(p,s)-D\theta(p,s).\end{aligned}$$

The functions $A(p)$, $B(p)$, $C(p)$ and the constant D are given by Snyder[1] and by Rossi and Greisen.[3] $\varphi_P(p)$ is the Mellin transform of the initial spectrum of particles, and $\varphi_\gamma(p)$ is that for the photons:

$$\varphi_P(p)=\int_0^\infty P(x,0)x^p dx, \quad \varphi_\gamma(p)=\int_0^\infty \gamma(x,0)x^p dx.$$

It is to be noticed, first, that the form of Eqs. (4) depends on the homogeneity property of the asymptotic cross-sections; second, that this method brings the initial conditions in automatically and exactly; third, that the term $-pg(p-1,s)$ results from the collision loss term $\beta\partial P/\partial t$ and is the main source of difficulty with this approach.[4]

Equations (4) can be solved for g:

$$pg(p-1,s)+\left[s+A(p)-\frac{B(p)C(p)}{s+D}\right]g(p,s)=\varphi(p,s), \tag{5}$$

where

$$\varphi(p,s)=\frac{B(p)\varphi_\gamma(p)}{s+D}+\varphi_P(p). \tag{6}$$

$\theta(p,s)$ is given by

$$\theta(p,s)=\frac{C(p)g(p,s)+\varphi_\gamma(p)}{s+D}. \tag{7}$$

In what follows, we shall deal only with $g(p,s)$ inasmuch as exactly similar results for $\theta(p,s)$ can be found by using (7). We shall also suppress the letter s in $\varphi(p,s)$ for brevity. Finally, we write for the square bracket in (5)

$$G(p,s)=s+A(p)-\frac{B(p)C(p)}{s+D}\equiv\frac{[s-\mu(p)][s-\nu(p)]}{s+D}, \tag{8}$$

where μ and ν are functions given by Snyder[1] [his Eq. (17)], by Rossi and Greisen,[3] who call them λ_1 and λ_2, and by Bhabha and Chakrabarty,[2] who call them $-\lambda(p+1)$ and $-\mu(p+1)$. As $|p|\to\infty$, $G(p,s)\sim c_1\ln p$, where c_1 is a constant.

We thus have to solve the difference equation

$$pg(p-1,s)+G(p,s)g(p,s)=\varphi(p). \tag{9}$$

The condition on $g(p,s)$ which determines the particular one of the infinite manifold of solutions of (9) that yields the desired solutions of Eqs. (1) and (2) is that $g(p,s)$ must be a proper Mellin transform function in p. From (3) we see that, if the initial spectrum of particles contains none above $x_0=E_0/\beta$, then $g(p,s)$ increases as $p\to\infty$ less rapidly than x_0^p. That is, $x_0^{-p}g(p,s)\to 0$ as $p\to+\infty$. Consequently, we can solve (9) by iteration for $g(p,s)$, successively replacing p by $p+1$, $p+2$, $p+3$, $\cdots$, and eliminating the intermediate values of $x_0^{-p-m}g(p+m,s)$. We obtain in this way an infinite series, with a remainder which approaches zero. In the final result, x_0^{-p} can be factored out, and we have a convergent series

$$g(p,s)=\frac{\varphi(p+1)}{p+1}-\frac{\varphi(p+2)G(p+1,s)}{(p+1)(p+2)}+\frac{\varphi(p+3)G(p+1,s)G(p+2,s)}{(p+1)(p+2)(p+3)}-\cdots$$
$$+(-1)^m\frac{\varphi(p+m+1)G(p+1,s)G(p+2,s)\cdots G(p+m,s)}{(p+1)(p+2)\cdots(p+m+1)}+\cdots. \tag{10}$$

This series yields an appropriate Mellin transform in p, which can, in fact, be integrated termwise. But the mth term as a function of s behaves like s^m, and cannot be used in the Laplace inversion integral, which requires that the Laplace transform vanish as s^{-1} as $s\to+\infty$.

[3] B. Rossi and K. Greisen, Rev. Mod. Phys. 13, 240 (1941).

[4] F. L. Friedman, Cosmic Ray Shower Theory, MIT Laboratory for Nuclear Science and Engineering, Tech. Rpt. 31, pp. 43–45.

Thus we must sum the series (10), or obtain another representation for it. We shall first write the general term in such a way that we can replace the integer m by a complex variable σ, so that we can in the well-known way convert the series into a contour integral.

Now, the mth term of (10) contains m factors G in the numerator. Just as the denominator can be written as a ratio of two gamma-functions to suppress the variable number of factors, so we shall use the ratio of two new functions (definable as infinite products) to rewrite the numerator.

For the denominator, we have

$$(p+1)(p+2)\cdots(p+m+1)=\frac{\Gamma(p+m+2)}{\Gamma(p+1)}. \quad (11)$$

with $p\Gamma(p)=\Gamma(p+1)$.

For the numerator, we shall take

$$G(p+1,s)G(p+2,s)\cdots G(p+m,s)=\frac{L(p+m+1,s)}{L(p+1,s)} \quad (12)$$

where $L(p,s)$ must satisfy the recursion relation

$$G(p,s)L(p,s)=L(p+1,s). \quad (13)$$

Snyder[5] has shown how to solve equations of type (13) in a very general way for general values of p in terms of infinite products. His solution for this case can be written as follows:

$$L(p,s)=G(b,s)^{p-a}\lim_{N\to\infty}\prod_{j=0}^{N}\frac{G(a+j,s)}{G(p+j,s)}\times\left\{\frac{G(b+j+1,s)}{G(b+j,s)}\right\}^{p-a}$$

$$=\lim_{N\to\infty}G(b+N+1,s)^{p-a}\prod_{j=0}^{N}\frac{G(a+j,s)}{G(p+j,s)}. \quad (14)$$

The infinite product is convergent for a wide class of functions G. Indeed, if G satisfies a relation of the form

$$\frac{G(p_1+j,s)}{G(p_2+j,s)}=1+O\left(\frac{1}{j}\right)\quad\text{as}\quad j\to\infty \quad (15)$$

for any p_1, p_2 and s, the infinite product will be convergent.[6] Functions which behave like $p^{\pm r}$, $\ln p$, $p^{\pm r}e^{\lambda p}$, etc., will thus yield convergent products.

To see that (14) satisfies (13), write

$$\frac{L(p+1,s)}{L(p,s)}=G(b,s)\lim_{N\to\infty}\prod_{j=0}^{N}\frac{G(p+j,s)}{G(p+j+1,s)}\frac{G(b+j+1,s)}{G(b+j,s)}$$

$$=G(b,s)\lim_{N\to\infty}\left\{\frac{G(p,s)}{G(p+N+1,s)}\frac{G(b+N+1,s)}{G(b,s)}\right\}$$

$$=G(p,s)$$

by Eq. (15). Here a is a constant which merely determines that value of p for which $L=1$. When $p-a$ is an integer, (14) reduces to a finite product. Also, b is a convergence-controlling number which does not affect the value of L, since

$$\lim_{N\to\infty}\left[\frac{G(b_1+N+1,s)}{G(b_2+N+1,s)}\right]^{p-a}=1$$

(excepting the case of reference 6). We may, in fact, write the factor $G(b+N+1)^{p-a}$ as a product of several factors with different values of b and different exponents, provided the sum of the exponents is $p-a$. These values of b and the corresponding exponents can be so chosen that the product in (14) yields exact values *for any* N at specified values of p. Then for neighboring values of p the convergence will be especially rapid, and (14) will be useful for numerical work.[7]

For $G(p,s)=p$, L becomes $\Gamma(p)$; values calculated in the manner aforementioned yield extremely rapid convergence.[8]

A useful asymptotic expression for $L(p,s)$ may be obtained by writing $\ln G(p,s)=\ln L(p+1,s)-\ln L(p,s)\simeq\partial/\partial p[\ln L(p,s)]$ and using $G(p,s)\simeq c_1\ln p$ yielding on integration

$$L(p,s)\simeq(c_1\ln p)^p \quad (16)$$

as $|p|\to\infty$.[9]

We may now write the mth term of the series (10) in a form which does not involve a variable number of factors, and which allows m to be replaced by σ. To make the writing simpler, we shall first write

$$\frac{L(p+m+1,s)}{L(p+1,s)}=Q(p+1,m,s)$$

$$=G(b,s)^m\prod_{j=0}^{\infty}\frac{G(p+j+1,s)}{G(p+j+m+1,s)}\left\{\frac{G(b+j+1,s)}{G(b+j,s)}\right\}^m. \quad (17)$$

$Q(p+1,m,s)$ obeys the recursion relations

$$G(p,s)Q(p+1,m,s)=Q(p,m+1,s) \quad (18a)$$

and

$$G(p+m,s)Q(p,m,s)=Q(p,m+1,s). \quad (18b)$$

We also have

$$Q(p,0,s)=1. \quad (19)$$

The series (10) for $g(p,s)$ now becomes

$$g(p,s)=\sum_{m=0}^{\infty}(-1)^m\varphi(p+m+1)\frac{\Gamma(p+1)}{\Gamma(p+m+2)}\times Q(p+1,m,s), \quad (20)$$

[5] H. S. Snyder, Phys. Rev. **75**, 906 (1949).

[6] If $G=e^{\lambda p}$ where λ is any function of s, the convergence is trivial. If a factor $e^{\lambda p}$ is included in G, (15) will be altered by a factor $e^{\lambda(p_1-p_2)}$ but the convergence will be unaffected.

[7] See Eq. (25) of reference 1, and the discussion following.

[8] H. S. Snyder (private communication).

[9] I wish to thank Mr. I. Bernstein for informing me of this asymptotic expression.

and we can write $g(p, s)$ as a contour integral as follows

$$g(p, s)=\frac{1}{2\pi i}\int_{C_\sigma} d\sigma \frac{\pi}{\sin\pi\sigma}\frac{\phi(p+\sigma+1)\Gamma(p+1)}{\Gamma(p+\sigma+2)} \times Q(p+1, \sigma, s). \quad (21)$$

where C_σ is a contour from $+\infty$ around the origin in the positive sense, and back to $+\infty$. It is readily shown that the contour can be shifted to C_σ', a contour parallel to the imaginary axis, cutting the real axis between -1 and 0. The negative of the integral must be taken if C_σ' is described in the usual positive sense.

Since $Q(p+1. \sigma, s)$ behaves like s^σ for large $|s|$, we see that the integral over σ will in general behave like s^δ where $-1<\delta<0$. We can now write the inverse Laplace and Mellin transforms, since we have the correct behavior in s and p:

$$P(x, t)=\frac{-1}{(2\pi i)^2}\int_{C_s} e^{st}ds\int_{C_p} x^{-p-1}dp\int_{C_{\sigma'}} d\sigma\frac{\pi}{\sin\pi\sigma} \times\frac{\Gamma(p+1)}{\Gamma(p+\sigma+2)}Q(p+1, \sigma, s)\varphi(p+\sigma+1) \quad (22)$$

where C_s and C_p are contours parallel to the imaginary axis in the s-plane and p-plane, respectively, each taken to the right of all singularities. A similar formula can easily be obtained for $\gamma(E, t)$.

We thus have achieved a solution of our problem, Eqs. (1) and (2), in the form of triple complex integrals. The evaluation of these integrals is naturally not simple. One can evaluate one integral as a series of residues, reduce a second by restricting our attention to finding an integral spectrum for the total number of particles (or for low energies, expanding by residues again in powers of x) and calculate the last integral by the method of steepest descents. It is also possible to use a double saddle-point method for two integrals simultaneously.[2]

We shall first show how Snyder's result can be obtained. We shall restrict ourselves to electron-initiated showers, with

$$P(x, 0)=\delta(x-x_0); \quad \gamma(x, 0)=0, \quad (23)$$

or $\phi(p, s)=x_0{}^p$.

The first step is to evaluate the s integral, interchanging the order of integration. Let us write $m=\sigma$ in (17), set $b=0$ and use (8).

$$Q(p+1, \sigma, s)=\lim_{N\to\infty}\frac{[s-\mu(N+1)]^\sigma[s-\nu(N+1)]^\sigma}{[s+D]^\sigma} \times\prod_{j=0}^{N}\frac{[s-\mu(p+j+1)][s-\nu(p+j+1)]}{[s-\mu(p+\sigma+j+1)][s-\nu(p+\sigma+j+1)]}. \quad (24)$$

Poles occur for

$$\left.\begin{aligned} s&=\mu(p+n+\sigma+1)\\ \text{and}\quad s&=\nu(p+n+\sigma+1)\end{aligned}\right\} n=0, 1, 2, \cdots. \quad (25)$$

As $p\to\infty$, $\mu(p)\to -D$, $\nu(p)\to-\infty$ so the point $s=-D$ is the limit point of one series of poles, and need not be treated itself. The residue of Q at $s=\mu(p+n+\sigma+1)$ is then

$$\lim_{N\to\infty}\left\{\frac{[\mu(p+n+\sigma+1)-\mu(N+1)]^{\sigma+n+1}[\mu(p+n+\sigma+1)-\nu(N+1)]^{\sigma+n+1}}{[\mu(p+n+\sigma+1)+D]^\sigma}\right\} \cdot\left\{\prod_{j=0}^{N}\frac{[\mu(p+n+\sigma+1)-\mu(p+j+1)][\mu(p+n+\sigma+1)-\nu(p+j+1)]}{[\mu(p+n+\sigma+1)-\mu(p+\sigma+n+j+2)][\mu(p+n+\sigma+1)-\nu(p+\sigma+n+j+2)]}\right\} \cdot\left\{\frac{\prod_{k=0}^{n}[\mu(p+n+\sigma+1)-\mu(p+N+\sigma+k+2)][\mu(p+n+\sigma+1)-\nu(p+N+\sigma+k+2)]}{[\mu(p+n+\sigma+1)-\mu(N+1)]^{n+1}[\mu(p+n+\sigma+1)-\nu(N+1)]^{n+1}}\right\} \cdot\left\{\frac{1}{\mu(p+n+\sigma+1)-\nu(p+n+\sigma+1)}\prod_{l=0}^{n-1}\frac{1}{[\mu(p+n+\sigma+1)-\mu(p+l+\sigma+1)][\mu(p+n+\sigma+1)-\nu(p+l+\sigma+1)]}\right\} \quad (26)$$

where the third brace { } contains factors that cancel with those added in the second brace to maintain symmetry. The factors dividing this third product are also inserted in the first numerator; they allow the

expression in the third brace to approach 1 as $N\to\infty$. Thus we may write, using (24) to shorten the writing,

$$P(x,t)=\frac{-1}{(2\pi i)^2}\int_{C_p}\left(\frac{x_0}{x}\right)^{p+1}\Gamma(p+1)dp\int_{C_\sigma'}\frac{\pi d\sigma}{\sin\pi\sigma}\,\frac{x_0{}^\sigma}{\Gamma(p+\sigma+2)}\,\frac{1}{\mu(p+n+\sigma+1)-\nu(p+n+\sigma+1)}$$
$$\cdot\sum_{n=0}^{\infty}\left\{\frac{e^{\mu(p+n+\sigma+1)t}[\mu(p+n+\sigma+1)+D]^{n+1}Q(p+1,\,\sigma+n+1,\,\mu(p+n+\sigma+1))}{\prod_{l=0}^{n-1}[\mu(p+n+\sigma+1)-\mu(p+l+\sigma+1)][\mu(p+n+\sigma+1)-\nu(p+l+\sigma+1)]}\right.$$
$$\left.-\frac{e^{\nu(p+n+\sigma+1)t}[\nu(p+n+\sigma+1)+D]^{n+1}Q(p+1,\,\sigma+n+1,\,\nu(p+\sigma+n+1))}{\prod_{l=0}^{n-1}[\nu(p+n+\sigma+1)-\mu(p+l+\sigma+1)][\nu(p+n+\sigma+1)-\nu(p+l+\sigma+1)]}\right\}. \quad (27)$$

Equation (27) is identical with Snyder's[1] Eq. (38) as can be seen if we write

$$\sigma+n+1=-s \quad \text{(Snyder's } s\text{, not ours!)}$$
$$p+\sigma+n+1=y;\quad dp=dy. \quad (28)$$

We then set

$$Q(p+1,\,\sigma+n+1,\,\mu(p+n+\sigma+1))=Q(y+s-1,\,-s,\,\mu(y))=\frac{K_\mu(y,s)}{\Gamma(s+1)}, \quad (29)$$

and

$$Q(p+1,\,\sigma+n+1,\,\nu(p+n+\sigma+1))=K_\nu(y,s)/\Gamma(s+1).$$

We use the formulas for Snyder's $A_n(y)$ and $B_n(y)$ given in the note at the end of his paper. Finally, we can use Snyder's arguments to justify displacing the contour for the y integration n places to the left, to bring it from having a real part $n+\epsilon$ to having a real part ϵ, $1>\epsilon>0$.

To arrive at the Bhabha-Chakrabarty result,[2] we shall write in (22), $p+\sigma+2=\lambda$, $dp=d\lambda$ (λ is identical with Bhabha-Chakrabarty's s), and keep the λ-integration path fixed by shifting the p contour C_p to the right as C_σ' is shifted to the left. We evaluate the σ integral first, at the poles $\sigma=-m-1$, $m=0,\,1,\,2,\,\cdots$. The resulting series is divergent, but if we take only a finite number of poles, leaving a remainder, and then carry out the inverse Laplace transform on each term, the resulting series of p integrals is convergent. Thus we write, after taking residues in σ,

$$P(x,t)=\sum_{m=0}^{\infty}\frac{x^{-m}}{2\pi i x_0}\int dx\left(\frac{x_0}{x}\right)^{\lambda}\frac{\Gamma(\lambda+m)}{\Gamma(\lambda)}(-1)^m\frac{1}{2\pi i}$$
$$\times\int_{C_s}e^{st}ds\,Q(\lambda+m,\,-m-1,\,s). \quad (30)$$

Using (18a) and (19) repeatedly, we see that

$$Q(\lambda+m,\,-m-1,\,s)=\prod_{k=0}^{m}\frac{1}{G(\lambda+k-1,\,s)}, \quad (31)$$

and that the functions

$$\psi_m(\lambda,t)=\frac{1}{2\pi i}\int_{C_s}e^{st}ds\,Q(\lambda+m,\,-m-1,\,s) \quad (32)$$

may be found by the theorem of convolution integrals (faltungs-integrals) from

$$\psi_0(\lambda,t)=\frac{1}{2\pi i}\int e^{st}ds\frac{s+D}{[s-\mu(\lambda-1)][s-\nu(\lambda-1)]}. \quad (33)$$

Equation (33) readily yields $B-C$'s formula (8),[2] and their convolution integrals (11) and (13) are readily deduced from Eqs. (31), (32) and (33). We thus arrive at their expression (14) for the electron spectrum, and may treat it as they did.

The methods of this paper are clearly applicable to a rather general class of differential-integral equations, and in particular should be useful for further work in cascade theory. In fact, Bernstein has shown[10] that corrections to Snyder's results can be made by methods related to those of this paper, using more accurate but inhomogeneous cross sections for the elementary processes.

[10] I. Bernstein, Ph.D. Thesis, New York University (1950).

The Differential Range Spectrum of Cosmic-Ray Mesons*

LAWRENCE GERMAIN†
Department of Physics, University of California Berkeley, California
(Received May 18, 1950)

A counter-controlled cloud chamber has been used to investigate the differential range spectrum of mesons at sea level. The chamber contains eight lead plates each 7½ in. wide and one-half in. thick. A lead absorber of variable thickness, up to 27 in., may be placed above the chamber. The number of mesons observed the stop in the chamber per unit time has been found for various thicknesses of absorber above the chamber. A plot of the counting rate of particles which stop *versus* the thickness of absorber above the chamber reveals a broad low peak which has its maximum at a 6-in. thickness of absorber. The counting rate at the peak is 2.20×10^{-6} count/sec./sterad/g, about 10 percent higher than the counting rate with no absorber. Correction has been made for particles lost through scattering in the absorber. The corrected results show a more marked peak whose maximum occurs with a 9-in. thickness of absorber. The counting rate at the maximum of the corrected curve is 3.73×10^{-6} count/sec./sterad/g.

I. INTRODUCTION

IT is well known that mesons found in cosmic rays have a large spread in energy and therefore a large spread in range. The number of mesons having a range greater than R, when given as a function of R, is called the integral range spectrum of the mesons, while the number of mesons having a range between R and $R+dR$ as a function of R is called the differential range spectrum. Rossi[1] has given both differential and integral range spectrum curves drawing upon the results of several workers.

The differential range spectrum can be measured either directly or indirectly. Indirect measurements can be obtained by differentiating integral spectrum data or by measuring the differential momentum spectrum and converting the momentum values to ranges by the use of range-momentum curves. The integral spectrum has been investigated by several authors.[2–9] The momentum spectrum has been found by Wilson,[10] Jones,[11] and Blackett and Brode.[12]

There are two methods for measuring the differential range spectrum directly. Both involve a counter telescope to define the incoming particles with absorber of variable thickness in or above the counter telescope and an absorber below the telescope in which the mesons are to be stopped. In the delayed coincidence method the number of delayed coincidences between counters placed around the lower absorber with the counters in the counter telescope is measured. The number of mesons which stopped can be found from the number of decay electrons thus observed. If an element of large Z is used as the absorber this method will detect only positive mesons. The anticoincidence method consists of a measurement of the number of anticoincidences between the counter telescope and counters placed below the lower absorber. This tells the number of particles which enter the lower absorber but which fail to penetrate it. Delayed coincidence measurements have been made by Sands[9] and Shamos and Levy.[13] Some data have been obtained by Koenig[14] using the anticoincidence method. Later and more extensive data have been obtained by Rogozinski and Lesage,[15] Kellerman and Westerman,[16] Kraushaar,[17] and Sands.[9]

Each of these two methods has disadvantages. The The energy spectrum of the decay electrons is not well known, and it is difficult to correct for the number of decay electrons which do not reach the delay coincidence counters. Thus it is difficult to obtain absolute values for the values of the differential range spectrum with this method, but relative values can be found easily. While the anticoincidence method tells the number of particles which do not penetrate the lower absorber, it says nothing about their natures and there is no way to tell the mesons from the electrons or protons with small absorber thicknesses.

The present experiment was a measurement of the differential range spectrum at sea level using the anticoincidence method. The nature of the particle was determined with the aid of a cloud chamber. The absorber in which the particles were to stop took the form of several lead plates in a cloud chamber. The nature of the track of the stopped particle determined whether it was an electron, proton, or meson. Thus the difficulty cited above has been circumvented.

* Assisted by the joint program of the ONR and AEC.
† Now at Reed College, Portland, Oregon.
[1] B. Rossi, Rev. Mod. Phys. 20, 537 (1948).
[2] A. Emhart, Zeits. f. Physik 106, 751 (1937).
[3] V. C. Wilson, Phys. Rev. 53, 337 (1938).
[4] Nielsen, Reyerson, Nordheim, and Morgan, Phys. Rev. 59, 547 (1941).
[5] Rossi, Hillsberry, and Hoag, Phys. Rev. 57, 461 (1940).
[6] Bernardini, Cocciapuoti, Ferretti, Piccioni, and Wick, Phys. Rev. 58, 1017 (1940).
[7] D. B. Hall, Phys. Rev. 66, 321 (1944).
[8] Carr, Schein, and Barbour, Phys. Rev. 73, 1419 (1948).
[9] Matthew Sands, Phys. Rev. 77, 180 (1950).
[10] J. G. Wilson, Nature 158, 415 (1946).
[11] H. Jones, Rev. Mod. Phys. 11, 235 (1939).
[12] P. M. S. Blackett and R. B. Brode, Proc. Roy. Soc. A154, 573 (1936).
[13] M. H. Shamos and M. G. Levy, Phys. Rev. 73, 1396 (1948).
[14] H. P. Koenig, Phys. Rev. 69, 590 (1946).
[15] A. Rogozinski and M. Lesage, Comptes Rendus 227, 1027 (1948).
[16] E. W. Kellerman and K. Westerman, Proc. Phys. Soc., Lond. A62, 356 (1949).
[17] W. L. Kraushaar, Phys. Rev. 76, 1045 (1949).

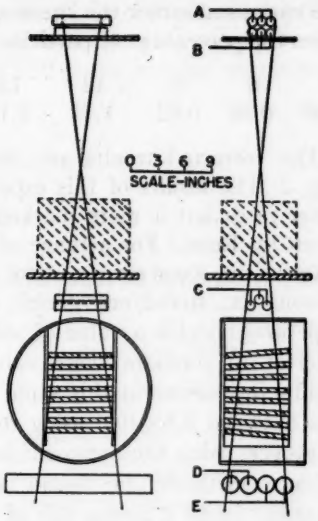

FIG. 1. Apparatus for observation of meson range spectrum.

This work was undertaken with two results in mind. In the first place, there are no extensive direct measurements of the differential range spectrum over a large spread of ranges. In the second place, it is desirable to perform experiments dealing with slow mesons or mesons that stop in such a manner that the total range of the mesons in the apparatus corresponds to a maximum value of the differential range spectrum, for in this case the rate of gathering data will be a maximum. Thus it is of interest to see whether a considerable peak is to be found in the differential range spectrum, as would be expected from an examination of the momentum spectrum.

II. APPARATUS

The apparatus is shown schematically in Fig. 1. The cloud chamber was 41.5 cm in diameter and had an illuminated region 12.7 cm deep. The eight lead plates were each 19 cm wide and 1.32 cm thick. The cloud chamber was tripped by every (A, B, C—D, E) event. Stereoscopic pictures of each expansion were taken.

It was found that it was not possible to identify the particles which stopped in the top plate in the chamber. Furthermore, identification of the particles stopping in the second plate was not reliable. Therefore only six of the plates in the chamber were used for the observation of stopped particles. Since this amounted to about three inches of lead, lead was added above the chamber in three inch intervals from zero up to 27 inches. However, no measurements were made with 18 or 24 inches of lead above the chamber. There were certain other absorbers which were in the solid angle at all times: roof, cloud chamber walls, Geiger counter walls, and stands supporting the absorber and counters. These absorbers were equivalent to 17.3 g/cm² of lead. No correction need be made for the fact that particles travelling at an angle to the vertical penetrate more absorber than vertical particles because the counter dimensions are small compared with their separation.

III. RESULTS

The results are given in Table I and are shown in the form of a histogram in Fig. 2. The errors given are probable errors based on the number of counts. The conversion from g/cm² of lead to g/cm² of air was made with the aid of range-momentum curves given by Rossi and Greisen.[18]

A glance at the histogram shows that the measured peak in the differential range spectrum is very low. The counting rate at the peak is only about 10 percent greater than the counting rate with no lead above the chamber. This in itself shows that placing lead above a chamber will not greatly increase the number of mesons stopping in the chamber. This means that experiments which deal with slow mesons cannot be speeded up by placing an absorber above the apparatus.

IV. CORRECTIONS

While the experimental results give the number of mesons stopping in the chamber, they do not accurately represent the true differential range spectrum of the mesons in the solid angle defined by the apparatus, since some particles which should be counted are lost from the apparatus because of scattering. Mesons that are going to stop in the chamber must have a relatively low energy when passing through the absorber above the chamber. Particles of low energy are severely scattered in the absorber. There are two ways in which this scattering may cause particles to be lost to the apparatus. In the first place, many of the particles emerging from counter C will no longer be going to the right direction to hit the plates in the cloud chamber. In the second place, some particles which have passed through counter B and are travelling in such a direction that they should hit counter C will be scattered away from counter C. This effect is largely compensated by particles which are scattered in such a direction that they hit counter C when they would not have done so if there were no scattering. However, the net effect is a loss of particles. Calculations of both of these corrections have been made. The first of these two corrections is by far the larger, and will be considered first.

TABLE I. Experimental results.

Thickness of lead absorber above chamber (inches)	Stopped particles	Minutes	Counts/min. ($\times 10^{-4}$)	Counts/sec./cm²/sterad/g/cm² of air ($\times 10^{-4}$)
0	64	11,589	5.52±0.47	2.02±0.20
3	64	11,360	5.63±0.48	2.06±0.20
6	72	11,995	6.00±0.48	2.20±0.21
9	70	12,185	5.74±0.46	2.10±0.20
12	70	13,391	5.23±0.42	1.91±0.18
15	53	12,214	4.34±0.40	1.59±0.17
21	50	14,285	3.50±0.33	1.28±0.14
27	51	25,919	1.97±0.18	0.72±0.08

[18] B. Rossi and K. Greisen, Rev. Mod. Phys. 13, 240 (1941).

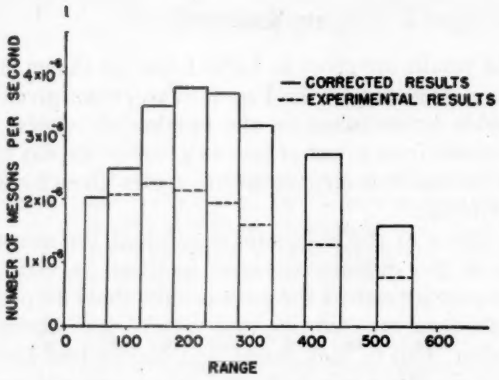

FIG. 2. Corrected and uncorrected observations of the differential range spectrum of mesons at sea level. The range is measured in grams per square centimeter of air.

Rossi and Greisen[18] have derived a formula for the mean square scattering angle, considering energy losses in the absorber. Assuming that the scattering angles are distributed according to a Gaussian distribution with the mean square given by the Rossi and Greisen formula, one can calculate the fraction of the particles with such an energy that they should stop in a given plate and which would be travelling at such an angle that they get to the plate. These values were calculated for each plate in the chamber and then averaged to give the fraction of the mesons received with various thickness of absorber. The results are as follows:

t (inches)	3	6	9	12	15	21	27
f (percent)	83.9	63.9	56.8	53.3	51.5	49.7	49.0

The corrections are seen to be large. About one-half of the desired mesons are lost to the apparatus when large thicknesses of absorber are used.

The second correction has been worked out in a two-dimensional case assuming a uniform distribution of the scattered particles from the vertical to the maximum allowable angle, rather than a Gaussian one. Since the correction is a small one, these assumptions have little effect when both corrections are considered. The percent loss of mesons depends on the fractional loss of momentum, λ. The loss is proportional to

$$\{\lambda+(1-\lambda)[\lambda+2\ln(1-\lambda)]\}\cdot 1/\lambda^3.$$

This relation between the percentage loss and the fraction of momentum lost was derived by Foldy[19] and put in the form used here by Wouthuysen.[20] The calculation of the percentage lost involves also the distance between the counters of the telescope and the mean square displacement due to scattering in the absorber. The results of this correction, averaged over all of the plates in the chamber and given as the percentage of the particles scattered away from the lower counter, are given below for each thickness of absorber used. The top line gives the various absorber thicknesses, while the bottom line gives the percentage of particles lost.

3	6	9	12	15	21	27 (inches)
0.08	0.36	0.82	1.44	2.12	3.62	5.85

The corrected results are shown in Table II and Fig. 2. The results of this experiment give somewhat lower rates but a more marked peak than the curve given by Rossi.[1] For a range of between 100 and 200 g/cm² of air, Rossi gives a meson flux of about 5.5×10^{-6} mesons/sec./sterad/cm²/g/cm² of air. The present experiment yields a value of about 3.5×10^{-6}. It is of interest to compare these values with other recent results on mesons in this same range interval. Sands[9] has obtained 5.5×10^{-6} using the coincidence method. However, using the anticoincidence and delayed coincidence methods, he found a value of 3.1×10^{-6}. Koenig[14] found a meson flux of 3.7×10^{-6} by the anticoincidence method, and Steinberger[21] obtained 4.36×10^{-6} using the delayed coincidence method. The anticoincidence experiments of Kellerman and Westerman[11] when reduced to the above units yield a result of the order of 2×10^{-6}. Kraushaar[17] has found the meson flux to be 5.5×10^{-6}. While Kraushaar used the anticoincidence method, he did not find the meson flux directly from the anticoincidence counting rates but found the fraction of the particles which stop in an absorber. The absolute number of particles stopping can then be found from the value of the integral spectrum at that range. Thus it appears that meson flux measurements made employing the coincidence method yield larger results than measurements using the other methods. It is true that the coincidence method is by far the simplest, and therefore one would place more faith in results obtained by that method. However, the possibility exists that the coincidence method detects some particles which are not mesons and therefore gives a value which is somewhat high. Merkle[22] has found about equal numbers of protons and mesons in the energy region below 300 Mev. If, as this result indicates, the proton flux at sea level is greater than had

TABLE II. Corrected results

Thickness of lead absorber above chamber (inches)	Total range of particles stopped in the chamber (g/cm² of air)	Counting rate counts/sec./cm²/sterad/g/cm² of air
0	27 to 80	2.02×10^{-6}
3	69 to 125	2.46×10^{-6}
6	123 to 179	3.45×10^{-6}
9	171 to 232	3.73×10^{-6}
12	230 to 286	3.64×10^{-6}
15	284 to 340	3.15×10^{-6}
21	394 to 450	2.67×10^{-6}
27	504 to 560	1.56×10^{-6}

[19] L. L. Foldy, Phys. Rev. 75, 311 (1949).
[20] S. Wouthuysen, private communication.
[21] J. Steinberger, Phys. Rev. 75, 1137 (1949).
[22] T. C. Merkle, private communication.

been thought, the results of the coincidence method would be expected to be too large. However, very few protons were identified in the photographs obtained in the present experiment.

The author is indebted to William B. Fretter who suggested and directed this research and to Professor Robert B. Brode whose interest and helpfulness greatly facilitated the work.

PHYSICAL REVIEW VOLUME 80, NUMBER 4 NOVEMBER 15, 1950

Latitude and Altitude Dependence of the Local Hard Showers of Cosmic Rays*

T. G. WALSH† AND O. PICCIONI
Brookhaven National Laboratory, Upton, Long Island, New York

(Received July 17, 1950)

The latitude effect of the local hard showers penetrating at least 350 g/cm² of lead has been measured at two airplane altitudes, and found to be (12±2) percent between Rome, New York, and Canal Zone.

The two separate latitude effects, obtained respectively at 30,500 ft. (300 g/cm²) and at 25,000 ft. (383 g/cm²) coincide within the experimental errors. This slow dependence on altitude of the latitude effect seems to allow an estimate of the energy of the hard shower producing particles as they arrive at the apparatus. An average energy of 20 to 30 Bev is obtained from the present data and the current ideas on the absorption of the nucleonic component. This large value is discussed in connection with other experiments and in view of the fact that at sea level or at mountain altitudes pi-mesons of that energy have a large probability of undergoing a nuclear collision before decaying into mu-mesons.

The measured altitude dependence of hard showers gives for the absorption mean free path of the producing radiation in air, the value of 112±2 g/cm², if interpreted in terms of a simple exponential. However, because of the geometry of the apparatus, the value 140 g/cm², as obtained from the data according to the Gross transform, seems to be more acceptable when referred to strictly vertical particles.

The latitude effect of the normal penetrating component was 1.33 at 30,500 ft., 1.24 at 25,000 ft., and 1.08 at sea level.

I. INTRODUCTION

LOCAL hard showers (*HS*) have been the object of several investigations[1] and their connection with the nucleonic component of the cosmic rays is now fairly well established. The present research leads to an estimate of the energy of the hard shower producing particles which are mainly protons and neutrons, at least when the observations are performed at airplane altitudes. We have obtained such an energy estimate by measuring the latitude dependence of the rate of occurrence of *HS* at two altitudes, 30,500 ft. (300 g/cm²) and 25 000 ft. (383 g/cm²).

Previous information on this subject was available before we performed our experiment. Appapillai and Mailvaganam[2] reproduced the apparatus of Broadbent and Jánossy[1] at the latitude 4°S and did not find large latitude effect at sea level. However, in general, the energies of the secondary nucleons which actually produce a *HS* are smaller than the energies of their primaries. Therefore, any estimate of the energy of the secondary particles based on latitude effect is the more reliable the smaller the depth of the atmosphere at which the experiment is performed. For this reason the present measurements were taken aboard a B-29 aircraft. Also, the apparatus (Fig. 1) was designed so that it would detect particles of lower energy than that of Appapillai and Mailvaganam. In order to obtain a measurable effect we used a relatively small thickness of absorbing material and disposed the counters in such a geometry that even a *HS* of two particles could give a registered count. Both of these features help to make the rate of registered *HS* large enough to obtain good statistical accuracy. Yet, in spite of the simple geometry, the fraction of *HS* produced by mu-mesons was, as we shall show later, as small as two percent at airplane altitudes. Like other experimenters, we believe that these spurious *HS* are produced by mu-mesons by means of knock-on electrons or by electromagnetic radiation, and that their contribution to the *HS* intensity is the greater the less severe we make the requirements for *HS* detection.

II. THE APPARATUS

As may be seen from Fig. 1, our disposition of counters is somewhat similar to that used by Tinlot,[1] but our geometry is not expected to favor vertical particles as was the case with Tinlot's geometry. Therefore, the *HS* dependence on altitude obtained by

* The present research has been carried out under the auspices of the AEC.

† Work performed in partial fulfillment of the requirements of Fordham University for the Degree of Doctor of Philosophy.

[1] We quote only a few papers in which references are made that will allow the collection of a complete bibliography: Wataghin, de Souza Santos, and Pompeia, Phys. Rev. **57**, 61 (1940). L. Jánossy and P. Ingleby, Nature **145**, 511 (1940). D. Broadbent and L. Jánossy, Proc. Roy. Soc. **A190**, 497 (1947). W. B. Fretter, Phys. Rev. **73**, 41 (1948). Rochester, Butler, Mitza, and Rosser, Rev. Mod. Phys. **21**, 20 (1949). J. Tinlot, Phys. Rev. **74**, 1197 (1948). O. Piccioni, Phys. Rev. **77**, 1 (1950).

[2] V. Appapillai and A. W. Mailvaganam, Nature **162**, 887 (1948).

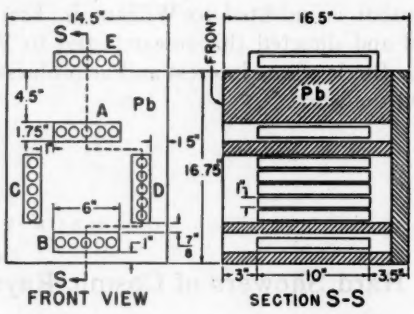

FIG. 1. Experimental arrangement of the counters and absorbers.

us will approach the value typical for a non-directional detector, while the dependence observed by Tinlot is, presumably, intermediate between that of a completely "vertical" and a non-directional apparatus.

The electronic circuit which was connected to our apparatus had a resolving time of one microsecond, and registered the coincidences AB, ABC, $AB(C+D)$, and $AB(C+D)E$. By the expression $(C+D)$ we mean that if either of the trays C or D were discharged, a coincidence was registered. The coincidences ABC were also registered in order to have a check on the behavior of the apparatus through the ratio $AB(C+D)/ABC$, which was constant over the whole period of time covered by the experiment. The counting rate of each tray, and the size of the pulses at each counter, were checked every working day. The voltages of the counters were adjusted individually such that the size of the pulses at all of the counters could be made equal to a constant value. Throughout the entire length of the experiment not a single counter needed to be replaced, and the electronic apparatus worked very satisfactorily.

The coincidences AB are due for the most part to mu-mesons, while the coincidences ABC and $AB(C+D)$ represent HS. We are interested in determining an upper limit for the percentage of spurious HS. Between sea level and 25,000 ft. the rate AB increases by a factor of about 4, and the rate $AB(C+D)$ by a factor of 118. If we call K the factor of increase for the true HS ($K \geqq 118$), the fraction S of $AB(C+D)$ associated with the normal penetrating particles at 25,000 ft. is $4(K-118)/118(K-4)$. Since K is, at most, 360 (absorption mean free path $=110$ g/cm^{-2}), S turns out to be less than 2.5 percent. An even smaller fraction would result by taking into account that the increase of AB is presumably much larger than the increase of the mu-particles having enough energy to produce a spurious HS.

The tray E was, for the first flights, an extension tray placed three feet away from the main apparatus. The $AB(C+D)E$ rate thus gave an indication of what percentage of the HS were accompanied by large air showers. Since this percentage, as expected because of previous information,[3] turned out to be very low, about two percent, the measurements with the extension tray E were discontinued. In the second series of flights at Rome, New York, and at Canal Zone, the tray E was placed on top of the apparatus and used as an additional HS tray.

The flights were performed at Rome, New York, geomagnetic latitude 55° 8′N and at the Canal Zone, geomagnetic latitude 20° 42′N. The aircraft first made a series of flights at Rome and at Canal Zone, and subsequently performed another series flying again at Rome and at Canal Zone. The data are shown in Tables I and II. The complete agreement between the results of the first and the second series gives us full confidence in the data. The errors shown in the table are the usual statistical errors, but for the HS data it has been checked that the individual measurements, made under the same conditions, did not differ from the average by more than the expected amount.

III. THE ABSORPTION MEAN FREE PATH

When we average the measurements at Canal Zone and at Rome, New York, we obtain an absorption mean free path of 112±2 g/cm², if we take the simple exponential law for the altitude dependence; that is, if we assume that all of the detected particles were traveling vertically. However, it is reasonable to believe that our apparatus, because of its geometry, made no important selection in favor of vertical particles. This fact explains, at least qualitatively, the difference between our value of 112 g/cm² and the one obtained by Tinlot of 118 g/cm². For if our apparatus makes no selection at all as to the direction of the arriving particles, and if collisions in air, as according to Walker,[4] do not

TABLE I. Observed data at Rome, New York, and the Canal Zone.

	Rome, New York (geomagnetic latitude N 55° 8′)					Canal Zone (geomagnetic latitude N 20° 42′)				
Atmos. depth (g/cm²)	Time (hours)	$AB(C+D)$ (hr.$^{-1}$)	$AB(C+D)E$ (hr.$^{-1}$)	ABC (hr.$^{-1}$)	AB* (hr.$^{-1}$)	Time (hours)	$AB(C+D)$ (hr.$^{-1}$)	$AB(C+D)E$ (hr.$^{-1}$)	ABC (hr.$^{-1}$)	AB* (hr.$^{-1}$)
273	2.5	1585±25		885±19	17760±84					
300						8	1122±12		630±10	12352±40
383	9.2	597±8		336±6	12000±38	9.97	538±8		310±6	9710±31
1030	417.5	5.05±0.1	1.35±0.06	2.65±0.08	2940±3	28.6	4.67±0.4		2.65±3	2710±10
300 (2nd series)	6.4	1268±14	318±7	717±12	16576±51	9.4	1120±10	274±5	640±8	12416±36

* Errors shown are statistical errors only.

[3] J. Tinlot and B. Gregory, Phys. Rev. 75, 519 (1949). G. Cocconi and K. Greisen, Phys. Rev. 74, 62 (1948).
[4] W. D. Walker, Phys. Rev. 77, 686 (1950).

result in an important angular spread of the high energy nucleons, the *HS* rate should be taken as proportional to the value given by the Gross transform:

$$G=\int_0^{\pi/2} \sin\theta \exp[-x/L\cos\theta]d\theta.$$

From this expression and our data we obtain $L=140$ g/cm².

In principle, the experimental curve of the altitude dependence, extended to lower altitudes than 25,000 ft. and particularly to sea level, should show whether the expression $[G]$ or the simple exponential represents correctly the altitude dependence of the *HS* detected with our apparatus. However, the distinction is rather uncertain for the following reason. The two functions, once they are brought to fit the points at 30,500 ft. and 25,000 ft., give two sea level values whose ratio is only 1.7, and the indeterminacy of the rate of spurious *HS* produced by mu-mesons makes it impossible to estimate the true *HS* rate at sea level with an error much less than a factor of 2. On the other hand, if we should take the apparatus under a few thousand g/cm² of solid material, an uncertainty would still be present, since it cannot be assumed that the rate of spurious *HS* is proportional to the total intensity of mu-mesons.

IV. THE LATITUDE EFFECT

From the data we obtain readily the latitude effect for the total penetrating component (AB) and for the $HS[AB(C+D)]$, both at 30,500 ft. and 25,000 ft. We shall indicate the latitude effect by the ratio of the intensity at Rome to the intensity at the Canal Zone. The total penetrating component undergoes a latitude effect of 1.33 at 30,500 ft., of 1.24 at 25,000 ft., and of 1.08 at sea level. The *HS* rate exhibits a latitude effect of 1.12 ± 0.02, if we take the average of the measurements at 30,500 ft. and 25,000 ft.

Because of the latitude effect obtained, it is evident that a particle must have an energy above a certain limit in order to generate a *HS* recorded in our apparatus. The probability P for a particle to produce a *HS* is presumably a function $P(E)$ of the particle's energy, E. It is reasonable to assume that $P(E)$ is a monotonic function increasing with E, but we do not know how rapid this increase is. We can consider two different types of function for $P(E)$. (a) Sharp cut-off; $P(E)$ is a step function equal to zero for energies less than a cut-off value E_c, and constant for $E>E_c$. (b) Smooth cut-off; $P(E)$ is zero for $E<E_c'$, increases linearly for $E_c'<E<E_s'$, and is constant for $E>E_s'$. We can choose for E_s' a value large enough so that E_c', to be determined, will turn out to be two or three times smaller than E_s'. Then, the function (b) will be substantially different from the function (a).

For the energy spectrum of the primaries, we take a power law with the exponent -1.8 (integral spectrum), which seems to be the best value for large energies.

TABLE II. Latitude effect of hard showers.

Atmos. depth (g/cm²)	Latitude effect = Intensity at Rome / Intensity at Canal Zone			
	$AB(C+D)$	$AB(C+D)E$	ABC	AB
300	1.13 ± 0.015	1.16 ± 0.035	1.12 ± 0.02	1.33
383	1.11 ± 0.02		1.08 ± 0.03	1.24
1030				1.085

The geomagnetic cut off, averaged over a solid angle of semi-aperture 30°, is 11 Bev at the Canal Zone, while at Rome it is 2 Bev.

In evaluating the energy cut-off introduced by the apparatus, the process by which high energy nucleons are absorbed in the atmosphere plays an important role. The value of the absorption mean free path alone does not allow us to give a unique interpretation of the observed latitude effect. The nucleonic absorption may be due either to catastrophic collisions with a cross section about half of the geometrical cross section of air nuclei, or to collisions causing a partial loss of energy with a cross section equal to the geometrical value. If the collision cross section is independent of the nucleonic energy, then under the first hypothesis the observed exponential law for the intensity of fast nucleons *versus* atmospheric depth is immediately explained. The energy spectrum of the nucleons would be the same at any depth and the latitude effect would not depend on altitude. The last two consequences are obvious, because the nucleons detected, say, at 30,500 ft., in any arbitrary interval of energy, would be the primary nucleons which did not have any collision before arriving on the apparatus. Thus, their number would be an energy-independent fraction of the number of the primaries in the given energy interval. On the other hand, one can conceive, and this is more likely to be true, that the collisions of fast nucleons with air nuclei do not result in a total energy loss for the colliding nucleons. If, as Heitler and Jánossy[5] assume, the probability of a certain energy loss is a function of the fractional energy loss only, we can account for the observed exponential absorption if we take for the energy spectrum of the primaries the function $E^{-(\gamma+1)}dE$. The collision cross section may then be equal to the geometrical cross section of air nuclei.

As to the interpretation of our experiment in the scheme of Heitler and Jánossy, one notices that nucleons of energy E_s detected at a certain atmospheric depth, x, are secondaries of primaries of energy E_p larger than E_s. The average ratio between E_p and E_s increases with x, with the result that the latitude effect of *HS* would decrease with increasing atmospheric depth. This last point would allow a very significant check on the type of absorption process which takes place in the atmosphere. However, the two altitudes at which we have

[5] W. Heitler and L. Jánossy, Proc. Phys. Soc. London A62, 374 (1949).

experimented do not differ sufficiently to allow us to reach a definite conclusion concerning the altitude dependence of the latitude effect. We obtain a latitude effect of 1.13 ± 0.015 at 300 g/cm² and 1.11 ± 0.02 at 383 g/cm², the difference being smaller than the statistical error. A computation performed following the mathematical scheme of Heitler and Jánossy predicts a difference slightly larger than our experimental error. Thus, rather than proving the validity of a certain type of absorption process, the present experiment indicates that the true process is such that it gives a non-rapid increase of the latitude effect with altitude. Consequently, our conclusions concerning the energy of the hard shower producing particles seem not to be critically bound to any particular absorption process. In computing the minimum energy and the average energy for our *HS* events we shall distinguish four cases according to the two above mentioned schemes for the nucleonic absorption and the two types of functions for $P(E)$.

Aa. Catastrophic collisions; sharp cut-off: in this case, the energy cut-off E_c is obtained from the equation $(E_c/11 \text{ Bev})^{-1.8}=1.12$, where 11 Bev is the geomagnetic cut-off for the vertical at the Canal Zone. The geomagnetic cut-off at Rome plays no part because it is clearly smaller than the cut-off of the apparatus. For the Canal Zone we take the value for the vertical direction, since it is close to the average for all of the useful directions. The above equation gives $E_c=10.5$ Bev and $(E)_{Av}$, the average energy of a hard shower producing particle, is $(1.8/0.8)\times10.5$, or 24 Bev.

Ab. Catastrophic collisions; smooth cut-off: $P(E)=0$ for $E<E_c'$; $P(E)=1$ for $E>E_s'$; $P(E)=(E-E_c')/(E_s'-E_c')$ for $E_c'<E<E_s'$. The value of E_c' is derived from the two equations:

$$\frac{1}{E_s'-E_c'}\int_{E_c'}^{E_s}(E-E')E^{-2.8}dE + \int_{E_s'}^{\infty}E^{-2.8}dE=1.12K \quad \text{(Rome, N. Y.)}$$

$$\frac{1}{E_s'-E_c'}\int_{11}^{E_s'}(E-E_c')E^{-2.8}dE + \int_{E_s'}^{\infty}E^{-2.8}dE=K. \quad \text{(Canal Zone)}$$

For $E_s'=20$ Bev the value of E_c' which best fits the two equations is $E_c'=8.5$ Bev, which in turn gives an average energy $(E')_{Av}=35$ Bev. As expected, a function of type *Ab* gives a smaller value for the minimum energy and a larger value for the average energy, than the step function, *Aa*.

Ba. Non-catastrophic collisions; sharp cut-off: following the scheme of Heitler and Jánossy we computed the value $E_c''=9$ Bev for the cut off energy, and the value $(E'')_{Av}=20$ Bev for the average energy.

Bb. Non-catastrophic collisions; smooth cut-off: the exact computation in this case is somewhat tedious, and was not carried out in view of the approximations and uncertainties already present in the adopted scheme for the nucleonic absorption and in the assumed cut-off function $P(E)$. One notices that according to the Heitler-Jánossy theory the nucleonic spectrum at airplane altitude is already close to a power law for energies around 10 Bev. Therefore, the value of E_c''' deduced from (*Ba*) through the proportion $E_c'''/E_c''=E_c'/E_c$ is not expected to differ substantially from the value one would obtain by a detailed calculation. With an analogous proportion for $(E''')_{Av}$, we have $E_c'''=7.3$ Bev; $(E''')_{Av}=30$ Bev. Thus, the minimum energy which a fast particle arriving on our apparatus must have in order to produce a *HS* with any appreciable probability, appears to be between 7 and 11 Bev, and the average energy between 20 and 35 Bev.

The above values are rather large if we consider that, in the limit, a *HS* producing two penetrating particles of range larger than 300 g/cm² is all that is required by the apparatus. One would think that nucleons of 2 or 3 Bev should be able to produce a *HS* in our apparatus, and the fact that a much larger energy is needed deserves a special explanation. One such explanation, could be the following. All of the secondary particles produced in a *HS* interact strongly with nuclei and undergo severe absorption in the lead of the apparatus. Thus the energy necessary to penetrate the absorber is much larger than we would compute from ionization losses. However, this assumption is not absolutely necessary to explain the present results. First, the production of photo-electron showers by the colliding nucleon presumably represents an important energy loss. Second, from the latitude effect of our *AB* coincidence rate, due mainly to mu-mesons, one can argue that the primary particles producing these mu-mesons with enough energy to reach tray *B*, have a minimum energy not much smaller than the minimum energy computed for the *HS* producing particles. Thus one would draw the conclusion that the very process of meson production is such that the mesons produced are not likely to have energies of the order of 1 Bev unless the producing nucleons have energies of the order of 10 Bev.

A good confirmation of our conclusions on the minimum value for E_c lies in the findings of McMahon, Rossi, and Burditt,[5a] who observed a latitude effect of

[5a] McMahon, Rossi, and Burditt, Echo Lake Conference on Cosmic Rays, 1949, Phys. Rev. **80**, 157 (1950).

1.17 ± 0.03 for the nucleons able to produce bursts in an ion chamber. From the size of the bursts the authors computed that the minimum energy of such nucleons was appreciably larger than 5 Bev.

V. THE ABSOLUTE INTENSITY

It is of interest to deduce from our experiment an approximate value for the absolute intensity of fast nucleons, in order to see how it compares with the known measurements of the primary flux. Such a comparison is most conveniently done with the Canal Zone data, since the obtained latitude effect is small enough to make it clear that most of the primaries arriving at high latitudes do not contribute to our *HS* counting rate.

According to Dwight, Sabin, Stix, and Winkler,[6] the vertical primary flux at 20°N is 0.031 ± 0.001 cm^{-2} sec.$^{-1}$ sterad.$^{-1}$. Since it is presumed that, at the top of the atmosphere, the primary intensity is constant for all directions in the upper hemisphere, a sphere of 1 cm^2 cross section would be crossed by $2\pi\times0.03$ particles sec.$^{-1}$, that is, the value of the flux integrated over all directions. Using the Gross transform ($L=140$), one finds that the integrated flux would equal 5.77×10^{-3} particles sec.$^{-1}$ cm^{-2} at the atmospheric depth of 300 g/cm^2. At that depth the $[AB(C+D)]$ counting rate of our apparatus was 0.31 sec.$^{-1}$. That is, the apparatus would be equivalent to a sphere of 55-cm^2 cross section which would detect all nucleons of energies larger than the geomagnetic cut-off at the Canal Zone (11 Bev). Such a cross section is small enough compared with the active surface of each tray, 300 cm^2, to show that our *HS* rate, I, and the large value of approximately 10 Bev for the minimum energy E_c are not in conflict with the value of the primary flux. Indeed, the product IE_c is too small, so that either a value of the primary flux smaller than 0.03 particles cm^{-2} sec.$^{-1}$ sterad.$^{-1}$, or a value of E_c larger than 10 Bev would lead to an estimated cross section of the apparatus reasonably larger than 55 cm^2.

A primary flux of 0.03 particles cm^{-2} sec.$^{-1}$ sterad.$^{-1}$ thus appears to be about the maximum value compatible with the present experiment.

As to a lower limit for the primary flux, we notice that the useful cross section S of the apparatus must be smaller than 500 cm^2, which is the geometrical cross section of the lead assembly. Actually, the data with the additional tray E on top of the apparatus indicate that S is appreciably less than 500 cm^2, for otherwise the fraction of *HS* detected by E should be less than the experimental value ($\sim1/4$), taking into account that presumably half of the *HS* producing particles are not ionizing. Our lower limit for the primary flux would thus be some five times smaller than our upper limit of 0.03 particles cm^{-2} sec.$^{-1}$ sterad.$^{-1}$. Both values, however, do not result from a direct determination. Our main purpose, in comparing our limits for the primary flux with the value given by Dwight and others, was to see whether the comparison would show the computed *HS* energy to be too large. It does not.

In agreement with our conclusions, Sitte,[7] working at mountain altitudes, argued that the absolute rate of the *HS* indicates a large value for the energy of the *HS* producing particles.

VI. DISCUSSION

The large value of the average energy of the *HS* producing particles, as deduced from the 12 percent latitude effect at 30,500 ft., is based on the current ideas concerning the process by which the nucleonic component arises from the primary particles, and the process by which it is absorbed in the atmosphere. If these processes should actually be entirely different from the assumed ones, our conclusion concerning the energy of *HS* producing particles might need to be changed. As an obvious example, the small latitude effect obtained for the mu-mesons does not allow us to conclude that the average energy of detected mesons is over 10 Bev.

As far as the absorption process is concerned, we have computed the minimum energy E_c for the *HS* producing particles according to two different schemes of nucleonic absorption: by catastrophic collisions and by non-catastrophic collisions. The difference between the two values is not very important. If we assume some other absorption process which would lead to a larger degradation of the energy, we could hardly avoid the consequence that the latitude effect should depend on the altitude much more than is shown experimentally. Thus, it is unlikely that the true absorption process would lead to a value for E_c substantially lower than we have computed.

As to the process by which the nucleonic component arises from the primary particles, we believe it to be the same process which causes the absorption throughout the atmosphere. Indeed, for all nuclear phenomena, like ion chamber bursts, photographic emulsion stars, and slow neutrons, it appears that when the observations are performed above airplane altitudes up to very small atmospheric depths, no change is observed which could not fit our current ideas on the birth of the nucleonic component, except perhaps some dependence of the cross sections on particle energy.

The value of about 10 Bev for E_c seems, therefore, to be acceptable on the basis of the observed latitude effect. We have already remarked that our rate of occurrence can well be accounted for as given by particles of such a high energy, descendants of primaries the flux of which is known.

The large value obtained for the energy of the *HS* producing particles suggests that in the measurements of the altitude dependence of the *HS*, performed between sea level and mountain altitudes, one might

[6] Dwight, Sabin, Stix, and Winkler, Phys. Rev. **78**, 324(A) (1950).

[7] K. Sitte, Proc. Phys. Soc. London **A63**, 295 (1950).

expect a contribution from pi-mesons. Such a contribution could result in an increase of the absorption mean free path of the *nucleons*, with respect to the case in which pi-mesons decay before interacting. That is because at a given absorber depth there could be production of nucleons by pi-mesons, if the absorber is dense enough that pi-mesons undergo nuclear interactions before decaying. With the value found for the mean energy of the *HS* producing particles, we see that at sea level or at mountain altitudes, the decay process does not prevent the interaction. Let us consider the experiment of George and Jason[8] (GJ), who used an apparatus with 60 cm of Pb and required sevenfold coincidences. The energy required by their apparatus must be several times larger than that required in our experiment. To make a rough estimate of the energy difference we observe that our *HS* rate, interpolated to 3450 meters above sea level, is about $40h^{-1}$, while the apparatus of GJ recorded a rate of $5h^{-1}$, even though it had a useful cross section twice as large as ours. Interpreting the difference between the two rates, normalized for equal cross sections of the apparatuses, as due to two different energy cuts in the integral spectrum $E^{-1.8}$, we find that the apparatus of GJ was detecting *HS* of energy four times as large as ours. One would thus think, as a rough approximation, that the mean energy of the particles producing *HS* in their apparatus was about 80 Bev. Now, at sea level or at mountain altitudes, a pi-meson of about 20 Bev has an equal probability of colliding with an air nucleus as it has of decaying. Then, at the energy of the experiment of GJ the contribution of pi-mesons is expected to be almost as important as if the absorber were a dense material. On the contrary, in our experiment, as well as in Tinlot's, performed with small apparatuses and at airplane altitudes, the decay process is expected strongly to prevent the collision processes. Now, GJ measured an absorption mean free path of 115 g/cm², which is about the same value as was obtained by Tinlot and by ourselves at airplane altitudes. Thus, there is no evidence of an important contribution of pi-mesons to the reproduction of the *HS* component. The possibility that the other parameters which determine the absorption mean free path, like the exponent of the power spectrum and the fractional energy loss (see Heitler and Jánossy[5]), would change at high energy just to balance the effect of pi-mesons does not seem likely.

[8] E. P. George and A. C. Jason, Proc. Roy. Soc. (to be published).

One may see that in the scheme of Heitler-Jánossy the absorption mean free path of the fast nucleons is increased by less than 20 percent if one assumes that for one-half of the events all of the energy lost in one elementary collision goes into the production of one pi-meson which has the same properties of interaction as a nucleon. For the other half of the events it is assumed that a neutral meson is produced. Therefore, our conclusion does not imply any limit for the interaction cross section of pi-mesons; it implies, however, that even in a dense material the high energy nucleonic component would decrease with a mean free path not much larger than in air, if the only difference between the absorption in air and in dense material were due to pi-mesons.

On this subject Rediker and Bridge[9] have recently performed an experiment which shows that the nuclear interactions detected with an ion chamber decrease, under a graphite absorber, as $\exp(-X/500)$, where X is in g/cm². The energy of such nuclear interactions is presumably not much lower than that of our *HS* events. This result seems to show a strong contribution of unstable particles, most likely pi-mesons, to the interacting component. The question arises whether such evidence can be brought into agreement with our conclusions. We can think of two possibilities. (a) Pi-mesons have a larger absorption mean free path than nucleons have in air; then the energy at which the contribution of pi-mesons becomes appreciable in air would be larger than we have computed. (b) The nucleonic component under graphite does not decrease with a mean free path of 500 g/cm², but that value represents the decrease of the rate of all the events produced by pi-mesons and by nucleons. Possibly, the energy of the pi-mesons is smaller than the energy of the nucleons which produce the same events.

We are indebted to the Air Materiel Command, particularly to the 3171 Electronics Squadron, and to the Atmospheric Physics Laboratory of the Air Force Cambridge Research Laboratory, for their cooperation and assistance. We are also grateful to the pilots: Lt. C. C. Davis, Capt. H. Norton, Lt. D. Paulsel, and Capt. S. Casselman.

Thanks are due to T. H. Johnson, H. S. Snyder, and G. A. Snow for their many useful and stimulating discussions.

The important help of C. S. Kemic is gratefully acknowledged.

[9] R. H. Rediker and H. S. Bridge, Phys. Rev. 79, 206(A) (1950).

Momentum Distribution of Charged Cosmic-Ray Particles at Sea Level*

DONALD A. GLASER,† BERNARD HAMERMESH,‡ AND GEORGE SAPONOV§
California Institute of Technology, Pasadena, California

(Received July 27, 1950)

A new measurement of the momentum distribution of high energy charged cosmic-ray particles at sea level has been made with a magnetic spectrograph which uses two counter-controlled cloud chambers and a large electromagnet. The spectrum is extended beyond previous determinations to a momentum of 80 Bev/c. For the 1547 measureable sets of tracks recorded the positive–negative ratio is 1.26 ± 0.06. Up to the highest momenta measured the differential spectrum can be represented by an expression of the form $1/p^s$ with $s=1.9$. The positive excess and positive–negative ratio appear to be functions of momentum with the positives predominating at about 1.3 Bev/c. Except for this the positive and negative spectra are very similar.

Although the effect is barely outside statistical uncertainty there seems to be an anomalous dip in the momentum distribution at about 3 Bev/c. There seems to have been a small diurnal variation in the spectrum during the time occupied by the experiment, 1 Bev/c particles being favored during the day, and 3 Bev/c and 6 Bev/c particles being favored at night. These effects are discussed and the present results are compared with data of other experimenters.

I. INTRODUCTION

SEVERAL determinations of the cosmic-ray momentum spectrum have been made by observing curvatures of tracks in a counter-controlled cloud chamber immersed in a uniform magnetic field.[1–8] All of them agree in the gross features of the distribution; a rise at the low end to a maximum at about 1 Bev/c and then a decrease in intensity which falls off roughly as the inverse square of the momentum out to a momentum of about 10 Bev/c which is the upper limit of previous measurements.

This experiment is an extension of the magnetic deflection method to higher momenta and to higher accuracy in the range already investigated. It was undertaken in order to study the form of the spectrum above 10 Bev/c, and to reexamine the part below 10 Bev/c with higher resolving power in a search for properties of the distribution such as positive-negative ratio that might vary with momentum. Two cloud chambers are used, one placed above and the other below a region of fairly strong and uniform magnetic field in air. Straight tracks are observed in the chambers and the angular deflections of the particles in traversing the field are obtained from stereographic pictures which give the angles between the tracks. A pair of Geiger counters in coincidence triggers the cloud chambers. Figure 1 shows the main parts of the apparatus schematically.

In spite of its increased difficulty as compared with the conventional method, the two-chamber method offers several advantages for this kind of measurement. Since the chambers are not in the gap, the required field can be produced more economically; the chambers are easier to photograph and insulate thermally against distortions due to convection currents in the chambers, and tracks which are not straight because of scattering or distortions can be rejected easily and objectively. A final advantage of the present method is the ease and accuracy with which the deflection angle can be measured as compared with the difficult task of measuring curvatures directly. We have introduced a new source of uncertainty with the present arrangement, however, that is, the scattering in the material separating the sensitive volumes of the two chambers. It turns out that the effect of scattering is not serious as will be shown by a simple calculation which has been checked experimentally.

II. THE APPARATUS AND ITS OPERATION

The experiment described here was performed at Pasadena, California, at an elevation of about 800 feet above sea level. All of the particles observed entered the apparatus from a nearly vertical direction after passing through a roof of duraluminum about 2 mm thick which constituted the only solid material above the top counter. The magnetic field was oriented nearly north and south and was horizontal. Data included in this survey were recorded between May 27 and September 9, 1949, during which time the apparatus was operated continuously day and night except when repairs and adjustments were necessary. Pictures were taken at the rate of six or seven an hour during normal operation. The magnet gives a very nearly uniform field of about 9000 Gauss at 3.3 kilowatts. It will be shown later that this uniformity in the vertical direction is not necessary for this experiment, but that the quantity characterizing the magnetic field which is relevant here is the line integral $\int B dl$, taken along a vertical straight line at

* Assisted by joint program of the ONR and AEC.
† Now at University of Michigan, Ann Arbor, Michigan.
‡ National Research Fellow 1946–1948. Now at the Argonne National Laboratory.
§ Now at Rand Corp., Santa Monica, California.
[1] P. Kunze, Zeits. f. Physik **80**, 559 (1933).
[2] C. D. Anderson and S. H. Neddermeyer, Int. Conf. Phys., London, 177 (1934).
[3] L. LePrince-Ringuet and J. Crussard, J. de phys. et rad. **8**, 207 (1937).
[4] P. M. S. Blackett and R. S. Brode, Proc. Roy. Soc. **A154**, 573 (1936).
[5] P. M. S. Blackett, Proc. Roy. Soc. **A159**, 1 (1937).
[6] H. Jones, Rev. Mod. Phys. **11**, 235 (1939).
[7] D. J. Hughes, Phys. Rev. **57**, 592 (1940).
[8] J. G. Wilson, Nature **158**, 415 (1946).

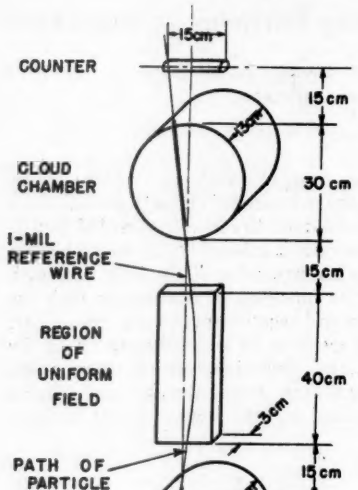

FIG. 1. Arrangement of apparatus showing the path of a typical particle which passes through the two counters, two cloud chambers, and the region of uniform magnetic field. The 1-mil tungsten wire furnishes a reference direction for measuring angles in the photographs.

the center of the gap. Its value is $(3.9\pm0.2)\times10^5$ Gauss-cm for this experiment.

The cloud chambers are of the conventional moving-piston design and have a sensitive volume 30 cm in diameter and 13 cm deep. Each chamber is photographed stereographically by means of two cameras placed about 140 cm in front of the chamber, one of which looks along the chamber axis. The axis of the second camera is parallel to the axis of the first but is displaced 25 cm to the side. A 6-foot length of 1-mil tungsten wire is stretched vertically the whole length of the apparatus just in front of the cloud chambers to provide a reference direction in the pictures with respect to which angles may be measured on the films. Two Geiger counters in a double coincidence circuit are placed one above the top chamber and one below the bottom one in such a way that only a particle passing through the uniform portion of the field and the center portions of the cloud chambers trip the apparatus except, of course, for scattered particles and accidental coincidences.

III. THEORY OF THE MEASUREMENTS

To an approximation sufficient for this experiment, the magnetic field used here can be considered to be uniform except for variations due to fringing at the top and bottom of the magnet. Particles which get near the edge of the pole pieces in the horizontal direction are quickly lost from the field. Those few which do get bent back into the field can be found by examining full scale projections of the pictures.

The equation of motion of a particle carrying a single electronic charge and moving in a plane perpendicular to a magnetic field of flux density B is

$$pc=3\times10^{-7}B(y)\rho(y'', y') \quad (1)$$

if y is the distance in cm measured in the direction in which B varies (vertical here), ρ is the radius of curvature of the path in cm, B is the magnetic induction in Gauss, y' and y'' are derivatives with respect to distance taken in the plane of motion and perpendicular to the y axis, and p is the momentum in Bev/c. If ds is the arc length along the path and φ is the angle between the path and the y axis

$$\rho=ds/d\varphi=dy/(\cos\varphi d\varphi). \quad (2)$$

Since p is a constant of the motion we can substitute (2) into (1) and integrate to get

$$pc=\left[3\times10^{-7}\int_{y1}^{y2}B(y)dy\right]\Big/(\sin\varphi_2-\sin\varphi_1). \quad (3)$$

Hence the momentum of the particle is determined by a vertical line integral of the magnetic induction and the angles of entry and exit of the particle. The integral is evaluated from a plot of the magnetic flux density in the region between the two chambers including the region of fringing. Inside the chambers the field is too weak to cause observable deflections. Once the magnetic flux integral is measured, we need only two angles to determine the momentum.

IV. ERRORS AND CORRECTIONS TO THE OBSERVATIONS

Since the particles observed here move in very nearly plane curves, it is sufficient for a calculation of the momentum to determine the projections of the angles of entry and exit on a plane perpendicular to the magnetic field. The maximum error in momentum that can result from neglecting the angle of tilt of the actual motion is less than 0.02 percent. These projected angles can be found from the central cameras alone with sufficient accuracy for the particles of momentum less than 10 Bev/c, but for the higher energy particles it is necessary to measure the side views and make a sterographic correction.

In the absence of the magnetic field the solid angle into which a given point on the top counter will accept particles which pass through both counters depends only the size and position of the bottom counter. For the two counters used here the integrated aperture of the instrument is 0.0822 cm²-steradian. Due to the magnetic field the particles move in curved trajectories so that the limiting paths are different from those found without the field in such a way that the effective solid

angle of the instrument is reduced. A straightforward though somewhat tedious calculation has been made to evaluate the amount of this effect. At 3 Bev/c and above the solid angle is within one percent of the no-field value. Below this momentum one must apply a correction to the observed momentum distribution to obtain the true distribution. At 2.4 Bev/c one must add three percent, at 1.5 Bev/c, 10 percent, at 1.0 Bev/c, 24 percent, and at 0.7 Bev/c, 60 percent. Particles of momentum less than about 0.3 Bev/c cannot trip the apparatus.

In addition to the magnetic deflections on which this experiment is based, the charged particles observed will suffer various amounts of angular deviation due to scattering by the walls of the cloud chambers and the gas in the space between the chambers. To estimate the effect of this scattering on the momentum distribution, we assume all the particles observed to be mu-mesons and consider coulomb scattering only since nearly all of the penetrating component at sea level is thought to consist of high energy mu-mesons and the nuclear cross sections for fast mu-mesons are small. Williams[9] has considered the problem of the multiple and plural scattering of fast charged particles and concludes that, for all but the largest net angles of scattering, a suitable Gaussian distribution represents the distribution of scattering angles quite well. In the present experiment large deflection angles are excluded by the counter geometry. Using Williams' result calculated for mu-mesons it is found that the probability of a given fractional change in apparent momentum due to scattering is independent of the momentum. Most scatterings (35 out of 36) are found to change the momentum by less than 10 percent of itself. One out of 600 scatterings changes it by more than 15 percent and one out of 10,000 by more than 20 percent for the 2 cm of glass scatterer assumed here.

By starting with some hypothetical momentum distribution which can be represented analytically, one can estimate the effect of scattering on the shape of the momentum spectrum. A distribution that rises linearly from zero to a peak at 1 Bev/c and then falls off as $1/p^2$ is a fairly good approximation to the observed curve. When Williams' Gaussian scattering results are applied to this distribution, it is found that the sharp peak is reduced by about nine percent, that the ordinates of the distribution are increased by less than 0.3 percent between 0.1 Bev/c and 0.5 Bev/c and increased by about the same percent between 3 Bev/c and 100 Bev/c. Hence, the general form of the spectrum is not altered by scattering of the particles although any sharp peaks that might be present in the true distribution will be smeared out somewhat. A no-field run of 107 tracks gives good agreement with the theoretically predicted root mean square scattering angle.

In each picture the angle between the track image and the reference wire image was measured by projecting the films full scale onto a protractor of one meter radius. It was possible in this way to measure angles to about 0.001 radian. The errors in momentum assigned on the various curves shown are derived from the root mean square deviations in angle measurements obtained by several remeasurements of some of the tracks. These independent remeasurements permit an estimate of errors due to chamber distortions and track thickness. We have assumed that it is impossible for a whole track 10 inches long to remain straight after being rotated by gas flow in the chamber. Such gas flow results in kinking the tracks into a more or less severe S shape. Photographic distortions were found to be negligible compared with the errors due to the thickness of the tracks and chamber distortions.

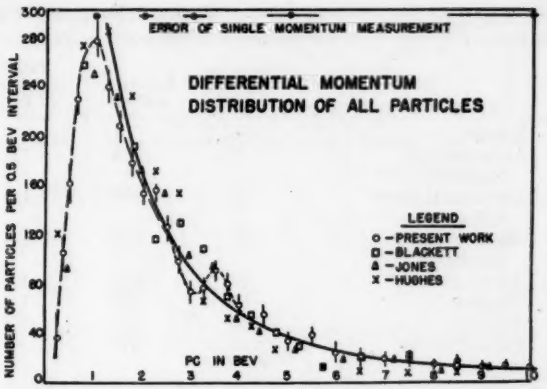

FIG. 2. The dashed curve represents the raw data; the full curve results after correction for the magnetic cut-off effect at low momenta. A possible anomaly at 3 Bev/c is shown dotted.

V. RESULTS AND CONCLUSIONS; COMPARISON WITH OTHER EXPERIMENTS

1547 measureable pairs of photographs were taken in this experiment, 127 of them representing particles of momentum greater than 10 Bev/c. Figure 2 shows the differential momentum distribution of the particles of momentum less than 10 Bev/c. Each point represents the number of particles found in 0.5 Bev/c interval centered about the momentum plotted as abscissa. Vertical bars indicate the standard deviations of these numbers and the horizontal bars are errors in momentum derived from the mean error of the angle measurements. The dashed curve follows the raw data; the full curve has been corrected for the variation of the aperture of our instrument with momentum. After the correction is applied it is at best difficult to determine the position of the maximum point of the distribution since the instrument is very strongly biased against particles of low momentum when operated at high magnetic field strengths. An unusual feature of the distribution is the apparent irregularity at about 3.5 Bev/c which is shown dotted in Fig. 2. Overlapping intervals have been used to plot the low end of the spectrum in order to represent the data in more detail. As a result only half the points

[9] E. J. Williams, Proc. Roy. Soc. A169, 531 (1939).

TABLE I. Summary of momentum distribution surveys.

Reference	Resolving power in Bev/c	Number of particles	Peak of distribution in Bev/c	Exponent of power law	Positive–negative ratio	Means of limiting electrons
Kunze[a]	3	61	—	—	1	single tracks*
Anderson and Neddermeyer[b]	5	78	1.0	−1.7	1.2	single tracks
LePrince-Ringuet and Crussard[c]	20	300	1.0	—	1.7	magnetic cutoff
Blackett and Brode;[d] Blackett[e]	20	829	1.0	−1.9	1.2	magnetic cutoff
Jones[f]	10	923	1.0	−1.9	1.3	10 cm lead
Hughes[g]	16	674	1.0	−2.5	1.2	10 cm lead
Wilson[h]	20	424	0.8	−1.8	—	lead
Present work	80	1547	—	−1.8 below 10 Bev/c −2.1 above 10 Bev/c	1.26±0.06	magnetic cutoff

* Not counter-controlled.
[a] See reference 1.
[b] See reference 2.
[c] See reference 3.
[d] See reference 4.
[e] See reference 5.
[f] See reference 6.
[g] See reference 7.
[h] See reference 8.

shown at the low end are statistically independent. Blackett[5] found a similar irregularity at somewhat lower momentum. At Manchester where his measurements were made, the minimum momentum a proton requires to arrive from the vertical direction is about 2 or 3 Bev/c; at Pasadena this value is 7 Bev/c. One might reasonably expect some characteristics of the spectrum, therefore, to be different in the two places.

Table I contains a summary of the salient features of all of the surveys of the momentum distribution published to date in which counter-controlled cloud chambers and magnetic fields were used. We have taken the resolving power to be that value of the momentum at which the error in determining the momentum reaches 100 percent. For comparison we have plotted the results of the three of the previous surveys in which the largest numbers of measurements were reported. After normalization to include the same number of particles between about 1 Bev/c and 10 Bev/c we find Jones' data agree excellently with the present work. Blackett's data also lie closely on our curve except for the anomaly at 2.5 Bev/c. Hughes' data seem to lie consistently below our results for momenta above 3 Bev/c and consistently above for lower values of the momentum. Though the statistics are not good enough in any one of these experiments to establish the presence of an irregularity around 3 Bev/c, all of them seem to show some evidence for it. Adding all the data together might be the wrong thing to do, however, if the suspected effect is latitude sensitive. In comparing the various sets of data, it should be observed that the resolution of the present experiment is roughly twice that of Blackett's in the range below 10 Bev/c. The other authors did not give a detailed error estimate. Figures 3 and 4 show the differential momentum distributions of positive and negative particles, respectively.

In Fig. 5 is plotted the distribution of the excess of positive over negative particles, the full curve representing the data after correction for magnetic biasing. There seems to be a concentration of positive particles around 1.3 Bev/c with a gradual tailing off toward high momenta. Again the normalized data of previous experiments are replotted and verify in a general way the present results although the poorer statistics and resolv-

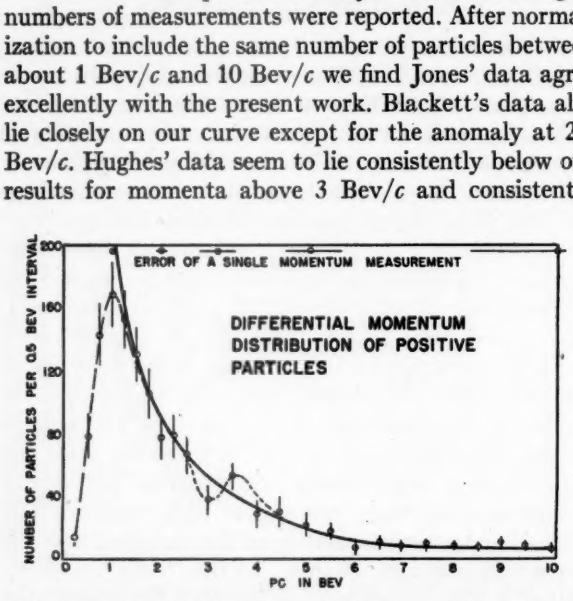
ERROR OF A SINGLE MOMENTUM MEASUREMENT
DIFFERENTIAL MOMENTUM DISTRIBUTION OF POSITIVE PARTICLES
NUMBER OF PARTICLES PER 0.5 BEV INTERVAL
PC IN BEV

FIG. 3. The dashed curve represents the raw data; the full curve results after correction for the magnetic cut-off effect at low momenta. A possible anomaly at 3 Bev/c is shown dotted.

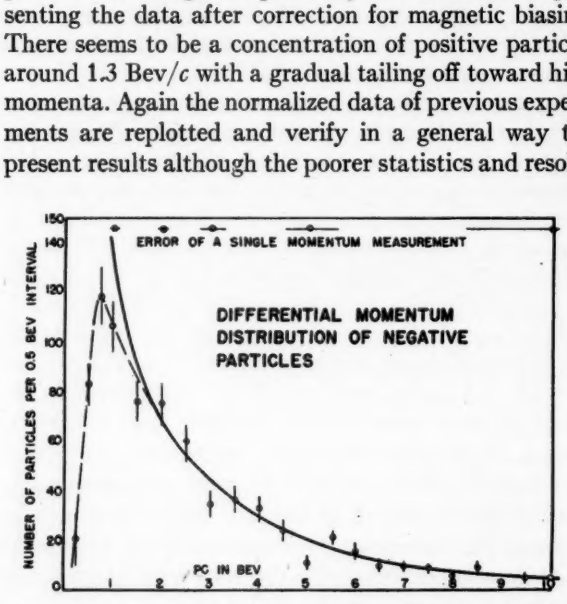
ERROR OF A SINGLE MOMENTUM MEASUREMENT
DIFFERENTIAL MOMENTUM DISTRIBUTION OF NEGATIVE PARTICLES
NUMBER OF PARTICLES PER 0.5 BEV INTERVAL
PC IN BEV

FIG. 4. The dashed curve represents the raw data; the full curve results after correction for the magnetic cut-off effect at low momenta. The low point at 3 Bev/c is similar to the corresponding one in Fig. 3.

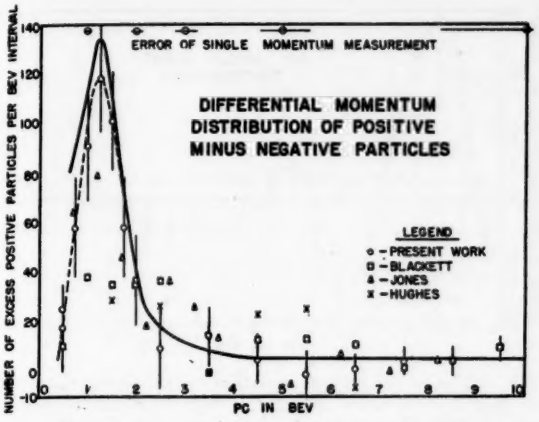
ERROR OF SINGLE MOMENTUM MEASUREMENT
DIFFERENTIAL MOMENTUM DISTRIBUTION OF POSITIVE MINUS NEGATIVE PARTICLES
LEGEND
o - PRESENT WORK
□ - BLACKETT
Δ - JONES
x - HUGHES
NUMBER OF EXCESS POSITIVE PARTICLES PER BEV INTERVAL
PC IN BEV

FIG. 5. The dashed curve represents the raw data; the full curve results after correction for the magnetic cut-off effect at low momenta.

ing powers of the earlier results wash out the sharp peak to a large extent.

Corresponding to the variation of the positive–negative excess with momentum, the ratio of positives to negative seems to vary with momentum, the ratio having a peak at about 1.5 Bev/c. In Table II are listed the values of the positive–negative ratio computed for 2 Bev/c intervals centered about the momentum values tabulated.

Actually the apparent variation of the positive–negative ratio is not outside the statistical uncertainty for this experiment alone, but Owen and Wilson[10] have recently found an indication of similar behavior with better statistics. We also agree with Brode[11] who finds the ratio 1.37 ± 0.04 in a range around 1.5 Bev/c.

The over-all ratio of positives to negative is 1.26 ± 0.06; the ratio for the 127 particles of momentum greater than 10 Bev/c is 1.2 ± 0.2.

Figure 6 shows the differential momentum distribution for particles between 10 Bev/c and 100 Bev/c. Plots of the positive and negative spectra separately are similar but the statistics do not permit a very critical comparison.

In order to compare these results with the theory and make various calculations, it is desirable to try to find some simple analytical representation for the cosmic-ray momentum distribution. As is shown in Fig. 7 the data are well-fitted by a distribution of the form $1/p^s$ with $s=1.8\pm0.2$ from 2.5 Bev/c to 10 Bev/c and $s=2.1\pm0.6$

TABLE II. Ratio of numbers of positive to negative particles.

Center of 2-Bev/c momentum interval	Positive–negative ratio
1.5 Bev/c	1.36 ± 0.1
2.5	1.24 ± 0.1
3.5	1.15 ± 0.1

[10] B. G. Owen and J. G. Wilson, Proc. Phys. Soc. London **A62**, 601 (1949).
[11] R. B. Brode, Phys. Rev. **76**, 468 (1949).

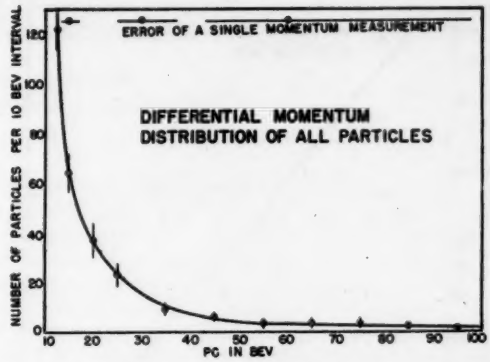
ERROR OF A SINGLE MOMENTUM MEASUREMENT
DIFFERENTIAL MOMENTUM DISTRIBUTION OF ALL PARTICLES
NUMBER OF PARTICLES PER 10 BEV INTERVAL
PC IN BEV

FIG. 6. Distribution for 112 particles of momenta between 10 Bev/c and 100 Bev/c.

from 10 Bev/c to about 70 Bev/c. For simplicity in calculations $s=1.9$ is quite good for the whole range. A fairly good fit can also be obtained with an exponential law, $\exp(-kp)$, but at least three different values of k are needed to cover the whole range of momenta. Similarly the integral spectrum can be represented by $1/p^n$ with $n=1.2$ as shown in Fig. 8 in good agreement with the result for the differential spectrum. The upper end of the integral spectrum is somewhat uncertain because of the uncertainty in the number of particles above 100 Bev/c apparent momentum. Fifteen such particles were found and a $1/p^2$ law for the differential spectrum when extended to infinite momentum predicts twelve particles. No significant differences between the analytical behaviors of the positive and negative distributions were found.

It was possible to divide all the particles observed here into two groups; those that occurred at night and those that came in when the sun was above the horizon in Pasadena. By chance the running times of the apparatus at night and during the day gave nearly equal

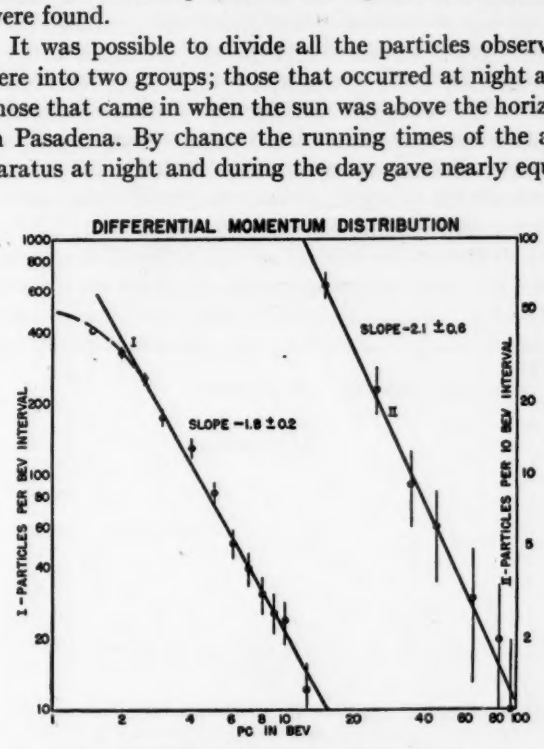

FIG. 7. Logarithmic plot of total differential momentum distribution.

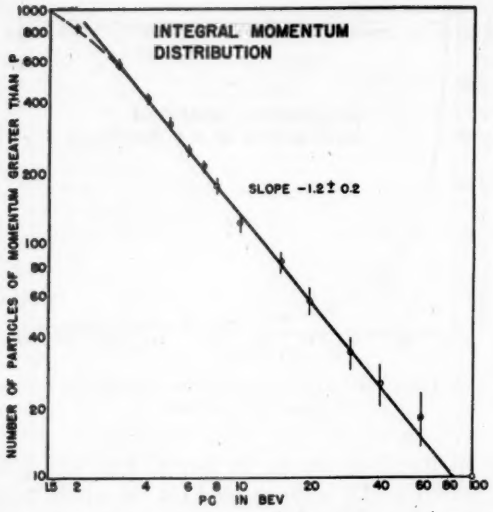

FIG. 8. Logarithmic plot of total integral momentum distribution.

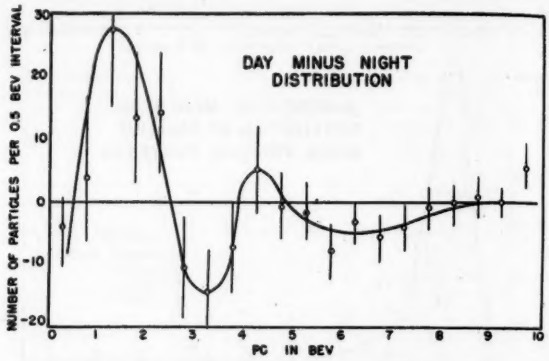

FIG. 9. Plot of the diurnal variation of the differential momentum distribution. Each ordinate is the difference between the number of particles occurring during the day and the number occuring during the night for the 0.5 Bev/c interval placed symmetrically about the plotted abscissa.

numbers of night time and daytime particles. In Fig. 9 is plotted the momentum distribution of the day particles minus the night particles. Although the statistical accuracy is poor, there seems to be some indication of a variation favoring 1 Bev/c particles during the day and 3 Bev/c and 7 Bev/c particles at night. Perhaps it is not an accident that this 3 Bev/c irregularity coincides with that of the whole momentum spectrum. Above 10 Bev/c the same number of particles occurred during the day as at night. In a recent paper, K. Dwight[12] gives a calculation of the diurnal variation in primary intensity at the top of the atmosphere due to the combined magnetic fields of the earth and the sun, assuming that the sun actually has a permanent field. A rough extrapolation of his results to latitude 33° gives the following expectation. At Pasadena no singly charged primary particle of momentum less than 7 Bev/c can hit the earth at the vertical. Above 10 Bev/c little diurnal effect is expected at Pasadena, while between 7 Bev/c and 10 Bev/c one expects an effect, the time of maximum intensity occurring at different times for different momenta. To calculate how rapidly the time of maximum intensity varies with momentum requires considerable numerical work and, in any event, the total variation is not expected to exceed 10 percent. Since the curve shown in Fig. 9 is presumably for meson secondaries, it would be surprising if any diurnal variation should survive at sea level at all. This is a point that might bear further examination experimentally. There was no evidence of a correlation with sidereal time.

Rossi[13] has compared previous measurements of the sea level momentum spectrum with the intensity *versus* depth curve for charged cosmic-ray particles deep underground to see whether ionization loss alone is sufficient to explain the rate of absorption of the cosmic rays. He finds good agreement out to a momentum of 10 Bev/c, one point at 20 Bev/c being in apparent disagreement indicating that the more energetic particles lose energy at a greater rate than can be accounted for by ionization loss alone. When our data are normalized to compare with Rossi's curve, we confirm in a rough way the discrepancy above 10 Bev/c. Calculations are now under way to determine whether radiation and pair production losses are sufficient to account for the discrepancy.

In conclusion the authors wish to thank Professor Carl D. Anderson for his continued interest and assistance and Professor Robert B. Leighton for assistance in the design of the cloud chambers.

[12] K. Dwight, Phys. Rev. **78**, 40 (1950).

[13] B. Rossi, Rev. Mod. Phys. **20**, 537 (1948).

The Measurement of Gamma-Ray Energies with Single Crystals of NaI(Tl)

R. HOFSTADTER AND J. A. MCINTYRE
Palmer Physical Laboratory, Princeton University,† Princeton, New Jersey*

(Received July 12, 1950)

A new method is described for determining gamma-ray energies and intensities. The basis of the method is the observation of narrow pulse distributions (lines) in the scintillations of NaI(Tl). Due to the presence of the iodine component, pair production and the photoelectric process produce relatively sharp lines in the pulse distributions. The Compton process may also be used in determining gamma-energies. Approximate theoretical curves of the pulse distribution are shown. Experimental spectra resemble the theoretical patterns, except for differences in intensities discussed in the text. Electronic as well as photographic techniques for obtaining spectra are described. With these methods well known spectra are confirmed and new results in the case of Ga^{66} are given. With a source of less than 10^{-9} curie of K^{40} the energy of the gamma-ray has been determined to within two percent. The method described should make possible a new approach to the study of weak gamma-radioactivities and unknown gamma-ray spectra.

IN an earlier paper[1] one of the authors showed that sodium iodide, activated by a small thallium impurity, was a useful material for detecting gamma-rays in the device now called a scintillation counter. In those studies it was also shown that gamma-rays of different energies could be distinguished by their corresponding pulse size distributions. It was stated, furthermore, that the rules for distinguishing gamma-rays of different energies were not clear. Since that time much progress has been made in the solution of this problem and the main point of this paper is to report on some aspects of this new knowledge.[2] It was also demonstrated[1] that potassium iodide was a useful material, but since its pulses are smaller than those of NaI it will not be considered below.

Gamma-rays interact with matter by the three well-known processes of Compton effect, photoelectric effect, and pair production. In sodium the photoelectric and pair production processes are rather unimportant compared with the Compton effect for energies up to about 5 Mev. In iodine, on the contrary these effects are by no means negligible and in fact offer new possibilities for energy measurements with gamma-rays.

Figure 1 shows the variation of absorption coefficient[3] for the iodine constituent (85 percent by weight) of NaI. Thallium is present to less than 0.5 percent by weight and will be neglected in the approximations discussed. On the basis of these cross sections and neglecting the small contribution due to sodium,[4] the curves of Figs. 2, 3, 4 show approximations to the pulse distributions which may be expected theoretically for gamma-rays of the indicated energies. In these figures the photoelectric (*Ph*) and pair (*P*) pulse distributions have been calculated on the following assumptions. (1) All photoelectric processes result in the production of electrons in the NaI crystal with the full energy of the gamma-ray. (2) The pulse distributions are Gaussian and due entirely to the statistics of the photo-multiplier tube. (3) Approximately 1000 electrons are produced at the photo-multiplier cathode surface for a 1.0-Mev electron[5] in the crystal. (4) The pair energy is the gamma-energy minus 1.02 Mev and all pair pulses are uniform and subject to the statistical width considerations just described. The Compton distributions in the figures have been corrected only partially (in the energy regions near the high energy edges) for the broadening effects due to statistics of the photo-multiplier since these distributions are already continua and the figures are only approximations to the actual pulse distributions. The areas under the various Gaussian components have been chosen according to the data in Fig. 1. In the assumption (1) above, it is suggested that

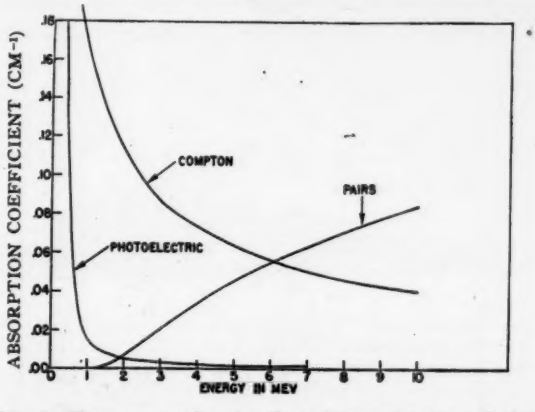

FIG. 1. The cross section for the primary processes of photoelectric capture, Compton scattering and pair production in the iodine constituent of NaI(Tl).

* Earlier reports of this work were given at the Meeting of the Metropolitan Section of the American Physical Society, Brookhaven, March 31–April 1, 1950, and at the Mexico City Meeting of the American Physical Society, June 21–23, 1950.

† This work was partially supported by the U. S. Army Signal Corps and by the joint program of the ONR and AEC.

[1] R. Hofstadter, Phys. Rev. **75**, 796 (1949); **74**, 100 (1948).

[2] Work in some respects similar to that here reported was also done by S. A. E. Johansson, Arkiv f. Fysik **18**, 171 (1950). R. W. Pringle, K. I. Roulston, and S. Standil, Phys. Rev. **78**, 627 (1950). P. R. Bell and J. M. Cassidy, Phys. Rev. **79**, 173 (1950).

[3] R. G. Evans, *Advances in Biological and Medical Physics* (Academic Press, Inc., New York, 1948), Vol. 1, pp. 167–168.

[4] If it is desired to include the effect of sodium the Compton curve should be increased by 21 percent, the pair curve increased by four percent and the photoelectric curve should remain unaffected.

[5] J. A. McIntyre and R. Hofstadter, Phys. Rev. **78**, 617 (1950).

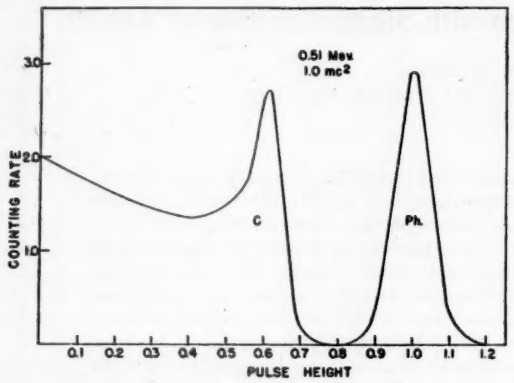

FIG. 2. Approximate pulse distribution to be expected in a NaI(Tl) single crystal when struck by 0.51-Mev gamma-radiation if only primary processes occur.

the energy is the full energy of the gamma-ray and *not* that energy minus the binding energy of a K, L, etc. electron. For if a K, L electron is set free the subsequent x-ray produced will also be captured, perhaps after degradation, so that eventually electrons are produced with all the energy of the x-ray.

Assumption (3) indicates a figure, 1000 electrons/Mev, which differs by a factor of two from a previous estimate.[5] The difference arises from (a) inclusion in this estimate of the statistical widening of the pulses due to variable multiplication at the dynodes of the multiplier and (b) use in this estimate of the standard deviation in place of the half-width at half maximum used earlier, by mistake. The number of electrons N corresponding to a peak of standard deviation σ and mean value V is

$$N=[r/(r-1)](V/\sigma)^2,$$

where r is the mean value of the multiplication factor at the dynodes. r is assumed to be 4 for this calculation.

We have found experimental evidence for the reality of the curves of Figs. 2, 3, 4. Furthermore, this evidence opens up an entirely new and most powerful method of investigating the energies and intensities of gamma-rays. An example discussed below (K^{40}) shows that sources as weak as 0.001 microcurie can be investigated successfully so that the gamma-ray energy can be found to within two percent or better.

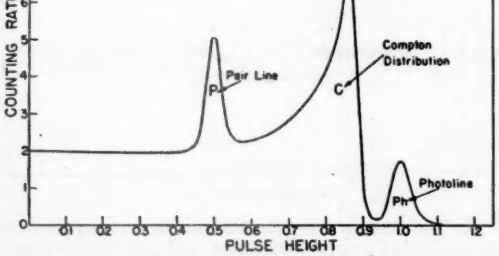

FIG. 3. Approximate pulse distribution to be expected in a NaI(Tl) single crystal when struck by 2.04-Mev gamma-radiation if only primary processes occur.

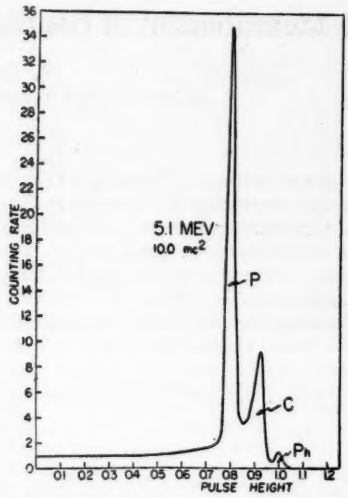

FIG. 4. Approximate pulse distribution to be expected in a NaI(Tl) single crystal when struck by 5.1-Mev gamma-radiation if only primary processes occur.

Figure 5 shows the experimentally observed pulse distribution in Au^{198} which has principally a gamma-ray line at 0.411 Mev. The curve shown was taken with a differential discriminator,[5] an EMI photo-multiplier tube (35 μa/lumen) and a 0.5-in. crystal cube of NaI,

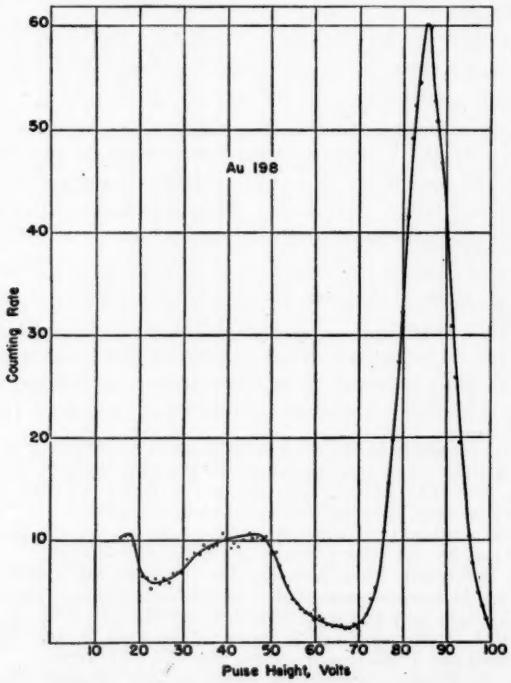

FIG. 5. Experimental discriminator pulse distribution observed with Au^{198} 0.411-Mev gamma-radiation. Data have been taken with a single channel discriminator. The photo-peak at 85.5 volts is quite accurately Gaussian. To obtain counts per second multiply ordinate scale by 1.06.

FIG. 6. The pulse distribution for Au^{198} photographed on an oscilloscope screen. The bright band at the top is the photo-peak at 0.411 Mev. Below the gap lies the Compton distribution, with a relatively sharp edge. Superposed on the Compton distribution is a low energy gamma-ray at 0.075 Mev.

in a collimated arrangement of the gamma-rays in which the beam struck the middle third of the crystal and had about a 1° angular width. For this energy the curve taken without collimation is very similar. The peak at 85.5 volts is due to the photoelectric effect and also to gamma-rays scattered by the Compton process whose second-scattered (third, etc.) gamma-rays are finally completely captured by the crystal. The broad distribution peaking near 48 volts is due to the Compton effect as a primary process, the scattered gamma-ray escaping the crystal. Also indicated near 19 volts is partial evidence of another peak. Figure 6 shows the pulse distribution for Au^{198} as photographed on an oscilloscope screen. One sees clearly the "photoelectric" line at the top, the broad Compton distribution and the low energy peak corresponding to the flattening near 19 volts in Fig. 5. The low energy peak corresponds to an energy of about 0.075 ± 0.006 Mev.

This line has not been reported in the literature[6] although its low energy may have made its detection difficult. An x-ray line of mercury following internal conversion of the 0.411-Mev line is a possibility. A similar K x-ray line has been observed recently by Hill[7] in Au^{199}. On the other hand, since only rough chemical separation has been employed, an impurity might be the source of this line. Other structure in this spectrum will be discussed below.

Figures 5 and 6 show a strong resemblance to Fig. 2 when the proper correction is made for cross sections at the energy 0.411 Mev. At 0.411 Mev the areas under the Compton curve and under the photoelectric peak should be approximately equal if only primary processes occur. Nevertheless the area under the "photoelectric" peak is too large to be given by this simple theory. This fact has led us to suggest[5] that secondary processes contribute to the photoelectric peak.

The photo-line of Fig. 5 has been fitted empirically by a Gaussian curve. The fit is excellent and within the experimental error at every point above a counting rate of 5, in the ordinate units of Fig. 5. The half-width, assuming only statistical causes of broadening, results in an assignment of about 400 electrons at the photocathode for the energy 0.411 Mev. This value is in agreement with the figure 1000 electrons/Mev obtained previously from the Co^{60} lines and a different crystal.

Au^{198}, because of the low energy of the gamma-ray, offers no evidence of pair production. The second case to be discussed, Na^{24}, does indeed show a pair line. Na^{24} has two gamma-rays of energy 1.38 Mev, 2.76 Mev. The pulse distribution taken with the differential discriminator has been published recently.[8] Figure 7 shows the pulse distribution photographed on the oscilloscope screen. At the top the weak photoelectric line (2.76 Mev) appears. Under it one can see the broader, more intense Compton distribution due to the 2.76-Mev line. Below it is the strong pair line at 1.74 Mev. Below the pair line lie the 1.38-Mev photo-line and the Compton distribution of the 1.38-Mev line. Between the pair line (1.74 Mev) and the Compton distribution of 2.76 Mev there is a weak band easily observed in the original plate. This band appears in the position to be expected if either of the gamma-rays produced on annihilation of the pair-produced positron is captured in the crystal. Figure 2 of an earlier publication[8] also shows this band. With a larger crystal this band will undoubtedly become more prominent, because of increased capture of annihilation radiation.

It may be observed that the Compton peaks have a characteristic shape (Fig. 2 of reference 8); they are sharp on the high energy side and show a gradual falling off on the low energy side. This feature will be of help in analyzing unknown spectra.

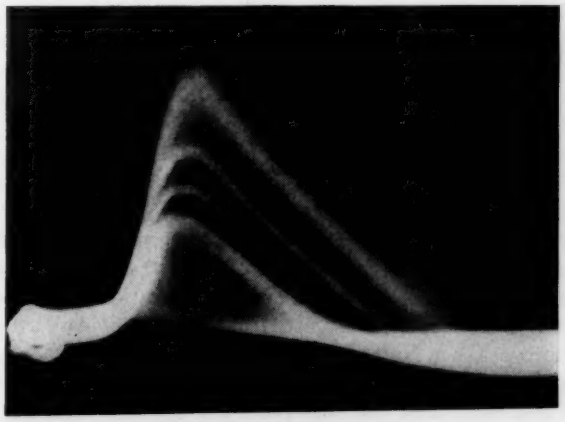

FIG. 7. The pulse distribution for Na^{24} photographed on an oscilloscope screen. The weak 2.76-Mev photo-peak appears at the top. Below it lies the Compton distribution and the prominent pair peak of the 2.76-Mev radiation. Between the pair peak and the Compton edge lies a weak band due to capture of annihilation radiation in the crystal. The photo-peak of 1.38 Mev lies above the continuum due to the Compton effect for 1.38 Mev.

[6] A. C. G. Mitchell, Rev. Mod. Phys. **22**, 36 (1950).
[7] R. D. Hill, Phys. Rev. **79**, 413 (1950).
[8] R. Hofstadter and J. A. McIntyre, Phys. Rev. **79**, 389 (1950), Fig. 1.

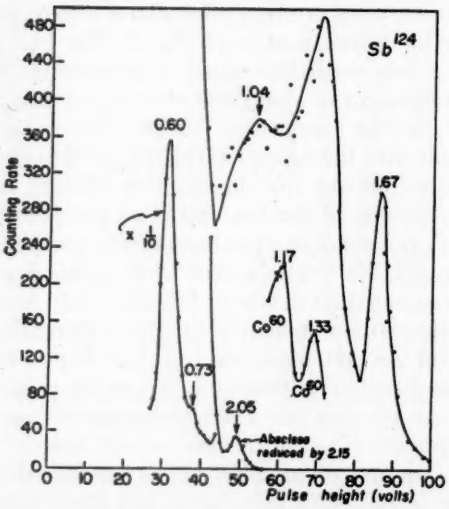

FIG. 8. The discriminator run for Sb^{124} using a collimated source. Co^{60} calibration lines are also shown.

It is clear from the figures shown that single crystal pulse distribution curves can be used to determine gamma-ray energies by locating correlated triads of peaks (*Ph*, *C*, *P*) when the energy is greater than 1.02 Mev and correlated pairs of peaks for lower energies. In fact, the interval between the pair line and photoline offers an internal calibration scheme.[9] However, it is also clear that the presence of numerous peaks due to a single line will make for troubles in analyzing a complex spectrum of gamma-rays. A larger crystal will add more bands and therefore more complexity, as evidenced in the case of the Na^{24} example. In such cases other methods[8,10] involving two or more crystals in coincidence will be useful. Perhaps an organic crystal which interacts essentially by Compton processes with the gamma-rays will also be useful as a rough indication of the more prominent gamma-ray lines.

The gamma-rays 1.38 and 2.76 Mev in Na^{24} are of equal intensity. If only primary processes occur in the gamma-ray—NaI(Tl) interactions, the ratio of intensities of the various peaks should be given by the curves of Fig. 1. Comparing the areas of Peaks II, III, and V, respectively, in Fig. 1 of the earlier paper[8] we obtain the respective relative values 1.21, 1.00, 0.48. According to the theoretical curves of Fig. 1 these ratios should be 0.64, 1.00, 0.25. As suggested in the case of Au^{198} the photo-peaks in Na^{24} also have contributions of secondary origin and are larger than the theory indicates. It is also clear that the pair peak III has lost intensity, because of absorption of annihilation radiation in the crystal, to the band between III and IV. A further small contribution to the photopeak arises from simultaneous capture of two annihilation quanta. Intensities cannot be determined therefore at first glance and corrections will be required for the secondary processes of capture. Nevertheless, rough intensities can be told at a glance. It is also probably true that the curves of Fig. 1 of this paper have not been verified completely and further work along these lines may show what corrections are needed to make them more perfect.

Figure 8 shows the more complex spectrum of Sb^{124}. The known gamma-rays[6] of Sb^{124} are located at 0.603, 0.650, 0.714, 1.71 and 2.06 Mev. Their intensities are given roughly by Kern *et al.*[11] Figure 8 shows also the Co^{60} (1.33, 1.17 Mev) photo-lines, useful in calibration of the scale. The known lines[11] are all shown, except the weak line at 0.650 Mev which is apparently concealed in the much more intense 0.603-Mev line. The unusual

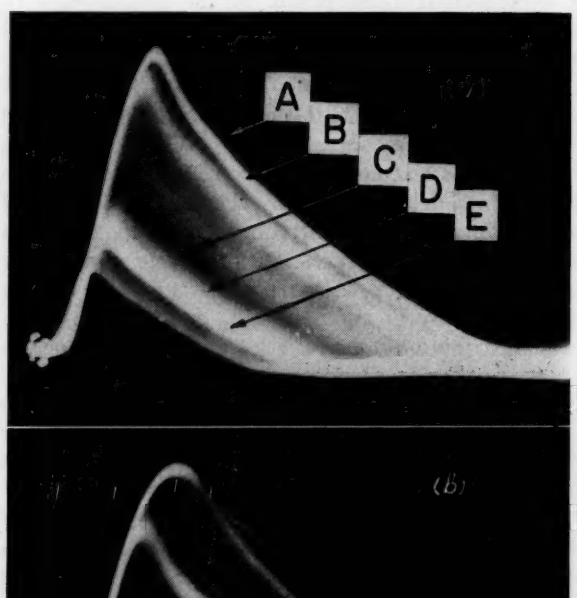

FIG. 9. (a) Photographic representation of Sb^{124}. *A* represents the weak 2.05-Mev photo-line. *B* is the 1.67 photo-line. *C* represents the weak pair line of 2.05 Mev. *D* (see also Fig. 9b) represents the weak 0.73 photo-line and *E* the strong 0.60 photo-line.

(b) Expanded photographic representation of Sb^{124} obtained by increasing the gain of the amplifier. The higher energy peaks are crowded into the topmost edge. The bright band in the middle is the 0.60-Mev photo-line and under it lies the Compton distribution for this line. Above the 0.60-Mev photo-line is the weak 0.73-Mev line observed in Fig. 9a. The unusual crowding of topmost peaks is not typical and resulted from special settings of oscilloscope amplifier gain.

[9] Let the photo-line have the position V_1 and the pairline the position V_2. The energy of the gamma-ray, E, is then

$$E=\frac{2mc^2}{\left[1-\left(\frac{V_2}{V_1}\right)\right]}.$$

[10] R. Hofstadter and J. A. McIntyre, Phys. Rev. **78**, 619 (1950).

[11] Kern, Zaffarano, and Mitchell, Phys. Rev. **73**, 1142 (1949).

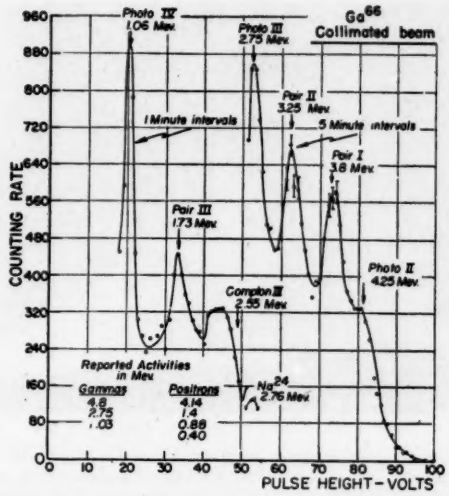

FIG. 10. Discriminator spectrum of Ga^{66}. Na^{24} photo-line is used as a reference (below). A pair line is observed at about 62 volts corresponding to a new gamma-line at 4.27 Mev.

shape of our 1.67-Mev line at higher energies is probably due to the superposition of the 2.05-Mev Compton distribution and the 1.67 photo-line. The band at 1.04 Mev is probably due to pair production of the 2.05 line. The pair peak of 1.67 Mev is weak and is concealed under the 0.603-Mev line. The differences between our observed energies and those previously reported are within our experimental error (~two percent) but this error does not represent a real measure of the possible accuracy of this method. Careful temperature control of the electronic parts is an essential element in making precise measurements of energy. In the time available we have unfortunately not been able to eliminate drifts of the discriminator and associated equipment. Our voltage control of the photo-multiplier however has been better than ±0.1 percent.

Figures 9a and 9b show the photographed pulse distributions in Sb^{124}. The strong peak at *B* in Fig. 9a is the 1.67-Mev photo-line. The weak peak at *A*, above *B*, is due to the 2.05 line. At *C* is the pair line 1.04 Mev. *D* is the 0.73-Mev photo-line and *E* the 0.60-Mev photo-line. Figure 9b was taken with greater amplifier gain, resulting in distortion and crowding together of the higher energy lines, but shows clearly the weak 0.73 Mev above the prominent 0.603-Mev photo-line near the center of the pattern.

Another example of a complex scheme is provided by Ga^{66}. In this case we have found evidence for a new gamma-ray line near 4.30 Mev which decays with the known half-life of Ga^{66}. We are also able to estimate rough intensities of the gamma-lines in this spectrum. Figure 10 shows the spectrum observed with the differential discriminator. Figure 11 shows the lower part of the spectrum enlarged by increase of amplifier gain. The peak at 3.25 Mev is believed to represent the pair line of a new gamma ray of intensity roughly equal to that of the 4.8-Mev line.[12] Figure 12a shows the oscilloscopic representation and Fig. 12b a second representation with increased amplifier gain. A discriminator curve of the lowest region, not shown, shows peaks[13] at 0.296 Mev and 0.186 Mev. These and other curves show that the photo-line at 1.06 Mev has an area about twice that of the 2.75-Mev pair line. Referring to Fig. 1 this means that the 1.06-Mev line is about twice as intense as the 2.75-Mev line. However, as we have previously observed, the photo-peak is usually larger than expected by about a factor of two and a corrected ratio of intensities of 1:1 for these gamma-lines seems to be reasonable.[14] It is interesting, and in good agreement with Moffat and Langer's energy level scheme for Zn^{66} that our new line at 4.27 Mev fits in with the proposed level at 4.29 Mev.

Three final examples are given, the first of which relates to an important point requiring consideration when observing single crystal spectra. The latter two illustrate the power of the method. Figure 13 shows the oscilloscopic representation of Co^{60} uncollimated. In addition to showing the two photo-lines and the composite Compton peak, there is a small band located near 0.2 Mev. This does not represent a real gamma-line and does not appear in the same strength when a collimated beam is used. It is believed that this peak is due to back scattered gamma-rays, captured (mainly photoelectrically) by the NaI and produced in the surroundings of the crystal and perhaps also at crystal

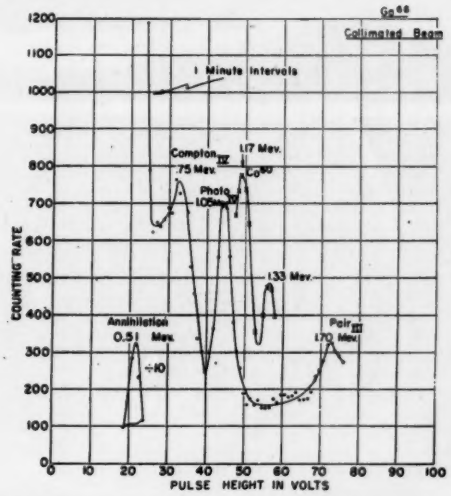

FIG. 11. Expanded discriminator run of the lower energy part of the Ga^{66} spectrum.

[12] R. D. Moffat and L. M. Langer, Phys. Rev. **79**, 237 (1950).

[13] The peaks at 0.296 and 0.186 Mev have not been followed to see whether they have the same decay period as Ga^{66}, and are quite probably due to Ga^{67} made by $(\alpha,2n)$ reaction on Cu^{65}. Ga^{67} has a half-life of 78 hours and has gamma-lines at 0.30, 0.18 and 0.093 Mev. We have not looked for the lowest energy gamma-line in our work.

[14] A private communication from Dr. L. M. Langer informs us that the ratio 300:1 reported in the abstract (reference 12) was a typographical error and the actual ratio is close to unity, as we find.

edges by Compton processes. Probably other "ghosts" due to multiple scattering will also appear.

Figure 14 shows a double exposure of the gamma-rays from a source of Au^{198}. The upper band was exposed for about 700 seconds and the lower intense band (0.411-Mev photo-line) for about 2 seconds. It therefore appears that this gold sample, made in the pile, shows another line at 0.66 Mev in addition to those at 0.411 Mev and at 0.075 Mev. Initial measurements with the differential discriminator showed that the weaker line at 0.66 Mev was present to about 1 part in 250 compared to the main line at 0.411 Mev. Subsequently the 0.66-Mev line grew stronger relative to the 0.411-Mev line. After the gold activity had decayed further, a second line at about 0.86 Mev appeared and possibly a third at a higher energy. The impurity responsible for these lines is unknown but may be Ag^{110} formed by neutron capture in Ag^{109}. Ag^{110} has strong gamma-lines at 0.66, 0.88 and 1.5 Mev.

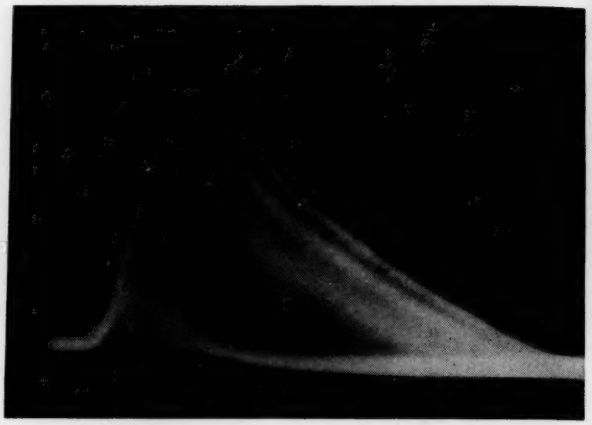

FIG. 13. Co^{60} photographic representation observed with uncollimated source. Weak band near bottom of pattern is a spurious peak produced by backscattered gamma-rays. The two photo-peaks are shown at top.

We have also examined the spectrum of K^{40}, using an enriched sample of this material.[15] The amount of K^{40} used was 0.6 mg and represents an effective source strength of less than 0.001 microcurie gamma-ray activity. Figure 15 shows the data observed with this source. The background was made negligible by enclosure of the detecting apparatus in a 6.0-inch wall lead house. The two peaks of Na^{24} (1.38-Mev photo-line and 1.74-Mev pair line) and the 1.33-Mev peak of Co^{60} were used for calibration. From these data the photo-line of K^{40} appears at 1.48 ± 0.02 Mev which agrees with other recent determinations[2,16] within the experimental error. Photographs of the oscilloscopic representation

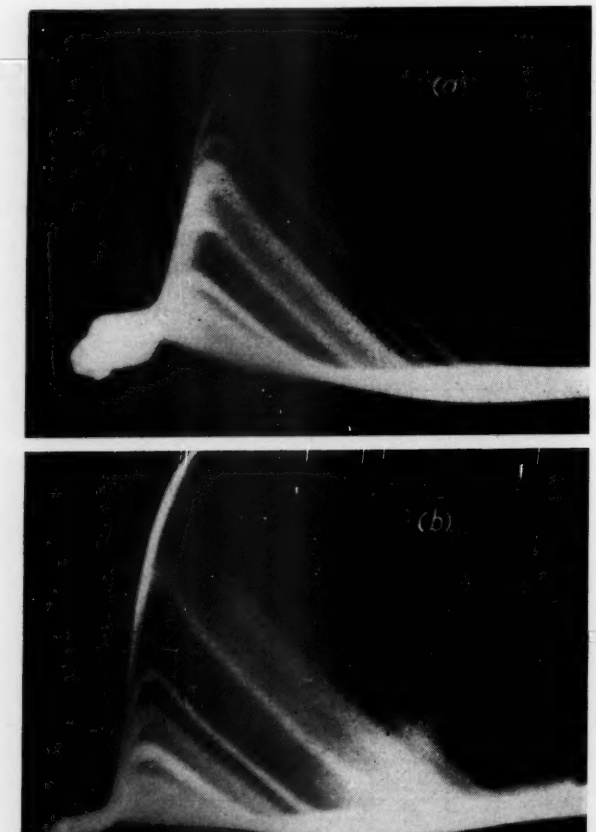

FIG. 12. (a) Photographic representation of Ga^{66}. The three higher energy peaks corresponding to Pair I, Pair II, Photo III appear at the top followed below by the broad Compton distribution of the 2.75-Mev line.

(b) Expanded photographic representation of Ga^{66} emphasizing low energy peaks. The very bright band at the bottom is the annihilation radiation photo-peak. Above it are the Compton distribution and photo-peak of the 1.05-Mev line. There is a gap leading to the 1.73-Mev pair peak which is superposed on the 2.75-Mev Compton distribution.

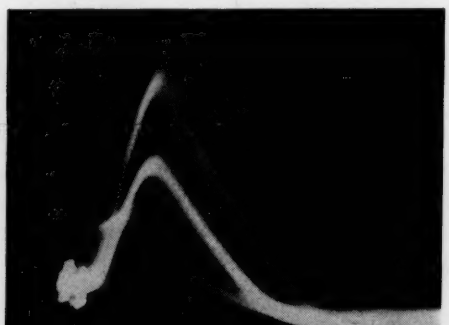

FIG. 14. Double exposure of Au^{198} gamma-rays. Peak at top is due to weak 0.66-Mev gamma-ray present initially to about one part in 250 of the strong 0.411-Mev gamma-ray whose photo-peak stands out sharply in the photograph.

[15] We are indebted to Dr. C. S. Wu (Columbia University) and the Isotopes Branch ORNL, for putting sources of enriched K^{40} at our disposal.

[16] Pringle, Standil, and Roulston, Phys. Rev. 77, 841 (1950). P. R. Bell and J. M. Cassidy, Phys. Rev. 77, 409 (1950).

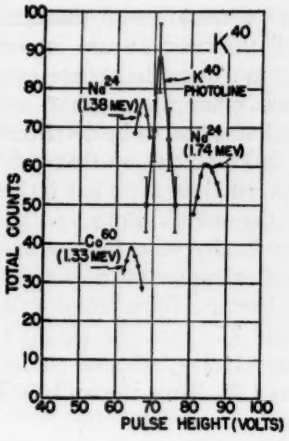

FIG. 15. The photo-line of K^{40} and Na^{24} and Co^{60} calibration lines. The source strength was less than 10^{-9} curie. The data were taken in about five hours. The K^{40} energy is 1.48 ± 0.02 Mev.

of the pulses in K^{40} show that there is no other gamma-ray present with an intensity greater than about 10 percent of the 1.48-Mev line. Our success with the photographs of oscilloscope patterns suggests that this technique will be valuable for work with weak sources since it serves the purpose of a multichannel discriminator. Densitometer traces we have made of gamma-ray patterns resemble the discriminator curves very closely. For initial spotting of gamma-ray lines this technique will probably not be surpassed.

We are greatly indebted to Drs. Dean Cowie and P. Abelson of the Carnegie Institution of Washington for supplying us with sources of Ga^{66}. We wish to thank Drs. E. P. Tomlinson and J. L. Simons for sources of Au^{198}.

PHYSICAL REVIEW VOLUME 80, NUMBER 4 NOVEMBER 15, 1950

Photo-Disintegration Cross Sections of Deuterium and Beryllium for the Gamma-Rays of Sodium 24 and Gallium 72

ARTHUR H. SNELL, E. C. BARKER, AND R. L. STERNBERG
Oak Ridge National Laboratory, Oak Ridge, Tennessee

(Received June 22, 1950)

Photo-neutron yields from spheres of D_2O and Be containing Na^{24} and Ga^{72} gamma-ray sources were measured by spatial integration of induced foil activities in a large paraffin block. A standard neutron source was used to calibrate the apparatus.

The Ga^{72} and Na^{24} sources were subsequently dissolved, and their radioactive strengths were measured by beta-counting of aliquots. The data so obtained, when combined with the known wall thickness of the spheres led to the following results after the application of appropriate corrections:

(1) Photo-disintegration cross section of D at 2.76 Mev: 14.3×10^{-28} cm²
(2) Photo-disintegration cross section of Be at 2.76 Mev: 6.74×10^{-28} cm²
(3) Cross section of D at 2.50 Mev multiplied by intensity of 2.50 Mev line in quanta per Ga^{72} beta-emission: 2.81×10^{-28} cm²
(4) Sum of cross sections of Be at 1.84, 2.20 and 2.50 Mev weighted according to respective gamma-intensities in Ga^{72}: 2.16×10^{-28} cm²

These results are believed accurate within 8 percent. Agreement with theory is discussed for both D and Be.

I. INTRODUCTION

THE measurements to be described in this paper were made in 1945–46. At that time a rather complete survey of photo-neutron yields was envisaged. Since circumstances have prevented the completion of such a survey, we describe here our study of the yields from Na^{24} and Ga^{72}. The results may be of interest inasmuch as very little has been published on this subject. Comparable work which has come to our attention is that of Russell, Sachs, Wattenberg, and Fields[1] and Wilson, Collie, and Halban.[2]

It is easy to see from first principles that if a gamma-emitting radioactive source is placed in a small spherical cavity in the center of a sphere of beryllium or heavy water, the number of photo-neutrons emitted per second will be given by

$$S = QN(\Sigma_i \alpha_i \sigma_i) \qquad (1)$$

where Q is the number of radioactive transformations taking place per second within the source, N is the wall thickness of the spherical shell expressed in terms of the number of Be or D atoms per square centimeter, α_i is the relative intensity (i.e., the mean number of quanta per radioactive transformation) of the ith gamma-ray above the photo-neutron threshold for beryllium (1.67 Mev) or deuterium (2.235 Mev), and σ_i is the (γ, n) cross section at the energy of the ith gamma-ray. This expression will hold so long as there is negligible neutron and gamma-ray absorption in the spherical shell. We are here concerned with the experimental measurement of the $\Sigma_i \alpha_i \sigma_i$. In the case of Na^{24} this leads to a value for the photo-dissociation cross sections at 2.76 Mev,

[1] Russell, Sachs, Wattenberg, and Fields, Phys. Rev. **73**, 545 (1948).
[2] Wilson, Collie, and Halban, Nature **163**, 245 (1949), and supplementary communication from Professor Halban.

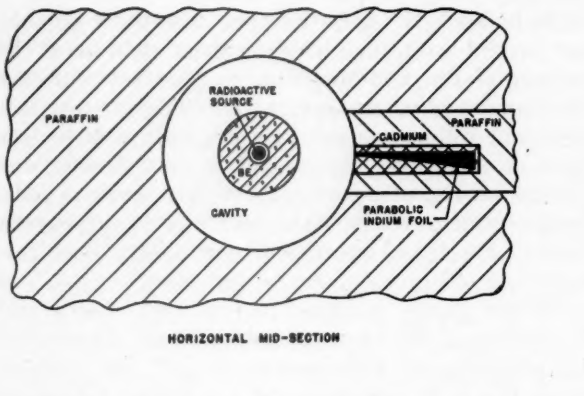

FIG. 1. Experimental arrangement used for measuring photo-neutron yields. The beryllium sphere was chosen for indication in the sketch, but the D_2O sphere was nearly the same size and had similar geometry. The 2-g Ra source placed in the beryllium sphere, without the covering plug, constituted the standard (photo-neutron) source used for calibration purposes.

and in the case of Na^{24} a direct comparison with theory is possible. Even for the more complicated decay scheme of Ga^{72} comparison with theory can be instructive, although it is less satisfactory because of the difficulty of measuring the α's with precision.

II. EXPERIMENTAL

The radioactive sources consisted of several grams of NaF or Ga_2O_3 contained in Lusteroid tubes and activated in the Oak Ridge Nuclear Reactor to a strength of a few tenths of a curie. They were first placed in the beryllium and heavy water spheres, and the photo-neutron outputs were measured; they were then dissolved, and aliquots were taken for absolute beta-counting. For a closer discussion, we shall describe severally the measurements of N, Q, and S.

The Spheres

The beryllium sphere had an average diameter of 10.05 cm and departed from sphericity by less than 0.10 cm along various diameters. A radial recess 2.22 cm in diameter and 6.36 cm deep permitted the insertion of the radioactive source (Fig. 1). After the source was in place, a beryllium plug was inserted over it so as to complete the shell. Let us call $(10.05-2.22)/2=3.91$ cm the "nominal" wall thickness. This is not the correct wall thickness to use in our formula because of two factors: first, the source cavity was cylindrical rather than spherical, so that some kind of average wall thickness had to be determined; second, the source was of finite extent, so that the γ-rays did not in general proceed along radii but rather had slightly longer paths in the metal. Both of these effects were estimated graphically; the former involved a reduction of the nominal wall thickness by a factor 0.92 and the latter an increase by a factor 1.04, together yielding a final value 3.75 cm. The weight of the sphere without plug was 911.2 g, whence the mean density of the metal was 1.78. Thus the wall thickness N in terms of atoms per cm^2 was 4.46×10^{23}.

The D_2O sphere was contained in a shell spun of brass $\frac{1}{2}$ mm thick. It was slightly smaller in diameter than the beryllium sphere, and had an entrant brass tube to contain the radioactive source, with a covering cap containing about 6 g of D_2O. The nominal wall thickness of D_2O was 2.86 cm. Corrections were again determined graphically. The cavity shape correction reduced the nominal wall thickness by a factor 0.889 and the finite source size correction increased it by a factor 1.03; thus the final value was 2.62 cm, whence $N=1.75\times10^{23}$. The weight of D_2O in the sphere was close to 270 g.

III. THE NEUTRON MEASUREMENTS

The photo-neutron sources were placed in a paraffin pile and the space-integrated radioactivity induced in cadmium-covered indium foils was compared with that induced by a calibrated neutron source of known intensity. In the actual experimental arrangement, (Fig. 1) each source was placed at the center of a spherical cavity, 24 cm in diameter, centered in the paraffin. The whole paraffin pile measured $54\times48\times32$ inches; it had been built by the Metallurgical Laboratory group under L. Szilard, and it was fortunately available to us for this work. Rather than measure the indium resonance activity distributions explicitly to compare the (activity$\times r^2$) integrals, we cut parabolic indium foils and laid them between sheets of cadmium, 0.020 inch thick, in the equatorial plane of the paraffin geometry. The width of any element of the foil was then proportional to the square of the radial distance of that element from the center of the total geometry, and the narrow end of the foil came to the boundary of the cavity in the paraffin. The foils had to be about 15 cm long in order to cover the region containing the indium resonance neutrons. After irradiation, the foils were removed and wrapped in a standard way about a thin-walled Geiger counter.

The standard source happened also to be a photo-source, consisting of a capsule containing 1935 mg of radium bromide placed in our beryllium sphere, without the beryllium plug. The absolute neutron output of this combination could be derived by comparisons that had

been made with the following three independently standardized Ra–Be sources:

(1) A source known as Source *I* in the Metallurgical Laboratory literature. This source had been calibrated absolutely by Anderson *et al.*[3] by a method depending on the calculation by diffusion theory of the slow neutron flux emerging from a pile of pure graphite with the source buried in it. Source *I* had been compared[4] with another Ra–Be source known as Source *II*, which in turn had been compared with our standard photo-source by Bernstein *et al.*[5] The results were: for Source *II*, 12.8×10^6 neutrons per second, and for our photo-source, 4.09×10^6 neutrons per second.

(2) Source *II* had been independently absolutely calibrated by Agnew *et al.*[6] in a water tank containing boron. The result, 14.0×10^6 neutrons per second, was somewhat higher than the above figure obtained by comparison with Source *I*, and led through the same intercomparison by Bernstein to the figure 4.48×10^6 neutrons per second by our photo-source.

(3) A Los Alamos source known as No. 44. Absolute standardization of this source had been carried out carefully by Walker[7] (result: 5.90×10^6 neutrons per second) and comparison with our Ra–Be photo-source was possible through two linkages. In the first place, Bernstein[5] had compared our Ra–Be photo-source with a Ra–B source known as No. 37, and Walker had compared No. 37 with No. 44. Walker's result for No. 37 was 4.28×10^6 neutrons per second, and this led through Bernstein's comparison to a strength of 4.13×10^6 neutrons per second for our photo-source.

The second comparison arose through the fact that Bernstein had also intercalibrated sources 37 and *II*; therefore the chain 44→37→*II*→(Ra–Be photo-source) could be set up. Using Walker's figure of 4.28×10^6 for No. 37, Bernstein's comparison gave 12.9×10^6 neutrons per second for Source *II*, in close agreement with the graphite pile calibration mentioned in paragraph (1) above. The derived strength for our photo-source was 4.12×10^6 neutrons per second.

As a final figure for the strength of the Ra–Be photo-source substandard, we have chosen 4.17×10^6 neutrons per second. This result comes from weighting the calibration of source No. 44 slightly more favorably than the earlier calibrations of Sources *I* and *II*.

IV. THE RADIOACTIVE SOURCE STRENGTHS

After the radioactive sources had been dissolved, the solutions were stirred thoroughly and two or three aliquots consisting of about 10^{-6} of the total were taken volumetrically. These samples were then evaporated on thin backing, and counted under a mica-window counter. The counting efficiency was determined by means of a separated UX_1 sample for which a specific activity of 724 disintegrations per minute per milligram was assumed. Suitable corrections were evaluated and applied for window absorption, backscatter, counting loss, and counts arising from the gamma-rays.

V. TREATMENT OF DATA AND RESULTS

Several different parabolic indium foils were used, and each was calibrated by three separate activations with the Ra–γ–Be standard source (4.17×10^6 neutrons per sec.) If a fraction, k, of the neutrons from the source is absorbed in the foil, and if the beta-particles are counted with an efficiency E_f, then E_fk is given by (saturation activity of foil in counts per sec.)/4.17×10^6. Thus E_fk was determined for the various foils; the values had a spread over a range of 4 percent in the neighborhood of 7.77×10^{-6}.

Now if we take the zero of time at the instant of starting the exposure of the parabolic indium foil to the photo-neutron sources under investigation, application of the laws of radioactive decay yields without approximation the following expressions for $\Sigma_i\alpha_i\sigma_i$ in terms of the parameters of the experiment:

$$\sum_i \alpha_i\sigma_i=\frac{1}{E_fk}\left(\frac{E_\beta A}{N}\right)\left(\frac{\lambda_f-\lambda_s}{\lambda_s}\right)\times\left\{\frac{e^{-\lambda_s t_2}-e^{-\lambda_s t_3}}{(e^{-\lambda_f t_a}-e^{-\lambda_f t_b})(e^{-\lambda_s t_1}-e^{-\lambda_f t_1})}\frac{N_f}{N_A}\right\}. \quad (2)$$

The symbols hitherto undefined have the following meanings: λ_f and λ_s are the decay constants of the indium foil and the radioactive source respectively, A is the aliquot fraction, E_β is the efficiency of counting the beta-particles of the aliquot, t_1 is the time of the end of the exposure of the indium foil (60 min. throughout), t_2 is the time of the start of the aliquot count and t_3

TABLE I. The figures in column 2 give results uncorrected for gamma-ray absorption and neutron slowing down in the spheres. Column 5 gives the results corrected for these effects as explained in the text. Columns 3 and 4 give the numbers of independent foils activated and aliquots taken and counted. Column 6 gives standard yields as derived from the figures of column 5, and column 7 gives comparable figures obtained by other workers.

1	2	3	4	5	6	7
Photo-source	$\Sigma\alpha_i\sigma_i$ before correction	Number of parabolic foils activated	Number of aliquots counted	$\Sigma\alpha_i\sigma_i$ after correction	Standard yield*	Standard yield (Russell *et al.*)
Na–Be	$6.02\pm0.04\times10^{-28}$ cm²	7	7	$6.74\pm0.04\times10^{-28}$ cm²	14.1×10^4	14×10^4
Na–D_2O	13.4 ± 0.2	6	8	14.3 ± 0.2	27.0	29
Ga–Be	1.83 ± 0.02	7	7	2.16 ± 0.03	4.5	5.9
Ga–D_2O	2.58 ± 0.04	7	7	2.81 ± 0.04	5.3	6.9

* Neutrons per second per curie of radioactive material situated 1 cm from 1 g of deuterium or beryllium.

[3] Anderson, Fermi, Roberts, and Whitaker, MDDC 880, unpublished.
[4] M. D. Whitaker and J. H. Roberts, Metallurgical Laboratory Report CP-10, unpublished.
[5] S. Bernstein, private communication.
[6] Agnew, Anderson, Miller, Roberts, Whitaker, and Wollan, MDDC 878, unpublished.
[7] R. L. Walker, MDDC 414, unpublished.

TABLE II. Summary of knowledge of the gamma-rays of Ga^{72} above the Be(γ, n) threshold.

Gamma-ray energies		Gamma-ray intensities (α_i)*		σ(Be) Theor.	$\alpha_i\sigma$(Theor.)	
MZK	Haynes	MZK	Haynes	Guth and Mullin	MZK (ref. 10)	Haynes (ref. 11)
1.81 Mev	1.87 Mev	0.102	0.078±0.02	7.5×10^{-28} cm²	0.76×10^{-28} cm²	0.59×10^{-28} cm²
2.18	2.21	0.33	0.33 ±0.05	5.4	1.78	1.78
2.50	2.51	0.154	0.265±0.04	5.8	0.89	1.54
				$\Sigma_i\alpha_i\sigma_i$ (Theor.):	3.43×10^{-28} cm²	3.91×10^{-28} cm²

* Quanta per $Ga^{72}-Ge^{72}$ radioactive transformation.

is the time of its conclusion ($t_3-t_2=10$ min. throughout), N_A is the total number of beta-counts registered in the interval t_3-t_2 from the aliquot, t_a (5 min. throughout) and t_b (55 min. throughout) are the beginning and conclusion times of the foil count measured from the *end* of the activation of the indium foil, and N_f is the number of foil counts observed in the interval t_b-t_a. Usually, t_2 was less than two half-lives of the radioactive source.

In a typical experiment two or three foils were activated from one of the sources placed in one of the spheres, after which the source was transferred to the other sphere and two or three more foils were activated. After dissolving the source two or three aliquots were taken. For a given photo-source Eq. (2) was applied to all of the possible foil-aliquot combinations, and the resulting values of $\Sigma_i\alpha_i\sigma_i$ were averaged with equal weight. The whole procedure was carried through for three or four freshly pile-irradiated radioactive sources. For example, in the case of Na$-D_2O$ three Na^{24} samples were used from which a total of six foils were activated and eight aliquots were counted. The possible foil-aliquot combinations per Na^{24} source added to give a total of sixteen determinations of $\Sigma_i\alpha_i\sigma_i$—not all independent, but all approximately equally reliable. The mean of these sixteen "determinations" is listed in column 2 of Table I, together with its "probable error" as derived from the spread of the individual values.

VI. CORRECTIONS

There are several corrections which clearly should be considered for the values of $\Sigma_i\alpha_i\sigma_i$ thus obtained. All of these are in the direction of increasing $\Sigma_i\alpha_i\sigma_i$. They are as follows:

A. Absorption of the γ-Rays in the Sphere

Our spheres were sufficiently large to make this a correction worth stating explicitly. If one assumes in a spherical geometry a wall thickness (R_2-R_1) and allows for the Compton absorption of the gamma-quanta in the material of thickness ($r-R_1$) inside of a shell at thickness dr and radius r, one obtains instead of (1) the following expression for the photo-neutron source strength:

$$S=QN\,\Sigma_i\{1-\exp[-\mu_i(R_2-R_1)]\}(\alpha_i\sigma_i/\mu_i)$$

Where μ_i is the total Compton absorption coefficient in cm^{-1} for the ith gamma-ray. This derivation assumes that any scattering of the original gamma-quantum will remove it from the picture so far as photo-neutron generation is concerned. Actually, it is seen that only a few percent of the quanta make either a Compton or a nuclear collision, so that the chance that any one of them will make a subsequent nuclear collision is negligible. Also there is a good chance that the original collision will reduce the energy of the quantum below the (γ, n) threshold. The assumption is therefore justified. The correction factors thus evaluated for $\Sigma_i\alpha_i\sigma_i$ are as follows: for Na$-D_2O$, 1.05; for Na$-$Be, 1.11; for Ga$-D_2O$, 1.06; for Ga$-$Be, 1.14.

B. Absorption of the Gamma-Rays in the Radioactive Source

Here the assumption was made that the average path length traversed by the gamma-quanta in the cylindrical radioactive sources was equal to the radius of the source. This was close to 1 cm. On this basis, the correction factors to be applied to were as follows: for NaF sources, 1.01; for Ga_2O_3 sources, 1.02.

C. The Slowing Down of Neutrons to below Indium Resonance before Escaping from the Sphere

Here we have adopted the corrections evaluated by Bernstein. In his work, using a radium gamma-source in the D_2O and Be spheres, the neutron distribution in the paraffin had been determined with cadmium-covered indium foils. These distributions, in terms of foil activity $\times r^2$, were extrapolated according to a purely r^2-decrease across the cavity in the paraffin to the outer surface of the sphere, and thence taken to decrease linearly to zero at the center of the sphere. The fragment of area under the foil activity $\times r^2$ curve thus obtained within the boundary of the sphere was compared with the total area under the curve as it extended into the paraffin. When allowance was made for the difference in slowing down density in the material of the sphere and the paraffin, it was thus estimated that 1 percent of the neutrons were slowed to indium resonance within both the beryllium and D_2O spheres. Although these corrections were evaluated for a radium source, we have applied them without change to our various source-sphere combinations.

D. Parasitic Capture of Neutrons above the Indium Resonance Level in the Source Material and, in the Case of the D_2O, in the Brass Shell of the Sphere

This we take to be negligible. One of the advantages of using the indium resonance activations instead of thermal activations is simply the great reduction in this effect.

Column 3 of Table I gives our values of $\Sigma_i \alpha_i \sigma_i$ after the application of these corrections.

VII. ERRORS

The probable errors of the means of the individual "determinations" of given in Column 5 of Table I show that the data are quite good so far as internal consistency is concerned. With regard to absolute values, systematic errors contribute the main uncertainties. In all, the probable precision of the various parts of the measurement can be summarized thus:

(1) Counting errors, as judged from the scatter of the data 1%
(2) Absolute calibration of Ra—Be photosource substandard 6%
(3) Systematic errors in absolute beta-count of aliquots 4%
(4) Wall thickness uncertainty 2%

Thus the over-all absolute precision can be estimated as probably about 8 percent. Clearly the relative values will be considerably more accurate, in that item 2 will not be involved, and 3 would be expected to be reduced.

In the case of the gallium, three separate Ga_2O_3 sources were activated, and each of these was used in the D_2O and in the Be. Consequently the ratio (standard yield in Be)/(standard yield in D_2O) should be especially accurate,[7a] because errors in the radioactive source strength determination are not involved; the only errors should be those of items 1 and 4. In this respect it is gratifying to note excellent agreement with the same ratio as derived from the work of Russell *et al.* (Table I), where it should also be particularly accurate for like reasons. Unfortunately our work with sodium involved only one source used both in D_2O and in Be; there were in addition two other sources used only in D_2O and two more used only in Be. Thus the Be/D_2O yield ratio is not expected to be so accurate as in the case of gallium. This may be part of the reason for the fact that the agreement with Russell *et al.* is also not as good; however, it is doubtful whether the disagreement can be considered significant inasmuch as their stated precision for the Be/D_2O yield ratios is 7 percent, and ours (for Na) is probably 3 or 4 percent.

VIII. DISCUSSION

We shall divide the discussion of our results into four paragraphs, of which the latter two are predominantly concerned with comparison with theory.

(1) *Sodium*—Since there is widespread agreement[8] that one 2.76 Mev gamma accompanies each beta-transition in Na^{24}, and since there is a negligible number of cross-over transitions with the cascading 1.38 Mev gamma,[9] we can drop our α_i notation and accept the figures 14.3 and 6.74×10^{-28} cm² as our results for the photo-disintegration cross sections respectively of deuterium and beryllium at 2.76 Mev.

(2) *Gallium*—The rather complicated decay scheme of Ga^{72} has been studied by Mitchell, Zaffarano, and

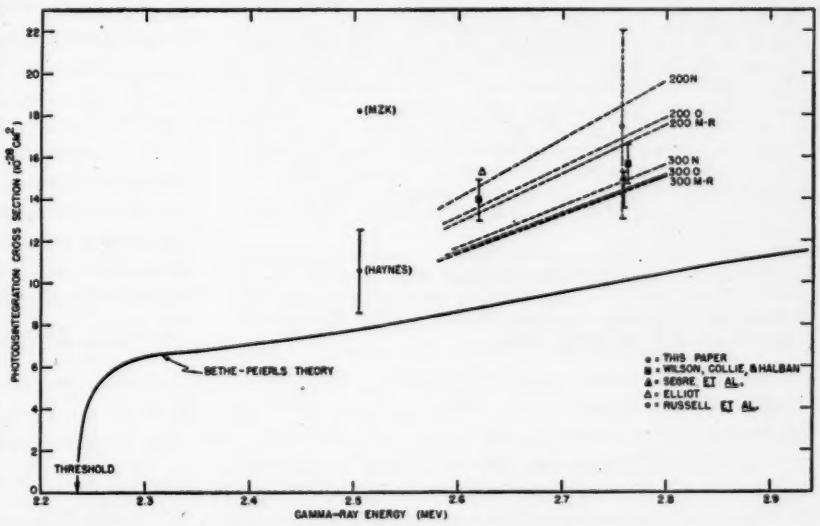

FIG. 2. Cross-section data on the photo-disintegration of the deuteron. The dashed lines are drawn through the points at 2.62 and 2.76 Mev as calculated theoretically by Hansson and Hulthén; the figures 200 and 300 refer to the assumed meson mass, and *N*, *O* and *M-R* refer, respectively, to calculations based upon the neutral meson theory, no interaction in the ^3P state, and the Møller-Rosenfeld theory. The experimental points attributed to Elliott and Segrè have been quoted by Wattenberg [A. Wattenberg, "Photoneutron Sources," Preliminary Report No. 6, Nuclear Science Series, Division of Mathematical and Physical Sciences, National Research Council]; the former has also been quoted by Sargent [B. W. Sargent, National Research Council of Canada, Division of Atomic Energy, Report PD-206, unpublished.]. The two points at 2.50 Mev are derived according to discrepant measurements of the intensity of this gamma-ray in Ga^{72} (see text).

[7a] The term "standard yield" is defined in the footnote for Table I.

[8] References to Na^{24} include among others: J. Itoh, Proc. Phys. Math. Soc. Japan **23**, 605 (1941); Elliot, Deutsch, and Roberts, Phys. Rev. **63**, 386 (1943); H. Maier-Leibnitz, Zeits. f. Physik **122**, 233 (1944); K. Siegbahn, Phys. Rev. **70**, 127 (1946); Cook, Jurney, and Langer, Phys. Rev. **70**, 985 (1946); E. C. Barker, Phys. Rev. **71**, 453 (1947).

[9] Bishop, Wilson, and Halban, Phys. Rev. **77**, 416 (1950).

Kern[10] and by Haynes.[11] The results for the lines above the beryllium (γ, n) threshold are summarized in columns 1 to 4 of Table II. The intensity values are based in both cases on the assumption that every Ga^{72} beta-emission is followed sooner or later by a gamma-quantum in the 0.835 Mev line. The 2.50 Mev quantum is the only one above the deuterium threshold, so that in this case we can deduce corresponding cross section values. Using our $\alpha\sigma$ value 2.81×10^{-28} cm² from Table I one obtains, in fact, photo-disintegration cross section values of 18.2×10^{-28} cm² on the MZK intensity[10] and 10.6×10^{-28} cm² on the Haynes intensity.[11] Comparison with other results (Fig. 2) shows that the former figure seems improbably high, while the latter figure appears reasonable even if inaccurate.

(3) *Deuterium*—In order to see how the present measurements agree with previous experimental results and with theory, the published data on the total photo-disintegration cross section of deuterium in this energy range have been assembled in Fig. 2. In this figure, dashed straight lines have been drawn joining the points calculated by Hansson and Hulthén[12] for 2.62 and 2.76 Mev, with (1) a meson mass of 200 m, (N) on the neutral meson theory; (0) on the assumption of no interaction in the ^3P state; and ($M-R$) on the Møller-Rosenfeld theory; and (2) with a meson mass 300 m and the same respective theoretical bases N, 0 and $M-R$.*

A glance at the figure shows that the experimental results agree rather well with the modern theory, but that they are not yet sufficiently accurate for a critical comparison. It is also clear that it will be difficult in this energy region to obtain experimental results accurate enough to favor definitely one or other of the alternates N, 0 or $M-R$. Hansson and Hulthén have implied that for comparisons of this accuracy the theory might also be due for refinement. All that can be said at this time is that our result at 2.76 Mev seems to join others in favoring a meson mass greater than 200 m.

(4) *Beryllium*—Our cross section 6.74×10^{-28} cm² at 2.76 Mev is in good agreement with the results of Russell *et al.*[1] and of Segrè and also Elliot as quoted by Guth and Mullin.[13] Guth and Mullin have treated the photo-disintegration of Be^9 theoretically on the basis of a model consisting of a Be^8 core plus an orbital neutron, and have succeeded in showing that a combination of $P-S$ and $P-D$ transitions can lead to a threshold maximum-minimum curve for the dependence of the cross section on gamma-ray energy in agreement with the type of variation found experimentally. The well depth describing the interaction of the Be^8 core with the orbital neutron appears in the theory as an adjustable parameter. Taking the published theoretical curve at its face value, one finds that with good agreement with experiment at 2.76 Mev, the cross sections at the Ga^{72} gamma-ray energies are as listed in the fifth column of Table II. The following two columns combine these cross sections with the MZK[10] and the Haynes[11] intensities to yield $\alpha_i\sigma_i$ values which on addition yield the sums 3.43 and 3.91×10^{-28} cm² for comparison with our photo-neutron result (Table I) 2.16×10^{-28} cm². There is, therefore, a discrepancy between theory and experiment so far as the summed results are concerned. Considering especially the evidence from deuterium that the Haynes intensity for the 2.50 line is approximately right, one is faced with a rather strong implication that the Guth-Mullin curve lies too high in the region below 2.76 Mev.

We are much indebted to S. Bernstein for advice, equipment and information, without which these measurements would have been much more time-consuming. We wish also to thank M. E. Rose for theoretical consultations, L. D. Norris for help in the absolute beta-counting, and the Subcommittee on Neutron Standards (Division of Mathematical and Physical Sciences, National Research Council) for information on the intercalibration of neutron sources. Correspondence with A. Wattenberg, H. Halban, L. G. Elliott, and R. L. Walker on various aspects of the work is gratefully acknowledged.

[10] Mitchell, Zaffarano, and Kern, Phys. Rev. **73**, 1424 (1948).
[11] S. K. Haynes, Phys. Rev. **74**, 423 (1948).
[12] I. F. E. Hansson and L. Hulthén, Phys. Rev. **76**, 1163 (1949).
[13] E. Guth and C. J. Mullin, Phys. Rev. **76**, 234 (1949).

* *Note added in proof:* I. F. E. Hansson has just published (Phys. Rev. **79**, 909 (1950)) the results of an extension of the Hansson-Hulthén computations, so that theoretical cross sections are now available for the Ga^{72} gamma-ray energy. For the sake of completeness we shall quote his figures for the total photo-disintegration cross section of the deuteron at 2.52 Mev, with binding energy 2.237 Mev. They are as follows, in units 10^{-28} cm²: 200-N, 11.82; 200-O, 11.14; 200-MR, 10.96; 300-N, 10.13; 300-O, 9.96; 300-MR, 9.96.

The reader should also be aware that an extensive experimental investigation of the photo-disintegration cross sections for the gamma-rays of Ga^{72}, ThC″ and Na^{24} has recently been completed by Hedgran, Siegbahn, du Toit, Bishop, Collie, Halban, and Wilson (Phys. Rev., in publication).

Deuteron Bombardment of C^{14}

EMMETT L. HUDSPETH* AND CHARLES P. SWANN
Bartol Research Foundation of the Franklin Institute,† Swarthmore, Pennsylvania

AND

N. P. HEYDENBURG
Carnegie Institution of Washington, Department of Terrestrial Magnetism, Washington, D. C.

(Received July 13, 1950)

Bombardment of C^{14} by deuterons produces three nuclear reactions, yielding neutrons, α-particles, and protons, and leads thereby to the formation of N^{15}, B^{12}, and a new radioactive isotope, C^{15}. The half-life of this sixth isotope of carbon is 2.4 sec., and the end point of the β-ray spectrum lies at 8.8 Mev.

Approximate values for relative yields from the various reactions are given, the neutron spectrum is obtained, and the nature of the γ-rays emitted during bombardment is reported.

I. INTRODUCTION

THE radioactive isotope C^{14} can be produced in an atomic pile in quantities sufficient to utilize it as a target material. We have obtained from Oak Ridge several milligrams of $BaCO_3$ which is enriched in C^{14} by about 40 percent.

Thin targets can be prepared from this material by a method previously described.[1] For our purposes, however, targets were prepared by forming a slurry of $BaCO_3$ on a silver disk.[2] Targets usually weighed 200–400 $\mu g/cm^2$, which corresponds to a thickness of 25 to 50 kv for deuterons of energy about 1 Mev. Targets of this type were bombarded with deuterons accelerated in the Van de Graaff generator at the Bartol Foundation[3] or in the larger generator at the Carnegie Institution of Washington[4] (in the case of the $C^{14}(d, p)C^{15}$ reaction). Three different reactions have been observed, yielding neutrons, protons, and α-particles. Only the neutrons have been observed "directly," from proton recoil data; protons and α-particles produced by deuteron bombardment are inferred from the formation of radioactive isotopes.

II. NEUTRON SPECTRUM OF $C^{14}(d, n)N^{15}$

We have used photographic plates to observe the neutrons from the bombardment of C^{14} by deuterons.[3] Ilford C.2 plates with emulsion thickness of 100μ were exposed at 0° and at 90° to a deuteron beam of energy 1.26 Mev. Exposure was made with the edge of the plates about 1 cm from the target and continued for about 6 μa-hr. Development and fixing of the plates were performed by following the procedure of Blau and De Felice,[5] and proton recoils were observed and measured with a microscope. Only recoils which were within 12° of the forward direction and which lay wholly within the emulsion were counted. Our earlier data[3] have been extended by one of us (CPS) and the results are shown in Figs. 1a and 1b.

The residual nucleus N^{15} has excited levels which have been previously established by other reactions. The neutron groups which may be expected from $C^{14}(d, n)$ should correspond to Q-values which leave N^{15} excited to levels[6] of 8.2 Mev (if the bombarding energy is sufficient), 7.2, 6.0(?), 5.39 Mev, and the ground state. At 0° to a deuteron beam of energy 1.26 Mev, we could therefore anticipate groups of neutrons of energies 9.1, 3.8, 3.2, 2.0, and 1.0 Mev; at 90°, the energies become 8.5, 3.4, 2.9, 1.7, and 0.8 Mev. The arrows in Figs. 1a and 1b are placed at abscissas corresponding to these energies. Calculated Q-values from the data of Fig. 1a are 8.15, 2.83, 1.87, and 0.71 Mev; Fig. 1b yields Q-values of 8.18, 2.83, 1.83, and 0.71 Mev. The curves show considerable asymmetry in the groups, and this would indicate fine structure.

The reaction $C^{12}(d, n)$ also takes place during bombardment, but its Q-value (−0.28 Mev) is too near the −0.18 Mev value anticipated for one of the groups from $C^{14}(d, n)$ to make resolution possible. It is obvious, however, that the total yield of neutrons from C^{14} bombardment at 1.26 Mev is considerably greater than the yield of neutrons from bombardment of C^{12}. Correction for track length and emulsion thickness shows that the relative yield from C^{14} bombardment is at least two or three times as great as the yield from C^{12} bombardment.

III. THE REACTION $C^{14}(d, \alpha)B^{12}$

Bombardment of C^{14} with deuterons leads to the production of a β-emitter of very short half-life. Absorption of the β-rays in aluminum showed[3] that their maximum energy was about 13 Mev, and the shape of the absorption curve was identical (Fig. 2) to that which had been previously observed in this laboratory for the β-rays from B^{12}. No attempt was made to measure the half-life of the β-emitter formed in the bombardment of C^{14}, other than to observe visually that the β-emission stopped essentially simultaneously with the cessation

* Present address: Department of Physics, University of Texas, Austin, Texas.

† Assisted by the Joint Program of the ONR and AEC.

[1] Shoupp, Jennings, and Sun, Phys. Rev. 75, 1 (1949).

[2] Several of these targets were kindly prepared by Dr. E. Shapiro.

[3] E. L. Hudspeth and C. P. Swann, Phys. Rev. 78, 337 (1950).

[4] Hudspeth, Swann, and Heydenburg, Phys. Rev. 77, 736 (1950).

[5] M. Blau and J. A. De Felice, Phys. Rev. 74, 1198 (1948).

[6] The data are summarized by W. F. Hornyak and T. Lauritsen, Rev. Mod. Phys. 20, 217 (1948).

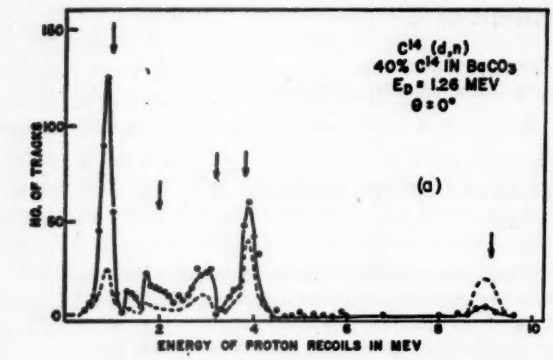

FIG. 1. Neutron spectrum from bombardment of C^{14} by deuterons. The intense group just below 1 Mev comes largely from bombardment of C^{13}. Arrows indicate positions of groups anticipated from known levels of N^{15}. (a) Observations at 0° to the bombarding beam, (b) observations at 90°.

of bombardment. These facts, together with the expected possibility of the reaction, serve to confirm the formation of B^{12} from $C^{14}(d, \alpha)$. B^{12} has a known half-life of 0.02 sec. and emits β-rays of maximum energy 13.4 Mev. The calculated Q-value for the reaction is 0.25 Mev.

The yield of β-rays from the $C^{14}(d, \alpha)B^{12}$ reaction was measured at a bombarding voltage of 750 kev. The cross section was found to be approximately 1.7×10^{-27} cm², which is somewhat greater (by a factor of nearly two) than the cross section for the $B^{11}(d, p)B^{12}$ reaction at this same bombarding voltage. The yield was observed to rise rapidly with increased bombarding voltage, indicating a much steeper excitation curve for $C^{14}(d, \alpha)B^{12}$ than for $B^{11}(d, p)B^{12}$ up to about 1.3 Mev.

IV. PRODUCTION OF C^{15}

The $C^{14}(d, p)C^{15}$ was expected to occur in our bombardments when the energy of the deuteron beam was sufficiently great. Assuming the mass of C^{15} to be 15.0165, as estimated by Bethe,[7] the Q-value for this reaction should be about -2 Mev. This estimate of the mass of C^{15} would make it stable against disintegration into C^{14} and a neutron by only 100 kv.

In order to bombard C^{14} with deuterons of higher energy than we can conveniently produce at the Bartol Foundation, we have utilized the larger generator at the Carnegie Institution of Washington.[4] We had supposed initially that any C^{15} produced might have a short half-life, so that it would yield β-rays which could be confused with the β-rays from the decay of B^{12} formed in the competing $C^{14}(d, \alpha)B^{12}$ reaction. The estimated maximum energy of the β-rays from C^{15} is 10.8 Mev (using a C^{15} mass of 15.0165), which is comparable to the maximum energy of 13.4 Mev for the β-rays from B^{12}. While bombarding C^{14} with deuterons of energy about 2 Mev, however, we found that the activity of the target was quite appreciable for several seconds after the beam was shut off. This activity could not be due to B^{12}, and we therefore ascribed it to the decay of C^{15}. The half-life of this isotope was determined by following the activity of the target; counts were recorded after the bombarding beam had been shut off for varying lengths of time. The mean of three sets of data (using varying thicknesses of absorber between coincidence counters) showed the half-life to be 2.4 sec., with an estimated error of not more than 10 percent.

The nature of the β-ray spectrum of C^{15} was investigated by absorption of the β-rays in aluminum. Coincidence counters were used for detection; varying thicknesses of aluminum absorber were placed between the source and the first counter, with $\frac{1}{8}$ in. of aluminum absorber between the counters (to prevent coincidences from the decay of N^{13} which was built up in activity through bombardment of normal carbon in the target). The absorption curve is shown in Fig. 3. The extrapolated end-point lies at 4.6 g/cm² of aluminum absorber (with correction for thickness of counter walls, etc.),

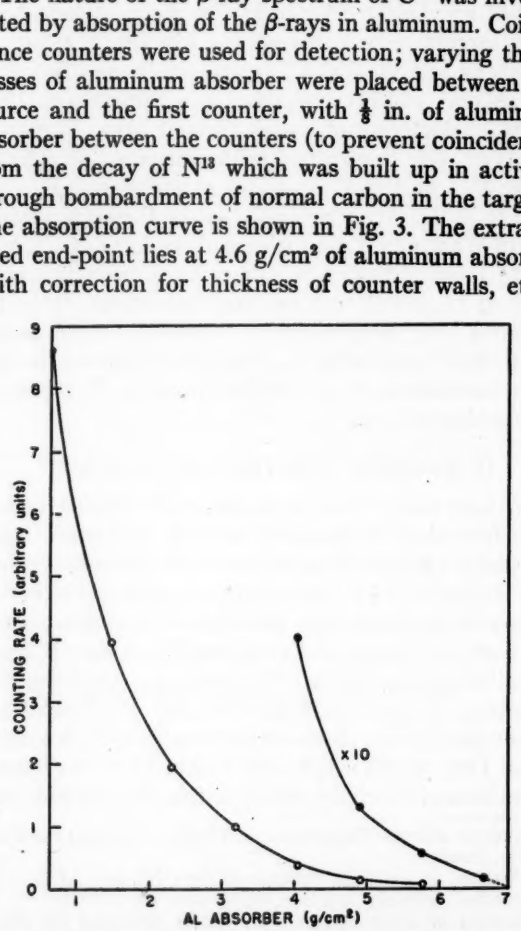

FIG. 2. Absorption of β-rays produced in the reaction $C^{14}(d, \alpha)B^{12}$. The shape of the spectrum and the extrapolated end point are identical with that observed for the β-rays obtained from deuteron bombardment of B^{11}.

[7] H. A. Bethe, *Elementary Nuclear Theory* (John Wiley and Sons, New York, 1947).

which corresponds to a maximum β-ray energy of 8.8 ± 0.5 Mev. This value of the energy, together with the half-life measurement of 2.4 sec., indicates that the $C^{15}-N^{15}$ decay is a first-forbidden transition. The calculated mass of C^{15}, based on the end-point of the β-ray spectrum and using the mass of N^{15} as[7] 15.00489, is 15.01434, which is about 2 Mev lower than the estimated value. It is not certain, however, that decay of C^{15} is to the ground state of N^{15}; some evidence for delayed emission of γ-rays was found (indicated by "background" in the absorption of β-rays described above).

The Q-value for the $C^{14}(d, p)C^{15}$ reaction is certainly somewhat greater than -1.2 Mev, since a rough excitation curve (Fig. 4) showed that the yield at a bombarding voltage of 1.4 Mev is quite appreciable. The indication of a weak resonance at 1.9 Mev bombarding energy was checked in two independent runs; at the time of these observations we did not have an opportunity to take more extensive data.

The yield from the $C^{14}(d, p)C^{15}$ reaction has been compared approximately with the yield from $C^{14}(d, \alpha)B^{12}$ by observation of the β-rays emitted during bombardment and also by the delayed activity of the bombarded target. With deuterons of 1.4 Mev, the formation of B^{12} is roughly seven times as probable as is the formation of C^{15}; at 2.6 Mev the formation of C^{15} is about seven times as probable as the formation of B^{12}.

V. γ-RAYS FROM $C^{14}(d, -)$

The bombardment of C^{14} with deuterons would lead to γ-ray emission through the excitation of states in N^{15}, formed in the reaction $C^{14}(d, n)$. The calculated Q-value for $C^{14}(d, \alpha)B^{12}$ is 0.25 Mev, while the Q-value for $C^{14}(d, p)C^{15}$ is negative. We should therefore expect γ-rays to be associated primarily with the excited states of N^{15} only; the neutron spectra (Fig. 1) indicate that a known excited state at 5.39 Mev is produced in our bombardments, and that transitions from this state to the ground state should yield an intense γ-ray. Of course γ-rays from higher excited states are expected, but our data on the neutron spectrum show that the 5-Mev γ-ray should be the most intense.

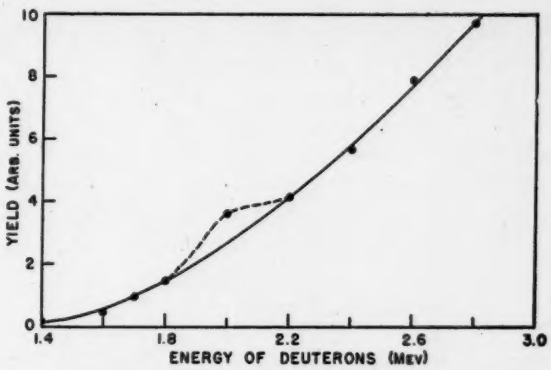

FIG. 4. Rough excitation curve for $C^{14}(d, p)C^{15}$. The point at 2.0 Mev lies off the smooth curve by about four times the statistical probable error.

We have analyzed the γ-radiation from a target of normal $BaCO_3$ and of a target of this same substance enriched in C^{14}; the bombarding voltage was 1 Mev. The relative abundance of normal carbon in the two targets was determined by following the decay of N^{13} in both cases. Varying thicknesses of aluminum absorber were placed between coincidence counters (with sufficient absorber before the first counter to stop all β-rays), and the results shown in Fig. 5 were obtained. Curves A and B were normalized by utilizing the comparative data on N^{13} decay, and curve C therefore represents an absorption curve of the γ-rays emitted when C^{14} is bombarded by deuterons. The absorption

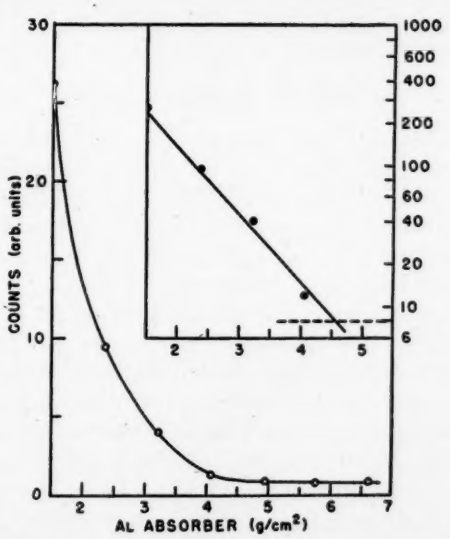

FIG. 3. Absorption of β-rays from C^{15}. The end point at 4.7 g/cm³ corresponds to a maximum β-ray energy of 8.8 Mev.

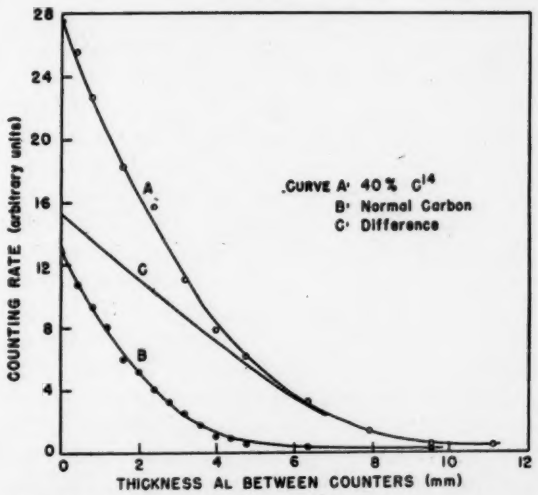

FIG. 5. Absorption of the Compton electrons produced by γ-rays emitted during bombardment of normal carbon and of C^{14} by deuterons. Targets were in the form of $BaCO_3$. Curve C represents the absorption involving γ-rays emitted during bombardment of C^{14} only.

curve drops to half-value at about 3.7-mm absorber; this corresponds to a γ-ray of nearly 6-Mev energy. The quarter-value thickness is nearly 6.0 mm; this would indicate a γ-ray of energy slightly over 7 Mev. It is reasonable therefore[8] to assume that most of the γ-radiation lies in the vicinity of 6 Mev, while more energetic lines are also present but of somewhat weaker intensity. This interpretation is of course quite consistent with the nature of the neutron spectrum, which in turn shows the existence of anticipated levels in N^{15}.

[8] Fowler, Lauritsen, and Lauritsen, Rev. Mod. Phys. 20, 256 (1948).

ACKNOWLEDGMENTS

The writers wish to acknowledge the technical assistance of Mr. J. T. Peoples and the continued interest of Dr. W. F. G. Swann, Director of the Bartol Research Foundation.

* Note added in proof: L. Yaffe and W. H. Stevens, Phys. Rev. 79, 893 (1950), have attempted to observe the reaction $C^{14}(n,)C^{15}$. The reaction was not observed, and it was concluded that the cross-section must be less than 1 microbarn.

PHYSICAL REVIEW VOLUME 80, NUMBER 4 NOVEMBER 15, 1950

Radioactive Isotopes of Rubidium*

D. G. KARRAKER AND D. H. TEMPLETON
Department of Chemistry and Radiation Laboratory, University of California, Berkeley, California
(Received July 10, 1950)

Neutron deficient isotopes of rubidium have been prepared from bromine by bombardment with helium ions in the Berkeley 184-inch and 60-inch cyclotrons. The properties of these isotopes are as follows:

Isotope	Half-life	Type of radiation	Energy in Mev: Particles	Gamma-rays	Produced by
Rb^{84}	34 days	β^+, K, ϵ^-	1.53(β^+) 0.37(ϵ^-)	0.85	Br-α-n
Rb^{83}	107 days	K	—	—	Br-α-2n
Rb^{82}	6.3 hr.	β^+, K	0.670	1.2, 0.7	Br-α-n Br-α-3n
Rb^{81}	4.7 hr.	β^+, K	0.990	0.95	Br-α-2n Br-α-4n

The mass numbers were determined with a mass spectrograph. Rb^{81} has been shown to decay to the 13-sec. krypton, thereby assigning it to Kr^{81}. Electrons from the conversion of a 190-kev gamma-ray caused by this krypton are observed with the Rb^{81} radiations.

I. INTRODUCTION

As part of a general program in this laboratory of investigation of the properties and mass assignments of radioactive isotopes, we have studied four neutron deficient isotopes of rubidium by mass-spectrographic and counting methods. The results of this work will be a basis for the assignment of some new strontium radioactivities now being studied, and perhaps ultimately of light yttrium and zirconium isotopes.

Barber[1] has assigned a 40-day positron-emitter to Rb^{84}; we have confirmed this assignment, but observe 34 days as the half-life. A 6.5-hour rubidium has been reported by Hancock and Butler.[2] Our mass-spectrographic results showing that there are actually two isotopes of about this half-life, at masses 81 and 82, have already been described.[3] However, subsequent experiments with a beta-spectrometer have yielded more accurate values for their properties than were reported there. A new 107-day activity assigned to Rb^{83} is also described in this paper.

II. CHEMICAL SEPARATIONS

Rubidium activities were produced by bombardment of bromine (as ammonium or cuprous bromide) with helium ions in the Berkeley 60-inch and 184-inch cyclotrons. Two principal procedures were used to separate the rubidium from the target material. In the case of ammonium bromide targets, 20 to 30 μg of inactive rubidium was added to the dissolved target material, the solution was evaporated to dryness and the ammonium bromide target material sublimed off by strong heating. The rubidium activities remained behind and were dissolved in a small volume of water. This solution was divided into two portions. The major portion was used without further purification for mass spectrographic determination of the mass numbers. The remainder was purified further by scavenging with precipitates of silver chloride, strontium carbonate, ferric

* This work was performed under the auspices of the AEC.
[1] W. C. Barber, Phys. Rev. 72, 1156 (1947).
[2] J. O. Hancock and J. C. Butler, Phys. Rev. 57, 1088 (1940).
[3] Reynolds, Karraker, and Templeton, Phys. Rev. 75, 313 (1949).

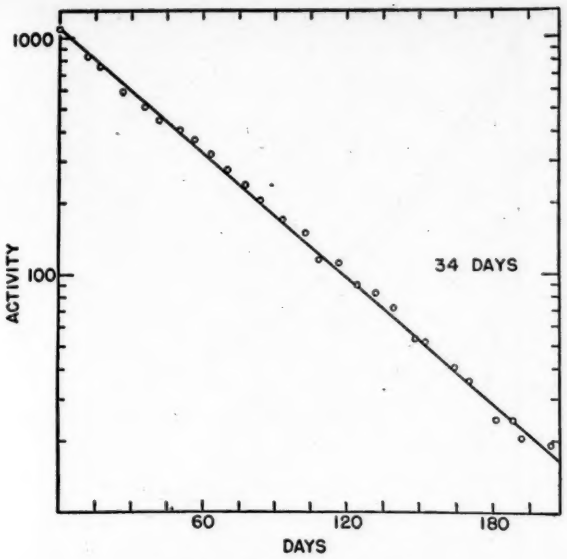

FIG. 1. Decay of 34-day Rb^{84}.

hydroxide, and lead sulfide. This repurified portion was used for decay and absorption measurements.

Cuprous bromide targets were used for the production of rubidium activity for the beta-ray spectrometer measurements. In this case, the target was dissolved in hot aqua regia, and about 0.5 mg of inactive rubidium carrier was added. The copper was removed by precipitation as the sulfide, and the solution was scavenged with lanthanum hydroxide and strontium carbonate precipitates. The remaining solution was evaporated to dryness and heated strongly to sublime off ammonium salts, leaving solid rubidium chloride behind.

III. MASS SPECTROGRAPH TECHNIQUES

For use in the mass spectrograph, the solution of the active rubidium chloride, with a few micrograms of stable rubidium carrier, was evaporated on the tungsten filament of the ion source. The rubidium was ionized by heating the filament with an electric current. The Rb^+ ions, after acceleration by a voltage drop and resolution by a 60° magnetic field, were collected on an Eastman III-0 spectrographic plate, with the stable rubidium serving as a mass marker. The location of radioactivity on the plate was determined, before it was developed, by the photographic transfer technique. The exposures used for obtaining transfers ranged from a few hours to six weeks. In some cases a Geiger-Müller counter, provided with a slit, was used, but the slit did not shield the counter perfectly from adjacent mass numbers.

IV. RADIOACTIVITY MEASUREMENTS

Decay and absorption measurements were made with end-window Geiger-Müller counters filled with argon and alcohol, with a window thickness of ca 4 mg/cm² mica. Aluminum absorption measurements were made

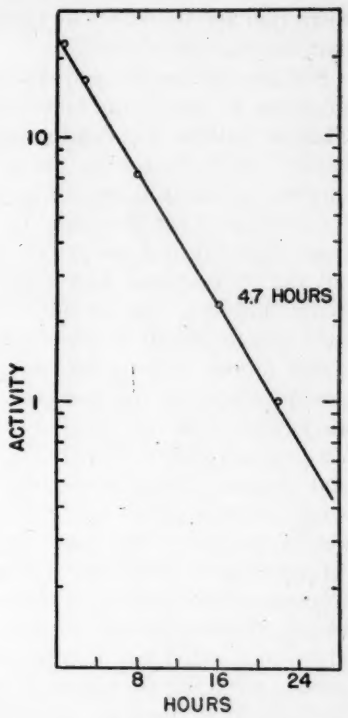

FIG. 2. Decay of Rb^{81}, measured by decay of the electron line of Kr^{81}.

in the conventional manner. After an aluminum absorption measurement, sufficient beryllium to absorb all particles present was interposed between the sample and the counter. An aluminum absorption measurement of electromagnetic radiation was then made. Subtraction of the electromagnetic radiation from the total, after

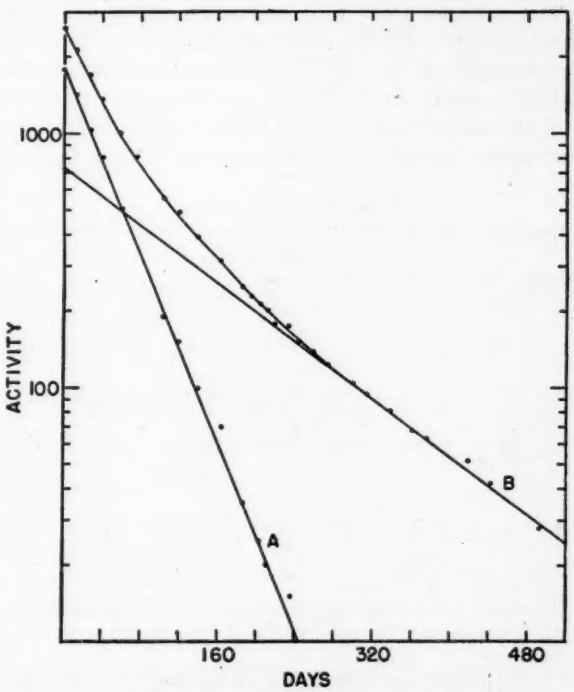

FIG. 3. Decay of long-lived rubidium activities; (A) 34-day Rb^{84}; (B) 107-day Rb^{83}.

correction for the effect of the beryllium, yielded the particle absorption curve.

Soft electromagnetic components of appropriate half-thickness in aluminum were interpreted as K x-rays. Their abundance was determined by subtraction of the harder components from the curve for aluminum absorption of electromagnetic radiation, with correction for the effect of the beryllium. Lead absorption measurements were taken at low geometry, using counters without the conventional lead shield. Lead absorbers were placed between two beryllium absorbers of sufficient thickness to absorb all secondary particles. Krypton K x-rays (about 13 kev) were assumed to count with 1.5 percent efficiency and gamma-rays over 0.5 Mev with an efficiency of 1.0 percent per Mev. Approximate branching fractions for the decay *via* positron emission and electron capture were estimated on the basis that K x-rays are emitted in only half of the electron capture events, because of the Auger effect.[4] It is assumed that all positrons in the proper angular interval are counted. Capture of electrons from shells other than K is neglected. The results will be in error if there are present highly converted low energy gamma-rays whose conversion electrons are too weak to have been observed. No correction has been made for backscattering from the sample.

For samples of low activity, rough measurements of the particle energies were made with a crude 180° magnetic spectrometer with about a 4-cm radius. Its use was necessary to determine the energy limit of the Rb^{84} positrons, and it also served to distinguish the sign of the particles in preliminary work.

The particles from Rb^{81} and Rb^{82}, which were prepared in high intensity, were observed with a beta-ray spectrometer of the 255° double-focusing type, similar to that invented by Svartholm and Siegbahn,[5] but with a 25-cm radius instead of the 12-cm radius of their first instrument. Samples were mounted on 1- to 4- mg/cm² mica backing with between 0.2 and 1.0 mg of material in the sample. The backscattering from these samples was quite marked at low energies, but was not serious in the region of interest (above 300 kev).

TABLE I. Isotope chart.[a]

Element	Mass Number 79	80	81	82	83	84	85
Sr						stable	70 min. I.T. / 65 days K
Rb			4.7 hr. β^+, K	6.3 hr. β^+, K	107 days K	34 days β^+, K	stable
Kr	34 hr. β^+, K	stable	13 sec. I.T.?	stable	113 min. I.T. / stable	stable	4 hr. β^- / 10 yr. β^-
Br	stable	4.4 hr. I.T. / 18 min. β^-, β^+	stable	34 hr. β^-	2.4 hr. β^-	30 min. β^-	3 min. β^-

[a] G. T. Seaborg and I. Perlman, Rev. Mod. Phys. 20, 585 (1948).

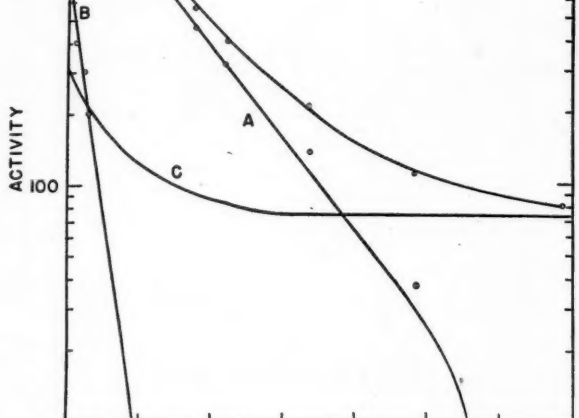

FIG. 4. Aluminum absorption of Rb^{84}; (A) 1.5-Mev positrons; (B) 0.37-Mev electrons; (C) K x-rays and gamma-rays.

V. MASS ASSIGNMENTS

In every bombardment of bromine with helium ions, which ranged in energy from 18 to 100 Mev, two main activities were observed in rubidium decay measurements, one of 5–6 hours half-life and one of the order of 1 to 3 months. Rubidium produced at bombardment energies of 40 to 100 Mev, when mass analyzed, gave photographic transfers at masses 81 and 82 in a few hours.[3] Direct measurement of the decay with the slit counter showed that both masses were of the order of six hours in half-life, with mass 82 being slightly longer lived than 81. Transfers exposed for several weeks showed radioactivity at masses 83 and 84 as well as at 81 and 82. Since masses 83 and 84 did not transfer in a few hours, they are known to be the long-lived activities.

Rubidium produced from bromine by 18-Mev helium ions gave radioactive transfers only at masses 82 and 84, showing that the major activities produced in these bombardments were the (α, n) products. Decay measurements on these activities showed the half-life of the short component (mass 82) to be 6.3 hours, corresponding to the 6.5-hr. activity previously identified by Hancock and Butler[2] (erroneously assigned to mass 84) and also showed a 34-day positron activity (Fig. 1) now assigned to mass 84, corresponding to the 40-day rubidium reported by Barber.[1]

[4] A. H. Compton and S. K. Allison, *X-rays in Theory and Experiment* (D. Van Nostrand Company, Inc., New York, 1935), p. 482.
[5] N. Svartholm and K. Siegbahn, Arkiv Mat., Astron. Fys. 33A, 1 (1946).

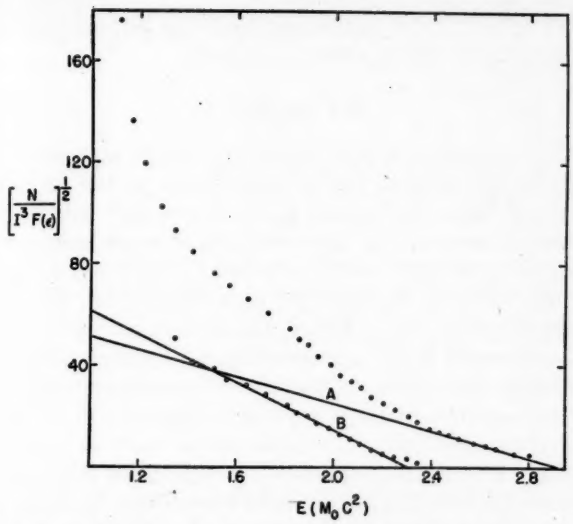

FIG. 5. Kurie plot of positrons of Rb^{81} and Rb^{82}; (A) $E_{max}=2.92$ m_0c^2 or 990 kev; (B) $E_{max}=2.30$ m_0c^2 or 670 kev.

Absorption and crude spectrometer measurements on the activities produced at low energy showed that Rb^{82} had virtually no conversion electrons compared to its positrons, whereas a strong conversion electron line had been observed from rubidium made at higher energy. Further work (described below) established that this line was due to a 13-sec. Kr^{81} daughter of Rb^{81}. Decay of this electron line, followed in the double-focusing spectrometer, gave a half-life of 4.7 hours for the half-life of Rb^{81} (Fig. 2). The half-life of Rb^{83} was determined by following the decay of a sample of rubidium activity produced by 60-Mev helium ion bombardment of bromine, very similar to the sample which gave a radioactive transfer at masses 83 and 84. Resolution of the decay curve showed a 107-day activity, assigned to mass 83, as well as the 34-day Rb^{84} (Fig. 3). The mass relations of these isotopes are shown in Table I. Radiation characteristics of each isotope will be discussed individually.

VI. RADIATION CHARACTERISTICS

34-day Rb^{84}

Measurements on the crude magnetic spectrometer have shown that Rb^{84} has positrons of 1.5-Mev energy limit, as determined by a Kurie plot of the spectrum. A broad electron distribution was also observed centered about 0.37 Mev. The width of the distribution showed that the electrons were complex. There may have been a small contribution from the 107-day Rb^{83}, although it was not observed to be present. Since Sr^{84} is found in nature, Rb^{84} is presumed to be unstable with respect to negative beta-decay, but we cannot say from these data whether any of the negative electrons observed are beta-particles. K x-rays have been identified by absorption in aluminum (Fig. 4), and a gamma-ray of 0.85 Mev (half-thickness, 8.5 g/cm² Pb) has been identified by absorption in lead. It is assumed that Rb^{83} did not affect the absorption measurements, since the decay curve indicated pure Rb^{84}. The ratio of positrons to K x-rays to gamma-rays, estimated from the absorption curve, was 0.15:1:*ca.* 0.6. From these data the mode of decay is estimated to be about 93 percent by K electron capture and seven percent by positron emission. Negative beta-decay would amount to about three percent if all the negative electrons observed were beta particles.

In a recent abstract Beckham and Pool[6] have listed properties of this isotope which are in reasonable agreement with those described above. They found the half-life to be 38 days, somewhat greater than our value. However, their bombardment of krypton with 10-Mev deuterons can be expected to produce Rb^{83} in smaller yield than Rb^{84}, but yet in amount large enough to influence the slope of the decay curve.

107-day Rb^{83}

The amounts of this activity available were so small that precise measurement of its radiations was not attempted. The ratio of particles to K x-rays to gamma-rays is very roughly 0.3:1:2. It is thus indicated that decay is to a large extent by electron capture. No positrons were detected, but the sensitivity for detection was poor.

Nothing can be said concerning the presence or absence of the 113-min. isomeric state[7] of Kr^{83} as a daughter of this activity; no experiments were at-

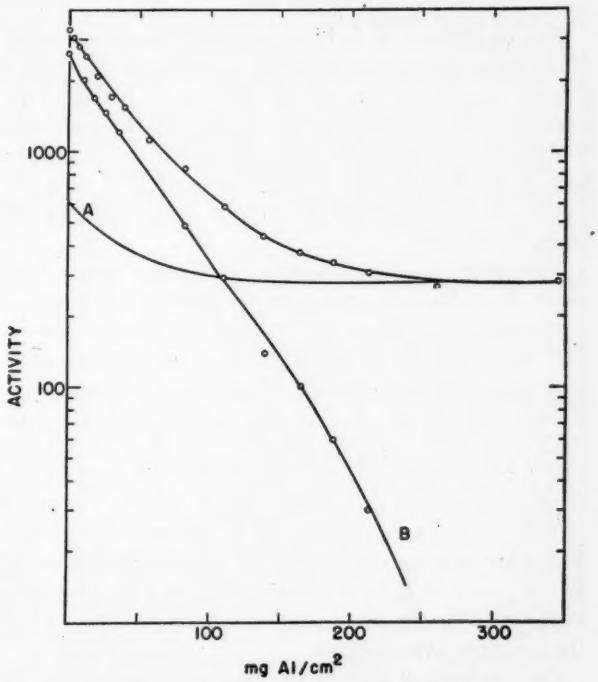

FIG. 6. Aluminum absorption of Rb^{83}; (A) K x-rays and gamma-rays; (B) 0.67-Mev positrons.

[6] W. C. Beckham and M. L. Pool, Phys. Rev. 80, 125 (1950).
[7] G. T. Seaborg and I. Perlman, Rev. Mod. Phys. 20, 585 (1948).

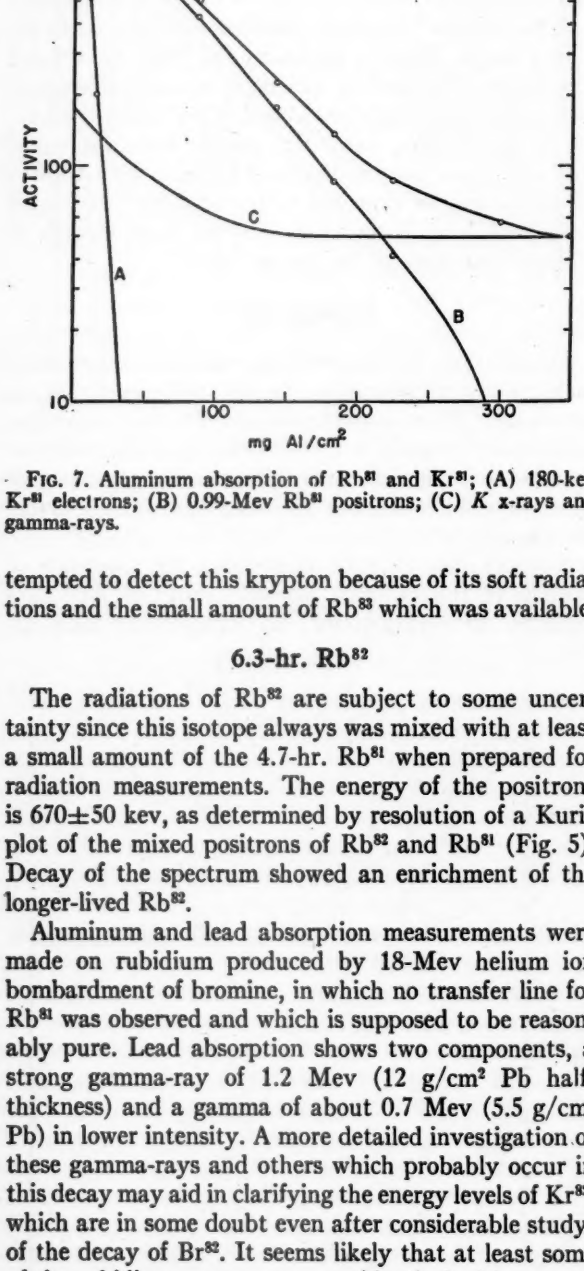

FIG. 7. Aluminum absorption of Rb^{81} and Kr^{81}; (A) 180-kev Kr^{81} electrons; (B) 0.99-Mev Rb^{81} positrons; (C) K x-rays and gamma-rays.

tempted to detect this krypton because of its soft radiations and the small amount of Rb^{83} which was available.

6.3-hr. Rb^{82}

The radiations of Rb^{82} are subject to some uncertainty since this isotope always was mixed with at least a small amount of the 4.7-hr. Rb^{81} when prepared for radiation measurements. The energy of the positrons is 670±50 kev, as determined by resolution of a Kurie plot of the mixed positrons of Rb^{82} and Rb^{81} (Fig. 5). Decay of the spectrum showed an enrichment of the longer-lived Rb^{82}.

Aluminum and lead absorption measurements were made on rubidium produced by 18-Mev helium ion bombardment of bromine, in which no transfer line for Rb^{81} was observed and which is supposed to be reasonably pure. Lead absorption shows two components, a strong gamma-ray of 1.2 Mev (12 g/cm² Pb half-thickness) and a gamma of about 0.7 Mev (5.5 g/cm² Pb) in lower intensity. A more detailed investigation of these gamma-rays and others which probably occur in this decay may aid in clarifying the energy levels of Kr^{82}, which are in some doubt even after considerable study[8] of the decay of Br^{82}. It seems likely that at least some of the rubidium gamma-rays are identical with some of the bromine gamma-rays.

On the basis of aluminum absorption measurements, (Fig. 6), the ratio of positrons to K x-rays to gamma-rays is 0.12:1:0.9, suggesting that this isotope decays about 94 percent by electron capture.

4.7-hr. Rb^{81}

The radiations of Rb^{81} are subject to the same uncertainties as those of Rb^{82} and are open to the further error of being confused with its 13-sec. Kr^{81} daughter. Measurement of the positron and electron energies, originally thought to be associated with Rb^{81}, in the double-focusing spectrometer gave 990±50 kev for the range of the positron (Fig. 5) and showed intense K and L conversion lines corresponding to a gamma-ray of 193±10 kev. The energy of this gamma-ray corresponds, within limits of error, to a gamma-ray of 187 kev found by Creutz, and co-workers[9] to be associated with a 13-sec. krypton activity produced by bombardment of bromine with protons of low energy. By flaming a strong sample of Rb^{81} to drive off the krypton, and observing of the growth of activity of the electron line in the crude spectrometer, Rb^{81} was shown to have a krypton daughter with a half-life of 10±6 sec.

In the same bombardments that Creutz and co-workers observed the 13-sec. Kr^{81}, they also observed a 55-sec. krypton isomeric transition with a strong conversion electron corresponding to a gamma of 127 kev. These activities were produced by bombarding bromine (masses 79 and 81) with protons of 5–6 Mev energy, and both isotopes are thought to be products of p, n reactions. Electrons from the 127-kev gamma were not observed by beta-ray spectrometer measurements of our rubidium activity. If the 55-sec. krypton does belong at mass 81, the amount formed by decay of Rb^{81} must be less than five percent as much as the 13-sec. activity.

Absorption data were taken on Rb^{81} samples prepared by bombardment of bromine with 100-Mev helium ions. A mass spectrographic transfer plate showed that the ratio of mass 81 to mass 82 was approximately 4. The data presented are corrected for the presence of the Rb^{82}.

Absorption in lead shows a gamma-ray of 0.95 Mev (9.5 g/cm² Pb half-thickness). Absorption in aluminum (Fig. 7) has given the positron to K x-ray to gamma-ratio as 0.1:1:0.6 after half of the x-rays observed were assumed to be due to the krypton daughter. It is estimated from this ratio that 87 percent of the decay is by electron capture. The number of conversion electrons from the 13-sec. krypton daughter is approximately three times the number of positrons of the rubidium parent.

We are indebted to F. L. Reynolds for assistance with the mass spectrograph and to G. D. O'Kelley for help with the beta-spectrometer. We are grateful to J. T. Vale and B. Rossi and the crews of the 184-inch and 60-inch cyclotrons for their cooperation which made these experiments possible.

[8] Siegbahn, Hedgran, and Deutsch, Phys. Rev. 76, 1263 (1949); A. C. H. Mitchell, Rev. Mod. Phys. 22, 36 (1950).

[9] Creutz, Delsasso, Sutton, White, and Barkas, Phys. Rev. 58, 481 (1940).

The Radioactivity of Ga^{66}

LAWRENCE M. LANGER AND R. DOUGLAS MOFFAT
Department of Physics, Indiana University, Bloomington, Indiana*
(Received July 17, 1950)

The disintegration of Ga^{66} results in four positron groups with end-point energies and relative intensities of 4.144 Mev, 87 percent; 1.4 Mev, 4.3 percent; 0.878 Mev, 6.9 percent; and 0.403 Mev, 1.7 percent. Nuclear gamma-rays having energies of 1.03 Mev, 2.75 Mev and 4.8 Mev are observed. Measurement of the associated Auger electrons at 7.3 kev indicates that 34 percent of all disintegrations are by *K*-electron capture. The 4.14-Mev positron spectrum is found to have a shape characteristic of an allowed transition. In consideration of its high *ft*-value, it is therefore inferred that this transition is once forbidden with a change of parity and a spin change of 0 or 1 unit. Furthermore, this transition does not go to the ground state of Zn^{66}, but rather appears to be followed by the 1.03-Mev gamma-ray. The direct 5.17-Mev transition between ground states is found to proceed in less than 0.4 percent of the positron decays. This transition is apparently twice forbidden with a spin change of 3 units and is effectively outcompeted by the other less forbidden modes of decay.

I. INTRODUCTION

THE radioactivity of the 9.4-hr. transition from Ga^{66} to Zn^{66} has been investigated by means of a large, high resolution, magnetic spectrometer. The original interest in the problem arose from the fact that, on the basis of the previously reported[1] absorption end point of 3.1 Mev, the comparative half-life ($ft \sim 10^7$) suggested that the positron spectrum might exhibit a shape different from that generally associated with allowed transitions. Further support for this idea was based on the predictions of the nuclear shell models,[2,3] which indicate that the transition from the ground state of Ga^{66} to that of Zn^{66} should involve *no* change of parity and should therefore fall into the twice forbidden class.

The results of the spectrometer measurements soon showed that the disintegration is quite complicated. The positron spectrum was found to be complex and was resolved into four groups with end-point energies of 4.144 Mev, 1.4 Mev, 0.878 Mev and 0.403 Mev. Furthermore, it appears that the intense 4.144-Mev group does *not* go to the ground state of Zn^{66}, but instead is followed by a 1.03-Mev gamma-ray. The direct 5.17-Mev positron transition between the ground states has a relative intensity of less than 0.4 percent. This transition was too weak to afford a reliable measurement of its spectrum shape. The momentum distribution of the 4.144-Mev positron group is such that the conventional Fermi plot is a straight line. This would be consistent with this transition's being once forbidden with a change of parity and a change of 0 or 1 unit of angular momentum.[4]

In addition to the 1.03-Mev transition, gamma-radiation was measured corresponding to energies of 2.75 Mev and 4.8 Mev. On the basis of the data, a reasonable energy level scheme is proposed for the Zn^{66} nucleus.

From the high intensity of Auger electrons, it appears that the positron emission is in competition with considerable *K*-electron capture to one or more of the levels of Zn^{66}.

II. EXPERIMENTAL METHOD

The energy measurements were obtained with the aid of a high resolution, 180-degree focusing, 40-cm radius of curvature, shaped magnetic field spectrometer.[5]

For most measurements, a 2.3 mg/cm² mica end window counter was used as a detector. For studying the low energy Auger electrons, a second counter was employed whose window was one double layer of zapon, 150Å thick, supported by a grid of Lektromesh.[6] Since the filling gas will slowly diffuse through such a thin window, the 2 cm total pressure of two parts ethylene to one part argon was automatically maintained constant by means of a Cartesian Manostat.[7] This method proved to be completely satisfactory in keeping the counter operating under constant conditions. Since the apparatus is entirely mechanical, it does not suffer from the electrical contact difficulties encountered with other methods of pressure control.[8]

The Ga^{66} was prepared by bombarding a copper probe with alpha-particles in the cyclotron. The probe tip was dissolved in acid and the Ga completely separated as chloride by a repeated ether extraction. In addition to the 9.4-hr. Ga^{66} resulting from $Cu^{63}(\alpha, n)Ga^{66}$, there were also produced some 68-min. positron activity and 83-hr. gamma-activity from the reactions $Cu^{65}(\alpha, n)Ga^{68}$ and $Cu^{65}(\alpha, 2n)Ga^{67}$. The decay of the Ga^{66} activities was monitored and was found not to be influenced by the other periods during the time of the spectrometer runs. The measured half-life was 9.45 hr.

A thin positron source was prepared on a 0.00025-in.

* This work was assisted by a grant from the Frederick Gardner Cottrell Fund of the Research Corporation and by the joint program of the ONR and AEC.

[1] W. B. Mann, Phys. Rev. 52, 405 (1937).
[2] M. G. Mayer, Phys. Rev. 78. 16 (1950).
[3] E. Feenberg and K. C. Hammack, Phys. Rev. 75, 1877 (1949).
[4] L. M. Langer and H. C. Price, Phys. Rev. 76, 641 (1946).
[5] L. M. Langer and C. S. Cook, Rev. Sci. Inst. 19, 257 (1948).
[6] Langer, Motz, and Price, Phys. Rev. 77, 798 (1950).
[7] Obtainable from the E. Greiner Company.
[8] Ter-Pogossian, Robinson, and Townsend, Rev. Sci. Inst. 20, 289 (1949).

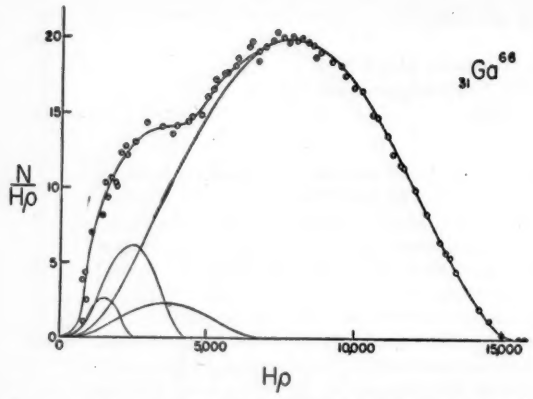

FIG. 1. Momentum distribution of the positrons of Ga^{66}.

Al backing by spreading, with the aid of insulin,[9] a rectangle 0.3 cm by 2.5 cm. A second positron source, 0.5 cm wide and 25 times more intense was prepared in a similar manner for the investigation of the weak high energy group. This source was also used in a search for internal conversion electrons.

For the study of Auger electrons, two sources were used. One was 1.0 cm by 2.5 cm on a thin backing[9] of LC 600. The upper and lower edges were grounded by tabs of Al leaf to prevent charging. The second Auger source was 0.4 cm wide and had a 0.00025-in. Al backing.

The photo- and Compton electrons from the gamma-radiation were investigated by containing a strong Ga source in a rectangular copper box whose front face was covered by a 0.4 cm by 2.5 cm radiator of 28 mg/cm² uranium.

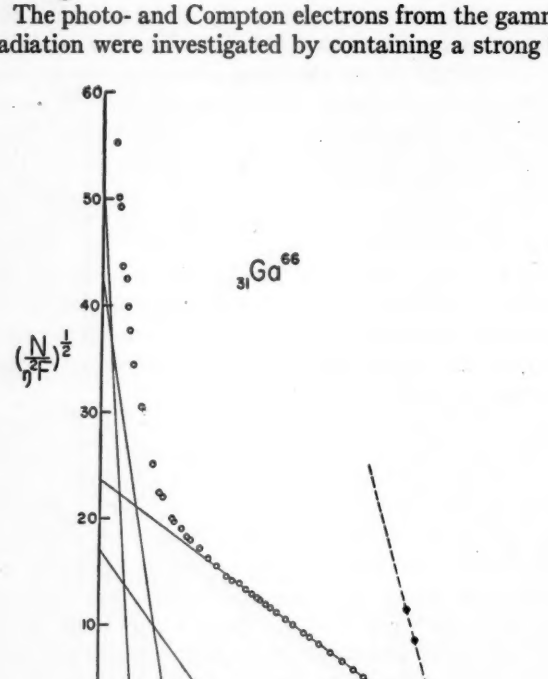

FIG. 2. Fermi plot of the spectra of Ga^{66}. The solid circles represent data obtained with a source 25 times more intense.

[9] L. M. Langer, Rev. Sci. Inst. 20, 216 (1949).

TABLE I. Beta- and gamma-rays of Ga^{66}.

		$_{31}Ga^{66}$ Mev	Intensity (%)
Beta	1	0.403	1.7
	2	0.878	6.9
	3	1.4	4.3
	4	4.144	87.0
	5	5.17(?)	<0.4
Gamma	1	1.03	1
	2	2.75	0.7
	3	4.8	...

Coincidence measurements were performed with the source located between end window Geiger counters spaced 4 cm apart. The beta-gamma-coincidence measurements were corrected for the additional background arising from the paired quanta from positron annihilation. The resolving time of the coincidence circuit was $\tau=0.44\times10^{-7}$ min. Weighed Al sheets were used for the absorbers.

III. RESULTS

The momentum distribution of the positrons of Ga^{66} is shown in Fig. 1. The obviously complex spectrum has been resolved into four groups on the basis of the Fermi plot shown in Fig. 2. Here it is clear that the intense 4.144-Mev group results in a straight line. The solid circles in Fig. 2 are the unadjusted data obtained with the more intense source mentioned above. In the proposed decay scheme (see Fig. 7) there exists the possibility of a 5.17-Mev transition directly to the ground state of Zn^{66}. The data show that this transition occurs in less than 0.4 percent of the positron decays. The measured intensity of this group was too small to yield any information about the spectrum shape of this presumably twice forbidden transition. The maximum energies and relative positron intensities are shown in Table I.

The distribution of Compton and photo-electrons ejected from the uranium radiator is shown in Fig. 3. K and L photo-lines may be seen which correspond to the 0.511-Mev annihilation radiation and to a 1.03-Mev gamma-ray. In addition, there is a K photo-peak from a gamma-ray of 2.75 Mev and a Compton distribution whose maximum energy corresponds to a gamma-ray energy[10] of 4.8 Mev. The areas under the 1.03 Mev and 2.75 photo-lines have been measured and compared, after correction by Gray's formula for the variation of photoelectric cross section with energy. The 2.75-Mev

[10] R. Hofstadter and J. A. McIntyre, in a private communication, confirm, by means of scintillation counting techniques, the existence of these gamma-rays. They also report a 4.25-Mev gamma which is not sufficiently resolved in the Compton distribution of Fig. 3. This gamma-ray could correspond to a transition to the ground state of Zn^{66} following on the 0.878-Mev positron decay from Ga^{66}.

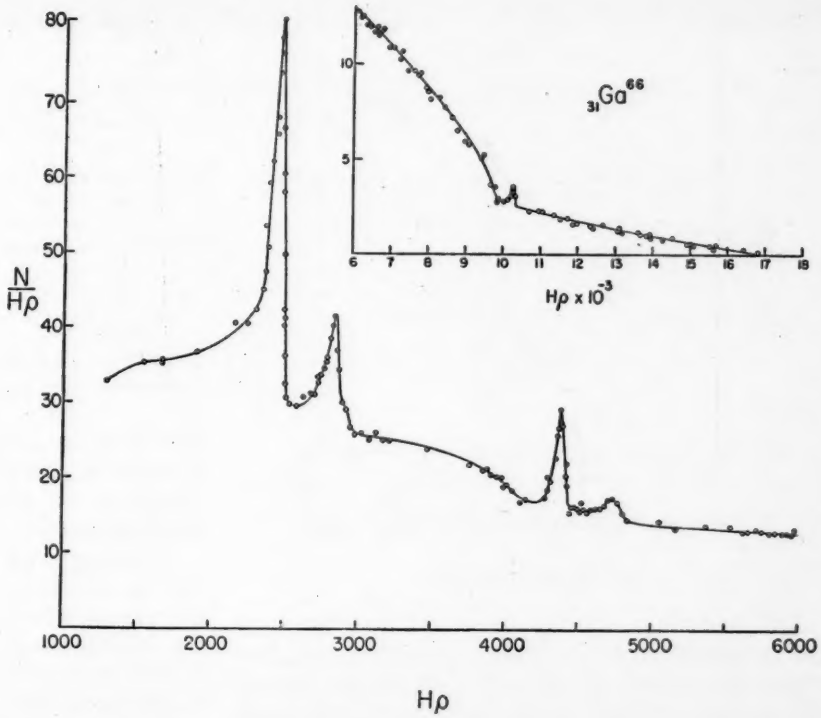

FIG. 3. Compton and photo-electrons ejected from a uranium radiator by the gamma-rays of Ga^{66}.

gamma-ray has 0.7 the intensity of that at 1.03 Mev. The intensity of the 0.511-Mev photo-line is here not indicative of the total positron activity because the copper box containing the source was not of sufficient thickness to cause annihilation of all positrons.

A careful search was made for internal conversion lines. The conversion electrons corresponding to the 1.03-Mev gamma-ray are shown in Fig. 4. Because of uncertainties in the distribution of K capture transitions and in the measurement of relative intensities, no reliable estimate could be made of the internal conversion coefficient.

Figure 4 also shows a continuous distribution of negatrons with most of the intensity concentrated in the region below 1500 Gauss-cm. The shape of this distribution shows no resemblance to that of a beta-ray spectrum and is attributed to bremsstrahlung and possibly to negatrons from pairs internally produced by the high energy gamma-rays.

Figure 5 shows a line of Auger electrons of 7.34 kev energy. Since the amount of internal conversion is relatively small, practically all of the Auger electrons are attributable to the rearrangement of the atomic electrons following K electron capture. The area under the line corresponds to 28 percent of the total positron intensity. Using a value of 0.46 for the fluorescence yield[11] in Zn, one concludes that 34 percent of all disintegrations are by K electron capture.

Beta-gamma-coincidences per recorded beta-ray are plotted in Fig. 6, as a function of Al absorber thickness placed before the beta-counter. The extremely low value of the ordinate for beta-energies above 1.4 Mev is interpreted to be indicative of a lifetime of the 1.03-Mev level in Zn^{66} comparable to or longer than the resolving time of the apparatus.

The decay scheme of Fig. 7 is proposed after the following considerations. (1) The 2.75-Mev gamma-ray energy fits well the observed difference between the 4.144-Mev and 1.4-Mev positron end points. (2) Since the 1.03-Mev gamma-ray is the most intense, it must follow the 2.75-Mev gamma-ray and hence the 4.144-Mev beta-group. (3) This scheme provides a means of energy release following the lowest energy (0.403-Mev) beta-group and removes the necessity of associating the 4.8-Mev gamma-ray with a level fed only by K electron capture.

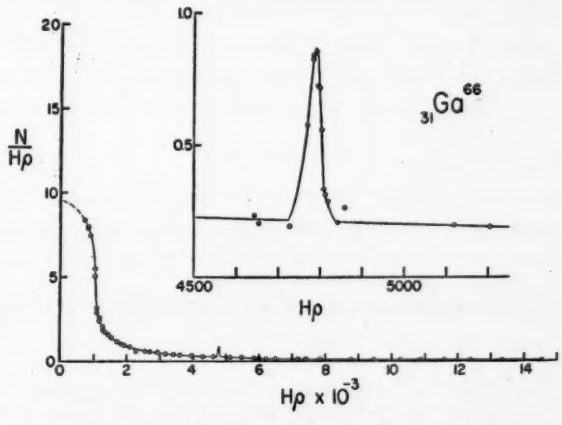

FIG. 4. Negatron distribution from a Ga^{66} source showing the internal conversion of the 1.03-Mev gamma-ray.

[11] Compton and Allison, *X-Rays in Theory and Experiment* (D. Van Nostrand Company, Inc., New York, 1935), p. 489.

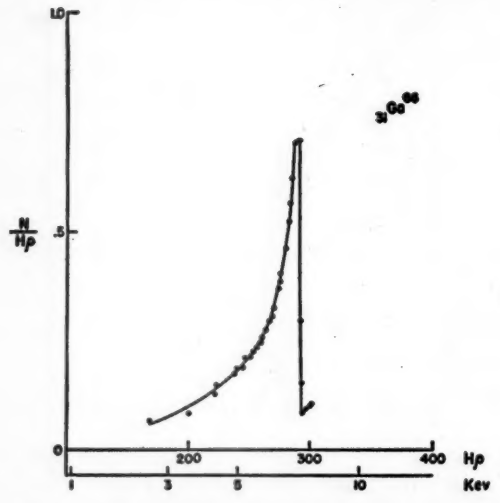

FIG. 5. Auger electrons following K electron capture.

IV. CONCLUSIONS

The momentum distribution of the positrons from Ga^{66} is complex. With the help of the Fermi theory, four groups are resolved with end points and relative intensities as shown in Table I. The most intense group, with an end point at 4.144 Mev, apparently does not represent a transition directly to the ground state of Zn^{66}, but rather to an excited state 1.03 Mev above the ground level. The intensity of the 5.17-Mev direct transition is less than 0.4 percent of the positron decays.

On the basis of the observed energies and intensities and taking into account the 34 percent of K electron capture, one finds, in order of decreasing end-point energy, the following values for $\log(ft)$, a measure of the comparative half-life of the individual positron groups: 7.84, 7.11, 6.29, 6.37.

The shape of the spectrum of the 4.144-Mev positron transition is of the allowed form. In consideration of the relatively high ft-value, one must infer therefore that

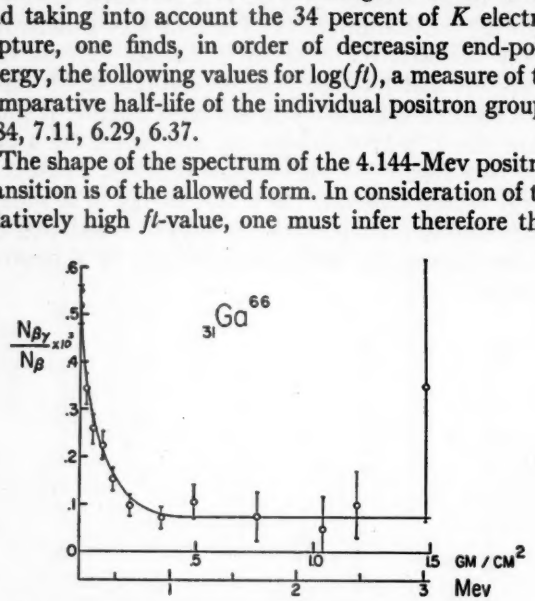

FIG. 6. Beta-gamma-coincidences as a function of positron energy.

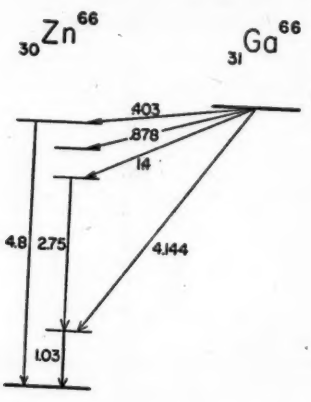

FIG. 7. Disintegration scheme for the Ga^{66}-Zn^{66} decay.

this transition is of the once forbidden type, involving a change of parity and a spin change of 0 or 1; a spin change of two units should have resulted in a unique forbidden shape.[4]

According to the nuclear shell model,[2] the 31st proton and the 35th neutron in Ga^{66} should each separately be in $P_{\frac{1}{2}}$ levels. According to Nordheim,[12] one might expect the resultant state of Ga^{66} to have even parity and a spin of 3. Since the ground state of Zn^{66} is that of an even-even nucleus, it is presumed to have *even* parity and zero spin. The transition between the ground states of Ga^{66} and Zn^{66} is then *twice* forbidden with a spin change of 3 units and is effectively outcompeted by the other less forbidden transitions. From the fact that the 4.144-Mev positron transition does not exhibit a forbidden shape, one may infer further that the 1.03-Mev excited state in Zn^{66} has a spin of at least 2 and odd parity. The 1.03-Mev gamma-transition would then involve a change of parity and a change of at least 2 units of angular momentum. The character of the radiation would then be at least magnetic quadrupole or electric octopole. The experimental absence of coincidences between the 4.144-Mev positron group and the 1.03-Mev gamma-ray suggests a relatively long lifetime for the excited state of Zn^{66}. This, of course, is only reasonable if the 1.03-Mev gamma-radiation is of high polarity.[13]

In addition to the 1.03-Mev gamma-radiation, evidence was found for quanta of 2.75-Mev and 4.8-Mev energy.

Figure 7 shows an energy level scheme which appears to be reasonably consistent with the observed data.

The authors would like to take this opportunity to thank Professor M. B. Sampson and the cyclotron crew for their kind cooperation.

[12] L. W. Nordheim, Phys. Rev. 78, 294 (1950).
[13] E. Segrè and A. C. Helmholz, Rev. Mod. Phys. 21, 271 (1949).

Luminescence and Trapping in Zinc Sulfide Phosphors with and without Copper Activator*†

RICHARD H. BUBE
Radio Corporation of America, RCA Laboratories Division and Princeton University, Princeton, New Jersey
(Received June 2, 1950)

A comprehensive study of ZnS:[Zn] and ZnS:[Zn]:Cu phosphors has been carried out with the use of glow curves, phosphorescence emission decay curves, and spectral distribution curves of emission during excitation by 3650A ultraviolet. The principal contributions of the study are (1) glow curves and spectral emission curves for nine samples each of cubic and hexagonal ZnS with copper activator in proportions from zero to 3000 parts per million, (2) a direct proof for ZnS-type phosphors of the equation of trap emptying proposed by Randall and Wilkins, (3) a detailed extension of the study of retrapping by the method indicated by Wilkins and Garlick, (4) a determination of the number of electron traps in ZnS as a function of heating temperature in preparation, (5) an analysis of glow and decay curves by means of the equation of Randall and Wilkins, and (6) suggestions concerning the identity of traps and luminescence centers on the basis of a study of the crystal structures of cubic and hexagonal ZnS.

I. INTRODUCTION

THERE are two basic types of *centers* involved in the luminescence process of ZnS phosphors. The first of these is the *luminescence center*, which is made up of an imperfection[1] and its surroundings in the crystal. When a luminescence center is excited, an electron is raised from a ground state to an excited state, from which the electron may make a radiative return transition at a later time. The probability that this return transition is dissipative rather than radiative increases with temperature. The second type of center is the *trapping center*. This center is also made up of an imperfection and its surroundings in the crystal, but an electron in a trapping state is effectively in an excited state from which a transition to a ground state cannot be directly made. The nature of the luminescence center determines the spectral distribution of the emission of the phosphor, whereas the nature of the trapping center (in phosphors for which a temperature-independent exponential decay is not found) is a major factor in determining how the emission will decrease with time after the cessation of excitation. In such phosphors the phosphorescence emission, i.e., the emission caused by the radiative transitions of electrons with apparent excited-state lifetimes of greater than 10^{-8} sec., is due to the thermal freeing of trapped electrons followed by their capture by a luminescence center.

Since the paper of Randall and Wilkins,[2] which contained the first quantitative analysis of glow curves (curves of thermally stimulated phosphorescence emission as a function of temperature after low temperature excitation) together with corresponding decay curves, other measurements on trapping in ZnS phosphors have been concerned with the applicability of the equation of Randall and Wilkins, the importance of retrapping, and the connection between trapping and the preparation process.

In general, a different group of investigators has studied the luminescence emission of ZnS phosphors during excitation. Among the principal problems were the nature of the luminescence centers, and the role of chloride added in the preparation of these phosphors.

The present paper contains measurements primarily made on two series of ZnS:[Zn]:Cu phosphors,[3] all prepared in an identical manner from spectroscopically pure ZnS, in such a way that the effect of varying crystal structure and activator proportions may be obtained.

Two problems are treated in the present study. (1) Is the equation of trap emptying of Randall and Wilkins[2] applicable to ZnS:[Zn]:Cu phosphors? (2) What information can be obtained concerning the identity of trapping centers and of luminescence centers in ZnS:[Zn]:Cu from a study of glow curves, decay curves, spectral distribution curves, and crystal structure?

II. THEORY

The theory of Randall and Wilkins[2] for the emptying of traps assumes that the probability of an electron escaping from a trap is given by the equation

$$P=\nu_a e^{-\epsilon/kT}, \qquad (1)$$

where ν_a is a frequency factor, the "attempt-to-escape" frequency, and the exponential term is a Boltzmann factor involving the trap depth ϵ, and the temperature T. The attempt-to-escape frequency may be interpreted as the number of times per second that thermal quanta from crystal vibrations attempt to eject the electron

* This paper is part of a dissertation presented in May, 1950 to the Physics Department of Princeton University in partial fulfillment of the degree of Doctor of Philosophy. It was presented before the New York meeting of the Physical Society, February 4, 1950.

† This work was done under contract between the ONR and RCA.

[1] The term "imperfection" is used to mean any distortion of the regular crystal configuration, whether it be caused by added impurities or by inherent crystal defects, such as interstitial or omission defects.

[2] J. T. Randall and M. H. F. Wilkins, Proc. Roy. Soc. **A184**, 366, 390 (1945).

[3] The expression [Zn] will be used to indicate the unknown activator for the blue luminescence emission of "pure" ZnS. In the author's opinion, the conventional contention that interstitial zinc is this activator has not been proven.

from the trap, multiplied by the probability of a transition from the trap to the conduction band. The Boltzmann factor is the probability of the electron having an energy sufficient to escape on any one of these attempts. The straightforward use of this equation requires the assumption that electrons freed from traps are not retrapped, that ν_a and ϵ are independent of temperature, and that freed electrons undergo radiative, rather than dissipative, transitions.

The decay equation derived from Eq. (1) gives

$$I_t = n_0 P e^{-Pt}, \tag{2}$$

where n_0 is the number of electrons trapped in traps of depth ϵ at $t=0$.

If β is the linear heating rate, the equation for the glow curve which results from Eq. (1) is

$$I_G = n_0 P \exp\left(-\int P/\beta dT\right). \tag{3}$$

Maximizing this equation for I_G with respect to T, gives the trap depth in terms of the temperature, T_G, for maximum I_G:

$$\epsilon = (\ln \nu_a) k T_G (1+f) \tag{4}$$

in terms of the quantity f which is given by

$$f = \ln(T_G^2 k/\beta\epsilon)/\ln\nu_a. \tag{5}$$

This theory has been extended by Garlick *et al.*[4] to cases where retrapping does occur. In particular, calculations were made for the case in which the probability of an electron being retrapped was equal to the probability of an electron being captured by a luminescence center.

For this case, the equivalent equation to Eq. (2) for the decay is

$$I_t = n_0 P/[1+Pt]^2 \tag{6}$$

if the traps have been saturated. For long times of decay, this becomes approximately

$$I_t \approx n_0/Pt^2. \tag{7}$$

The glow curve equation for this case, equivalent to Eq. (3) is

$$I_G = n_0 P \Big/ \left[1+\int P/\beta dT\right]^2. \tag{8}$$

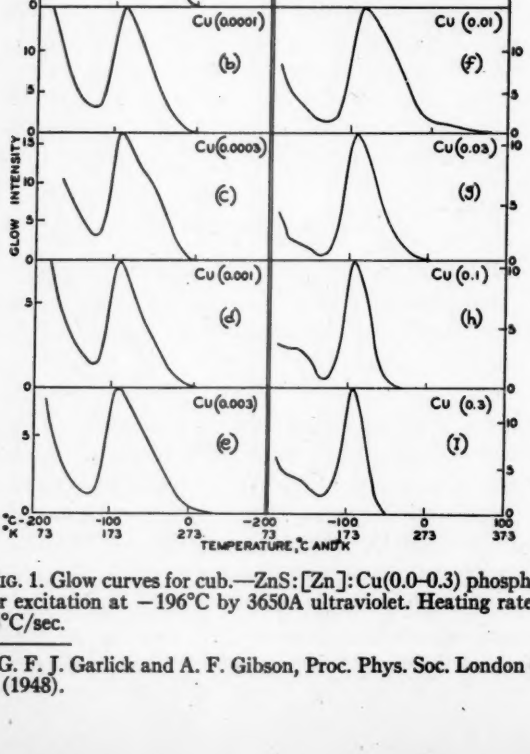

FIG. 1. Glow curves for cub.—ZnS:[Zn]:Cu(0.0–0.3) phosphors after excitation at −196°C by 3650A ultraviolet. Heating rate of 0.33°C/sec.

[4] G. F. J. Garlick and A. F. Gibson, Proc. Phys. Soc. London **60**, 574 (1948).

III. EXPERIMENTAL

Eighteen samples of cubic and hexagonal ZnS:[Zn]:Cu(0.0–0.3) [5] with logarithmically increasing proportions of copper make up the phosphor series with which the largest part of the experimental work was done. They were prepared[6] from the same lot of highly purified ZnS (RCA 33-Z-19),[7] in which there were no spectroscopically detectable[8] impurities. Copper, as $CuCl_2$, and two percent of a water solution of purified NaCl were added in the preparation of these phosphors. The cubic-structure samples were heated for twenty minutes at 950°C; the hexagonal-structure samples were heated for five minutes at 1250°C. Only the cores of the samples were used.

The phosphor to be tested was settled from chemically pure anhydrous methyl alcohol suspension onto the platinized bottom of a metal cup which was inside an evacuable container.[9] The other side of the bottom of this cup could be brought into contact with liquid nitrogen.

The phosphor was excited by 3650A ultraviolet from a 100-watt C-H4 mercury projector spot lamp placed approximately five centimeters from the entrance window. The emitted light was observed by a multiplier photo-tube (usually RCA 1P28) connected to a sensitive microammeter (2×10^{-8} amp. full scale). Linear heating rates were obtained by applying increasing voltages to heating coils around the metal cup at empirically determined times during the heating period.

The spectral distributions of the eighteen sample phosphors were measured at room temperature with an automatic recording spectroradiometer.[10] Excitation was by a 100-watt C-H4 mercury projector lamp 15-cm distant, through two Corning 5840 filters.

[5] Proportions of activator are given in weight percent.
[6] Prepared by P. R. Celmer of these laboratories.
[7] H. W. Leverenz, *An Introduction to Luminescence of Solids* (John Wiley and Sons, Inc., New York, 1950).
[8] Spectrographic analysis by S. Larach of these laboratories.
[9] Apparatus originally designed by R. E. Shrader and F. E. Williams.
[10] V. K. Zworykin, J. Opt. Soc. Am. **29**, 84 (1939).

Glow curves obtained at slow warming rates and measurements of phosphorescence emission decay at long times of decay were measured using a special apparatus with an especially well-insulated inner chamber.[11]

IV. RESULTS: PART I. GLOW AND DECAY CURVES

Glow Curves

The glow curves of the cubic and hexagonal ZnS:[Zn]:Cu(0.0–0.3) phosphors excited at −196°C by 3650A ultraviolet and heated at a rate of 0.33°C/sec. are given in Figs. 1 and 2. The glow curves are plotted with equal peak values because the effort to obtain phosphor layers of uniform thickness[12] was only approximately successful. Small differences in the intensities recorded are not significant.

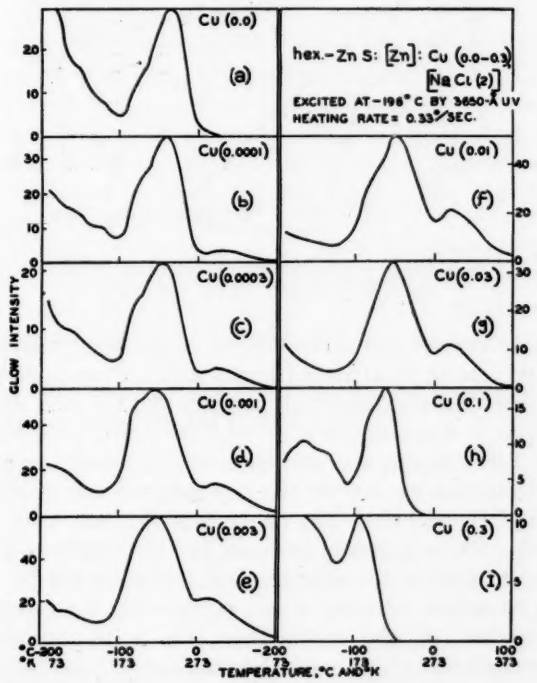

FIG. 2. Glow curves for hex.—ZnS:[Zn]:Cu(0.0–0.3) phosphors after excitation at −196°C by 3650A ultraviolet. Heating rate of 0.33°C/sec.

These curves show that (1) a large fraction of the traps[13] found in ZnS:[Zn]:Cu phosphors are present in the phosphors with no added copper, (2) the incorporation of copper affects the shape of the glow curve for hexagonal phosphors more than for cubic phosphors, (3) the incorporation of copper up to a critical proportion causes the appearance of deep traps, and (4) the incorporation of copper in proportions greater than this critical proportion causes the disappearance of the deep traps caused by copper, and also of some of the deeper traps present before the addition of any copper.

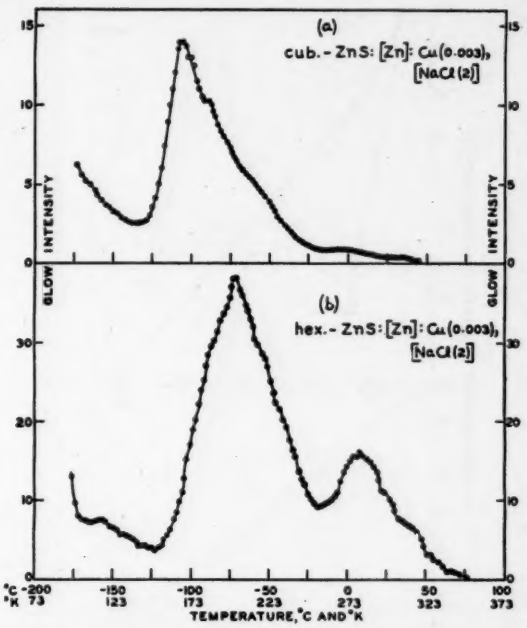

FIG. 3. Glow curves for cubic and hexagonal ZnS:[Zn]:Cu(0.003) phosphors after excitation at −175°C by 3650A ultraviolet. Heating rate of 0.033°C/sec.

Both blue and green emission, corresponding to the blue and green emission bands found during excitation (see Results: Part II, Fig. 13) are found during the glow experiment for low copper proportions. Only the emission of the green band, however, is found in glow curves for copper proportions equal to or greater than 0.003 percent. All quantitative analyses of glow curves and decay curves are based on phosphors which give only green phosphorescence emission.

The shapes of the glow curves, especially for high copper proportions where deep traps disappear, suggest the presence of a limited number of component glow curves, each being caused by traps of one depth.

Glow Curves with Slower Heating Rate

One method of testing for such component glow curves is to measure glow curves at a slower heating rate, for which an increase in resolution is obtained by a decrease in the width of a glow curve. Figure 3 gives examples of glow curves obtained at a heating rate of 0.033°C/sec. for cubic and hexagonal ZnS:[Zn]:Cu-(0.003) phosphors. These curves are reproducible in general shape, but peak intensities differ by as much as 15 percent.

A comparison of the glow curves at 0.33°C/sec. and 0.033°C/sec. shows a general increase in detectable structure for the latter. Although the shifts of the major glow peaks are in agreement with the shifts predicted by the simple theory [Eqs. (4) and (5)], these results

[11] Apparatus designed by H. W. Leverenz.
[12] The thickness affects the over-all intensity observed.
[13] When the total number of traps, regardless of depth, is under discussion, the plural "traps" will be used. When the number of different trap depths is under discussion, the term "trap depth" will be used. For example, the number of traps is very large, but the number of trap depths may be small.

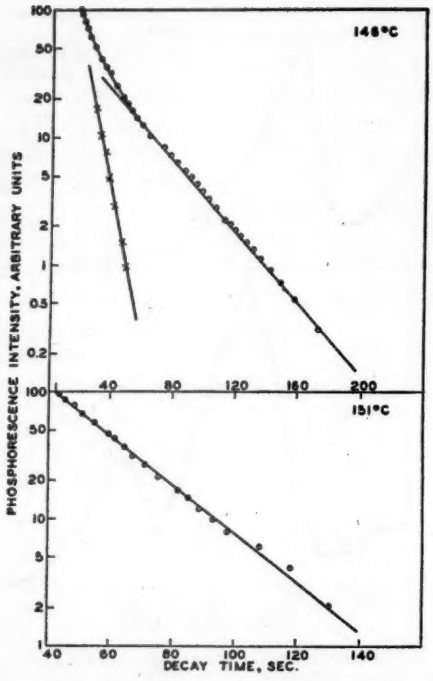

FIG. 4. Decay of phosphorescence emission for hex.—ZnS:[Zn]:Cu(0.01) at 146° and 151°C.

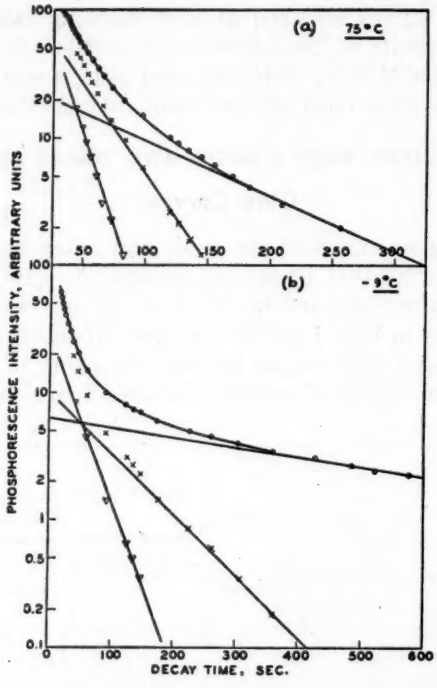

FIG. 6. Decay of phosphorescence emission for hex.—ZnS:[Zn]:Cu(0.01) at 75° and −9°C.

are inconclusive as far as the presence of component glow peaks is concerned.

Decay Curves

Typical decay curves for hex.—ZnS:[Zn]:Cu(0.01) at high temperatures (near the temperature at which the glow intensity becomes zero) are given in Fig. 4. The decay is exponential for long times of decay. If the final exponential portion is subtracted (Curve for 146°C), another exponential curve is found.

The agreement between the exponential decays at seven temperatures between 135° and 168°C and Eq. (2) is shown in Fig. 5. The logarithm of the decay constant is found to vary linearly with $1/T$, as predicted.

Figure 6 gives the decay curves for this same phosphor at 75° and −9°C. If the assumption is made that these decay curves, and others like them for other temperatures, are to be analyzed into a series of exponentials, at least three exponentials are required for each decay curve. It is possible to start with the exponential found at high temperatures and by successive subtraction of exponentials to analyze the experimental curves into a set of exponentials. The analysis of the curves for 75° and −9°C in this way is shown in Fig. 6. Although the set of exponentials obtained in this way cannot be said to be unique because of the increasingly larger errors attendant on the subtractions, the least number of exponentials which would be required is estimated.

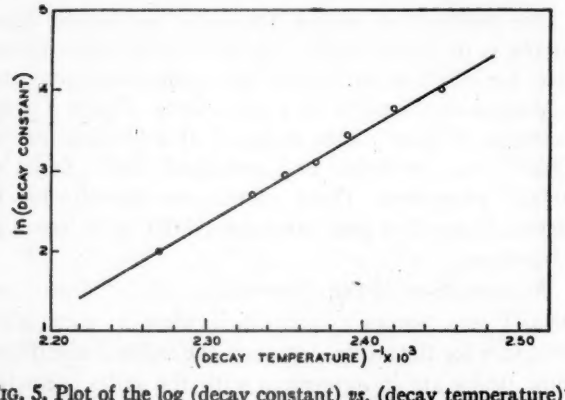

FIG. 5. Plot of the log (decay constant) *vs.* (decay temperature)$^{-1}$ for hex.—ZnS:[Zn]:Cu(0.01).

Glow Curves after Various Periods of Decay

A glow curve for traps of one depth [Eq. (3)] has the same shape and peak temperature regardless of the

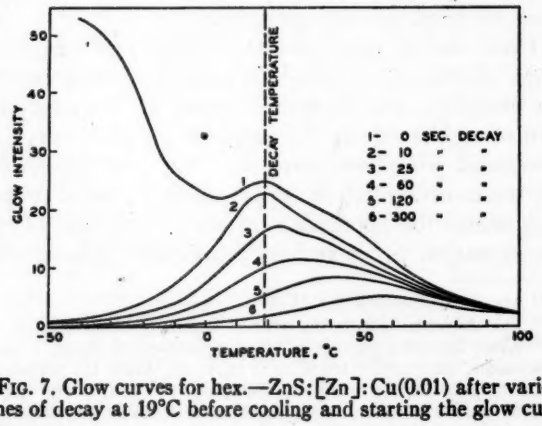

FIG. 7. Glow curves for hex.—ZnS:[Zn]:Cu(0.01) after various times of decay at 19°C before cooling and starting the glow curve run.

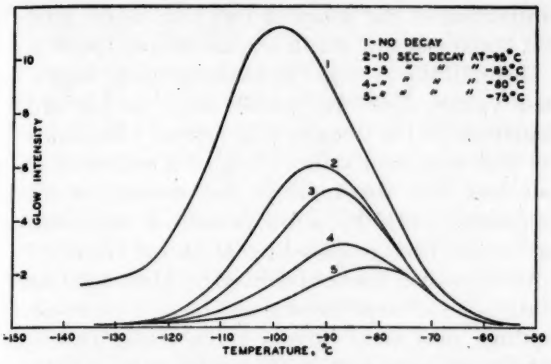

FIG. 8. Glow curves for cub.—ZnS:[Zn]:Cu(0.3) after various times of decay at temperatures between −75° and −95°C before cooling and starting the glow-curve run.

number of electrons trapped. Figures 7 and 8 show glow curves of hex.—ZnS:[Zn]:Cu(0.01) and cub.—ZnS:[Zn]:Cu(0.3) after various periods of decay at different temperatures. The phosphor was excited and then allowed to decay for the designated period. Then it was rapidly cooled to liquid nitrogen temperature, and the glow curve was measured.

The peak of the glow curve shifts continuously to higher temperatures with increasing periods of decay. The major glow peaks of Figs. 7 and 8, therefore, cannot be caused by traps of a single depth.

Glow Curves after Different Excitation Intensities and Periods; Retrapping (?)

Wilkins and Garlick[14] introduced a method for testing for the presence of retrapping. They used a hex.—ZnS:[Zn]:Cu phosphor with two distinct glow peaks: a low temperature peak caused by shallow traps and a high temperature peak caused by deep traps. When the phosphor was excited with very low intensity so that most of the traps were empty, they expected that the presence of retrapping by the deep traps of electrons freed from the shallow traps in the course of the glow curve run would make itself evident. Such retrapping would make the high temperature glow peak much more intense relative to the low temperature peak than was found in a glow curve obtained after high excitation intensity.

Measurements of this type have been extended over wide ranges of exciting intensity and periods of excitation. Figure 9 shows the results for hex.—ZnS:[Zn]:Cu(0.01) for excitation intensities varying by a factor of 10^4. A fixed excitation period of five minutes was used. The curves are normalized in this case so that the intensity of the shallow-trap peak remains fixed.

Analogous results obtained by variation of the excitation period are shown in Fig. 10. An excitation intensity was used that was 0.3 percent of the normal intensity used in Figs. 1 and 2.

For the sake of calculations, the glow curve is

[14] M. H. F. Wilkins and G. F. J. Garlick, Nature 161, 565 (1948).

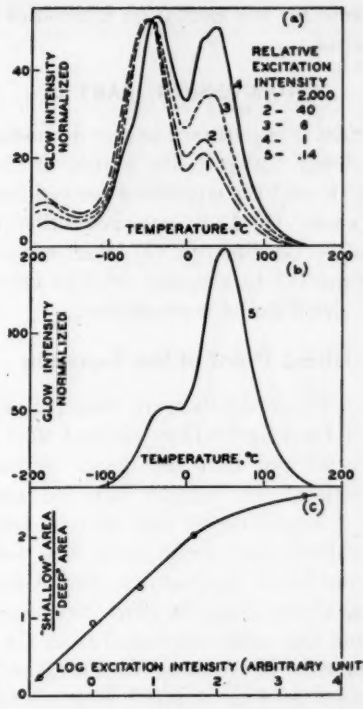

FIG. 9. Glow curves for hex.—ZnS:[Zn]:Cu(0.01) after excitation at −196°C by different excitation intensities.

divided into two major sections: (1) shallow traps between −100° and 0°C, and (2) deep traps above 0°C. The area under the glow curve for any portion of the curve is proportional to the number of electrons in traps which are responsible for the glow in that portion of the curve. Reducing the excitation intensity or the period of excitation causes an increase in the relative intensity of deep trap peaks with respect to shallow trap peaks.

Figures 9-c and 10-d show that the ratio of the areas of low temperature and high temperature glow peaks

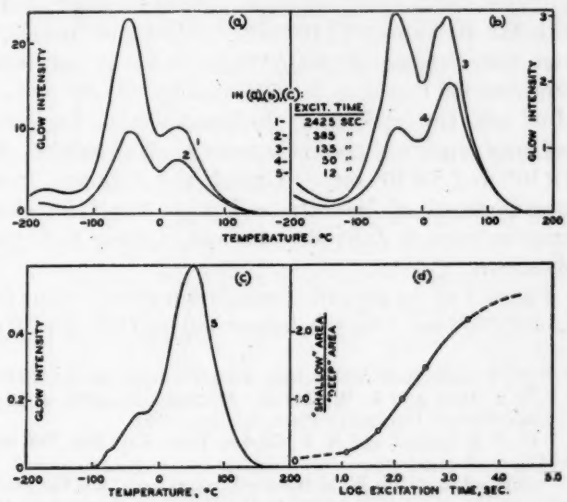

FIG. 10. Glow curves for hex.—ZnS:[Zn]:Cu(0.01) after excitation at −196°C for different excitation times.

approaches zero for low excitation intensities and short excitation periods.

V. DISCUSSION: PART I

Of fundamental importance in any discussion of glow curves and decay curves is the extent of the applicability of Eq. (1) and the equations derived from it. It is necessary to ask: (1) Is it experimentally possible to verify this equation directly? (2) What range of values may ν_a be expected to assume? (3) Can retrapping be neglected in ZnS:[Zn]:Cu phosphors?

Direct Proof of the Equation

Traps of a single depth were found in KCl:Tl by Buenger and Flechsig.[14a] They showed that the decay was exponential and that the decay constant varied with temperature in the manner expected from Eq. (2).

Traps of a single depth and with a temperature-dependent exponential decay were also found for a $SrSiO_3$:Eu phosphor by Garlick and Gibson.[4] The value of ϵ calculated from the glow curve was different, however, from the value calculated from the decay.

A direct proof of the equation for ZnS-type phosphors is demonstrated by Figs. 4 and 5. Exponential decay is found at high temperatures, for which the decay constant varies with temperature as expected from Eq. (2). The deepest trap in ZnS:[Zn]:Cu phosphors is found to have a trap depth of 1.00 ev.

Values of ν_a

The following values of ν_a have been reported in the literature: (1) 2.9×10^9 sec.$^{-1}$, Buenger and Flechsig,[14a] with traps of a single depth in KCl:Tl; (2) $10^{8\pm1}$ sec.$^{-1}$, Randall and Wilkins[2] from measurements of glow curves after various periods of decay, assuming a distribution of traps with the same ν_a, for ZnS phosphors and for calcium and strontium sulfides; (3) 10^{11} sec.$^{-1}$, Randall and Wilkins,[2] from similar measurements with cadmium borate and cadmium chlorophosphate, both with Mn activator; (4) 10^{10} sec.$^{-1}$, Mott and Gurney,[15] from the decrease of photo-conductivity at low temperatures for *F*-centers in alkali halides; (5) 10^{11} sec.$^{-1}$, Mott and Gurney,[15] from the cross section for luminescence capture of photo-electrons in alkali halides; (6) 6×10^6 to 2.5×10^7 sec.$^{-1}$, Garlick and Gibson,[16] from measurements of dielectric relaxation times for electrons in traps in ZnS:[Zn]:Cu and in other ZnS-type phosphors.[17]

Figure 5 of the present investigation gives a value for ν_a of 3×10^{10} sec.$^{-1}$ for the deepest trap in ZnS:[Zn]:Cu. Subtraction of the decay of this trap depth gives the next shallowest trap depth a value of ν_a of 7×10^9 sec.$^{-1}$.

Theoretically ν_a might be expected to be larger than these values, about 10^{12} to 10^{13} sec.$^{-1}$ or the order of magnitude of the frequency of crystal vibrations. The fact that measured values are several orders of magnitude less than this indicate the presence of a small transition probability in the process of trap emptying, such as has been proposed by Mott and Gurney.[15]

An expression has been derived by Mott and Gurney[15] relating the attempt-to-escape frequency for an electron captured in a state (luminescence center or trapping state) to the cross section for capture of an electron into the state. For an equilibrium condition, the rate of capture of electrons by the state was equated to the rate of escape of electrons from the state. In this case, the relation is found:

$$\nu_a/\sigma=(2(6)^{\frac{1}{2}}\pi^{\frac{1}{2}}mk^2/h^3)T^2, \tag{9}$$

where σ is the cross section for electron capture.

Because all of the reported values of ν_a lie above 10^6 sec.$^{-1}$, this value may be taken as a minimum to be considered for use in Eq. (1).

Importance of Retrapping

The study of glow and decay curves has led Wilkins, Garlick, Gibson, and Williams[4,14,18] to come to the conclusion that retrapping is negligible. In general their work has been non-quantitative and only partially conclusive.

The fact that the decay measured at high temperatures in the present investigation was found to be exponential, and that the decay constant varied with temperature in the manner predicted by Eq. (2), (Fig. 5), shows that at least for the deepest trap in ZnS:[Zn]:Cu retrapping is completely negligible. If retrapping did occur, a decay given by Eq. (6) would be expected, with a variation of the intensity according to t^{-2} at long decay times [Eq. (7)]. Retrapping of electrons by traps of the same depth as those from which they were freed does not occur in this case where a direct test was possible.

Figures 9 and 10 provide information on retrapping by deeper traps than those from which the electrons were freed. The relative intensity of the high temperature glow peak increases as the total number of electrons trapped decreases.

This dependence of glow-curve shape on excitation conditions could be caused by a larger probability for capture by a deep trap than by a shallow trap. Because there are many more shallow than deep traps in ZnS:[Zn]:Cu phosphors, the relative number of electrons trapped in shallow traps would increase as the total number of trapped electrons increased, and as saturation of the deep traps was approached. If the variations of glow-curve shape were caused by a larger

[14a] W. Buenger and W. Flechsig, Zeits. f. Physik **67**, 42 (1931).

[15] N. F. Mott and R. W. Gurney, *Electronic Processes in Ionic Crystals* (Oxford University Press, London, 1940).

[16] G. F. J. Garlick and A. F. Gibson, Proc. Roy. Soc. **188**, 485 (1947).

[17] Omitted from this lisi of reported values for ν_a are the much lower values reported in reference 18. These are obtained by the rather arbitrary analysis of a glow curve tnto four component curves.

[18] F. E. Williams and H. Eyring, J. Chem. Phys. **15**, 298 (1947).

capture probability for deep traps, the ratio of high temperature glow-peak area to low temperature glow-peak area should approach a constant value for low intensities and short excitation periods. This constant value would be the ratio of the capture probabilities multiplied by the ratio of the number of traps. The measurements of Figs. 9-c and 10-d show that a value of zero is the probable lower limit of the ratio of high temperature to low temperature glow-peak area. This result means that a simple difference in capture probabilities is not the cause of the changes in glow-curve shape with excitation conditions, unless the probabilities are different by a factor of 20 or more.

The glow-curve variations could be caused alternatively by the retrapping by non-filled deep traps of electrons freed from shallower traps in the course of the glow curve run. A certain area, corresponding to the number of electrons retrapped, would be displaced from the low temperature glow peak.

The glow-curve difference could not be caused by a larger probability of escape for electrons in shallow traps as compared to deep traps during excitation, because both the shallow traps and the deep traps have glow peaks far above the excitation temperature of -196°C.

If it is assumed that the whole dependence of the glow-curve intensities on excitation conditions is due to retrapping, a measure of the maximum amount of retrapping which could occur is obtained.

The glow curve for a high excitation intensity and long excitation period is used as a standard. Excitation for still longer times or at still higher intensities does not appreciably change the glow intensity or the relative intensities of high and low temperature glow peaks. Let the area measured under the low temperature glow peak for high excitation intensity and long excitation periods be L, and for a lower intensity and shorter period L'. Similarly let the respective high temperature glow-peak areas be H and H'. L is the number of shallow traps. H is the number of deep traps. R is the number of electrons retrapped, and is found from

$$(L'+R)/(H'-R)=L/H.$$

The number of electrons initially available for retrapping will be $(L'+R)$. The number of deep traps initially empty will be $[H-(H'-R)]$. The proportion of freed electrons retrapped, P_r, is $R/(L'+R)$. The number of initially empty deep traps per retrapped electron is $[H-(H'-R)]/R$.

A plot of P_r as a function of the number of deep traps initially empty is given in Fig. 11-b for the hex.—ZnS:[Zn]:Cu(0.01) phosphor of Figs. 9 and 10, and in Fig. 11-a for a cub.—ZnS:[Zn]:Cu(0.01) phosphor. The actual proportion of electrons retrapped is much less in cubic than hexagonal phosphors, because there are many less deep traps in the cubic phosphor.

The proportion of electrons retrapped is small until 80 or 90 percent of the deep traps are initially empty.

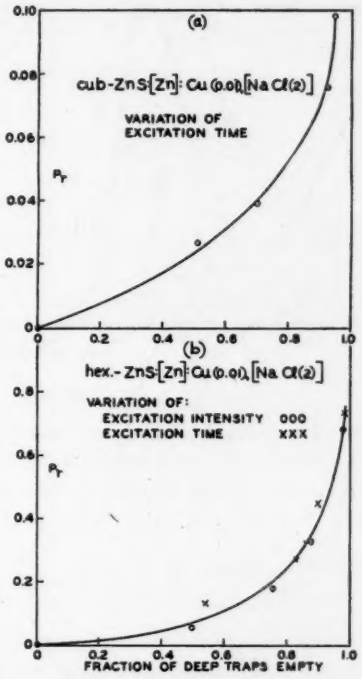

FIG. 11. Proportion of electrons freed from shallow traps which are retrapped by deep traps in the course of the glow-curve run as a function of the number of deep traps initially empty, for cubic and hexagonal ZnS:[Zn]:Cu(0.01).

The curve of Fig. 11-b shows that the proportion of electrons retrapped does not depend on whether changes in the number of electrons initially trapped were achieved by low excitation intensities or low excitation times.

The number of empty deep traps (at the start of the glow-curve run) per retrapped electron may be calculated for further information about the importance of retrapping. For excitation conditions such that less than 75 percent of the deep traps are initially empty, less than 20 percent of the freed electrons are retrapped. Over this range of excitation conditions, there are between 4 and 7 deep traps initially empty for every electron retrapped by these deep traps. For excitation conditions such that about 97 percent of the deep traps are initially empty, there are about 30 empty deep traps for every retrapped electron.

Although retrapping may occur, therefore, if a sufficient number of empty traps are present in which electrons may be stably retrapped,[19] retrapping does not play a role in the normal measurements of glow and decay curves for ZnS:[Zn]:Cu phosphors where initial excitation conditions are such that the number of empty traps is very small.

[19] The retrapping of electrons by empty *shallow* traps (still deep enough, however, to empty slowly at the operating temperature) after the electrons had been freed from *deep* traps by infrared has been reported by Garlick and Mason, J. Electrochem. Soc. **96**, 90 (1949), and D. Curie, Comptes Rendus **230**, 1400 (1950).

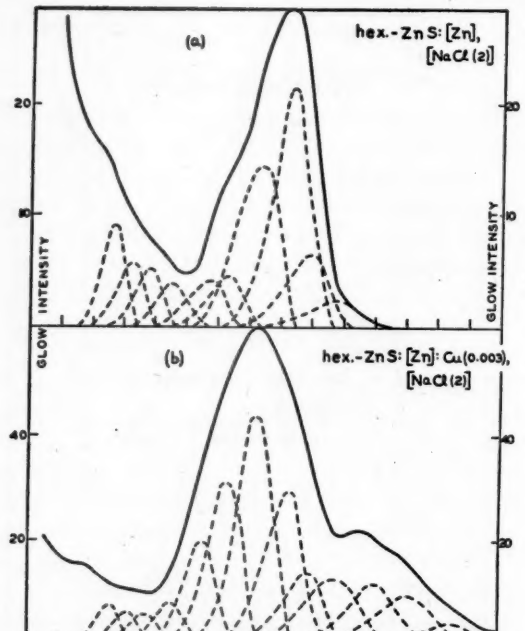

FIG. 12. Analysis of glow curves for hexagonal ZnS:[Zn] phosphor and for hex.—ZnS:[Zn]:Cu(0.003), using Eq. (3) for the shape of the component glow curves.

Analysis of Glow and Decay Curves

These results justify the use of Eq. (1) with a value of ν_a of greater than 10^6 sec.$^{-1}$.

Correlation between glow curves and decay curves for KCl:Tl was obtained (for decay curves near room temperature) by Randall and Wilkins[2] using Eq. (1) with the assumption of a narrow distribution of trap depths.

Because the glow curve of a ZnS phosphor was found by Randall and Wilkins to have an approximately exponential variation with temperature at room temperature, a continuous distribution of traps was assumed at room temperature such that the number of traps of a given depth decreased exponentially with increasing depth. Calculation using Eq. (1) showed that such a distribution of traps should give rise to a power-law decay. General agreement between glow curves and decay curves at this temperature was reported. Exact power-law decay is not found experimentally for any of the phosphors described in the present paper (an exponential variation of the glow curve with temperature was not found either), but approximate power-law decay is found for many temperatures for which the variation of the glow curve with temperature is not even approximately exponential.

The only previously reported separation of the glow curve into component curves where separate peaks are not found in the glow curve, was that done by Williams and Eyring[19] on the basis of absolute rate theory.[20] This theory gives an equation of exactly the same form as Eq. (1). A glow curve for a ZnS:[Zn]:Cu phosphor was approximately fitted by four component glow curves. Correlation with decay curves was not checked. This analysis gave low values of ν_a.

An analysis of the glow and decay curves of the present paper with the use of Eq. (1) gives the following results:

(1) Extremely low values of ν_a would be necessary to fit the experimental glow curves with two simple component curves calculated from Eq. (3). A reasonable fit between $-110°$ and 30°C may be obtained using $\nu_a = 10$ sec.$^{-1}$, but calculated decay curves do not agree with experimental decay curves.

(2) An estimate of the least number of component glow curves that would be needed to fit the experimental curve and still have ν_a be at least 10^6 sec.$^{-1}$ is obtained by dividing the widths of the experimental glow curves by the width of the calculated glow curve for $\nu_a = 10^6$ sec.$^{-1}$. At least three component curves would be needed to fit the principal central peak, and at least three or four component curves would be needed to fit the high temperature peak. Allowing for three or four subsidiary component curves to fill in the edges gives a total of at least 10 component curves.

(3) Figures 7 and 8 show that the glow maximum shifts to increasingly higher temperatures with increasing periods of decay before the glow-curve measurement. At least three component curves with $\nu_a = 10^6$ sec.$^{-1}$ would be required to fit the region over which the peak shifts in Fig. 7, and similarly at least two component curves would be required to explain Fig. 8.

(4) Glow curves measured at slow heating rates (Fig. 3) show no great increase in resolution of component detail, as might be expected if the number of component curves were small.

(5) Every measured decay curve (except at very high temperatures) must be analyzed into at least three exponentials, if it is to be analyzed into exponentials at all. Each exponential is attributable to a certain trap depth. It is possible for two exponentials at two different temperatures to refer to the same trap depth (since the decay constant is temperature dependent), but even allowing for such identities, at least about 12 different trap depths are required to describe the decay curves between $-83°$ and 200°C.

(6) The glow curves of Figs. 1 and 2 have been analyzed into a set of twelve component curves with $\nu_a = 10^8$ sec.$^{-1}$ for temperatures above $-100°$C. These curves were chosen, first by noting (*a*) the apparent maxima and (*b*) gross inconsistencies with the asymmetry required by the calculated glow curves, and then by filling in with other curves required to make a good fit with the experimental curve (Fig. 12). It is possible to analyze all the curves of Figs. 1 and 2 into the same set of 12 component curves. Too much significance cannot be attached to the exact details of these analyses.

Until clearly distinct peaks are observed in the glow

[20] Glasstone, Laidler, and Eyring, *The Theory of Rate Processes* (McGraw-Hill Book Company, Inc., New York, 1941).

curves, however, or until some means of resolving separate trap depths is found, it may only be said that the presence of a series of discrete trap depths in ZnS:[Zn]:Cu phosphors is plausible. The possibility remains that a continuum of trap depths followed by one or two discrete deep trap depths might also describe the experimental results.

VI. RESULTS: PART II

Emission Spectra

The spectral emissions of cubic and hexagonal ZnS:[Zn]:Cu(0.0–0.3) phosphors excited by 3650A ultraviolet at 24°C are given in Fig. 13. The curves are plotted to scale.

The emission of the ZnS:[Zn] phosphors without added copper is blue. Incorporation of copper up to a certain critical proportion causes the appearance of a green emission, and a decrease in intensity of the blue emission. Further incorporation of copper causes a blue band to appear. At very high copper proportions all visible emission disappears except a broad green band.

Spectrographic analysis[21] shows that the amount of copper added in the preparation of each phosphor is present in the phosphor sample. This means that changes in the spectral emission are not caused by differences between the amount of copper actually in the phosphors and the amount added in the preparation.

Of special interest is the emission for the highest proportion of copper used. Figure 14 is a tracing of the actual pen-drawing of the automatic recording spectroradiometer for the spectra of the cubic and hexagonal

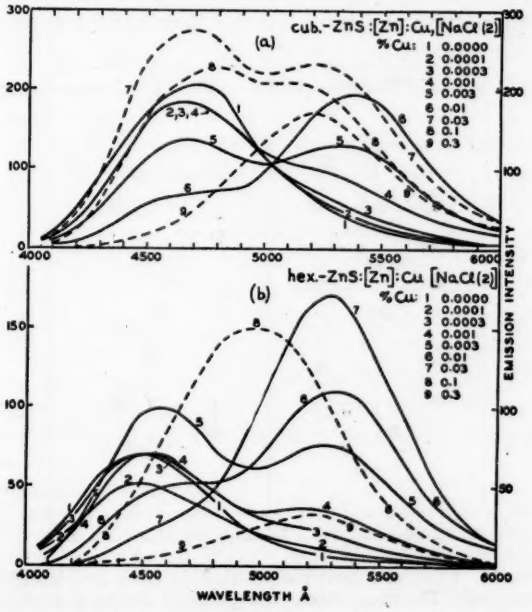

FIG. 13. Luminescence emission spectra for cubic and hexagonal ZnS:[Zn]:Cu(0.0–0.3) during excitation by 3650A ultraviolet at 24°C.

[21] Spectrographic analysis by S. Larach.

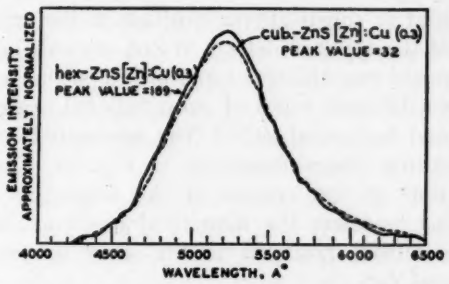

FIG. 14. Trace of the pen-drawing of the automatic recording spectroradiometer for the spectral curves of cubic and hexagonal ZnS:[Zn]:Cu(0.3).

ZnS:[Zn]:Cu(0.3). Although the actual intensity of the cubic emission is about five times greater than that of the hexagonal emission, the gain was adjusted so that both curves were drawn to about the same scale. The spectral curves are strikingly similar.

Effects of Chemical and Physical Variations on Emission and Glow Curves

One of the principal correlations found is that a decrease in the ratio of green to blue intensity during excitation, caused by some chemical or physical change, is accompanied in general by an increase in the glow intensity for shallow traps for temperatures −170° to −100°C, and a decrease in the glow intensity for deep traps at higher temperatures. This change is caused by heating or preparing phosphors in an atmosphere containing hydrogen. Another way of causing this change is to recrystallize a cubic ZnS:[Zn]:Cu(0.01) phosphor to form a hexagonal ZnS:[Zn]:Cu(0.01) phosphor. The change, in this case, is stopped by the addition of sufficient chloride in the recrystallization.

Although the use of chloride in the preparation of phosphors was found to increase the number of traps and the intensity of the excited emission, and to affect the ratio of shallow to deep traps, it was also found that the presence of chloride or other halide is not essential for the presence of luminescence emission or trapping (Fig. 15). "Pure" ZnS, the same as was used in the preparation of the ZnS:[Zn]:Cu series, was heated at various temperatures from 950° to 1340°C with no additives whatsoever. Figure 15 shows that the logarithm of the number of traps increases linearly with the reciprocal of the heating temperature. (The number of traps is proportional to the area under the glow curve.) The intensity of the blue emission also increases as the heating temperature of the phosphor increases.

VII. GENERAL DISCUSSION

Nature of Crystal Defects in ZnS

Because a large number of traps are found in the same energy range both for ZnS:[Zn]:Cu phosphors and for ZnS:[Zn] phosphors without added Cu, these traps are the result of crystal defects in ZnS. It is also true that the activating impurity must occupy either an

interstitial or substitutional position in the crystal. A study of the types of defects in ZnS crystals is useful.

There are two different types of interstitial positions and two different types of substitutional positions in cubic and hexagonal ZnS.[22] The interstitial positions are pictured diagrammatically in Fig. 16. The small black dots at the centers of the respective crystal diagrams represent the interstitial positions. None of the interstitial positions is the same in cubic and hexagonal ZnS.

A Zn substitutional position in cubic ZnS, however, is identical with a Zn substitutional position in a hexagonal ZnS out to third nearest neighbors; similarly for *S* substitutional positions.

This striking difference between interstitial and substitutional positions naturally leads to a new analytical approach: Luminescence phenomena caused by impurities in interstitial positions will be different when observed in cubic and hexagonal ZnS phosphors, whereas luminescence phenomena caused by impurities in substitutional positions will be identical or practically identical whether observed in cubic or hexagonal ZnS phosphors. The validity of this approach depends on the assumption that simple defect formation does not alter symmetry relations in the crystal.

Use of the Analytical Approach

The use of this approach together with the experimental results of this paper leads to the following set of hypotheses which are able to explain all of the results found in this study.

(1) Trapping centers are located at substitutional sites, principally omission defects, in ZnS phosphors.

The general variation of glow with temperature is the same for all the curves of Figs. 1 and 2. The shallowest traps give a glow with a minimum at −120°C, the central peak is the principal peak and extends from −120° to 0°C or a little above, and the deep traps caused by copper extend from 0° to over 100°C. As a special example, the principal glow peaks for cubic and hexagonal ZnS:[Zn]:Cu(0.3) are almost identical.

The same set of component glow curves describes all of the curves of Figs. 1 and 2.

The variation of the number of traps with heating temperature (Fig. 15) for "pure" ZnS is exactly the same as the variation of the number of omission defects.[15] A reasonable value of 2.2 ev is found for the activation energy for omission-defect formation. (It is true that the number of interstitial defects varies with heating temperature in the same way, but with an activation energy of 4.4 ev.)

(2) The luminescence emission for which the Cu is responsible depends on the position of Cu in the crystal structure.

Because Fig. 13 has shown that the spectral curves for low copper proportions have different blue and green

[22] P. P. Ewald and C. Herman, *Strukturbericht* (Akademische Verlagsgesellschaft mbH, Leipzig, 1931), pp. 76–79.

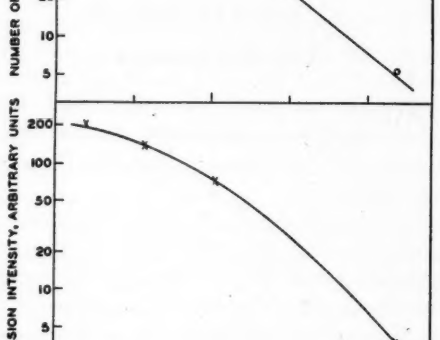

FIG. 15. The variation of the number of traps and of the blue emission intensity with preparation heating temperature for "pure" ZnS:[Zn].

bands for cubic and hexagonal phosphors, the impurities responsible for these emissions are located at interstitial sites. This agrees with the findings of Riehl and Ortmann,[23] and Seitz.[24,25]

The work of other investigators has included measurements on the spectra of ZnS:[Zn]:Cu phosphors up to the proportion of Cu for which a blue band reappears.

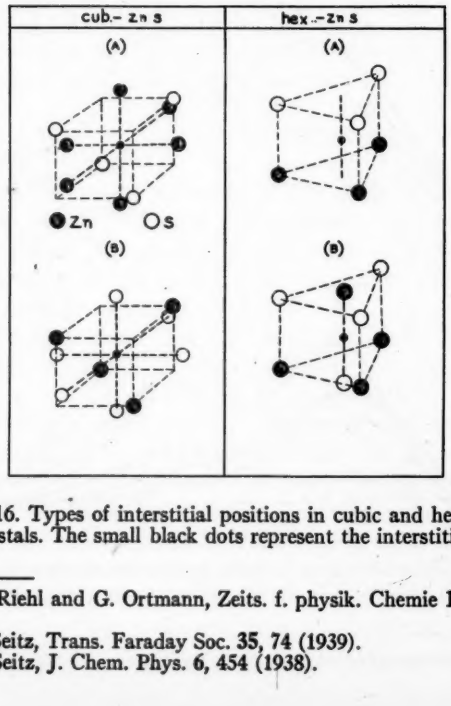

FIG. 16. Types of interstitial positions in cubic and hexagonal ZnS crystals. The small black dots represent the interstitial positions.

[23] N. Riehl and G. Ortmann, Zeits. f. physik. Chemie **188**, 109 (1941).
[24] F. Seitz, Trans. Faraday Soc. **35**, 74 (1939).
[25] F. Seitz, J. Chem. Phys. **6**, 454 (1938).

But, previous to this present paper, there has been no mention[26] to the knowledge of the author of the return of the emission to a broad green band for very high copper proportions, which band (Fig. 14) is almost identical for cubic and hexagonal ZnS:[Zn]:Cu(0.3). This identity of the emission bands for cubic and hexagonal phosphors means that the copper responsible for this emission is located in substitutional sites.

The reappearance of a blue band in the curves of Fig. 13 at a critical copper proportion marks the entrance of copper into substitutional sites. At low copper proportions, copper is located predominantly in interstitial positions and is responsible for a green emission. At some critical proportion, more copper is located in substitutional sites and is responsible for a blue emission. At very high copper proportions, only a broad green emission caused by pairs of substitutionally located copper ions is found.

(3) The effect of Cu on traps depends on the position of Cu in the crystal structure.

A comparison of Figs. 1 and 2 and Fig. 13 shows that deep traps are caused by copper when it is responsible for a green emission. The effect of interstitial copper is to perturb neighboring omission defects and cause deeper trap depths.

When copper gives rise to a blue emission, and for all larger proportions of copper, traps are destroyed. When copper enters substitutional positions, it destroys the traps which existed previously at those omission defects.

Shallow traps are located at sulfur omissions because these are the most likely to form. Because the entrance of copper into substitutional positions occurs at Zn positions, however, neighboring zinc and sulfur omission defects are indicated as trapping centers of intermediate depth.

(4) The role of the chloride, or other halide, in ZnS phosphors is to assist the temperature-dependent formation of defects.

An increase in the number of traps and of the intensity of the luminescence emission, which may be achieved by the use of chloride in the preparation, can be achieved also by merely raising the heating temperature of phosphor formation sufficiently (Fig. 15).

The use of chloride, bromide, or iodide in ZnS phosphors all give rise to the same spectral distribution of the emission.[27] This would hardly be expected if the chloride were an inherent part of the emission center, as was originally proposed by Kroeger *et al.*[28,29] Recently Kroeger[30] has altered this view in favor of one more compatible with these results. If the effect of the chloride were simply to increase the formation of defects, however, the luminescence emission would be characteristic of the defect and its surrounding in the crystal, and would not be dependent on the way it had been formed.

The emission change from green to blue and the destruction of deep traps when cub.—ZnS:[Zn]:Cu(0.01) is recrystallized into hex.—ZnS:[Zn]:Cu(0.01) indicates the entrance of copper into substitutional positions. The addition of chloride in the recrystallization prevents this by acting to keep copper in interstitial positions.

VIII. CONCLUSIONS

A large number of traps are present in ZnS:[Zn] phosphors with no added impurity. The incorporation of copper up to 0.01 percent causes the appearance of traps which are deeper than those present before the addition of copper. Incorporation of copper in amounts of more than 0.01 or 0.03 percent causes the traps due to copper, and also some of the deeper traps present before the addition of copper, to disappear. In proportions up to 0.01 percent, the copper is found to be responsible for a green luminescence emission. At about the proportion for which the deep traps start to disappear, a blue band is found. For very high proportions of copper, a green band is found that is almost identical for both cubic and hexagonal phosphors. These results may be explained by assuming a transition from interstitial copper to substitutional copper.

Equation (1) of Randall and Wilkins[2] was proven directly for a ZnS-type phosphor from measurements of decay at high temperatures. The deepest traps in ZnS:[Zn]:Cu phosphors have a single trap depth of 1.00 ev, and an attempt-to-escape frequency of 3×10^{10} sec.$^{-1}$. Subtraction of this decay yields for the next deepest trap depth, a single depth of 0.89 ev, and an attempt-to-escape frequency of 7×10^{9} sec.$^{-1}$.

The present measurements, together with previously published results of other investigators, favor the assumption that the probable range of values for the attempt-to-escape frequency is between 10^{8} and 10^{10} sec.$^{-1}$, with a minimum of about 10^{6} sec.$^{-1}$.

The agreement of the decay with Eq. (1) at high temperatures, indicates that retrapping of electrons by traps of the same depth as those from which they were freed does not occur. If retrapping did occur, the shape of the decay curve would be given by Eq. (6) instead of by an exponential.

The other possibility of retrapping is that freed electrons may be retrapped in deeper traps than those from which they were freed. It is shown for the hexagonal ZnS:[Zn]:Cu phosphors, assuming the maximum amount of retrapping possible, that there are at least four to seven empty deep traps for every electron retrapped. Normal measurements, therefore, which are

[26] Except reference 7.

[27] Spectral curves obtained by the Chemico-Physics Section of the RCA Laboratories show that spectral distributions are the same whether chloride, bromide, or iodide is used, although the efficiencies are slightly different.

[28] F. A. Kroeger and J. E. Hellingman, J. Electrochem. Soc. **93**, 156 (1948); **95**, 68 (1949).

[29] Kroeger, Hellingman, and Smit, Physica **15**, 990 (1949).

[30] F. A. Kroeger and J. Dikhoff, Physica **16**, 297 (1950). From the sizes of the ionic radii, it would be expected that a change from interstitial to substitutional Cu would also mean a change from Cu^{+} to Cu^{++}. Kroeger has proposed that the presence of Cl^{-} aids the formation of Cu^{+} on the basis of charge compensation.

obtained after excitation by high intensity and for a long time, at least for ZnS:[Zn]:Cu phosphors, are not affected by retrapping.

The existence of a series of discrete trap depths, at least 12 in number between −100° and 200°C, appears plausible. Definite evidence, however, was not obtained that a continuous distribution of trap depths, followed by one or two discrete depths, could not give an alternative description of the observed results.

A study of the crystal structure of ZnS indicates that interstitial positions are all different in cubic and hexagonal ZnS, whereas substitutional positions are the same out to third nearest neighbors. A new analytical approach was indicated, therefore, which states that, if formation of simple defects does not alter symmetry relations, luminescence phenomena caused by impurities in interstitial positions should be different when observed in cubic and hexagonal ZnS phosphors, but that luminescence phenomena caused by impurities in substitutional positions should be the same or practically the same when observed in cubic and hexagonal ZnS phosphors.

The similarity in trap depths found for cubic and hexagonal phosphors leads to the hypothesis that trapping centers are located in substitutional sites, primarily omission defects. This hypothesis and the previously mentioned analytical approach may be used to interpret many observations of luminescence emission and glow curves.

The author wishes to express his sincere appreciation to H. W. Leverenz and Dr. R. E. Shrader for many valuable discussions, suggestions, and encouragement throughout the work; to Professor R. Hofstadter[31] of Princeton University for his capable advice and guidance; and to the entire staff of the Chemico-Physics section at the RCA Laboratories for the assistance they gladly and skillfully contributed at various phases of the work.

The author also wishes to thank Dr. V. K. Zworykin of the Radio Corporation of America, and the ONR for enabling a concentrated program of this type to be carried out.

[31] Present address: Physics Dept., Stanford University.

PHYSICAL REVIEW VOLUME 80, NUMBER 4 NOVEMBER 15, 1950

Quantum Electrodynamics of Charged Particles without Spin

F. ROHRLICH
Laboratory of Nuclear Studies, Cornell University, Ithaca, New York
(Received June 19, 1950)

Feynman's formulation of quantum electrodynamics is shown to be equivalent to the Schwinger-Tomonaga theory also for spinless charged particles (mesons) as developed by Kanesawa and Tomonaga. The divergencies of the scattering matrix are analyzed to all orders in the fine-structure constant and it is found that mass and charge renormalizations do *not* remove all divergencies, unlike the electron case. The remaining divergence is associated with the meson-meson interaction and occurs in all orders of radiative corrections except the lowest (second) order in which the process can exist. In order to make the scattering matrix completely finite a direct interaction term $\lambda\phi^*(x)\phi^*(x)\phi(x)\phi(x)$ in the Hamiltonian must be postulated. The infinite coupling constant λ is to be renormalized by an infinite renormalization. One obtains a finite amount of direct interation which must be determined from experiment. The identical cancellation of certain divergencies to all orders of the fine-structure constant and valid for spin 0, ½, and 1 is proven in the Appendix.

I. INTRODUCTION

THE theory of the interaction of elementary particles has been formulated in two equivalent ways by Schwinger and Tomonaga, and by Feynman. So far the equivalence has been proven explicitly only for the interaction of electrons with the electromagnetic field,[1] but there seems to be little doubt that it holds also for the interaction of the electromagnetic field with particles of other spin and for nuclear interactions as described by meson theories. Also, a consistent separation and removal of divergencies to all orders in the coupling constant has so far been shown possible only for the quantum electrodynamics of the electron. Dyson[2] showed that this could be achieved by a consistent procedure of mass and charge renormalization. The resultant finite effects as far as they have been calculated seem to agree well with experiments. This theory is therefore outstanding as the only one both as to finiteness to all orders and correctness.[3]

This success of the theory of the interaction of electrons, positrons, and photons warrants a similar investigation for other elementary particles. As a first step

[1] F. J. Dyson, Phys. Rev. 75, 486 (1949). In the following quoted as I.

[2] F. J. Dyson, Phys. Rev. 75, 1736 (1949). In the following quoted as II.

[3] For an extension of these results to the interaction of spinless mesons with nucleons see P. T. Matthews, Phil. Mag. 41, 185 (1950) and Phys. Rev. (to be published).

in this direction the interaction of positively and negatively charged spinless mesons with the electromagnetic field is considered in this paper.

We first show the equivalence of the Schwinger-Tomonaga theory[4] and the Feynman theory[5] for this case. In Section III a sufficient condition for the finiteness of the number of primitive divergencies of the scattering matrix is derived. These divergencies are enumerated and the unexpected divergence of meson-meson interaction is found. All divergencies are then separated from the finite observable parts of the S matrix and are removed by renormalization (Section IV). For this purpose a direct meson-meson interaction must be introduced whose coupling constant must be renormalized together with the mass and charge of the mesons. A finite and unambiguous S matrix is obtained. Section V deals with the explicit calculation of the infinite parts of some primitive divergent processes to lowest order. In Section VI the results are summarized and the determination of the coupling constant of direct interaction from experiment is discussed. The two appendices prove the cancellation of spurious charge and wave function renormalization and show the asymptotic behavior of the finite parts of primitive divergent processes.

II. EQUIVALENCE OF THE THEORIES OF FEYNMAN AND KANESAWA-TOMONAGA

Let $\phi(x)$ and $A_\mu(x)$ denote the meson field and the electromagnetic field. The interaction of the two fields will be given by the Tomonaga-Schwinger equation[6]

$$i\delta\Psi[\sigma]/\delta\sigma(x)=\mathfrak{H}[x]\Psi[\sigma], \tag{1}$$

where

$$\mathfrak{H}[x]=ieA_\mu(\phi^*\partial_\mu\phi-(\partial_\mu\phi^*)\phi)+e^2\phi^*\phi(A_\mu A_\mu+(n_\mu A_\mu)^2) \tag{2}$$

is the Hamiltonian in the interaction representation. This Hamiltonian is obtained from the Heisenberg representation by a unitary transformation and fulfills the integrability condition

$$\delta^2\Psi[\sigma]/\delta\sigma(x)\delta\sigma(x')=\delta^2\Psi[\sigma]/\delta\sigma(x')\delta\sigma(x)$$

or

$$[\mathfrak{H}[x],\mathfrak{H}[x']]=i\frac{\delta\mathfrak{H}[x']}{\delta\sigma(x)}-i\frac{\delta\mathfrak{H}[x]}{\delta\sigma(x')}. \tag{3}$$

As can be seen by generalizing the Hamiltonian for a flat surface to one for a space-like surface, Eq. (3) leads to the introduction of normal-dependent terms only for derivative coupling. These terms therefore occur for bosons but not for electrons.

The formal solution of (1) is

$$\Psi[\sigma]=S[\sigma,\sigma_0]\Psi[\sigma_0], \tag{4}$$

which expresses the state of the system on the space-like surface σ in terms of the given state on σ_0. The "propagation matrix"

$$S[\sigma,\sigma_0]=1+(-i)\int_{\sigma_0}^{\sigma}\mathfrak{H}[x^1]d_4x'+(-i)^2\int_{\sigma_0}^{\sigma}dx^1\int_{\sigma_0}^{\sigma(x')}\mathfrak{H}[x^1]\mathfrak{H}[x^2]d_4x^2+\cdots$$

can be symmetrized in the time coordinates of the intermediate states to give (see Dyson I)

$$S[\sigma,\sigma_0]=1+\sum_{n=1}^{\infty}((-i)^n/n!)\int_{\sigma_0}^{\sigma}P\left(\prod_{k=1}^{n}\mathfrak{H}[x^k]d_4x^k\right). \tag{5}$$

P denotes the ordering operator in time: The factors $\mathfrak{H}[x^1]$, $\cdots\mathfrak{H}[x^n]$ are to be arranged in increasing (decreasing) order of the parameter labeling the family of space-like surfaces between σ_0 and σ when read from right to left and the integration extends from σ_0 to the later (earlier) surface σ. $S[\sigma,\sigma_0]$ is symmetrical in past and future and is unitary. It follows from the Hermitian property of $\mathfrak{H}[x]$ that

$$\begin{aligned}S^{-1}[\sigma,\sigma_0]&=S^\dagger[\sigma,\sigma_0]\\&=1+\sum_{n=1}^{\infty}(i^n/n!)\int_{\sigma_0}^{\sigma}P^{-1}\left(\prod_{k=1}^{n}\mathfrak{H}[x^k]d_4x^k\right)\\&=1+\sum_{n=1}^{\infty}((-i)^n/n!)\int_{\sigma}^{\sigma_0}P\left(\prod_{k=1}^{n}\mathfrak{H}[x^k]d_4x^k\right)\\&=S[\sigma_0,\sigma].\end{aligned} \tag{6}$$

P^{-1} denotes the ordering operator which arranges the factors in opposite order to P. Equation (6) is consistent with the propagation property of $S[\sigma,\sigma_0]$,

$$S[\sigma,\sigma_0]=S[\sigma,\sigma_1]S[\sigma_1,\sigma_0], \tag{7}$$

$$S[\sigma_0,\sigma_0]=1. \tag{7'}$$

The propagation matrix satisfies the equations

$$i\delta S[\sigma,\sigma_0]/\delta\sigma(x)=\mathfrak{H}[x]S[\sigma,\sigma_0], \tag{8a}$$

$$i\delta S[\sigma,\sigma_0]/\delta\sigma(x^0)=-S[\sigma,\sigma_0]\mathfrak{H}[x^0]. \tag{8b}$$

These equations are equivalent to (5), (6), and (7). As a special case of the propagation matrix we obtain the

[4] The Schwinger-Tomonaga theory was first applied to the electromagnetic interaction of spinless mesons by S. Kanesawa and S. Tomonaga, Prog. Theor. Phys. 3, 1 (1948). For a treatment with Kemmer-Duffin matrices see M. Neuman and W. H. Furry, Phys. Rev. 76, 1677 (1949); R. G. Moorhouse, Phys. Rev. 76, 1691 (1949).

[5] R. P. Feynman, Phys. Rev. 76, 749, 769 (1949).

[6] Throughout this paper we use the units $\hbar=c=1$. $\partial_\mu=\partial/\partial x_\mu$. Otherwise we use the same notation as Schwinger with $x\equiv(x_1, x_2, x_3, x_4=ix_0)$ and $d_4x=dx_1dx_2dx_3dx_0$. In particular a square bracket surrounding an argument indicates a functional, and we use Heaviside-Lorentz units.

scattering matrix

$$S=S[\infty,-\infty]$$

$$=1+\sum_{n=1}^{\infty}((-i)^n/n!)\int_{-\infty}^{\infty}P\left(\prod_{k=1}^{n}\mathfrak{H}[x^k]d_4x^k\right) \quad (5')$$

as given in I.

The non-linearity in the electromagnetic field of the interaction Hamiltonian for spinless mesons as compared to the interaction Hamiltonian for electrons is of great importance; the Compton effect to lowest order will be partially due to a direct interaction. If an unquantized external electromagnetic field is acting on the system, its potential $A_\mu^e(x)$ will superimpose linearly on the radiation field potential $A_\mu(x)$. The resulting interaction Hamiltonian

$$\mathfrak{H}^i[x]=ie(A_\mu+A_\mu^e)(\phi^*\partial_\mu\phi-(\partial_\mu\phi^*)\phi)$$

$$+e^2\phi^*\phi[(A_\mu+A_\mu^e)(A_\mu+A_\mu^e)+[n_\mu(A_\mu+A_\mu^e)]^2] \quad (9)$$

cannot be written as the sum of the interaction Hamiltonians with the radiation field and with the external field, but it will contain a cross term $\mathfrak{H}^c[x]$

$$\mathfrak{H}^i[x]=\mathfrak{H}[x]+\mathfrak{H}^c[x]+\mathfrak{H}^e[x], \quad (9')$$

$$\mathfrak{H}^c[x]=2e^2\phi^*\phi(A_\mu A_\mu^e+n_\mu A_\mu n_\nu A_\nu^e). \quad (10)$$

$\mathfrak{H}[x]$ describes the interaction of the mesons with their own radiation field and with photons in the absence of an external field, as given by Eq. (2). $\mathfrak{H}^e[x]$ is defined as (2) with A_μ replaced by A_μ^e. It is the interaction of the mesons with the external field in the absence of a quantized electromagnetic field (no radiative corrections and no photons present). The cross term, $\mathfrak{H}^c[x]$, permits the mesons to emit or absorb a photon under the simultaneous action of an external field. The fundamental Eq. (1) now becomes

$$i\delta\Psi[\sigma]/\delta\sigma(x)=\mathfrak{H}^i[x]\Psi[\sigma] \quad (1')$$

and yields as before the scattering matrix

$$S=1+\sum_{n=1}^{\infty}((-i)^n/n!)\int_{-\infty}^{\infty}P\left(\prod_{k=1}^{n}\mathfrak{H}^i[x^k]d_4x^k\right) \quad (11)$$

of which (5′) is a special case.

If one restricts himself to the problem of a single charged particle interacting with an external electromagnetic field taking account of radiative corrections, it is possible to obtain an effective interaction Hamiltonian to lowest order in the external field by a unitary transformation which eliminates the explicit appearance of the virtual radiation field. In the electron case, the effective Hamiltonian of this special problem lends itself to a simple physical interpretation which gives a link between the physical pictures underlying the Tomonaga-Schwinger and the Feynman theory. A similar transformation can be carried out in the case of integral spin, but due to the non-linearity in the electromagnetic field as manifested in the cross term (10), this transformation will depend on the external field.[7] The effective Hamiltonian thus constructed is not any simple physically meaningful quantity even in the special case considered. On the other hand, the S matrix (11) is perfectly general and does constitute the main link between the two theories, both in its physical meaning and in its mathematical character.

In evaluating the S matrix one takes the expectation value in occupation number space of the operator (11), corresponding to the number of mesons and photons emitted and absorbed, and inserts the external field of the particular problem under consideration. $S(\sigma,\sigma_0)$ then expresses the probability amplitude for a system of mesons and photons as given on σ_0 to arrive on σ in a specified way after interaction with the given external field. This includes in general all radiative corrections.

The physical idea underlying the Feynman theory is to follow one possible world line of each participating particle from the initial to the final space-time point during which time the particles interact with each other and with the external field. One constructs the probability amplitude for this case by a specified procedure from the "propagation functions" for the individual particles, and then sums over all possible world lines between the two space-time points. The propagation functions are related to the particles in a similar way as the propagation matrix $S(\sigma,\sigma_0)$ is related to the whole system. They are the probability amplitudes for arrival at a specified space-time point for a particle that started out at an other given space-time point; their propagation property is manifested by an equation similar to Eq. (7) (cf. Feynman[5]). It follows that the resultant integral has the same physical interpretation as does the S matrix. In the remainder of this section we shall show that it is also mathematically identical with the scattering matrix (11). This will be done by deriving from (11) the Feynman procedure for the construction of the S matrix.

We assume first that no external field is acting ($A_\mu^e=0$). The S matrix is given by (5′). The general problem to be solved will be to find the radiative corrections of order n' (an even number) for a system

[7] It would seem at first that the use of the Kemmer-Duffin matrices, β_μ, may not lead to a cross term since the equations of motion in the Heisenberg representation are linear in the electromagnetic field. However, in the interaction representation the Hamiltonian contains the quadratic terms

$$(e^2/m)(\bar\psi\beta_\mu\beta_\nu\psi+\bar\psi\beta_\mu(n_\lambda\beta_\lambda)^2\beta_\nu\psi)A_\mu A_\nu$$

(see Newmann and Furry, and Moorhouse, reference 4), of which only the second, normal-dependent term can be ignored, since it cancels out in the S matrix. Therefore, the interaction with an external field leads to a cross term also here. Note, however, that the Kemmer-Duffin matrices do permit one to write the S matrix formally as if the interaction were linear in the field, such that only single-corner diagrams need to be considered. Notwithstanding this advantage we have preferred not to use the Kemmer-Duffin matrices in this paper, because their singular character partially overestimates the divergencies of the S matrix.

involving the interaction of m mesons[8] and p photons. All terms in (5′) with

$$p+n' \geqslant n \geqslant \begin{cases} (p+n')/2, & p \text{ even} \\ (p+n'+1)/2, & p \text{ odd} \end{cases}$$

will contribute. $n'+p$ is the power to which the electric charge e occurs; n is the number of Hamiltonians in the integrand and is equal to the number of four-vectors $x_\mu{}^k$ ($k=1, 2, \cdots n$) over which the integration is carried out. For each value of n the integrand will contain terms of all orders between e^n and e^{2n}. Only the term of order $e^{n'+p}$ will contribute in our problem. This term will be a sum of P brackets, each being a product of $2n-n'-p$ factors A_μ, $n'+p-n$ factors $A_\mu A_\mu+(n_\mu A_\mu)^2$, $n+p$ factors ϕ^*, and $n+p$ factors ϕ; the latter two will sometimes be preceded by a differentiation operator. From each product we now select p operators A_μ corresponding to the emission and/or absorption of p photons, m operators ϕ, each for either a positive ingoing or a negative outgoing meson, and m operators ϕ^*, each for either a negative ingoing or a positive outgoing meson. The remaining operators ϕ and ϕ^*, possibly preceded by a differentiation operator, will combine in pairs $\phi(x^i)\phi^*(x^k)$ to give vacuum expectation values; similarly, the remaining factors A_μ have to combine in pairs to give vacuum expectation values. In order to make this possible n' has to be even as mentioned previously. Since each pair of operators refers to a different particle, the P bracket will break up into P brackets of pairs, and one obtains the following vacuum expectation values of P brackets:

$$\langle P(A_\mu(x^i), A_\nu(x^k))\rangle_0=\tfrac{1}{2}\delta_{\mu\nu}D_F(x^i-x^k), \tag{12}$$

$$\langle P(\phi(x^i), \phi^*(x^k))\rangle_0=\tfrac{1}{2}\Delta_F(x^i-x^k), \tag{13}$$

$$\begin{aligned}&\langle P(\partial_\mu{}^{(i)}\phi(x^i), \phi^*(x^k))\rangle_0\\ &=\tfrac{1}{2}\partial_\mu{}^{(i)}\Delta^{(1)}(x^i-x^k)+\tfrac{1}{2}i\epsilon(x^i, x^k)\partial_\mu{}^{(i)}\Delta(x^i-x^k)\\ &=\tfrac{1}{2}\partial_\mu{}^{(i)}\Delta_F(x^i-x^k)-\tfrac{1}{2}i\Delta(x^i-x^k)\partial_\mu{}^{(i)}\epsilon(x^i, x^k),\end{aligned} \tag{14a}$$

$$\begin{aligned}&\langle P(\phi(x^i), \partial_\mu{}^{(k)}\phi^*(x^k))\rangle_0\\ &=\tfrac{1}{2}\partial_\mu{}^{(k)}\Delta_F(x^i-x^k)-\tfrac{1}{2}\Delta(x^i-x^k)\partial_\mu{}^{(k)}\epsilon(x^i, x^k),\end{aligned} \tag{14b}$$

$$\begin{aligned}&\langle P(\partial_\mu{}^{(i)}\phi(x^i)\partial_\nu{}^{(k)}\phi^*(x^k))\rangle_0\\ &=\tfrac{1}{2}\partial_\mu{}^{(i)}\partial_\nu{}^{(k)}\Delta^{(1)}(x^i-x^k)\\ &\qquad+\tfrac{1}{2}i\epsilon(x^i, x^k)\partial_\mu{}^{(i)}\partial_\nu{}^{(k)}\Delta(x^i-x^k)\\ &=\tfrac{1}{2}\partial_\mu{}^{(i)}\partial_\nu{}^{(k)}\Delta_F(x^i-x^k)\\ &\quad-\tfrac{1}{2}i(\partial_\mu{}^{(i)}\epsilon(x^i, x^k))(\partial_\nu{}^{(k)}\Delta(x^i-x^k))\\ &\qquad-\tfrac{1}{2}i\partial_\mu{}^{(i)}(\Delta(x^i-x^k)\partial_\nu{}^{(k)}\epsilon(x^i, x^k)).\end{aligned} \tag{15}$$

These equations are a direct consequence of the definition of P

$$P(A(x^i), B(x^k))=\tfrac{1}{2}\{A(x^i), B(x^k)\}+\tfrac{1}{2}\epsilon(x^i, x^k)[A(x^i), B(x^k)]$$

(the brackets { } and [ ] denote the anticommutator and the commutator, and $\epsilon(x^i, x^k)=1$ or -1 for $\sigma(x^i)$ later or earlier than $\sigma(x^k)$), of the commutation relations

$$[A_\mu(x^i), A_\nu(x^k)]=i\delta_{\mu\nu}D(x^i-x^k), \tag{16}$$

$$[\phi^*(x^i), \phi(x^k)]=i\Delta(x^i-x^k), \tag{17}$$

and of the vacuum expectation values

$$\langle\{A_\mu(x^i), A_\nu(x^k)\}\rangle_0=\delta_{\mu\nu}D^{(1)}(x^i-x^k), \tag{18}$$

$$\langle\{\phi^*(x^i), \phi(x^k)\}\rangle_0=\Delta^{(1)}(x^i-x^k). \tag{19}$$

The functions D, $D^{(1)}$, Δ, and $\Delta^{(1)}$ are defined as in Schwinger's papers,[9] the functions D_F and Δ_F as in I. The relation between them is

$$D_F=D^{(1)}+i\epsilon D, \tag{20a}$$

$$\Delta_F=\Delta^{(1)}+i\epsilon\Delta. \tag{20b}$$

One now observes that,

$$\Delta(x^i-x^k)\partial_\mu{}^{(i)}\epsilon(x^i, x^k)=-2\Delta(x^i-x^k)n_\mu\delta(n_\lambda(x_\lambda{}^i-x_\lambda{}^k))=0$$

and that,

$$\begin{aligned}&(\partial_\mu{}^{(i)}\Delta(x^i-x^k))\partial_\nu{}^{(k)}\epsilon(x^i, x^k)\\ &\quad=n_\mu\delta(x_\lambda{}^i-x_\lambda{}^k+n_\lambda n_\sigma(x_\sigma{}^i-x_\sigma{}^k))2n_\nu\delta((x_\lambda{}^i-x_\lambda{}^k)n_\lambda)\\ &\quad=2n_\mu n_\nu\delta(x^i-x^k).\end{aligned}$$

The first expression vanishes because the δ-function of the time-like vector $n_\lambda(x_\lambda{}^i-x_\lambda{}^k)$ restricts the argument of the Δ-function to space-like vectors. As can be seen from Eq. (17), the Δ-function of space-like argument vanishes, since two operators of space-like separation commute. Therefore, the second term on the right side of Eqs. (14a) and (14b) vanishes, and (15) becomes

$$\langle P(\partial_\mu{}^{(i)}\phi(x^i)\partial_\nu{}^{(k)}\phi^*(x^k))\rangle_0=\tfrac{1}{2}\partial_\mu{}^{(i)}\partial_\nu{}^{(k)}\Delta_F(x^i-x^k)-in_\mu n_\nu\delta(x^i-x^k). \tag{15′}$$

Consider first only the P brackets arising from the meson field, such that for a particular value of n we will have $2n-n'-p$ factors A_μ and $n'+p-n$ factors $A_\mu A_\mu+(n_\mu A_\mu)^2$, as mentioned above. Let one of the latter factors have the argument x^i. Clearly, this argument can be chosen in n different ways, since there are n dummy variables. There will therefore be a normal-dependent term in the integrand containing the factor

$$((-i)^n/n!)ne^2\phi^*(x^i)\phi(x^i)(n_\lambda A_\lambda(x^i))^2. \tag{21}$$

[8] Any annihilated or created meson pair is counted here as one meson.

[9] J. S. Schwinger, Phys. Rev. **74**, 1439 (1948); **75**, 651 (1949); **76**, 790 (1949).

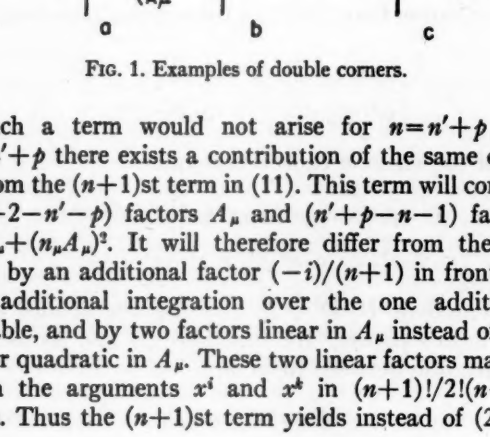

FIG. 1. Examples of double corners.

Such a term would not arise for $n=n'+p$; for $n<n'+p$ there exists a contribution of the same order n' from the $(n+1)$st term in (11). This term will contain $(2n+2-n'-p)$ factors A_μ and $(n'+p-n-1)$ factors $A_\mu A_\mu+(n_\mu A_\mu)^2$. It will therefore differ from the nth term by an additional factor $(-i)/(n+1)$ in front, by one additional integration over the one additional variable, and by two factors linear in A_μ instead of one factor quadratic in A_μ. These two linear factors may be given the arguments x^i and x^k in $(n+1)!/2!(n-1)!$ ways. Thus the $(n+1)$st term yields instead of (21)

$$[(-i)^{n+1}/(n+1)!][(n+1)!/2!(n-1)!]ieA_\mu(x^i)$$
$$\times(\phi^*(x^i)\partial_\mu{}^{(i)}\phi(x^i)-(\partial_\mu{}^{(i)}\phi^*(x^i))\phi(x^i))$$
$$\times\int ieA_\nu(x^k)(\phi^*(x^k)\partial_\nu{}^{(k)}\phi(x^k)$$
$$-(\partial_\nu{}^{(k)}\phi^*(x^k))\phi(x^k))d_4x^k. \quad (22)$$

Since (22) contains one pair $\phi^*\phi$ more than does (21), it will give rise to one P bracket more. From (13), (14), and (15′) it is seen that only the terms in (22) involving two derivatives lead to normal-dependent terms; these are with the help of (15′)

$$[(-i)^{n+1}/(n+1)!][(n+1)!/2!(n-1)!](-e^2)$$
$$\times\int A_\mu(x^i)A_\nu(x^k)(-\phi^*(x^i)\phi(x^k)$$
$$\times\langle P(\partial_\mu{}^{(i)}\phi(x^i),\ \partial_\nu{}^{(k)}\phi^*(x^k))\rangle_0$$
$$-\phi(x^i)\phi^*(x^k)\langle P(\partial_\mu{}^{(i)}\phi^*(x^i),\ \partial_\nu{}^{(k)}\phi(x^k))\rangle_0)d_4x^k$$
$$=[(-i)^n/n!]\cdot in/2\cdot e^2\int A_\mu(x^i)A_\nu(x^k)in_\mu n_\nu$$
$$\times(\phi^*(x^i)\phi(x^k)+\phi(x^i)\phi^*(x^k))\delta(x^i-x^k)d_4x^k$$
$$=-[(-i)^n/n!]ne^2\phi^*(x^i)\phi(x^i)(n_\mu A_\mu(x^i))^2. \quad (22')$$

This term, therefore, exactly cancels the term (21). It follows that for the case $A_\mu{}^e=0$ all normal-dependent terms cancel identically.[10]

The S matrix for $A_\mu{}^e\neq 0$ can be obtained from the S matrix for $A_\mu{}^e=0$ by the replacement $A_\mu\to A_\mu+A_\mu{}^e$. However, the above argument [following Eq. (15′)] is independent of such a replacement. The identical cancellation of all normal-dependent terms is therefore generally valid. In the following we shall drop these terms in the scattering matrix.

One can write the Hamiltonian

$$\mathfrak{H}^i[x]=ie\phi^*(x)(A_\mu+A_\mu{}^e)(\partial_\mu-\partial_\mu{}^*)\phi(x)$$
$$+e^2\phi^*(x)(A_\mu+A_\mu{}^e)(A_\mu+A_\mu{}^e)\phi(x).$$

∂_μ and $\partial_\mu{}^*$ are defined to act only on $\phi(x)$ and $\phi^*(x)$, respectively. All P brackets of pairs $\phi(x^i)\phi^*(x^k)$ will be given by (13) and the differentiations are properly taken into account by inserting for each linear factor $A_\mu(x)+A_\mu{}^e(x)$ a factor $\partial_\mu-\partial_\mu{}^*$ between the pair of P brackets containing x, e.g., $\Delta_F(x'-x)(\partial_\mu-\partial_\mu{}^*)\Delta_F(x-x'')$. ∂_μ and $\partial_\mu{}^*$ will therefore act, respectively, on the first and the second variable in the argument of Δ_F.

For the general case $A_\mu{}^e\neq 0$ we may look for the radiative corrections of order n' for a system of m mesons and p photons interacting with each other and with an external field to order f' in this field. The terms of (11) contributing in this case will be given by

$$n_{\max}=p+f'+n'\geqslant n\geqslant\begin{cases}(p+f'+n')/2, & p+f' \text{ even}\\ (p+f'+n'+1)/2, & p+f' \text{ odd}\end{cases} \quad (23)$$

where n and n' are defined as before. The term with the largest contributing n will involve only those parts of $\mathfrak{H}[x]$ which are linear in A_μ and/or only those parts of $\mathfrak{H}^e[x]$ which are linear in $A_\mu{}^e$. It will not involve $\mathfrak{H}^c[x]$. We now associate a definite set of integration variables with the operators referring to the real particles and external fields, and determine a definite division of the remaining operators into P brackets of pairs as described before. It is easily seen that for each such choice the integral can be brought into a one-to-one correspondence with a Feynman diagram, in complete analogy with the electron case as given in I. Each of the $n_{\max}=p+f'+n'$ variables x^k will be represented by a world point in a space-time diagram. Each operator $A_\mu(x^i)$ annihilating an incoming (creating an outgoing) real photon will be represented by a photon world line drawn from the point x^i to $-\infty$ $(+\infty)$ with an arrow in its positive time direction of propagation. Each external field $A_\mu{}^e(x^i)$ will be represented by a cross at the point x^i. Each operator $\phi(x^i)$ annhihilating a positive meson (or creating a negative meson), and each operator $\phi^*(x^i)$ creating a positive meson (or annihilating a negative meson) will be represented by a meson world line from x^i to $-\infty$ (or $+\infty$) and $+\infty$ (or $-\infty$), respectively, with arrows in the positive (or negative) time direction of propagation. The world lines of real mesons and photons will be called "external lines." Each function $D_F(x^i-x^k)$ resulting from the vacuum expectation value of the P bracket of a pair $A_\mu(x^i)A_\nu(x^k)$ according to (12) will be represented by an "internal photon line" from the point x^i to the point x^k without an arrow. Each function $\Delta_F(x^i-x^k)$ resulting from the vacuum expectation value of a P bracket of a pair

[10] A similar proof for a different case was sketched by P. T. Matthews, Phys. Rev. 76, 684 (1949).

$\phi^*(x^i)\phi(x^k)$ according to (13), (14), or (15′) will be represented by an "internal meson line" from x^i to x^k with an arrow pointing from x^i to x^k. The resulting diagram will contain meson lines which, following the arrows, will lead from $-\infty$ (or $+\infty$) through the diagram to $+\infty$ (or $-\infty$) for positive (or negative) mesons without ever meeting each other. It will also contain, in general, lines which are composed of internal meson lines only, and which form "closed loops" with all arrows pointing in the same sense. The meson lines will be interconnected by internal photon lines such that each point of the diagram has exactly one (internal or external) meson line incident and one (internal or external) meson line outgoing in the sense of the arrows. It will also be either one end of an internal or external photon line or it will contain a cross indicating the action of the external field.

A typical integral may lead to a diagram where all lines are interconnected, or to one which consists of two or more unconnected parts. Assume that such a part is not associated with external meson or photon lines, or with the external field. In this case it will correspond to a part of the integrand which can be integrated independently of the rest, yielding a constant numerical factor. When all radiative corrections were taken into account one would find that each diagram is associated with all possible unconnected diagrams of this kind. These unconnected diagrams and their corresponding integrals evidently occur when one calculates the S matrix for a vacuum remaining a vacuum when no mesons, photons, or external fields are present. Since this process has unit probability these numerical factors will add up to a phase factor which we may choose to be unity. It follows that all disconnected diagrams without external lines or crosses can be disregarded and their corresponding integrals put equal to zero.

We have seen above that for $n=n_{\max}$ each point or "corner" of a diagram has exactly three lines—two meson lines and one photon line—connecting it with the remainder of the diagram. (The photon line may be replaced by a cross indicating the action of $A_\mu{}^e$.) In the quantum electrodynamics of the electron these are the only diagrams possible. We shall call them "single-corner diagrams," because there is only a single A_μ or $A_\mu{}^e$ associated with each corner.

For $n<n_{\max}$ the integrals will not correspond to single-corner diagrams. Consider the case $n=n_{\max}-1$. The diagram corresponding to this integral will again have n corners, since n is the number of integration variables (in terms of four-vectors). It will therefore have one corner less than the diagram discussed previously. The integral will also differ from the previous one in that two factors containing a single operator $A_\mu(x^k)$ or $A_\mu{}^e(x^k)$ each will be replaced by one factor containing $A_\mu(x^k)A_\mu(x^k)$, $A_\mu{}^e(x^k)A_\mu{}^e(x^k)$ or $A_\mu(x^k)A_\mu{}^e(x^k)$. These factors arise from the terms of $\mathfrak{IC}$ and $\mathfrak{IC}^e$ quadratic in the electromagnetic field, or from $\mathfrak{IC}^e$. The point

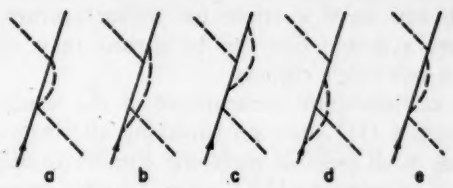

FIG. 2. Diagram a can be obtained by shrinkage of internal meson lines from any one of the diagrams b, c, d, and e. It has therefore weight 4.

x^k will therefore be associated with *two* electromagnetic field operators. We will refer to such a point as a "double corner." A double corner at x^k can arise from any of the following combinations:

$$A_\mu(x^k)A_\mu(x^k),\quad A_\mu(x^k)A_\mu{}^e(x^k),\quad A_\mu{}^e(x^k)A_\mu{}^e(x^k), \tag{24a}$$

$$A_\mu(x^k)\langle P(A_\mu(x^k)A_\nu(x^i))\rangle_0,$$
$$A_\mu{}^e(x^k)\langle P(A_\mu(x^k)A_\nu(x^i))\rangle_0, \tag{24b}$$

$$\langle P(A_\lambda(x^e)A_\mu(x^k))\rangle_0\langle P(A_\mu(x^k)A_\nu(x^i))\rangle_0,$$
$$\langle P(A_\mu(x^k)A_\mu(x^k))\rangle_0. \tag{24c}$$

The first line refers to "external double corners" with two external photon lines, one external photon line and one cross, or two crosses at the point x^k, respectively (see Fig. 1). The second line gives "mixed double corners." These are corners with one internal photon line and either one external photon line or one cross. Finally, there can be "internal double corners" where two internal photon lines meet, or where the two ends of one internal photon line meet, as sometimes happens. The diagram with $n=n_{\max}-1$ will also lack one pair $\phi\phi^*$ as compared to the one with $n=n_{\max}$. Since the same number of real mesons are involved this means that there will be one $\langle P(\phi(x^k)\alpha^*(x^e))\rangle_\lambda$ less, corresponding to one missing internal meson line. Let x^i and x^k be two adjacent corners connected by one internal meson line in a single-corner diagram from $n=n_{\max}$. There will be one of the diagrams arising from $n=n_{\max}-1$ which differs from this one only with respect to the corners x^i and x^k; i.e., it will have one double corner x^i, say, instead of the two single corners. The photon lines (or crosses) associated with x^i and x^k will now meet at this double corner. Therefore to every diagram with a double corner there corresponds a single-corner diagram from which it can be obtained by "shrinkage" of one internal meson line to zero. It is clear that the next smaller value of n will lead to diagrams with two double corners which can again be obtained from diagrams with one double corner by shrinkage of one internal meson line, or from single-corner diagrams of shrinkage of two meson lines. This process can be continued until all (or all but one) corner of the single-corner diagrams have been shrunk into double corners, corresponding to the integral with $n=n_{\max}/2$ [or $(n_{\max}+1)/2$] as seen from (23). Since there occur in $\mathfrak{IC}^i$ never more than two operators A_μ and/or $A_\mu{}^e$ with the same argument, no

diagram can have a triple (or higher) corner, and, therefore, a meson line can be shrunk only when it connects two single corners.

It is an immediate consequence of the structure of the integrals (11) that, on shrinking all single-corner diagrams in all possible ways one obtains all diagrams with one or more double corners ("double-corner diagrams") which correspond to the integrals with $n<n_{\max}$. However, it can occur that shrinkage of two different single-corner diagrams may lead to the same double-corner diagram. The number of times a particular double-corner diagram arises from shrinkage will be called its "weight." As an example the diagram *a* of Fig. 2 can be obtained by shrinkage from each of the single-corner diagrams *b*, *c*, *d*, or *e*. It has therefore weight 4.

We shall first calculate the weight directly from the integrals. One observes that

$$\begin{aligned}&\langle P(A_\lambda(x^e)A_\mu(x^k)A_\mu(x^k)A_\nu(x^i))\rangle_0\\&=\delta_{\mu\sigma}\langle P(A_\lambda(x^e)A_\mu(x^k)A_\sigma(x^k)A_\nu(x^i))\rangle_0\\&=2\langle P(A_\lambda(x^e)A_\mu(x^k)))\rangle_0\langle P(A_\mu(x^k)A_\nu(x^i))\rangle_0\\&\qquad+\langle P(A_\lambda(x^e)A_\nu(x^i)))\rangle_0\langle P(A_\mu(x^k)A_\mu(x^k)))\rangle_0.\end{aligned}$$

Each internal double corner [first term of (24c)] will therefore contribute a factor 2 to the weight of the diagram, except when it stems from a single internal photon line [second term of (24c) and Fig. 3a]. However,

$$\begin{aligned}&\langle P(A_\mu(x^k)A_\mu(x^k)A_\nu(x^i)A_\nu(x^i))\rangle_0\\&\qquad=2\langle P(A_\mu(x^k)A_\nu(x^i)))\rangle_0\langle P(A_\mu(x^k)A_\nu(x^i)\rangle_0\\&\qquad\qquad+\langle P(A_\mu(x^k)A_\mu(x^k)))\rangle_0\langle P(A_\nu(x^i)A_\nu(x^i)))\rangle_0,\end{aligned}$$

such that, when two internal double corners are connected to each other by two photon lines, their combined contribution to the weight of the diagram will be 2 rather than 4 (Fig. 3*b*). Each mixed double corner also contributes a factor 2: the second combination (24b), because of the factor 2 in $\mathfrak{H}^c$ of Eq. (10), and the first one, because each $A_\mu(x^k)$ may occur inside the P bracket.

$$\begin{aligned}&\delta_{\mu\sigma}\langle P(A_\mu(x^k)A_\sigma(x^k)A_\nu(x^i))\rangle_1\\&\quad=\delta_{\mu\sigma}A_\mu(x^k)\langle P(A_\sigma(x^k)A_\nu(x^i))\rangle_0\\&\qquad\qquad+\delta_{\mu\sigma}A_\sigma(x^k)\langle P(A_\mu(x^k)A_\nu(x^i))\rangle_0\\&\quad=2A_\mu(x^k)\langle P(A_\mu(x^k)A_\nu(x^i))\rangle_0.\end{aligned}$$

There will also be a factor 2 from $\mathfrak{H}^c$ in the external double corner arising from $A_\mu A_\mu{}^*$ in (24a). In the first term of (24a) each of the operators $A_\mu(x^k)$ may be associated with either of the two real photons emitted or absorbed. One is thus lead to two integrals which eventually are identical. It is convenient, therefore to write only one integral for each factor $A_\mu A_\mu$ and to give it weight 2, thereby permitting only one choice of association.

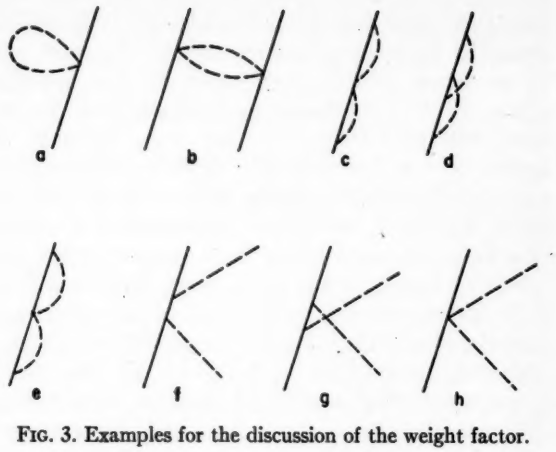

FIG. 3. Examples for the discussion of the weight factor.

We summarize these considerations in the simple weight formula

$$w=2^g,\quad g=d-d_f-a-b, \tag{25}$$

where d is the number of double corners, d_f is the number of double corners with two crosses, a is the number of closed photon lines (Fig. 3*a*), and b is the number of pairs of double corners connected by two photon lines (Fig. 3*b*).

It remains to show that w of (25) is exactly the number of different single-corner diagrams which by shrinkage give the same double-corner diagram. Clearly, when two (internal or external) photon lines end at neighboring single corners, they can come in "parallel" or "crossed," as is shown for the corners 1 and 2 of Figs. 3*c*, *d* and Figs. 3*f*, *g*. The two corresponding single-corner diagrams will both shrink to the same double-corner diagram (Figs. 3*e*, *h*). Furthermore, an external photon line (or cross) can be incident on either side of an internal single corner. The two diagrams will again shrink to the same mixed double corner. On the other hand, there is obviously only one way to obtain a double corner with 2 crosses or with a closed photon line. Finally, it is seen that the double-connected double corners of Fig. 3*b* can be obtained in only 2 ways rather than 4 ways, i.e., from either of the two diagrams Figs. 12*a* and *b*.

The above analysis shows that all single-corner diagrams from the integral $n=n_{\max}$ together with all different double-corner diagrams obtained from them by shrinkage and weighted according to Eq. (25) give exactly all diagrams resulting from the S matrix (11) for n satisfying (23).

We can now formulate a recipe for the calculation of the S matrix (11). Gives m mesons and p photons in interaction with each other and with an external field, we can find the radiative corrections of order n' which are of order f' in the external field, by the following procedure:

(1) Draw all possible connected single-corner dia-

grams with $n=n_{\max}=n'+p+f'$ corners, m external meson lines, p external photon lines, and f' external field interactions.

(2) Find all possible double-corner diagrams by shrinkage of the single-corner diagrams.

(3) Write down an integral for each diagram as follows:

(a) Label the corners with x^1, x^2, $\cdots x^n$ and associate with each single corner one, with each double corner two polarizations μ, ν, $\cdots$.

(b) At each corner x^k with polarization μ insert $A_\mu{}^e(x^k)$ for a cross, $A_\mu(x^k)$ for an external line, and $\phi(x^k)$ or $\phi^*(x^k)$ for an external meson line according to its arrow direction in or out of the diagram.

(c) For each two corners x^i and x^k insert for each connecting photon line a factor $\frac{1}{2}\delta_{\mu\nu}D_F(x^i-x^k)$, and for each connecting mesons line a factor $\frac{1}{2}\Delta_F(x^i-x^k)$, if the arrow points from x^k to x^i.

(d) For each single corner x^k with polarization μ insert $ie(\partial_\mu{}^{(k)}-\partial_\mu{}^{*(k)})$ where $\partial_\mu{}^{*(k)}$ differentiates one term of the form $\Delta_F(x^i-x^k)$ or $\phi^*(x^k)$ and $\partial_\mu{}^{(k)}$ differentiates one term of the form $\Delta_F(x^k-x^i)$ or $\phi(x^k)$.

(e) For each double corner x^k with polarizations μ and ν insert $e^2\delta_{\mu\nu}$.

(f) Integrate over all x^k ($k=1, 2, \cdots n$) and multiply by $(-i)^n w$, where w is given for each diagram by (25). (Note that the factor $1/n!$ occurring for each such diagram is canceled, since there are $n!$ ways of labeling the same diagram with x^1, $\cdots x^n$ which all give the same integral.)

(4) Sum these integrals and find that part of the S matrix (11) which satisfies (23) for the problem under consideration.

For actual calculations it will be convenient to work in momentum space. The Fourier transforms are[11]

$$A_\mu(x)=(2\pi)^{-2}\int A_\mu(k)\delta(k^2)\exp(ik_\lambda x_\lambda)d_4k, \tag{26a}$$

$$A_\mu{}^e(x)=(2\pi)^{-2}\int A_\mu{}^e(k)\exp(ik_\lambda x_\lambda)d_4k, \tag{26b}$$

$$\phi(x)=(2\pi)^{-2}\int \phi(p)\delta(p^2+m^2)\exp(ip_\lambda x_\lambda)d_4p, \tag{27a}$$

$$\phi^*(x)=(2\pi)^{-2}\int \phi^*(p)\delta(p^2+m^2)\exp(-ip_\lambda x_\lambda)d_4p, \tag{27b}$$

$$D_F(x)=(2\pi)^{-2}\int \frac{1}{\pi}\delta_+(k^2)\exp(ik_\lambda x_\lambda)d_4k$$

$$=-2i(2\pi)^{-4}\int\left(\frac{1}{k^2}+i\pi\delta(k^2)\right)\exp(ik_\lambda x_\lambda)d_4k, \tag{28a}$$

$$\Delta_F(x)=(2\pi)^{-2}\int \frac{1}{\pi}\delta_+(p^2+m^2)\exp(ip_\lambda x_\lambda)d_4p$$

$$=-2i(2\pi)^{-4}\int\left(\frac{1}{(p^2+m^2)}+i\pi\delta(p^2+m^2)\right)\times\exp(ip_\lambda x_\lambda)d_4p. \tag{28b}$$

The functions $\delta_\pm(x)$ are defined by

$$\delta_\pm(x)=\left(\frac{1}{2\pi}\right)\int_0^\infty \exp(\pm i\alpha x)d\alpha=\tfrac{1}{2}\delta(x)\pm\frac{1}{(2\pi i x)}. \tag{29}$$

When the transformation to momentum space is carried out in this way, and when all the integrations over x^1, $\cdots x^n$ are performed, the resultant S matrix will be very similar in form to the S matrix in coordinate space. In fact, it can be obtained from the latter by simple replacements, such that we can restate the construction recipe (3) for momentum space:

(3′) Write down an integral in momentum space for each diagram as follows:

(a′) Label all meson lines with four-momenta p, p', p'', $\cdots$, all photon lines with momenta k, k', k'', $\cdots$, and all crosses with q, q', q''. Associate with each single corner one, with each double corner two polarizations μ, ν, $\cdots$.

(b′) Insert $A_\mu{}^e(q)$ for a cross, $A_\mu(k)$ for an external photon line, and $\phi(p)\delta(p^2+m^2)$ or $\phi^*(p)\delta(p^2+m^2)$ for an external meson line pointing into or our of the diagram, respectively.

(c′) Insert for each internal photon line a factor $\delta_{\mu\nu}$ times the photon propagation function[11] $1/k^2$; insert for each internal meson line the meson propagation function $1/(p^2+m^2)$.

(d′) Insert for each single corner with polarization μ a factor[12] $(p_\mu+p_\mu')\delta(p-p'\pm k)$, where p_μ and p_μ' are the momenta associated with the meson lines leading into and out of the corner, and k is the momentum associated with the internal or external photon line ending there. If there is a cross instead of an external photon line k is to be replaced by q.

(e′) For each double corner insert a factor $-\delta_{\mu\nu}\delta(p-p'\pm k\pm k')$. One or both of the photon momenta k, k' may be replaced by external field momenta q, q'.

(f′) Integrate over all momenta and multiply each integral by its respective weight w as given in Eq. (25). Multiply each integral by the same factor

$$(-i)^{(n_{\max}-E)/2}(e/4\pi^2)^{n_{\max}}. \tag{30}$$

This factor depends only on the number of participating particles and on the order of approximation. E is the total number of external lines and crosses,

$$E=2m+p+f'. \tag{31}$$

[11] When the integrations in the S matrix are carried out in the manner explained in II, the δ-functions in Eqs. (28a) and (28b) can be dropped.

[12] It is clear that, if at one end of an internal photon line the δ-function is (arbitrarily) written with $+k$, the δ-function at the other end of the same internal photon line must be written with $-k$.

These rules follow from the rules (3) given above in the following way. Let F_m and F_p be the number of internal photon lines and meson lines for a given diagram. The structure of the diagrams tells us that

$$2F_p=n', \quad F_m=n-m \tag{32}$$

and that the total number of internal lines

$$F=F_m+F_p=n+\tfrac{1}{2}(n_{\max}-E)=\tfrac{1}{2}(3n_{\max}-E)-d \tag{33}$$

where $d=n_{\max}-n$ is the total number of double corners. The integral in coordinate space for a particular diagram will be multiplied by its weight w and by $(-i)^n$ as explained in rule (3f). The Fourier transforms (26) to (29) yield an additional factor $(2\pi)^{-2E}$ and rule (3'b') for the external lines and crosses, a factor $(-i)^F(2\pi)^{-4F}$ and rule (3'c') for the internal lines, a factor $(-e)^s(2\pi)^{4s}$ and rule (3'd') for the single corners (s is the number of single corners), and a factor $(-e^2)^d(2\pi)^{4d}$ and rule (3'e') for the double corners. The factors $(2\pi)^{4s}$ and $(2\pi)^{4d}$ came from the x-integrations which each yield $(2\pi)^4$ and a δ-function. Thus the total factor is

$$(-i)^{-m+n'/2}(e/4\pi^2)^{n_{\max}}$$
$$=i^{m-n'/2}(\alpha/\pi)^{n'/2}(e/4\pi^2)^{p+l'}(1/2\pi)^{n'}, \tag{30'}$$

which is the same as (30). In (30') we inserted the fine-structure constant $\alpha=e^2/4\pi\cong 1/137$. It should be noted that the factor (30') is also valid for the electron case where double-corner diagrams do not exist, and where $n=n_{\max}$ always. Equation (30') shows that the natural expansion parameter in perturbation theory is[13] α/π.

The rules (1), (2), (3'), and (4) are those of the Feynman theory[14] for the construction of the scattering matrix. We have thus shown that Feynman's S matrix is identical with the S matrix (11) of the Schwinger-Tomonaga theory.

III. ENUMERATION OF POSSIBLE PRIMITIVE DIVERGENCIES

A primitive divergent diagram is defined (as in I) as a diagram whose integral diverges such that when any of the internal lines is cut and thus replaced by two external lines, the resulting integral is convergent.

It is easy to enumerate the possibly primitive divergent processes for the interaction of any type of "source particles" (charged particles of spin 0, $\frac{1}{2}$, 1, nucleons) with any type of corresponding "interaction particles" (photons, mesons) and external fields. For all these cases it is sufficient to restrict oneself to single-corner diagrams, as will be proven in the next section for charged spinless mesons interacting with photons and an external field. Each single corner of these diagrams will either have one external field acting or none. In the first case there will be a cross at that corner and but two "source lines" or two "interaction lines" leading to it. In the second case there will always be exactly two source lines and one interaction line. A typical diagram will have n corners, E_i external lines corresponding to E_i ingoing and/or outgoing interaction particles, and E_s external source lines corresponding to $E_s/2$ participating source particles. There may also be external fields interacting f_s times with the source particles and f_i times with the interaction particles. The resulting diagrams will therefore have

$$F_i=\tfrac{1}{2}(n-E_i-f_s+f_i) \tag{34a}$$

internal interaction lines and

$$F_s=n-f_i-E_s/2 \tag{34b}$$

internal source lines, yielding

$$F=\tfrac{1}{2}(3n-f_i-f_s-E_i-E_s)=\tfrac{1}{2}(3n-E) \tag{34c}$$

internal lines. $E=E_s+E_i+f_s+f_i$ is the total number of external lines and crosses.

Quite generally, an internal line will correspond to a propagation function which is a polynomial divided by a quadratic in the momentum associated with it. The propagation functions

$$1/k^2, \quad 1/(p^2+m^2), \quad (ip_\mu\gamma_\mu-m)/(p^2+m^2) \tag{35}$$

are examples for a photon, a spinless meson, and a Dirac particle (electron or nucleon), respectively. We shall denote the degree of the polynomial in the numerator of the propagation function of source and interaction particles by D_s and D_i. Each corner will contain a δ-function of the three associated momenta and a polynomial of degree D_c.

$$(p_\mu+p_\mu')\delta(p-p'+k), \quad \gamma_\mu\delta(p-p'+k)$$

are examples for the interaction of spinless mesons with photons, and of nucleons (or electrons) with mesons of spin 1 (or photons).

Consider a single-corner diagram which is at most primitive divergent when integrated over the F internal momentum four-vectors. The n δ-functions of the corners permit to eliminate $n-1$ of them, since the last δ-function will contain the external momenta only, expressing energy-momentum conservation. The integral will be convergent if the degree of the denominator exceeds the degree of the numerator (including the differentials d_4p, d_4p', $d_4k\cdots$) by at least one. Since the degree of the denominator is $2F$, as seen from (35), the convergence condition is

$$D_{\text{den}}-D_{\text{num}}-4(F-n+1)\geq 1$$

or

$$4n-2F-D_{\text{num}}=n+E-D_{\text{num}}\geq 5 \tag{36}$$

by (34c).

With the above definitions

$$D_{\text{num}}=D_sF_s+D_iF_i+D_cn$$
$$=D_s(n-f_i-E_s/2)+\tfrac{1}{2}D_i(n-E_i-f_s+f_i)+D_cn.$$

[13] As will be shown in the next section, the number of non-trivial integrations is $F+1-n_{\max}=1-m+n'/2$. Each of these contribute a factor $i\pi^2$, such that there remains only one factor i and the factor $\pi^{-n'}$ is replaced by π^{1-m}.

[14] They are given for spinless mesons in Feynman's second paper, reference 5. Note, however, that Feynman uses Gaussian units and a different definition of the metric tensor.

Equation (36) becomes

$$n(1-D_s-D_c-Di/2)+E+D_s(f_i+E_s/2)+\tfrac{1}{2}D_i(E-E_s-2f_i)\geqslant 5. \quad (37)$$

This inequality is a sufficient convergence condition for a diagram which is not worse than primitively divergent.[15] The condition is not necessary, because the highest powers of the internal momenta may cancel identically in the integrand.[16] Further cancellation may occur between different diagrams for the same process, such that a process may be completely finite, although (37) is not fulfilled for each individual diagram. Such cancellation indeed occurs in the scattering of light by light and associate phenomena (see items 4a and 4b below) via particles of spin 0, $\frac{1}{2}$, and 1, but it requires the inclusion of possible double-corner diagrams.

If a process involving $E_s/2$ source particles and E_i interaction particles is to yield convergent results in arbitrary high order, (37) requires that the coefficient of n be positive. Therefore,

$$D_s+D_c+D_i/2\leqslant 1 \quad (38)$$

must be satisfied for the elimination of primitive divergencies.

All meson theories of nuclear forces have $D_s=1$ [see (35)] and therefore (38) would require $D_c=D_i=0$. This implies mesons of spin 0 and no derivative coupling;[17] i.e., scalar (or pseudoscalar) theory with scalar (or pseudoscalar) coupling. For those two cases the convergence condition (37) yields

$$E+\tfrac{1}{2}E_s+f_i=\tfrac{3}{2}E_s+E_i+2f_i+f_s\geqslant 5. \quad (39)$$

This condition is the same for the electrodynamics of the electron (see I) and the same *possible* primitive divergencies arise. However, the scattering of mesons by mesons (via nucleons) does not converge as does the corresponding scattering of light by light in electrodynamics. As mentioned previously, the latter is formally due to fortuitous cancellation, but has a deeper reason in the condition of gauge invariance. The divergence of meson-meson scattering cannot be removed by mass or charge renormalization. An infinite direct interaction must be introduced into the Hamiltonian which cancels the divergence.[18] This procedure together with mass and charge renormalization removes all the infinities from the S matrix.

In quantum electrodynamics we have $D_i=0$, and (38) permits either $D_s=1$ and $D_c=0$ or $D_s=0$ and $D_c=1$. The former values arise for the electron (see I), the latter for the spinless meson. Since f_i cannot occur here, the convergence condition (37) is

$$E_s+E_i+f_s=E\geqslant 5. \quad (40)$$

This condition, however, need only be applied to diagrams with $n\geqslant E$ for the following reason. Clearly, the integral will converge if the $n-1$ available δ-functions eliminate all internal momenta, i.e., if $F=n-1$. From (34c) we see that this means $n=E-2$, and that $n-E$ is always an even number. Therefore only diagrams with $n\geqslant E$ can diverge.

The possible primitive divergencies are therefore the following:[19]

(1) The meson self-energy[20] ($E_s=2$, $E_i=f_s=0$, quadratic divergence).

(2a) The photon self-energy ($E_i=2$, $E_s=f_s=0$, quadratic divergence).

(2b) The polarization of the vacuum ($f_s=2$, $E_s=E_i=0$, quadratic divergence).

(3) The "Lamb shift" and radiative corrections to the scattering of a meson in an external field to first order in this field ($E_s=2$, $F_s=1$, $E_i=0$, linear divergence).

(4a) The scattering of light by light ($E_i=4$, $E_s=f_s=0$, logarithmic divergence).

(4b) The scattering of light by an external field to second order in this field ($E_i=2$, $F_s=2$, $E_s=0$, logarithmic divergence).

(5a) The radiative corrections of the "Compton effect" ($E_s=2$, $E_i=2$, $f_s=0$, logarithmic divergence).

(5b) The radiative corrections to "bremsstrahlung," i.e., emission or absorption of a photon by a meson in an external field to first order in that field ($E_s=2$, $E_i=1$, $f_s=1$, logarithmic divergence).

(5c) The "Lamb shift" and radiative corrections to meson scattering to second order in the external field ($E_s=2$, $F_s=2$, $E_i=0$, logarithmic divergence).

(6) The radiative corrections to meson-meson scattering[20] ($E_s=4$, $E_i=f_s=0$, logarithmic divergence).

There is actually one more possible divergent process, i.e., the scattering of light by an external field to first order in that field ($E_i=2$, $f_s=1$, $E_s=0$, linear divergence). However, this process involves a closed loop with an odd number of corners and therefore vanishes identically by Furry's theorem. This theorem is obviously valid here as in the electron case, because ϕ and the charge conjugate solution ϕ^* fulfill the same equation except for a change in the sign of the charge e. Since two internal meson lines with opposite arrows correspond to vacuum expectation values of operators which are charge conjugate to each other, two closed loops with n corners each and opposite arrow directions will differ only in the respective factors e^n and $(-e)^n$. If n is odd two diagrams which differ only in the arrow

[15] The use of Kemmer-Duffin matrices for spin 0 and 1 leads to a sufficient condition which is more restrictive (see reference 7).

[16] Such cancellation seems very fortuitous and indeed occurs only if the combination of propagation function and coupling exhibit a certain "redundancy" as in the case of vector mesons interacting with photons.

[17] The propagation functions and couplings for various meson theories are given in Feynman's second paper, reference 5.

[18] Very recently this program was carried through to all order in the coupling constant by P. T. Matthews (see reference 3).

[19] This result and the conclusions of Section V of this paper were first presented by the author at the New York meeting of the American Physical Society January 1950. See Phys. Rev. 78, 346 (1950).

[20] Note that according to our definition of n', the lowest order to which the process occurs is the second-order radiative correction, $n'=2$.

direction of their closed loop of n corners will cancel identically. This result is unchanged by shrinkage of any of the meson lines in the closed loop.

In the next section we shall show how the infinities can be separated and removed from the S matrix by renormalizations, such that the resultant, renormalized S matrix leads to finite values for all the processes (1) to (6).

IV. REMOVAL OF THE DIVERGENCIES BY RENORMALIZATION

A. General Considerations

The divergence properties of single-corner diagrams derived in the last section can easily be generalized to double-corner diagrams. According to rule (3′) of Section II the shrinkage of two neighboring single corners involves the replacement of a factor

$$\delta(p-p''+k)(p_\mu+p_\mu'')(p''^2+m^2)^{-1}(p_\nu''+p_\nu') \times\delta(p''-p'+k')$$

by

$$-\delta_{\mu\nu}\delta(p-p'+k+k')$$

and also requires a corresponding change in the weight factor. We have, therefore, one δ-function less, but also one less integration over internal momenta, such that the number of independent variables remains unchanged. Since the difference $D_{\text{den}}-D_{\text{num}}=0$ in both factors, the resultant double-corner diagram will diverge (or converge) exactly as the original diagram. It follows that every primitive divergent single-corner diagram yields by shrinkage a double-corner diagram of the same order of divergence. The list of primitive divergents (1) to (6) is therefore also valid for the corresponding double-corner diagrams.

An unambiguous separation of a primitive divergent integral into an infinite and a finite part can be accomplished as for the electron (see **II**) by a Maclaurin expansion of the integrand in terms of the external momenta p_μ

$$R(p,l)=R(0,l)+p_\mu(\partial/\partial p_\mu)R(0,l) +\tfrac{1}{2}p_\mu p_\nu(\partial^2/\partial p_\mu\partial p_\nu)R(0,l)+\cdots. \quad (41)$$

$R(p,l)$ is the integrand after the integrations over the δ-function are carried out and the operators ϕ^*, ϕ, A_μ, and A_μ^* are omitted. p_μ and l_μ are typical external and internal momenta, respectively. Since each differentiation increases $D_{\text{den}}-D_{\text{num}}$ by unity, a logarithmically, linearly, or quadratically divergent integral will have an expansion of R in which only the first one, two, or three terms give divergencies. The form of the divergent terms follows from relativistic invariance.

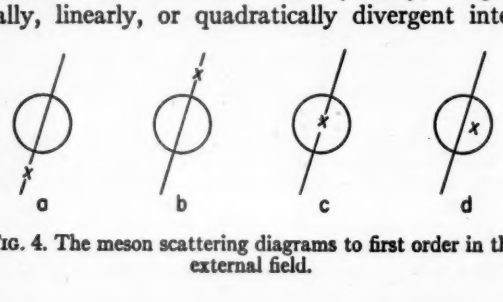

FIG. 4. The meson scattering diagrams to first order in the external field.

For example, the first term of (41) for the scattering of light by light, and of light by an external field yields a logarithmically divergent integral whose integrand is

$$A_\mu(p^1)A_\nu(p^2)A_\lambda(p^3)A_\sigma(p^4)T_{\mu\nu\lambda\sigma}\delta(p^1+p^2+p^3+p^4)$$

and

$$A_\mu(p^1)A_\nu(p^2)A_\lambda(p^3)A_\sigma(p^4)U_{\mu\nu\lambda\sigma}\delta(p^1+p^2+p^3+p^4), \quad (42)$$

respectively, after the integrations over the internal momenta $l^{(i)}$ are carried out. The tensors $T_{\mu\nu\lambda\sigma}$ and $U_{\mu\nu\lambda\sigma}$ are independent of the p^k, such that the terms (42) are gauge-variant. Since the theory is gauge-invariant the sum of the terms (42) over all diagrams of any given order n' must vanish;[21] i.e., $\Sigma T_{\mu\nu\lambda\sigma}=0$ and $\Sigma U_{\mu\nu\lambda\sigma}=0$. This will be verified to lowest order ($n'=0$) in the next section. We are therefore permitted to regard the processes of type (4) in the list of primitive divergencies as completely finite.

These arguments may not seem to be satisfactory, since $T_{\mu\nu\lambda\sigma}$ and $U_{\mu\nu\lambda\sigma}$ are divergent integrals. In view of these and similar arguments further on, we assume, therefore, that all integrations are carried out with regulators. This implies the introduction in the Lagrangian of auxiliary fields with suitably chosen masses and coupling constants.[22] The conditions on the auxiliary masses and coupling constants are such that all integrals which diverge worse than logarithmic are put equal to zero. Logarithmically divergent integrals become finite, but regulator-dependent. The masses are assumed to become infinite after the integration is completed, such that originally convergent integrals remain unaltered and independent of the regulators.[23] The use of regulators makes the arguments concerning divergencies, like the one following (42), mathematically meaningful.[24]

[21] A formal proof can be given in complete analogy with the one for the electron case given by J. C. Ward, Phys. Rev. **77**, 293 (1950), since the relation (A4) (see Appendix I) which is needed in this proof is obviously valid.

[22] The introduction of the auxiliary fields in the Lagrangian rather than in the S matrix is required, because they change the equations of motion and the momentum energy tensor, as is seen in the calculation of the self-stress. For the problems considered in this paper, however, it is irrelevant where the regulators are introduced. See F. Rohrlich, Phys. Rev. **77**, 357 (1950).

[23] The notion of logarithmic divergence and cut-off dependence are in this sense equivalent. Also, in the following, "finite" and "convergent" will mean "finite and cut-off independent" unless otherwise stated.

[24] Note that the use of regulators does not imply a loss of generality, since all one can study meaningfully is how the S matrix would behave if the theory were finite (which here also requires the assumption of the—unproven—existence of the expansion in the fine-structure constant). The finiteness of the theory achieved in this way guarantees gauge-invariance. The charge-renormalization procedure is not a requirement of gauge-invariance. Mass, charge, and direct interaction renormalization are required only in order to avoid imposing conditions on the regulators in addition to those which guarantee finiteness (e.g., $\Sigma c_i \ln m_i=0$ instead of the weaker condition $\Sigma c_i \ln m_i=$finite). Whether or not such conditions are introduced is irrelevant for

We now return to Eq. (41) for the purpose of general arguments. Again, on the basis of relativistic invariance the first, linearly divergent term of a primitive divergent meson scattering diagram (item 3 on the list of divergencies) is seen to vanish identically, such that these diagrams actually diverge only logarithmically. The second term of (41) gives therefore the only infinite term which is of the form

$$\phi^*(p^1)\phi(p^2)(p_\mu{}^1+p_\mu{}^2)A_\mu{}^e(p^1-p^2) \qquad (43)$$

after the integration over the internal momenta l has been performed. A similar term containing $(p_\mu{}^1-p_\mu{}^2)\times A_\nu{}^e(p^1-p^2)$ must vanish identically, since it is not gauge-invariant.

Similarly, the only divergent term of a primitive divergent diagram of type (5) (Compton effect and related phenomena) will be of the form

$$\phi^*(p^1)\phi(p^2)A_\mu(k)A_\mu(p^1-p^2+k). \qquad (44)$$

Consider now the radiative corrections of order n' to the scattering of a meson by an external field. The diagrams for this process can be divided into four groups as is indicated schematically in Fig. 4. The circle means any complex diagram of $n=n'-d$ corners. The cross indicates that the external field acts before (case *a*), after (case *b*), or during (cases *c* and *d*) the emission and absorption of the virtual photons. In case *c* the external field acts on the meson line which passes through the diagram, in case *d* it acts on a closed loop. Assume that in some way we eliminated all divergencies from the meson self-energy diagrams resulting from Fig. 4 when the external field is omitted. For Fig. 4*d* this diagram is identically zero, because of the odd-cornered loop. Figure 4*d* is therefore to be understood as containing all meson self-energy diagrams to which a closed loop is connected by one or more photon lines in such a way that the order of the total diagram is the same as that of the other diagrams of Fig. 4. The action of the external field will modify our integrals in such a way that they will all diverge; for example Fig. 4*a* will yield the expression

$$\phi^*(p^1)1/((p^1)^2+m^2)(p_\mu{}^1+p_\mu{}^2)A_\mu{}^e(p^1-p^2)\phi(p^2) \qquad (45)$$

which is singular, since p^1 satisfies $(p^1)^2+m^2=0$.

Equation (41) permits us to separate the infinite parts of (45) unambiguously, as will be described later. These infinite parts will be called "wave function renormalization" (cases *a* and *b*), "spurious charge renormalization" (case *c*), and "true charge renormalization" (case *d*) (see Fig. 4). For reasons which will become clear in the following we shall refer to all infinities arising from closed loops as "true charge renormalization." As is shown in Appendix I, the wave function renormalization and the spurious charge renormalization cancel identically to every order n'. In the next section this will be verified to lowest order ($n'=2$) by direct calculation.—The only remaining charge renormalizations of the processes of type (3) are therefore the "true" charge renormalizations, i.e., those which arise from the action of external fields on closed loops (Fig. 4*d*).

Consider next the radiative corrections of order n' of the Compton effect and related phenomena [type (5)]. These diagrams can again be separated into several groups as shown in Fig. 5 for the scattering of an electron by an external field to second order in this field. Figures 5*a* and *b* are all the meson scattering diagrams of Fig. 4 preceded and followed by a scattering. Figures 5*c* and *d* are all the meson self-energy diagrams of order n' preceded and followed by a double scattering in a double corner. Figures 5*e*, *f*, and *g* are the diagrams in which, respectively, both, one, or none of the two external field actions occur on the through-going meson line. (Figure 5*f* has to be understood in an analogous way to Fig. 4*d*.) When they are not acting on the latter they act necessarily on closed loops.

Let us assume that all infinities have been removed from the radiative corrections of order n' to the meson self-energy and to the scattering of an electron by an external field to *first* order in that field as was described before. Those diagrams of Figs. 5*a* and *b* which are derived from Figs. 4*a*, *b*, and *c* by an additional scattering will not give divergencies, since they will result in expressions of the form

$$\phi^*(p^1)(2p_\mu{}^1-q_\mu)A_\mu{}^e(q)1/[(p^1-q)^2+m^2](p_\nu{}^1+p_\nu{}^2-q_\nu)A_\nu{}^e(p^1-p^2-q), \qquad (46)$$

which are not singular as (45), due to the equations of motion. The other diagrams in the group Figs. 5*a* and *b* —derived from Fig. 4*d*—will give wave function renormalizations which exactly cancel the spurious charge renormalizations of Fig. 5*f*, for these divergencies will be of the same form as those of Fig. 4. On the other hand, the double corners added to the meson self-

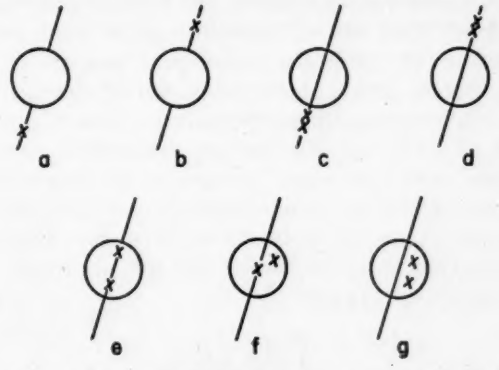

FIG. 5. The meson scattering diagrams to second order in the external field. If the crosses are replaced by photon lines these diagrams represent the Compton effect.

the physical results of quantum electrodynamics, but not always for meson theory. Since the introduction of such conditions is quite arbitrary, physical results will remain unaffected only if the divergence is a mass or charge normalization. They can therefore safely be introduced in the case of spin ½, but for the spin 0 case discussed here it would determine arbitrarily the amount of direct meson-meson interaction which is experimentally observable (see Section VI). An experimental check on this procedure is therefore possible.

energies in Figs. 5*c* and *d* again give rise to terms similar to (45), i.e.,

$$\phi^*(p^1)1/[(p^1)^2+m^2]A_\mu{}^e(q)A_\mu{}^e(p^1-p^2-q)\phi(p^2). \quad (45)$$

As before, this wave function renormalization will exactly cancel the spurious charge renormalization of Fig. 5*e*. Again, the only remaining charge renormalization will arise from the action of $A_\mu{}^e$ on closed loops (Fig. 5*g*). This will be verified by direct calculation to lowest order ($n'=2$) in the next section, but is true to all orders as proven in Appendix I. Corresponding arguments hold for the other processes of type 5 in which one or both $A_\mu{}^e$ are replaced by A_μ.

We see, therefore, that all "true" charge renormalizations arise from closed loops only. But we have seen before that all closed loops with an odd number of single corners (or closed loops resulting from these by shrinkage) contribute an identically vanishing factor to the integrals. For all other closed loops (which may be *part* of a diagram) the only terms which could give rise to charge renormalization [see Eq. (41)] vanish identically as was seen for the case of four corners. The only exceptions are: (1) the closed loops with two "external lines," i.e., with only two lines connecting to the other part of the diagram, and (2) the closed loops with one cross and one line connecting to the other part of the diagram. These two diagram parts may be thought of as the virtual occurrence of the processes of type 2 of our list of primitive divergences, i.e., photon self-energy parts and vacuum-polarization parts. It follows that *no primitive divergent diagram other than of type (2) can contain true charge renormalizations.*

We summarize these considerations: When the spurious infinities (spurious charge renormalization and wave function renormalization) are separated properly they will cancel identically, such that the only infinities which still have to be removed from the S matrix are those arising from diagrams (or diagram parts) of type (1), (2), and (6). These are the infinities associated with mass, charge, and direct interaction.

B. Separation of Divergencies

Most diagrams do not satisfy the condition that their integrals converge if any one of the internal momenta is held fixed. They will have more divergent terms in the expansion (41) than the primitive divergents of the same process. Such diagrams are called "reducible." They will contain primitive divergent parts of the types (1) to (6). We further distinguish between "proper" and "improper" diagrams, the latter being diagrams which can be separated into two unconnected diagrams by cutting only one internal line. Primitive divergent diagrams are proper, but not *vice versa.*

Consider the integral

$$\int R(p,l)d_4l \quad (47)$$

over all internal momenta, where $R(p,l)$ is defined as in (41) but does not necessarily refer to a primitive divergent diagram. The integral (47) for the radiative corrections of order n' of the processes of type (1) to (6) [except (4)] will be denoted, respectively, by

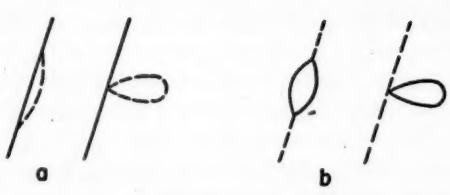

FIG. 6. The only primitive divergent self-energy diagrams. *a*: Meson self-energy. *b*: Photon self-energy.

$$\Sigma^{(n')}(p), \quad \Pi^{(n')}(k), \quad \Lambda_\mu{}^{(n')}(p^1,p^2),$$
$$\Omega_{\mu\nu}{}^{(n')}(p^1,p^2,k), \quad \Xi^{(n')}(p^1,p^2,p^3). \quad (48)$$

They may occur as virtual or as real processes. Where they refer to proper diagrams a star is added; the sum over all n' is indicated by omission of the superscript (n'), i.e., $\Sigma^*(p)$ is the sum over all proper self-energy diagrams. A left superscript p indicates that the proper diagram is primitive divergent.

Let $S(p)=(p^2+m^2)^{-1}$ and $D(k)=(k^2)^{-1}$ be the propagation functions of the mesons and photons. If we insert all possible radiative corrections into a meson line and sum them, we replace $S(p)$ in the integral by

$$S'(p)=S(p)+S(p)\Sigma(p)S(p)$$
$$=S(p)+S(p)\Sigma^*(p)S'(p). \quad (49a)$$

Similarly

$$D'(k)=D(k)+D(k)\Pi^*(k)D'(k). \quad (49b)$$

In order to write similar equations for $\Omega_{\mu\nu}$ and Ξ one must limit the definition of "proper diagrams" as follows. A proper "Compton effect" diagram [generally: diagram of type (5)] is one that is not only proper in the above-mentioned sense but also cannot be split into two Compton effect diagrams by cutting one meson line and one photon line. Similarly, a proper meson-meson interaction diagram is not only proper in the above sense but also cannot be split into two meson-meson interaction diagrams by cutting two meson lines. With these definitions of "proper" one finds

$$\Omega_{\mu\nu}(p^1,p^2,k)=\Omega_{\mu\nu}{}^*(p^1,p^2,k)+\int\Omega_{\mu\lambda}{}^*(p^1,t,k)S(t)$$
$$\times D(p^1+t+k)\Omega_{\lambda\nu}(t,p^2,p^1+t+k)d_4t \quad (49c)$$

and

$$\Xi(p^1,p^2,p^3)=\Xi^*(p^1,p^2,p^3)+\int\Xi^*(p^1,p^2,t)S(t)$$
$$\times S(p^1+p^2+t)\Xi(t,p^1+p^2+t,p^3)d_4t. \quad (49d)$$

When (48) refers to primitive divergents the separation (41) yields unambiguously:

$${}^p\Sigma^{(n')}(p)=e^{n'}[A^{(n')}+B^{(n')}S^{-1}(p)$$
$$+S^{-1}(p)S_e{}^{(n')}(p)], \quad (50a)$$

$$^{p}\Pi^{(n')}(k)=e^{n'}[C^{(n')}D^{-1}(k)+D^{-1}(k)D_c^{(n')}(k)], \quad (50b)$$

$$^{p}\Lambda_\mu^{(n')}(p^1,p^2)=e^{n'}[L^{(n')}(p_\mu{}^1+p_\mu{}^2)+L_{\mu c}^{(n')}(p^1,p^2)], \quad (50c)$$

$$^{p}\Omega_{\mu\nu}^{(n')}(p^1,p^2,k)=e^{n'}[O^{(n')}\delta_{\mu\nu}+O_{\mu\nu c}^{(n')}(p^1,p^2,k)], \quad (50d)$$

$$^{p}\Xi^{(n')}(p^1,p^2,p^3)=e^{n'}[X^{(n')}+R^{(n')}(p^1,p^2,p^3)+M_c^{(n')}(p^1,p^2,p^3)]. \quad (50e)$$

The term $R^{(n')}$ in (50e) will be explained in Section VI. The constants $A^{(n')}$, $B^{(n')}$, $C^{(n')}$, $L^{(n')}$, $O^{(n')}$, and $X^{(n')}$ are finite but cut-off dependent, and are "regulated" logarithmically divergent integrals. All divergencies higher than logarithmic are put equal to zero by the use of regulators.[24] $B^{(n')}$ is the "wave function renormalization," $L^{(n')}$ and $O^{(n')}$ are the "spurious charge renormalizations." As was explained before, they cancel identically (see Appendix I) such that

$$-B^{(n')}=L^{(n')}=O^{(n')}. \quad (51)$$

We are therefore effectively left with the primitive divergents $^{p}\Sigma$, $^{p}\Pi$, and $^{p}\Xi$. It should be mentioned at this point that the only primitive divergent $^{p}\Sigma$ and $^{p}\Pi$ are those shown in Fig. 6.

The convergent parts of (50) are defined as follows:

$$S_c^{(n')}(p)=0 \text{ for } p^2+m^2=0, \quad (52a)$$

$$D_c^{(n')}(k)=0 \text{ for } k^2=0 \quad (52b)$$

$$L_{\mu c}^{(n')}(p^1,p^2)=0 \text{ for } p^1=p^2 \text{ and } (p^1)^2+m^2=0 \quad (52c)$$

$$O_{\mu\nu}^{(n')}(p^1,p^2,k)=0 \text{ for } k=0 \text{ (gauge invariance)} \quad (52d)$$

$$M_c^{(n')}(p^1,p^2,p^3)=0 \text{ for } \mathbf{p}^1=\mathbf{p}^2=\mathbf{p}^3=0, \quad (p^1)^2=(p^2)^2=(p^3)^2=-m^2. \quad (52e)$$

For a discussion of (50e) and (52e) see Section VI.

All convergent functions thus defined increase at most as a power of the logarithm for large values of the arguments, except $L_{\mu c}$ which increases linearly (times a power of the logarithm). Their effect is therefore to "smear out" the propagation functions S and D, and the corner functions $p_\mu+p_\mu'$ and $\delta_{\mu\nu}$. Similarly M_c could be regarded as a smearing out of a direct (δ-function) interaction between two mesons. (See also Appendix II.)

We can now define an unambiguous method for the separation of all infinities from any diagram. We first adopt as a "hierarchy" of divergencies the list of Section III. Any primitive divergence higher on the list has preference in separation from any lower one. However, the succession of the divergencies of type (1) and (2) may be interchanged.

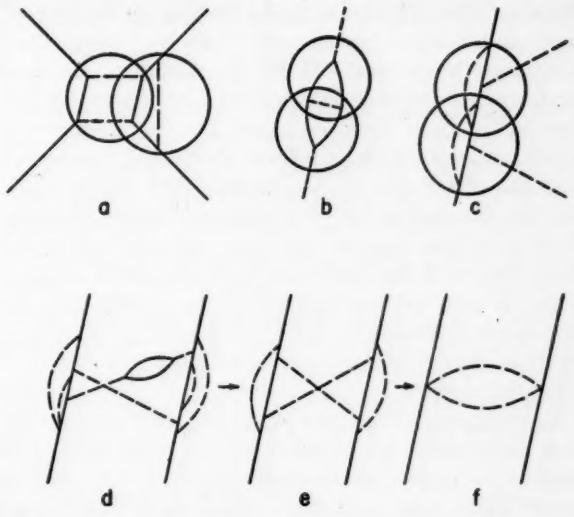

FIG. 7. Diagrams *a*, *b*, and *c* are examples of ambiguity in reduction. *b* and *c* are *b*-divergencies. Diagrams *e* and *f* illustrate the successive steps in the reduction of diagram *d*.

Every reducible diagram of a given order contains proper irreducible, and therefore at most primitively divergent, parts. The divergencies of these primitive divergent parts are to be separated according to (50). The divergent parts are then to be dropped. This separation is indicated in the diagram as follows: The replacement of $^{p}\Sigma^{(n')}(p)$ by $e^{n'}(p^2+m^2)S_c^{(n')}(p)$ in the integral is indicated by replacing the self-energy part $S(p)^{p}\Sigma^{(n')}(p)S(p)$ in the diagram by an effective meson line $e^{n'}S(p)S_c^{(n')}(p)$. (See also Appendix II.) Similarly a photon self-energy part $D(k)^{p}\Pi^{(n')}(k)D(k)$ is replaced by an effective photon line $e^{n'}D(k)D_c^{(n')}(k)$. The replacement of the primitive divergent parts of type (3), (5), and (6) by their finite parts is indicated in a diagram by replacing these parts by effective corners: type (3) will give an effective single corner, type (5) an effective double corner, and type (6) a direct interaction corner, where four meson lines meet.

This procedure would carry through without difficulty were it not for the fact that some primitive divergent parts may "overlap" as shown in Fig. 7; i.e., that they may have one or more lines in common. If two primitives of different types overlap (Fig. 7*a*), the hierarchy decides in which part the divergencies are to be separated out first. If the two primitives are of the same type (Figs. 7*b* and *c*) we are faced with the so-called *b*-divergencies. Dyson has shown how to proceed in this case (**II**, p. 1749); i.e., the divergencies of each of the two parts are to be separated out. Any ambiguities which may arise in this connection are eliminated in our case by the use of regulators.

In this way one obtains diagrams which may again contain primitive divergent parts. Some of these parts may contain effective single and double corners and

effective lines. These are to be treated as "ordinary" single and double corners, and "ordinary" lines. Their divergence properties will be the same as those of "ordinary" primitive divergencies (see Appendix II); they differ from them at most by the power of a logarithm as mentioned before. Therefore, this reduction procedure can be continued until the diagram becomes irreducible, i.e., it becomes either an improper diagram whose proper parts are at most primitive divergent, or it becomes a proper irreducible diagram which is also at most primitive divergent. The last separation if necessary, is then completed and a finite result is obtained. An example of such a reduction is indicated in Figs. 7*d*, *e*, *f*.

Suppose that all integrations over the internal photon lines have been carried out and the reduced diagram consists of proper parts which contain only internal *meson* lines. Any such part which does not contain corners coupling to photons or external fields involves necessarily only "direct interaction corners." Let us investigate the possible primitive divergencies in such a diagram. With the notation of Section III we find with $D_e=0$, $E_i=f_i=0$,

$$F=F_s=2n-E_s/2,$$
$$D_{\text{num}}=0, \quad D_{\text{den}}=2F,$$
$$E_s\geqslant 5.$$

Since E_s is obviously even, the two primitive divergent processes are those with $E_s=2$ (quadratic) and $E_s=4$ (logarithmic). They are shown in Figs. 8*a* and *b*. All other divergent diagrams contain these as parts. For example, the diagram Fig. 8*c* contains two primitive divergencies of type Fig. 8*b*. Possible action of external fields or photons will clearly improve the order of divergence by one each, such that in general

$$E_s+E_i+f_i=E\geqslant 5,$$

which is identical with (40). We have thus shown that the introduction of direct interaction corners by the reduction procedure will yield "effective" diagrams of the same type and divergence properties as the original diagrams. Thus, by counting the external lines Figs. 8*a* and *b* are identified as primitive self-energy and meson-meson interaction which diverge exactly as the original processes. Their divergencies are to be separated out as in (50).

In this way we split the S matrix into a finite and an infinite (i.e., cut-off dependent) part in an unambiguous way. The infinite part is to be dropped. We shall now justify the omission of the infinite part by showing that these parts are equivalent to infinite factors which can be consistently incorporated into the finite parts in such a way that they constitute renormalizations of the constants originally entering the theory: The mass and charge of the mesons and the constant of direct interaction. The latter which has not entered into the theory as developed so far, has to be introduced in order to justify the omission of the terms arising from X in (50e).

FIG. 8. Typical diagrams resulting from direct meson-meson interaction. *a*: primitive divergent meson self-energy. *b*: Primitive divergent meson-meson scattering. *c*: Reducible meson-meson scattering.

C. Removal of the Divergencies by Renormalization

The meson mass m entering the Klein-Gordon equation is the "mechanical" mass and can be written $m_1-\delta m$ where m_1 is the observed and δm the electromagnetic mass. The term $-\delta m$ will always appear together with the self-energy term Σ^*, such that (49a) becomes

$$S'(p)=S(p)+S(p)(\Sigma^*(p)-\delta m)S'(p). \tag{54a}$$

When the divergent parts of the effective meson line function $S'(p)$ are dropped, one is left with the finite function S_1'. Following Dyson we set out to prove that

$$S'=Z_2S_1'(e_1), \tag{53a}$$

where e_1 is the renormalized (observed) charge and Z_2 is an infinite constant. Similarly it should be possible to write the finite effective photon propagation function $D_1'(e_1)$ obtained by dropping the divergent terms in D' of (49b) as

$$D'=Z_3D_1'(e_1). \tag{53b}$$

Radiative corrections to a given diagram can be obtained not only by inserting corrections into the meson and photon lines S and D but also by inserting single-corner parts, i.e. diagrams of type Figs. 4*c* and *d* into single corners $C_\mu=p_\mu+p_\mu'$, and Compton effect diagrams (Figs. 5*e*, *f*, *g*) into double corners $C_{\mu\nu}=\delta_{\mu\nu}$. Making such insertions to all orders will amount to a replacement of C_μ by C_μ' and of $C_{\mu\nu}$ by $C_{\mu\nu}'$ where according to (49c)

$$C_\mu=C_\mu+\Lambda_\mu, \tag{54b}$$

$$C_{\mu\nu}'=C_{\mu\nu}+\Omega_{\mu\nu}{}^*+\int(C_{\mu\lambda}+\Omega_{\mu\lambda}{}^*)S'D'C_{\lambda\nu}. \tag{54c}$$

It is important that $\Omega_{\mu\nu}{}^*$ are the proper Compton diagrams as defined preceding to Eq. (49c) and do not contain diagrams followed (or preceded) by emission (or absorption), i.e., Figs. 5*a–d*. These diagrams would otherwise be counted twice.

When the divergent parts of these functions are dropped one obtains $C_{\mu 1}'$ and $C_{\mu\nu 1}'$. Their relation to the functions (54) should be

$$C_\mu'=Z_1{}^{-1}C_{\mu 1}'(e_1), \tag{53c}$$

$$C_{\mu\nu}'=Z_4{}^{-1}C_{\mu\nu 1}'(e_1). \tag{53d}$$

Finally radiative corrections can be obtained by replacing a direct interaction corner M by all meson-meson interaction diagrams. For this purpose we assume first that there exists a direct interaction term

$$\lambda\phi^*(x)\phi^*(x)\phi(x)\phi(x) \tag{55}$$

in the Lagrangian of our theory. Such a term would then appear additive to the interaction Hamiltonian (2). λ is an infinite constant. It is completely within the philosophy of the present theory to renormalize this coupling constant λ, since also the coupling constant e is being renormalized; thus we put $\lambda=\lambda_1-\delta\lambda$ where λ_1 is finite and is to be determined from experiment.

It follows from (49d) that each direct interaction corner M which is replaced by all possible meson-meson interactions to yield M' can be written

$$M'=\lambda_1-\delta\lambda+\Xi^*+\int(\lambda_1-\delta\lambda+\Xi^*)S'S'M'. \tag{54d}$$

When the divergent parts are dropped it gives $M_1'(e_1)$. One should thus obtain the renormalization of M' which for $\lambda_1=0$ is of the form

$$M'=Z_5^{-2}M_1'(e_1). \tag{53e}$$

The finite functions S_1', D_1', $C_{\mu 1}'$, $C_{\mu\nu 1}'$, and M_1' are well determined by the reduction procedure given in (B). It is therefore only a question of the structure of the diagrams whether or not Eqs. (53) can be fulfilled by proper choice of δm, $\delta e=e_1-e$, and $\delta\lambda$. Since Eqs. (53) are interdependent but should reproduce themselves upon insertion into each other, this procedure will prove the consistency of the renormalization program.

Consider any single-corner diagram $\Delta^{(n')}$ of order n'. Replace all lines and corners by the completely corrected lines and corners (i.e., S by S', D by D', etc.) and find $\Delta'^{(n')}$. Consider now the first radiative correction to the original diagram, $\Delta^{(n'+2)}$. It can be obtained by inserting a photon line between two meson lines thereby increasing the number of S functions by two, the number of D functions by one and the number of C_μ functions by two. It will also add a factor e^2 to the integral. We now again make the replacement $S\to S'$, $D\to D'$, $C\to C_\mu'$, etc. and find $\Delta'^{(n+2)}$. When Eqs. (53) are applied to $\Delta'^{(n')}$ and $\Delta'^{(n'+2)}$ they should result in the finite renormalized diagrams $\Delta'^{(n')}(e_1)$ and $\Delta'^{(n'+2)}(e_1)$. This is only possible consistently if the additional factor in $\Delta'^{(n'+2)}$, i.e.,

$$e^2S'S'D'C_\mu'C_\nu'=e_1^2S_1'D_1'C_{\mu 1}'C_{\nu 1}',$$

or with (53)

$$e_1^2=Z_2^2Z_3Z_1^{-2}e^2. \tag{56}$$

It is clear that the photon line inserted into $\Delta^{(n')}$ could have both ends in the same double corner. This would add instead the factor $e^2S'D'C_{\mu\nu}'=e_1^2S_1'D_1'C_{\mu\nu 1}'$ by the same argument as before

$$e_1^2=Z_2Z_3Z_4^{-1}e^2. \tag{57}$$

Equation (56) and (57) are compatible if and only if

$$Z_4=Z_1^2Z_2^{-1}. \tag{58}$$

One can now proceed just as in II. From Fig. 6*a* we see that Σ^* consists of one S function, one D function, two C_μ, and a factor e^2. Replacement by the primed functions and use of (53) and (56) gives $\Sigma^*-Z_2^{-1}\Sigma^*(e_1)$. Therefore (54a) with the separation (50a) yields

$$S'=S+Z_2^{-1}(SA(e_1)+B(e_1)+S_c(e_1))S'-\delta mSS'$$

which should reduce to its finite part

$$S_1'(e_1)=S+S_c(e_1)S_1'(e_1)$$

due to the renormalization (53a). This is indeed the case provided

$$\delta mZ_2=A(e_1) \tag{59}$$

and

$$Z_2=1+B(e_1). \tag{60}$$

In the same way, the structure of Fig. 6*b* leads to $\Pi^*=Z_3^{-1}\Pi^*(e_1)$ and (49b) becomes with (50b)

$$D'=D+Z_3^{-1}(C(e_1)+D_c(e_1))D'.$$

This reduces to

$$D_1'(e_1)=D+D_c(e_1)D_1'(e_1)$$

due to (53b) provided

$$Z_3=1+C(e_1). \tag{61}$$

For the renormalization of C_μ we see from (56) and Fig. 10 that $\Lambda_\mu=Z_1^{-1}\Lambda_\mu(e_1)$ such that (54b) with the separation (50c) becomes

$$C_\mu'=C_\mu+Z_1^{-1}(C_\mu L(e_1)+L_{\mu c}(e_1))$$

which reduces to its finite part

$$C_{\mu 1}'(e_1)=C_\mu+L_{\mu c}(e_1)$$

due to (53c) provided

$$Z_1=1-L(e_1). \tag{62}$$

As is proved in Appendix I [Eq. (A11)] $B+L=0$, since it is true in each order. Therefore (60), (62), and (58) give at once

$$Z_1=Z_2=Z_4, \tag{63}$$

and (56) simplies to

$$e_1^2=Z_3e^2=(1+C(e_1^2))e^2. \tag{56'}$$

Equation (63) is another statement of the cancellation of spurious charge and wave function renormalization. This cancellation occurs explicitly in Eq. (56) such that the complete "true" charge renormalization is due only to the renormalization of D' of (53b). Since any insertions into the D lines always reduce to effective diagrams of the form Fig. 6*b*, we find again that only closed loops with two single corners or one double corner yield charge renormalization.

We also observe that Z_4 the renormalization associated with the Compton effect diagrams is already determined by Z_1 and Z_2 which is actually a consequence of gauge invariance (see the remark at the end of Appendix I).

The above analysis which resulted in the determination of the Z_i in terms of the infinite integrals can, of course, in principle be continued for $C_{\mu\nu}'$ and M'. This would result, of course, in the same equations as above. From Fig. 11 and Eq. (56) one finds

$$\Omega_{\mu\nu}{}^*=Z_2Z_1^{-2}\Omega_{\mu\nu}{}^*(e_1).$$

The renormalization of S' and D' in the integral (54c), observing that there are two more factors of e to be renormalized (one of the "external" charges of each diagram connected by D') yields

$$C_{\mu\nu}'=C_{\mu\nu}+Z_2Z_1^{-2}\Omega_{\mu\nu}{}^*(e_1)$$

$$+Z_1{}^2Z_2\int(C_{\mu\lambda}+Z_2Z_1^{-2}\Omega_{\mu\lambda}{}^*(e_1))S'(e_1)D'(e_1)C_{\lambda\nu}'. \quad (64)$$

This should reduce to $C_{\mu\nu_1}'(e_1)$ due to (53d). However, the analysis cannot be carried further, because $C_{\mu\nu_1}'(e_1)$ is not known in closed form. Although it is uniquely determined by the reduction prescription, it is not possible to write down its form. This is already indicated by the fact that the integral in (64) diverges even if the factors of the integrand are replaced by their finite parts. The reason for this apparently unexpected divergence is to be found in the b-divergences of the type shown in Fig. 7c. Whenever these diagrams occur the separation into proper diagrams of type (5) (Compton effect, etc.) becomes ambiguous. Of course, it is irrelevant which separation is chosen, but it is due to this ambiguity that the separation of the infinite parts of the two diagrams of type (5) thus obtained does not completely separate out all infinite terms. Since the integral in (64) is just based on this separation one cannot expect it to be finite. On the other hand, only some of the improper diagrams of type (5) will contain b-divergencies; it will therefore not be possible to write down a closed analytic expression correct for all cases.

One may argue that the renormalization procedure has to be consistent even if one restricts $C_{\mu\nu}'$ to proper diagrams omitting the integral in (64). One finds in this case from (50d)

$$C_{\mu\nu}'=C_{\mu\nu}+Z_2Z_1^{-2}(O(e_1)C_{\mu\nu}+O_{\mu\nu}(e_1))$$

which reduces to

$$C_{\mu\nu_1}'(e_1)=C_{\mu\nu}+O_{\mu\nu}(e_1)$$

due to (53d) provided

$$Z_4=1-O(e_1) \quad (65)$$

and Eq. (58) holds. Equations (66) and (62) combined with the result of Appendix I (A12) confirm $Z_2=Z_4$ found previously [Eq. (65)].

Finally we turn to the meson-meson interaction and observe that the same difficulty encountered in the integral of (54c) is also present in (54d). The case is completely analogous to the one discussed above. If we restrict ourselves to $\lambda_1=0$ and to proper Ξ, one finds from Fig. 12 that $\Xi^*=Z_2^{-2}\Xi^*(e_1)$. Therefore, with (50e)

$$M'=-\delta\lambda+Z_2^{-2}(X(e_1)+M_e(e_1)+R(e_1))$$

which reduces to

$$M_1'(e_1)=M_e(e_1)+R(e_1)$$

due to (53e) provided that

$$\delta\lambda=Z_2^{-2}X(e_1) \quad (66)$$

and that

$$Z_5=Z_2. \quad (67)$$

We have so far restricted ourselves to $\lambda_1=0$ in (54d). For this case the discussion of this section shows the consistency of the removal of all divergencies by renormalization. If $\lambda_1\neq 0$ two additional types of divergencies arise. First, the divergencies due to the direct interaction term λ_1 itself which gives rise to divergent diagrams like those of Fig. 8. They can be separated into a finite part and an infinite part analogous to (50e). The latter must be canceled by a renormalization $\delta\lambda_1$ which is independent of e_1.

Second, there are radiative corrections of diagrams like Fig. 8. They diverge exactly like the effective diagrams encountered previously where the direct interaction corner was due to Ξ rather than (55). Their separation according to (50) of infinite and finite parts will result in infinite parts which depend on e_1 and on λ_1. These have to be canceled by a term $\delta\lambda_{1e}$.

We thus find that if $\lambda_1\neq 0$, $\delta\lambda=\delta\lambda_1+\delta\lambda_{1e}+\delta\lambda_e$, where $\delta\lambda_e$ is independent of λ_1 and is determined by (66). Since the reduction procedure uniquely separates the infinite parts which in turn define $\delta\lambda$, this quantity is well defined. The finite scattering matrix will then be a well-defined function of λ_1 and will be given as a power series in λ_1.

Before we turn to a discussion of the physical meaning and determination of λ_1 (Section VI), we shall give some examples which illustrate some of the results obtained so far.

V. THE PRIMITIVE DIVERGENT PROCESSES TO LOWEST ORDER

The second-order meson self-energy and vacuum polarization have been treated repeatedly by various authors. There is no need to give these calculations here.

A. Scattering of Light by Light

There are three kinds of diagrams, corresponding to the number of double corners (Fig. 9). From (30′) we see that they will all be of the form

$$(e/4\pi^2)^4A_\mu(k^1)A_\nu(k^2)A_\lambda(k^3)A_\sigma(k^4)$$

$$\times T_{\mu\nu\lambda\sigma}(k^1,k^2,k^3,k^4)\delta(k^1+k^2+k^3+k^4).$$

The diagram Fig. 9*a* gives with regulators

$$T_{\mu\nu\lambda\sigma}{}^{(a)}(1234)=\Sigma c_i\int\frac{(2p_\mu-k_\mu{}^1)(2p_\nu-2k_\nu{}^1-k_\nu{}^2)(2p_\lambda-2k_\lambda{}^1-k_\lambda{}^3)(2p_\sigma+k_\sigma{}^4)d_4p}{[p^2+m_i{}^2][(p-k^1)^2+m_i{}^2][(p-k^1-k^2)^2+m_i{}^2][(p+k^4)^2+m_i{}^2]}.$$

We introduce auxiliary variables[25] and combine the denominator to give the fourth power of a quadratic form. On shifting the origin of the p space the divergent part of the integral is found to be [see Eq. (41)]

$$T_{\mu\nu\lambda\sigma}{}^{(a)}=\Sigma c_i 3!\int_0^1 dx\int_0^x dy\int^y dz\frac{16p_\mu p_\nu p_\lambda p_\sigma d_4p}{(p^2+m_i{}^2)^4}.$$

The integral vanishes unless the μ, ν, λ, σ are equal in pairs. One finds that $p_\mu p_\nu p_\lambda p_\sigma$ in the integral can be replaced by

$$(1/24)(\delta_{\mu\nu}\delta_{\lambda\sigma}+\delta_{\mu\lambda}\delta_{\nu\sigma}+\delta_{\mu\sigma}\delta_{\nu\lambda})p^2p^2$$

and the integration can be carried out over four-dimensional spherical coordinates with volume element $2\pi^2p^3dp$ as explained in **II**. One finds

$$T_{\mu\nu\lambda\sigma}{}^{(a)}=(16/24)2\pi^2i(\delta_{\mu\nu}\delta_{\lambda\sigma}+\delta_{\mu\lambda}\delta_{\nu\sigma}+\delta_{\mu\sigma}\delta_{\nu\lambda})\times\Sigma c_i\tfrac{1}{2}\ln(M_c{}^2/m_i{}^2)\equiv\tfrac{2}{3}Q_{\mu\nu\lambda\sigma},$$

where M_c is an upper cut-off mass. The relation $\Sigma c_i=0$ was used. There are 24 permutations of the four corners in Fig. 9*a* which can be obtained from six of them by cyclic permutations. Therefore there are six diagrams of the type Fig. 9*a* which need to be taken into account. These six are 1234, 1324, 1243, and their "charge—conjugates," obtained by reversing the sense of all the arrows, i.e., 4321, 4231, 3421. The latter three are identical with the former three by Furry's theorem. Since $T_{\mu\nu\lambda\sigma}{}^{(a)}$ is invariant under the concomitant permutation of 1234 and $\mu\nu\lambda\sigma$, we find for the sum of divergent parts of the three essentially different diagrams of the form Fig. 9*a*

$$\Sigma T_{\mu\nu\lambda\sigma}{}^{(a)}=2Q_{\mu\nu\lambda\sigma}.$$

Each of these three diagrams gives four diagrams of type Fig. 9*b* by shrinkage of the meson lines. The one actually drawn gives

$$T_{\mu\nu\lambda\sigma}{}^{(b)}(1234)=\Sigma c_i\int(-\delta_{\mu\sigma})\times\frac{(2p_\nu-2k_\nu{}^1-k_\nu{}^2)(2p_\lambda-2k_\lambda{}^1-2k_\lambda{}^2-k_\lambda{}^3)d_4p}{(p^2+m_i{}^2)[(p-k^1)^2+m_i{}^2][(p-k^1-k^2)^2+m_i{}^2]}.$$

As before one finds, since $p_\nu p_\lambda$ can be replaced by $\frac{1}{4}\delta_{\nu\lambda}p^2$,

$$T_{\mu\nu\lambda\sigma}{}^{(b)}=2!\int_0^1 dx\int_0^x dy\Sigma c_i\frac{4p_\nu p_\lambda d_4p}{(p^2+m_i{}^2)^3}\delta_{\mu\sigma}=-i\pi^2\delta_{\mu\sigma}\delta_{\nu\lambda}\Sigma c_i\ln(Mc^2/m_i{}^2).$$

[25] See R. P. Feynman, reference 5, p. 785.

The three other ways of shrinkage of 1234 will give the same result with $\delta_{\mu\sigma}\delta_{\lambda\nu}$ replaced by $\delta_{\mu\nu}\delta_{\lambda\sigma}$, $\delta_{\nu\lambda}\delta_{\mu\sigma}$, and $\delta_{\lambda\sigma}\delta_{\mu\nu}$, respectively. The sum of all diagrams Fig. 9*b*, resulting from 1234 is therefore

$$-2\pi^2i(\delta_{\mu\sigma}\delta_{\nu\lambda}+\delta_{\mu\nu}\delta_{\lambda\sigma})\Sigma c_i\ln(M_c{}^2/m_i{}^2).$$

The results from shrinkage of 1324 are obtained from this by replacing μ, ν, λ, σ by μ, λ, ν, σ, respectively, yielding

$$-2\pi^2i(\delta_{\mu\sigma}\delta_{\nu\lambda}+\delta_{\mu\lambda}\delta_{\nu\sigma})\Sigma c_i\ln(M_c{}^2/m_i{}^2)$$

and similarly from 1243, replacing μ, ν, λ, σ instead by μ, ν, σ, λ,

$$-2\pi^2i(\delta_{\mu\lambda}\delta_{\nu\sigma}+\delta_{\mu\nu}\delta_{\lambda\sigma})\Sigma c_i\ln(M_c{}^2/m_i{}^2).$$

Therefore,

$$\Sigma T_{\mu\nu\lambda\sigma}{}^{(b)}=-4Q_{\mu\nu\lambda\sigma}.$$

The same result could have been obtained by drawing all diagrams of type Fig. 9*b* and multiplying by the weight factor 2.

Each of the diagrams of the type Fig. 9*b* can be shrunk once to yield a diagram of Fig. 9*c*. The one drawn is

$$T_{\mu\nu\lambda\sigma}{}^{(c)}(1234)=\Sigma c_i\int\frac{(-\delta_{\mu\sigma})(-\delta_{\nu\lambda})d_4p}{[(p-k')^2+m_i{}^2][p^2+m_i{}^2]},$$

$$T_{\mu\nu\lambda\sigma}{}^{(c)}=\delta_{\mu\sigma}\delta_{\nu\lambda}\Sigma c_i\int_0^1 dx\int\frac{d_4p}{(p^2+m_i{}^2)^2}=\delta_{\mu\sigma}\delta_{\nu\lambda}i\pi^2\Sigma c_i\ln(M_c{}^2/m_i{}^2).$$

The four diagrams *b* resulting from 1234 will on shrinkage give two diagrams *c* as the one just calculated and two diagrams with $\delta_{\mu\sigma}\delta_{\nu\lambda}$ replaced by $\delta_{\mu\nu}\delta_{\lambda\sigma}$. Summing again over the permutations μ, λ, ν, σ and $\mu\nu\sigma\lambda$ corresponding to the diagrams resulting from 1324 and 1243 we find

$$\sum T_{\mu\nu\lambda\sigma}{}^{(c)}=2Q_{\mu\nu\lambda\sigma}.$$

The sum of all diagrams Fig. 9 is therefore

$$\sum T_{\mu\nu\lambda\sigma}{}^{(a)}+\sum T_{\mu\nu\lambda\sigma}{}^{(b)}+\sum T_{\mu\nu\lambda\sigma}{}^{(c)}=0$$

as required by gauge invariance.

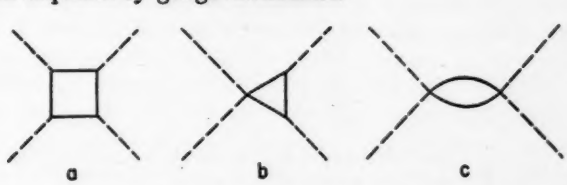

FIG. 9. The scattering of light by light in lowest order.

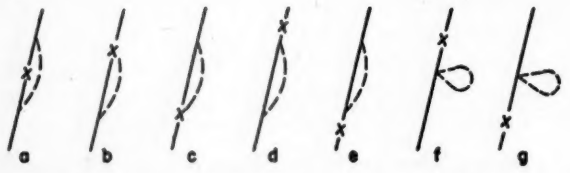

FIG. 10. Meson scattering to first order in the external field and in lowest order of correction. Note that the diagrams describing the effect of vacuum polarization were omitted here.

B. Lamb Shift and Associated Phenomena

In this process as well as in the Compton effect dealt with subsequently, we want to show how the spurious charge renormalizations and wave function renormalizations cancel. For this purpose we will content ourselves to show the cancellation of the divergent upper limit of the integrals, and we shall ignore "infrared divergencies" and finite renormalizations. In this way we shall greatly simplify the discussion, and we do not need to introduce regulators.

The diagrams are shown in Fig. 10. Apart from uninteresting constants Fig. 10*a* gives

$$\Lambda_\mu^{(a)}(p,p')=\int\frac{(2p_\lambda-k_\lambda)(2p_\lambda'-k_\lambda)(P_\mu+2k_\mu)d_4k}{k^2(k^2+2p\cdot k)(k^2+2p'\cdot k)},\quad(68)$$

where k is the momentum of the virtual photon, $P=p+p'$ and $p^2=p'^2=-m^2$. It is now convenient to introduce the variable $k'=k+\frac{1}{2}P$ which will enable us to eliminate the linearly divergent term correctly. One finds after putting $p=p'$

$$\Lambda_\mu^{(a)}(p,p)=\int\frac{(p+k')^2\cdot 2k_\mu' d_4k'}{(k'-p)^2(k'^2-p^2)}.$$

For large k' we can put $(k'-p)^{-2}=(1+2k\cdot p/k^2)/k'^2$. The linearly divergent term now vanishes because of symmetry and the remainder gives for large k

$$L^{(a)}p_\mu=p_\mu\int d_4k/(k^2)^2\equiv p_\mu I.$$

In the same way Figs. 10*b* and *c* give together

$$\Lambda_\mu^{(b)}(p,p')+\Lambda_\mu^{(c)}(p,p')$$
$$=2\int\left[\frac{-\delta_{\mu\nu}(2p_\nu+k_\nu)}{k^2(k^2+2p\cdot k)}+\frac{-\delta_{\mu\nu}(2p_\nu'+k_\nu)}{k^2(k^2+2p'\cdot k)}\right]d_4k,$$

where the factor 2 is the weight factor. For large k we can again put $(k^2+2p\cdot k)^{-1}=(1-2p\cdot k/k^2)/k^2$ and find

$$L^{(b)}+L^{(c)}=-3I,\quad L=L^{(a)}+L^{(b)}+L^{(c)}=-2I.\quad(69)$$

The remaining diagrams of Fig. 10 will give wave function renormalizations.

$$\Lambda_\mu^{(d)}+\Lambda_\mu^{(e)}=\tfrac{1}{2}P_\mu\int\left[\frac{(2\bar p-k)^2d_4k}{[(\bar p-k)^2+m^2]k^2(\bar p^2+m^2)}\right.$$
$$\left.+\frac{(2\bar p'-k)^2d_4k}{[(\bar p'-k)^2+m^2]k^2(\bar p'^2+m^2)}\right],\quad(70a)$$

$$\Lambda_\mu^{(f)}+\Lambda_\mu^{(g)}=\tfrac{1}{2}P_\mu\int\left[\frac{-\delta_{\nu\nu}}{(\bar p^2+m^2)k^2}+\frac{-\delta_{\nu\nu}}{(\bar p'^2+m^2)k^2}\right]d_4k.\quad(70b)$$

From these integrals first the mass renormalization has to be subtracted, i.e., we have to subtract

$$\tfrac{1}{2}P_\mu\int\left[\frac{(2p-k)^2}{(k^2-2p\cdot k)k^2(\bar p^2+m^2)}\right.$$
$$\left.+\frac{(2p'-k)^2}{(k^2-2p'-k)k^2(\bar p'^2+m^2)}\right]d_4k$$
$$+\tfrac{1}{2}P_\mu\int\left[\frac{-\delta_{\mu\nu}}{(\bar p^2+m^2)k^2}+\frac{-\delta_{\nu\nu}}{(\bar p'^2+m^2)k^2}\right]d_4k.\quad(71)$$

One observes that the diagrams Fig. 10*f* and *g* exactly cancel out. They do not contribute to observable effects. It can easily be seen that these double-corner self-energy terms will always behave in this manner.

$\bar p_\mu$ and $\bar p_\mu'$ of (70) obey $p^2=p'^2=-m^2$ only after (71) has been subtracted. One therefore replaces them first by $(1+\epsilon)p_\mu$ and $(1+\epsilon)p_\mu'$ and passes to the limit $\epsilon\to 0$ in the difference (70)–(71). The resultant linearly divergent integral may be treated similarly to (68) and yields after an easy calculation the wave function renormalization

$$B=2I,\quad(72)$$

which exactly cancels the spurious charge renormalization (69).

C. Compton Effect and Associated Phenomena

We will here be concerned with the radiative correction to the scattering of an electron by an external field to second order in that field. The diagrams are those of the Lamb shift (Fig. 10) preceded or followed by an additional scattering, those containing true charge renormalizations (i.e., diagrams with parts of the form Fig. 6*b*), and those shown in Fig. 11. The latter are special cases of Figs. 5*c*, *d*, *e*. The calculation is carried out as in Section B. One finds

$$\Omega_{\mu\nu}^{(a)}=\int\frac{(2p_\lambda+k_\lambda)(2p_\lambda'+k_\lambda)(2p_\mu+2k_\mu+q_\mu)(2p_\nu'+2k_\nu+q_\nu')}{k^2(k^2+2p\cdot k)[(k+q)^2-2p\cdot(k+q)](k^2+2p'\cdot k)}d_4k+(\text{same with }\mu,\nu\text{ and }q,q'\text{ interchanged})$$

which for large k_μ yields

$$O^{(a)}\delta_{\mu\nu}=2\int d_4k\cdot 4k_\mu k_\nu/(k^2)^3=2\delta_{\mu\nu}I.$$

Similarly, with weight factor 2

$$\Omega_{\mu\nu}{}^{(b)}=2\int\frac{(2p+k)\cdot(2p'-k)(-\delta_{\mu\nu})}{k^2(k^2+2p\cdot k)(k^2+2p'\cdot k)}d_4k,$$

$$O^{(b)}=-2I,$$

$$\Omega_{\mu\nu}{}^{(c)}+\Omega_{\mu\nu}{}^{(d)}=2\int\frac{(2p_\lambda+k_\lambda)(-\delta_{\lambda\nu})(2p_\mu+2k_\mu+q_\mu)d_4k}{k^2(k^2+2p\cdot k)[(k+q)^2+2p\cdot(k+q)]}$$

$$+2\int\frac{(2p_\lambda'+k_\lambda)(-\delta_{\lambda\nu})(2p_\mu'+2k_\mu+q_\mu)d_4k}{k^2(k^2+2p'\cdot k)[(k+q)^2+2p'\cdot(k+q)]}$$

$$+(\text{same with }\mu,\ \nu\text{ and }q,\ q'\text{ interchanged}),$$

$$O^{(c)}+O^{(d)}=-4I.$$

The last spurious charge renormalization diagram, Fig. 11*e*, has weight 4

$$O_{\mu\nu}{}^{(e)}=4\int\frac{(-\delta_{\mu\lambda})(-\delta_{\lambda\nu})d_4k}{k^2[(k+q)^2+2p\cdot(k+q)]}$$

$$+(\text{same with }\mu,\ \nu\text{ and }q,\ q'\text{ interchanged}),$$

$$O^{(e)}=8I.$$

Together they give

$$O=O^{(a)}+O^{(b)}+O^{(c)}+O^{(d)}+O^{(e)}=4I. \tag{73}$$

The sum of the wave function renormalization diagrams, Fig. 11*f* and *g*, obviously yield the same integrals as Figs. 10*d* and *e*, except that P_μ in the latter is to be replaced by $-2\delta_{\mu\nu}$. One therefore finds at once from (70) and (72)

$$B=-4I$$

which again cancels (73).

D. Meson-Meson Scattering

The diagrams for this process to fourth order are shown in Fig. 12. The circle in Fig. 12*e* stands for *all* the Lamb shift diagrams with the external field replaced

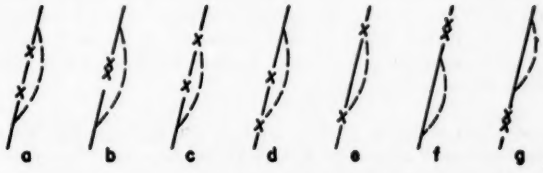

FIG. 11. Meson scattering to second order in the external field and in lowest order of correction. When the crosses are replaced by photon lines these diagrams represent the first radiative corrections to Compton scattering. Note that these are not *all* of the diagrams for these processes (see text).

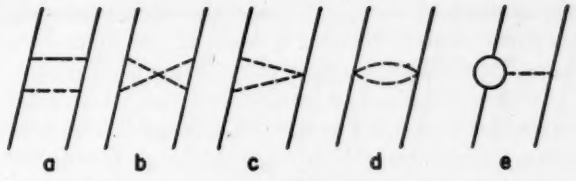

FIG. 12. The first radiative correction to meson-meson scattering. The circle in *e* stands for all single-corner parts in that order of correction.

by a photon line. Therefore, the sum of all diagrams *e* contains only true charge renormalizations. One finds, observing the weight factors:

$$\Xi^{(a)}=\int\frac{(2p^1-k)\cdot(2p^2+k)(p^1+p^3-k)\cdot(p^2+p^4+k)}{k^2(k+p^3-p^1)^2(k^2-2p^1\cdot k)(k^2+2p^2\cdot k)}d_4k,$$

$$\Xi^{(b)}=\int\frac{(2p^1-k)\cdot(2p^4-k)(p^1+p^3-k)\cdot(p^2+p^4-k)}{k^2(k+p^3-p^1)^2(k^2-2p^1\cdot k)(k^2-2p^4\cdot k)}d_4k,$$

$$\Xi^{(c)}=-2\int\frac{(2p^1-k)\cdot(p^1+p^3-k)}{k^2(k+p^3-p^1)^2(k^2-2p^1\cdot k)}d_4k$$

$$-2\int\frac{(2p^2+k)\cdot(p^2+p^4+k)}{k^2(k+p^3-p^1)^2(k^2+2p^2\cdot k)}d_4k,$$

$$\Xi^{(d)}=2\int\frac{(-\delta_{\mu\nu})(-\delta_{\nu\mu})}{k^2(k+p^3-p^1)^2}d_4k.$$

Thus, with (50e)

$$X=X^{(a)}+X^{(b)}+X^{(c)}+X^{(d)}=I+I-4I+8I=6I.$$

From this and Eq. (66) one finds $\delta\lambda$.

VI. DISCUSSION OF THE RESULTS

First, the equivalence of the Kanesawa-Tomonaga theory with the Feynman theory is established by proving the identity of the scattering matrices of the two theories. Second, the divergencies of the S matrix are investigated and an unambiguous way for the separation of the finite and infinite parts is given. Finally, all divergencies are removed by renormalization.

One finds that the quantum electrodynamics of spinless particles is in many ways similar to the one for particles of spin $\frac{1}{2}$. There are, however, these essential differences. The non-linear terms of the interaction Hamiltonian give rise to double corners in the diagrams; this in turn is closely related to the fact that both the Lamb shift diagrams and the Compton effect diagrams lead to divergencies. However. these divergencies are shown to be entirely spurious. But the divergent Compton effect diagrams give rise to a *b*-divergence problem which is much more complicated than the *b*-divergence problem in the electron case. In the latter these divergencies occur only in very special cases since they are there only associated with electron

and photon self-energy diagrams of which there exist only two primitive divergent ones. In the spinless case there is an infinite number of b-divergent diagrams.

Further complication arises from the meson-meson interaction which is found to be divergent. This divergence necessitates the introduction of a direct interaction term into the Hamiltonian. It is this point which deserves further clarification.

As is well known, the long range of the Coulomb potential causes the scattering amplitude to become arbitrary large for small enough energy-momentum transfer $\Delta=p^1-p^3$. Terms of the type $1/\Delta$ arising, for example, in fourth order are physically undistinguishable from similar terms arising in second order. It is therefore satisfactory to see them arise only in connection with charge renormalization, i.e., they come from those fourth-order diagrams which are derived from Lamb shift diagrams, but not from Ξ. There are, however, corrections to the Coulomb potential at smaller distances from terms of the type $\ln\Delta$ occurring in ${}^p\Xi$. These terms have to be separated from ${}^p\Xi$ in the separation (50e) with the definition (52e) of M_c.

Consider a primitive divergent meson-meson scattering diagram ${}^p\Xi(p^1\ p^2\ p^3, p^4)$ for initial four-momenta p^1, p^2 and final four-momenta p^3, p^4 where $p^1+p^2=p^3+p^4$ because of energy-momentum conservation. Introduce regulators and photon masses, the latter to properly take into account the infra-red divergencies. The result of the various integrations will contain constant, logarithmically cut-off dependent terms X which are defined within an additive cut-off independent constant X'. One can now define a term R which is logarithmically divergent for $\Delta=p^1-p^3=0$,

$$R=r\ln(\Delta/m), \tag{74}$$

where

$$r=\lim_{\Delta\to 0}({}^p\Xi-X)/\ln(\Delta/m). \tag{75}$$

m is the meson mass. The limit is taken with p^1+p^3 and p^2+p^4 held fixed. r will be a function of these two combinations only. The finite function

$$M_c={}^p\Xi-X-R$$

is now defined within the constant X'.

This constant can be defined by defining R [e.g., as in (74)] and M_c [e.g., by choosing the definition (52e)]. The direct or contact interaction is then solely due to λ_1 which has to be found from experiment. However, we do not intend to imply that the interaction $R+M_c$ thus defined is free from contact interaction. In fact, there seems to be no simple unambiguous way of defining such a contact-free interaction.[26] The separation into contact and contact-free interaction must therefore be regarded as arbitrary. One might indeed equally well choose $\lambda_1=0$, i.e., one may renormalize λ to zero, and leave M_c undetermined within the additive constant X' which is to be determined by experiment.

I would like to thank Professors R. P. Feynman and N. M. Kroll for many helpful discussions throughout this work. The author is also grateful to Professor H. A. Bethe for his valuable criticism of the manuscript.

Note added in proof: The integrals in equations (49c and d) and therefore also in equations (54c, d) and (64) are oversimplified and consequently incorrect. However, they have not been used in the arguments so that the results and conclusions remain unaffected.—This author believes that the existence proof by construction of the finite S matrix as outlined in section VB should be supplemented by a mathematical formulation of this procedure. This would enable one to give a detailed proof of the consistency of the renormalization program (section VC). But it requires a detailed analysis of the treatment of b-divergencies; these have not been considered in this paper. Such analysis should furnish the correct integrals of (49c and d).

APPENDIX I. CANCELLATION OF SPURIOUS CHARGE RENORMALIZATION AND WAVE FUNCTION RENORMALIZATION

The proof presented here will be given in complete generality, valid for spin 0, $\frac{1}{2}$, and 1, and for the formulation with and without Kemmer-Duffin matrices in the cases of integer spin.

Let ψ be the source field and

$$S^{-1}(p)\psi=0 \tag{A1}$$

the equation of motion of the free field. $S(p)$ is the propagation function of the source particles. The coupling to the electromagnetic field $A_\mu{}^e(q)$ is given by the operator $C_\mu(p, p')$ where $p_\mu-p_\mu'=q_\mu$. This operator represents the single corner of a diagram, e.g., it is γ_μ for spin $\frac{1}{2}$ and it is $p_\mu+p_\mu'$ in our formulation of spin 0.

As is obvious from an expansion[27] of $S^{-1}(p-A)$,

$$C_\mu(p, p)=\partial S^{-1}(p)/\partial p_\mu. \tag{A2}$$

If (A1) is quadratic in p there will also be a quadratic term in $A_\mu{}^e$ with coefficient

$$C_{\mu\nu}=-\frac{1}{2}\frac{\partial^2 S^{-1}(p)}{\partial p_\mu\partial p_\nu}=-\frac{1}{2}\frac{\partial C_\mu(p, p)}{\partial p_\nu}. \tag{A3}$$

From (A2) the identity

$$-\partial S(p)/\partial p_\mu=S(p)C_\mu(p, p)S(p) \tag{A4}$$

is an immediate consequence. If p_μ satisfies (A1) we find the useful relation

$$\lim_{p_\mu'\to p_\mu} S(p')(p_\mu'-p_\mu)C_\mu(p, p)\psi=\psi. \tag{A5}$$

A proper Lamb shift diagram $\Lambda_\mu{}^*$ is obtained by inserting into a proper source particle self-energy diagram Σ^* the action of $A_\mu{}^e(q)$. If this is done in a source line $S(p')$, it will replace it by $S(p')C_\mu(p', p')S(p')$ for $q=0$. If it is done at a single corner it will produce a double corner with coupling function $2C_{\mu\nu}$ again for $q=0$. In all cases considered here either $C_\mu(p, p)$ is a constant and no double corner exists [$S^{-1}(p)$ is linear] or $C_{\mu\nu}$ is a constant [$S^{-1}(p)$ is quadratic]. The factor 2 which enters here in a natural way is the weight factor.

[26] Two possible definitions of a contact-free meson-meson interaction seem to be of particular interest. First, there is the analogy with the electron case in which the corresponding interaction is well defined and may be considered as not containing a direct interaction. Second, one might use regulators with the additional condition $\Sigma c_i\ln m_i=0$ for a contact free interaction. One then does not need a direct interaction term (55). The amount of contact interaction is $\Sigma c_i\ln m_i=0$ (see also footnote 24). Further investigation of these points may show that the two definitions proposed here are actually identical.

[27] The coupling of the electromagnetic field A_μ to the bare particles by replacing p_μ by $p_\mu-A_\mu$ is a requirement of gauge-invariance. Since the whole proof is based on this fact, the cancellation of the renormalizations can therefore be thought of as a consequence of gauge-invariance.

Summing over all possible insertions of $A_\mu^e(0)$ we find with (A3) and (A5),

$$\Lambda_\mu^*(p, p) = -\partial\Sigma^*(p)/\partial p_\mu. \quad \text{(A6)}$$

If Σ^* is of order n', Λ_μ^* will be of the same order. We now assume that all primitive divergent parts of lower order have been properly replaced by their finite parts, such that $\Sigma^{*(n')}$ and $\Lambda_\mu^{*(n')}$ are primitive divergent effective diagrams, i.e., they will contain effective lines and corners. Therefore, a separation of the form (50c) is possible and since $L_{\mu e}^*(p, p)\psi = 0$ by definition we find

$$e^{n'} L^{(n')} C_\mu(p, p) = -\partial\Sigma^*(p)/\partial p_\mu. \quad \text{(A7)}$$

It is to be noted here that we have not excluded the action of the electromagnetic field in closed loops, but that these contributions vanish by Furry's theorem, for the even number of corners of the loops in Σ^* becomes odd by the action of A_μ^e. Therefore (A7) gives correctly the spurious charge renormalization of the diagrams *c* of Fig. 4.

Repeating this insertion process we find from a separation of the form (50d) of the primitive divergent diagram of type (5) (Compton effect and related phenomena) $\Omega_{\mu\nu}^{*(n')}(p, p)$ since $O_{\mu\nu}^{*(n')}(p, p) = 0$

$$2e^{n'} O^{(n')} C_{\mu\nu} = -\partial\Lambda_\mu^{*(n')}(p, p)/\partial p_\nu = \partial^2\Sigma^{*(n')}(p)/\partial p_\mu \partial p_\nu. \quad \text{(A8)}$$

From (A5), (A7), and (A8) it follows therefore that

$$O^{(n')} = L^{(n')}. \quad \text{(A9)}$$

Clearly, if $C_{\mu\nu} = 0$, $O^{(n')}$ does not exist and the processes of type (5) are convergent. $O^{(n')}$ is the spurious charge renormalization arising from the diagrams of Fig. 5*e*.

Let $\Sigma^{*(n')}(p')$ be an effective, but primitive divergent diagram. Then the separation (50a) is valid and the diagrams 4*a* and *b* give

$$C_\mu(p', p')S(p')\Sigma^{*(n')}(p') = e^{n'} C_\mu(p', p')(A^{(n')} S(p) + B^{(n')} + S_e^{(n')}(p')). \quad \text{(A10)}$$

The first term will be canceled by the mass renormalization which can be written

$$e^{n'} C_\mu(p', p')S(p')\Sigma^{*(n')}(p),$$

where p_μ, in contradiction to p_μ', satisfies (A1). We subtract it from (A10) and expand $\Sigma^{*(n')}(p')$ near p. Comparing the infinite terms on both sides we find for the wave function renormalization constant

$$e^{n'} B^{(n')} = S(p')[\partial\Sigma^{*(n')}(p)/\partial p_\lambda](p_\lambda' - p_\lambda).$$

This yields with (A7) and the identity (A5) as we pass to the limit $p_\mu' \to p_\mu$

$$B^{(n')} + L^{(n')} = 0. \quad \text{(A11)}$$

Equation (A11) expresses the identical cancellation of the infinities arising from Figs. 4*a*, *b*, and *c*. It is to be noted that the wave function renormalization constant for each of the diagrams 4*a* and *b* is only $\frac{1}{2}B^{(n')}$ since it is associated with the outgoing source line which is shared by the next scattering process.

On calculating the wave function renormalization for the diagrams of type (5) (Figs. 5*c* and *d*) we observe that one simply has to replace $C_\mu(p', p')$ of (A10) by $2C_{\mu\nu}$ and one finds from (A11) and (A9)

$$B^{(n')} + O^{(n')} = 0 \quad \text{(A12)}$$

which expresses the identical cancellation of the divergencies of Figs. 5*c*, *d*, and *e*.

It may be remarked that (A12) can be concluded from (A11) alone since the requirement of gauge invariance connects the fundamental single corner and double corner parts of the Hamiltonian (2), and a consistent charge renormalization procedure has to yield $(e+\delta e)^2$ in front of the latter if it yields $e+\delta e$ in front of the former. The above proof, however, is not based on the consistency of the charge renormalization procedure.[28]

APPENDIX II. ON THE ASYMPTOTIC BEHAVIOR OF PRIMITIVE DIVERGENT INTEGRALS

Consider a primitive divergent integral which involves an integration over a single internal momentum t only. Assume that auxiliary variables $x, y, \cdots$ are used to combine the denominators[5] of a single-corner diagram. The integral will be of the form

$$\int dxdy\cdots d_4 t P_n(t, p^i)/[(t - \Sigma a_j p^j)^2 + b^2]^F, \quad \text{(A13)}$$

where F is the number of internal lines, n the number of corners, and $P_n(t, p^i)$ a polynomial of order n in t whose terms are of the form $(p^i)^{r+s}$ with $r+s \leqslant n$. The α_j are polynomials in $x, y, \cdots$ and b^2 is quadratic in all the p^i with coefficients which are polynomials in $x, y, \cdots$. If we use regulators we are permitted to shift the variable $t \to t + \Sigma\alpha_j p^j$. The result of the t integration will, for any of the p^i large, behave as $(p^i)^{n-2F+4}$. From (34c) and the fact that only diagrams with $n \geqslant E$ can diverge $n - 2F + 4 \leqslant 4 - E$. Comparison with (40) shows that (A13) diverges for large p^i at most as the t integration itself. The same result can be derived for integrals with more than one t integration. Therefore the convergent functions introduced in (50) behave asymptotically as follows: $S_e \sim O(1)$, $D_e \sim O(1)$, $L_{\mu e} \sim O(p)$, $O_{\mu\nu} \sim O(1)$, $M_e \sim O(1)$, where $O(1)$ may imply a logarithmic dependence. This justifies the interpretation as smearing-out functions [as given following Eq. (52)] and it proves that diagrams with effective lines and corners diverge in the same way as those with ordinary lines and corners.

[28] For spin $\frac{1}{2}$ such a proof to second order was first given by R. P. Feynman, reference 5, p. 778. Also for spin $\frac{1}{2}$ and based on the charge renormalization procedure a proof was given by J. C. Ward, Phys. Rev. 78, 182 (1950).

On the Hall Effect in Ferromagnetics

EMERSON M. PUGH, N. ROSTOKER, AND A. SCHINDLER
Carnegie Institute of Technology, Pittsburgh, Pennsylvania
(Received May 22, 1950)

With precise measurements at magnetic fields well above those required for saturation, it is shown that the Hall electric field per unit current density consists of two distinct parts. Its value averaged between poles is given by R_0H+R_1M, where H and M are the magnetizing force and average intensity of magnetization, respectively. in the sample.

The value $R_0=-0.611\times10^{-12}$ volt-cm/amp.-oersted indicates 1.16 s-band electrons with no d-band conduction, 0.6 s-band electrons with 30 percent d-band conduction, or something intermediate between these two.

The value $R_1=-74.9\times10^{-12}$ volt-cm/amp.-oersted suggests the existence of a very large average magnetic field acting on the conduction electrons. An explanation for this is suggested.

I. INTRODUCTION

IT has long been known[1] that the Hall electromotive force in practically all of the ferromagnetic materials is directly proportional, at low magnetic fields, to the intensity of magnetization, M. The accuracy with which the Hall e.m.f. follows this rule is very high; for example, when measurements are made while the M of the material is carried around a hysteresis loop,[2] the measured e.m.f.'s follow curved loops when plotted against either H or B, but follow precise straight lines when plotted against M.

Following a suggestion of Smith and Sears[3] one of us proposed[4] that for ferromagnetics the Hall relation should be written as:

$$e_H=-E_H/ib=R_0H+R_1M, \qquad (1)$$

where E_H=the Hall e.m.f., e_H=Hall electric field per unit current density, i=the current density in the ferromagnetic, b=the width of the plate between the Hall probes, and H=the magnetic field which in a thin plate perpendicular to the field is given by $H=B-4\pi M$, B being the magnetic induction.

R_0 and R_1 are Hall coefficients and $|R_1|\gg|R_0|$ in most ferromagnetic materials. R_0 is too small to be easily detectable in bars of ferromagnetics shaped to facilitate simultaneous magnetic and Hall e.m.f. measurements.

Using the more conventional plate-shaped samples of nickel, which are more suitable for high field measurements, it has been shown that the Hall e.m.f. does increase in fields beyond those required for saturation and is linear with H in this region. Furthermore, the slope of this straight line of E_H *versus* H is close to the slope predicted by theory. Figure 1 shows a plot of E_H *versus* H measured in an annealed plate of 99.6 percent pure nickel at 28.5, 20.3, and 14.3°C. The experimental points taken at fields well above those required to saturate the nickel fall quite accurately on a straight line whose slope determines the value of R_0. The intercept of this line with the $H=0$ axis, together with the separately determined saturation magnetization of the nickel, determines the value of R_1. At 20.3°C these values, when corrected for the Ettingshausen effect, are $R_0=-0.611\times10^{-12}$ volt-cm/amp.-oersted and $R_1=-74.9\times10^{-12}$ volt-cm/amp.-oersted. In Fig. 2 values of R_1 are plotted as a function of temperature over the small range of temperatures for which they have been determined. Over the observed range of temperatures there is no significant variation of R_0 with temperature, while R_1 appears to increase rather rapidly with increasing temperature.

In 1910 Smith[5] published a rather complete study of the Hall effect in nickel over a wide range of temperatures, which agrees as well as could be expected with the results reported here. Since he did not measure the saturation magnetization of his samples as a function of temperature and since he did not employ very high fields, it is impossible to calculate reliable values of R_0 and R_1 from his data. This is especially true in the neighborhood of the Curie temperature where the saturation magnetization needs to be known with great accuracy. Nevertheless, R_0 and R_1 have been calculated from Smith's data by using accepted values for the magnetic properties of nickel and these are plotted in Fig. 3. If the behavior in the immediate neighborhood of the Curie temperature is ignored, R_0 remains constant while R_1 increases with temperature. It is particularly noteworthy that R_0 is the same above the Curie temperature as below. This is just what should be expected, since R_0 should be the ordinary Hall coefficient depending chiefly upon the number of conduction carriers (electrons and holes), which should not change with temperature. Experimentally, then, the Hall effect in ferromagnetics separates into two distinct phenomena which can be analyzed separately. The two effects will be called ordinary (proportional to H) and extraordinary (proportional to M) to distinguish them from the terms "normal" and "abnormal," which have so often been used to designate negative and positive Hall coefficients, respectively.

[1] A. Kundt, Wied. Ann. 49, 257 (1893).
[2] E. M. Pugh and T. W. Lippert, Phys. Rev. 42, 709 (1932).
[3] A. W. Smith and R. W. Sears, Phys. Rev. 34, 1466 (1929).
[4] E. M. Pugh, Phys. Rev. 36, 1503 (1930).
[5] A. W. Smith, Phys. Rev. 30, 1 (1910).

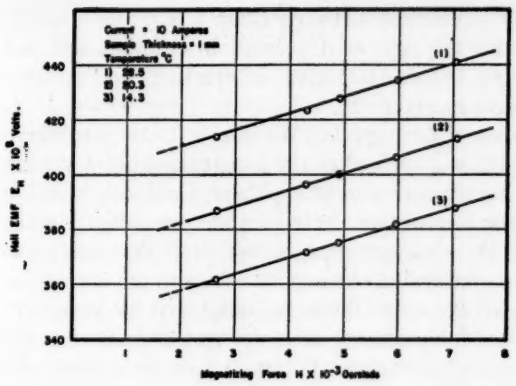

FIG. 1. Hall electromotive force in a magnetically saturated sample of nickel.

II. EXTRAORDINARY EFFECT

The extraordinary Hall e.m.f. is the one which is usually measured, since it is obtainable at low fields with relatively insensitive instrumentsThe coefficient R_1 is far too large to agree with generally accepted theories. To obtain a better understanding of this effect one must take the modern domain theory of magnetization into consideration. According to this theory, a current passing through a ferromagnetic material is passing through domains that are magnetized to saturation at all times. When the measured value of magnetization is less than the saturation value, the domains are oriented in different directions. Under these circumstances the Hall electric field per unit current in each domain is given by an expression of the form:

$$\mathbf{e}_H = R_1 \mathbf{m} \times \mathbf{i}, \tag{2}$$

where $\mathbf{m}$=vector intensity of magnetization in the domain, R_1=a constant which is the same for each domain, and $\mathbf{i}$=vector current density assumed to be of unit magnitude and parallel to the x-axis. A rectangular parallelopiped as shown in Fig. 4 is employed and E_H is measured between probes located at $(x, 0, z)$ and (x, b, z). The current density $\mathbf{i}$ is assumed to be uniform and parallel to the x-axis. The macroscopically

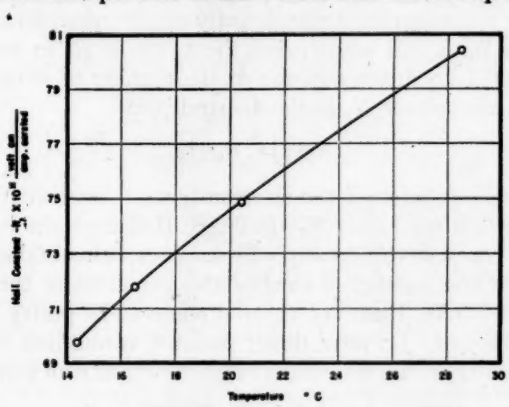

FIG. 2. Temperature dependence of extraordinary Hall constant R_1 in nickel.

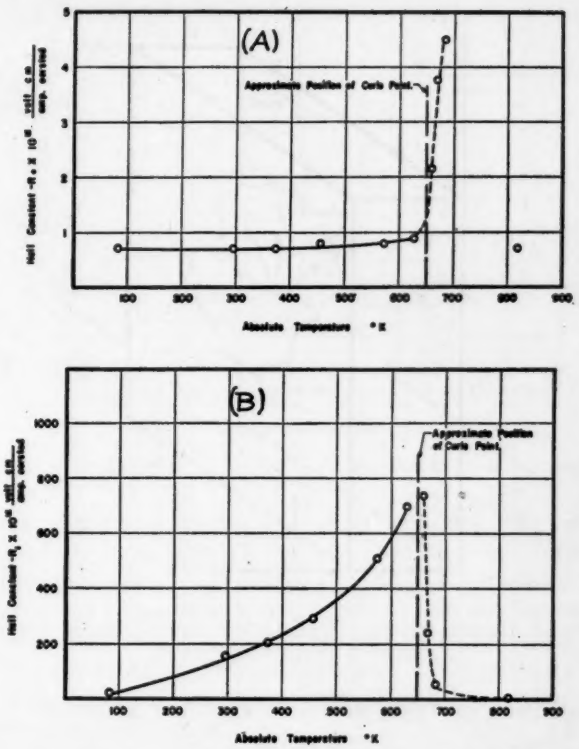

FIG. 3. (A) Temperature dependence of ordinary Hall constant R_0 in nickel (calculated from data of A. W. Smith). (B) Temperature dependence of extraordinary Hall constant R_1 in nickel (calculated from data of A. W. Smith).

measured M is parallel to the z-axis and is the average of the z-component of $\mathbf{m}$. For convenience this average may be taken along a line parallel to the y-axis; thus

$$M = (1/b)\int_0^b (\mathbf{m}\cdot\mathbf{k})dy.$$

M is assumed to be uniform throughout the specimen in the sense that it has the same value when averaged over any volume whose dimensions are small compared with the dimensions of the block, but large compared with the dimensions of the domains.

The average Hall electric field e_H is given by

$$e_H = (1/b)\int_0^b \mathbf{e}_H\cdot\mathbf{j}dy = (R_1/b)\int_0^b (\mathbf{m}\times\mathbf{i})\cdot\mathbf{j}dy,$$

and since $(\mathbf{m}\times\mathbf{i})\cdot\mathbf{j} = (\mathbf{i}\times\mathbf{j})\cdot\mathbf{m} = \mathbf{k}\cdot\mathbf{m}$, it may be expressed in terms of M as

$$e_H = -E_H/b = R_1 M. \tag{3}$$

Although the Hall effect is of different direction and magnitude in each domain, the resultant macroscopic effect is proportional to the intensity of magnetization, and the result would be the same if the magnetization were regarded as a simple uniform field in the z direction. Furthermore the macroscopic Hall constant is the same as the Hall constant for the domains.

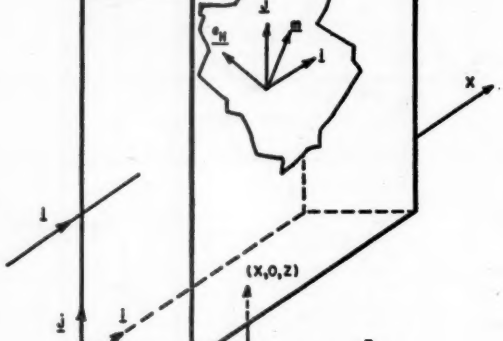

FIG. 4. Domain structure in Hall effect sample (relative size of domain is greatly exaggerated).

The complete expression for $\mathbf{e}_H$ in the domain is

$$\mathbf{e}_H=(R_0\mathbf{H}+R_1\mathbf{m})\times\mathbf{i}. \tag{2.1}$$

This leads to the following expression for the observable Hall e.m.f.:

$$E_H=-ibR_0[H+4\pi\alpha M], \quad \alpha=R_1/4\pi R_0. \tag{4}$$

Equation (2) for the Hall effect in domains is what would be expected on the basis of Lorentz forces acting on conduction electrons; and, since this leads to the correct empirical formula (1) for the observed Hall effect with the same macroscopic Hall constants, it is probable that conduction electrons in domains are subjected to a Lorentz magnetic force-field $\mathbf{H}+4\pi\alpha\mathbf{m}$. The effective uniform field acting on conduction electrons would be

$$h=H+4\pi\alpha M. \tag{5}$$

The most recent work on effective Lorentz force-fields acting on charged particles has been carried out by Wannier[6] in connection with the deflection of beams of cosmic-ray particles by a ferromagnetic medium whose magnetism is due to electron spins. Wannier finds that the effective uniform Lorentz field for a beam of high velocity charged particles is

$$h=H+2\pi(p+1)M, \tag{6}$$

where p is the probability of coincidence of beam particles and "magnetic" electrons compared to the random probability of such coincidences. (By random probability is meant the coincidence probability of beam particles and magnetic electrons in the absence of any interaction between them.) Wannier considered in detail the case of Coulomb interaction and found that $p>1$ for attractive interaction and $p<1$ for repulsive interaction.

Webster[7] first applied Wannier's ideas to conduction electrons and arrived at the conclusion that p should be very nearly zero due to repulsive Coulomb interaction between conduction electrons and "magnetic" electrons. There is no assurance, however, that Webster's speculations concerning conduction electrons are correct, since many of the approximations employed by Wannier are doubtful for particles of energy as low as the energy of conduction electrons. This fact has been pointed out by Wannier.

The experimental evidence from the Hall effect in nickel indicates that $p=2\alpha-1$ must be considerably greater than unity. Values of the field parameter α from the extraordinary Hall effect are shown in Fig. 5. It is difficult to understand how α can attain such large values on the basis of Wannier's analysis for beams of negative particles or Webster's considerations of conduction electrons. However, from the work of previous investigators it may be concluded that for p to be greater than unity there must be a correlation in position between the conduction electrons and the locations of strong magnetic fields that is more than random. It is likely that there is such a correlation between the conduction electrons and "magnetic" holes characteristic of ferromagnetics. This type of process appears to offer the only possibility of explaining the unusually large value of the field parameter α within existing framework of concepts.

No attempt will be made in this paper to explain quantitatively the large value of α. However, experimental and theoretical researches are being carried on which will appear in forthcoming papers.

III. ORDINARY EFFECT

The ordinary Hall e.m.f. is measured at magnetic fields well above those required to saturate the material, and is expressed by the first term of Eqs. (1) or (4). It is generally supposed[8] that in nickel the 3*d*-band does not contribute significantly to electrical conduction. With this assumption the value of R_0 in nickel should be a direct measure of the number of electrons per unit volume N_s in the 4*s*-band; i.e.,

$$N_s=|1/R_0ec|,$$

where e=charge of the electron (e.s.u.), c=velocity of light (cm/sec.), and R_0=ordinary Hall constant (stat-volt-cm/stat-volt-oersted). From the experimental value of R_0, the number of electrons n_s per atom in the 4*s*-band is 1.16. However, $n_s=0.6$ seems to be pretty well established.[9] Its most direct measure is obtained from the value of the saturation magnetization, which yields

[6] G. H. Wannier, Phys. Rev. 72, 304 (1947). (Wannier uses the symbol b in place of h.)

[7] D. L. Webster, Am. J. Phys. 14, 360 (1946).

[8] N. F. Mott, Proc. Roy. Soc. A153, 699 (1935–6).

[9] N. F. Mott, Proc. Phys. Soc. London 47, 571 (1935).

0.6 Bohr magnetons per atom of nickel. Ferromagnetism results from exchange forces which align as many as possible of the spins of the 3*d* electrons parallel to the field, the balance being antiparallel. If n_p and n_a are the number per atom of 3*d* electrons whose spins are aligned with the field parallel and antiparallel, respectively, then $n_p-n_a=0.6$. Then, since $n_s+n_p+n_a=10$ for nickel and since it is assumed that $n_p=5$, $n_s=0.6$. The assumption that $n_p=5$ is made because calculations[9] indicate that the parallel half of the 3*d* should be full. However, if this assumption is eliminated and instead the Hall effect measurements are taken at face value, then there are three equations for the three unknowns n_s, n_p, and n_a. For nickel these are

$$n_s+n_p+n_a=10, \quad n_p-n_a=0.6, \quad n_s=1.16. \qquad (7)$$

The solution of these equations gives $n_p=4.72$ and $n_a=4.12$. However, there is another possible explanation of the experimental results obtained here.

The above explanation assumed that the 3*d*-band does not contribute significantly to the electrical conduction. Let us suppose that the 3*d*-band does contribute to the conduction and that $n_p-n_a=0.6=n_s$. The total conductivity $\sigma=\sigma_d+\sigma_s$, where σ_d and σ_s are the conductivities due to the 3*d*- and 4*s*-bands, respectively. Since the *d*-band is nearly full, its conductivity is caused by holes and should contribute a positive Hall e.m.f., whereas the *s*-band should contribute a negative Hall e.m.f. This could account for the small observed value of R_0. Under these circumstances its value is given by:

$$R_0=-\frac{n_d\sigma_s^2-n_s\sigma_d^2}{n_dn_s\sigma^2}\frac{1}{Nec}=\frac{-1}{n_s'Nec}. \qquad (8)$$

(N = the number of atoms per unit volume),

where n_d is the number of holes per atom in the 3*d*-band and n_s' (=1.16 in nickel) is the apparent number of electrons in the conduction band as measured by the Hall effect. Solving (8) gives

$n_s=n_s'[(\sigma_s^2/\sigma^2)-(n_s\sigma_d^2/n_d\sigma^2)]$ or, since $n_s=n_d$,
$n_s=n_s'(\sigma_s-\sigma_d)/\sigma$.

Putting $n_s=0.6$ and $n_s'=1.16$ gives $\sigma_d/\sigma_s=0.3$.

IV. CONCLUSIONS

(1). The Hall effect in nickel has been separated into two terms, the "ordinary" Hall effect caused by a uniform field (the magnetizing force) and the "extraordinary" Hall effect due to magnetization. The empirical expression (Eq. 1) for the Hall effect satisfies the requirements of the domain theory of ferromagnetism if the Hall effect is due to Lorentz type magnetic forces where the average Lorentz magnetic force-field is $h=H+4\pi\alpha M$. This appears to be the only possible explanation of the experimental facts at present although it is conceivable that other types of forces may also contribute to the Hall effect in nickel. The surprisingly large value of the field parameter α is interpreted as being due to strong correlation between the positions of conduction electrons and the locations of very high magnetic fields identified with the *d*-band "magnetic" holes. The reason for this strong correlation is the effectively attractive interaction between *s*-band electrons and *d*-band holes.

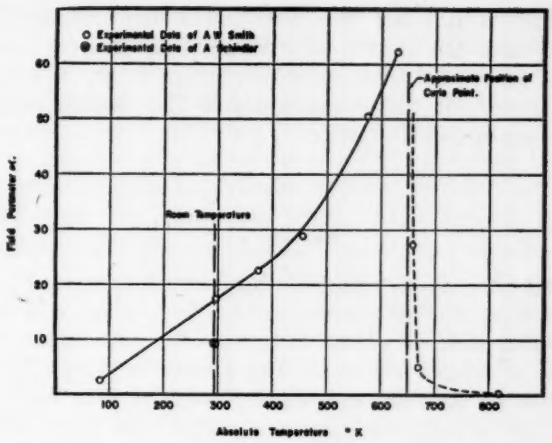

FIG. 5. Temperature dependence of field parameter α in nickel.

(2). The "ordinary" Hall effect involves a Hall constant R_0 which corresponds closely to the Hall constant of the conventional theory of Hall effect due to a uniform magnetic field. As such it should be a measure of the number of conduction particles. There is a relatively small but real discrepancy between the number of *s*-band electrons predicted by the measured value of R_0 and the generally accepted value. Two distinct interpretations have been suggested.

(a) One interpretation assumes that the conduction by holes is negligible. The numbers of electrons in the *s*- and *d*-bands are then calculated by means of Eq. (7). From the experimental value of R_0 we obtain $n_s=1.16$ for the *s*-band, and $n_p=4.72$, $n_a=4.12$ for the *d*-band. Since the Hall effect measurements were made at room temperature and the magnetization at room temperature differs from that at 0°K only by a factor of the order of 0.96, this calculation would be approximately correct for room temperature.

The parallel *d*-band in nickel is generally regarded as being filled at low temperatures. It follows that there must be 0.6 electrons per atom in the *s*-band. Although there must be a change in the distribution of parallel and antiparallel spin electrons in the *d*-band at higher temperatures, it seems highly improbable that there would be as large a change in the numbers of electrons in the *s*- and *d*-bands as indicated by the above calculations at the temperatures and field strengths associated with these Hall effect measurements. It is thus clear that the above interpretation of the ordinary Hall constant R_0 is at variance with established concepts.

(b) The other interpretation assumes that the parallel

d-band is full but the hole conduction cannot be neglected. The experimental value of R_0 then requires that $\sigma_d/\sigma_s=0.3$. According to existing theory of conductivity[8] for temperatures above the characteristic temperature of the lattice

$$\frac{\sigma_d}{\sigma_s}=\frac{m_s\tau_d}{m_d\tau_s}, \tag{9}$$

where m_s = effective mass of s-band electrons, m_d = effective mass of d-band electrons (absolute value), τ_s = relaxation time of s-band electrons, and τ_d = relaxation time of d-band electrons. The specific heat measurements of Keesom and Clark[10] indicate that $m_s/m_d \cong 1/28$, which would give $\tau_d/\tau_s \cong 8$. No physically significant calculations have yet been given for τ_d/τ_s, but it is plausible that $\tau_d > \tau_s$ because of the low velocity of d-band electrons relative to the velocity of s-band electrons.

[10] W. H. Keesom and C. W. Clark, Physica **2**, 513 (1935).

Of the two possible interpretations of the experimental value of R_0, the latter, in which the negative Hall effect from s-band conduction is counteracted by the positive Hall effect due to hole conduction, appears to be the most likely alternative. The result $\sigma_d/\sigma_s=0.3$ does not appear to contradict any existing experimental evidence. It is believed that this is the only quantitative evaluation of the conductivity ratio that has been attempted. Furthermore, it is necessary that $\sigma_d/\sigma_s>1$ for Co and Fe to produce the observed positive Hall effects, unless some agency entirely different from hole conduction is responsible for these positive Hall effects.

It is expected that a clearer understanding of the hole conduction will be achieved with the completion of measurements of R_0 and R_1 that are now being carried out on the Ni—Cu and the Ni—Co series of alloys.

The authors are grateful for helpful discussions with a number of individuals including F. Seitz and G. Wannier and to the International Nickel Company for supplying the nickel samples.

PHYSICAL REVIEW VOLUME 80, NUMBER 4 NOVEMBER 15, 1950

Magneto-Hydrodynamic Shocks*

F. DE HOFFMANN AND E. TELLER
Los Alamos Scientific Laboratory, Los Alamos, New Mexico

(Received July 10, 1950)

A mathematical treatment of the coupled motion of hydrodynamic flow and electromagnetic fields is given. Two simplifying assumptions are introduced: first, the conductivity of the medium is infinite, and second, the motion is described by a plane shock wave. Various orientations of the plane of the shock and the magnetic field are discussed separately, and the extreme relativistic and unrelativistic behavior is examined. Special consideration is given to the behavior of weak shocks, that is, of sound waves. It is interesting to note that the waves degenerate into common sound waves and into common electromagnetic waves in the extreme cases of very weak and very strong magnetic fields.

I. INTRODUCTION

IT has been shown recently that the interaction between hydrodynamic motion and magnetic fields in a conducting liquid is of importance in problems of astrophysics, geophysics, and the behavior of interstellar gas masses.[1] The non-linear character of the hydrodynamic equations raises difficulties in the treatment of these problems. So far only the linear problem of sound propagation has been treated[2] and this one only for a transverse wave propagating along the lines of force. It is the purpose of the following investigation to clarify the behavior of plane waves in magneto-hydrodynamics. The non-linear case of shock waves will be of primary interest and the simpler behavior of sound waves will be obtained by considering shocks of small amplitude. Two special cases of magneto-hydrodynamic waves are well known in physics. One is the hydrodynamic shock and the other the pure electromagnetic wave. It will be clear from the formalism which we are going to develop that these can be obtained from the magneto-hydrodynamic shock as limiting cases. In order to permit a treatment of waves which are similar to electromagnetic waves we shall need to discuss shock velocities which are close to the velocity of light. We therefore must include a relativistic treatment.

In order to limit ourselves to the simplest possible case we shall make the assumption that the conductivity is infinite. One consequence of this assumption is that the self-induction will prevent a change in the magnetic fields if the substance carrying the magnetic field is at rest. Actually the conductivity is finite. However, the

* This document is based on work performed at Los Alamos Scientific Laboratory of the University of California under the auspices of the AEC.

[1] H. Alfvén, Arkiv. f. Mat. Astron. Fysik **29A**, 12 (1943). E. C. Bullard, Proc. Roy. Soc. A **197**, 433 (1949)—See this paper for additional bibliography. E. Fermi, Phys. Rev. **75**, 1169 (1949). C. Walen, Arkiv. f. Mat. Astron. Fysik **30A**, 15 (1944).

[2] H. Alfvén, Arkiv. f. Mat. Astron. Fysik **29B**, 2 (1943).

time in which magnetic fields can change appreciably is proportional to the conductivity times the square of the linear dimensions of the system under consideration. In the applications to cosmic problems the linear dimension is usually so great that changes of the magnetic field in a system at rest are effectively excluded even if the conductivity is moderate. Thus the case of infinite conductivity will furnish us with a good model of the situations of interest.

If the conducting liquid is in motion it can flow freely along the magnetic lines of force without affecting the latter. If, on the other hand, material streams in a direction perpendicular to the lines of force, these will behave as though they were firmly attached to the fluid. This can be seen by the following qualitative argument. Consider an imaginary closed path which moves along with the liquid. Since the conductivity is infinite, the e.m.f. along this path must at all times be zero. It follows that the magnetic flux enclosed by the closed path is time independent. Since this statement holds for any closed path, it follows that no sidewise shift of magnetic lines with respect to the fluid is possible.

It also follows from the above assumption that the electric fields vanish in a coordinate system that is at rest in the liquid. The vector $\mathfrak{D}$ will vanish in the same system and it is unnecessary to introduce the dielectric constant. As a further simplification we shall assume $\mathfrak{H}=\mathfrak{B}$ so that only the six vector $\mathcal{E}$, $\mathfrak{H}$ is needed to describe the electromagnetic field.

While most of the derivations will refer to a general equation of state of matter, we shall be interested in particular in the case in which the fluid is an ideal gas for which γ, the ratio of specific heats at constant volume to constant pressure, is a fixed number. This is a satisfactory approximation for the equation of state within stars and for interstellar gases. In the latter case the effective value of γ may depend on the presence of dust and on the question of whether or not equilibrium with radiation is established.

II. LONGITUDINAL AND TRANSVERSE SHOCKS

In normal shock hydrodynamics it is proved that the motion in a shock proceeds perpendicularly to the shock front. We shall see later that in magneto-hydrodynamics this is no longer necessarily so. When treating shocks whose direction of propagation is parallel or perpendicular to the magnetic force lines, one obtains solutions of the shock equations if one assumes that all motion is parallel to the direction of shock propagation. These shocks we shall call longitudinal shocks. In addition we shall consider discontinuities in which the motion of material is along the surface of discontinuity (and therefore perpendicular to the direction of propagation). These are transverse shocks. These transverse shocks have in normal hydrodynamics a propagation velocity equal to zero and are there called slipstreams rather than shocks. In magneto-hydrodynamics transverse shocks have a finite propagation velocity if the magnetic field is perpendicular to the shock front; the propagation velocity of transverse waves is zero (as in normal hydrodynamics) when the magnetic field is parallel to the shock front. All this will be proved later.

In the case of a transverse shock the magnetic lines of force will have in general a different direction before and after the shock has passed and therefore the expression "transverse shock" does not apply in a strict sense. The only case in which this expression may be applied is that of a weak transverse shock, i.e., in transverse sound propagation, in which case the magnetic lines are only slightly different in direction before and after the passage of the wave. These are in fact the magneto-hydrodynamic waves discussed by Alfvén[2] and they possess the velocity $\mathfrak{H}/(4\pi\rho)^{\frac{1}{2}}$. It will be observed that for a vanishing magnetic field this velocity goes to zero. We shall not treat this transverse sound wave in detail here because its properties will be obtained by appropriate specialization from the oblique shock equation.

In the following Sections III and IV we discuss the longitudinal shocks for the cases of shock propagation parallel and perpendicular to $\mathfrak{H}$. The discussion of oblique shocks in which the terms transverse and longitudinal motion do not apply directly will be reserved for a final Section V.

III. PARALLEL SHOCKS

We shall assume that the shock propagates in the x direction, i.e., that its plane is the $y-z$ plane. The magnetic fields have components only along the x direction. It is easy to see that in this case the hydrodynamic motion is not coupled to the magnetic field and the shock proceeds as in ordinary hydrodynamics. We give a detailed discussion, however, in order to introduce the proper relativistic terminology. There are two kinds of coordinate systems which are relevant:

(a) *The co-moving systems:* These systems are those in which the observer is at rest relative to the medium on the one or other side of the shock. They will be denoted by a prime. Owing to the infinite value of the conductivity all electric fields vanish in the primed systems.

(b) *The shock system:* This system is one in which the observer is at rest relative to the shock front and will be denoted by unprimed letters. Viewed from this coordinate system the flow will appear time-independent.

We denote the two regions on either side of the shock by 1 and 2, respectively. In the region 1 the flow velocity v_1 will be directed toward the shock plane; in region 2 the velocity v_2 is directed away from that plane.

According to the definition of the parallel shock all components of the magnetic fields vanish with the exception of[3] $\mathfrak{H}_{1,x}'$ and $\mathfrak{H}_{2,x}'$. By a Lorentz transforma-

[3] The index 1 or 2 will always appear at the bottom of the quantity it qualifies as the first subscript. It is separated from the symbols of the coordinates (x, y, z, t, or in general n) by a comma. If no index 1 or 2 appears the formula applies to both 1 and 2.

tion we find

$$\left.\begin{array}{llll}\mathcal{E}_{1,x}=0 & \mathcal{H}_{1,x}=\mathcal{H}_{1,x}' \\ \mathcal{E}_{1,y}=0 & \mathcal{H}_{1,y}=0 \\ \mathcal{E}_{1,z}=0 & \mathcal{H}_{1,z}=0\end{array}\right\}, \tag{1}$$

and

$$\left.\begin{array}{llll}\mathcal{E}_{2,x}=0 & \mathcal{H}_{2,x}=\mathcal{H}_{2,x}' \\ \mathcal{E}_{2,y}=0 & \mathcal{H}_{2,y}=0 \\ \mathcal{E}_{2,z}=0 & \mathcal{H}_{2,z}=0\end{array}\right\}. \tag{2}$$

Furthermore, $\mathrm{div}\mathcal{H}=0$, so that

$$\mathcal{H}_{1,x}=\mathcal{H}_{2,x}. \tag{3}$$

We see that on the boundary $\mathrm{curl}\mathcal{E}$ vanishes and hence $\partial\mathcal{H}/\partial t=0$ as was to be expected.

In order to set up the relativistic shock equations we define the quantity η' as the relativistic energy density for the primed system:

$$\eta' c^2=n'(m_0' c^2+E'), \tag{4}$$

where n' is the density of particles, m_0' the average rest mass, and E' the excess energy per particle over and above the rest energy. We shall restrict the discussion to fluids. For these the energy momentum stress tensor has a particularly simple form in the primed system: only the diagonal components T_{nn}' differ from zero.

$$T_{xx}'=p'-(\mathcal{H}_x')^2/8\pi, \tag{5}$$

$$T_{yy}'=T_{zz}'=p'+(\mathcal{H}_x')^2/8\pi, \tag{6}$$

$$T_{tt}'=\eta'+(\mathcal{H}_x')^2/8\pi c^2, \tag{7}$$

where p' is the pressure in the co-moving system.

If one performs the Lorentz transformation to the shock system which moves with a velocity v relative to the primed system, he obtains for the tensor:

$$T=\begin{vmatrix} \dfrac{\eta' v^2+p'}{1-(v^2/c^2)}-\dfrac{(\mathcal{H}_x')^2}{8\pi} & 0 & 0 & \dfrac{-[v\eta'+(v/c^2)p']}{1-(v^2/c^2)} \\ 0 & p'+\dfrac{(\mathcal{H}_x')^2}{8\pi} & 0 & 0 \\ 0 & 0 & p'+\dfrac{(\mathcal{H}_x')^2}{8\pi} & 0 \\ \dfrac{-[v\eta'+(v/c^2)p']}{1-(v^2/c^2)} & 0 & 0 & \dfrac{\eta'+(v^2/c^4)p'}{1-(v^2/c^2)}+\dfrac{(\mathcal{H}_x')^2}{8\pi c^2} \end{vmatrix}. \tag{8}$$

Equation (8) will hold on both sides of the shock; i.e., all quantities should be given the subscript 1 or all quantities the subscript 2.

One group of shock equations is obtained from the fact that the four-dimensional divergence of T vanishes:

$$\mathrm{div}T=0. \tag{9}$$

Since the flow depends only on the x coordinate, we know that $\partial/\partial y$ and $\partial/\partial z$ are zero and since the shock system is stationary, $\partial/\partial t$ is zero. Thus $\partial T_{xx}/\partial x=0$ and $\partial T_{xt}/\partial x=0$ and in general all components T_{xn} are independent of x. This statement continues to hold across the shock discontinuity, since it must hold in any approximation in which the shock is replaced by an increasingly steep but continuous change of the physical variables. We therefore find that the xx components of the tensors T_1 and T_2 are equal and similarly the xt components of these tensors are equal. Recalling that

$$\mathcal{H}_{1,x}'=\mathcal{H}_{2,x}' \tag{10}$$

we obtain

$$(\eta_1' v_1^2+p_1)/(1-v_1^2/c^2)=(\eta_2' v_2^2+p_2)/(1-v_2^2/c^2) \tag{11}$$

and

$$\left(\eta_1' v_1+\frac{v_1}{c^2}p_1'\right)\Big/\left(1-\frac{v_1^2}{c^2}\right)=\left(\eta_2' v_2+\frac{v_2}{c^2}p_2'\right)\Big/\left(1-\frac{v_2^2}{c^2}\right). \tag{12}$$

An additional shock equation is obtained from the conservation of particles; i.e., the number of particles arriving and leaving per unit time must be equal:

$$n_1 v_1=n_2 v_2. \tag{13}$$

This may be written in the co-moving systems as

$$n_1' v_1(1-v_1^2/c^2)^{-\frac{1}{2}}=n_2' v_2(1-v_2^2/c^2)^{-\frac{1}{2}}. \tag{14}$$

Equations (11)–(13) do not contain[4] $\mathcal{H}$. It is easy to see that these equations reduce to the Rankine-Hugoniot equations in the non-relativistic approximation. In fact, (14) reduces to the equation of conservation of mass. Neglecting v^2/c^2 and replacing η' by nm_0 in (11) one obtains the unrelativistic equation for the conservation

[4] They are the same equations as have been derived by A. H. Taub, Phys. Rev. 74, 328 (1948), for relativistic shocks, with a slightly different notation.

of momenta. The leading term in (12) is identical with (14). If one expands (12) in powers of v^2/c^2, subtracts (14), and substitutes from (4), the leading terms in the difference give

$$c^{-2}[\tfrac{1}{2}n_1m_0v_1^3+n_1E_1+p_1v_1] = c^{-2}[\tfrac{1}{2}n_2m_0v_2^3+n_2E_2+p_2v_2]. \quad (15)$$

This is the Rankine-Hugoniot equation expressing conservation of energy.

IV. PERPENDICULAR SHOCK

The shock again propagates in the x direction and owing to the infinite value of the conductivity all electric fields vanish in the primed systems. According to the definition of the perpendicular shock all components of the magnetic fields vanish with the exception of $\mathfrak{H}_{1,y}'$.

By a Lorentz transformation we find

$$\left.\begin{array}{ll} \mathcal{E}_{1,x}=0 & \mathfrak{H}_{1,x}=0 \\ \mathcal{E}_{1,y}=0 & \mathfrak{H}_{1,y}=\dfrac{\mathfrak{H}_{1,y}'}{[1-(v_1/c)^2]^{\frac{1}{2}}} \\ \mathcal{E}_{1,z}=\dfrac{(v_1/c)\mathfrak{H}_{1,y}'}{[1-(v_1/c)^2]^{\frac{1}{2}}} & \mathfrak{H}_{1,z}=0 \end{array}\right\}. \quad (16)$$

$$T=\begin{vmatrix} \dfrac{\eta'v^2+p'+[(\mathfrak{H}_y')^2/8\pi][1+(v^2/c^2)]}{1-(v^2/c^2)} & 0 & 0 & \dfrac{-[v\eta'+(v/c^2)p'+(v/c^2)(\mathfrak{H}_y')^2/4\pi]}{1-(v^2/c^2)} \\ 0 & p'-\dfrac{(\mathfrak{H}_y')^2}{8\pi} & 0 & 0 \\ 0 & 0 & p'+\dfrac{(\mathfrak{H}_y')^2}{8\pi} & 0 \\ \dfrac{-[v\eta'+(v/c^2)p'+(v/c^2)(\mathfrak{H}_y')^2/4\pi]}{1-(v^2/c^2)} & 0 & 0 & \dfrac{\eta'+(v^2/c^4)p'+[(\mathfrak{H}_y')^2/8\pi c^2][1+(v^2/c^2)]}{1-(v^2/c^2)} \end{vmatrix}. \quad (23)$$

We introduce the energy density η in the unprimed system

$$\eta=\eta'/[1-(v/c)^2] \quad (24)$$

and define the auxiliary quantity

$$p=p'/[1-(v/c)^2]. \quad (25)$$

To simplify the notation for the remainder of this section we set $\mathfrak{H}=\mathfrak{H}_y$, $\mathfrak{H}'=\mathfrak{H}_y'$. Making use of (16) we get

$$\mathfrak{H}=\mathfrak{H}'/[1-(v/c)^2]. \quad (26)$$

Thus, in analogy to the treatment presented for the parallel shock, Eq. (23) with the use of Eqs. (24) through (26) yields

$$\eta_1v_1^2+p_1+(\mathfrak{H}_1^2/8\pi)=\eta_2v_2^2+p_2+(\mathfrak{H}_2^2/8\pi) \quad (27)$$

$$\eta_1v_1+(v_1p_1/c^2)+(v_1\mathfrak{H}_1^2/c^24\pi) = \eta_2v_2+(v_2p_2/c^2)+(v_2\mathfrak{H}_2^2/c^24\pi). \quad (28)$$

$\mathfrak{H}_{1,y}$ and $\mathfrak{H}_{2,y}$ are related by virtue of the fact that we have assumed the magnetic force lines to be attached to the particles. Thus, the density of magnetic force lines is proportional to the density of particles and we have

$$\mathfrak{H}_{1,y}'/n_1'=\mathfrak{H}_{2,y}'/n_2' \quad (17)$$

or since

$$n_1'=n_1[1-(v_1/c)^2]^{\frac{1}{2}}, \quad (18)$$

it follows that

$$\mathfrak{H}_{1,y}/n_1=\mathfrak{H}_{2,y}/n_2. \quad (19)$$

Equation (19) is merely a special case of the general statement that the density of magnetic lines of force divided by the density of particles in a perpendicular shock will retain the same value in all coordinate systems. Furthermore because of Eq. (13)

$$\mathfrak{H}_{1,y}v_1=\mathfrak{H}_{2,y}v_2. \quad (20)$$

Finally, since

$$\mathcal{E}_{2,z}=(v_2/c)\mathfrak{H}_{2,y}, \quad (21)$$

we have

$$\mathcal{E}_{2,z}=\mathcal{E}_{1,z}, \quad (22)$$

so that in the shock system curl$\mathcal{E}=0$ at the boundary, which yields $\partial\mathfrak{H}/\partial t=0$ as expected.

The energy-momentum tensor follows from (16) as:

RELATIVISTIC IDEAL GAS

The first use we shall make of these equations will be to derive the sound velocity for a monoatomic gas in the extreme relativistic case. We must, therefore, find the relevant equation of state. For a relativistic gas we may write

$$\eta'c^2=A\int[P^2c^2+m_0^2c^4]^{\frac{1}{2}}P^2dP \times\exp[-(P^2c^2+m_0^2c^4)^{\frac{1}{2}}/kT], \quad (29)$$

$$p'=\frac{Ac^2}{3}\int\frac{P^4dP}{(P^2c^2+m_0^2c^4)^{\frac{1}{2}}} \times\exp[-(P^2c^2+m_0^2c^4)^{\frac{1}{2}}/kT], \quad (30)$$

where P is a momentum and A a normalization constant. In the extreme relativistic case

$$kT\gg m_0c^2, \quad P^2c^2\gg m_0^2c^4 \quad (31)$$

and Eqs. (29) and (30) are related by

$$\eta' c^2 = 3p' \tag{32}$$

and also using (24) and (25)

$$\eta c^2 = 3p. \tag{33}$$

Since we are interested in the sound velocity, the quantities in Eqs. (27) and (28) carrying subscripts 1 and 2 differ by infinitesimal amounts. If we take the differences of the two sides of these two equations and divide by $v_2 - v_1 = dv$, we get using (33)

$$\frac{d}{dv}\left[\eta v^2 + \frac{\eta c^2}{3} + \frac{\mathfrak{M}^2}{8\pi}\right] = 0 \tag{34}$$

$$\frac{d}{dv}\left[\frac{4}{3}\eta v + \frac{v}{c^2}\frac{\mathfrak{M}^2}{4\pi}\right] = 0. \tag{35}$$

Similarly, from (20)

$$d(\mathfrak{M}v)/dv = 0. \tag{36}$$

Using the last four equations and eliminating η, $d\eta/dv$, $d\mathfrak{M}/dv$ as well as re-introducing p' and $\mathfrak{M}'$ we find

$$(3v^2 - c^2)/(c^2 - v^2) = r, \tag{37}$$

where

$$r = 9(\mathfrak{M}')^2/16\pi\eta' c^2. \tag{38}$$

Thus, when $\mathfrak{M}' = 0$, i.e. there is no applied magnetic field, the sound velocity is

$$v = c/\sqrt{3}. \tag{39}$$

When $\mathfrak{M}' \to \infty$, then

$$v \approx c. \tag{40}$$

At intermediate values of $\mathfrak{M}$ we find

$$v = c[(1+r)/(3+r)]^{\frac{1}{2}}. \tag{41}$$

Equation (40) shows that the sound velocity becomes equal to the light velocity when the contribution of matter to the energy momentum tension tensor becomes relatively unimportant. This agrees with expectation. One may find it surprising that in the absence of a magnetic field the sound velocity[5] is $c/\sqrt{3}$ while the velocity of the particles in the extreme relativistic case is equal to c. The reason is that in the random thermal motion the particles move obliquely in the propagating wave.

THE LIMITING CASE $v \to c$

We have seen above that, in the special case of an extremely relativistic equation of state, v is equal to c in the case $\mathfrak{M}' \to \infty$. We shall now investigate the conditions necessary for $v \to c$.

First we shall assume that $v_1 \approx c$ and $v_2 \approx c$. Making use of the contraction

$$\mu = (1 - v^2/c^2)^{-\frac{1}{2}} \tag{42}$$

we thus wish to examine the case $\mu_1 \gg 1$; $\mu_2 \gg 1$. In the approximation $v_1 = v_2$ Eq. (14) reduces to

$$n_1'\mu_1 = n_2'\mu_2. \tag{43}$$

Similarly, Eq. (20) becomes $\mathfrak{M}_1 = \mathfrak{M}_2$ or

$$\mathfrak{M}_1'\mu_1 = \mathfrak{M}_2'\mu_2. \tag{44}$$

Equations (27) and (28) then reduce to the same statement, namely,

$$\eta_1 c^2 + p_1 = \eta_2 c^2 + p_2. \tag{45}$$

Multiplying (28) by $-c$, adding (27), and retaining terms of the order $(c - v_1)$, $(c - v_2)$, and $(\mathfrak{M}_1 - \mathfrak{M}_2)$ one obtains

$$\left.\begin{aligned} -\eta_1 c^2\left(1 - \frac{v_1}{c}\right) + p_1\left(1 - \frac{v_1}{c}\right) + \frac{\mathfrak{M}_1^2}{8\pi} - \frac{v_1\mathfrak{M}_1^2}{4\pi c} \\ = -\eta_2 c^2\left(1 - \frac{v_2}{c}\right) + p_2\left(1 - \frac{v_2}{c}\right) + \frac{\mathfrak{M}_2^2}{8\pi} - \frac{v_2\mathfrak{M}_2^2}{4\pi c} \end{aligned}\right\}. \tag{46}$$

Using the approximation

$$\mu^2 \approx \tfrac{1}{2}(1 - v/c)^{-1} \tag{47}$$

and the equation

$$\frac{H_1^2}{8\pi} - \frac{v_1\mathfrak{M}_1^2}{4\pi c} = \left(1 - \frac{v_1}{c}\right)^2 \frac{\mathfrak{M}_1^2}{8\pi} - \frac{v_1^2\mathfrak{M}_1^2}{8\pi c^2}. \tag{48}$$

Equation (46) can be written as

$$\frac{-\eta_1 c^2}{(\mu_1)^2} + \frac{p_1}{(\mu_1)^2} + \frac{\mathfrak{M}_1^2}{16\pi(\mu_1)^4} = \frac{-\eta_2 c^2}{(\mu_2)^2} + \frac{p_2}{(\mu_2)^2} + \frac{\mathfrak{M}_2^2}{16\pi(\mu_2)^4}. \tag{49}$$

Equations (45) and (49) can be written as

$$(\mu_1)^2\eta_1' c^2 + (\mu_1)^2 p_1' = (\mu_2)^2\eta_2' c^2 + (\mu_2)^2 p_2', \tag{50}$$

$$-\eta_1' c^2 + p_1' + (\mathfrak{M}_1')^2/16\pi(\mu_1)^2 = -\eta_2' c^2 + p_2' + (\mathfrak{M}_2')^2/16\pi(\mu_2)^2. \tag{51}$$

Examine now Eqs. (50) and (51) for the special case of a weak shock (sound velocity). In particular, we shall investigate whether $v \approx c$ is consistent with the presence of a cold ideal gas (i.e., non-relativistic equation of state of the matter). Then

$$\eta' c^2 = n' m_0 c^2 + (3n'kT/2) \tag{52}$$

$$p' = n'kT. \tag{53}$$

Hence our equations become

$$d(n'\mu)/d\mu = 0 \tag{54}$$

$$d(\mathfrak{M}'\mu)/d\mu = 0 \tag{55}$$

$$\frac{d}{d\mu}\mu^2\left(n' m_0 c^2 + \frac{5}{2}n'kT\right) = 0 \tag{56}$$

$$\frac{d}{d\mu}\left[-\left(n' m_0 c^2 + \frac{1}{2}n'kT\right) + \frac{(\mathfrak{M}')^2}{16\pi\mu^2}\right] = 0. \tag{57}$$

[5] A. R. Curtis, Proc. Roy. Soc. **A200**, 248 (1950).

Since for our unrelativistic equation of state $kT \ll m_0$, we find that (54) and (56) yield

$$n' m_0 c^2 + \frac{5}{2}\mu n' \frac{d(kT)}{d\mu} = 0. \tag{58}$$

From (54), (55), and (57) it follows that

$$n' m_0 c^2 - \tfrac{1}{2}\mu n' [d(kT)/d\mu] - [(\mathfrak{H}')^2/4\pi\mu^2] = 0. \tag{59}$$

Eliminating $d(kT)/d\mu$ from (58) and (59) one obtains

$$(\mathfrak{H}')^2/8\pi = 3\mu^2 n' m_0 c^2/5. \tag{60}$$

Thus it is seen that for $v \approx c$ there is indeed a possibility that the material stays cold provided the magnetic energy is considerably greater than the rest energy. Equations (60) and (41) show that the sound velocity approaches light velocity for both the unrelativistic and the relativistic ideal gas, provided that the magnetic energy density becomes large compared with the material energy density.

We shall now enquire in greater generality whether the case of a predominant magnetic field will indeed have as a consequence that the propagation velocity is close to the velocity of light. We assume that $(1-v_1/c)$ is not small compared with unity and we shall show that (except for quite peculiar equations of state) this is incompatible with the assumption that $\mathfrak{H}^2/8\pi$ is large compared with the material energy density.

If the magnetic terms dominate comparison of (20), (27) and (28) shows that $v_1 \approx v_2$ and $\mathfrak{H}_1 \approx \mathfrak{H}_2$. If in addition $(1-v_1/c) \ll 1$ and also $\mu^2 \gg 1$ do not hold, it follows that

$$\left.\begin{aligned} v &= \tfrac{1}{2}(v_1+v_2) \approx v_1 \approx v_2 \\ \mu^2 &= \tfrac{1}{2}(\mu_1^2+\mu_2^2) \approx \mu_1^2 \approx \mu_2^2 \\ \mathfrak{H} &= \tfrac{1}{2}(\mathfrak{H}_1+\mathfrak{H}_2) \approx \mathfrak{H}_1 \approx \mathfrak{H}_2. \end{aligned}\right\} \tag{61}$$

Equations (13), (20), (27), and (28) can be written in powers of the quantities $\Delta v = v_1 - v_2$, $\Delta\eta = \eta_1 - \eta_2$, $\Delta p = p_1 - p_2$ and $\Delta\mathfrak{H} = \mathfrak{H}_1 - \mathfrak{H}_2$ as follows:

$$\mathfrak{H}\Delta v + v\Delta\mathfrak{H} = 0 \tag{62}$$

$$v^2\Delta\eta + v(\eta_1+\eta_2)\Delta v + \tfrac{1}{4}\Delta\eta(\Delta v)^2 + \Delta p + (\mathfrak{H}\Delta\mathfrak{H}/4\pi) = 0 \tag{63}$$

$$\left.\begin{aligned} v\Delta\eta + \frac{\eta_1+\eta_2}{2}\Delta v + \frac{v}{c^2}\Delta p + \frac{(p_1+p_2)}{2c^2}\Delta v \\ + \frac{v\mathfrak{H}\Delta\mathfrak{H}}{4\pi c^2} + \frac{\Delta v(\Delta\mathfrak{H})^2}{16\pi c^2} = 0 \end{aligned}\right\}. \tag{64}$$

Multiplying (64) by v and subtracting from (63) we get

$$\frac{\Delta p}{\mu^2} + \frac{\mathfrak{H}\Delta\mathfrak{H}}{4\pi\mu^2} = \frac{v\Delta v}{2c^2}\left\{-(\eta_1+\eta_2)c^2 + (p_1+p_2) + \frac{(\Delta\mathfrak{H})^2}{8\pi}\right\} - \frac{\Delta\eta}{4}(\Delta v)^2. \tag{65}$$

The last term on the right-hand side is of higher order and may be neglected. The first term can be transformed with the help of (62)

$$\frac{v\Delta v}{2c^2}\left\{-(\eta_1+\eta_2)c^2 + (p_1+p_2) + \frac{(\Delta\mathfrak{H})^2}{8\pi}\right\} = -\frac{\mathfrak{H}\Delta\mathfrak{H}}{2}\left(\frac{v^2}{c^2}\right)\left\{\frac{-(\eta_1+\eta_2)c^2 + (p_1+p_2) + (\Delta\mathfrak{H})^2/8\pi}{\mathfrak{H}^2}\right\}. \tag{66}$$

The bracket on the right-hand side of (66) is small compared with unity. Thus all of the right-hand side of (65) is negligible and one obtains

$$\Delta p = -\mathfrak{H}\Delta\mathfrak{H}/4\pi. \tag{67}$$

Next (63) will be multiplied by (v/c^2) and subtracted from (64)

$$\frac{v\Delta\eta}{\mu^2} = -\frac{\Delta v}{2c^2}\left\{(\eta_1+\eta_2)(c^2-2v^2) + (p_1+p_2) + \frac{(\Delta\mathfrak{H})^2}{8\pi}\right\} + \frac{v(\Delta v)^2}{4c^2}\Delta\eta. \tag{68}$$

The last term on the right-hand side of (68) is small compared with the left hand side and will be neglected. Transforming the first term in a manner similar to (66) and using (67) leads to the result

$$c^2\Delta\eta = -\tfrac{1}{2}\mu^2\Delta p + \left\{\frac{(\eta_1+\eta_2)(c^2-2v^2) + (p_1+p_2) + (\Delta\mathfrak{H})^2/8\pi}{(\mathfrak{H}^2/4\pi)}\right\}. \tag{69}$$

It is seen from (69) that

$$c^2|\Delta\eta| \ll |\Delta p|. \tag{70}$$

Dividing by μ one has

$$c^2|\Delta\eta'| \ll |\Delta p'|. \tag{71}$$

Condition (71) does not seem to be in direct contradiction to any general law but it requires a somewhat peculiar equation of state. For the extreme relativistic ideal gas Eq. (32) states that $c^2\Delta\eta' = 3\Delta p'$, which contradicts (71). In general, using (4), and introducing

$$\left.\begin{aligned} n' &= \tfrac{1}{2}(n_1'+n_2') \approx n_1' \approx n_2' \\ \Delta n' &= n_1' - n_2' \\ \Delta E' &= E_1' - E_2' \end{aligned}\right\} \tag{72}$$

we get

$$c^2\Delta\eta' = [m_0c^2 + \tfrac{1}{2}(E_1'+E_2')]\Delta n' + n'\Delta E'. \tag{73}$$

With the help of (41), (62), and (67) the quantity $\Delta n'$ can be expressed in terms of $\Delta p'$.

$$c^2\Delta\eta' = -\frac{\mu^2 n'[m_0c^2 + \tfrac{1}{2}(E_1'+E_2')]}{[(\mathfrak{H}')^2/4\pi]}\Delta p' + n'\Delta E'. \tag{74}$$

Here the coefficient of $\Delta p'$ is small compared with unity and it follows from (74) and (71) that

$$n'|\Delta E'|\ll|\Delta p'|. \tag{75}$$

Remembering that $(\Delta n'/n')\ll 1$ and applying (71) to the non-relativistic case one sees that we are indeed led to this strange conclusion: The particle density changes little and the energy density (exclusive of rest energy) changes by a negligible amount compared to the change in pressure. This is not absurd but quite unusual.

Thus for the extreme relativistic ideal gas and for most non-relativistic equations of state one may conclude that $(1-v_1/c)\ll 1$ is not compatible with predominance of magnetic field energies. It seems the rule that the propagation velocity of the shock approaches c as $(\mathfrak{C}')^2/8\pi$ becomes the leading term in the energy density.

NON-RELATIVISTIC PERPENDICULAR SHOCK

Equation (27) may be written as

$$\frac{n_1'(m_0'+E_1'/c^2)v_1^2+p_1'+(\mathfrak{C}_1')^2/8\pi}{1-(v_1/c)^2} = \frac{n_2'(m_0'+E_2'/c^2)v_2^2+p_2'+(\mathfrak{C}_2')^2/8\pi}{1-(v_2/c)^2}. \tag{76}$$

To obtain the non-relativistic approximation we neglect all terms containing c^{-2}. Setting the material density

$$\rho'=n'm_0' \tag{77}$$

and dropping the primes for simplicity in the non-relativistic case we get the equation

$$p_1+\rho_1v_1^2+(\mathfrak{C}_1)^2/8\pi=p_2+\rho_2v_2^2+(\mathfrak{C}_2)^2/8\pi, \tag{78}$$

which expresses conservation of momentum.

If in Eq. (28) all terms containing c^{-2} should be dropped, the result would be identical with the conservation of matter, Eq. (13),

$$\rho_1v_1=\rho_2v_2. \tag{79}$$

Expanding (14) and (28) in powers of v^2/c^2 and subtracting the highest remaining terms gives the non-relativistic approximation to the energy equation

$$E_1\rho_1v_1+\tfrac{1}{2}\rho_1v_1^3+p_1v_1+v_1(\mathfrak{C}_1)^2/4\pi = E_2\rho_2v_2+\tfrac{1}{2}\rho_2v_2^3+p_2v_2+v_2(\mathfrak{C}_2)^2/4\pi. \tag{80}$$

We may derive the sound velocity in this case from Eqs. (78) and (80). By reasoning analogous to that presented in obtaining Eqs. (34) and (35) we find that

$$(dp/dv)+2\rho_0v+(v^2d\rho_0/dv)-(\mathfrak{C})^2/4\pi v=0 \tag{81}$$

$$\rho_0v+v^2d\rho_0/dv=0 \tag{82}$$

and hence

$$v=\left(\frac{dp/dv}{d\rho_0/dv}+\frac{\mathfrak{C}^2}{4\pi\rho_0}\right)^{+\frac{1}{2}} \tag{83}$$

which reduces to the familiar expression for the sound velocity in case the magnetic field vanishes. In case the magnetic field dominates, (83) reduces to

$$v=\mathfrak{C}/(4\pi\rho_0)^{\frac{1}{2}}. \tag{84}$$

This formula for the sound velocity looks like the Alfvén velocity. This agreement is fortuitous. The derivation of the Alfvén velocity is given later under the section treating the oblique shock.

Equations (78) and (80) can be simplified by the substitutions

$$p_1^*=p_1+(\mathfrak{C}_1)^2/8\pi \tag{85}$$

$$E_1^*=E_1+(\mathfrak{C}_1)^2/8\pi\rho_1 \tag{86}$$

with analogous equations for p_2^* and E_2^*. In fact, the quantities p^* and E^* are the sums of material and magnetic pressures and energies.

Equations (78) and (80) then become the familiar Rankine-Hugoniot equations with p and E replaced by their respective starred quantities which include the appropriate electromagnetic contribution. A solution of these equations yields the familiar shock equations.

$$v_1-v_2=\left[(p_2^*-p_1^*)\left(\frac{1}{\rho_1}-\frac{1}{\rho_2}\right)\right]^{\frac{1}{2}} \tag{87}$$

$$E_2^*-E_1^*=\left(\frac{1}{\rho_1}-\frac{1}{\rho_2}\right)\left(\frac{p_1^*+p_2^*}{2}\right). \tag{88}$$

IDEAL GAS

Let us now specialize the previous section for the case of an ideal gas; i.e., let

$$E=p/(\gamma-1)\rho. \tag{89}$$

Here γ satisfies the inequality $1<\gamma\leqslant 3/5$. Using (17) we define the constant

$$\nu=\mathfrak{C}_1/\rho_1=\mathfrak{C}_2/\rho_2. \tag{90}$$

Then we may verify that the following relation holds between E^* and p^*:

$$E^*=\frac{p^*}{(\gamma-1)\rho}+\frac{(\gamma-2)}{(\gamma-1)}\frac{\rho\nu^2}{8\pi}. \tag{91}$$

Substituting (91) into (88) we find

$$p_2^*\left[\frac{1}{2\rho_1}-\frac{1}{2\rho_2}-\frac{1}{(\gamma-1)\rho_2}\right]-p_1^*\left[\frac{1}{2\rho_2}-\frac{1}{2\rho_1}-\frac{1}{(\gamma-1)\rho_1}\right] = \frac{\nu^2}{8\pi}\frac{(\gamma-2)}{(\gamma-1)}(\rho_2-\rho_1). \tag{92}$$

In ordinary shock hydrodynamics of an ideal gas for $\rho_2>\rho_1$ it follows that $p_2>p_1$ and $(\rho_2/\rho_1)<(\gamma+1)/(\gamma-1)$. Thus $(\gamma+1)/(\gamma-1)$ is the maximum compression obtainable. Similar relations are true in magneto-

hydrodynamic shocks. For this purpose we set

$$\alpha=(\gamma+1)/(\gamma-1) \tag{93}$$

$$\beta=-\left(\frac{\nu^2}{4\pi}\right)\frac{\gamma-2}{\gamma-1}. \tag{94}$$

We note that $\alpha>1$ and that for the case of interest to us, namely, $\gamma<2$, the expression $\beta>0$. Equation (92) may then be written as

$$p_2^*\left[\frac{\alpha}{\rho_2}-\frac{1}{\rho_1}\right]-p_1^*\left[\frac{\alpha}{\rho_1}-\frac{1}{\rho_2}\right]=\beta(\rho_2-\rho_1). \tag{95}$$

Assuming $(\rho_2-\rho_1)>0$ we see that $(\alpha/\rho_1-1/\rho_2)>0$ and therefore from (95), $(\alpha/\rho_2-1/\rho_1)>0$ or

$$(\rho_2/\rho_1)<\alpha=(\gamma+1)/(\gamma-1). \tag{96}$$

Since, furthermore, $(\alpha/\rho_2)-(1/\rho_1)<(\alpha/\rho_1)-(1/\rho_2)$ follows from $\rho_2>\rho_1$, it can be further seen from (95) that $p_2^*>p_1^*$.

STABILITY AND CHANGE OF ENTROPY

We shall now investigate whether a compressive shock $\rho_2>\rho_1$ is thermodynamically stable, i.e., whether the entropy increases in a compressive shock. For this purpose plot p_2^* against $1/\rho_2$ for given p_1^* and ρ_1 as indicated in Fig. 1. We introduce the notation $1/\rho=x$. Point 1 represents the initial condition of the gas. Then we draw the locus of all possible shocks with 1 as the initial point. Examples of such points are k and l. Let these be infinitesimally close. Now consider the difference dS of entropy between points k and l. This is given by

$$dS=dQ/T, \tag{97}$$

where dQ is the heat added to get from k to l:

$$dQ=E_l^*-E_k^*+p_k^*(x_l-x_k) \tag{98}$$

but from Eq. (88)

$$E_l^*-E_k^*=\tfrac{1}{2}(p_l^*-p_k^*)(x_1-x_k) -\tfrac{1}{2}(p_1^*+p_k^*)(x_l-x_k) \tag{99}$$

so that

$$dQ=\tfrac{1}{2}[(p_l^*-p_k^*)(x_1-x_k)+(p_k^*-p_1^*)(x_l-x_k)]. \tag{100}$$

Consider now a move from point k to point l. Then (x_l-x_k) is negative and dp_2^* is positive. Moreover, *if* the curve is everywhere concave then

$$(x_1-x_k)/(p_k^*-p_1^*)>(x_k-x_l)/(p_l^*-p_k^*) \tag{101}$$

so that dQ_2 and hence dS is positive. If now we consider another point j, then we can repeat the argument for this point. Thus eventually we can by differential regression arrive at point 1. Hence point l has higher entropy than point 1 provided that the curve is concave throughout. This argument is analogous to the usual argument in hydrodynamics, except that of course E^* is replaced by E and p^* by p.

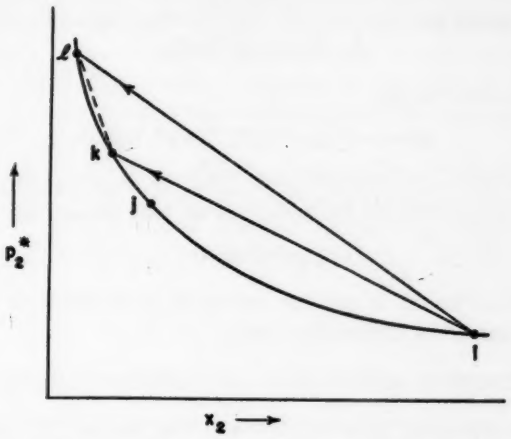

FIG. 1. The pressure p_2^* *versus* $1/\rho_2$ in a compressive shock.

We shall now prove that indeed for an ideal gas a plot of p_2^* *vs.* x_2 is concave throughout. From Eq. (95) we find

$$\frac{d^2p_2^*}{dx_2^2}=\frac{2\alpha(\alpha p_2^*+p_1^*)}{(\alpha x_2-x_1)^2} +\frac{2\beta}{x_2^2}\left\{\frac{\alpha}{(\alpha x_2-x_1)^2}+\frac{1}{x_2(\alpha x_2-x_1)}\right\}. \tag{102}$$

However, Eq. (96) shows that in general $(x_1/x_2)<\alpha$, so that $(\alpha x_2-x_1)>0$. Hence $d^2p_2^*/dx_2^2>0$ at all points and thus the entropy indeed increases in a compressive shock for an ideal gas.

In the limiting case of sound waves the entropy tends to zero. It is of interest to investigate the entropy change for weak shocks.[6] Let the entropy S and the inverse density x be the independent variables and expand E_2^* and p_2^* in powers of $\Delta x=x_2-x_1$, and $\Delta S=S_2-S_1$. Then

$$E_2^*=E_1^*+(\partial E^*/\partial x)_S\Delta x+\tfrac{1}{2}(\partial^2E^*/\partial x^2)_S(\Delta x)^2 +\tfrac{1}{6}(\partial^2E^*/\partial x^3)_S(\Delta x)^3+(\partial E^*/\partial S)_{\Delta x}\Delta S+\cdots. \tag{103}$$

Since we have seen that E^* plays the role of the actual total energy and p^* of the pressure, we have from thermodynamics:

$$(\partial E^*/\partial x)_S=-p^* \tag{104}$$

and

$$(\partial E^*/\partial S)_x=T. \tag{105}$$

We can see this in a more formal way by recalling that

$$E^*=E+(\nu^2/8\pi x) \tag{106}$$

$$p^*=p+(\nu^2/8\pi x^2) \tag{107}$$

and carrying out the indicated differentiations in (104) and (105) and using (87) we find

$$\tfrac{1}{6}(\partial^2p^*/\partial x^2)_S(\Delta x)^2-T_1\Delta S/\Delta x =\tfrac{1}{4}(\partial^2p^*/\partial x^2)_S(\Delta x)^2+\tfrac{1}{2}(\partial p^*/\partial S)_x\Delta S. \tag{108}$$

[6] This derivation for the case of conventional hydrodynamics is given in a private communication by R. W. Goranson, entitled "Seminar Notes," dated May 13, 1949.

For small Δx

$$T_1/\Delta x \gg \tfrac{1}{2}(\partial p^*/\partial S)_s \tag{109}$$

holds and we get

$$\Delta S = -[(\Delta x)^3/12T_1](\partial^2 p^*/\partial x^2)_S. \tag{110}$$

Now for a compressive wave $(\Delta x)^3$ is negative and for the special case of the ideal gas we have shown that

$$d^2p_2^*/dx^2 > 0 \tag{111}$$

so that the ΔS is positive, which is in accord with the general proof previously given.

ENERGY DISSIPATION IN A STRONG SHOCK

In ordinary hydrodynamics strong shocks transform a considerable portion of the kinetic energy into heat. It is of interest to determine whether in the presence of a magnetic field this continues to be true or whether the magnetic field can act as a sort of cushion producing elastic recoil where normal hydrodynamics would predict a strongly inelastic collision. For the sake of simplicity only transverse shocks are considered.

Let us therefore investigate whether the following assumptions are consistent. First, we have a strong shock, i.e., the relation $|v_1-v_2| \ll |v_1|$ does not hold, and second,

$$\left.\begin{aligned} E_1 &\ll \rho_1 v_1^2 \\ p_1 &\ll \rho_1^2 v_1^2 \end{aligned}\right\} \tag{112}$$

and

$$\left.\begin{aligned} E_2 &\ll \rho_2 v_2^2 \\ p_2 &\ll \rho_2^2 v_2^2 \end{aligned}\right\}. \tag{113}$$

Now we make use of these assumptions in (78) and (80) and obtain

$$\rho_1 v_1^2 + (\mathfrak{H}_1)^2/4\pi = \rho_2 v_2^2 + (\mathfrak{H}_2)^2/4\pi \tag{114}$$

$$\tfrac{1}{2}\rho_1 v_1^3 + (\mathfrak{H}_1)^2 v_1/8\pi = \tfrac{1}{2}\rho_2 v_2^3 + (\mathfrak{H}_2)^2 v_2^2/8\pi. \tag{115}$$

Let us, in accordance with (13), set

$$M = \rho_1 v_1 = \rho_2 v_2 \tag{116}$$

and divide (114) and (115) by M^2. Then, using (90)

$$\frac{1}{M}(v_1 - v_2) = \frac{\nu^2}{8\pi}\left(\frac{1}{v_1^2} - \frac{1}{v_2^2}\right) \tag{117}$$

$$\frac{1}{2M}(v_1^2 - v_2^2) = \frac{\nu^2}{4\pi}\left(\frac{1}{v_2} - \frac{1}{v_1}\right). \tag{118}$$

We note that in (117) and (118) the pressure and internal energy terms are neglected as compared with terms containing difference of velocities. This is justified because according to the definition of a strong shock (v_1-v_2) is not very much less than v_1 and hence the differences retained in (117) and (118) are not small.

Dividing now (118) into (117) we find

$$\frac{2}{v_1+v_2} = \frac{1}{2}\left(\frac{1}{v_1} + \frac{1}{v_2}\right) \tag{119}$$

or

$$4 = 2 + (v_1/v_2) + (v_2/v_1). \tag{120}$$

Equation (120) is satisfied only if $v_1 = v_2$; i.e., for sound velocity and *not* for a strong shock. Thus the assumptions (112) and (113) require $|v_1-v_2| \ll v_1$ and the magnetic field does not provide the cushioning effect.

V. OBLIQUE SHOCK

In order to simplify the treatment of the oblique shock we shall introduce a convenient coordinate system. Consider first the co-moving system on side 1 of the shock. As usual we shall denote the quantities in this system by primes. Thus $\mathcal{E}_{1,x}' = \mathcal{E}_{1,y}' = \mathcal{E}_{1,z}' = 0$. Further we choose our coordinate system such that the shock front is perpendicular to the x axis and the y axis is so oriented as to make $\mathfrak{H}_1'$ lie in the xy plane. In consequence $\mathfrak{H}_{1,z}' = 0$. We shall assume obliquity of the shock so that $\mathfrak{H}_{1,x}' \neq 0$ and $\mathfrak{H}_{1,y}' \neq 0$. Now make a transformation to a system in which the shock is stationary and whose velocity relative to the primed system is parallel to the magnetic lines of force.[7] This "shock system" will be denoted by unprimed symbols. In particular then

$$\mathfrak{H}_{1,x}/\mathfrak{H}_{1,y} = v_{1,x}/v_{1,y} = \phi_1. \tag{121}$$

Since $\mathbf{v}_1$ and $\mathfrak{H}_1$ are parallel, it follows that

$$\mathcal{E}_{1,x} = \mathcal{E}_{1,y} = \mathcal{E}_{1,z} = 0. \tag{122}$$

Because $\mathfrak{H}_1$ lies in the xy plane, we find $\mathfrak{H}_{1,z} = 0$ and $v_{1,z} = 0$. Since our transformation is such that the translation is along the lines of force, the direction or magnitude of the magnetic field does not change, i.e.,

$$\mathfrak{H}_{1,x} = \mathfrak{H}_{1,x}' \neq 0, \quad \mathfrak{H}_{1,y} = \mathfrak{H}_{1,y}' \neq 0. \tag{123}$$

In order to find the electromagnetic fields on the other side of the shock we note that the equation $\operatorname{div}\mathfrak{H} = 0$ becomes

$$\mathfrak{H}_{1,x} = \mathfrak{H}_{2,x} \neq 0. \tag{124}$$

The particular simplicity of our coordinate system lies in the fact that

$$\mathcal{E}_{2,x} = \mathcal{E}_{2,y} = \mathcal{E}_{2,z} = 0. \tag{125}$$

This can be seen as follows. Consider the co-moving system for side 2. In this system $\mathcal{E}_2' = 0$ and hence $\mathcal{E}_2' \cdot \mathfrak{H}_2' = 0$. Since the quantity $\mathcal{E} \cdot \mathfrak{H}$ is a relativistic invariant, we find $\mathcal{E}_2 \cdot \mathfrak{H}_2 = 0$. Thus $\mathcal{E}_2$ is perpendicular to $\mathfrak{H}_2$. Furthermore, the shock system is stationary so that $\dot{\mathfrak{H}} = 0$ and hence $\operatorname{curl}\mathcal{E} = 0$ at the shock front. Since

[7] It should be noted that such a transformation obviously cannot be made for the limiting case of the perpendicular shock. In the latter case the magnetic lines of force are perpendicular to the x direction and thus along the shock front. Hence no motion along the shock front can bring the shock front to rest.

$\mathcal{E}_1=0$, it follows that $\mathcal{E}_2$ is perpendicular to the shock front. Considering $\mathfrak{C}_{2,x}\neq 0$, the vector $\mathcal{E}_2$ cannot be perpendicular to both the shock front and the magnetic field. We must therefore (as stated in (125)) set $\mathcal{E}_2=0$. In order that no electric fields arise on side 2 because of the transformation from the primed to the unprimed system, $\mathbf{v}_2$ must be parallel to $\mathfrak{C}_2$.

$$\mathfrak{C}_{2,z}/\mathfrak{C}_{2,y}=v_{2,z}/v_{2,y}=\phi_2, \tag{126}$$

$$\mathfrak{C}_{2,z}/\mathfrak{C}_{2,y}=v_{2,z}/v_{2,y}=\phi_3. \tag{127}$$

The picture obtained in our particular coordinate system is the following. The shock is stationary. Material streams in from one side and out on the other. The streamlines are oblique to the shock front. One expects that the streamlines are refracted in the shock front. They are everywhere parallel to the magnetic lines of force which, therefore, are similarly refracted. It is known that no oblique shocks are possible in an isotropic medium in the absence of magnetic fields because the shock front can transfer momentum to the streaming material only in a direction perpendicular to the front. The refraction of magnetic lines makes this type of momentum transfer possible.

To obtain the quantitative effect of this momentum transfer we now evaluate the T_{xn} components of the energy momentum tensor. For the system with a velocity v relative to the co-moving system one finds

$$T_{xx}=p'+(v_x^2/c^2)\mu^2(p'+c^2\eta')+(\mathfrak{C}^2/8\pi)-(\mathfrak{C}_x)^2/4\pi \tag{128}$$

$$T_{xy}=(v_xv_y/c^2)\mu^2(p'+c^2\eta')-(\mathfrak{C}_x\mathfrak{C}_y/4\pi) \tag{129}$$

$$T_{xz}=(v_xv_z/c^2)\mu^2(p'+c^2\eta')-(\mathfrak{C}_x\mathfrak{C}_z/4\pi) \tag{130}$$

$$T_{xt}=(-v_x/c^2)\mu^2(p'+c^2\eta'). \tag{131}$$

In (128) through (130) we have written $\mathfrak{C}$ instead of $\mathfrak{C}'$, since it has been shown that in the present case the two vectors are equal. Equations (128) through (131) apply to side 1 or 2 of the shock depending on whether all quantities carry subscript 1 or 2. Because of our assumptions, $T_{1,xz}=0$ holds and according to (9) it follows that also $T_{2,xz}=0$.

The most natural way in which to satisfy these equations is to assume $v_{2,z}=\mathfrak{C}_{2,z}=0$. This, indeed, seems to follow from symmetry. We shall see, however, in the further discussion that $v_{2,z}=\mathfrak{C}_{2,z}=0$ does not hold in a particular degenerate case. We shall exclude at first such a degeneracy by demanding the following conditions.

Case I, $T_{xy}\neq 0$

Equation (127) and comparison of (129) and (130) show that

$$T_{xz}=v_zT_{xy}/v_y. \tag{132}$$

From $v_{1,z}=\mathfrak{C}_{1,z}=0$ we get $T_{1,xz}=0$ and from (9) we get $T_{2,xz}=0$. This last statement is compatible with (132) and $T_{xy}\neq 0$ only if $v_{2,z}=0$. It then follows that $\mathfrak{C}_{2,z}$ is also zero and the whole phenomenon takes place in the xy plane.

The equations in this case are fairly involved. We limit ourselves to the derivation of formulas for the non-relativistic sound velocity. In the non-relativistic case[8] Eqs. (128), (129), and (131) read as follows:

$$\rho_1v_{1,x}^2+p_1+(\mathfrak{C}_{1,y})^2/8\pi=\rho_2v_{2,x}^2+p_2+(\mathfrak{C}_{2,y})^2/8\pi \tag{133}$$

$$\rho_1v_{1,x}v_{1,y}-(\mathfrak{C}_{1,x}\mathfrak{C}_{1,y}/4\pi)=\rho_2v_{2,x}v_{2,y}-(\mathfrak{C}_{2,x}\mathfrak{C}_{2,y}/4\pi) \tag{134}$$

$$E_1\rho_1v_{1,x}+\tfrac{1}{2}\rho_1(v_{1,x}^2+v_{1,y}^2)v_{1,x}+p_1v_{1,x}=E_2\rho_2v_{2,x}+\tfrac{1}{2}\rho_2(v_{2,x}^2+v_{2,y}^2)v_{2,x}+p_2v_{2,x}. \tag{135}$$

Equating the expressions for mass flow and the magnetic flux on the two sides of the shock and replacing the difference of the two sides of these equations by differentials we find

$$v_xd\rho+\rho dv_x=0 \tag{136}$$

$$d\mathfrak{C}_x=0. \tag{137}$$

From (121) and (126)

$$\mathfrak{C}_x/\mathfrak{C}_y=v_x/v_y=\phi. \tag{138}$$

Equations (136), (137), and (138) in combination with (133), (134), and (135) then yield

$$-v_x^2+\frac{dp}{d\rho}+\frac{(\mathfrak{C}_x)^2}{4\pi}\phi\frac{d\phi}{d\rho}=0 \tag{139}$$

$$-\phi v_x^2+\rho v_x^2\frac{d\phi}{d\rho}-\frac{(\mathfrak{C}_x)^2}{4\pi}\frac{d\phi}{d\rho}=0 \tag{140}$$

$$\rho v_x\frac{dE}{d\rho}+v_x^3\left(-1+\phi\frac{d\phi}{d\rho}\rho-\phi^2\right)-\frac{v_x}{\rho}p+v_x\frac{dp}{d\rho}=0. \tag{141}$$

Substituting the values of $dp/d\rho$ and $d\phi/d\rho$ obtained from (139) and (140) into (141) we find that (141) reduces merely to the adiabatic condition

$$dE/d\rho=p/\rho^2. \tag{142}$$

Elimination of $d\phi/d\rho$ between Eqs. (139) and (140) yields the desired equation for v_x^2

$$4\pi\rho(v_x^2)^2-\left(4\pi\rho\frac{dp}{d\rho}+\mathfrak{C}_x^2+\phi^2\mathfrak{C}_x^2\right)v_x^2+\mathfrak{C}_x^2\frac{dp}{d\rho}=0. \tag{143}$$

Thus the general expression for v_x^2 is given by

$$v_x^2=\frac{4\pi\rho(dp/d\rho)+\mathfrak{C}_x^2(1+\phi^2)\pm[\{4\pi\rho(dp/d\rho)+(\mathfrak{C}_x)^2(1+\phi^2)\}^2-16\pi\rho(\mathfrak{C}_x)^2(dp/d\rho)]^{\frac{1}{2}}}{8\pi\rho}. \tag{144}$$

[8] Since we are discussing the non-relativistic case, primes can be dropped.

It might be noted that the sum of the solutions (where the two solutions are denoted by a subscript + or −) is given by

$$(v_x^2)_+ + (v_x^2)_- = (dp/d\rho) + (\mathcal{H}^2/4\pi\rho), \tag{145}$$

which is the sum of the squares of the ordinary sound velocity and the Alfvén velocity (84). The product of the solutions of (144) yields

$$(v_x)_+(v_x)_- = (\mathcal{H}_x^2/4\pi\rho)(dp/d\rho), \tag{146}$$

which is the product of the squares of the ordinary velocity and the Alfvén velocity for $\mathcal{H}_x$.

Two special cases of (144) are of particular interest to us. The first case is $\mathcal{H}_y \to 0$. There (144) reduces to

$$(v_x^2)_+ = dp/d\rho \tag{147}$$

$$(v_x^2)_- = (\mathcal{H}_x)^2/4\pi\rho. \tag{148}$$

The first solution is the familiar velocity for the parallel longitudinal shock in hydrodynamics. The second solution corresponds to the transverse shock and is indeed identical with that derived by Alfvén[2] for this case.

The second case of interest to us is that where $\mathcal{H}_x \to 0$; then (144) reduces to

$$8\pi\rho v_x^2 = 4\pi\rho(dp/d\rho) + \mathcal{H}_y^2 \pm [4\pi\rho(dp/d\rho) + \mathcal{H}_y^2] \tag{149}$$

and

$$(v_x^2)_+ = 0 \tag{150}$$

$$(v_x^2)_- = (dp/d\rho) + (\mathcal{H}_y)^2/4\pi\rho. \tag{151}$$

The first solution is the hydrodynamic transverse velocity which (as in normal hydrodynamics) is equal to zero. The second of these solutions is the magnetohydrodynamic velocity for the perpendicular longitudinal shock previously expressed by Eq. (83).

Case II. $T_{xy} = 0$

In this case (132) shows that $T_{2,xz} = 0$ is compatible with $v_x \neq 0$, $\mathcal{H}_x \neq 0$. The assumption $T_{xy} = 0$ will be used in the form

$$(v_x v_y/c^2)\mu^2(p' + c^2\eta') = \mathcal{H}_x\mathcal{H}_y/4\pi. \tag{152}$$

Using (121), (126), and (127) it follows that

$$(v_x^2/c^2)\mu^2(p' + c^2\eta') = (\mathcal{H}_x)^2/4\pi. \tag{153}$$

Since $\mathcal{H}_{1,x} = \mathcal{H}_{2,x}$, the left side of (153) has the same value for subscripts 1 and 2:

$$[(v_{1,x})^2/c^2]\mu_1^2(p_1' + c^2\eta_1') = [(v_{2,x})^2/c^2]\mu_2^2(p_2' + c^2\eta_2'). \tag{154}$$

The condition $T_{1,xt} = T_{2,xt}$ and (131) leads to

$$(v_{1,x}/c^2)\mu_1^2(p_1' + c^2\eta_1') = (v_{2,x}/c^2)\mu_2^2(p_2' + c^2\eta_2'). \tag{155}$$

Combining (154) and (155) yields

$$v_{1,x} = v_{2,x} \tag{156}$$

and

$$\mu_1^2(p_1' + c^2\eta_1') = \mu_2^2(p_2' + c^2\eta_2'). \tag{157}$$

Thus from (128)

$$p_1' + (1/8\pi)(\mathcal{H}_{1,y})^2 = p_2' + (1/8\pi)[(\mathcal{H}_{2,y})^2 + (\mathcal{H}_{2,z})^2]. \tag{158}$$

Suppose now that we find a solution that is satisfied for a given $\mathcal{H}_{2,z}$ and corresponding $v_{2,z}$. We shall verify below that in this case there exists an entire set of solutions in which the values of $[(\mathcal{H}_{2,z})^2 + (\mathcal{H}_{2,y})^2]$ and $[(v_{2,z})^2 + (v_{2,y})^2]$ are maintained and μ_2, p_2 and η_2 are also unchanged. Physically this means that for each outgoing velocity $\mathbf{v}_2$ there is a whole set of solutions such that the $\mathbf{v}_2$'s describe a cone with the perpendicular to the shock front as the center line. We can easily verify that all the values corresponding to this cone are indeed solutions; $T_{2,xx}$ as expressed by Eq. (158) is unchanged, since $[(\mathcal{H}_{2,z})^2 + (\mathcal{H}_{2,y})^2]$ is maintained; $T_{2,xy}$ is still zero, since v_y and $\mathcal{H}_y$ are changed in proportion; $T_{2,xz}$ is still zero, since v_z and $\mathcal{H}_z$ are changed in proportion, and, lastly, $T_{2,xt}$ is not affected, since it does not depend on y or z components. Thus we see that if the condition $T_{1,xy} = 0$ is satisfied in the incident stream, the solution is degenerate and the direction of the outgoing stream is indeterminate. In this way out-of-the-plane solutions are compatible with the symmetry of the incident stream.

In order to simplify further discussion we shall consider here only the case $\mathcal{H}_{2,z} = v_{2,z} = 0$ and recognize that any such solution really corresponds to a cone of solutions. Then (158) reduces to

$$p_1' + (1/8\pi)[(\mathcal{H}_{1,x})^2 + (\mathcal{H}_{1,y})^2] = p_2' + (1/8\pi)[(\mathcal{H}_{2,x})^2 + (\mathcal{H}_{2,y})^2]. \tag{159}$$

Use of Eqs. (154) and (126) yields

$$p_1' + \tfrac{1}{2}(v_1/c)^2\mu_1^2(p_1' + c^2\eta_1') = p_2' + \tfrac{1}{2}(v_2/c)^2\mu_2^2(p_2' + c^2\eta_2'). \tag{160}$$

Since $(v/c)^2\mu^2 = \mu^2 - 1$, the use of Eq. (157) yields

$$p_1' - c^2\eta_1' = p_2' - c^2\eta_2'. \tag{161}$$

Thus Eqs. (157) and (161) together with the equation of state determine the nature of the solution. Clearly, a particular solution satisfying (157) and (161) is given by

$$\left.\begin{aligned} p_1' &= p_2' \\ \eta_1' &= \eta_2' \\ \mu_1^2 &= \mu_2^2 \end{aligned}\right\}. \tag{162}$$

Equations (162) then imply (for the case of $v_{2,z} = \mathcal{H}_{2,z} = 0$) that

$$v_{1,y} = \pm v_{2,y}, \quad \mathcal{H}_{1,y} = \pm\mathcal{H}_{2,y}. \tag{163}$$

The positive sign corresponds to no shock, the case of the negative sign we shall denote by the term "sym-

metrical shock." For the symmetrical shock $T_{1,xy}=T_{2,xy}$ implies that both these quantities vanish. Using (129), (121), and the definition of μ^2 one obtains for the velocity of the symmetrical shock[9]

$$v=\left[\frac{1}{c^2}+\frac{4\pi}{\mathfrak{IC}^2}\left(\frac{p'}{c^2}+\eta'\right)\right]^{-\frac{1}{2}}. \tag{164}$$

Note that Eq. (164) states that if $\mathfrak{IC}\to\infty$, then $v=c$.

Examine now whether (162) is the only condition satisfying Eqs. (157) and (161) or whether there are other solutions. Since $v_{1,x}=v_{2,x}$, the equation expressing the conservation of particles is

$$\mu_1 n_1'=\mu_2 n_2'. \tag{165}$$

Hence, use of Eq. (4) permits the rewriting of (161) and (157), respectively, as

$$n_1'm_0c^2+n_1'E_1'-p_1'=n_2'm_0c^2+n_2'E_2'-p_2' \tag{166}$$

$$\frac{m_0c^2}{n_1'}+\frac{n_1'E_1'+p_1'}{(n_1')^2}=\frac{m_0c^2}{n_2'}+\frac{n_2'E_2'+p_2'}{(n_2')^2}. \tag{167}$$

Multiplying Eq. (167) by $n_1'n_2'$, Eqs. (166) and (167) can be written as

$$m_0c^2\Delta n'=-\Delta(n'E')+\Delta p' \tag{168}$$

$$n_0c^2\Delta n'=+\Delta(n'E')+(p_1'n_2'/n_1')-(p_2'n_1'/n_2'). \tag{169}$$

We now assume that the equation of state is nonrelativistic on both sides of the shock. If we divide (168) by nm_0c^2, then we notice that

$$[-\Delta(n'E')+\Delta p']/nm_0c^2\ll 1 \tag{170}$$

so that

$$\Delta n'/n'\ll 1. \tag{171}$$

Hence Eq. (169) may be rewritten as

$$m_0c^2\Delta n'=+\Delta(n'E')+\Delta p'. \tag{172}$$

Combining (170) with (168) we find

$$\Delta p'\gg n'(\Delta E'). \tag{173}$$

Note that Eqs. (172) and (71) are identical. We have seen that the latter equation together with (171) requires a peculiar equation of state. Therefore, the symmetrical shock and the associated cone of solutions are as a general rule the only ones compatible with $T_{xy}=0$ and an unrelativistic equation of state.

If on both sides of the shock the extreme relativistic ideal gas law holds, $3p'=c^2\eta'$. This is evidently inconsistent with (161) except for $p_1'=p_2'$ and $\eta_1'=\eta_2'$. Thus we are brought back to (162).

[9] This agrees with the velocity given by H. Alfvén in his book, *Cosmical Electrodynamics* (Oxford University Press, London, 1950), p. 85, for a somewhat more specialized case.

The Surface Photoelectric Effect

M. J. BUCKINGHAM*
School of Physics, University of Sydney, Sydney, Australia
(Received February 10, 1950)

Theoretical expressions describing the photoelectric emission from a metal surface are derived, taking account of the dependence, established by Bardeen, of the effective surface barrier on the momentum of the impinging electron, due to exchange and correlation forces in the interior. This generalization reduces by a significant factor the magnitude of the theoretical expression for the absolute photoelectric yield. The shapes of the energy and spectral distributions of emitted photo-electrons are essentially unchanged, so that certain well-known disagreements between theoretical and observed distributions near the threshold remain unexplained. The influence of the transmission coefficient of the surface potential barrier on the photoelectric properties of a metal is discussed and an experiment is proposed for determining directly the variation with energy of the transmission coefficient, thus leading to information concerning the shape of the barrier.

I. INTRODUCTION

THE photoelectric current from a metal surface is influenced near the threshold, in its dependence on frequency and temperature, primarily by the factors describing the energy distribution of electrons in the metal and the transmission coefficient of the surface potential barrier. Existing theories dealing with the energy and spectral distributions of the emitted electrons make use of a free-electron model for the metal, with various assumptions concerning the surface barrier and the probability of excitation of the electrons. Rudberg[1] has examined and classified these assumptions.

The theory of the spectral and "normal" energy distributions, given by Fowler[2] and DuBridge[3] respectively, are based on the assumption of a barrier transmission coefficient which is constant for electrons with sufficient energy to escape, corresponding approximately to an image field barrier. While experimental results for a number of metal surfaces agree well[4] with these theories, results for sodium, which should approximate closely to the free-electron model, show marked systematic disagreements.[5,6] The work of Hill[7] on the total energy distribution for sodium shows that in this case also the image field theory is inadequate.

In an investigation of conditions at the surface of an ideal metal, Bardeen[8] has shown that, as a result of exchange and correlation forces in the electron gas the effective barrier for an electron depends in general on its momentum, and that the potential exhibits an asymptotic approach to an image field outside the surface. The exchange forces arise from the interaction in the motions of the electrons, due to the fact that electrons of parallel spin tend to keep apart, and Bardeen's calculations show that the effective surface barrier is due primarily to these forces, while the ordinary electrostatic forces are of minor importance.

It has been pointed out recently by Makinson[9] that the momentum-dependence of the barrier has a marked effect on formal expressions for the photoelectric current and may well alter considerably the quantitative conclusions from earlier theories. It is one of the purposes of the present paper to determine the modifications necessary in the theoretical description of the photoelectric effect, when account is taken of this dependence. It is found that this generalization introduces a significant factor into the theoretical value of the photoelectric yield, reducing the latter for sodium by a factor of about 3 near the threshold. However, it does not materially alter the distribution functions of the photo-electrons, so that it is insufficient to resolve the disagreements with experiment mentioned above.

Attempts have been made to explain these discrepancies by assuming that the cleanest sodium surfaces obtainable in practice are far from "ideal" and that instead of being nearly constant, the barrier transmission coefficient varies greatly with the energy of the emitted electrons. Houston[10] obtained agreement with experimental results for the spectral and "normal" energy distributions by assuming that the transmission coefficient vanishes linearly with diminishing energy of the ejected electron, while Hill[7] postulated a coefficient with a selective maximum in order to explain the observed total energy distribution. In Sections IV and V below this aspect is reviewed and an experiment is proposed which should allow a direct determination of the transmission coefficient as a function of energy.

II. THE EXCHANGE OPERATOR

It will be assumed[8] that the conduction electrons in the metal are subject to exchange interaction, but in the interior are otherwise free, moving in the "smeared" field of the combined positive and negative charges. The wave function then satisfies the unperturbed

* Now at Department of Theoretical Physics, The University, Liverpool, England.

[1] E. Rudberg, Phys. Rev. 48, 811 (1935).
[2] R. H. Fowler, Phys. Rev. 38, 45 (1931).
[3] L. A. Dubridge, Phys. Rev. 43, 727 (1933).
[4] See A. L. Hughes and L. A. DuBridge, *Photoelectric Phenomena* (McGraw-Hill Book Company Inc., New York, 1932).
[5] M. M. Mann and L. A. DuBridge, Phys. Rev. 51, 120 (1937).
[6] C. F. Overhage, Phys. Rev. 52, 1039 (1937).
[7] A. G. Hill, Phys. Rev. 53, 184 (1938).
[8] J. Bardeen, Phys. Rev. 49, 653 (1936).
[9] R. E. B. Makinson, Phys. Rev. 75, 1908 (1949).
[10] W. V. Houston, Phys. Rev. 52, 1047 (1937).

equation

$$-(\hbar^2/2m)\nabla^2 u+V(\mathbf{r})u-\mathfrak{A}(\mathbf{r})u=i\hbar\partial u/\partial t, \quad (1)$$

where $V(\mathbf{r})$ is the Coulomb potential energy and $\mathfrak{A}(\mathbf{r})$ represents the exchange operator, defined by

$$\mathfrak{A}(\mathbf{r})u_j(\mathbf{r})=\tfrac{1}{2}e^2\int\frac{\rho(\mathbf{r},\mathbf{r}')u_j(\mathbf{r}')d\mathbf{r}'}{|\mathbf{r}-\mathbf{r}'|},$$

in which $\rho(\mathbf{r},\mathbf{r}')$ is the Dirac density matrix,

$$\rho(\mathbf{r},\mathbf{r}')=\Sigma_i u_i^*(\mathbf{r})u_i(\mathbf{r}').$$

Dirac[11] has shown that if the exchange operator $\mathfrak{A}(\mathbf{r})$ acts on a plane-wave function $\exp(i\mathbf{k}\cdot\mathbf{r})$ in the interior of a metal, where all states for which $k=|\mathbf{k}|\leqq k_0$ are filled, it has the effect of multiplying the wave function by a constant, $A(k)$, given by

$$A(k)=(e^2k_0/2\pi)f(k/k_0),$$

where the function f is defined by

$$f(x)=2+(1/x)(1-x^2)\ln\{(1+x)/|1-x|\}.$$

The corresponding results for electrons near the surface have been calculated by Bardeen.[8]

The energy of an electron in the state $\mathbf{k}$ is then given by

$$\begin{aligned}E_k&=(h/\mu)k^2+V(-\infty)-A(k)\\&=(h/\mu)k^2-h\nu_k,\end{aligned} \quad (2)$$

where $\mu=8\pi^2m/h$ and $h\nu_k$ is the effective height of the surface potential barrier for this electron.

A good approximation to Dirac's theoretical expression[12] can be obtained near $k=k_0$ by putting

$$A(k)=A_0-\beta(h/\mu)k^2, \quad (3)$$

where A_0 and β are constants. The dimensionless quantity β can be regarded as a measure of the magnitude of the exchange energy; when the latter is neglected, $\beta=0$.

III. THE PHOTOELECTRIC CURRENT

By regarding as a small perturbation the incident plane waves of light of frequency ν, Makinson[9] has derived a formal expression, valid for any surface barrier, for the photoelectric current density from a simple metal. He showed that the contribution to the current, arising from electrons from the state $\mathbf{k}$, could be expressed in the form of the product of the electronic charge, the density of electrons in the state $\mathbf{k}$, the transmission coefficient of the surface barrier for the excited electrons, and an excitation function, $X(\mathbf{k},\nu)$. Thus

$$dJ=-e4|\alpha_k|^2D(r)X(\mathbf{k},\nu),$$

[11] P. A. M. Dirac, Proc. Camb. Phil. Soc. 26, 376 (1930).
[12] See reference 8, Fig. 1.

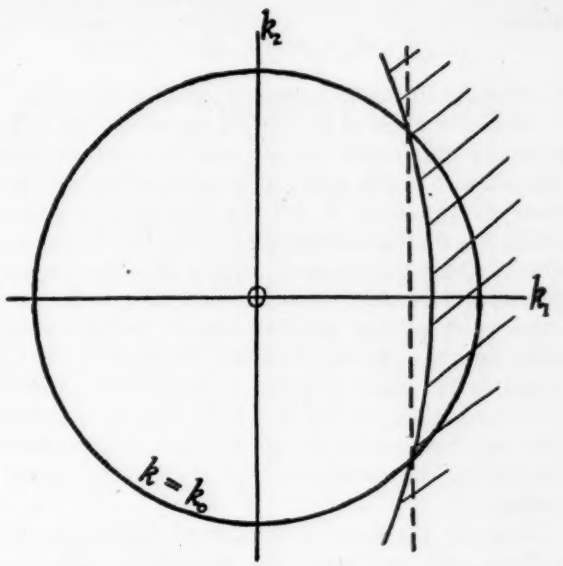

FIG. 1. Region of integration in $\mathbf{k}$-space, where $k_1>0$, $r^2>0$.

where at temperature T

$$|\alpha_k|^2=\frac{1}{8\pi^3}\frac{dk_1dk_2dk_3}{1+\exp[(E_k-E_0)/\kappa T]},$$

E_0 being the energy of the state with $k=k_0$; κ is Boltzmann's constant and k_1, k_2, k_3 are the components of $\mathbf{k}$ (k_1 normal to the surface and restricted to positive values). The transmission coefficient, $D(r)$, is a function of the normal component, r, of the wave vector of the emitted electron and is zero when $r^2<0$. From (2), r is given by

$$r^2=k_1^2+\mu(\nu-\nu_k).$$

By integration over all values of $\mathbf{k}$ we have for the photoelectric current density

$$J(\nu)=\frac{-e}{2\pi^3}\int\int\int\frac{D(r)X(\mathbf{k},\nu)dk_1dk_2dk_3}{1+\exp[(E_k-E_0)/\kappa T]}, \quad (4)$$

where the integration is over the volume of $\mathbf{k}$-space in which $k_1>0$ and $r^2>0$. This region is indicated by the shaded area in Fig. 1. In a model in which the electron density and threshold frequency are the same as in ours, but in which the effect of exchange energy is neglected, the curved boundary at the left of the region of integration would be replaced by the broken straight line shown in the figure. Thus we may expect a non-zero value of β to involve a reduction in the magnitude of the photoelectric current.

Now the total energy of the emitted electrons is

$$E=(h/\mu)(r^2+k_2^2+k_3^2)$$

and, if $(h/\mu)r^2=xE$, we can transform the integral in (4) to one over E and x, giving

$$J(\nu)=\frac{-e}{4\pi}\left(\frac{\mu}{h}\right)^2\frac{1}{1+\beta}\left[\int_0^\infty\int_0^1\frac{D(r)X(\mathbf{k},\nu)EdxdE}{k_1(1+e^x)}\right], \quad (5)$$

where

$$\chi=(E_k-E_0)/\kappa T=[E-h(\nu-\nu_0)]/\kappa T,$$

ν_0 being the threshold frequency, so that $h\nu_0=-E_0$.

An examination of the formal expression for $X(\mathbf{k}, \nu)$ given by Makinson[13] reveals that it is approximately independent of the value of β, at least for ν near ν_0. Near the threshold, k_1 will not differ greatly from k_0, which is a constant independent of β. Thus the expression in square brakets in (5), which gives the frequency dependence of $J(\nu)$, does not depend greatly on the value of β, so that we may expect the photoelectric yield near the threshold to be approximately proportional to the factor $(1+\beta)^{-1}$. From Bardeen's results, $\beta\sim 2$ for sodium, so that this factor can be of considerable significance and should be taken into account in theoretical calculations of the photoelectric yield of metals.

However, the shape of the spectral distribution of the current $J(\nu)$, and hence the logarithmic plots of the Fowler method,[2] are to a first approximation independent of the value of β.

This is also the case as shown below for the total and "normal" energy distributions of the emitted electrons, which are determined experimentally by measuring the photoelectric current as a function of the retarding potential between emitting and collecting surfaces.

Measurements of the *total* energy distribution are performed with a spherical collector surrounding a small central cathode, while for the *normal* energy distribution, plane parallel surfaces are employed. If U is the retarding potential in the former case, the current is given by the Eq. (5) with eU replacing zero as the lower limit of the integration with respect to E. In the latter case the expression for the current, when the retarding potential is V, is obtained from (5) by inserting eV and eV/E as the lower limits for the integrations over E and x, respectively. It is easily seen that, apart from the constant factors determining their absolute magnitudes, the two expressions obtained in this way are approximately independent of β when the frequency is not far from the threshold. This result was to be expected on physical grounds, since the energy distribution of the emitted electrons is largely determined by their *energy* distribution inside the metal and, unlike the *momentum* distribution, this is independent of β.

Actual computations, appropriate to sodium, have shown that the differences in the distribution functions for the cases $\beta=2$ and $\beta=0$ are, in fact, much too small to account for the disagreements with experimental results mentioned earlier, so that the explanation of these discrepancies must be looked for in other directions.

[13] In reference 9, $U_k(x)$ depends on the momentum of the electron and when operating on (u_k+v_k) in Eq. (3) of that paper should give $U_k(x)u_k+U_{k'}(x)v_k$, where $k'^2=q^2+k_x^2+k_z^2$. In the expressions following that equation, $U_k(x)$ should be replaced by $U_{k'}(x)$ and q redefined so that $q^2=r^2-(\mu/h)U_k'(x)$.

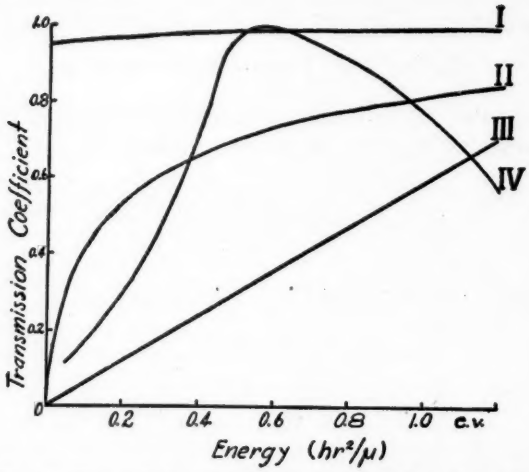

FIG. 2. Transmission coefficient as a function of energy for various potential barriers. (I) Image field barrier, (II) Square barrier, (III) Houston's barrier, (IV) Hill's barrier.

IV. THE SURFACE POTENTIAL BARRIER

In the general expression (5) for the photoelectric current, both the factors $X(\mathbf{k}, \nu)$ and $D(r)$ depend on the form of the surface potential barrier. As Makinson has shown, however, the excitation function $X(\mathbf{k}, \nu)$ does not in general vary sharply with $\mathbf{k}$ or ν near the threshold frequency, a fact shown explicitly for the image field and square barriers by the calculations of Hill. Thus, provided $h(\nu-\nu_0)$ is less than about one electron volt, we shall not be seriously in error if we regard $X(\mathbf{k}, \nu)$ as constant in performing the integrations in (5).

On the other term, $D(r)$, representing the transmission coefficient of the surface barrier, many of the properties of photoelectric emission depend. The fact that experimental results for sodium do not agree with the theory based on an image field barrier has inspired suggestions that the actual barrier has a transmission coefficient that is far from constant.

The transmission coefficient of a number of barriers is illustrated in Fig. 2 as a function of "normal" energy. Measurements of the *total* energy distribution were shown by Hill[7] to require a form of $D(r)$ with a selective maximum (curve IV), while Houston[10] explained results for the *spectral* and *normal* energy distributions by assuming a coefficient proportional to the normal energy (hr^2/μ) and illustrated by curve III in the figure.

Calculations by the present writer have shown that an agreement with experiment, about as close as that found by Houston,[14] can be obtained with the assumption of a square barrier,[15] for which the transmission

[14] See reference 10, Figs. 1 and 2.

[15] The saturation current is then given approximately by

$$J(\nu)\propto(\kappa T)^{5/2}F[h(\nu-\nu_0)/\kappa T],$$

where the function F is defined by

$$F(x)=\int_0^\infty f(y^2-x)dy,$$

in which f is Fowler's function

$$f(x)=\int_x^\infty \ln(1+e^{-y})dy.$$

coefficient is approximately proportional to the square root of the normal energy (curve II).

The present inconclusive state of knowledge in regard to the form of the surface potential barrier of sodium is illustrated by the fact that each type of transmission coefficient shown in Fig. 2 has some evidence to support it. Theoretical investigations by Bardeen indicate the image field curve I, while the results of experiment, summarized above, point to one or other of the remaining curves. In view of this uncertainty, experiments performed on the lines suggested in the next section should yield results of considerable value.

V. PROPOSED EXPERIMENT

Using the arrangement of spherical collector and small central cathode employed in experiments to determine the total energy distribution of emitted electrons, the photoelectric current is measured and plotted as a function of retarding potential, E/e, for incident light of various frequencies in the vicinity of the threshold. If the relative intensity of the light at different frequencies is measured, the sets of current readings can be adjusted in magnitude so that the value of (incident energy flux/frequency^2), is the same for each curve. After this adjustment the values of the current, $J(\nu, E)$, may be plotted against E on the same diagram and a point selected on each curve such that the value of $\chi=[E-h(\nu-\nu_0)]/\kappa T$ is the same at each point. Thus the distance in a direction parallel to the E axis, between the points on $J(\nu_1, E)$ and $J(\nu_2, E)$, for example, is $h(\nu_2-\nu_1)$. The points so obtained define a curve giving current, $C_\chi(E)$ say, as a function of E for a fixed value of χ; after repeating the process for other values of χ from about $+5$ to -10, a family of such curves can be drawn. An example of the type of result to be expected is sketched in Fig. 3.

It is shown below that, for those curves with $\chi>-1$, the differential function $dC_\chi(E)/dE$ is approximately proportional to the transmission coefficient, expressed as a function of E (compare Fig. 2). Thus

$$D\propto dC_\chi(E)/dE, \tag{6}$$

so that from the experiment described, a direct representation may be obtained of the variation with energy of the surface barrier transmission coefficient.

To establish (6) we note that, since the variation of $X(\mathbf{k}, \nu)$ and k_1 may be neglected when the frequency is near the threshold, (5) gives approximately,

$$J(\nu, E)\propto\int_E^\infty\int_0^1\frac{D(r)E'dxdE'}{1+e^{x'}}$$

$$=\int_E^\infty(1+e^{x'})^{-1}G(E')dE'$$

where

$$\chi'=[E'-h(\nu-\nu_0)]/\kappa T$$

and

$$G(E')=\int_0^{E'}D(\{\mu E/h\}^{\frac{1}{2}})dE=E'\int_0^1 D(r)dx,$$

since $hr^2/\mu=Ex$. Integrating by parts,

$$J(\nu, E)\propto(\kappa T)G(E)\log(1+e^{-\chi})+\cdots,$$

where the terms after the first are small for $\chi>-1$ and $\kappa T<E<1$ ev.

Then, when χ is kept constant,

$$C_\chi(E)\propto G(E)\log(1+e^{-\chi}),$$

so that

$$dC_\chi(E)/dE\propto D(\{\mu E/h\}^{\frac{1}{2}})\log(1+e^{-\chi}),\quad(\chi>-1),$$

giving (6).

It is easy to show that, for $\chi<-3$ and with the same approximations,

$$dC_\chi(E)/dE\propto G(E-\kappa T\chi)-G(E),\quad(\chi<-3),$$

a relation that may be used as a check on results obtained from curves with $\chi>-1$.

VI. CONCLUSION

There are important disagreements between experimental results and the simple theories of photoelectric emission based on a free-electron model with an image field barrier. Near the threshold frequency, the shapes of the observed spectral and energy distributions of photo-electrons from sodium do not agree with the Fowler and DuBridge theories, and it has been shown above that the generalization which includes the effect of exchange forces on the electrons does not improve the agreement.

This generalization does, however, reduce the magnitude of the calculated photoelectric yields of alkali metal surfaces by a factor of about 3, which should help in

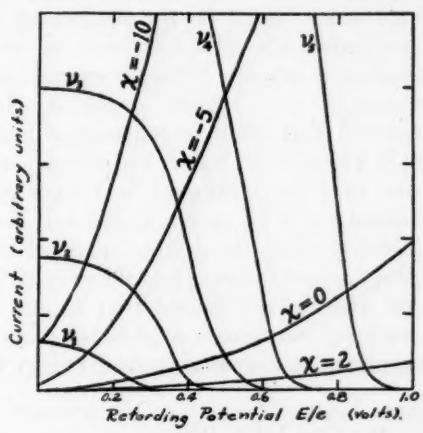

FIG. 3. Current, $J(\nu, E)$, *versus* retarding potential and a possible form for the constant-χ functions, $C_\chi(E)$.

bringing the calculated[16] yields into line with experiment.

The transmission coefficient of the surface barrier is an important factor in the description of photoelectric emission, and experiments such as that described, which could provide definite information on the barrier transmission coefficient, would be of great value, particularly as the special barriers assumed by certain authors to explain the normal and total energy distributions are very different, both from each other and from the theoretical barrier for an "ideal" metal.

The writer wishes to record his indebtedness to Dr. R. E. B. Makinson, who suggested this investigation, for many helpful discussions during its progress.

This work was carried out during the tenure of a Commonwealth Research Studentship at the University of Sydney.

[16] R. E. B. Makinson, Proc. Roy. Soc. **A910**, 367 (1937).

PHYSICAL REVIEW VOLUME 80, NUMBER 4 NOVEMBER 15, 1950

The Mechanism of Self-Diffusion in Alkali Metals

HEINZ R. PANETH
Department of Physics, University of Chicago, Chicago, Illinois
(Received June 26, 1950)

On the basis of calculations of the activation energies of various ring, vacancy, and interstitial mechanisms in alkali metals, the most probable mechanism of self-diffusion is found to be the rapid transmission of short linear regions of compression (referred to as "crowdions") along body-diagonals in the body-centered cubic lattice. The creation of crowdions, which can be regarded as interstitial atoms diluted over a region of about eight interatomic distances in a vernier-like fashion, occurs at the surface rather than in the interior of a perfect lattice. The calculation of the corresponding energy of formation depends on the empirical values for the work function, heat of sublimation, and ionization energy; for sodium, the total heat of activation for diffusion by crowdions is probably less than one-tenth of one electron volt.

I. INTRODUCTION

DIFFUSION in a periodic structure, such as a crystal lattice without macroscopic faults, is presumably the result of a large number of elementary steps from one stable configuration to the next equivalent one. While any elementary mechanism will in general involve the displacement of many atoms in the saddle point configuration (relaxation of neighboring atoms), we may distinguish between elementary steps resulting in the net displacement of one or of several atoms. The former type is only possible if we have either an interstitial atom or a vacancy in the lattice, while an example of the latter process is the cyclic interchange of two or more atoms, which would be the mechanism of self-diffusion in a perfect lattice. The exchange of two neighboring atoms in a metallic lattice is energetically unlikely because of their mutual repulsion. However, Zener[1] suggested that cyclic interchange of more than two atoms in a ring would reduce the activation energy required (due to mutual repulsion). Such steps involving the net displacement of many atoms are not energetically unlikely when the displacements of the individual atoms produce forces aiding the over-all motion. Huntingdon and Seitz[2,3] showed that in the case of copper a vacancy mechanism is probably dominant in accounting for the measured activation energy for self-diffusion.

The alkali metals present a structure which can be approximated by a particularly simple model of positive point charges embedded in a uniform negative charge density. Calculation of the activation energy of various elementary mechanisms in this model can be carried out rigorously involving essentially long-range Coulomb forces. It is found that insertion of an interstitial atom requires much less energy than in the case of copper,[2] where we have neighboring-shell-repulsion to contend with. The energetically favorable interstitial position is not, however, the geometrically obvious face center of the body-centered cubic structure, but between nearest neighbors, the insertion being accompanied by very considerable relaxation displacement along that line of nearest neighbors (forming the stable "crowdion" configuration). The elementary step in the diffusion process involves, then, the net displacement of about eight atoms forming the crowdion,[4] and requires very little activation energy of migration, due to the cooperative action of the several dipoles corresponding to the individual displacements of the ions. Vacancy and ring mechanisms are found to require much higher energies of formation and migration respectively.

The model adopted is a body-centered cubic lattice of positive point charges (each of one electronic charge in magnitude) embedded in a homogeneous negative charge density of constant value balancing the positive

[1] C. Zener, Acta Crys. 3, 346 (1950).
[2] H. B. Huntingdon and F. Seitz, Phys. Rev. **61**, 315 (1949).
[3] F. Seitz, Acta Crys. 3, 355 (1950).

[4] The term "crowdion" has been coined as a descriptive designation for a short linear region of compression.

charges. We are thus neglecting the finite size of the sodium ion core, and the increase in "free electron" density in the immediate neighborhood of the nucleus. Fuchs[5] has shown that this approximation introduces an error of about ten percent in the elastic constants for sodium. Allowing for relaxation of the electron distribution in the course of motion of the ions would always lower the activation energy, which is here calculated assuming a rigid uniform negative charge distribution throughout.

We designate by $2a$ the side of a cubic unit cell; for sodium, $a=2.12\times10^{-8}$ cm, and $e^2/a=6.80$ ev (where e is the electronic charge).

In the perfect lattice the least energy required for the simultaneous creation of a vacancy and an independent interstitial atom in the interior (allowing for relaxation in position of surrounding ions) was found to be about $0.6\,e^2/a$ corresponding to an activation energy of $0.3\,e^2/a$ for production of one vacancy. To avoid the necessity for creation of such vacancies and interstitial atoms, we might consider the alternate mechanism for diffusion, the cyclic interchange of atoms.

II. RING MECHANISMS

The most favorable ring mechanism involved the cyclic exchange of four nearest neighbors in a plane, and requires an activation energy of $0.24\,e^2/a$. The detailed results, involving the calculation of potentials by the Ewald method,[6] are as follows:

(a) self-potential at lattice point: $-1.820\,e/a$,
(b) hence, the energy required to remove 4 nearest neighbors to points of zero potential infinitely far apart: $+10.44\,e^2/a$,
(c) potential at point midway between nearest neighbor lattice points: $-0.200\,e^2a$.
(d) energy of repulsion for four ring atoms at mid-points, per atom: $+1.142\,e^2/a$,
(e) energy of attraction by holes created at lattice points ("hole effect") per atom at mid-point: $-3.371\,e^2/a$,
(f) hence, energy of activation for plane undistorted 4-atom ring: $0.70\,e^2/a$.

We now allow the ring to be distorted as it passes the half-way position; it is found that buckling of the ring out of the plane, or symmetric distortion in the plane along the equilibrium direction of the sides of the ring does not result in an appreciable lowering of the activation energy. On the other hand, we do gain by allowing relaxation in the position of the ions outwards from the mid-point positions. This is due to the fact that the repulsion energy term has a finite slope (when plotted against the distance from mid-point) already at the mid-point of the straight side, and therefore decreases faster at first, as we go out, than the attractive term due to the holes increases, the latter having a minimum for the undistorted position. The saddle point is found at an approximate distance of $a/4$ from the mid-point of the undistorted ring. Here we have a repulsion term of 0.875, and an attraction term of $-3.166\,e^2/a$ per atom. Strict calculation of the Ewald potentials then gives us an activation energy of $0.29\,e^2/a$.

Finally, we allow a group of eight and a group of four neighbors to relax simultaneously (relaxation of other ions is found to be negligible). Maximizing the energy gain, calculated in the dipole approximation for constant curvature in potential about the lattice point, we obtain a set of simultaneous linear equations for the values of the dipole displacements, and the relaxation energy is found to be $0.05\,e^2/a$, giving us a final activation energy of $0.24\,e^2/a$ for the ring motion.

These energies and those of some alternate ring mechanisms considered are listed in Table I.

It will be seen that the term corresponding to mutual repulsion of the ions in the saddle point configuration is, and hence the activation energy tends to be, reduced by avoiding acute angles in the ring.

TABLE I. Energies of various ring mechanisms.

Ring configuration	Activation energy	Repulsion energy per atom	Hole effect per atom
Undistorted plane nearest neighbor 4-ring without dipole relaxation	$0.70\frac{e^2}{a}$	$+1.142\frac{e^2}{a}$	$-3.371\frac{e^2}{a}$
Optimally distorted plane nearest neighbor 4-ring without dipole relaxation	0.29	+0.875	−3.166
with dipole relaxation	0.24		
Undistorted folded nearest neighbor 4-ring without dipole relaxation	1.122	+1.353	−3.516
Optimally distorted folded nearest neighbor 4-ring (dipole relaxation negligible)	0.504	+0.902	−3.155
Undistorted cube-face r-ring without dipole relaxation	0.85	+0.957	−2.898
Undistorted plane 6-ring (two sides $2a$, four sides $3a$ long) without dipole relaxation	1.06	+1.747	−3.585
Undistorted buckled 6-ring (6 equal obtuse angles) without dipole relaxation (effect of distortion $0.20\,e^2/a$)	0.51	+1.294	−3.906
Undistorted plane 8-ring (with 2 acute angles) without dipole relaxation	0.88	...	...
Undistorted buckled 8-ring (obtuse angles only) without dipole relaxation	0.48	...	...

III. LONG CHAIN MECHANISMS

This remark leads us to consider the limiting case of translation in a straight line. The energy *per atom* required for rigid translation of an infinite straight chain

[5] K. Fuchs, Proc. Roy. Soc. **A153**, 636 (1936); **A157**, 444 (1936).
[6] M. Born and M. Goeppert-Mayer, Handbuch der Physik, XXIV/2, 710.

FIG. 1. Diagram of crowdion. × denotes lattice positions; ● denotes ions.

of nearest neighbors (e.g., along the 1:1:1 direction) through the mid-points saddle position was calculated as follows:

(a) Self-potential at equilibrium position: $-1.8199 \pm 0.0004\ e/a$,
(b) potential at saddle point position: $-0.2004 \pm 0.001\ e/a$,
(c) interaction (hole and repulsion effect):

$$\frac{4}{\sqrt{3}}\sum_{n=1}^{\infty}\frac{(-1)^n}{n}\frac{e^2}{a}=-\frac{4}{\sqrt{3}}(\log 2)\frac{e^2}{a}$$

$$=-1.6008\frac{e^2}{a}\text{ per atom},$$

(d) hence, activation energy of chain shift without dipole relaxation: $0.0187\ e^2/a$ per atom,
(e) energy gain due to dipole relaxation of six neighboring chains (allowing for all three types of mutual interaction of the six claims): $0.0132\ e^2/a$ per atom.

The dipole relaxation in these neighboring chains is appreciable in spite of the small net electrostatic field acting, because of the shallow potential curvature along a chain corresponding to parallel dipole displacements.

We thus get an activation energy for rigid translation of a nearest-neighbor-chain of $0.0187-0.0132=0.0055\ e^2/a$ per atom.

This result, showing the ease of translation of straight chains of nearest neighbors (if it were not for the end effects resulting in an interstitial atom and a vacancy) owing to the cooperation of the parallel dipoles, suggested, first, consideration of rings formed by such chains. However, the repulsive effect (about $+0.02\ e^2/a$) at each corner, of which there must be at least 6 to avoid acute angles, did not allow this to be a favorable mechanism. The distortion relaxation was small, owing to the high potential curvature in that direction, corresponding to the shallow potential variation along the chain (the Laplacian of the potential being $\pi e/3a^3$ everywhere in the uniform negative charge distribution); similarly, it is a general result that the "better" the ring from the point of view of angles, the smaller the dipole relaxation of the surrounding atoms.

IV. THE CROWDION

However, the low energy per atom required to shift a straight chain (which only applies to nearest-neighbor-chains) suggests a large relaxation on placing an interstitial atom half-way between nearest neighbors, and indeed it is found that less energy is required to place an interstitial atom in such a position than in the more obvious face-centered position, though the latter is a position of lower potential when we ignore relaxation.

The Ewald potential at the center of a cube face is about $-0.34\ e/a$. By allowing the two nearest ions to move after having dropped a positive ion in the face center, we gain an additional relaxation energy of $0.381\ e^2/a$. On the other hand, the potential at the halfway point between nearest neighbors is calculated by the Ewald method to be only $-0.200\ e/a$, but allowing two atoms on either side along the 1:1:1 axis to relax we gain $0.535\ e^2/a$ in relaxation energy.

By allowing more atoms along the chain to relax simultaneously, we approach a relaxation energy which is nearly maximal for a "crowdion" of the form shown in Fig. 1. Each of the pair of ions nearest to the interstitial ion is displaced by an amount $p_1=\frac{1}{4}\sqrt{3}a$ along the line, $p_2=0.30a$, $p_3=0.2a$, $p_4=p_5\cdots=0$. The relaxation energy associated with this formation was calculated to be $-0.69\ e^2/a$ using the exact Ewald potential rather than the constant curvature approximation for p_1 (the latter giving too low a potential rise). The highest relaxation calculated by an approximate method (for a slightly different formation) was $-0.71\ e^2/a$.

However, the corresponding energy required for the formation of a vacancy is $+1.820-0.310=1.510\ e^2/a$, the relaxation being approximately the same ($0.310\ e^2/a$) whether we allow chain, or symmetric nearest neighbor, relaxation of 8 atoms.

Instead of creating the vacancy in the interior, we can, however, remove the positive ion from the surface of the crystal. In order to work out, then, the energy required to transfer a positive ion from the surface to an interstitial position half-way between nearest neighbors we shall make use of the empirical data relating to work function, ionization, and sublimation, giving us the work required to remove a positive ion from the surface to infinity.

The heat of sublimation of sodium at 20° was taken to be[7] 25.7 kcal./g-atom = 1.12 ev/g-atom. The ionization energy is 5.12 ev, and the empirical value taken for the work function[8] is 2.25 ev. We thus arrive at the value I for the energy required to remove a positive ion from the surface to infinity outside the crystal: $I=1.12+5.12-2.25=3.99$ ev. Allowing for errors in the experimental values, we take[9] $I=4.0\pm0.2$ ev.

In order to calculate the work required to bring a positive ion from infinity outside the crystal across the surface to an interstitial position in the interior of our lattice (thus standardizing our Ewald potentials to zero at infinity outside the crystal), we shall use an approximation[10] to our model of the crystal by considering it to

[7] W. Edmondson and A. Egerton, Proc. Roy. Soc. **A113**, 520 (1926).
[8] R. J. Maurer, Phys. Rev. **57**, 653 (1940).
[9] This shows that removal of one of the surface ions involved demands almost exactly half the energy required for removal of an interior lattice ion.
[10] The quality of this approximation is shown by F. Seitz, *The Modern Theory of Solids* (McGraw-Hill Book Company, Inc., New York, 1950), p. 364.

be made up of spheres of uniform negative charge density surrounding the positive lattice points, the volume of each sphere being equal to the volume of the polygon corresponding to each lattice point, the total charge of the sphere being of course normalized to unit electronic charge. We shall also use the Bardeen[11] correction to allow for electron redistribution at the surface of sodium.

The volume of the unit (polygonal) cell in a b.c.c. lattice is $4a^3$. The radius of a sphere of equal volume is given by $R=(3/\pi)^{\frac{1}{3}}a$. The potential at the center of such a sphere of uniform charge density normalized to $-e$ is $-1.5(3/\pi)^{-\frac{1}{3}}e/a=-1.524\,e/a$. On the other hand, we had calculated this self-potential by the Ewald method to be $-1.820\,e/a$. Thus, to standardize all Ewald potentials to zero at infinity outside the crystal, one must add $+0.30\,e/a$ to their values. In particular, the potential at the point midway between nearest neighbors is therefore $-0.20+0.30=+0.10\,e/a$, and the energy gained in bringing the positive ion from infinity to that position is $-0.10+0.70$ (relaxation) $=0.60\,e^2/a$.

Allowing for a redistribution of electronic charge at the surface of the crystal (compared to the interior) resulting in an average dipole of 0.15 ev, as calculated by Bardeen, the net energy required to remove a positive ion from the surface to form a crowdion in the interior is given by

$$4.15\text{ ev}-0.60\,e^2/a=0.61\,e^2/a-0.60\,e^2/a$$
$$=0.01\pm0.03\,e^2/a.$$

Thus the activation energy of formation for crowdions in sodium is less than 0.3 ev.

For the higher alkali metals the work function is practically the same, and the decreases in ionization and sublimation energy more than compensate the effect of the increase in interatomic distance on the relaxation and potential terms, so that we would expect a still lower activation energy of formation for crowdions (not taking into account the Bardeen correction).[12] In the case of lithium, the increase in ionization energy is small, the change in cell constant is more important, and we again expect a lower energy of formation for crowdions.

The activation energy associated with migration of such crowdions is small. Even for crowdions extending over only $4\cdot3^{\frac{1}{3}}a$, the difference in energy between the symmetric position considered above, and the configuration obtained by shifting the crowdion (whose amplitude of displacement is taken to vary linearly over its length) rigidly through half a spacing (*viz.* $3^{\frac{1}{3}}a/n$), is found to be only $0.05\,e^2/a$ ($=0.3$ ev for sodium).[13] The energy of creation calculated above, referring as it does to the position of the crowdion on the potential hump, is the total energy of activation (the unit jump for an atom being $3^{\frac{1}{3}}a/n$ in length, where na is the length of the crowdion).

The picture we arrive at is then as follows: Crowdions extending over about eight spacings are formed by the motion of ions situated initially at surface ledges and subject to Brownian collisions from one side. These crowdions travel rapidly along nearest-neighbor axes throughout the crystal. As the crowdion flies in a straight line and cannot turn corners without considerable additional activation energy, we might expect anisotropy under suitable conditions. For very large single crystals we might expect time effects such as freezing in of equilibrium concentrations on rapid cooling. Moreover, it might be possible to inhibit the formation of crowdions at the surface by non-mobile layers of foreign atoms. Foreign atoms in the interior of the lattice would not benefit preferentially by such a diffusion mechanism. Finally, as in the case of interstitial atoms, vacancies, and any other configurations assumed to exist under conditions where equilibrium concentrations are maintained, there is the possibility of detectable material flow under stationary temperature gradient conditions, though in this case a concentration gradient of crowdions is expected to be limited by an accompanying potential gradient.

For sufficiently low activation energy of migration, crowdions (which can be assigned definite mass) can be considered as particles with one degree of freedom of motion, and hence contribute to the specific heat and heat-conductivity.[14]

I wish to express my gratitude to Professor C. Zener for his helpful advice at all times.

[11] J. Bardeen, Phys. Rev. **49**, 653 (1936).

[12] However, our electrostatic model of the crystal becomes increasingly unreliable for the higher alkali metals.

[13] Compare the similarly low energy of activation of migration (0.5 ev) calculated by Huntingdon and Seitz (reference 2) for an ordinary interstitialcy in copper.

[14] The kinematics of non-stationary "slip-waves" have been worked out for a different model (involving nearest-neighbor elastic interactions along the chain) by J. Frenkel and T. Kontorova, J. Phys. (USSR) **1**, 137 (1939).

Piezoelectric Constants of Alpha- and Beta-Quartz at Various Temperatures

RICHARD K. COOK AND PEARL G. WEISSLER
National Bureau of Standards, Washington, D. C.
(Received April 24, 1950)

The adiabatic piezoelectric constants d_{11} and d_{14} of alpha-quartz have been measured between room temperature and 571.5°C. At the latter temperature, d_{11} is about one-half of its room temperature value, whereas d_{14} has increased by a factor of almost three. At 573°C (the inversion temperature) the crystal structure changes to that of beta-quartz, and d_{11} vanishes. The constant d_{14} for beta-quartz has been measured between 584°C and 626°C. d_{14} appears to be substantially constant over this short range of temperature, and differs from d_{14} for alpha-quartz at about 570°C by only a few percent. The piezoelectric constants were deduced from measurements (with a Q-meter technique) of the equivalent circuits of long thin bars driven electrically at frequencies near resonance.

I. INTRODUCTION

A KNOWLEDGE of the variation of the piezoelectric constants of quartz with temperature near 573°C (the inversion temperature of quartz) is desirable in the design of experiments for elimination of electrical (Dauphiné) twinning. Alpha-quartz, which is the stable crystalline form at temperatures below 573°C, is susceptible to such twinning. When alpha-quartz, of symmetry D_3 (in the Schoenflies notation), is heated to 573°C, the crystal structure changes suddenly to symmetry D_6. This form, stable above 573°C, is called beta-quartz, and is not susceptible to electrical twinning.

Alpha-quartz has two piezoelectric constants, d_{11} and d_{14}. d_{11} is the electric polarization per unit normal stress on a plane perpendicular to the electric axis. d_{14} is the electric polarization per unit shearing stress on a plane perpendicular to the optic axis. More precise definitions of piezoelectric constants, and a very complete summary of the measurements of the constants d_{11} and d_{14} for alpha-quartz, for temperatures from 4°K to 568°C, are given by W. G. Cady.[1] It appears that many of the early measurements at elevated temperatures were qualitative in character. However, Fréedericksz and Michailow[2] made quantitative measurements of d_{11} up to a temperature of 568°C. No measurements of d_{14} for alpha-quartz at elevated temperatures have been found in the literature.

For beta-quartz, the symmetry D_6 requires that $d_{11}=0$. However, d_{14} is not zero. No quantitative measurements have been found in the literature on the piezoelectric constant d_{14} for beta-quartz.

In view of the foregoing we have measured d_{11} up to a temperature of 571.5°C, and d_{14} up to a temperature of 626°C. Although some consideration was given to the idea of measuring the electric charges produced by transient loads, the technique finally adopted was a determination of the equivalent circuits of long thin bars driven electrically at frequencies near resonance. This method seemed to have the advantages of high precision, freedom from systematic errors due to the appreciable electrical conductivity of quartz at high temperatures, and ease of measurement with readily available electronic equipment.

The connection between the piezoelectric constants and the equivalent circuit of a bar is well known, and is summarized briefly in the following section.

II. EQUIVALENT CIRCUITS OF QUARTZ BARS

In the neighborhood of a resonant frequency, the equivalent circuit of a quartz bar can be represented very accurately by the circuit shown in Fig. 1. If ω_0 is the pulsatance (circular frequency) of the bar at resonance, $\omega_0^2 L_1 C_1 = 1$, where L_1 and C_1 are the series-chain inductance and capacitance, respectively. These depend on the piezoelectric constants and other physical constants of quartz, and are independent of frequency.

Consider a long thin quartz bar (Fig. 2) vibrating in its fundamental longitudinal mode. Its broad flat faces, perpendicular to the x-axis, are plated so as to be conducting. The capacitance C_1 is given by

$$C_1 = 8|d_{12}'|^2 l_w l/(\pi^2 l_t s_{22}'), \tag{1}$$

where $1/s_{22}'$ = Young's modulus of the bar in zero electric field (platings short-circuited), and the equivalent piezoelectric constant is

$$|d_{12}'| = (1/2)|(1+\cos 2\alpha)d_{11} - d_{14}\sin 2\alpha|. \tag{2}$$

Although the Young's moduli of the various bars used in the experiments could have been computed from values of the known zero-field compliances s_{ij}, it was found more convenient to determine the moduli from the measured resonant frequencies and bar lengths. If ρ is the density of quartz, then

$$s_{22}' = \pi^2/(\rho l^2 \omega_0^2). \tag{3}$$

Also, it was found to be easier to compute the bar thickness than to measure it directly. In terms of the mass m, the bar thickness is

$$l_t = m/(\rho l_w l). \tag{4}$$

[1] W. G. Cady, *Piezoelectricity* (McGraw-Hill Book Company, Inc., New York, 1946).
[2] V. Fréedericksz and G. Michailow, Zeits. f. Physik **76**, 328 (1932).

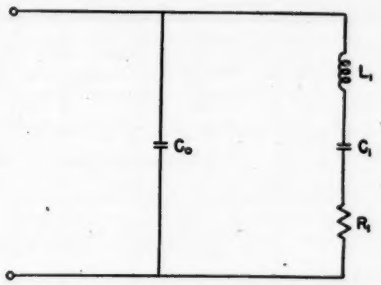

FIG. 1. Equivalent circuit of a quartz crystal bar near a natural frequency.

Combination of Eqs. (1)–(4) yields

$$|(1+\cos 2\alpha)d_{11}-d_{14}\sin 2\alpha| = \pi^2(mC_1)^{\frac{1}{2}}/(\sqrt{2}\rho l^2 l_w\omega_0). \quad (5)$$

By making measurements on two or more bars having different angles α, values of d_{11} and d_{14} can be deduced by means of Eq. (5). Only the absolute value, and not the sign, of d_{12}' can be determined from equivalent circuit measurements. This means physically that such measurements do not yield the phase angle between the mechanical vibration and the electric current.

Signs can be given to d_{11} and d_{14} on the basis of values given by Cady.[1] The signs are the same for both right and left quartz if one follows the Institute of Radio Engineers 1944 convention (described by Cady) for the choice of axes for quartz. This convention is used throughout this paper. We shall assume that the signs of d_{11} and d_{14} remain unchanged at the various temperatures used in the experiments.

Recently the I.R.E. 1944 convention was modified.[3] Under the new convention, the signs of d_{11} and d_{14} are different for right and left quartz.

III. TECHNIQUE OF MEASUREMENT OF EQUIVALENT CIRCUITS

The equivalent circuits of the quartz bars were found by means of a Q-meter circuit (Fig. 3). The basic idea

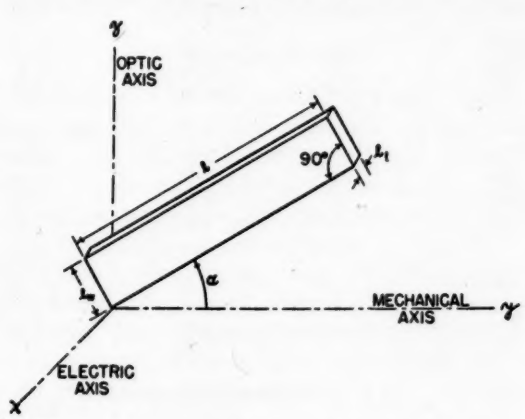

FIG. 2. Notation for quartz crystal bars.

[3] Proc. I.R.E. 37, 1378, December (1949).

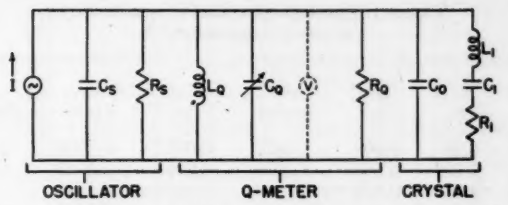

FIG. 3. Q-meter for measurement of equivalent circuits of crystal bars.

is that the reactance of the bar must be determined at two known frequencies at least, both very near the resonant frequency, in order to determine C_1 and L_1 with good precision.

By Thévenin's theorem, the source is representable by a generator, producing current I (independent of load), in shunt with a capacitance C_s and resistance R_s. The Q-meter, consisting of a voltmeter, a high Q coil, and a variable capacitor all connected in parallel, has an equivalent circuit consisting of an inductance L_Q, capacitance C_Q, and resistance R_Q. It is clear that the parallel combination C_s, C_Q, L_Q, and C_0 (the clamped capacitance of the crystal and its leads) can be adjusted to have zero admittance at the measuring frequency. The amount ΔC, by which the variable capacitance differs from the setting for zero admittance, can be either positive or negative. Hence a simplified version of the circuit is that shown in Fig. 4.

The pulsatance at resonance is found by successive approximations. At resonance, the reactance in the crystal's series chain is zero, and hence the voltage V is a minimum with respect to frequency changes. Then $V=IRR_1/(R+R_1)\approx IR_1$, if $\Delta C=0$, and if $R\gg R_1$ (which can be achieved easily). The resonant frequency is located approximately by finding a minimum in V, then ΔC is adjusted to zero, and the resonant frequency is then located as exactly as possible at the minimum in V. The values of I and R are then determined at the resonant frequency by disconnecting the crystal and observing V for two values of ΔC. This sequence of operations therefore yields the resonant pulsatance ω_0 and the series chain resistance R_1.

The next step is to change the frequency by a small amount (usually a few tenths of a percent), so that the new pulsatance is $\omega=\omega_0+\Delta\omega$. The crystal is connected into the circuit, and ΔC is adjusted until the voltage V is a maximum. An analysis of the circuit of Fig. 4

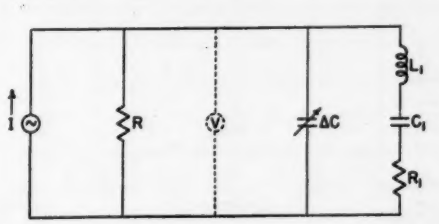

FIG. 4. Simplified version of Q-meter and equivalent circuit of crystal.

TABLE I. Physical constants of quartz bars (at room temperature).[a]

Bar	l, cm	l_w, cm	m, grams	l_t, cm	m', grams	α, degrees
C	6.98	0.699	1.2877	0.0997	1.2906	+18.5
D	7.02	0.698	1.2923	0.0996	1.2945	−45.0
E	5.00	0.499	0.3265	0.0495	0.3274	0.0
F	5.00	0.499	0.3263	0.0495	0.3275	+18.5

[a] The tabulated thicknesses l_t were computed on the assumption that the density of quartz at room temperature is $\rho=2.648$ g/cc. Direct measurements of l_t with a micrometer calipers yielded values which were systematically greater by about one percent. Allowance was made for the small thermal changes in density, linear dimensions, and angles of the bars, by means of the data given in *The Properties of Silica* by R. B. Sosman (Chemical Catalog Company, New York, 1927).

shows that when this occurs, then

$$\omega\Delta C=\frac{\omega L_1-1/\omega C_1}{R_1^2+(\omega L_1-1/\omega C_1)^2}, \tag{6}$$

and the combination of the capacitance ΔC and the series chain has an impedance (entirely real)

$$Z=[R_1^2+(\omega L_1-1/\omega C_1)^2]/R_1. \tag{7}$$

From Eq. (6) combined with $\omega_0^2 L_1 C_1=1$, we find

$$C_1=(2\Delta\omega/\omega_0)\Delta C[1+\Delta\omega/2\omega_0]\cdot[1+(\omega R_1\Delta C)^2+\cdots]. \tag{8}$$

It is evident that the precision of measurement of $\Delta\omega$, ω_0, and ΔC must each be approximately one percent or better if C_1 is to be obtained to within one percent. In order to improve the precision a little, several determinations of C_1 were made at several different frequencies, both above and below the resonant frequency (both positive and negative values of $\Delta\omega$).

IV. EXPERIMENTAL RESULTS AND DISCUSSION

The piezoelectric constants were deduced from measurements of the equivalent circuits of long thin bars driven electrically at frequencies near the resonant frequency for the fundamental longitudinal mode. The bars were cut with flat faces perpendicular (to within 0.1°) to the x-axis (electric axis) (Fig. 2). The flat faces were gold-plated. The platings were used as electrodes. The long dimensions of the bars lay in the yz-plane, and made known angles with the y-axis.

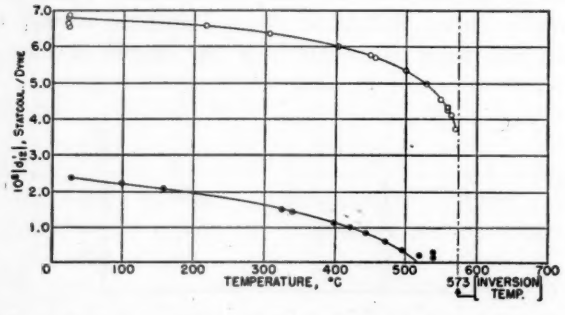

FIG. 5. $|d_{12}'|$ *vs.* temperature. Open circles are for bar E ($\alpha=0°$), and solid circles for bar D ($\alpha=-45°$).

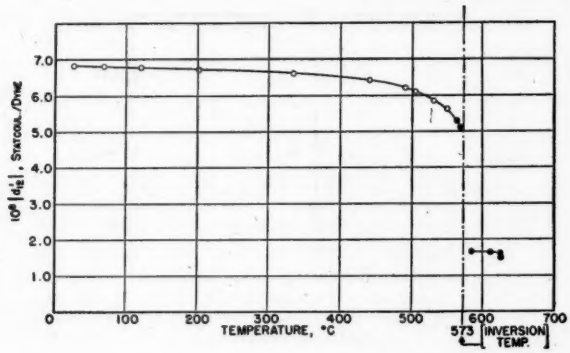

FIG. 6. $|d_{12}'|$ *vs.* temperature. Open circles are for bar C ($\alpha=18.5°$) and solid circles for bar F ($\alpha=18.5°$).

The physical constants of the bars at room temperature are given in Table I. m is the mass of a bar, and m' is the mass of a bar including its plated gold electrodes.

The results of determinations of $|d_{12}'|$ for the various bars are shown in Figs. 5 and 6. In general, it was not feasible, particularly at high temperatures, to determine $|d_{12}'|$ for two different bars at exactly the same temperature. Hence smooth curves were drawn through Cartesian plots of $|d_{12}'|$ against temperature. d_{11} and d_{14} were then computed from values of $|d_{12}'|$ read off at the same temperature from the curves for two differently oriented bars.

TABLE II. Piezoelectric constants of quarts at various temperatures.

Temperature °C	$10^8 d_{11}$ statcoulomb/dyne		$10^8 d_{14}$ statcoulomb/dyne
	Bars C and D	Bar E	Bars C and D
20	6.88	6.89	−2.04
50	6.84	6.86	−2.14
100	6.77	6.79	−2.33
150	6.69	6.70	−2.51
200	6.60	6.60	−2.69
250	6.50	6.49	−2.91
300	6.37	6.37	−3.15
350	6.22	6.21	−3.42
400	6.02	6.01	−3.74
450	5.74	5.74	−4.16
500	5.32	5.34	−4.72
			Bars E and C
520		5.08	−4.99
540		4.74	−5.24
550		4.53	−5.34
555		4.41	−5.40
			Bars E and F
560		4.26	−5.48
565		4.06	−5.54
570		3.81	−5.63
571.5		3.74	
573	Inversion temperature		
			Bar F
585			−5.69
612			−5.59
626			−5.47

The measurements on bar E (Fig. 5) yield d_{11} directly, and show a relatively wide spread at room temperatures. Each time d_{11} was determined at room temperature after this bar had been heated to temperatures near inversion, the value was found to be a little less than the preceding determination. We ascribe the gradual decrease to the incidence of electrical twinning caused by the heating. It was decided that the maximum value would be the best value of d_{11}.

The determinations of d_{11} and d_{14} are finally tabulated in Table II. Figure 7 is a graph of the tabulated values. The value of d_{14} at room temperature should be noted. We find it to be -2.04 (in units of 10^{-8} statcoulomb/dyne), which is in agreement with Cady's "best value" of -2.0 based mainly on static measurements. Mason,[4] however, finds a value of -2.56 by a dynamic method, which is not in agreement with Cady's and our values.

Saksena and Srivastava[5] have made quasi-empirical computations of the piezoelectric constants e_{11} and e_{14}. Their results are based on a calculation of the electric

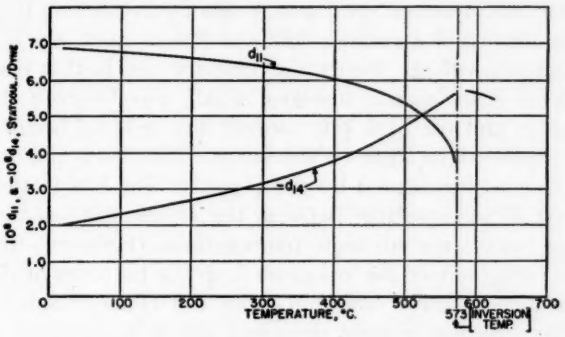

FIG. 7. Measured values of d_{11} and d_{14} for quartz as a function of temperature.

dipole moment caused by straining the covalent bonds in quartz. Our measurements of d_{11} and d_{14} can be used to get e_{11} and e_{14} by means of the equations

$$e_{11}=(c_{11}-c_{12})d_{11}+c_{14}d_{14}$$
$$e_{14}=2c_{14}d_{11}+c_{44}d_{14}, \tag{9}$$

in which the c's are the zero-electric-field elastic constants. However, the only measured elastic constants available at high temperatures are the zero-electric-charge ones determined by Atanasoff and Hart.[6] These were used to determine the experimental values shown in Fig. 8, and should not cause errors in e_{11} and e_{11} of more than a few percent. Also plotted in the same figure are the theoretical values found by Saksena and Srivastava. The agreement between the experimental and theoretical values of e_{11} is fairly good, but there are large discrepancies in the case of e_{14}.

[4] W. P. Mason, Bell Sys. Tech. J. 22, 178 (1943).
[5] B. D. Saksena and K. G. Srivastava, Proc. Ind. Acad. Sci. 28A, 423, 437 (1948). Also see Nature 161, 283 (1948).
[6] J. V. Atanasoff and P. J. Hart, Phys. Rev. 59, 85 (1941).

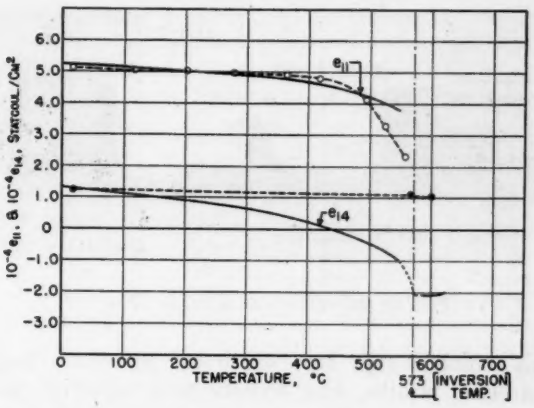

FIG. 8. e_{11} and e_{14} for quartz as a function of temperature. The solid lines are based on the experimental measurements. The open circles represent values of e_{11} computed by Saksena and Srivastava. The solid circles represent values of e_{14} computed by the same authors.

We estimate that the probable error in our measurement of d_{11} does not exceed one percent, and the probable error of d_{14} does not exceed two percent, at most temperatures. The errors are greater near the inversion temperature. The source of largest random error is probably the measurement of C_1. Figure 9 presents graphs of C_1, which should be practically independent of $\Delta\omega/\omega_0$, as a function of $\Delta\omega/\omega_0$. These graphs serve as an indication of the random errors to be expected.

Systematic errors might arise because bars of finite dimensions were used. For example, Eq. (1) is based on a calculation which assumes uniform polarization across the width of the bar when it vibrates, but actually the polarization in the middle is not quite the same as it is at the longitudinal edges. Bars of different sizes were used in order to find out whether systematic errors of significant amount were present. A study of the tabulated results (see Table II) seems to show no appreciable errors due to the finite size of the bars.

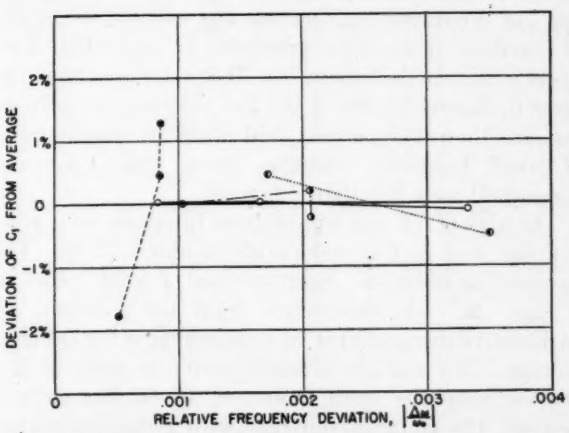

FIG. 9. Variations in C_1 as a function of $|\Delta\omega/\omega_0|$. Open circles are for bar D at 26°C. Solid circles for bar F at 626°C. Circles shaded on the left are for bar C at 492°C. Circles shaded on the right for bar E at 529°C.

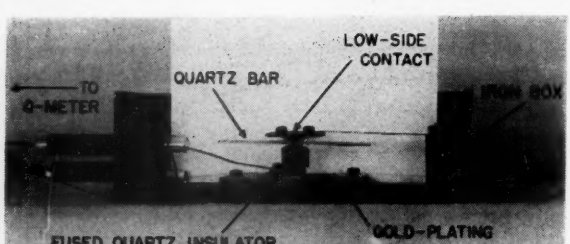

FIG. 10. Quartz crystal bar in its holder.

This indicates that bars which are ten times longer than their widths, and seventy to a hundred times longer than their thicknesses, can yield piezoelectric constants having systematic errors of less than about one percent.

The resistances R_1 and elastic compliances s_{22}' were obtained as by-products of the experiments. We hope to publish at a later date a detailed analysis of the variations of R_1 and s_{22}' with temperature.

V. APPARATUS

The Q-meter was constructed in the laboratory, largely from commercially available components. Since oscillators which could produce two frequencies differing by a few tenths of a percent, with the difference in frequency known to an accuracy of about one percent, were not readily available, a General Radio beat-frequency audio-oscillator was modified to yield such small frequency changes. These were produced by a low capacitance variable condenser connected in parallel with the main tuning condenser in the tank circuit. The oscillator covered the range from 167 to 187 kc/sec., whereas the quartz bars had resonant frequencies between 35 and 60 kc/sec. Therefore, a multivibrator was constructed and used to reduce the oscillator frequency. The multivibrator output was suitably filtered and amplified, and was then coupled to the remainder of the Q-meter by a capacitor of a few $\mu\mu$f. Frequency calibration was effected by means of standard frequencies generated by our High Frequency Standards Laboratory. It is estimated that the error in determination of the bar resonant frequencies was less than 0.05 percent, and errors in measurement of small frequency changes (from which $\Delta\omega$ was computed) were less than 2 percent.

The high Q coil was wound from Litzdraht on a glass cylinder, and had an inductance of about 22 mh. The variable air-dielectric capacitor had a least count of 0.2 $\mu\mu$f. ΔC was determined from the location, by variation of the capacitor, of a maximum in the Q-meter voltage. This was the greatest source of error in ΔC. We estimate the error, however, to be less than 2 percent. The voltages were read with a high impedance electronic voltmeter having five ranges. At 50 kc/sec., the Q-meter when tuned with the crystal disconnected had $R \approx 3.5 \times 10^6$ ohms, which is equivalent to $Q = 510$.

The crystal holder was a 15×4.5×4.5-cm iron box having 3-mm thick walls (Fig. 10). Contact was made with the bar platings, at the geometrical centers of the faces, by means of gold-alloy spherical surfaces having small fillings of pure gold at the points of contact. One contact (low side) was connected to the iron box, which served as an electrical shield, and which in turn was connected to the low side and shield of the Q-meter. The other spherical contact (high side) was mounted on a fused quartz insulating plate, and was connected to the high side of the Q-meter.

Preliminary experiments showed the fused quartz to have surprisingly large dielectric losses at temperatures above about 550°C. The losses were large enough to make precision measurements of the piezoelectric constants impossible. A screening system was devised to reduce this loss. The fused quartz insulator was plated with gold in such a way that the plating made no contact with either the iron box or the high side spherical contact, but so that the plating was geometrically between the spherical contact and the part of the box supporting the fused quartz. The gold plating (Fig. 10) was then used as a screen by connecting it to the output of a cathode follower whose input was the high side voltage. Hence the dielectric loss in that part of the fused quartz insulator which was between the screen and the high side contact was reduced because the potential difference was small. This loss is the one which was measured by the Q-meter. The loss in that part of the insulator between the screen and the iron box was large at high temperatures. However, the power to supply the loss came from the batteries of the cathode follower, and not from the Q-meter source. The screening system described above is identical in principle with the shielding system described by Daniels.[7]

The crystal holder was placed in the center of a tubular electric furnace 8 cm in diameter and 46 cm long, whose ends were plugged with asbestos fiber and blocks. The heating current was 60-cycle a.c. The temperature of the air within the iron box was measured by means of a chromel-alumel thermocouple and potentiometer. Because the resonant frequencies of the bars were strong functions of the temperature near inversion, it was found necessary to make measurements when the temperature was substantially stationary with time. In addition, this would reduce errors in temperature measurement due to systematic differences between the temperature of the air in the box and the temperature of the quartz bar. The error in determination of temperature of the bars is estimated to be less than 0.5°C.

We are particularly indebted to Messrs. M. Greenspan and R. P. DeAgro for assistance in the construction of apparatus and the collection of data.

[7] H. L. Daniels, Electronics 18, 125 (February, 1945).

PHYSICAL REVIEW VOLUME 80, NUMBER 4 NOVEMBER 15, 1950

Theory of Superconductivity*†

L. TISZA
Research Laboratory of Electronics and Department of Physics, Massachusetts Institute of Technology, Cambridge, Massachusetts
(Received June 1, 1950)

A quantum-mechanical model has been developed exhibiting the characteristic properties of superconductors. Localized "atomic" wave functions are used to construct many-electron wave functions obeying the exclusion principle and corresponding to definite electronic localization (ϕ-functions). The crystal translations will take these over into a set of, say ω, equivalent ϕ-functions. Quantum resonance of these provides a zero-order wave function with the correct symmetry properties. (Ψ-functions.) The ϕ-functions of small ω have a high translational symmetry and are referred to as "electron-lattices." The model has superconducting properties if its lowest state is described by a ψ-function obtained through the resonance of at least three resonating electron lattices, and if this state is somewhat depressed below the continuum of high ω-states. The latter can also be described in the standard band formalism. In the absence of external fields the lowest state is without a current. If the transition from ϕ- to ψ-functions is carried out in the presence of a magnetic field, one automatically obtains a current "induced" by the field, and connected with it by the well-known London relation. The present method is not adequate to prove that the conditions stated are actually satisfied in superconductors. Nevertheless, qualitative quantum-chemical arguments make it appear plausible that these conditions are satisfied in the regions of the periodic table where the actual superconductors are located. Conversely, if the theory is accepted, a rather detailed insight is gained into the quantum-chemical properties of superconductors. The recent experimental and theoretical work on the isotope effect is being discussed.

I. INTRODUCTION

WHEREAS we have a good understanding of the phenomenological aspects of superconductivity,[1] the question of the electronic mechanism is at present still completely open. The theories advanced so far can be classified by and large into three types. They assume that the system of superelectrons has the properties of a "crystal lattice," of an "ideal gas" or of a "gas of interacting particles."

The ideal gas type theories, assuming that the superelectrons are unusually weakly coupled with the lattice and with each other,[2] can be eliminated at once since they are in conflict with the general principle that approaching absolute zero the role of the various interactions is on the increase rather than on the decrease. Superconductors are no exceptions as the experimentally established drop in the entropy indicates.

The lattice type theories[3] have never been integrated into the quantum-mechanical theory of metals and their assumption of weak coupling between electron and ionic lattice is greatly objectionable.

The theories of the third type[4] start from the standard band theory of metals and try to refine this theory by introducing the interaction of the electrons. Although this approach is fundamentally not unsound, it led to great complexities without any convincing results. (See, however, Fröhlich's recent theory discussed in Section V.)

It is not hard to point out the root of the difficulties of the last approach. We know from the macroscopic theory[1] that the transition into the superconducting state is a sort of "ordering" or "condensation" phenomenon. The interaction of an electron pair leads essentially to the second virial coefficient of the electron gas. It is well known,[5] however, that the second virial coefficient, or virial coefficients up to any finite number for that matter, are inadequate to account for condensation.

A reasonable way out would be to choose more appropriate wave functions at the outset. Actually there is a standard alternate method to the Bloch procedure, namely the use of Heitler-London type localized atomic wave functions. It is hardly a coincidence that the well-known Heisenberg-Bloch theory of ferromagnetism (also an order-disorder phenomenon) was based on functions of this type.

In its original form this method had several shortcomings. The use of neutral atomic functions made it unsuitable for questions of conductivity, and the lack of orthogonality of the atomic functions rendered their use cumbersome. These difficulties, however, are not inherent in the method. Slater has pointed out[6] that the neutral atomic states can be augmented easily by polar states and Wannier has shown[7] that the Fourier transforms of orthogonal band functions form an orthogonal set of functions which provide a degree of localization approaching that of the atomic functions. Thus the use of such generalized atomic functions is completely jus-

* This work has been supported in part by the Signal Corps, the Air Materiel Command, and the ONR.
† Presented at the meeting of the A.P.S., New York, February 4, 1950.

[1] C. J. Gorter and H. Casimir, Physica **1**, 306 (1934); F. London, Phys. Rev. **74**, 562 (1948), also F. London, *Superfluids, The Macroscopic Theory of Superconductivity* (John Wiley and Sons, Inc., New York, 1950), Vol. I.

[2] F. Bopp, Zeits. f. Physik **107**, 623 (1937).

[3] J. J. Thomson, Phil. Mag. **44**, 657 (1922); R. de L. Kronig, Zeits. f. Physik **78**, 744 (1932); **80**, 203 (1933).

[4] J. C. Slater, Phys. Rev. **51**, 195 (1937); **52**, 214 (1937); W. Heisenberg, Zeits. f. Naturforsch. **2a**, 185 (1947); **3a**, 65 (1948); Ann. d. Physik 6F **3**, 289 (1948); M. Born and K. C. Cheng, J. de phys. et rad. Serie **8**, **9**, 249 (1948); also F. London, reference 1.

[5] J. E. Mayer and M. G. Mayer, *Statistical Mechanics* (John Wiley and Sons, Inc., New York, 1940), Chapts. 13, 14. B. Kahn and G. E. Uhlenbeck, Physica **5**, 399 (1938).

[6] For example, see J. C. Slater, Phys. Rev. **35**, 509 (1930).

[7] G. Wannier, Phys. Rev. **52**, 191 (1937); see also J. C. Slater, Phys. Rev. **52**, 198 (1937).

tified within the framework of the standard theory. They will provide the point of departure for our developments. These will be of a rather general nature and no specific assumptions will be made concerning the properties of the atomic functions.

II. THE WAVE FUNCTION OF SUPERCONDUCTORS

As a start in carrying out the program outlined in Section I, we discuss the localized wave functions of a solid in the absence of an external field. In order to emphasize the essential points of the argument, we discuss at first a greatly simplified case.

Consider a linear chain of N ions. This "fundamental domain" is periodically repeated so as to form a one-dimensional ideal lattice of the spacing a. We take a system of ν electrons per fundamental domain.

The Schrödinger equation of the system of electrons is

$$\mathcal{H}\Psi = E\Psi \tag{1}$$

with

$$\mathcal{H} = -(h^2/2m)\sum_j \nabla_j^2 + U(\mathbf{r}_1, \mathbf{r}_2, \cdots, \mathbf{r}_\nu), \tag{2}$$

where $\mathbf{r}_j$ represents the coordinates of the jth electron, U is the potential energy containing the interactions of the electrons with each other and with the ions. The other symbols have their usual meanings. U is periodic, i.e. it is invariant under the simultaneous translation of all the electrons:

$$T_l: \quad x_j \to x_j + la \quad j = 1, 2, \cdots \nu, \tag{3}$$

where x is the coordinate pointing along the chain and l is an integer.

We build up an approximate wave function of the solid from atomic wave functions: $u_{n_j}(\mathbf{r}_j)$ corresponding to the localization of the ith electron at the n_jth ion. We assume at first that there is a single wave function for every ion and neglect in particular spin and orbital degeneracy. We assume the functions u_{n_j} to be orthogonal.

Since we want to consider ionic states, we have to admit $\nu \leqq N$. The neutrality of the whole system can be assured by an adjustment of the potential U. This means physically that the number of conduction electrons outside a filled band is less than one per atom. If the degeneracy of the atomic functions were taken into account, ν could also exceed N.

We define many-electron functions of the following type:

$$\phi_{n_1 n_2 \cdots n_\nu} = \frac{1}{(\nu!)^{\frac{1}{2}}} \sum_P (-)^P P \varphi_{n_1 n_2 \cdots n_\nu}, \tag{4}$$

where

$$\varphi_{n_1 n_2 \cdots n_\nu} = u_{n_1}(\mathbf{r}_1) u_{n_2}(\mathbf{r}_2) \cdots u_{n_\nu}(\mathbf{r}_\nu) \tag{5}$$

and the summation is over all the permutations of the electrons. In certain connections $\varphi_{n_1 n_2 \cdots n_\nu}$ will prove to be an adequate "representative" of the determinant $\phi_{n_1 n_2 \cdots n_\nu}$. In $\varphi_{n_1 n_2 \cdots n_\nu}$ the individual electrons are localized. In contrast, $\phi_{n_1 n_2 \cdots n_\nu}$ is antisymmetric with respect to the permutation of the electrons, but it is still a localized state in the sense that we know of every ion whether or not its orbit u is occupied by an electron. These functions will be briefly referred to as ϕ-functions. Although satisfying the exclusion principle, they will not in general be satisfactory eigenfunctions of the Schrödinger equation (1) since they do not have the correct transformation properties respective to the crystal translations T_l defined in (3). The application of the operators T_l generates from every ϕ-function a whole set of new functions:

$$T_l \phi_{n_1 n_2 \cdots n_\nu} = \phi_{n_1 + l,\, n_2 + l \cdots n_\nu + l}. \tag{6}$$

The periodic boundary condition assures that each set contains at most N different functions. However, the symmetry of the charge distribution corresponding to $\phi_{n_1 n_2 \cdots n_\nu}$ may be such that some or all of the functions (6) are identical. Let ω be the smallest integer for which the set of numbers $n_1, n_2 \cdots n_\nu$ is (modulo N) identical with the set $n_1 + \omega, n_2 + \omega_1 \cdots n_\nu + \omega$. Then the operator T_ω is equivalent to a permutation of the electrons and we have

$$T_\omega \phi_{n_1 n_2 \cdots n_\nu} = \pm \phi_{n_1 n_2 \cdots n_\nu}, \tag{7}$$

where the sign depends on whether the permutation is even or odd.

The number of significantly different ϕ-functions or the degree of the translational degeneracy is ω.

It is an easy matter to use the set (6) of ϕ-functions to construct what we call Ψ-functions having the correct translational symmetry properties, but these may be devoid of physical meaning if strongly perturbed by ϕ-functions belonging to other sets. Postponing the discussion of this important point we first carry out formally the perturbation calculation within a single set of functions.

If no ambiguity arises, we will use the simplified notation:

$$\begin{aligned} \phi_{(l)} &\equiv \phi_{n_1 + l,\, n_2 + l, \cdots n_\nu + l}, \\ \varphi_{(l)} &\equiv \varphi_{n_1 + l,\, n_2 + l, \cdots n_\nu + l}. \end{aligned} \tag{8}$$

We must solve the secular determinant given by the matrix elements

$$\mathcal{H}_{ll'} = \int \phi_{(l)}^* \mathcal{H} \phi_{(l')} d\tau, \tag{9}$$

where $d\tau = d\mathbf{r}_1 d\mathbf{r}_2 \cdots d\mathbf{r}_n$.

Because of the translational symmetry $\mathcal{H}_{ll'}$ depends only on the difference of the indices, hence we use the abbreviated notation

$$\mathcal{H}_{ll'} \equiv \mathcal{H}_{l-l'}.$$

We assume for simplicity's sake that only neighboring atomic functions u_n and u_{n+1} overlap noticeably. Consequently all matrix elements (8) vanish except $\mathcal{H}_1$

and $\mathcal{H}_0$. Moreover

$$\mathcal{H}_1=\int \phi_{(0)}{}^*\mathcal{H}\phi_{(1)}d\tau=\int \varphi_{(0)}{}^*\mathcal{H}\varphi_{(1)}d\tau.$$

That is, the effect of exchange can be neglected for the calculation of $\mathcal{H}_1$ and the "representative term" can be used instead of the determinant ϕ. This is by no means true in case of $\mathcal{H}_0$ for which the exchange will be in general of importance. Standard methods lead to the zero-order wave function

$$\Psi_\kappa=\omega^{-\frac{1}{2}}\sum_{l=0}^{\omega-1}\exp(i\kappa l/N)\phi_{(l)},$$

$$\kappa=(0, 1, \cdots\omega-1)2\pi N_x/\omega \qquad (10)$$

and the corresponding energy value

$$E_n=\mathcal{H}_0+2\mathcal{H}_1\cos(\kappa/N). \qquad (11)$$

(It may be noted that $P=(\hbar\kappa/Na)$ is the so-called quasi-momentum of the electron system.)

We will find the current associated with the state (10). The so-called coarse-grained current density is

$$J_x=(e\hbar/mV)\sum_j\int\partial\Psi/\partial x_j d\tau, \qquad (12)$$

where V is the volume of the fundamental domain.

A straightforward calculation leads to

$$J_x=(ve\hbar/Vm^*a)\sin(\kappa/N), \qquad (13)$$

where the "effective mass" m^* is defined by the equation

$$1/m^*a=(2/m)\int\varphi_{(l)}\partial\varphi_{(l+1)}/\partial x_j d\tau. \qquad (14)$$

The ϕ-functions were assumed to be real. Of course, (14) is independent of the special choice of l and j.

The currents thus obtained are of a very special kind. They correspond to the organized drift of the electrons in the course of which the strong electronic correlation inherent in the ϕ-function representation is conserved. This is in contrast with the normal currents of the Bloch theory which are obtained by a random superposition of single-electron currents.

We now turn to the discussion of the validity of these results. In addition to several simplifying assumptions which we shall drop without altering our results essentially, we made the crucial assumption that the perturbation calculation can be carried out within a single set of ϕ-functions. In general, however, one will expect accidental degeneracies owing to the coincidence of the energies of ϕ-functions belonging to different sets. Consequently these functions may "mix" with the Ψ-function (10) destroying its high electronic correlation *provided the sets have the same* ω. Only in exceptional cases can one expect the correlation to survive the perturbation of other states.

At present we shall investigate the implication of such an exceptional situation without arguing the question of its actual occurrence. More precisely, we assume that the lowest state of the system corresponds to some regular charge distribution described by ϕ-functions of low translational degeneracy ($\omega\ll N$). Such states will be referred to as "electron-lattices." The resonance of these leads to a splitting into ω discrete levels adequately described by the Ψ-functions (10). Immediately joining the lowest state there are others obtained by removing a small number of electrons from the lowest configuration ("lattice defects"). The corresponding wave functions do not "mix" with the ground state because of their different symmetry numbers ω. A finite amount higher are the states in which the lattice "melts." Their representation in terms of Bloch function is undoubtedly more appropriate. On the other hand the Bloch function would be just as inappropriate to represent the discrete states as, say, free particle wave functions would be to represent a crystal.

Since κ is a multiple of $2\pi N/\omega$, it is obvious from (13) that a non-vanishing current can be obtained only for $\omega\geqq 3$. Even then the current vanishes for the ground state for which $\kappa=0$ or N/π, according to whether $\mathcal{H}_1<0$ or $\mathcal{H}_1>0$. Thus we have the general result that the lowest state of the system is always devoid of current. This fact is frequently referred to as Bloch's theorem and was considered as a baffling dilemma for any theory of superconductivity until the question was clarified by F. and H. London,[1] whose well-known phenomenological theory emphasized the importance of the magnetic field for superconductivity. The modification of the above results in a magnetic field will be the subject of the next section.

We will now rid our discussion of some of the simplifying assumptions introduced earlier.

The generalization from one to three dimensions could be carried out by a more complete notation, using vectorial indices and the like. In particular the degree of translational degeneracy of a ϕ-function will be characterized by a triple of numbers $\omega_1\omega_2\omega_3$. In a cubic crystal the functions with $\omega_1=\omega_2=\omega_3$ will likely be of special importance. At any rate in this general discussion we will continue to use a single number ω.

Less trivial is the generalization to the case in which the orbital and spin degeneracies of the single-electron wave functions are taken into consideration. Fortunately the great difficulties of constructing an antisymmetric wave function having a definite multiplicity (singlet in our case) need not be handled explicitly. The main point of our theory is that only the transition from the ϕ-functions to the Ψ-functions is treated in detail and the real difficulties are by-passed by the postulation of the ϕ-functions. Hence we shall satisfy

ourselves with the barest outline of how the ϕ-function could be constructed in principle.

The method to be used in a generalization of the Heitler-London-Slater-Pauling method of quantum chemistry.[8] An important intermediate step is the construction of bond wave functions corresponding closely to the valence bond pattern of the chemists. In the next step one considers the resonance between various valence bond structures. The result of this procedure will provide the ϕ-function and the energy $\mathcal{H}_0$. In the theory of the chemical bond this is usually the last step, since ionic states are mostly ignored. This is however not inherent in the method. Our ϕ-functions have an ionic character (except those with $\omega=1$). This is the reason they can be used to represent current carrying states.[8a]

Regarding the validity of our procedure we can repeat our reservations stated above: only in exceptional cases can it be expected that this particular sequence in the approximation is justified. However, we are interested in just such exceptional cases in which a small group of levels is depressed below the continuum.

At absolute zero the system is supposed to be in the lattice state ψ_κ with $\kappa=0$ or π/N (see above).

Slightly above $T=0$ the system is a mixture of electrons in the lattice state and of electrons "melted" from the lattice. The transition temperature is reached when the long range correlation of the electron lattice vanishes. We hope to come back to this question at a later time.

It is also plausible that an electric field would excite the system into the current carrying states[8b] and that dissipation owing to the lattice would not start before the energy is increased to the continuum.

The most important question is the behavior of the model in a magnetic field. This is the subject of the next section.

III. MAGNETIC FIELD AND SUPERCURRENT

Consider a system of the type discussed in Section II. Its lowest state Ψ_0 should arise through the resonance of a set of ϕ-functions with $\omega \geqq 3$. As emphasized above, there is no current associated with Ψ_0. The effect of switching on a magnetic field will be to introduce a phase difference into the resonance of the ϕ-functions and thus give rise to a current.

In spite of the fact that the above statement is rather plausible, since it is essentially Larmor's theorem, its formal proof is not quite straightforward; the presence of the magnetic field requires a drastic modification of the considerations of the last section.

Even though the magnetic field is homogeneous, say in the z direction, the Schrödinger equation contains the vector potential for which a possible choice is

$$\mathbf{A}=\tfrac{1}{2}\mathbf{H}\times\mathbf{r}. \tag{15}$$

The modified Schrödinger equation has no longer a translational symmetry. This renders it impossible to introduce currents of the type discussed in the last section. Those currents are linear, extending uniformly over the infinite crystal. In this respect they are analogous to the currents used in the theory of normal conductivity. Of course, in the latter case this infinite extension of the current is purely formal since the interaction with the lattice limits the "coherence length" of such a plane wave current to a free path.

The situation is quite different in the superconductor. The current elements are not limited by any damping mechanism and it is quite unrealistic to build up a supercurrent of unlimited linear current elements. In fact, the supercurrents consist of thin current filaments closing upon themselves. These current loops depend on the geometry of the conductor. It is of course desirable to separate the quantum-mechanical discussion from the boundary value problem and this is indeed possible, since any macroscopic current loop can be decomposed into elementary loops, as is done, for example, in the proof of Stokes' theorem. These loops or rings can be considered as large compared with a unit cell but small compared with macroscopic dimensions. *The translation group associated wtih these currents consists of the rotations of the ring rather than of the lattice.*

Accordingly we now consider N ions at the corners of a regular polygon represented by the vectors $\mathbf{R}_1$, $\mathbf{R}_2$, $\cdots\mathbf{R}_N$, the origin of the coordinate system being in the center of the polygon. A magnetic field $H=H_z$ is perpendicular to the plane of the ring. The Hamiltonian (2) is replaced by

$$\mathcal{H}=-(\hbar^2/2m)\sum_j[\nabla_j-(ie/\hbar c)\mathbf{A}(\mathbf{r}_j)]^2+U, \tag{16}$$

where $\mathbf{A}(\mathbf{r}_j)$ is the vector potential at the position of the jth electron. The electrostatic energy U is invariant under the rotations of the ring by the angle $2\pi/N$. These rotations operate only on the electrons and are not identity transformations of the crystal.

In case of a vanishing vector potential, there is a perfect formal analogy between the ring and the linear chain with cyclic boundary conditions. We again introduce ϕ-functions and find it convenient to use the "representative terms": $\varphi_{n_1 n_2 \cdots n_\nu}$.[8c] Furthermore the rotations of the ring lead to a set of functions $\varphi_{(l)}$ with $l=0, 1, \cdots\omega-1$.

In the presence of a magnetic field, however, the functions $\varphi_{(l)}$ with different indices will no longer be equivalent, since the rotation transfers the electrons to positions with different values of the vector potential.

[8] A concise account with references to the earlier literature is given by G. W. Wheland, J. Chem. Phys. 3, 230 (1935).

[8a] The case $\omega=2$ is of interest. Here two ionic states are in resonance. The corresponding Ψ-function is real, we have a standing wave and no current.

[8b] This case has been investigated by J. M. Luttinger.

[8c] This proves to be satisfactory since our main interest is in the current which is symmetric in the electron coordinates.

The same difficulty was encountered by Peierls[9] while computing the diamagnetism of electrons in a periodic field. He introduced the artifice of carrying out simultaneously with the translation a gauge transformation shifting the origin of the vector potential so that the combined transformations leave the Schrödinger equation invariant. The procedure was adapted by London[10] to ring molecules with the view of obtaining the diamagnetic anisotropy of aromatic compounds. We shall follow London's procedure closely. The new feature of the present discussion is the replacement of London's single electron functions by localized many-electron functions.

We are solving the Schrödinger equation by a function of the form:

$$\Psi=\omega^{-\frac{1}{2}}\sum_{l=0}^{\omega-1}c_l\exp\left[\frac{ie}{\hbar c}\sum_j \mathbf{A}_{n_j+l}\cdot\mathbf{r}_j\right]\varphi_{(l)}, \tag{17}$$

where $\mathbf{A}_{n_j+l}=\frac{1}{2}\mathbf{H}\times\mathbf{R}_{n_j+l}$ is the vector potential at the position of the n_j+lth ion. The coefficients c_l are obtained from the system of linear equations:

$$\sum c_l(\mathcal{H}_{ll'}-E\delta_{ll'})=0, \tag{18}$$

where E is the energy, $\delta_{ll'}$ the Kronecker symbol and

$$\mathcal{H}_{ll'}=\int\varphi_{(l)}{}^*\exp\left[\frac{ie}{\hbar c}\sum_j(\mathbf{A}_{n_j+l'}-\mathbf{A}_{n_j+l})\cdot\mathbf{r}_j\right]$$

$$\left\{-\frac{\hbar^2}{2m}\sum_j\left[\nabla_j-\frac{ie}{\hbar c}(\mathbf{A}(\mathbf{r}_j)-\mathbf{A}_{n_j+l'})\right]^2+U\right\}\varphi_{(l)}d\tau. \tag{19}$$

We evaluate the matrix elements (19) under the assumption that only neighboring wave functions overlap, i.e. $\mathcal{H}_{ll'}=0$ unless $l'=l$ or $l'=l+1$. We have

$$\mathcal{H}_{ll}=\mathcal{H}_0=\int\varphi_{(l)}{}^*\left\{-\frac{\hbar^2}{2m}\sum_j\left[\nabla_j-\frac{ie}{\hbar c}(\mathbf{A}(\mathbf{r}_j)-\mathbf{A}(\mathbf{R}_{n_j+l})\right]^2+U\right\}\varphi_{(l)}d\tau. \tag{20}$$

This expression is independent of l. It depends only quadratically on the magnetic field, corresponding to a small diamagnetic effect which we shall neglect. In the same approximation we can consider the $\varphi_{(l)}$ as real. On the other hand, $\mathcal{H}_{l\,l+1}$ depends essentially on the magnetic field through the exponential gauge factor.

The important contribution to the integral comes from the region $\mathbf{r}_j\approx\frac{1}{2}(\mathbf{R}_{n_j+l}+\mathbf{R}_{n_j+l+1})$ $j=1, 2, \cdots\nu$.

Using (15) and $\mathbf{H}=H_z\mathbf{k}$ we have

$$\tfrac{1}{2}\sum_j(\mathbf{A}_{n_j+l+1}-\mathbf{A}_{n_j+l})\cdot(\mathbf{R}_{n_j+l+1}+\mathbf{R}_{n_j+l})$$
$$=\tfrac{1}{2}H_z\sum_j(X_{n_j+l+1}Y_{n_j+l}-Y_{n_j+l+1}X_{n_j+l})=\nu H_zS/N,$$

where S is the area of the polygon. Introducing the notation

$$f=\nu eH_zS/\hbar c \tag{21}$$

we obtain

$$\mathcal{H}_{l\,l+1}=e^{if/N}\mathcal{H}_1, \quad \mathcal{H}_{l\,l-1}=e^{-if/N}\mathcal{H}_1 \tag{22}$$

with

$$\mathcal{H}_1=\int\varphi_{(l)}\left\{-\frac{\hbar^2}{2m}\sum_j\left[\nabla_j-\frac{ie}{\hbar c}(\mathbf{A}(\mathbf{r}_j)-\mathbf{A}_{n_j+l+1})\right]^2+U\right\}\varphi_{(l+1)}d\tau.$$

Again, as in the case of (20), this integral is independent of l and its dependence on the magnetic field is negligible. Equations (18) now become

$$c_{l-1}\mathcal{H}_1e^{-if/N}+C_l(\mathcal{H}_0-E)+C_{l+1}\mathcal{H}_1e^{if/N}=0. \tag{23}$$

These are solved by $c_l=e^{ipl/N}$ with $p=2\pi N/\omega$ $(0, 1, \cdots\omega-1)$. Hence

$$\psi_k=\frac{1}{\omega^{\frac{1}{2}}}\sum_{l=0}^{\omega-1}\exp\left[\frac{ipl}{N}+\frac{ie}{\hbar c}\sum_j\mathbf{A}_{n_j+l}\cdot\mathbf{r}_j\right]\varphi_{(l)} \tag{24}$$

and the energy

$$E=\mathcal{H}_0+2\mathcal{H}_1\cos[(p+f)/N]. \tag{25}$$

The quantum number p is analogous to κ introduced in (10) but it is connected with the rotation of the ring rather than with the translation of the lattice.

The current J_s along the ring associated with the state (24) is

$$J_s=\frac{e\hbar}{mV}\sum_j\int\Psi_k{}^*\frac{\partial}{\partial s}\psi_kd\tau-\frac{e^2}{mcV}\sum_j\int A_s(\mathbf{r}_j)\Psi_k{}^*\Psi_kd\tau, \tag{26}$$

where $\partial/\partial s$ indicates differentiation along the ring. Inserting (24) one obtains

$$J_s=-\frac{1}{\omega}\frac{e\hbar}{mV}\sum_j\left\{\int\varphi_{(l)}\frac{\partial}{\partial s}\varphi_{(l)}d\tau\right.$$
$$+\sin\frac{p+f}{N}\left[\int\varphi_{(l)}\frac{\partial}{\partial s}\varphi_{(l+1)}d\tau-\int\varphi_{(l+1)}\frac{\partial}{\partial s}\varphi_{(l)}d\tau\right]$$
$$\left.+(e/\hbar c)\sum_j\int[A_s(R_{n_j+l})-A_s(\mathbf{r}_j)]\varphi_{(l)}{}^2d\tau.\right\}$$

On integration by parts one sees that the first term vanishes and the next two terms are equal. The last term also vanishes since the bracket is linear in the coordinate.

[9] R. Peierls, Zeits. f. Physik **80**, 763 (1933).
[10] F. London, J. de phys. et rad., Serie 7, **8**, 397 (1937).

Hence we have

$$J_s=(eh/m^*aV)\sin[(p+f)/N] \tag{27}$$

with

$$1/m^*a=(2/m)\int \varphi_{(l)}\partial\varphi_{(l+1)}/\partial s d\tau. \tag{28}$$

It may be noted that the above results depend essentially on the condition $\omega\geqq 3$. For $\omega=1$ there is no degeneracy. In case $\omega=2$ one must put $f=0$ in (25) and (27) in order to obtain the correct solution which is thus independent of the magnetic field and no current is induced. This is in line with the exceptional nature of this case noted in Section II.

We shall find the current induced in the case $\omega\geqq 3$ if the magnetic field is turned on adiabatically while the system is in its ground state.

In the absence of a magnetic field the system can be described either in the present formalism or in that of the last section. The lowest state will be given by $p=0$ or $\kappa=0$, respectively. It is to be noted that no simple relation exists between the two sets of quantum numbers for the excited states of the system.

For the small magnetic fields to be considered the sine can be replaced by its argument and we obtain from (27) and (21)

$$J_s=\nu e^2H_zS/Vm^*caN.$$

Introducing the notation $n_s=\nu/V$ for the density of superconducting electrons and the London constant

$$\lambda=m^*/n_se^2 \tag{29}$$

we obtain

$$(aNc\lambda/S)J_s=(1/S)\oint c\lambda\mathbf{J}\cdot d\mathbf{s}=-H. \tag{30}$$

The negative sign expresses the fact that we have diamagnetism. This is evident since we have, according to (25) and (21),

$$\partial^2E/\partial H^2\sim\partial^2E/\partial p^2$$

with a positive proportionality constant and in the lowest state the latter quantity must be positive. Equation (30) is, of course, the London relation.

$$\mathrm{curl}(c\lambda\mathbf{J})=-\mathbf{H}. \tag{31}$$

It should be noted that at the present stage of the theory it is arbitrary that λ is placed *after* the curl operator.

In a certain sense (31) is only an approximation since the effective mass, and hence λ, is not necessarily a constant but could depend on the crystallographic orientation of the sides of the polygon. The same is true for the number ω. It remains to be seen whether or not single crystals lend themselves to a more detailed analysis. Recent results of Pippard[11] seem to indicate that λ has no simple tensor properties.

Finally a word about the destruction of superconductivity by a magnetic field. It follows both from the phenomenological theory and from the above discussion that in a magnetic field the superconductor contains an additional energy-term $\sim H^2/\lambda$. If this additional term is large enough to bridge the gap between the lowest state and the continuum, superconductivity will be destroyed.

IV. THE CLASSIFICATION OF SOLID TYPES

The results obtained in the last two sections are of a somewhat formal nature. We have found a set of conditions for superconductivity expressed in terms of the eigenfunctions and eigenvalues of a system of electrons in a periodical potential. It would be desirable, of course, to have some independent reasons why these conditions should be satisfied specifically in superconductors.

The most characteristic feature of these conditions is the requirement that the lowest state of the system should be built up by resonance of "electron lattices." These are essentially ionic states in which some ions or bonds have a surplus and others a defect of electrons, all arranged in some regular pattern. Is there any reason to expect such a rather unusual situation?

The distribution of the superconductors over the periodic table (Table I) provides us with a tentative answer to this question. It is seen that the superconductors are found in two groups commonly referred to as *hard* and *soft* superconductors. The former are transition metals; they are "hard" both mechanically and magnetically; i.e., their critical fields at absolute zero, H_c and the slopes of their threshold curves $-dH_c/dT$ are higher than the corresponding values of the second group.

In Table I we have indicated also Hume-Rothery's[12] classification of the crystals of the elements.

Class i contains the regular metals with cubic close-packed, body-centered and hexagonal close-packed structures.

Class iii contains insulators and semiconductors. In these crystals the atoms have a strong tendency to complete their octet shell by forming covalent bonds with as many close neighbors as indicated by their electronegative valence. This is also called the (8-N) rule.

Class ii contains the so-called irregular metals with more or less distorted metallic structures. They show slight remnants of the tendency to follow the (8-N) rule; e.g., Zn and Cd crystallize in a hexagonal structure with an axis ratio 1.9 instead of 1.63 in the close-packed case. In these elongated structures each atom has six neighbors lying in one plane, and at a greater distance three neighbors above, and three below. Hume-Rothery comments that this observance of the (8-N) rule "is very curious since there can be no question of building

[11] International Conference on the Physics of Very Low Temperatures. Cambridge, Massachusetts, Sept. 1949.

[12] W. Hume-Rothery, The Structure of Metals and Alloys, Inst. of Metals (London, 1936), p. 21.

TABLE I. Periodic table.

																H	He
Li	Be											B	C	N	O	F	Ne
Na	Mg											Al*	Si	P	S	Cl	A
K	Ca	Sc	Ti*	V*	Cr	Mn	Fe	Co	Ni	Cu	Zn*	Ga*	Ge	As	Se	Br	Kr
Rb	Sr	Y	Zr*	Nb*	Mo	Tc	Ru	Rh	Pd	Ag	Cd*	In*	Sn[a]	Sb	Te	I	Xe
Cs	Ba	La*–Lu	Hf*	Ta*	W	Re	Os	Ir	Pt	Au	Hg*	Tl*	Sn*[b] Pb*	Bi	Po	At	Rn
Fr	Ra	Ac	Th*	Pa	U*												
			Class i										Class ii			Class iii	

* Superconducting elements are starred.
[a] Grey tin.
[b] White tin.

up an octet of electrons by simple covalent bonds when there are only two electrons per atom, and these elements have normal metallic properties."

From the point of view of the present theory the above situation can be handled as follows.

In their lowest state class iii elements are described by a non-degenerate ϕ-function for which, in particular, $\omega = 1$. The reason for this is the existence of energetically advantageous closed-shell configurations; these may be atomic (rare gases), molecular, or extending over the whole crystal (diamond structure for *IVB* elements). The energy gap between the lowest state and the continuum of excited states is essentially determined by the excitation potential of the closed shell and can be several electron-volts, decreasing by and large while proceeding to the left or downwards in the periodic table.

For Cu, Ag, Au the gap has virtually vanished and we see no tendency of the outer electrons to form closed structures. This may be described also in Pauling's terminology according to which the metallic bonds are essentially resonating covalent bonds.[13] For class i the number of available orbits greatly exceeds the number of electrons.

Class ii elements which are practically identical with the soft superconductors show an intermediate behavior.[13a]

This means in the first place a very small value of the energy gap so that above the transition temperature we have a normal metal. In the second place the lack of electrons to fill up a closed structure makes it appear reasonable that the lowest state will be built up of ϕ-functions corresponding to some regular pattern of completely filled and completely empty shells. *This is precisely the situation postulated in Sections II and III.*

The value of ω and the assurance that it is larger than 2 could be obtained only through a more detailed investigation.

On the whole, for the soft superconductors we can give an affirmative answer to the question asked at the beginning of this section: it is plausible to assume that our postulates are selectively satisfied in this case.

The peculiar accumulation of the hard superconductors in a particular region among the transition metals makes it likely that the various *d*-electrons cannot be considered on an equal footing. The division of the *d*-electrons into two groups has already been proposed by Pauling.[14] As a slight modification of Pauling's idea we suggest the following working hypothesis.

Within the *d*-shell of the transition metals, one must distinguish a subshell which can be filled up by approximately half of the *d*-electrons. The corresponding wavefunctions (possibly after hybridization with *s* and *p* function) lend themselves to covalent binding. The rest of the *d*-electrons occupy unshared orbits and contribute to the ferromagnetism of the iron group.

We refer to Pauling's paper[14] for supporting evidence relating to interatomic distances, characteristic temperature, hardness, compressibility, coefficient of thermal expansion and the atomic saturation moments of the ferromagnetic elements.

Additional evidence is provided by electric resistivities (Table II). The well-known drop of resistivity from Ni to Cu is not only duplicated but exceeded by V and Cr, and likewise in the case of the heavier elements. Thus Cr seems to have an electronic structure of nearly one *s* electron outside a closed shell.[14a]

This situation is again consistent with our conditions for superconductivity. The ϕ-functions of the hard superconductors correspond to states in which part of

[13] L. Pauling, Nature **161**, 1019 (1948).
[13a] Hume-Rothery classified boron into class ii and Po, Bi into class iii. All these seem to be borderline cases. Whereas Bi is not yet superconducting, the gold-bismuth intermetallic compound is.

[14] L. Pauling, Phys. Rev. **54**, 899 (1938); J. Am. Chem. Soc. **69**, 542 (1947).
[14a] It may be noted that the resistivity data for the hard superconductors were taken almost at random from among unusually divergent experimental results. Some of the resistivities found in the literature are even considerably higher than those given in Table II.

TABLE II. Resistivity in microhm-cm.

Ti	50	V	60	Cr	2.6	Ni	10	Cu	1.6
Zr	40	Nb	13	Mo	5	Pd	11	Ag	1.5
Hf	32	Ta	13	W	5.5	Pt	10	Au	2.4

the subshells are completely filled at the expense of others.

It is interesting to note that the rare earths also show some tendency to have a stable half shell.[14] The theoretical basis for this tendency may be that in a half-filled shell the orbital part of the wave function will be completely anti-symmetric in the state of highest multiplicity, which is a very advantageous configuration for keeping the electrons apart. The resulting spin is saturated while forming covalent bonds with neighboring atoms. At any rate, it might be worth while to study samarium and europium for the possible occurrence of superconductivity.

Finally, it might be fair to state that some of the ferromagnetic alloys have saturation moments which do not follow Pauling's curve.[15] This may change his quantitative statements but hardly the general qualitative idea.

Pauling's concept of the transition elements has been criticized also by Seitz[16] since x-ray emission spectra of Ni and Cu failed to show evidence of the two types of *d*-electrons. The reinvestigation of the x-ray spectra with increasing resolving power would be highly desirable.

V. DISCUSSION. THE ISOTOPE EFFECT[16a]

The results of the theory can be summed up as follows:

(i) The introduction of many-electron wave functions (Ψ-functions) arising out of the resonance of ω localized ϕ-functions provides an enrichment of the standard formalism of the quantum theory of solids. This may be of importance for such low temperature phenomena in which the electronic correlations are of importance, in particular superconductivity. For the latter phenomenon seemingly contradictory features can be united for the first time in a single formalism. All this is achieved by means of symmetry considerations, hence these results are rigorous, but limited in scope.

(ii) The above mentioned rigorous results can be supplemented by tentative qualitative considerations which seem to indicate that the suggested model has generally reasonable properties. These considerations have at the same time a heuristic character and are suggestive of the direction in which the development of a quantitative theory should be sought.

We will take up these two items in some detail.

First, we explain the relation of the present formalism to that of the standard band theory in terms of an analogy: In the case of atoms, the total angular momentum is expressed rigorously by a quantum number. In addition approximate quantum numbers are significant for the spectrum. The choice of these varies with the nature of the coupling which may be, for example, of the *L–S* or *j–j* type.

In case of the electrons in an ideal crystal the exact quantum number is that corresponding to the total quasi-momentum. In the standard theory the approximate quantum numbers are those of the quasi-momenta $k_1, k_2, \cdots k_j, \cdots$ of the individual electrons, (*k–k* coupling). In the present theory: the numbers $n_1, n_2, \cdots n_j, \cdots$ describing the centers of localization of the individual electrons in an "electron lattice" or ϕ-function (*n–n* coupling).

The ϕ-functions are characterized by "symmetry numbers" ω indicating the number of ϕ-functions equivalent under the crystal translation. The resonance of these leads to the Ψ-functions labelled by the quantum numbers of the quasi-momentum of the electron lattice. The individual quasi-momenta are not described by "good quantum numbers."

In case of filled bands the two coupling cases lead to identical results. The total quasi-momentum is zero; i.e., the wave function is invariant under the crystal translations and $\omega=1$. Otherwise the two representations are not equivalent, at least not in first approximation.

Of course the *k–k* coupling applies in most instances and the *n–n* coupling should prevail, if at all, only for the lowest states, hence the relevance of this case near absolute zero. The lowest state is non-conducting if $\omega=1$ or 2 and superconducting if $\omega\geqq 3$. The supercurrent induced by a magnetic field appears inevitably from the combination of the requirements of translational degeneracy with gauge invariance.

It is interesting to recall in this connection that Gorter,[17] while tentatively extending Nernst's law to irreversible processes, and discussing the increase of the resistivity of gold at low temperatures, conjectured that at absolute zero every solid should be either an insulator or a superconductor.

It is also possible that ϕ-functions with $\omega=1$ or 2 will be useful in describing the low temperature transition of magnetite into a state of high resistivity.[18]

The present discussion is limited to the case of superconductivity. The various quantum-mechanical attempts to providing a theory for this phenomenon were beset by a peculiar difficulty. The existence of the supercurrent and also London's heuristic considerations

[15] R. M. Bozorth, *Ferromagnetism* (D. Van Nostrand Company, Inc., New York, to appear in 1951). My thanks are due to Dr. Bozorth for communication of some of his conclusions.

[16] F. Seitz, *The Modern Theory of Solids* (McGraw-Hill Book Company, Inc., New York, 1940), pp. 429 and 440.

[16a] Note added July 19, 1950. This section has been revised and extended to include the discussion of experimental and theoretical work on the isotope effect which came to the attention of the author after completion of the manuscript.

[17] C. J. Gorter, Physica **5**, 483 (1938).

[18] Verwey, Haayman, and Romeijn, J. Chem. Phys. **15**, 181 (1947).

suggest a description in momentum space. In fact, most theories attempt to make it plausible that the electrons tend to "bunch" in momentum space. It remains completely unexplained, however, why this should set in at a sharp temperature.

Recently[19] the author has advanced arguments in favor of a principle according to which sharp transitions in crystals should be describable in terms of parameters which are translational invariants. The gist of the idea is that microscopic crystal properties can generally be described in terms of normal coordinates which multiply with a phase factor for crystal translations, and only the normal coordinates with zero phase difference will "survive" the statistical averaging. These parameters could be called macro parameters (or, by an extension of a standard terminology: ergodic parameters), in contrast to the micro- or statistical parameters. Such macro parameters are, for example, the atomic parameters specifying the equilibrium positions of the atoms in the unit cell and the parameters of long range order. The corresponding statistical parameters are associated with the lattice vibrations, and the short range order. Actually, all phase transitions the mechanism of which is understood can be characterized in terms of macro parameters. At any rate it would seem reasonable to accept tentatively the principle in question as a heuristic rule.

The spatial order required by this rule is not easily reconciled with the otherwise more plausible momentum space representations and has indeed been ignored by all theories of which we are aware. Even the lattice type theories[3] violate our rule, since the symmetries of the electron and ion lattices were supposed to be unrelated.

It is thus significant that the present theory resolves this difficulty in a natural fashion. The ϕ-functions exhibit the spatial order required by the theory of phase transitions, at the same time the resonance process leading to the Ψ-functions can be described in terms of the momentum of the electron lattice.

It may be added that the present formalism conforms to London's phenomenological theory. The well-known relation connecting the supercurrent with the magnetic field has been derived and London's interpretation of this relation as a quantum-mechanical restriction is confirmed. For the explanation of the absence of dissipation we can do hardly better than refer to a recent paper of London (pp. 570–571 of reference 1).

We may sum up by saying that the present theory provides an explanation for superconductivity in terms of such basic concepts as symmetry with respect to translations, permutations (exclusion principle) and suitably located gaps in the energy spectrum. We thus have a logical extension of the standard theory which uses similar means to account for the differences between metals, insulators and semiconductors and for the striking range of electronic mobilities (differing by as much as 10^{16}). All this is possible since in quantum mechanics current is closely connected with translational degeneracy.

Of course, the standard theory includes also an impressive number of quantitative results and it remains to be seen whether the present ideas will be similarly substantiated. The difficulties are here considerably greater than in case of the single electron problem.

At present we shall survey a few tentative heuristic ideas which may point the way toward such a development.

The first question concerns the correlation of superconductivity with the chemical properties of elements. The discussion of Section IV has shown that it is plausible to assume that our conditions are satisfied in the two regions of the periodic table where the so-called hard and soft superconductors are located. Such an assumption fits in well with semi-empirical considerations of Pauling[13,14] and Hume-Rothery[12] obtained from a variety of independent evidence.

This discussion has been carried out by using the language of the valence bond theory. It is of interest to inquire into the nature of the energy difference between the normal and superconducting state from the point of view of the band theory.

It is well known that in the course of the superconducting transition the electrons at the tail end of the Fermi distribution get rid of their entropy; i.e., organize into an ordered pattern (the resonating electron lattice according to the present theory). In contrast to the ordered states the Fermi distribution implies some random charge fluctuation. It is thus inescapable that the normal and superconducting states should differ by a small amount of energy associated with these fluctuations.

This question is closely connected with the interesting isotope effect recently discovered by Maxwell[20] and Reynolds, Serin, Wright and Nesbitt.[21] The transition temperature of mercury was found to vary with the average atomic weight according to the relation

$$dT_c = -a dM \tag{32}$$

with $a \approx 0.007°\text{K}$ (mass numbers).

The present theory may be conceived as the first step of the standard adiabatic approximation[22] in which the electronic wave functions are considered in the field of nuclei at rest. In the first approximation of this procedure the atomic weight could influence the transition temperature only through the intermediary of the lattice constant. This would actually depend slightly on the zero point vibration and hence on the atomic weight, but this effect can be estimated to account for

[19] L. Tisza, National Research Council Symposium on Phase Transitions, August, 1948. To appear in book form. Also RLE M.I.T. Technical Report No. 127. M. J. Klein and L. Tisza, Phys. Rev. 76, 1861 (1949).

[20] E. Maxwell, Phys. Rev. 78, 477 (1950).

[21] Reynolds, Serin, Wright, and Nesbitt, Phys. Rev. 78, 487 (1950).

[22] See reference 16, p. 470.

only two to three percent of the observed effect. Hence we must conclude that for quantitative purposes the second approximation taking into account the nuclear motion cannot be ignored.

At low temperatures the nuclear motion means only the zero-point vibration. The corresponding charge fluctuation would interact with the electronic charge fluctuation discussed above. A quantitative discussion of this effect is outside the scope of the present method but seems to provide the most promising point of departure for the quantitative developments.

The present manuscript was essentially completed when Fröhlich's[23] theory of superconductivity came to the author's attention. (Compare also the recent note of Bardeen.[24]) This theory is based on the interaction of free electrons with the lattice vibrations and led to a brilliant prediction of the isotope effect. It is possible that this is the definitive theory of superconductivity rendering the ideas of the present paper obsolete.

It seems, however, not improbable that the two theories represent different aspects of the same phenomenon. Fröhlich's superconducting electrons moving in a parallel beam and exhibiting distance correlations may provide a one-electron approximation to our resonating electron lattices. We may be confronted with a situation as provided by the "magic numbers" in nuclei where a one-particle approximation leads to unexpectedly good results. On the other hand the many-electron treatment might be necessary to treat the phase transition aspects and the correlation with chemical properties as discussed in the last section. It is hard to see how these features could be incorporated into Fröhlich's theory.

If the second alternative were true, the lattice vibrations would influence the quantitative aspects of superconductivity without being responsible for it. At first sight the isotope effect would seem to preclude this interpretation.

Indeed, Serin, Reynolds and Nesbitt[25] and Herzfeld, Maxwell and Scott[26] have suggested the integrated formula

$$T_c = T_0(M_0/M)^\alpha \tag{33}$$

for the description of their experiments, Here T_0, M_0 are transition temperature and average atomic weight at a standard state, and $\alpha = \frac{1}{2}$.

Equation (33) implies $T_c = 0$ for $M = \infty$, which would mean that superconductivity is impossible for infinitely heavy ions.

This argument is not quite convincing, since there are infinitely many expressions which reduce in the narrow range of observations to the empirical relation (32).

One taken almost at random is

$$T_c = T_\infty(1+\beta/M), \tag{34}$$

which conforms to (32) equally as well as does Eq. (33), provided the constants are related as follows:

$$T_\infty = T_0(1-\alpha), \quad \beta = M_0\alpha/(1-\alpha).$$

Here T_∞ is the transition temperature for infinite atomic weight.

The question obviously needs further clarification.

The author is greatly indebted to Professor F. London for elaborate discussions on the nature of superconductivity and to Professor Slater for many critical comments.

[23] H. Fröhlich, Phys. Rev. 79, 845 (1950). The author is indebted to Dr. Fröhlich for sending his manuscript before publication.
[24] J. Bardeen, Phys. Rev. 79, 167 (1950).
[25] Serin, Reynolds and Nesbitt, Phys. Rev. 78, 813 (1950).
[26] Herzfeld, Maxwell, and Scott, Phys. Rev. 79, 911(L) (1950). The author is indebted to Dr. Maxwell for communicating his results before publication.

A Note on Tisza's Theory of Superconductivity

J. M. LUTTINGER*,†
Institute for Advanced Study, Princeton, New Jersey
(Received April 24, 1950)

The equation of F. London connecting the electric field and the current in a superconductor is derived on the basis of Tisza's theory of superconductivity.

I. INTRODUCTION

RECENTLY[1] Tisza has presented a quantum-mechanical model which gives superconductivity at absolute zero. It was shown there that the "magnetic" London equation

$$c\nabla\times(\Lambda\mathbf{J})=-\mathbf{H} \tag{1}$$

follows from the assumptions of the theory. The "electric" equation

$$\partial(\Lambda\mathbf{J})/\partial t=\mathbf{E}, \tag{2}$$

however, was not derived. It is the purpose of this note to complete the theory by providing a derivation of (2). Just as the Tisza derivation of (1) takes as its model the London theory of the diamagnetism of aromatic molecules,[2] we shall take as ours a calculation of the acceleration by an electric field of a strongly bound electron. The method of gauge transformations developed there will then be applied to Tisza's model to derive Eq. (2). For simplicity we shall restrict ourselves to one dimension throughout this note.

II. THE BEHAVIOR OF A STRONGLY BOUND ELECTRON IN AN EXTERNAL ELECTRIC FIELD

In this case the Hamiltonian is

$$\mathcal{H}=-(\hbar^2/2m)\nabla^2+\sum_k V_k+\varphi,$$

where V is the potential of the kth ion and $\varphi=-eEx$, the potential of the external field. The Schrödinger equation is

$$\mathcal{H}\Psi=i\hbar\partial\Psi/\partial t.$$

Now just as in the Bloch[3] theory of strongly bound electrons we make the assumption that

$$\Psi=\sum_r c_r(t)\exp(-i\varphi_r t/\hbar)u_r, \tag{3}$$

where u_r is the wave function of an electron bound to an isolated atom at the point r, and φ_r is the external potential at the point r (i.e. $\varphi_r=-eEX_r$). The extra factor $\exp(-i\varphi_r t/\hbar)$ is of the nature of a gauge transformation, as will be clear from what follows. Substituting (3) in the Schrödinger equation we obtain

$$\sum_r \exp(-i\varphi_r t/\hbar)[-(\hbar^2/2m)\nabla^2+V_r+(\varphi-\varphi_r)+\sum_{k\neq r}V_r-i\hbar\partial/\partial t]c_r(t)u_r=0. \tag{4}$$

Now for an electron bound to an atom we may assume that the electric polarizability is very small, so that one has approximately (if the energy of the state u_r is E_0)

$$[-(\hbar_i^2/2m)\nabla^2+V_r+(\varphi-\varphi_r)]u_r\cong E_0u_r.$$

Equation (4) then becomes

$$\sum_r \exp(-i\varphi_r t/\hbar)[E_0+\sum_{k\neq r}V_k-i\hbar\partial/\partial t]c_r(t)u_r=0. \tag{5}$$

One sees then that the function of the gauge transformation $\exp(-i\varphi_r t/\hbar)$ was to center the potential at each atom. Writing $c_r=a_r\exp(-iE_0t/\hbar)$, multiplying (5) by u_m^* and integrating, we obtain (assuming approximate orthogonality)

$$\sum_r \exp[i(\varphi_r-\varphi m)t/\hbar](u_m,(\sum_{k\neq r}V_k)u_r)a_r=i\hbar\partial a_m/\partial t, \tag{6}$$

where

$$(u_m,Fu_n)=\int d^3x u_m^*Fu_r.$$

Equation (6) may be solved by palcing

$$a_m=f_\kappa(t)\exp(i\kappa ma). \tag{7}$$

a is the lattice constant, N the number of ions, and $\kappa=2\pi n/N$, $n=0, 1, \cdots, N-1$.

We have assumed periodic boundary conditions. Substitution of (7) in (6) yields

$$[\sum_r \exp(ieEa(r-m)t/\hbar)\exp(i\kappa a(r-m)\times(u_n,(\sum_{k\neq r}V_k)u_r)]f_\kappa=i\hbar\partial f_\kappa/\partial t. \tag{8}$$

The quantity in Eq. (8) in square brackets is independent of m because of the lattice periodicity (the V_r's are the same potentials at different points). Then the matrix element can depend only on $m-r$. Put

$$(u_m,(\sum_{k\neq r}V_k)u_r)=v(m-r).$$

* Frank B. Jewett Fellow.
† Now at: Department of Physics, University of Wisconsin.
[1] L. Tisza, Phys. Rev. **80**, 717 (1950).
[2] F. London, Comptes Rendus **28**, 205 (1937).
[3] F. Bloch, Zeits. f. Physik **52**, 555 (1929).

Then (8) becomes

$$\{\sum_r \exp[i((eEart/\hbar)+\kappa ar)]v(r)\}f_\kappa = i\hbar\partial f_\kappa/\partial t.$$

It is easy to solve this equation for f_κ, but this is not necessary for our purposes. Looking at the wave function (3) we obtain

$$\Psi_\kappa = \exp(-iE_0t/\hbar)f_\kappa(t)\sum_m \exp[i(\kappa am+(rEamt/\hbar))]u_m$$

$$= e(-iE_0t/\hbar)f_\kappa(t)\sum_m \exp(i\bar{\kappa}am)u_m,$$

where $\bar{\kappa}\equiv\kappa+eEt/\hbar$, $\partial\bar{\kappa}/\partial t = eE/\hbar$ which is the well-known result of Bloch.[3]

III. APPLICATION TO TISZA'S MODEL

The method of Section II can be applied to Tisza's model in the following way. Call

$$\mathcal{H}_E = \mathcal{H}+U, \quad \mathcal{H} = -(\hbar^2/2m)\sum_i \nabla_i^2 + W,$$

$$U = -eE\sum x_i = -eEnX.$$

W is the interaction energy of the electrons among themselves and with the ions, X is the coordinate of the center of gravity of the electrons.

$$X = (1/n)\sum_i x_i.$$

The Schrödinger equation is then

$$\mathcal{H}_E\Psi = (\mathcal{H}+U)\Psi = i\hbar\partial\Psi/\partial t. \tag{9}$$

Define X_α as the position of the center of mass of the electron system in the configuration α (i.e., $x_i = (\nu_i+\alpha)a$ —we follow Tisza's notation throughout this section). Now we make the following substitution for Ψ

$$\Psi = \sum_{\alpha=0,\,1,\,\cdots,\,\omega-1} c_\alpha(t)\exp(ieEX_\alpha nt/\hbar)\varphi_{\nu+\alpha} \tag{10}$$

the φ_ν being defined as by Tisza.[1] Such an assumption is possible as long as the energy of the system remains small compared with the "gap" energy assumed by Tisza. We shall always choose times so short that this is so. The factor $\exp(ieEX_\alpha nt/\hbar)$ is the corresponding gauge transformation for our case. Substituting (10) in (9) we obtain

$$\sum_\alpha \exp(ieEnX_\alpha t/\hbar)[\mathcal{H}+(U-U_\alpha)-i\hbar\partial/\partial t]c_\alpha(t)\varphi_{\nu+\alpha} = 0, \tag{11}$$

where $U_\alpha = -eEX_\alpha n$. Multiplying (11) by $\varphi_{\nu+\beta}^*$ and integrating over-all electron coordinates we obtain (assuming approximate orthogonality for the φ_ν)

$$\sum_\alpha \exp(ieE(X_\alpha - X_\beta)nt/\hbar)$$

$$\times[\mathcal{H}_{\alpha\beta}+(\varphi_{\nu+\beta},\,(U-U_\alpha)\varphi_{\nu+\alpha})]c_\alpha = i\hbar\partial c_\beta/\partial t.$$

$\mathcal{H}_{\alpha\beta} = \mathcal{H}_{\alpha-\beta}$ is a function of $\alpha-\beta$ only, because of the translational invariance of the Hamiltonian. Now if we assume that the electron lattice corresponding to φ_ν is only very weakly polarizable (just as we assumed in II that the isolated atom was only slightly polarizable) then we may neglect the dependence of the φ_ν on the electric field. But for this to be possible matrix elements of the type $(\varphi_{\nu+\beta},\,(U-U_\alpha)\varphi_{\nu+\alpha})$ must be negligible. Dropping them, we obtain from (11)

$$\sum_\alpha \exp[ieE(X_\alpha - X_\beta)t/\hbar]\mathcal{H}_{\alpha-\beta}c_\alpha = i\hbar\left(\frac{\partial c_\beta}{\partial t}\right). \tag{12}$$

Noticing that $X_\alpha - X_\beta = a(\alpha-\beta)$ we can solve (12) with the substitution

$$C_\beta = f_k(t)\exp(2\pi ik\beta/\omega), \quad k = 0,\,1,\,\cdots,\,\omega-1. \tag{13}$$

Equation (12) then gives

$$(\sum_\alpha \exp(ienaeEt/\hbar)\mathcal{H}_\alpha)f_k(t) = i\hbar\partial f_k/\partial t. \tag{14}$$

As previously f_k can be determined easily from (14), but it is not necessary for our purposes.

The wave functions corresponding to (13) are

$$\Psi_k = f_k(t)\sum_\alpha \exp(2\pi ik\alpha/\omega)\exp(ineEX_\alpha t/\hbar)\varphi_{\nu+\alpha}.$$

The lowest state (say) is $k=0$

$$\Psi_0 = f_0(t)\sum_\alpha \exp(ieEntX_\alpha/\hbar)\varphi_{\nu+\alpha}.$$

Let us calculate the mean current density ($J(t)$ say) as a function of time for this state.

$$J(t) = (e_T/m_TV)(\Psi_0,\,P\Psi_0)/(\Psi_0,\,\Psi_0).$$

e_T = total charge $= ne$, m_T = total mass $= nm$, V = volume of metal, P = total momentum operator $= -i\hbar\sum_i \partial/\partial x_i = -i\hbar\partial/\partial X$,

$$(\Psi_0,\,P\Psi_0)/(\Psi_0,\,\Psi_0)$$

$$= (1/\omega)\sum_{\alpha,\beta}\exp(ieEn(X_\alpha - X_\beta)t/\hbar)(\varphi_{\nu+\beta},\,P\varphi_{\nu+\alpha})$$

$$= (1/\omega)\sum_\alpha\{\exp(ieEnta/\hbar)(\varphi_{\nu+\alpha-1},\,P\varphi_{\nu+\alpha})$$

$$+\exp(-ieEnta/\hbar)(\varphi_{\nu+\alpha+1},\,P\varphi_{\nu+1})+(\varphi_{\nu+\alpha},\,P\varphi_{\nu+\alpha})\},$$

if we assume that only nearest neighbors overlap appreciably. Now the third term is certainly zero (the φ_ν may be taken real), and further the matrix element $(\varphi_{\nu+1},\,P\varphi_\nu) = -(\varphi_\nu,\,P\varphi_{\nu+1})$ on integrating by parts. Therefore

$$(\Psi_0,\,P\Psi_0)/(\Psi_0,\,\Psi_0) = 2i(\varphi_\nu,\,P\varphi_{\nu+1})\sin(eEnta/\hbar)$$

$$= 2\hbar(\varphi_\nu,\,\partial\varphi_{\nu+1}/\partial X)\sin(eEnta/\hbar).$$

However the quantity $(\varphi_\nu,\,\partial\varphi_{\nu+1}/\partial X)$ is exactly the quantity defined as $(m/2m^*a)$ by Tisza so that we

obtain

$$J(t)=(e\hbar/Vam^*)\sin(eEnat/\hbar).$$

For $t\ll\hbar/eEna$ we have

$$J(t)=(ne^2/Vm^*)Et,\quad \partial J(t)/\partial t=(ne^2/Vm^*)E. \quad (15)$$

The quantity multiplying E in (15) is however exactly the quantity $1/\Lambda$ defined by Tisza so as to give Eq. (1). Therefore we obtain finally

$$\partial(\Lambda J)/\partial t=E. \quad (16)$$

This is Eq. (2). The fact that the same Λ occurs in both equations speaks to a certain extent for the internal consistency of the theory.

In conclusion I would like to thank Professor Tisza for allowing me to see his manuscript prior to publication, and for several valuable discussions.

PHYSICAL REVIEW VOLUME 80, NUMBER 4 NOVEMBER 15, 1950

Quantum Theory of the Longitudinal Electromagnetic Field

S. T. MA
University of Chicago, Chicago, Illinois
(Received April 24, 1950)

The special features of the quantum theory of the longitudinal electromagnetic field originated from the supplementary condition are discussed in connection with the vacuum expectation value of the bilinear form in the electromagnetic potentials. The present investigation confirms the view that the unified treatment of the electromagnetic field is valid for gauge-invariant integrals.

I. INTRODUCTION

PRIOR to the recent developments in quantum electrodynamics it was customary to eliminate the longitudinal electromagnetic field and its supplementary condition by a canonical transformation, and to deal with the interaction of the electron waves with the transverse photons, together with the Coulomb interaction of the electron waves that arises from the elimination of the longitudinal field.[1] In order to simplify the calculations, a unified treatment of the longitudinal and transverse components of the electromagnetic field has been generally adopted in recent works on quantum electrodynamics in dealing with the virtual processes.[2] Since the longitudinal field is no longer eliminated from the theory, it has become necessary to make a closer study of its properties.

In the following discussion we shall use the notation of Schwinger's papers with the constants c and $\hbar$ put equal to unity. In this notation the state vector representing the vacuum state of the free electromagnetic field satisfies the supplementary condition:

$$\frac{\partial}{\partial x_\mu}A_\mu(x)\Psi_0=0 \quad (1)$$

for the longitudinal field and the condition of vacuum:

$$\mathfrak{A}_\mu^{(+)}(x)\Psi_0=0 \quad (2)$$

for the transverse field. In Schwinger's formulation of quantum electrodynamics the elimination of virtual photons is achieved by evaluating vacuum expectation values of the form:

$$\langle\Omega\rangle_0=\Psi_0\dagger\Omega\Psi_0. \quad (3)$$

In order to do this in a covariant way, Eq. (2) is generalized into:

$$A_\mu^{(+)}(x)\Psi_0=0. \quad (4)$$

This generalized vacuum condition leads to the result:

$$\langle A_\mu(x)A_\nu(x')\rangle_0=i\delta_{\mu\nu}D^{(+)}(x-x'), \quad (5)$$

which forms the basis of the unified treatment of the electromagnetic field. Belinfante[3] has pointed out that Eq. (4) is incompatible with the supplementary condition. As a result of this incompatibility the vacuum expectation value

$$\left\langle A_\mu(x)\frac{\partial}{\partial x_\nu'}A_\nu(x')\right\rangle_0$$

derived from formula (5) does not vanish as it should. Nevertheless, it has been shown by Schwinger that direct calculations of the self-energy of the electron based on the rigorous method and the unified treatment give results which become identical after a gauge transformation. It has also been shown by Hu[4] that the two methods give the same result for the iterated form of the S-matrix. It is not clear from these investigations

[1] W. Heisenberg and W. Pauli, Zeits. f. Physik **59**, 168 (1930); E. Fermi, Rev. Mod. Phys. **4**, 125 (1932).

[2] T. Tati and S. Tomonaga, Prog. Theor. Phys. **3**, 391 (1948); J. Schwinger, Phys. Rev. **74**, 1439 (1948); **75**, 651 (1949); **76**, 790 (1949); R. P. Feynman, Phys. Rev. **74**, 1430 (1948); D. Rivier and E. C. G. Stueckelberg, Phys. Rev. **74**, 218 (1948); F. J. Dyson, Phys. Rev. **75**, 486, 1736 (1949).

[3] F. J. Belinfante, Phys. Rev. **76**, 226 (1949).

[4] N. Hu, Phys. Rev. **76**, 391 (1949); **77**, 150 (1950).

why two apparently incompatible mathematical schemes should lead to equivalent results.

The situation has been clarified by recent investigations of Dyson,[5] Coester and Jauch.[6] These authors have shown that it is possible to justify the unified treatment with no reference to either the traditional separate treatment of the electromagnetic field or the generalized vacuum condition, as long as we are dealing with gauge-invariant integrals. In Coester and Jauch's evaluation of the S-matrix the virtual photons are eliminated by using the commutation relations alone without any special consideration of the vacuum expectation value $\langle A_\mu(x)A_\nu(x')\rangle_0$. The vacuum expectation value of the bilinear form has been investigated by Dyson. Dyson shows that $\langle A_\mu(x)A_\nu(x')\rangle_0$ can be determined, except for an unknown function, from Eq. (2) and the equation:

$$\frac{\partial}{\partial x_\mu}A_\mu^{(+)}(x)\Psi_0=0, \tag{6}$$

which is the positive-frequency part of the supplementary condition. The result thus obtained is of the form:

$$\langle A_\mu(x)A_\nu(x')\rangle_0=i\delta_{\mu\nu}D^{(+)}(x-x')+\frac{1}{2}\frac{\partial^2}{\partial x_\mu\partial x_\nu}\Phi(x-x'), \tag{7}$$

Φ being a function left undetermined by the theory. From the special form in which Φ appears in Eq. (7) it can be seen that it contributes nothing to integrals of the form:

$$\int\int K_{\mu\nu}(x,x')\langle A_\mu(x)A_\nu(x')\rangle_0 d^4x d^4x', \tag{8}$$

if the tensor $K_{\mu\nu}$ satisfies the conditions of gauge invariance:

$$\frac{\partial}{\partial x_\mu}K_{\mu\nu}=0, \quad \frac{\partial}{\partial x_\nu'}K_{\mu\nu}=0, \tag{9}$$

and the integrals extend over the whole space. Since Eq. (7) differs from Eq. (5) only by the term involving the function Φ, it is justified to use formula (5) for the evaluation of gauge-invariant integrals.

It is interesting to find out whether it is possible to take into account the complete supplementary condition, Eq. (1), in the evaluation of the vacuum expectation value in question. It will be seen in the next section that this requires a slight modification in the way the vacuum expectation value is taken, but the result that follows from this modification bears out the view that the unified treatment of the electromagnetic field is valid for gauge-invariant integrals.

In connection with the exclusive use of the positive-frequency part of the supplementary condition, we note that Gupta[7] has recently proposed a modified formulation of quantum electrodynamics which consists in taking Eq. (6) instead of Eq. (1) as the supplementary condition. In the present note we shall be concerned with only the original formulation of the theory based on the supplementary condition (1). A systematic formulation of Gupta's idea is a problem for further investigation.

II. VACUUM EXPECTATION VALUE IN THE QUANTUM THEORY OF THE ELECTROMAGNETIC FIELD

Quantum-mechanical representations for the longitudinal electromagnetic field have been given by Fock and Podolsky,[8] Dirac,[9] and Wentzel.[10] In all of these representations the state vector satisfying Eq. (1) is infinite in magnitude. Since the state vector is not normalized in the conventional sense, the usual concept of expectation value does not exist. If we formally take the state vector to be normalized and apply the conventional rules for evaluating expectation values, contradictions of the following kind will arise.[11] From Eq. (1) and its Hermitian conjugate:

$$\Psi_0\dagger\frac{\partial}{\partial x_\mu}A_\mu(x)=0, \tag{10}$$

we obtain

$$\Psi_0\dagger\left[\frac{\partial}{\partial x_\mu}A_\mu(x), \quad A_\nu(x')\right]\Psi_0=0$$

or

$$\frac{\partial}{\partial x_\nu}D(x-x')\Psi_0\dagger\Psi_0=0,$$

which obviously cannot be true.

These features of the theory of the longitudinal electromagnetic field are typical of the theory of continuous spectrum. Consider for example a pair of canonically conjugate variables q, p satisfying the commutation relation:

$$[q,p]=i. \tag{11}$$

Let $\psi(q')$ be an eigenvector of q belonging to the eigenvalue q'. Then the normalization condition in the theory of discrete spectrum is replaced by the formula:

$$\psi(q')\dagger\psi(q'')=\delta(q'-q''), \tag{12}$$

and the matrix elements of p are of the form:

$$\psi\dagger(q')p\psi(q'')=-i\frac{\partial}{\partial q'}\delta(q'-q''). \tag{13}$$

[5] F. J. Dyson, Phys. Rev. 77, 420 (1950).
[6] F. Coester and J. M. Jauch, Phys. Rev. 78, 149 (Section V), 827 (1950).
[7] S. N. Gupta, Proc. Phys. Soc. London 63, 681 (1950); K. Bleuler (to be published).
[8] V. A. Fock and B. Podolsky, Physik. Zeits. Sowjetunion 1, 801 (1931); L. Rosenfeld, Zeits. f. Physik 76, 729 (1932); S. T. Ma, Phys. Rev. 75, 535 (1949); F. J. Belinfante (reference 3).
[9] P. A. M. Dirac, Ann. Inst. M. Poincaré, 9, 13 (1939).
[10] G. Wentzel, *Quantum Theory of Fields*, Interscience Publishers, New York (1949). The writer is grateful to Professor Wentzel for a discussion of this representation.
[11] This was pointed out to me by C. N. Yang several years ago.

It follows from Eqs. (12) and (13) that:

$$\psi\dagger(q')pq\psi(0)=0, \tag{14}$$

$$\psi\dagger(q')qp\psi(0)=i\delta(q'), \tag{15}$$

$$\psi\dagger(0)pq\psi(q')=-i\delta(q'), \tag{16}$$

$$\psi\dagger(0)qp\psi(q')=0. \tag{17}$$

These equations are mathematically consistent as long as q' is treated as a variable of integration. On the other hand, expectation values—diagonal matrix elements—calculated from these equations are usually divergent and ambiguous. In the first place, it follows from Eq. (12) that

$$\psi\dagger(0)\psi(0)=\delta(0),$$

which shows that $|\psi(0)|^2$ is infinite. As can be expected from this divergence, Eqs. (14) to (17) lead to contradictory results if q' is put equal to zero. For example, from Eqs. (14), (17) with $q'=0$ we have

$$\psi\dagger(0)[q, p]\psi(0)=0$$

or

$$\psi\dagger(0)\psi(0)=0.$$

In view of these special features of the longitudinal electromagnetic field, and of the fact that only the transverse photons are of physical interest, it seems more consistent to take the vacuum expectation value only for the transverse degrees of freedom. Let χ_0 and Φ_0 be the two factors of Ψ_0 referring, respectively, to the longitudinal and transverse degrees of freedom. These state vectors satisfy the equations:

$$\frac{\partial}{\partial x_\mu}A_\mu(x)\chi_0=0, \tag{18}$$

$$\mathfrak{A}_\mu^{(+)}(x)\Phi_0=0, \tag{19}$$

$$\Phi_0\dagger\mathfrak{A}_\mu^{(-)}(x)=0. \tag{20}$$

Instead of the quantities defined by Eq. (3) we consider the quantities $\Phi_0\dagger\Omega\Phi_0$. The latter quantities are operators when Ω involves the longitudinal variables, and operate on χ_0.

It follows from Eqs. (19) and (20) that:

$$\Phi_0\dagger\mathfrak{A}_\mu(x)\Phi_0=0, \tag{21}$$

$$\Phi_0\dagger\mathfrak{A}_\mu(x)\mathfrak{A}_\nu(x')\Phi_0=i\delta_{\mu\nu}D^{(+)}(x-x')+P_{\mu\nu}(x-x'), \tag{22}$$

where

$$P_{\mu\nu}(x)=-i\left\{\frac{\partial^2}{\partial x_\mu\partial x_\nu}+\left(n_\mu\frac{\partial}{\partial x_\nu}+n_\nu\frac{\partial}{\partial x_\mu}\right)n_\lambda\frac{\partial}{\partial x_\lambda}\right\}\mathfrak{D}^{(+)}(x). \tag{23}$$

Resolving $A_\mu(x)$ into the longitudinal and transverse components according to the general formula:

$$A_\mu(x)=n_\mu n_\lambda\frac{\partial}{\partial x_\lambda}[\Lambda(x)-L(x)]-\frac{\partial}{\partial x_\mu}L(x)+\mathfrak{A}_\mu(x), \tag{24}$$

where we write L instead of Schwinger's Λ', we have:

$$\Phi_0\dagger A_\mu(x)A_\nu(x')\Phi_0 =i\delta_{\mu\nu}D^{(+)}(x-x')+P_{\mu\nu}(x-x')+Q_{\mu\nu}(x-x') +R_{\mu\nu}(x-x')+\frac{\partial^2}{\partial x_\mu\partial x_\nu'}L(x)L(x'), \tag{25}$$

with:

$$Q_{\mu\nu}(x-x')=n_\mu n_\lambda\frac{\partial}{\partial x_\lambda}\frac{\partial}{\partial x_\nu'}[L(x), L(x')] =-in_\mu n_\lambda\frac{\partial}{\partial x_\lambda}\frac{\partial}{\partial x_\nu'}\mathfrak{D}(x-x'), \tag{26}$$

$$R_{\mu\nu}(x-x')=\left\{n_\mu n_\lambda\frac{\partial}{\partial x_\lambda}[\Lambda(x)-L(x)] -\frac{\partial}{\partial x_\mu}L(x)\right\}\left\{n_\nu n_\kappa\frac{\partial}{\partial x_\kappa'}[\Lambda(x')-L(x')] -\frac{\partial}{\partial x_\nu'}L(x')n_\mu n_\lambda[\partial/\partial x_\lambda][\Lambda(x)-L(x)]\right. \tag{27}$$

The supplementary condition (18) can be written in the form:

$$[\Lambda(x)-L(x)]\chi_0=0. \tag{28}$$

Hence:

$$\Phi_0\dagger A_\mu(x)A_\nu(x')\Phi_0\chi_0 =\left\{i\delta_{\mu\nu}D^{(+)}(x-x')+P_{\mu\nu}(x-x')+Q_{\mu\nu}(x-x') +\frac{\partial^2}{\partial x_\mu\partial x_\nu'}L(x)L(x')\right\}\chi_0. \tag{29}$$

The right-hand side of Eq. (29) may be replaced by:

$$i\delta_{\mu\nu}D^{(+)}(x-x')\chi_0 \tag{30}$$

in the integrand of a gauge-invariant integral, which shows that the state vector χ_0 is transformed into the same state vector multiplied by the factor $i\delta_{\mu\nu}D^{(+)}(x-x')$. Thus, formula (29), like formula (7), provides a justification for applying formula (5) to gauge-invariant integrals.

The integral (8) is gauge-invariant if (i) the tensor $K_{\mu\nu}$ satisfies the conditions of gauge invariance (9), and (ii) the integral extends over the whole space. Expressed or implied, the conditions of gauge invari-

ance have been used in all the recent investigations on the equivalence of the two methods of treating the longitudinal electromagnetic field. As the investigations of Wentzel and others show,[12] the evaluation of the induction tensor in the theory of vacuum polarization involves a great deal of ambiguity, so that gauge invariance of quantum electrodynamics is by no means a well-established fact at the present stage of the theory. However, gauge invariance is a basic requirement of a satisfactory formulation of quantum electrodynamics, and it is reasonable to take Eqs. (9) as an assumption or to ensure their validity by means of the regularization of Pauli and Villars.

For integrals which do not satisfy the requirement (ii), further investigation is necessary before the validity and limitation of the unified treatment can be established. For example, in Schwinger's calculations of the self-energy of the electron, the results obtained by the two methods of treating the longitudinal electromagnetic field become identical only after a gauge transformation. On the other hand, the requirement (ii) is satisfied by the iterated form of the S-matrix, so that the equivalence of the two methods of evaluating the S-matrix follows immediately from the above considerations.

[12] G. Wentzel, Phys. Rev. 74, 1070 (1948); W. Pauli and F. Villars, Rev. Mod. Phys. 21, 434 (1949).

PHYSICAL REVIEW VOLUME 80, NUMBER 4 NOVEMBER 15, 1950

Hall Coefficient and Resistivity of Thin Films of Antimony Prepared by Distillation*

W. F. LEVERTON† AND A. J. DEKKER
Department of Physics, University of British Columbia, Vancouver, Canada

(Received June 30, 1950)

An a.c. method is described for measuring the Hall coefficient. An apparatus for the preparation of very pure evaporated metal films is also described. This apparatus eliminates such sources of contamination as hot filaments.

The effect of annealing on both Hall coefficient and resistivity of evaporated films of antimony is examined. A tentative explanation is presented for the observed increase in the Hall coefficient and decrease in the resistivity. It is based on the assumption of partial recombination of electrons and holes.

The Hall coefficient of unannealed evaporated films is 0.215_9 c.g.s.m., and of annealed films is 0.24_14 c.g.s.m. with an accuracy of one percent.

The resistivity of our annealed films is 1.28 times that of bulk antimony.

I. INTRODUCTION

IF a conductor carrying a current is placed in a magnetic field at right angles to the current, a potential difference develops across the conductor in a direction perpendicular to both magnetic field and current flow. This potential difference is known as the Hall voltage

$$V=(RIH/t)\times10^{-9},$$

where I is the current in amperes, H is the magnetic field in gauss, t is the thickness of the conductor in cm in the direction of H, and R is the Hall coefficient of the conducting material in c.g.s. magnetic units.

Examination of the literature reveals that most observers have used direct current in their determinations of the Hall coefficient. Since such a determination measures the sum of the Hall and Ettingshausen voltages, the results must be corrected by measuring the latter separately. Since the voltages are very small, the Hall voltage determined in this manner may be in serious error where the Ettingshausen voltage is large compared with the Hall voltage. The Ettingshausen voltage may be eliminated by using Hall contacts of the same material as the sample; however, this is practicable only in a limited number of cases.

In the measurements described in this paper an alternating current was used in the determination of Hall coefficients. Since the temperature gradient which leads to the Ettingshausen effect requires a time of the order of seconds to become established,[1] use of alternating current completely eliminates this effect from the observed transverse voltage. A further advantage of the a.c. method is that it is much easier to amplify very small alternating voltages than to amplify direct voltages of the same magnitude.

Despite these advantages, few observers[1–3] have used a.c. methods. Smith[1] found the Hall coefficient of bismuth to be constant within experimental error for frequencies up to 120,000 cycles per second. Wood[2] found similar results for tellurium up to 10,000 cycles per second. Busch and Labhart[3] worked only at line frequency (50 cycles). Some early observers[4–6] used a.c. of the same frequency in both the Hall sample and in the

* Assisted by the Defence Research Board of Canada.

† Holder of National Research Council of Canada Studentship, 1948–49, 1949–50.

[1] A. Smith, Phys. Rev. 35, 81 (1912).
[2] L. A. Wood, Phys. Rev. 41, 231 (1932).
[3] G. Busch and H. Labhart, Helv. Phys. Acta 19, 463 (1946).
[4] T. Des Coudres, Physik. Zeits. 2, 586 (1901).
[5] Von Traubenberg, Ann. d. Physik 17, 78 (1905).
[6] H. Zahn, Ann. d. Physik 36, 553 (1911).

electromagnet producing the magnetic field. This, of course, resulted in a direct Hall voltage and did not eliminate the Ettingshausen effect.

Since antimony has a comparatively large Hall coefficient and since there is wide disagreement as to its correct value,[7] it was decided that a careful determination of the Hall coefficient of pure antimony would serve as a test of the measuring equipment and might also serve to resolve some of the disagreement.

An examination of the expression for the Hall voltage indicates that it can be increased (for any allowable Joule heating) by reducing the thickness of the sample. This suggested preparation of the samples as thin layers by evaporation in vacuum.

II. MEASURING APPARATUS

The magnetic field is supplied by a water-cooled electromagnet with four-inch diameter flat pole faces. This magnet will produce up to 14,000 gauss with a three-quarter-inch gap. The field is measured by means of a fluxmeter and search coils. The calibration of the fluxmeter was checked by means of accurately known fields produced in nuclear magnetic moments experiments in this department.

Current is supplied to the Hall sample by a 210-cycle R.C. oscillator. This frequency was chosen to minimize pick-up of harmonics of 60 cycles.

The amplifier for the Hall voltage has a high gain (up to 10^7) and is sharply tuned at 210 cycles ($Q>200$). The input impedance is high so that negligible current flows through the Hall contacts. The sharp frequency characteristic, obtained by using a parallel T feedback network, reduces the amount of tube noise amplified. The Hall voltage can be applied directly to the grid of the first tube or through a step-up transformer. The latter feature should be valuable in measuring very small Hall voltages, for the transformer will raise the signal voltage above the noise level of the first tube, thus improving the signal to noise ratio.

To measure the Hall voltage the sample is mounted on a piece of insulating board and held in place by clamping the ends between layers of tin foil. The clamps serve as electrodes for the primary current. The contacts for the Hall voltage are constructed as shown in Fig. 1. The ball bearing, free to roll in its mounting sleeve, makes a point contact which can be moved along the metal layer without scratching it. The Hall contacts are held at a fixed separation somewhat less than the width of the sample. Spring mounting assures good electrical contact. With current flowing but no magnetic field, the Hall contacts are adjusted so that their potential difference is small compared to the Hall voltage. This residual voltage (as well as the total voltage with magnetic field) is measured by noting the amplifier output and then substituting for the unknown voltage a known voltage which may be varied to give the same amplifier output.

[7] International Critical Tables 6, 415 (1929).

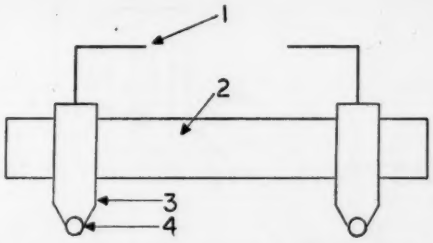

FIG. 1. Schematic diagram of movable Hall contacts. (1) Lead to amplifier; (2) lucite support; (3) brass sleeve; (4) steel ball bearing 1 mm in diameter. Distance between contacts is 2 cm.

This calibration voltage is developed across a standard resistance and may be calculated by measuring the current flowing through the standard resistance. This is repeated for each determination. By this method the accuracy of the measurements of Hall voltage does not depend on the long-time stability of the amplifier.

The same ammeter is used to measure both the current through the Hall sample and the calibration voltage. Since in the expression for the Hall coefficient the Hall voltage appears in the numerator and the primary current in the denominator, this arrangement tends to cancel any error in the ammeter calibration.

III. PREPARATION OF SAMPLES

The layers of antimony were prepared by evaporation in vacuum using glass microscope slides 2.5×7.5 cm as targets. At first a conventional vacuum evaporating apparatus with removable glass bell jar was used. To ensure uniformity of metal thickness along the sample multiple sources were used. The sources were 20-mil molybdenum wire wound in funnel-shaped spirals. The nominal thickness of the metal layers was determined by weighing and using the known sample area and the density of antimony in bulk. Layers from 0.2 to 10 microns in thickness were prepared with this apparatus. Their electrical resistivities ranged from 10 to 20 times greater than that for antimony in bulk. The layers were bright and highly reflecting but had a finely mottled or banded appearance. Annealing in vacuum reduced the resistivity somewhat but was limited by the fact that at temperatures above 400°C the antimony re-evaporated from the slides. Annealing at 500°C in an atmosphere of 20 to 25 cm Hg of carbon dioxide gas reduced the resistivity to five or six times that of antimony in bulk with only a small loss of metal due to re-evaporation.

Because of their high resistivities, these layers were considered unsatisfactory. In an effort to produce better layers, the vacuum evaporating apparatus shown in Fig. 2 was constructed. It is made entirely of Pyrex glass. Heat necessary for evaporation of the metal is supplied by a 700-watt furnace which is lowered over the apparatus down to level AA. This apparatus has several advantages over the conventional vacuum evaporating apparatus:

(1) It can be completely outgassed permitting more complete evacuation.

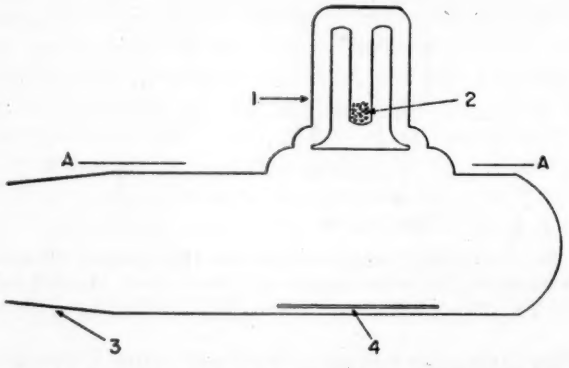

FIG. 2. Schematic diagram of evaporating apparatus. (1) 8 mm o.d. Pyrex glass tubing; (2) metal to be evaporated; (3) ground glass joint to liquid air trap and pumping system; (4) target (1×3-in. glass microscope slide).

(2) Metals other than that being evaporated, rubber gaskets, and hot filaments are eliminated, thus reducing the possibility of contamination.

(3) Impurities with boiling points lower than that of the metal to be evaporated tend to evaporate more rapidly and are concentrated in the first portion evaporated; impurities with higher boiling points tend to remain in the residual metal. Because of this fractional distillation, by discarding the initial and final portions, appreciable purification is achieved.

This apparatus will withstand temperatures up to 600°C. For evaporation at higher temperatures a similar apparatus could be constructed of fused quartz.

The thickness of layers prepared in this apparatus was uniform within one percent along the length of the sample. This was determined by weighing the antimony deposited on several small targets of known area placed at intervals along a 2.5×7.5 cm slide.

Layers of antimony from 0.1 to 3.0 microns in thickness have been prepared using this apparatus. All were highly reflecting and none showed any structure. Their electrical resistivities before annealing ranged from 1.8 to 2.2 times greater than that for antimony in bulk (1.2 to 1.4 after annealing in carbon dioxide).

During evaporation, the gas pressure was kept below 10^{-5} mm Hg and the antimony was heated to 580 to 600°C. Antimony was deposited at rates ranging from 2.6 to 33 micrograms/cm²/min. No variation of resistivity with thickness or rate of deposition was observed.

IV. PURITY OF SAMPLES

The antimony used was 99.8 percent pure. Maximum limits of impurities (in percent) were listed as arsenic 0.10, copper 0.03, iron 0.05, lead 0.04, tin 0.030, zinc 0.010.

Examination of the arc spectra of several of the evaporated layers showed that the concentration of each of these impurities was considerably lower than in the original bulk antimony. Arsenic and zinc were concentrated in the first fraction sublimed while copper, iron, lead, and tin were concentrated in the residual melt. The first fraction of each melt (about five percent of the total melt) produced a layer with resistivity from 3 to 11 times that of bulk antimony. This high resistivity was probably due to the increased concentration of arsenic.

V. EXPERIMENTAL RESULTS

1. Hall Coefficient

Unannealed Samples

The Hall coefficient R was measured in five unannealed samples of antimony. The voltage measured is that developed across the Hall contacts and must be multiplied by the ratio of sample width to separation of Hall contacts in order to obtain the Hall voltage. This ratio was 1.26_7.

There appears to be no variation of R with sample thickness from 0.7 to 1.1 microns, strength of applied magnetic field from 4000 to 12,000 gauss, nor with current density from 180 to 500 amp./cm². The mean value of R for these samples (22 determinations) was $+0.215_9$ c.g.s.m. at 20°C. The probable error of the mean was 0.000_4 c.g.s.m.

Annealed Samples

Antimony samples annealed in carbon dioxide at 20 cm Hg and 510°C for 45 minutes had a larger Hall coefficient than before annealing. Repeated annealing caused no further change in R. The Hall coefficient does not vary with thickness (0.8 to 1.9 microns), applied magnetic field (3000 to 12,000 gauss), or current density (140 to 460 amp./cm²).

The mean value of R for five annealed samples (35 determinations) was $+0.244_1$ c.g.s.m. at 20°C. The probable error of the mean was 0.000_2 c.g.s.m. The increase in R caused by annealing was 13 percent.

The accuracy of the measurement of the Hall coefficient is estimated to be within ±one percent, the chief sources of error being the determination of the uniformity of thickness of the layers (0.5 percent) and the measurement of the magnetic field (0.5 percent).

Impure Sample

As noted previously, the first sample prepared from each melt contained considerably more arsenic and zinc than did the original bulk antimony. The Hall coefficient of one of these impure samples was measured as follows, at 20°C.

Magnetic field (10^3 gauss)	Hall coefficient (c.g.s.m.)
3.96	$0.188_8 \pm 0.001_9$
12.24	$0.195_6 \pm 0.000_6$
Mean	0.192_2

The Hall coefficient of this sample was 11 percent lower than that of more pure samples (unannealed) and appeared to vary somewhat with magnetic field strength.

2. Resistivity Measurements

The resistivity ρ of a number of samples was measured at temperatures of 77 and 293°K.

Electron diffraction studies[8,9] have shown that evaporated antimony deposits are oriented with the principal axis perpendicular to the substrate; hence, the resistivity measurements were actually made perpendicular to the principal axis. The resistivity of bulk antimony perpendicular to the principal axis is[10] 42.6×10^{-6} ohm-cm at 293°K and[11] 8.2×10^{-6} ohm-cm at 77°K, hence

$$\Delta\rho/\Delta T=0.159\times10^{-6}\ \text{ohm-cm/°K}$$

over this temperature range. The mean value of $\Delta\rho/\Delta T$ for the unannealed samples was 0.154×10^{-6} ohm-cm/°K and for the unannealed samples 0.168×10^{-6} ohm-cm/°K.

In Fig. 3 resistivity is plotted against temperature for unannealed samples, annealed samples, and bulk antimony.

The resistivity of the evaporated layers can be represented conveniently as the sum of a temperature independent resistivity, ρ_0, and a temperature dependent resistivity, ρ^T, which varies approximately linearly with the absolute temperature

$$\rho=\rho_0+\rho^T.$$

ρ_0 was obtained by extrapolating the resistivity-temperature plot to 0°K.

The resistivity measurements are summarized in Table I.

Annealing greatly reduced ρ_0, but slightly increased ρ^T.

The mean room temperature resistivity of the annealed samples was 1.28 times that of bulk antimony. The lowest resistivity previously reported for evaporated layers was 1.35 times that of bulk antimony by Harris and Shaffer.[12] The resistivity of their samples was considerably more temperature dependent than that of bulk antimony, the smallest value of $\Delta\rho/\Delta T$ they reported was 0.185×10^{-6} ohm-cm/°K.

VI. DISCUSSION OF RESULTS

Antimony crystallizes in a trigonal structure. This structure differs from that of most other metals in that there are two atoms per elementary cell. According to the modern electron theory of solids, each energy band provides two possible energy states per elementary cell. Hence, a contribution of one electron per atom would completely fill a Brillouin zone. Antimony has five valence electrons per atom and it is generally assumed that these fill four bands completely, while the fifth band is nearly filled and the sixth nearly empty. The amount of overlapping of the fifth and sixth bands has been estimated by Brown and Lane[13] from measurements of the magnetic anisotropy of tin-antimony alloys. They conclude that there is about 1 free electron per 100 antimony atoms or 3.3×10^{20} electrons and an equal number of holes per cm³.

TABLE I. Resistivity data. (Resistivities in units of 10^{-6} ohm-cm.)

	ρ_{77}	ρ_{293}	$\Delta\rho/\Delta T$	$\rho_{293}{}^T$	ρ_0	$(\rho/\rho_{Sb})_{293}$
Unannealed samples	53	86	0.154	45	41	2.02
Annealed samples	18	54.5	0.168	49	5.5	1.28
Bulk antimony	8.2	42.6	0.159	46.6	−4.0	1.00

$\rho_{293}{}^T$ is the value of ρ^T at 293°K.
(ρ/ρ_{Sb}) is the ratio of resistivity to that of bulk antimony.

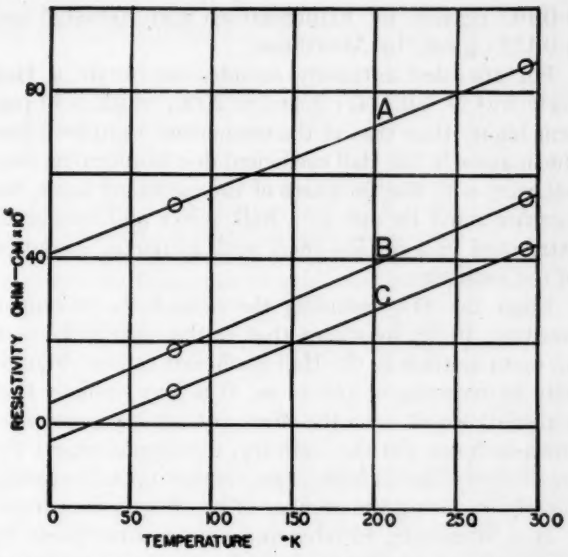

FIG. 3. Resistivity of evaporated deposits of antimony as a function of temperature. *A*—unannealed deposits; *B*—annealed deposits; *C*—single crystals, resistivity perpendicular to principal axis.

Apart from the relatively large number of free electrons and holes (even at $T=0$), which leads to a positive temperature coefficient of resistance, antimony may, in certain respects, be considered as a semiconductor. Its Hall coefficient should be given by the same formula which holds for a semiconductor with combined electron and hole conduction:

$$R=+\frac{3\pi}{8e}\cdot\frac{n_h b_h{}^2-n_e b_e{}^2}{(n_h b_h+n_e b_e)^2}, \qquad (1)$$

where e is the electronic charge, n_h, n_e are the densities of holes and electrons respectively, and b_h, b_e are their mobilities. For pure antimony, $n_h=n_e$ and since the Hall coefficient is positive, $b_h>b_e$.

Our result for the Hall coefficient of unannealed antimony, $+0.215_9$ c.g.s.m. at 20°C, is in agreement with the value +0.219 c.g.s.m. reported by Barlow[14] and by Zahn[15] but is in poor agreement with the value

[8] J. A. Prins, Nature **131**, 760 (1933).
[9] G. Hass, Kolloid Zeits. **100**, 230 (1946).
[10] P. W. Bridgman, Proc. Am. Acad. **63**, 351 (1929).
[11] W. J. De Haas, Proc. Royal Acad. Sci. Amsterdam **16**, 1110 (1914).
[12] L. Harris and L. H. Shaffer, Phys. Rev. **76**, 943 (1949).
[13] S. H. Brown and C. T. Lane, Phys. Rev. **60**, 895 (1942).
[14] G. Barlow, Ann. d. Physik **12**, 897 (1903).
[15] H. Zahn, Ann. d. Physik **14**, 886 (1904).

+0.192 c.g.s.m. by Ettingshausen and Nernst,[16] and +0.125 c.g.s.m. by Alterthum.[17]

For annealed antimony samples we obtain a Hall coefficient of $+0.244_1$ c.g.s.m. at 20°C, which is 13 percent higher than that of the unannealed samples. Since the increase in the Hall coefficient due to annealing does not vary with the thickness of the antimony layer, the increase must be due to a bulk effect and cannot be attributed to a surface effect such as partial oxidation of the antimony.

From Eq. (1), assuming the ratio b_e/b_h to remain constant, it can be shown that in the neighborhood of n_e/n_h an increase in the Hall coefficient can be obtained only by reducing n_e and/or n_h. It is very unlikely that annealing would have the effect of trapping either electrons or holes. On the contrary, one would expect the small crystallites to form larger crystals upon annealing, thereby reducing the number of possible surface traps.

It is interesting to refer to an observation made by Stephens[18] on antimony in bulk. Stephens measured the Hall coefficient of two antimony plates 0.5 cm in thickness, one consisting of large crystals, the other of smaller crystals. He found that the Hall coefficient of the first plate was 9 percent greater than that of the second.

On the basis of the foregoing discussion it seems reasonable to exclude an explanation based on trapping electrons or holes at the crystal boundaries. The following is suggested as a tentative explanation of the increase in R. The ratio b_e/b_h is assumed to remain practically constant during the annealing process. Our antimony layers as well as the plates used by Stephens were of very high purity; we will therefore assume that trapping by impurities may be neglected. (In any case we should not expect such trapping to be increased by annealing the samples.) Since trapping at crystal boundaries is also excluded, $n_e=n_h$. It is clear that the amount of overlapping of the fifth and sixth bands depends on the crystal structure. Since the behavior of the potential at the crystal boundaries will be different from that within the crystals, one might expect the extent of "average overlapping" to depend on the size of the crystals composing the sample. If we assume that crystal boundaries tend to increase the average overlapping, annealing would result in the recombination of a fraction of the free electrons and holes. Annealing would then have the effect of reducing the number of both electrons and holes and hence would increase the Hall coefficient.

Any interpretation of the effect of annealing on R must be in accord with the observed decrease in resistivity. The latter is an effect which is generally observed in evaporated layers. It is commonly assumed that by increasing the size of the crystallites, annealing reduces scattering by crystal boundaries. This would lead to a decrease in ρ_0, the temperature independent part of the resistivity. However, in addition to the decrease in ρ_0, we observed an increase of about nine percent in ρ^T, the temperature dependent part of the resistivity. This increase is consistent with the tentative explanation given above for the behavior of the Hall coefficient. If a number of free electrons and holes recombine upon annealing, ρ^T will increase.

One would expect the percentage increase in R and ρ^T on annealing to be the same. In view of the simplifying assumptions made, the observed increases of 13 percent and nine percent, respectively, seem to be in satisfactory agreement.

The authors wish to thank Dr. A. van der Ziel for his assistance in the design of the electronic equipment.

[16] A. Ettingshausen and W. Nernst, Sitz. Akad. Wiss. Wien **94 II**, 560 (1886).
[17] Alterthum, Ann. d. Physik **39**, 933 (1912).
[18] E. Stephens, Phil. Mag. **9**, 547 (1930).

PHYSICAL REVIEW VOLUME 80, NUMBER 4 NOVEMBER 15, 1950

The Superconductivity of Columbium

D. B. Cook, M. W. Zemansky,* and H. A. Boorse†
Pupin Physics Laboratories, Columbia University,‡ New York, New York
(Received June 26, 1950)

Isothermal critical magnetic field curves and zero field transitions for several annealed specimens of columbium have been measured by an a.c. mutual inductance method, at temperatures from 5.1°K to the zero field transition temperature. The $H-T$ curve was found to fit the usual parabolic relationship $H=H_0(1-T^2/T_0^2)$ with $H_0=8250$ oersteds and $T_0=8.65$°K. The initial slope of the curve was 1910 oersteds/deg. The electronic specific heat in the normal state calculated from the thermodynamic equations is $0.0375T$ and the approximate Debye characteristic temperature in the superconducting state, 67°K. Results on a different grade of columbium with a tantalum impurity of 0.4 percent, according to neutron scattering measurements, were in agreement with the data obtained from columbium of 0.2 percent maximum tantalum impurity.

I. INTRODUCTION

THE superconductivity of columbium was discovered by Meissner and Franz[1] who observed that the transition from the superconducting state to the normal state occurred between 8.18° and 8.74°K on a specimen of columbium containing 1.5 percent tin. On a specimen with reported impurities of 0.08 percent O and 0.02 percent Ta Meissner, Franz, and Westerhoff[2] observed the transition to occur between 9.20° and 9.35°K. Further observations of the transition by Bruksch, Ziegler, and Hickman[3] disclosed wide variations between three specimens which gave 5.09°, 8.64°, and 9.58° respectively. These investigators searched for impurities by the x-ray method which disclosed only a removable surface contamination of SiC. Transitions in magnetic fields were measured only in the liquid helium region, 1.4° to 4.2°K, by Daunt and Mendelssohn,[4] on a specimen of "about 99.8 percent purity."

II. PURITY OF COLUMBIUM

The lack of agreement among the transition temperatures suggests a greater variation of purity among the samples of columbium than is apparent from the numerical values of purity reported by the various investigators. It is difficult not only to obtain pure columbium, but also to measure accurately the purity of any given sample.

In the natural ores columbium is found in close association with the element tantalum. The chemical properties of the two are very similar and strict quantitative separation as well as the analysis of minute amounts of tantalum in columbium are problems to which no satisfactory solution has been found. Chemically the best method involves the difference of behavior of oxalotantalic and oxalocolumbic acids in dilute solutions of tannin. Other impurities have first to be removed by long and involved procedures.[5]

The spectra of the two elements are also very difficult to resolve from each other. The columbium lines interfere with tantalum lines to such a degree that the deliberate addition of tantalum to supposedly pure columbium cannot be detected until approximately 0.2 percent has been added.

Analysis by mass spectroscopy is a possibility but would have to be done without the convenience of using a gaseous compound to supply ions. X-ray examination of the crystal lattice is not suitable for analytical work, since the lattice spacings of columbium and tantalum are respectively 3.294 and 3.296A.[6]

It therefore appears that the spectrographic method is about as sensitive as any other for determining small tantalum impurities, and it has the advantage of providing a rapid means of surveying for other impurities.

The Fansteel Corporation, which appears to be the only refiner of columbium in this country, was reported to have improved the purity of its columbium production during the war. Therefore it was considered desirable to investigate the superconducting properties of this material, inasmuch as columbium has the highest superconducting temperature of any element and its $H-T$ curve had not been studied above 4.2°K.

The specimens used in this research were supplied by the Fansteel Corporation as Lot Cb-22 in 1947, with the maximum impurities quoted as 0.20 percent tantalum, 0.03 percent silicon, 0.01 percent iron, and 0.002 percent titanium. A spectrographic survey was conducted on this material using a comparison sample from the National Bureau of Standards (B. S. S. Steel No. 123) which contained known amounts of the following elements: Ag, Al, As, B, Be, Ca, Cb, Co, Cu, Mn, Mo, Ni, P, Si, Sn, Ta, Ti, V, W, and Zr. The only im-

* The City College of New York.
† Barnard College, Columbia University.
‡ Assisted by the ONR.
[1] W. Meissner and H. Franz, Zeits. f. Physik **63**, 558 (1930).
[2] Meissner, Franz, and Westerhoff, Ann. d. Physik **17**, 593 (1933).
[3] Bruksch, Ziegler, and Hickman, Phys. Rev. **42**, 554 (1942).
[4] J. G. Daunt and K. Mendelssohn, Proc. Roy. Soc. **A160**, 127 (1937).
[5] W. R. Schoeller, *The Analytical Chemistry of Tantalum and Niobium* (Chapman and Hall, Ltd., London, 1937). Also W. F. Hillebrand and G. E. F. Lundell, *Applied Inorganic Analysis* (John Wiley and Sons, Inc., New York, 1929), Chapter 38.
[6] Fansteel Corporation, Technical Bulletin on Columbium (1946).

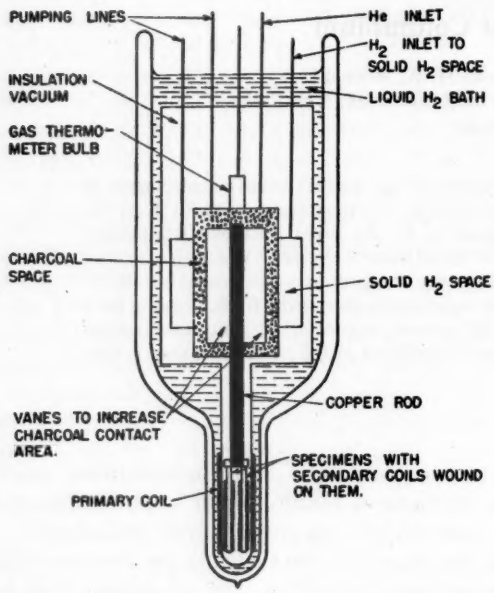

FIG. 1. Schematic diagram of the desorption cryostat.

purities indicated from the survey were iron and molybdenum, both exceedingly faint, and reported as not present in greater amounts than 0.1 percent.

A specimen of columbium produced by Fansteel prior to 1947 had been tested by means of the low velocity neutron spectrometer by Wu, Rainwater, and Havens.[7] One dip had been observed in the curve of transmission *versus* time of flight which coincided in energy value with the location of a large dip in tantalum. From the area of the weak dip in columbium it was estimated that the tantalum impurity might be 0.4 percent. From spectrographic evidence, a maximum of 1 percent of tantalum had been reported. A sample of this material was used for experimental comparison with the newer samples of columbium. After experimental data had shown the two materials to have the same superconducting properties in the annealed condition, a careful spectrographic comparison yielded the conclusion that the tantalum content was the same in both cases and of the order of 0.2 percent.

III. CRYOSTAT

To produce temperatures between 5 and 9°K required for this investigation, a helium desorption cryostat[8] was constructed, a schematic view of which is given in Fig. 1. The operation was briefly as follows: While liquid hydrogen was being transferred into the apparatus, the insulation vacuum space was filled with a few mm of helium gas to provide thermal contact between the hydrogen bath and the inner components of the apparatus. The latter consisted of concentric copper cylinders to which were attached a gas thermometer bulb and the specimens to be measured. The inner of the two concentric cylinders contained 200 cm³ of activated charcoal (Columbia 6-G, 8–14 mesh) supplied through the courtesy of Dr. L. I. Dana of the Linde Air Products Company. During the period of cooling through hydrogen temperatures, purified helium gas was adsorbed on the charcoal at pressures up to 50 lb./sq. in.

When thermal equilibrium at 20.4°K had been reached, the gas thermometer system was filled with helium to 1 atmos. pressure. Some of the liquid hydrogen from the outer bath was then admitted to the annular space surrounding the charcoal cylinder, by means of a small valve manipulated by a retractable rod. A high vacuum was then established in the insulation-vacuum container, and the internal apparatus, thus thermally isolated from the 20.4° bath, was cooled to 10° by pumping on the liquid hydrogen in the annular space. Adsorption of helium was continued during this operation.

When equilibrium at 10° had been reached, helium was desorbed from the charcoal by a fast mechanical pump. The lowest temperature attained varied from 4.9° upwards, depending upon the rate of pumping and the amount of solid hydrogen remaining to be cooled down with the apparatus. At maximum pumping speed the minimum temperature was reached in about 10 minutes. The temperature would remain constant for a few minutes and then would rise under continued pumping at an average rate of 0.007 deg./min. Temperatures could be held constant within 0.01° for long periods provided less gas was desorbed initially, thus conserving more of the available refrigeration for control purposes. One desorption cycle was sufficient for at least three hours of experimentation, provided the outer liquid hydrogen bath was maintained at the approximate level indicated in Fig. 1.

IV. THERMOMETRY

Since vapor pressure methods of thermometry are not available between 5° and 9°, a helium gas thermometer was used to measure temperatures directly. The gas thermometer consisted of a bulb of volume 3.862 cm³, made of an alloy of 96 percent silver and 4 percent copper, the silver being chosen because of its minimal tendency to adsorb helium on its surface, and copper added to improve machinability. The bulb was attached to the top of the desorption chamber and connected to a constant volume mercury manometer through a capillary tube of 0.4-mm bore.

Neglecting, as a first approximation, the volume and temperature gradients in the capillary, the gas thermometer may be regarded as consisting of two volumes; V_b, that of the bulb, and V_r, that at room temperature. Since gas pressures in the thermometer system were at most 1 atmos., the gas law could be taken, with sufficient accuracy, to include only the second virial

[7] Wu, Rainwater, and Havens, Phys. Rev. 71, 174 (1947).
[8] F. Simon, Physik Zeits. 27, 790 (1926).

coefficient. Thus, at the filling temperature T_f,

$$\left.\begin{aligned} p_f V_b &= n_b(RT_f + B_f p_f), \\ \text{and} \quad p_f V_r &= n_r(RT_r + B_r p_f), \end{aligned}\right\} \tag{1}$$

where the subscripts b, f, and r respectively designate values appropriate to the bulb, to the filling temperature, and to room temperature. R is the gas constant, n is the number of moles of gas in a given volume V, and B is the value of the second virial coefficient appropriate to the given temperature. When the bulb is at temperature T,

$$\left.\begin{aligned} pV_b &= n_b'(RT + B_T p), \\ pV_r &= n_r'(RT_r + B_r p). \end{aligned}\right\} \tag{2}$$

Here the respective numbers of moles have changed but the total number of moles is the same as before, except for the very small effect of adsorption which is neglected. Therefore, since $n_b + n_r = n_b' + n_r'$,

$$\frac{p_f V_b}{T_f + (B_f p_f/R)} + \frac{p_f V_r}{T_r + (B_r p_f/R)} = \frac{pV_b}{T + (B_T p/R)} + \frac{pV_r}{T_r + (B_r p/R)}. \tag{3}$$

Solving (3) for T and dividing all terms by V_b we obtain

$$T = \left[\frac{1}{\dfrac{p_f}{T_f + (B_f p_f/R)} + \dfrac{p_f V_r/V_b}{T_r + (B_r p_f/R)} - \dfrac{pV_r/V_b}{T_r + (B_r p/R)}} - \frac{B_T}{R}\right] p. \tag{4}$$

The dependence of thermometer sensitivity, dT/dp, on the choice of T_f and of the ratio S, defined as V_r/V_b, is seen by letting $B=0$ in Eq. (4) and differentiating T with respect to P. Thus

$$\frac{dT}{dp} = \frac{(p_f/T_f) + S(p_f/T_r)}{\{(p_f/T_f) - (S/T_r)(p_f - p)\}^2}. \tag{5}$$

From Eq. (5) it is seen that, when $S=0$, dT/dp is given by T_f/p_f. In order to make dp/dT as large as possible (dT/dp as small as possible) the filling pressure p_f was chosen as 1 atmos. and the filling temperature as 20.4°, the temperature of the liquid hydrogen bath. The room temperature volume V_r was chosen to be moderately large (28.771 cm²; $S=6.41$) to provide a small increase in sensitivity.[9] Under the given conditions dT/dp at 7°K ($p=0.42$ atmos.) was 0.024 deg./mm Hg. The manometer was read to the nearest 0.5 mm, providing a thermometer sensitivity of 0.01°.

The filling conditions were such that the correction for gas imperfection amounted to 0.1 to 0.2°, since the filling pressure corresponded to an ice point pressure of about 13 atmos. This correction was applied by finding the difference $T - T^*$ between the true temperature T and the quantity T^* measured assuming $B=0$.

If Eq. (3) is divided by V_b, and B is set equal to zero, T^* is given by

$$T^* = \frac{p}{p_f/T_f + p_f S/T_r - pS/T_r}, \tag{6}$$

whereas $T - T^*$ is given by

$$T - T^* = \left[\frac{p_f\left(T_f + \dfrac{B_f p_f}{R}\right)\left(T_r + \dfrac{B_r p_f}{R}\right)\left(T_r + \dfrac{B_r p}{R}\right)}{p_f\left(T_r + \dfrac{B_r p_f}{R}\right)\left(T_r + \dfrac{B_r p}{R}\right) + p_f S\left(T_f + \dfrac{B_f p_f}{R}\right)\left(T_r + \dfrac{B_r p}{R}\right) - pS\left(T_f + \dfrac{B_f p_f}{R}\right)\left(T_r + \dfrac{B_r p_f}{R}\right)} - \frac{pT_f T_r}{p_f T_r - ST_f(p - p_f)} - \frac{B_T p}{R}\right]. \tag{7}$$

The virial coefficients were obtained from the work of Keesom and Walstra,[10] the numerical magnitudes referring to the amount of gas occupying unit volume at 0°C, the pressure being expressed in atmos. The appropriate value of R is then 0.00366 atmos./deg. Since $B_r \sim 5\times10^{-4}$, the terms $B_r p/R$ and $B_r p_f/R$ can be neglected with respect to T_r without introducing errors greater than 0.05 percent. The term $B_f p_f/R$ is more important when compared with T_f, where it introduces an error of 0.25 percent if neglected. Since the precision of

[9] A. H. Woodcock, Can. J. Research **A16**, 133 (1938).
[10] W. H. Keesom and W. K. Walstra, Physica **13**, 225 (1947).

FIG. 2. Transitions of columbium cylinder in transverse fields.

the over-all experiment did not appear to warrant temperature measurements more accurate than 0.02°, and since the indicated approximations would introduce an error of no more than 0.02° at 7°K, all three aforementioned terms can be dropped in the calculations, whereupon Eq. (7) reduces to

$$T-T^*=-B_T p/R. \tag{8}$$

The procedure involved in determining temperatures was to use Eq. (6) to determine T^* and then to use Eq. (8) to correct T^* to the true temperature T. Small correction terms were calculated to take account of the volumes of gas in the various temperature regions of the capillary tube.

The performance of the thermometer was verified at the transition temperature of lead which agreed, within the indicated accuracy, with earlier values for the lead transition in zero field.[11] The triple point of hydrogen was checked on each run. At this temperature the error introduced by neglecting $B_f p_f/R$ with respect to T_f was 0.03°K. The determinations averaged 13.98°K when this error was compensated for, while 13.96°K is the value for the triple point of normal hydrogen quoted by Woolley, Scott, and Brickwedde.[12]

V. METHOD

The experimental specimens were attached to the solid hydrogen and charcoal compartments of the cryostat by means of a $\frac{1}{4}$-in. copper rod which was fastened inside the charcoal space to six large copper vanes, as indicated in Fig. 1. The rod terminated at its lower end in a plate to which four specimens, each with its own secondary coil, could be attached by means of copper set screws.

In the experiments here described the transitions were measured by observation of the magnetic permeability of cylindrical samples of columbium in small alternating magnetic fields. This method, described by Webber, Reynolds, and McGuire,[13] has the advantage of requiring no electrical connections to columbium, which is difficult to solder, electroplate, or weld. The dimensions of the cylinders were 2 mm in diameter by 5 cm long. Each was used as the core of the secondary coil of a mutual inductance, the primary of which was actuated by an audio oscillator at 1000 cycles/sec. Variations of frequency between 500 and 2000 cycles/sec., as well as of amplitude over the full range available, were found to have no effect on the observed transitions. The maximum a.c. field in the secondary coil was about 5 oersteds with the oscillator set at full gain.

The e.m.f. induced in the secondary coil was dependent upon the permeability of the superconducting cylinder upon which it was wound. When the core was superconducting this secondary e.m.f. had a small residual value that was due to the flux threaded by the actual windings of the secondary. When a transition to the normal state occurred, the signal increased to a steady maximum value. The opposite change occurred in a transition from the normal to the superconducting state. The e.m.f. induced in the secondary coil was successively amplified, filtered to remove 60 cycle background, and rectified for observation on a recording potentiometer.

The bottom of the cryostat was designed to permit insertion into the pole gap of an electromagnet by means of which magnetic fields were applied transversely to the superconducting specimens. The measurement of the field at the center of the $1\frac{5}{16}$ in. gap was effected with the aid of single layer search coils of 1 cm diameter, attached to a sensitive fluxmeter calibrated by a standard mutual inductance. The absolute accuracy of determining magnetic fields was two percent or better. Hysteresis in the magnet was avoided as a systematic error by measuring magnetic transitions in the direction of increasing magnetic fields only, from the superconducting to the normal state rather than *vice versa*. Between transitions the magnet was cyclically demagnetized. For measurements of transitions in small, longitudinal magnetic fields, a solenoid was used.

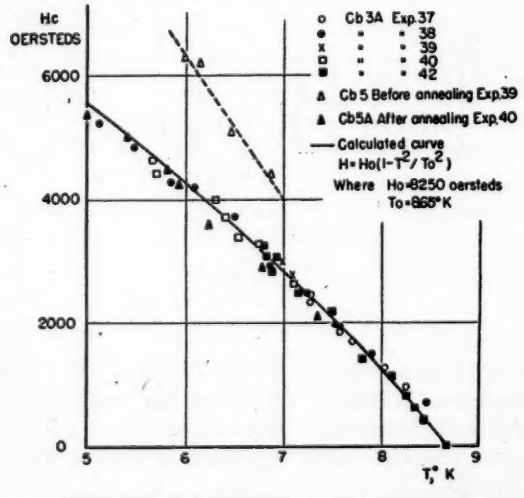

FIG. 3. Magnetic fields at completion of $s-n$ transitions in Cb.

[11] Boorse, Cook, and Zemansky, Phys. Rev. 78, 635 (1950).
[12] Wooley, Scott, and Brickwedde, J. Research Nat. Bur. of Stand. 41, 379 (1948).
[13] Webber, Reynolds, and McGuire, Phys. Rev. 76, 293 (1949).

VI. RESULTS

The measurements on columbium were made on a series of vacuum annealed samples. The detailed data given in this paper refer to the sample denoted as 3A which was given an additional heat treatment of five hours at 1000°C in a vacuum of 10^{-6} mm. The latter process was carried out at the Research Laboratory of the General Electric Company through the courtesy of Dr. F. Hubbard Horn. Two other samples annealed by Fansteel, as well as a cylindrical capsule of columbium powder were also tested and found to agree with sample 3A.

A few typical isothermal transitions in transverse magnetic fields are shown in Fig. 2. In each of the transitions the temperature was maintained constant to within 0.05°K or less. The transitions were measured in the direction of increasing magnetic fields. A number of check transitions taken in the reverse direction showed that the behavior of the sample was reversible. The critical field values are the values of H at which the sample *completes* the transition from the superconducting to the normal state. This identification is supported by the results of Webber, Reynolds, and McGuire[13] on monocrystalline tin where the $H-T$ curve thus obtained was in agreement with the generally accepted curve of de Haas and Engelkes.[14] Using a polycrystalline sample of very pure lead we have similarly verified points on the $H-T$ curve of Daunt[15] for lead.

The results of five experiments taken over a period of several months are plotted in Fig. 3. It should be emphasized that every point of Fig. 3 is the result of a complete transition curve comprising from 5 to 15 individual points. In addition to the data shown, points on the $H-T$ curve near T_0 were checked by measurements in a longitudinal field. Since the available longitudinal fields did not exceed 500 oersteds, data of this kind could be obtained only in the immediate neighborhood of T_0.

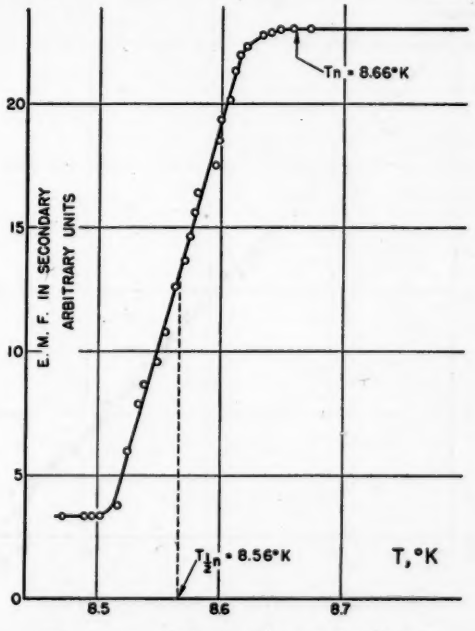

FIG. 4. Zero field transition of columbium.

TABLE I. Successive observations of zero field transitions in columbium 3A.

Expt. no.	$T_{\frac{1}{2}n}$, °K	T_n, °K	Expt. no.	$T_{\frac{1}{2}n}$, °K	T_n, °K
37	8.98	9.08	42	8.57[a]	8.64[a]
37	8.98[a]	9.08[a]	42	8.57	8.65
42	8.56	8.64	42	8.58	8.67
42	8.56	8.66	43	8.54[a]	8.65[a]
42	8.58	8.66	43	8.53	8.66
42	8.57	8.67	43	8.54[a]	8.65[a]
42	8.59	8.66	43	8.53	8.65
				$T_{\frac{1}{2}n}$	T_n
Average values in experiments			42, 43:	8.56°K	8.65°K
Mean deviations			42, 43:	0.01°	0.01°

[a] Indicates observation on $n-s$ transition. The other points were taken on $s-n$ transitions.

The zero field transitions of this specimen had a characteristic temperature width of 0.15°K, as is shown by a typical transition plotted in Fig. 4. The traditional way of quoting the temperature value of such a transition is to give the value of the temperature $T_{\frac{1}{2}n}$ at which the transition (in resistance or permeability) has reached the half-way point between superconducting and normal values. The intersection of the $H-T$ curve with the T axis, however, can be expected to correspond not to $T_{\frac{1}{2}n}$ but to the temperature T_n at which the zero field transition to the normal state is finally completed. In cases where the transition in zero field occurs over a very narrow range of temperatures, this difference is negligible, but in the present measurements this was not the case. Therefore, in tabulating transition temperatures in Table I both $T_{\frac{1}{2}n}$ and T_n are given.

It will be noted that two values of the zero field transition were observed at $T_n=9.08°$ on the first experimental run after reannealing, whereas transitions were thereafter repeatedly observed in the neighborhood of $T_n=8.65°$. The $H-T$ curve was not displaced by this change except in the immediate vicinity of the zero field transition temperature. The value $T_n=8.65°$ was not only obtained as the result of 12 successive observations but also correlated exactly with T_0 as determined independently from the magnetic transition data assuming the parabolic law $H=H_0(1-T^2/T_0^2)$. The results with $T_n=9.08°$ are included as an indication of the experimental fact that columbium can undergo changes perhaps in the course of temperature cycling, which alter its zero field transition by a fraction of a degree without affecting the critical field properties beyond the immediate temperature neighborhood.

In the comparison experiments on the specimen of

[14] W. J. De Haas and A. D. Engelkes, Physica 4, 325 (1937).
[15] J. G. Daunt, Phil. Mag. 28, 24 (1939).

TABLE II. Critical magnetic fields necessary to complete $s \rightarrow n$ transitions in columbium containing 0.4 percent tantalum according to reference 7.

Sample No. 5 Before annealing			Sample No. 5A After annealing		
Expt. no.	T°K	H_c, kilo-oersteds	Expt. no.	T°K	H_c, kilo-oersteds
			40	5.0	5.4(2)
39	6.48	5.10	40	5.4	4.84
39	6.88	4.40	40	5.80	4.50
39	6.00	6.28	40	5.94	4.24
39	6.15	6.20	40	6.23	3.60
			40	6.80	2.88
			40	7.35	2.09

columbium 5 tested in the cyclotron experiments,[7] the first observations were made on the sample as machined into cylindrical form, and the second after annealing for three hours at 1000°C in a fused silica tube evacuated to 10^{-5} mm. The first set of $H-T$ data were higher than corresponding results in the purer specimen 3A, but after the annealing process, the results on 5A came into agreement with those of 3A. The data are given in Table II, and the complete $H-T$ curve in Fig. 3 includes these points.

VII. DISCUSSION

The $H-T$ curves of most superconductors have been observed to agree approximately with an equation of the form

$$H=H_0(1-T^2/T_0^2). \tag{9}$$

To test the validity of this equation in connection with the present results, a graph of H *versus* T^2 is shown in Fig. 5. A least squares analysis of the magnetic points alone yields the values $H_0=8250$ oersteds and $T_0=8.65$°K. It is seen therefore that this value of T_0 is in agreement with the average experimental value of T_n given in Table I for experiments 42 and 43. Values of H_0 ranging from 7280 oersteds to 8050 oersteds and of T_0 from 9.0°K to 8.71°K have been given in preliminary reports of this work.[16,17] The values $H_0=8250$ oersteds and $T_0=8.65$°K are the result of a careful reevaluation of all the experimental data and are believed to represent the best values obtainable from these data. The present experimental values of the critical field extrapolated to the temperature range 1 to 4°K are about three times greater than those obtained by Daunt and Mendelssohn.[4] The reason for this is by no means clear. It is to be noted that the Daunt and Mendelssohn results were obtained on a single sample of which no detailed analysis was given and the authors indicated that their experiment was of a preliminary nature.

The value of dH/dT at T_0 is 1910 oersteds/deg., which is larger than the corresponding value for any other superconductor except vanadium[13] which has a value of about 4000 oersteds/deg.** As a necessary consequence of the large values of H_0 and dH/dT at T_0, the derivable thermodynamic quantities are much larger in magnitude for columbium than for other superconducting elements. The entropy change of the transition at any given temperature T is given by

$$S(n)-S(s)=-(VH/4\pi J)dH/dT, \tag{10}$$

where V=atomic volume in cm³/mole, J=mechanical equivalent of heat, the magnetic fields are expressed in oersteds, and the entropy change is calculated in units of cal./mole deg.

In the case of columbium, the atomic weight is 92.91, which divided by the density determined for our specimens, 8.55, gives 10.87 cm³/mole. Substituting the experimental values of H_0 and T_0 in Eq. (9) we find that

$$H=8250-110T^2,$$
$$dH/dT=220T.$$

Substitution of these values into Eq. (10) leads to the result

$$S(n)-S(s)=0.0375T-0.00100T^3.$$

The change of specific heats $C_p(n)-C_p(s)$ between the two states is derived from Eq. (10) as

$$C_p(n)-C_p(s)=(VT/4\pi J)\{(dH/dT)^2+H(d^2H/dT^2)\}. \tag{11}$$

When the experimental values are substituted into Eq. (11), the difference between the two specific heats becomes

$$C_p(n)-C_p(s)=0.0375T+0.00150T^3. \tag{12}$$

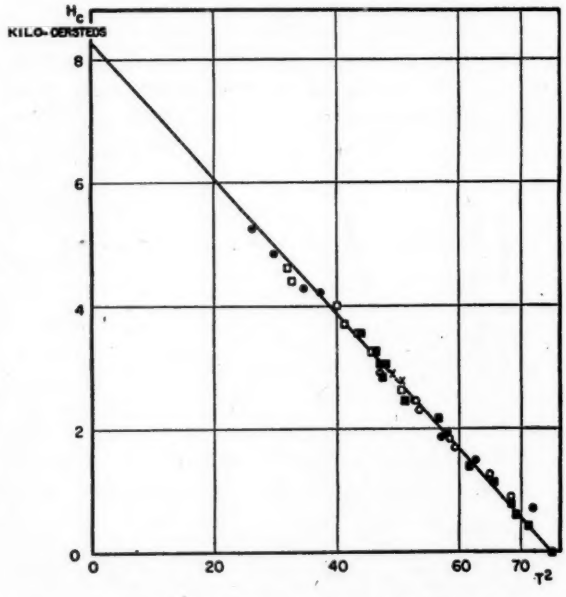

FIG. 5. Verification of the parabolic relation.

[16] Cook, Zemansky, and Boorse, Phys. Rev. **79**, 212 (1950).
[17] Cook Zemansky, and Boorse, Phys. Rev. **78**, 820 (1950).

** *Note added in proof:* Since this paper was submitted, the $H-T$ curve of vanadium was determined by A. Wexler and W. S. Corak, Phys. Rev. **79**, 737 (1950), who give the value dH/dT =400 oersteds/deg.

The specific heat $C_p(n)$ of a metal in the normal state and at low temperatures can be expressed in the form

$$C_p(n)=\gamma T+464.4T^3/\Theta_n^3, \quad (13)$$

where the term proportional to T is contributed by the conduction electrons, and the second term by lattice vibrations at low temperatures, Θ_n being the Debye characteristic temperatures of the normal state.

In all calorimetric experiments on superconductors the electronic contribution to specific heat has been zero, while the Debye term remains but with a different value Θ_s of the characteristic temperature. Therefore $C_p(s)$ can be written

$$C_p(s)=464.4T^3/\Theta_s^3. \quad (14)$$

If Eqs. (12), (13), and (14) are combined it is seen that the value of the constant γ of the electronic specific heat term is

$$\gamma=0.0375,$$

and that

$$\Theta_s^{-3}-\Theta_n^{-3}=0.00150/464.4=3.24\times10^{-6}.$$

The value of Θ_n can be estimated from Lindemann's empirical equation,[18]

$$\Theta=c(T_m/AV^{\frac{1}{3}})^{\frac{1}{2}}.$$

where A is the atomic weight, V the atomic volume (cm³/mole), T_m the melting point in °K, and c a constant having values from 115 to 142 as determined from known Debye Θ values. Using $c=135$, $A=92.91$, $V=10.87$ cm³/mole and $T_m=2415°C=2688°K$, the value of Θ_n for Cb is 330°K, so that $\Theta_n^{-3}=0.04\times10^{-6}$, which leads to an estimate of Θ_s as ~67°K.

The electronic specific heat of columbium calculated from $H-T$ measurements is higher than calorimetric values that have been observed in other transition metals. This, however, is not surprising in view of its observed magnetic behavior. The occurrence of large values of γ has been observed only in the "transition metals" in which the d-bands are partially filled, and this circumstance has been accounted for by extending the free electron theory of Sommerfeld by an appropriate quantum-mechanical treatment to include the effects of the nuclei and bound electrons on the conduction electrons, as well as interaction terms between the conduction electrons themselves. It is the latter type of interaction that has so far provided the best possibility of accounting for the larger values of γ although compensating effects and the extreme difficulty of the calculation make a detailed prediction impossible.[19]

The authors wish to express their appreciation to Messrs. Albert Brown, Robert C. Block, J. Gregory Dash, and Leonard Lesensky for their assistance in performing the experiments, as well as to Miss Marian Lamson and Mr. John Dunbar of Professor T. I. Taylor's laboratory in the Department of Chemistry, Columbia University, for spectrographic analyses.

[18] Lindemann, Physik Zeits. **11**, 609 (1910).

[19] E. Wigner, Trans. Faraday Soc. **34**, 678 (1938).

Ferromagnetic Resonance in Nickel Ferrite

W. A. YAGER, J. K. GALT, F. R. MERRITT, AND E. A. WOOD
Bell Telephone Laboratories, Murray Hill, New Jersey

(Received July 21, 1950)

The ferromagnetic resonance phenomenon in single crystals of NiO Fe_2O_3 has been studied at room temperature at 24,000 Mc/sec. Small samples were used in order to avoid electromagnetic cavity-type resonances. The g-factor observed is 2.19. The first-order magnetocrystalline anisotropy constant K_1 was found to be -6.27×10^4 ergs/cc. The absorption line was very narrow (half-widths less than 100 oersteds) and fit a resonance curve quite satisfactorily.

I. INTRODUCTION

FERROMAGNETIC resonance, originally discovered by Griffiths[1] and explained phenomonologically by Kittel,[2] has now been discussed by several authors.[3] The phenomenon has been studied in ferrites in the form of ceramics by Hewitt[4] and by Beljers[5] and in the form of single crystals of Fe_3O_4 by Bickford.[6]

We have studied the resonance behavior of single crystals of NiO Fe_2O_3 with a view to examining some of the fundamental properties of ferrites. The investigation was carried out at a frequency of approximately 24,000 Mc/sec. on spherical samples. In order to avoid electromagnetic cavity type resonances in our samples we have found it necessary to use spheres whose diameter was less than 0.1 cm. Most of our data were taken on spheres of diameter about 0.038 cm.

We have examined the field at resonance and the line width as a function of crystallographic orientation. From the first of these we find the magnetocrystalline anisotropy. The growth of the crystals and measurements of several of their properties are described elsewhere.[7]

II. EXPERIMENTAL

A block diagram of the r-f equipment used for the measurements is shown in Fig. 1. The signal oscillator is monitored with a crystal detector so that its output can be held constant. This output passes through an attenuator and then through the test cavity in which our sample is mounted. This signal is then mixed with the signal from a beat oscillator and the difference frequency passes through an attenuator, is amplified in the i-f amplifier, then detected and applied to the vertical plates of an oscilloscope. Since the beat oscillator is swept at 60 cycles over a frequency band larger than the two megacycle band width of the i-f amplifier, and since the same 60-cycle signal is used for the horizontal oscilloscope sweep the detected signal is just the shape of the i-f response curve. The peak height on the oscilloscope can be adjusted by means of the i-f attenuator, and when this height is held at a constant level the attenuator reading is a measure of the signal amplitude transmitted through the test cavity.[7a] The procedure for deriving the characteristics of the sample from signals measured in this way is given below.

A detailed picture of the test cavity showing how the sample is mounted is given in Fig. 2. By rotating the phosphor-bronze rod while the sample is in place, data can be taken at various orientations of crystal axes with respect to the r-f and steady magnetic fields.

The spherical shape of the samples was achieved using a device developed for the purpose by Bond.[8] We have produced spheres with diameters from 0.02 to 0.10 cm with the device without difficulty.

The sample is mounted on a rod as shown in Fig. 2, with its crystal axes oriented in a predetermined way. In order to do this, the crystal is first adjusted to the desired orientation by means of x-ray techniques while it is mounted on an adjustable head and can therefore be rotated by measured angles. It is attached to this head with rochelle salt which is melted and then allowed to solidify around the sample. When the head adjustments have been made, and the desired crystal axis is parallel to the axis of the head, the sample is transferred to the rod. This is done outside the cavity, and the rod is put in place in the cavity later. The head and the rod are placed in aligned V-blocks so that the ends of both can be brought together with the sample between them. The end of the rod, which is polystyrene, is softened with benzene and pressed against the sample until the benzene has evaporated and the polystyrene is hard. The rochelle salt is then dissolved away with water, and the sample is left imbedded in the polystyrene. A final Laue photograph is taken to check the sample orientation after it is affixed to the polystyrene. This was always within a degree or two of the desired position for the spheres on which data were taken.

From the description of the apparatus given above it

[1] J. H. E. Griffiths, Nature **158**, 670 (1946).
[2] C. Kittel, Phys. Rev. **71**, 270 (1947).
[3] W. A. Yager and R. M. Bozorth, Phys. Rev. **72**, 80 (1947); J. L. Snoek, Nature **160**, 60 (1947); Physica **14**, 207 (1948); A. F. Kip and R. D. Arnold, Phys. Rev. **75**, 1556 (1949); D. Polder, Phil. Mag. **40**, 99 (1949); J. M. Richardson, Phys. Rev. **75**, 1630 (1949); J. H. Van Vleck, Phys. Rev. **78**, 266 (1950).
[4] W. H. Hewitt, Jr., Phys. Rev. **73**, 1118 (1948).
[5] H. G. Beljers, Physica **14**, 629 (1949).
[6] L. R. Bickford, Jr., Phys. Rev. **78**, 449 (1950).
[7] Galt, Matthias, and Remeika, Phys. Rev. **78**, 391 (1949).

[7a] The crystal converter is driven hard by the beat oscillator signal, and under these conditions the difference frequency output is proportional to the signal from the test cavity. This proportionality has been checked experimentally in this set-up.
[8] W. L. Bond (to be published).

will be clear that we measure the *variation* in the signal transmitted through the cavity as we change the steady magnetic field H_z. All measurements are taken with the cavity tuned to resonance. From these data we find the variation in ferromagnetic resonance energy absorption with H_z in the following way. From Eqs. IV(14) and IV(16) in Slater's[9] review article on microwave electronics, when the cavity is at resonance the ratio of signal power out to signal power incident on the input window is:

$$\frac{P_{out}}{P_{inc}}=\frac{4Q_L^2}{Q_{ext_1}Q_{ext_2}}, \tag{1}$$

where Q_L is the loaded Q and Q_{ext_1} and Q_{ext_2} are the input and output Q's respectively. Here:

$$\frac{1}{Q_L}=\frac{1}{Q_{ext_1}}+\frac{1}{Q_{ext_2}}+\frac{1}{Q_a}, \tag{2}$$

where Q_a is the unloaded Q of the cavity. Q_a takes account of losses in the sample as well as in the other components of the cavity. From Eqs. (1) and (2):

$$\frac{1}{Q_a}=2\frac{V_{inc}}{V_{out}}\frac{1}{(Q_{ext_1}Q_{ext_2})^{\frac{1}{2}}}-\frac{1}{Q_{ext_1}}-\frac{1}{Q_{ext_2}}, \tag{3}$$

where V_{inc}/V_{out} is the square root of P_{inc}/P_{out}.

Now if a reference point is established at very large H_z where the ferromagnetic resonance energy absorption is zero, Q_a at that H_z involves all the other losses in the cavity, including the dielectric losses in the sample. If a prime is used to denote quantities at the reference point Eq. (3) gives;

$$\frac{1}{Q_a}-\frac{1}{Q_a'}=2\frac{V_{inc}'}{V_{out}'}\frac{1}{(Q_{ext_1}Q_{ext_2})^{\frac{1}{2}}}\left(\frac{V_{out}'}{V_{out}}-1\right), \tag{4}$$

where we have used the fact that the incident signal is held constant during the experiment and therefore $V_{inc}'/V_{inc}=1$. Now if (1) is used to determine Q_L at the reference point and it is called Q_L', Eq. (4) becomes:

$$\frac{1}{Q_a}-\frac{1}{Q_a'}=\frac{1}{Q_L'}\left(\frac{V_{out}'}{V_{out}}-1\right). \tag{5}$$

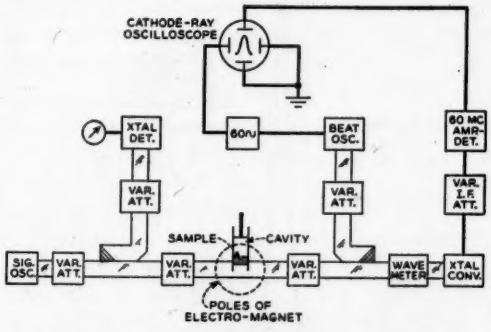

FIG. 1. Block diagram of the r-f equipment.

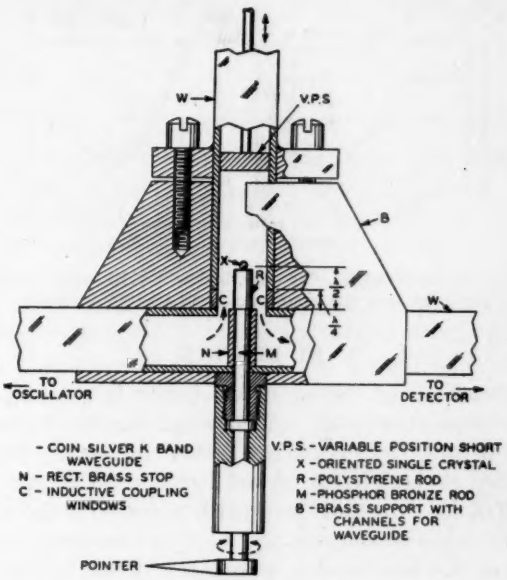

FIG. 2. Schematic diagram of the transmission cavity for magnetic resonance absorption measurements at 1.25-cm wave-length. W-coin silver K band wave guide.

In terms of energy dissipated per unit time, this can be written as:

$$w_m=(w_{ext_1}+w_{ext_2}+w_{cav}+w_{diel})[(V_{out}'/V_{out})-1], \tag{6}$$

where w_m is the energy dissipated due to ferromagnetic resonance, w_{ext_1} and w_{ext_2} are the energies lost through the input and output windows of the cavity, w_{cav} is the energy lost in the cavity outside the sample and w_{diel} is the *dielectric* energy loss in the sample. We assume that $(w_{ext_1}+w_{ext_2}+w_{cav}+w_{diel})$ is independent of the applied field H_z.

Two methods were used to measure the steady field H_z. One was the conventional rotating coil technique. The voltage induced in a coil rotating in a field H_z is a measure of the field. With this method we are able to obtain accuracies of ± 0.5 percent. The other method which was used for most of the readings was the measurement of the resonance frequency of protons in the field. From this and the value of the gyromagnetic ratio γ for the proton as measured by Thomas, Driscoll, and Hipple[10] the value of the field is obtained using the relation $\omega=\gamma H$. We have used a superregenerative circuit similar to that of Roberts[11] to detect the resonance. The protons were contained in a sample of polyisobutylene. The line observed is narrow enough to give an accuracy of ± 0.02 percent in the measurement, and not so sharp and intense as to cause overcoupling troubles.

[9] J. C. Slater, Rev. Mod. Phys. 18, 441 (1946). There is a misprint in Eq. IV(14) in this reference. It should read:

$$\frac{P}{\frac{1}{2}Z_0A\bar{A}}=\frac{4Q_L^2}{Q_{ext_1}}\left(\frac{1}{Q_a}+\frac{1}{Q_{ext_2}}\right).$$

[10] Thomas, Driscoll, and Hipple, Phys. Rev. 75, 902 (1949).

[11] A. Roberts, Rev. Sci. Inst. 18, 845 (1947).

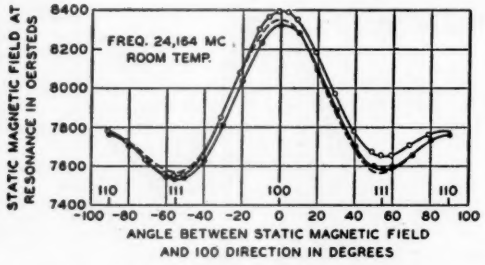

FIG. 3. Variation of H_{res} for directions in a (110) plane with the angle between the steady field and a [100] direction.

III. RESULTS

Because a crystal of nickel ferrite is magnetically anisotropic, the steady field at which maximum absorption occurs, H_{res}, is different when the steady field is applied along different crystal directions. The variation of H_{res} for directions in a (110) plane with the angle between the steady field and a [100] direction is shown in Fig. 3. Data for two spheres are shown by the two solid curves. As we shall see presently, the magnetocrystalline anisotropy constant K_1 can be determined from these data.

The width of the absorption line has required some care in its determination. Our first measurements were made on a sphere approximately 0.10 cm in diameter. The line observed is shown in the top half of Fig. 4. The essential structure of this line was the same at all crystallographic orientations. One large line and two small ones always occurred, and the separations remained quite constant. This behavior seems to be caused by electromagnetic cavity type resonances in the sample.[11a] As we go up the resonance curve $(\epsilon\mu)^{\frac{1}{2}}$ reaches a value such that a half-wave-length of electromagnetic radiation is of the order of the diameter of the sphere, and resonance occurs. We do not know enough about ϵ to check this relation by calculating $(\epsilon\mu)^{\frac{1}{2}}$; when we use smaller samples, however, a single narrow line occurs as we should expect and H_{res} is not the same as that for the maximum absorption in the larger sphere. Furthermore our best estimates of ϵ make this explanation plausible. The line obtained in a small sample at the same crystallographic orientation is plotted in the lower half of Fig. 4. It is believed to be the narrowest ferromagnetic resonance line thus far observed.

We have observed no large variation in the line width with the crystallographic orientation of the steady field. In one case the width varied from 70 oersteds when H_s was along the [100] direction in the (110) plane to 77 oersted when H_s was along the [111] direction in the (110) plane. Variations of this size occur from sample to sample, however.

We have also found that varying the position of the sample in the r-f field of the test cavity has no appreciable effect on line width. This result seems to indicate that the dielectric losses are independent of the magnetic losses, and thus to justify the assumption stated just after Eq. (4).

[11a] The authors are indebted to Dr. C. Kittel for suggesting this explanation.

IV. THEORY

Using Kittel's theory for the relationship between H_{res} and crystallographic direction,[12] we can account for the data of Fig. 3 and can derive the value of the magnetocrystalline anisotropy constant K_1. According to Kittel, the general resonance condition is:

$$\omega=\gamma H_{eff}, \tag{7}$$

where γ is the gyromagnetic ratio $ge/2mc$ and g is the spectroscopic splitting factor.[13] If the z axis is taken along the steady applied field:

$$H_{eff}=\{[H_z+(N_y+N_y^e-N_z)M_z] \times[H_z+(N_x+N_x^e-N_z)M_z]\}^{\frac{1}{2}}. \tag{8}$$

N_x, N_y, N_z are the usual demagnetizing factors. N_x^e and N_y^e are effective demagnetizing factors, which are a convenient way of taking account of the variation in the resonance field due to the presence of magnetic anisotropy. Each of these factors takes account of one component of the torque on the magnetization due to the anisotropy. The values of N_x^e and N_y^e to be used in analyzing the data in Fig. 3 where the steady applied

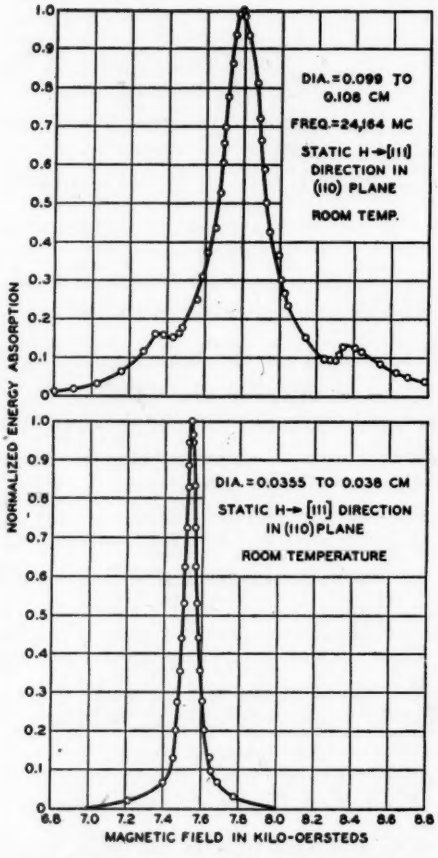
NORMALIZED ENERGY ABSORPTION
DIA.=0.099 TO 0.108 CM
FREQ.=24,164 MC
STATIC H→[111] DIRECTION IN (110) PLANE
ROOM TEMP.
DIA.=0.0355 TO 0.038 CM
STATIC H→[111] DIRECTION IN (110) PLANE
ROOM TEMPERATURE
6.8 7.0 7.2 7.4 7.6 7.8 8.0 8.2 8.4 8.6 8.8
MAGNETIC FIELD IN KILO-OERSTEDS

FIG. 4. Structure of the absorption line.

[12] C. Kittel, Phys. Rev. 73, 155 (1948).
[13] C. Kittel, Phys. Rev. 76, 743 (1949).

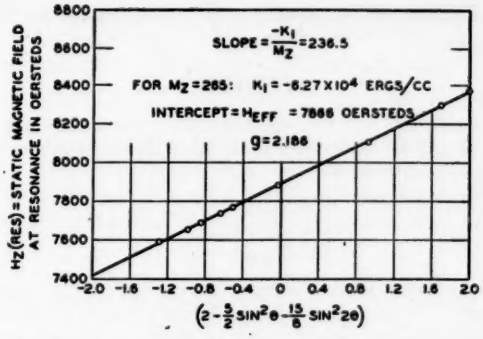
SLOPE = $\frac{-K_1}{M_z}$ = 236.5
FOR M_z = 265: K_1 = -6.27 X 10⁴ ERGS/CC
INTERCEPT = H_{EFF} = 7866 OERSTEDS
g = 2.186
H_z(RES) = STATIC MAGNETIC FIELD AT RESONANCE IN OERSTEDS
$(2-\frac{5}{2}\sin^2\theta-\frac{15}{8}\sin^2 2\theta)$

FIG. 5. Variation of the static magnetic field at resonance as determined by Eq. (12). *Note added in proof:* $g=2.186$ should read $g=2.19$.

field is always in the (110) plane have been derived by Bickford.[6] They are:

$$N_x^e=(2-\sin^2\theta-3\sin^2 2\theta)K_1/M_z^2,$$
$$N_y^e=2(1-\sin^2\theta-\tfrac{3}{8}\sin^2 2\theta)K_1/M_z^2, \quad (9)$$

where θ is the angle between the steady applied field and a [100] crystal direction.

Since we deal with spheres, $N_x=N_y=N_z$, and Eq. (8) becomes:

$$H_{eff}=[(H_z+N_y^eM_z)(H_z+N_x^eM_z)]^{\frac{1}{2}}. \quad (10)$$

It turns out from our measurements that $N_y^eM_z$ and $N_x^eM_z$ are only about five percent of H_z, so that the square roots above can be developed by the binomial theorem, and we have to a very good approximation:

$$H_{eff}=H_z+\tfrac{1}{2}(N_x^e+N_y^e)M_z, \quad (11)$$

$$H_z=H_{eff}-(2-5/2\sin^2\theta-15/8\sin^2 2\theta)K_1/M_z. \quad (12)$$

Clearly K_1/M_z and hence K_1 can be determined from the slope of a plot of H_z *vs.* the quantity in brackets in Eq. (12). The dotted line in Fig. 3 is a plot of H_z *vs.* θ as given by Eq. (12). We attribute the deviation of the data from this curve to the fact that the samples were not perfect spheres. In calculating K_1 we have eliminated this effect by using the average of four experimental values of H_z in the plot *vs.* the quantity in brackets in Eq. (12) for each value of θ; we get four values of H_z by using the data at $+$ and $-\theta$ on both spheres. The plot of these averaged values of H_z *vs.* the quantity in brackets in Eq. (12) is shown in Fig. 5. Clearly the averaging process has eliminated deviations of the sort appearing in Fig. 3. The slope of this plot can be determined to an accuracy of ± 2 percent. Using a value of 265 c.g.s units for [7,14] M_s, we find:

$$K_1=-6.27\times 10^4 \text{ ergs/cc},$$

as compared with

$$K_1=-6.2\times 10^4\pm 10 \text{ percent ergs/cc},$$

recently obtained from hysteresis loop measurements.[7]

Experimentally, we measure H_z and θ while ω and therefore H_{eff} is held constant. We may then use Eq. (12) to find H_{eff} and from this obtain g using Eq. (7). This is done most easily using the intercept of the line in Fig. 5 with the vertical axis. In this way we obtain:

$$g=2.19.$$

The shape of the resonance line can be accounted for by Kittel's equation of motion[12] plus a damping term the magnitude of which is determined by the line width. From such an equation of motion, assuming simple harmonic time dependence in the usual way, one finds the usual sort of resonance curves for the real and imaginary parts of the permeability ($\mu=\mu'-j\mu''$). The formulas are worked out here in greater detail than usual in order to compare our data with these resonance curves. Several damping terms have been suggested[2,12]; we have used one of the general form first put forward by Landau and Lifshitz.[15]

The equation of motion is:

$$d\mathbf{M}/dt=\gamma[\mathbf{M}\times\mathbf{H}]-\gamma\alpha/M(\mathbf{M}\times[\mathbf{M}\times\mathbf{H}]), \quad (13)$$

where α is a parameter, determined from the line width, which measures the magnitude of the damping force on the precessing dipole moment of the sample.

As we have said, an expression for $\chi_x=M_x/H_x$ and thus for μ' and μ'' may be derived from Eq. (13). The demagnetizing fields and the effective fields caused by magnetocrystalline anisotropy enter into these formulas, however, since they affect the effective field inside the material. There is thus no general way of plotting curves for μ' and μ'' which are characteristic of the material and independent of sample shape. The formulas for μ' and μ'' for spherical samples are given in the appendix [Eqs. (A-2)].

The parameter α is determined from the line width by means of the following relation (see appendix):

$$\alpha/(1+\alpha^2)^{\frac{1}{2}}=[(l_xl_y)^{\frac{1}{2}}/(l_x+l_y)]2\Delta H/H_{res}. \quad (14)$$

$2\Delta H$ is the width of the absorption line at points such that $\mu''=\frac{1}{2}\mu''_{res}$. Since α is small for the lines observed here, we use the approximation $(1+\alpha^2)^{\frac{1}{2}}=1$. With α determined, Eqs. (A-2) are complete, and give formulas for μ' and μ'' *vs.* H_z if ω is constant or *vs.* ω if H_z is constant. The value of α obtained with Eq. (14) from our data is approximately:

$$\alpha=4.5\times 10^{-3}.$$

The relaxation time associated with the resonance is $2Q/\omega$, where Q is $H_{res}/2\Delta H$ for the absorption line. Equation (14) then gives:

$$\tau=-\frac{2}{\omega}\frac{H_{res}}{2\Delta H}=-\frac{2}{\omega}\frac{(1+\alpha^2)^{\frac{1}{2}}}{\alpha}\frac{(l_xl_y)^{\frac{1}{2}}}{l_x+l_y}, \quad (15)$$

and our data yield:

$$\tau=1.5\times 10^{-9} \text{ sec.}$$

[14] C. Guillaud and M. Roux, Comptes Rendus **229**, 1133 (1949).

[15] L. Landau and E. Lifshitz, Physik. Zeits. Sowjetunion **8**, 153 (1935).

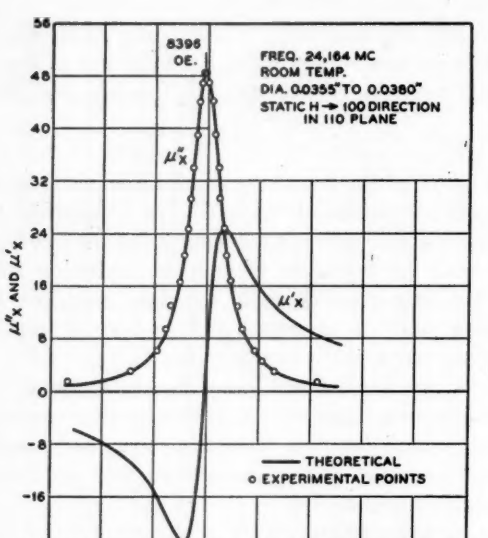

FIG. 6. Resonance curves for μ_x' and μ_x''.

The variation of μ'' with H_z as determined from experiment may be compared with Eqs. (A-2) over the whole range of variation of H as follows. The values of μ'' are first determined from the energy absorbed in the sample as given by Eq. (6). For the energy absorbed we write:

$$w_m = K\mu'', \tag{16}$$

where K is a constant proportional to the integral of H^2 over the volume of the sphere. Equation (6) then becomes:

$$\left(\frac{K}{w_{\text{ext}_1}+w_{\text{ext}_2}+w_{\text{cav}}+w_{\text{diel}}}\right)\mu'' = \left(\frac{V_{\text{out}}'}{V_{\text{out}}}-1\right). \tag{17}$$

We determine $K/(w_{\text{ext}_1}+w_{\text{ext}_2}+w_{\text{cav}}+w_{\text{diel}})$ from Eq. (17) by using Eqs. (A-2) in the appendix to calculate μ'' at one point (say at maximum) and measuring $[(V_{\text{out}}'/V_{\text{out}})-1]$ at the same point. The values of μ'' can then be obtained at all other fields from Eq. (17) and compared with the curve obtained from Eqs. (A-2). Figure 6 shows a plot of the data at various points treated in this way, with the curve obtained from Eqs. (A-2) superposed. No data were taken on μ' but the theoretical curve is shown. The data fit the theoretical curve quite satisfactorily.

V. DISCUSSION

It should be noted that the g value observed here for $NiFe_2O_4$ is consistent with a very simple picture in which we attribute the whole magnetization to Ni^{++} ions as the Néel picture does for an inverse spinel of this type. The g value is then also identified with that of the Ni^{++} ions, and since the d-shell in these ions is more than half full, the g value is expected to be larger than 2.

The authors wish to express their gratitude to Dr. C. Kittel for helpful discussions of this problem, and to H. G. Hopper, W. L. Bond, and J. Andrus for technical assistance.

APPENDIX

We assume $\exp(j\omega t)$ time dependence for the x and y components of M and H, and substitute in Eq. (13) using values of the internal fields as given by:

$$\begin{aligned} H_x &= H_{x\text{app}} - N_x^e M_x, \\ H_y &= -N_y^e M_y, \\ H_z &= H_{z\text{app}}. \end{aligned} \tag{A-1}$$

Only the effective demagnetizing factors caused by anisotropy enter here. The usual ones N_x, N_y, N_z are equal for the spherical case and cancel out, so they may be dropped. We assume that $\mathbf{M}\cdot\mathbf{H} = M_z H_z$ so that the last term in Eq. (13) may be written: $\gamma\alpha(\mathbf{H}M_z - \mathbf{M}H_z)$.

The resulting equations for μ' and μ'' are:

$$\frac{\mu'-1}{4\pi} = \frac{1-\dfrac{\omega^3}{\gamma^3 l_x l_y H_z^3(1+\alpha^2)^2}\left(1-\alpha^2\dfrac{l_z}{l_y}\right)}{\left[1-\dfrac{\omega^2}{\gamma^2}\dfrac{1}{l_x l_y H_z^2(1+\alpha^2)}\right]^2}\frac{M_z}{l_z H_z}, \tag{A-2}$$

$$+\frac{\alpha^2}{1+\alpha^2}\frac{(l_x+l_y)^2}{l_x l_y}\frac{\omega^2}{\gamma^2}\frac{1}{l_x l_y H_z^2(1+\alpha^2)}$$

$$\frac{\mu''}{4\pi} = \frac{\dfrac{\alpha}{1+\alpha^2}\dfrac{\omega}{\gamma}\dfrac{1}{l_y H_z}\left[\dfrac{\omega^2}{\gamma^2}\dfrac{1}{l_x l_y H_z^2(1+\alpha^2)}+\dfrac{l_y}{l_x}\right]}{\left[1-\dfrac{\omega^2}{\gamma^2}\dfrac{1}{l_x l_y H_z^2(1+\alpha^2)}\right]^2}\frac{M_z}{l_z H_z},$$

$$+\frac{\alpha^2}{1+\alpha^2}\frac{(l_x+l_y)^2}{l_x l_y}\frac{\omega^2}{\gamma^2}\frac{1}{l_x l_y H_z^2(1+\alpha^2)}$$

where

$$l_x H_z = H_z + N_x^e M_z; \quad l_y H_z = H_z + N_y^e M_z. \tag{A-3}$$

The resonance denominator makes it possible for us to calculate the field at resonance quite easily. It is:

$$H_{res} = (\omega/\gamma)[l_x l_y(1+\alpha^2)]^{-\frac{1}{2}}. \tag{A-4}$$

This checks Eq. (8) except for the factor $1/(1+\alpha^2)^{\frac{1}{2}}$ which determines the change in the resonant field caused by the damping term in the equation of motion.

If H_z is off the resonant value sufficiently to reduce μ'' to one-half of its maximum value, H_z at this point is: $H_z = H_{res}+\Delta H$. From (A-3) it is clear that at this point the two terms in the denominator are approximately equal, and therefore:

$$1-\frac{\omega^2}{\gamma^2}\frac{1}{l_x l_y H_z^2(1+\alpha^2)} = \frac{\alpha}{(1+\alpha^2)^{\frac{1}{2}}}\frac{l_x+l_y}{(l_x l_y)^{\frac{1}{2}}}\frac{1}{(l_x l_y)^{\frac{1}{2}}H_z(1+\alpha^2)^{\frac{1}{2}}}\frac{\omega}{\gamma}. \tag{A-5}$$

This can be written as:

$$\left(\frac{\gamma}{\omega}(l_x l_y)^{\frac{1}{2}}H_z(1+\alpha^2)^{\frac{1}{2}} - \frac{\omega}{\gamma}\frac{1}{(l_x l_y)^{\frac{1}{2}}H_z(1+\alpha^2)^{\frac{1}{2}}}\right) = \frac{\alpha}{(1+\alpha^2)^{\frac{1}{2}}}\frac{l_x+l_y}{(l_x l_y)^{\frac{1}{2}}}.$$

Now if (A-4) is used for ω/γ this becomes:

$$\frac{H_z}{H_{res}} - \frac{H_{res}}{H_z} = \frac{2\Delta H}{H_{res}} = \frac{\alpha}{(1+\alpha^2)^{\frac{1}{2}}}\frac{l_x+l_y}{(l_x l_y)^{\frac{1}{2}}}. \tag{A-6}$$

Equation (14) follows from Eq. (A-6) immediately.

Equations (A-2) can be simplified considerably if (A-4) is examined from a different point of view, and it is noted that the resonance frequency ω_0 associated with each field H_z is $\gamma(l_x l_y)^{\frac{1}{2}}H_z(1+\alpha^2)^{\frac{1}{2}}$. If we use this abbreviation, and the definition of τ given in Eq. (15), Eqs. (A-2) become:

$$\begin{aligned} \frac{\mu'-1'}{4\pi} &= \frac{1-(\omega^2/\omega_0^2)[1-\alpha^2(l_x/l_y)]}{(1-\omega^2/\omega_0^2)^2+(4/\omega_0^2\tau^2)}(M_z/l_z H_z), \\ \frac{\mu''}{4\pi} &= \frac{(2/\omega_0\tau)[(\omega^2/\omega_0^2)+(l_y/l_x)]l_x/(l_x+l_y)}{(1-\omega^2/\omega_0^2)^2+(4/\omega_0^2\tau^2)}(M_z/l_z H_z). \end{aligned} \tag{A-7}$$

This form reveals the resonance character of the formulas clearly.

Letters to the Editor

PUBLICATION of brief reports of important discoveries in physics may be secured by addressing them to this department. The closing date for this department is five weeks prior to the date of issue. No proof will be sent to the authors. The Board of Editors does not hold itself responsible for the opinions expressed by the correspondents. Communications should not exceed 600 words in length.

Nuclear Disintegrations at 29,000 Meters above Sea Level

M. M. ADDARIO AND S. TAMBURINO
Institute of Physics, University of Catania, Catania, Italy
September 22, 1950

ILFORD C2 photographic plates, 100μ thick, carried up to 29,000 m above sea level (14 g cm^{-2} residual atmosphere) at 55° N geom. latitude, were explored to study the heavily ionizing particles released in nuclear disintegrations.[1] Eighty-four stars of 3 or more prongs were analyzed.

I. An estimate was made of what fraction of the stars produced at 14 g cm^{-2} of residual atmosphere is generated by the nucleons of the primary cosmic radiation. Following the method used by Bernardini *et al.*,[2] the cross section for star production was computed from the formula: $\sigma=N/MI$, where $N=(1.55\pm0.09)\times10^{-2}$ is the number of stars cm^{-3} sec.$^{-1}$ we observed at 29,000 m. This figure is corrected for the stars produced during the ascent and the descent of the balloon; $M=4.72\times10^{22}$ is the number of atoms cm^{-3} of emulsion, H-atoms disregarded; $I=2\pi I_0\exp(-h/\lambda)+(h/\lambda)E_i(-h/\lambda)$ is the intensity of the primary nucleons at 29,000 m; in this formula $I_0=0.12$ cm^{-2} sec.$^{-1}$ sterad.$^{-1}$ is the intensity of the primary nucleons at the top of the atmosphere, $h=14$ g cm^{-2}, and $\lambda=65$ g cm^{-2} is the interaction mean free path of nucleons for star production in air, corresponding to the average geometrical cross section of the nuclei in the air.

With the above values, we obtained $\sigma=(0.78\pm0.05)\times10^{-24}$ cm^2. If the cross section for the star production in the plates equals the average geometrical cross section of the nuclei in the emulsion, $\sigma_{Av}=0.8\times10^{-24}$ cm^2, one deduces that $\sigma/\sigma_{Av}=0.98\pm0.06$, which would indicate that *practically all of the stars observed at 14 g cm^{-2} residual atmosphere are produced by primary nucleons.*

II. The atomic number Z of the particles emitted in the stars observed was established and the ratio of the number of particles with $Z\geq2$ to the number of particles with $Z=1$ was computed for stars of different sizes. The results are given in column 3 of Table I.

TABLE I. Nature of the particles emitted from stars of different sizes produced at 29,000 m and at mountain elevation (H.L.P.'s data).

(1) No. of prongs	(2) No. of stars observed	(3) No. of part. with $Z\geq2$ / No. of part. with $Z=1$ at 29,000 m	(4) No. of α-particles / No. of protons at ~4000 m (H.L.P.)
3–6	32	0.63±0.18	0.65±0.09
7–9	25	0.52±0.12	0.85±0.13
10–14	16	0.61±0.12	0.77±0.09
≥15	11	0.58±0.11	0.59±0.06

In column 4 are given the ratios of the number of α-particles to the number of protons, obtained by Harding, Lattimore, and Perkins[3] (H.L.P.), at mountain elevation.

As the meanings of their and our ratios do not differ substantially, the two sets of data are comparable. They agree within the statistical errors, and show no variation with the star size and with the elevation at which the event occurred. We can therefore conclude that *the evaporation process does not vary appreciably with the excitation energy and with the energy of the star producing radiation.*

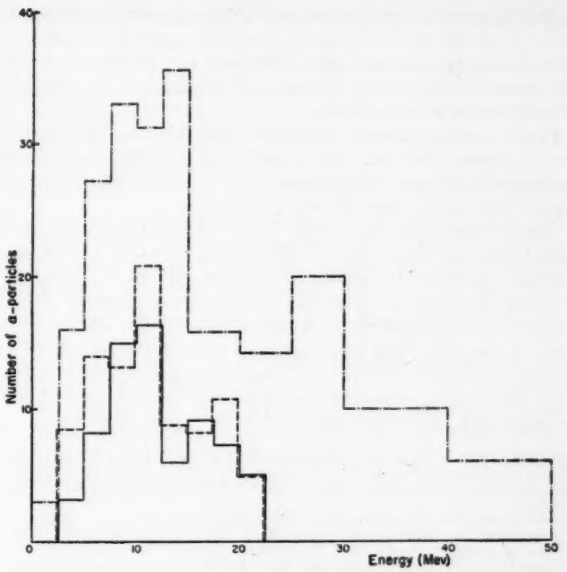

FIG. 1. Energy distribution of the α-particles emitted from the stars observed, ———— stars with number of prongs ≤9, at 29,000 m; - - - - - - - stars with number of prongs >9, at 29,000 m; —·—·— stars with number of prongs >9, at mountain elevation (H.L.P.'s data).

III. The energy distribution of the α-particles emitted from the 84 stars was studied. The results obtained for stars with number of prongs ≤9 and number of prongs >9 are plotted in Fig. 1, corrected to take into account the fact that, the larger the path of a particle, the greater is its probability of emerging from the emulsion. H.L.P.'s results obtained at mountain elevation are plotted in the figure of comparison.

It appears from the figure that *at 29,000 m stars of all sizes can emit α-particles with energies lower than the potential barrier of the nuclei in the emulsion* (~18 Mev for the heavy nuclei).

It is interesting to recall that H.L.P. obtained an indication, at mountain elevation, that practically all of the α-particles produced in stars of 2 or 3 prongs have energies above the potential barrier. Now, the 11 stars with 3 prongs observed in our plates gave rise to 8 α-particles ending in the emulsion, out of which 5 had energies lower than 8.5 Mev.

If this discrepancy between the energy distribution of the α-particles released in stars produced at mountain and balloon elevations is real, one must assume that the production of α-particles with energies lower than the potential barrier is a feature characteristic of the nuclear disintegrations in which very high energies are involved.

This would support H.L.P.'s argument that a nucleus hit by a very energetic particle may emit heavy unstable fragments which, in their turn, will disintegrate and produce α-particles with energies smaller than the potential barrier of the original nucleus.

Table II. Spatial distribution of the star pairs observed at 29,000 m and at mountain elevation. r is the distance between the centers of the stars of the pair, and r_p is its projection on the plane of the plate. P is the number of pairs observed, with the stars at distance r (or r_p), and Q is the number of "chance pairs" calculated using Perkins' formula.

	r_p (microns)	50	100	200	300	400	500	600	700
29,000 m (Addario and Tamburino)	$\frac{P-Q}{Q^{\frac{1}{2}}}$	6.85	2.93	1.43	1.15	1.15	1.24	0	0.9
	r_p (microns)	67	131	191	251	381	508	635	762
3650 m (Li and Perkins)	$\frac{P-Q}{Q^{\frac{1}{2}}}$	3.3	2.8	2.2	1.7	1.9	2.5	2.4	1.2
	r (microns)	50	100	150	200	250			
3600 m (Heidmann and Leprince-Ringuet)	$\frac{P-Q}{Q^{\frac{1}{2}}}$	10	8	5	4	4			

Such an interpretation is supported by the following experimental facts: (a) some stars emit heavy nuclear fragments; (b) in some stars forked tracks have been observed; (c) several stars show collimated beams of 2, 3, or more α-particles; (d) in some stars 2 recoil fragments are visible.

IV. An anomalous spatial distribution of the stars was observed in our plates, like that first found at mountain elevation by Leprince-Ringuet and Heidmann, and by Li and Perkins.[4] (Our plates, like theirs, were exposed vertically.)

The number P of pair of stars present in our plates was determined and the number Q of "chance pairs" was computed using Perkins' formula. In Table II is given the ratio $(P-Q)/Q^{\frac{1}{2}}$, between the observed deviation from chance association and the calculated one, for different distances between the centers of the stars of the pair. This ratio is greater than unity for practically all pairs observed. Perkins' and Leprince-Ringuet's data are also given in the table for comparison. Our ratios agree, regarding order of magnitude, with those observed at mountain elevation.

[1] We are deeply grateful to Professor F. Oppenheimer for giving us these plates. Details concerning the exposure of the plates and the procedures of the analysis are to be found in an article which will soon appear in *Nuovo Cimento*.
[2] Bernardini, Cortini, and Manfredini, Phys. Rev. **76**, 1792 (1949).
[3] Harding, Lattimore, and Perkins, Proc. Roy. Soc. **A196**, 325 (1949).
[4] L. Leprince-Ringuet and J. Heidmann, Nature **161**, 844 (1948). T. T. Li and D. H. Perkins, Nature **161**, 844 (1948).

On the Forward Scattering of 3.1-Mev Neutrons by the Deuteron

JUMPEI SANADA AND SHOTARO YAMABE
Department of Physics, Osaka University, Osaka, Japan
September 27, 1950

THE scattering of neutrons by deuterons was studied from a theoretical point of view by Massey and Buckingham.[1] They gave for 2.53-Mev neutrons two angular distribution curves which are shown in Fig. 1 with full lines; the one was deduced from the ordinary forces between nucleons and the other from the exchange forces. Coon and Barschall[2] measured the angular distribution experimentally, analyzing the distribution in energy of the recoiling deuteron in an ionization chamber. Their results are plotted in Fig. 1 with solid circles. They were in favor of the predictions of the theory of exchange forces. However, the results obtained by Darby and Swan[3] using a Wilson chamber fitted the angular distribution corresponding to the theory of ordinary forces and are plotted also in Fig. 1 with solid triangles.

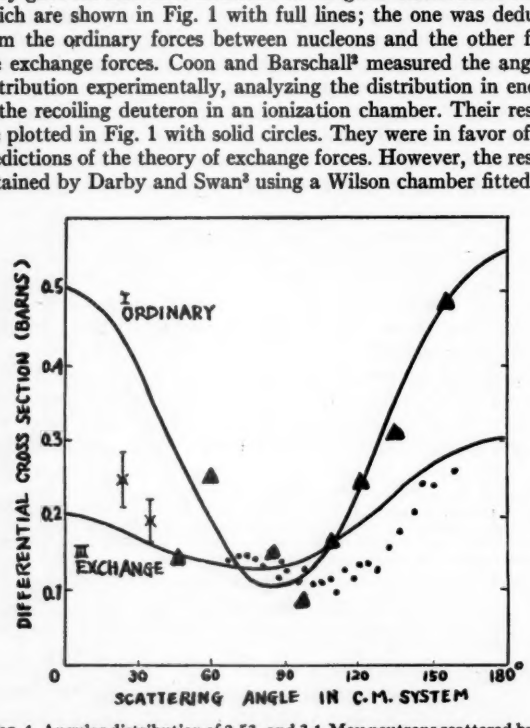

FIG. 1. Angular distribution of 2.53- and 3.1-Mev neutrons scattered by the deuteron. The full-line curves are according to the theory on the respective assumption of ordinary and exchange forces. The solid circles give the observation of Coon and Barschall, which is adjusted to give agreement between theory and experiment near 90°. The solid triangles give the observation of Darby and Swan, which is adjusted to agree with curve I (ordinary forces) near 120°. All above relate to 2.53-Mev neutrons. Two crosses are the results of the present observations for 3.1-Mev neutrons.

TABLE I. The differential scattering cross section of 3.1-Mev neutrons scattered by the deuteron in the center-of-mass system.

Scattering angle	Differential cross section
25±4 deg.	0.249±0.039 barn
35±6	0.191±0.029

It seems to be of interest to investigate the scattering in the forward direction, considering the two different results for the backward scattering. We measured the absolute values of the forward differential scattering cross section for 3.1-Mev neutrons using heavy water as a ring scatterer. The procedures were the same as those applied when we measured the angular distribution of 3.1-Mev neutrons from the d–d reaction scattered by proton using water as ring scatterer.[4]

Since the quantity of heavy water available was only 70 g, we could not extend the range of the scattering angle. The results are tabulated in Table I and plotted with crosses in Fig. 1.

In the neighborhood of the scattering angle 30° the theoretical differential scattering cross sections for 3.1-Mev neutrons are almost the same as those for 2.53-Mev neutrons in the case of ordinary forces, while they decrease by about ten percent from those for 2.53-Mev neutrons in the case of exchange forces.[5] We may conclude that our results of the differential scattering cross section lie between the curves corresponding to the theory of ordinary forces and that of exchange forces.

[1] H. S. Massey and R. A. Buckingham, Phys. Rev. **71**, 558 (1947). We could not refer to their original paper in Proc. Roy. Soc., until this letter was written.
[2] J. H. Coon and H. H. Barschall, Phys. Rev. **70**, 592 (1946).
[3] J. F. Darby and J. B. Swan, Nature **161**, 22 (1948).
[4] Oda, Sanada, and Yamabe, unpublished. See Kikuchi, Aoki, and Wakatuki, Proc. Phys. Math. Soc. Japan **21**, 410 (1939).
[5] C. L. Critchfield, Phys. Rev. **73**, 1 (1948).

The Shape of the Low Energy Beta-Spectrum of Rb^{86}

HERBERT R. MUETHER AND STUART L. RIDGWAY
Palmer Physical Laboratory, Princeton University, Princeton, New Jersey*
September 11, 1950

BETA-GAMMA-ANGULAR correlation has been reported for the low energy beta-group of Rb^{86} in coincidence with the 1.08-Mev gamma-ray.[1-3] Theory predicts such correlation only for forbidden-shape beta-spectra.[4] We have measured the low energy spectrum by a coincidence technique to avoid subtraction of the high intensity (80 percent) 1.8-Mev beta-group.

A conventional thick magnetic lens beta-ray spectrometer was modified to count only beta-rays coincident with a gamma-ray. The beta-scintillation counter ($\frac{1}{8}$-in. thick anthracene and a magnetically shielded E.M.I. photo-multiplier) had uniform efficiency for 100–1000-kev electrons. The Lucite-shielded NaI(Tl) gamma-scintillation counter, essentially a hemisphere concentric with the source, gave inappreciable backscattering and had sufficiently isotropic efficiency (15 percent rise near 50°, as checked with collimated 1.1- to 1.3-Mev Co^{60} source) to give no spectrum distortion by an energy-dependent angular correlation.

For a satisfactory coincidence rate the solid angle and momentum acceptance of the spectrometer were increased. Corrections for the resulting 15 percent resolution were made near the end point.

In checking the instrument with Au^{198} (one gamma per beta), the coincidence spectrum showed the expected allowed shape with end point at 972±10 kev. The low energy Cs^{137} spectrum was examined with the beta-counter alone, and the first-forbidden correction $a\ (=p^2+q^2)$ transformed the data into a straight line with end point at 515±10 kev.

Cs^{134} impurity was chemically removed from the Oak Ridge Rb^{86} as checked by gamma-ray spectra before and after. The sources

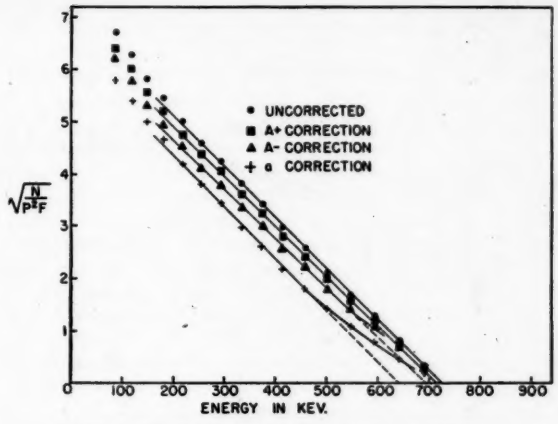

FIG. 1. Fermi plots for Rb^{86} low energy spectrum.

(0.4 mg/cm² and 1.0 mg/cm²) were prepared by evaporation of RbCl in vacuum on mica foils of approximately 2 mg/cm² thickness.

Figure 1 shows the Fermi plot analysis of the low energy Rb^{86} data. Points show the data without forbidden corrections and with first-forbidden corrections[5] a, A_+, and A_-. The $A_\pm'$ and $A_\pm''$ corrections differ insignificantly from the $A_\pm$ corrections, the energy-independent term $(\alpha z/2R)^2$ dominating the energy-dependent terms. A straight line fits best the uncorrected Fermi plot or the A_+ correction, and fits rather poorly the A_- correction; the a correction seems definitely excluded. The corrections yield different extrapolated end points and may also be compared on this basis.

Figure 2 shows the Fermi plot analysis of the high energy beta-spectrum (three percent resolution), and indicates a first-forbidden spectrum with the a correction giving a straight line with end point at 1.80±0.01 Mev. The gamma-ray energy was found to be 1.076±0.003 Mev, as measured by photo-electrons from a U radiator and calibrated with Co^{60}. These results are in agreement with those of Zaffarano, Kern, and Mitchell,[6] although these authors did not attempt to fit a forbidden correction to their data.

A search with a crystal gamma-ray spectrometer[7] failed to show any other gamma-radiation from Rb^{86}, and it is concluded that the end point of the low energy beta-spectrum should be the difference between the high energy end point and the gamma-ray energy, or 724±11 kev. Table I shows the extrapolated end points obtained from the various curves in Fig. 1. Thus on the basis of end points and shapes, type a can be ruled out entirely, and types A_-, A_-' and A_-'' seem quite unlikely. Of the remaining two, the existence of beta-gamma-correlation[1-3] seems to rule out the allowed transition.

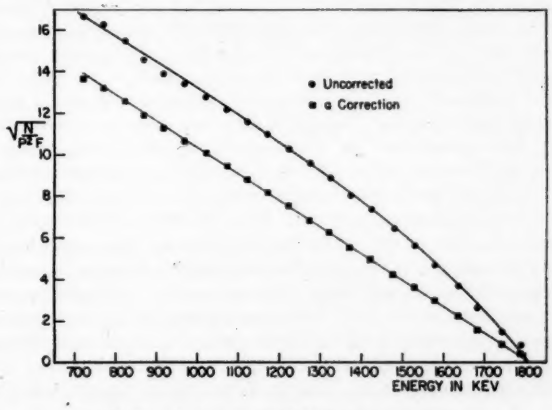

FIG. 2. Fermi plots for Rb^{86} high energy spectrum.

Further elimination may be made on the basis of a level scheme with specific spin assignments. Sr^{86} (even-even) should have ground-state spin zero. Selection rules for a first-forbidden transition of type a (such as the Rb^{86} high energy component has been shown to be) allow a transition to spin zero only from spin two. Hence we suggest the level scheme and spin assignments of Fig. 3,

TABLE I. Extrapolated end points.

Correction End points	Allowed 726±10	A_+, A_+', A_+'' 714±10	A_-, A_-', A_-'' 696±10	$a=p^2+q^2$ 640±10

with change of parity as required for those first-forbidden beta-interactions under discussion.

The coefficient R/Q in the beta-gamma-correlation function $1+(R/Q)\cos^2\theta$ is observed[1-3] to be positive. It is interesting to note that, on the basis of reference (4), this sign is consistent with the proposed level scheme only for types $A_\pm'$ of all thoses cited in

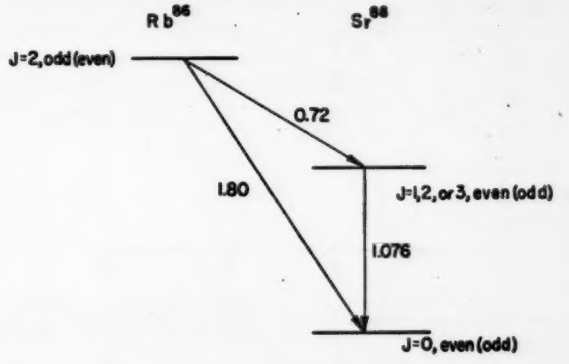

FIG. 3. Decay scheme of Rb^{86}.

Table I, except possibly for the intermediate state $J=3$, for which there are no angular correlation calculations. These A_+' and A_-' corrections arise from matrix elements $\int\sigma\times\mathbf{r}$ in the first-forbidden tensor and axial vector interactions, respectively. The former of these is somewhat more likely on the basis of our data.

The authors are deeply indebted to Professor R. Sherr for his interest and helpful suggestions during the course of this experiment and to Professor D. R. Hamilton for his extensive assistance in the interpretation of the results.

* Supported by the joint program of the ONR and AEC.

[1] D. J. Stevenson and M. Deutsch, Phys. Rev. 78, 640 (1950).
[2] T. B. Novey, Phys. Rev. 78, 66 (1950).
[3] R. Stump and S. Frankel, Phys. Rev. 79, 243 (1950).
[4] D. L. Falkoff and G. E. Uhlenbeck, Phys. Rev. 79, 334 (1950).
[5] E. J. Konopinski, Rev. Mod. Phys. 15, 209 (1943). (Our notation is the same as that introduced by Konopinski on page 227.)
[6] Zaffarano, Kern, and Mitchell, Phys. Rev. 74, 682 (1948).
[7] R. Hofstadter and J. A. McIntyre, Phys. Rev. 79, 389 (1950).

On the Deviations of Nuclear Magnetic Moments from the Schmidt Limits*

L. L. FOLDY AND F. J. MILFORD
Case Institute of Technology, Cleveland, Ohio
September 11, 1950

ASSUMING that magnetic moments of odd nuclei arise solely from the orbital and spin magnetic moments of the odd nucleon, one easily finds that the magnetic moment of an odd proton or odd neutron nucleus of spin I should have one of two values (the Schmidt limits) depending on the relative orientation of the orbital and spin angular moments.[1] Experimentally determined moments partially corroborate the above model in that almost without exception they lie between the Schmidt limits and

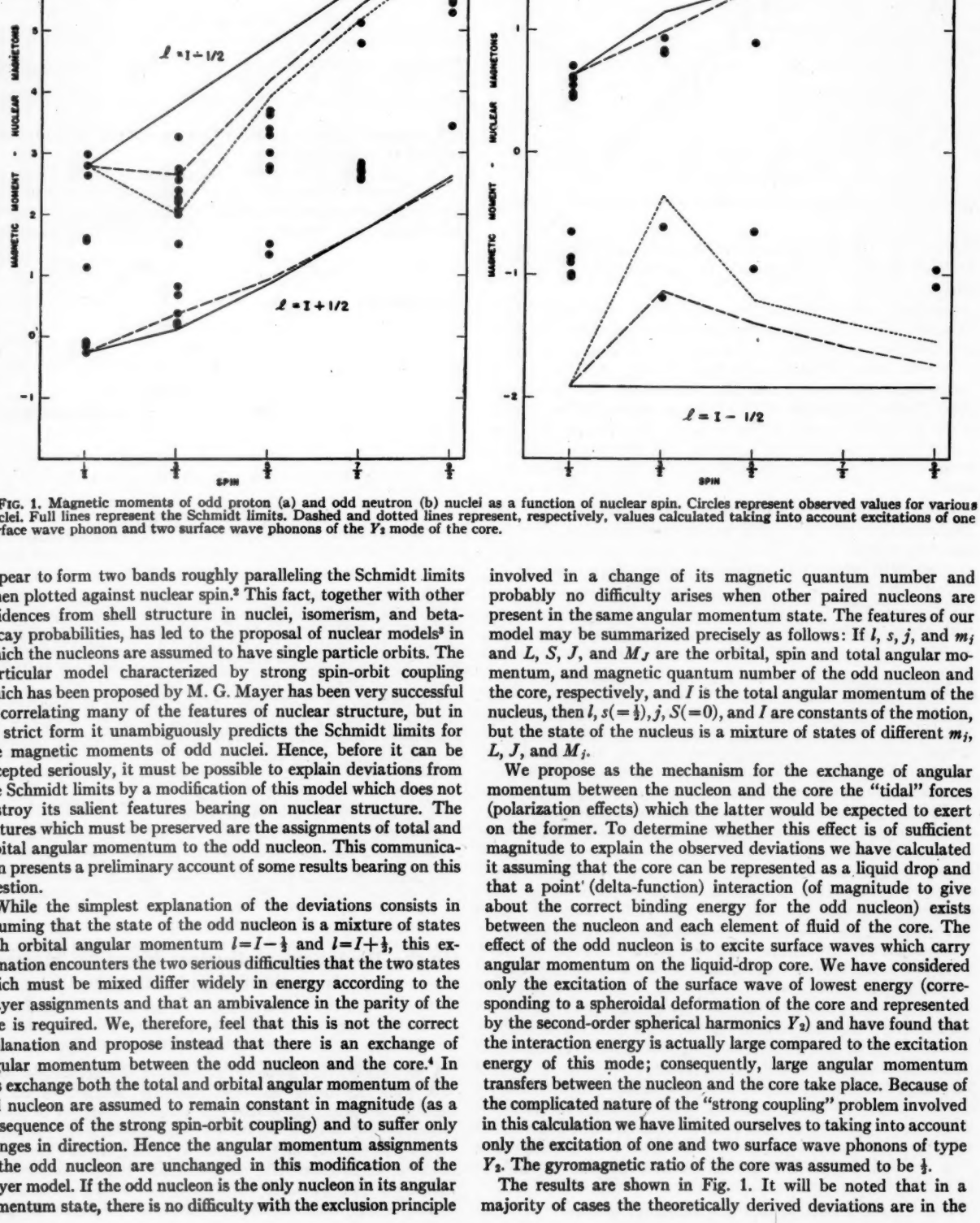

FIG. 1. Magnetic moments of odd proton (a) and odd neutron (b) nuclei as a function of nuclear spin. Circles represent observed values for various nuclei. Full lines represent the Schmidt limits. Dashed and dotted lines represent, respectively, values calculated taking into account excitations of one surface wave phonon and two surface wave phonons of the Y_2 mode of the core.

appear to form two bands roughly paralleling the Schmidt limits when plotted against nuclear spin.[2] This fact, together with other evidences from shell structure in nuclei, isomerism, and beta-decay probabilities, has led to the proposal of nuclear models[3] in which the nucleons are assumed to have single particle orbits. The particular model characterized by strong spin-orbit coupling which has been proposed by M. G. Mayer has been very successful in correlating many of the features of nuclear structure, but in its strict form it unambiguously predicts the Schmidt limits for the magnetic moments of odd nuclei. Hence, before it can be accepted seriously, it must be possible to explain deviations from the Schmidt limits by a modification of this model which does not destroy its salient features bearing on nuclear structure. The features which must be preserved are the assignments of total and orbital angular momentum to the odd nucleon. This communication presents a preliminary account of some results bearing on this question.

While the simplest explanation of the deviations consists in assuming that the state of the odd nucleon is a mixture of states with orbital angular momentum $l=I-\frac{1}{2}$ and $l=I+\frac{1}{2}$, this explanation encounters the two serious difficulties that the two states which must be mixed differ widely in energy according to the Mayer assignments and that an ambivalence in the parity of the core is required. We, therefore, feel that this is not the correct explanation and propose instead that there is an exchange of angular momentum between the odd nucleon and the core.[4] In this exchange both the total and orbital angular momentum of the odd nucleon are assumed to remain constant in magnitude (as a consequence of the strong spin-orbit coupling) and to suffer only changes in direction. Hence the angular momentum assignments to the odd nucleon are unchanged in this modification of the Mayer model. If the odd nucleon is the only nucleon in its angular momentum state, there is no difficulty with the exclusion principle involved in a change of its magnetic quantum number and probably no difficulty arises when other paired nucleons are present in the same angular momentum state. The features of our model may be summarized precisely as follows: If l, s, j, and m_j and L, S, J, and M_J are the orbital, spin and total angular momentum, and magnetic quantum number of the odd nucleon and the core, respectively, and I is the total angular momentum of the nucleus, then l, $s(=\frac{1}{2})$, j, $S(=0)$, and I are constants of the motion, but the state of the nucleus is a mixture of states of different m_j, L, J, and M_j.

We propose as the mechanism for the exchange of angular momentum between the nucleon and the core the "tidal" forces (polarization effects) which the latter would be expected to exert on the former. To determine whether this effect is of sufficient magnitude to explain the observed deviations we have calculated it assuming that the core can be represented as a liquid drop and that a point' (delta-function) interaction (of magnitude to give about the correct binding energy for the odd nucleon) exists between the nucleon and each element of fluid of the core. The effect of the odd nucleon is to excite surface waves which carry angular momentum on the liquid-drop core. We have considered only the excitation of the surface wave of lowest energy (corresponding to a spheroidal deformation of the core and represented by the second-order spherical harmonics Y_2) and have found that the interaction energy is actually large compared to the excitation energy of this mode; consequently, large angular momentum transfers between the nucleon and the core take place. Because of the complicated nature of the "strong coupling" problem involved in this calculation we have limited ourselves to taking into account only the excitation of one and two surface wave phonons of type Y_2. The gyromagnetic ratio of the core was assumed to be $\frac{1}{2}$.

The results are shown in Fig. 1. It will be noted that in a majority of cases the theoretically derived deviations are in the

right direction and of the proper order of magnitude to accord with the observed moments. The results are not sensitive to the strength of the interaction provided it is large compared with the core level spacing. It would be of interest to continue the calculations further by taking account of higher order excitation of the Y_2 modes as well as other modes which can be excited, but the labor involved appears prohibitive at present.

Before taking the proposed model too seriously, however, one should observe certain of its limitations. First, the model predicts that spin ½ nuclei have magnetic moments coinciding with the Schmidt limits; there are a considerable number of observed exceptions. Secondly, the model predicts (small) deviations in the wrong direction for nuclei with $1=I+\frac{1}{2}$ for $I>5/2$ resulting in additional discrepancies particularly for the compact group of odd proton nuclei with $I=7/2$. To just what extent and in what direction the model must be modified to explain these discrepancies is not clear.

* This work was supported in part by the AEC and by a grant-in-aid to one of the authors (L.L.F.) from the Scientific Research Society of America. A detailed report of the calculations will be published in the future.

[1] T. Schmidt, Zeits. f. Physik **106**, 358 (1937).

[2] H. H. Goldsmith and D. R. Inglis, *The Properties of Atomic Nuclei I* (Information and Publications Division, Brookhaven National Laboratory, Upton, New York, October 1, 1948).

[3] L. W. Nordheim, Phys. Rev. **75**, 1894 (1949); M. G. Mayer, Phys. Rev. **75**, 1969 (1949); **78**, 16 (1950); Haxel, Jensen, and Suess, Phys. Rev. **75**, 1766 (1949); E. Feenberg and K. C. Hammack, Phys. Rev. **75**, 1877 (1949); E. Feenberg, Phys. Rev. **77**, 771 (1950).

[4] In this connection, see J. Rainwater, Phys. Rev. **79**, 432 (1950).

Cascade Processes Recorded in an Emulsion Chamber Exposed in the Stratosphere

HERMAN YAGODA
Experimental Biology and Medicine Institute of the National Institutes of Health, Public Health Service, Bethesda, Maryland

September 22, 1950

A LUCITE frame supporting 5 disks of emulsion (5 cm diameter, cast between 1200 and 2400 microns thick) was exposed in the stratosphere at λ 55°N for 6.8 hr. at an average elevation of 90,000 ft. The disks developed uniformly and the tracks of singly charged particles at the minimum of ionization exhibited 23 grains per 100 microns.[1] Intensity measurements on the number of low energy mesons created in one of the 1200 micron disks have been made, a phenomenon particularly suited to the emulsion chamber owing to the greater probability of the ejected particles terminating their range within the thick recording medium. In a volume of 1.5 ml a total of 8 events were observed in which either Π^+- or Π^--mesons were created, the range of the ejected particles residing between 213 and 9150 microns. This corresponds to an observational intensity of 19±7 per cc per day, which is about 8 times greater than that observed in plates of comparable sensitivity coated 300 microns thick.[2]

One of these events exhibiting the termination and decay of a Π^+-meson (Fig. 1) is of particular interest as this track is the wide angle member of a 17-particle shower initiated by a relativistic alpha-particle. With the exception of track 10, which produces a small star, the remaining shower particles leave the disk after traversing 14 to 20 mm of emulsion[3] without appreciable increase in grain density. The emission of the slow Π^+ at a large angle with the shower axis provides further evidence for the Bethe mechanism of plural-multiple meson production.[4]

In this preliminary survey no attempt was made to count or identify all the incident heavy primaries, but a large number were observed to stop within the disk either by ionization or nuclear capture processes. An exceptionally heavy track (maximum core diameter 8 microns, total diameter including delta-rays measuring up to 30 microns) came to rest after traversing 15 mm of the disk. On the basis of a thin down length of 700 microns its charge[5] is estimated at 49±3. The track may possibly have been produced by a tin nucleus, as this element has the greatest astrophysical abundance of the elements with atomic numbers[6] between 45 and 55.

A cascade initiated by a heavy primary of charge 18.1±1.3 as estimated by delta-ray counts is described in Fig. 2. At point C the incident particle produces a nuclear disruption constituted of six shower particles $C_1 \cdots C_6$, and 15 evaporated nucleons, and a heavy residual fragment emerges co-linear with the primary. This residual fragment has a charge of 10.2±0.7, continues for a distance of 8.9 mm and while still moving at relativistic speed produces a narrow angle shower (tracks $N_1 \cdots N_6$) without any associated slow nucleons. In the second shower particles N_1 and N_3 have a recorded range of 7 mm at the points of emergence from the disk and both show a continuous grain density of 4×minimum, and hence are probably relativistic alpha-particles. Tracks N_2, N_4, N_5, and N_6 have minimum ionization grain density and are probably a mixture of fast mesons and protons.

The charge of the incident primary and that of the co-linear heavy fragment indicate that the particles are very probably argon and neon nuclei respectively. While the masses of the particular isotopes are not determinate, A^{36} and Ne^{20} are distinct possibilities. These isotopes have a particularly stable nuclear shell-structure, and if tracks ZC and CN were produced by them, the event suggests that in the interaction of heavy primaries with nuclei in the emulsion a preferential shearing may occur such that units constituted of integral multiples of the helium structure may emerge as sub-units of the interacting nuclei. This implies that the incident argon nucleus also originated from a more complex

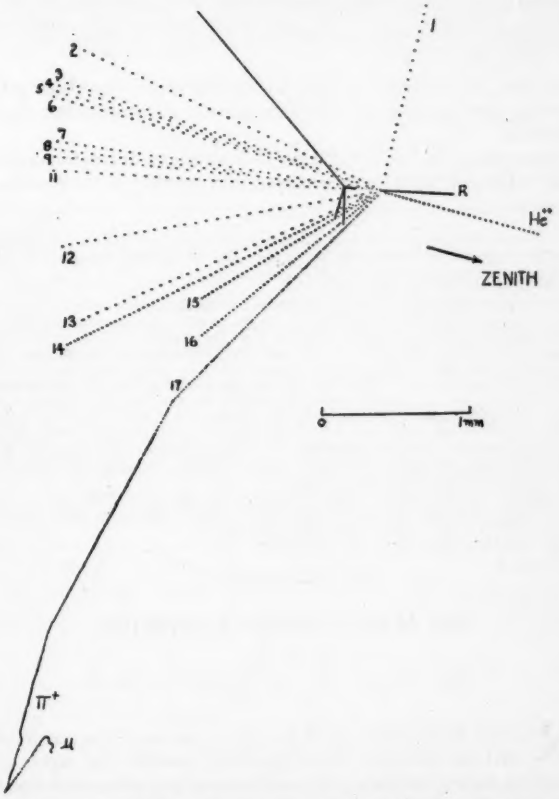

FIG. 1. Wide-angle shower initiated by a relativistic alpha-particle. This event is noteworthy in that only a single slow nucleon, track R, is associated with the star. Tracks 3–6 and 7–11 are produced by singly charged minimum ionization particles and constitute narrow angle showers of 0.05 and 0.04 radians, respectively. Particle 10 is captured in flight and forms a 4-pronged star 240 microns distant from the origin. Tracks 14, 15, and 16 have a grain density close to 4×minimum. Track 14 was followed for a distance of 14.2 mm until it escaped from the recording medium, without exhibiting an increase in grain count. Track 17 terminates in the emulsion with a range of 4800 microns, and is identified as a Π^+-meson by the decay track of the μ^+-meson which has a range of 520 microns (corrected for dip). The center of the shower occurred at a depth of 890 microns and the μ^+-particle terminated 10 microns below the upper surface of the 1200-micron disk.

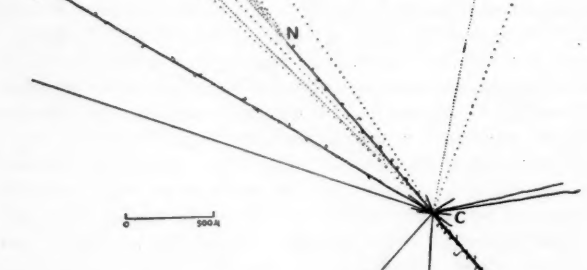

FIG. 2. Cascade processes initiated by a heavy primary. The event extends along a total length of 42.2 mm. In order to reproduce its more important features tracks ZC (23 mm), CN (8.9 mm), and NN_1 (10.3 mm) have been greatly shortened in the facsimile drawing. The scale applies only to the evaporated low energy nucleons. Among these, track G (range 2620 microns) is of particular interest because of its high charge $Z=5\pm1$ and the 28 micron electron track originating from its rest point. This corresponds to an energy of about 70 kev, a value consistent with the beta-decay spectrum of C^{14}.

structure, a concept not at variance with Spitzer's hypothesis concerning the acceleration and breakdown of interstellar dust particles.[7]

Opportunity is taken to thank the ONR and the aeronautical staff of General Mills for the exposure and recovery of the emulsion chamber.

[1] A brief description of the emulsion casting and development procedures has been presented, H. Yagoda, Phys. Rev. 79, 207 (1950). Working details will be presented in a manuscript in preparation.
[2] H. Yagoda (to be published).
[3] In assembling the chamber, the upper surface of each disk is infected at two fixed points with a polonium-coated needle. An autoradiograph of these points develops on the lower face of the adjoining disk. It is thus possible to follow dense tracks through the chamber by measuring the coordinates of the tracks with reference to these orientation marks. In order to allow for small differences in shrinkage incurred in the processing, a coordinate net is printed photographically on the surface of each disk prior to development. In this particular event the shower tracks escaped from the chamber owing to the small angle with the plane of the disk. Experiments are now in progress toward increasing the area of the chamber, and one disk measuring 9 cm in diameter and 1500 microns thick has been cast and dried successfully.
[4] M. M. Shapiro and H. Yagoda, Phys. Rev. 80, 283 (1950).
[5] Freier, Lofgren, Ney, and Oppenheimer, Phys. Rev. 74, 1820 (1948).
[6] H. Brown, Rev. Mod. Phys. 21, 628 (1949).
[7] L. Spitzer, Phys. Rev. 76, 583 (1949).

Are Mesons Complex Particles?

M. EL NADI
Faculty of Science, Fouad the I University, Cairo, Egypt
June 20, 1950

RECENTLY Fermi and Yang[1] have discussed the possibility that the meson is not an elementary particle, but rather is a complex entity, consisting of a nucleon and an anti-nucleon bound together. A similar suggestion was put forward a few years ago by de Broglie[2] for particles of spin one, in general. De Broglie's theory was developed in a direction different from that of Fermi and Yang. The assumption that the meson is complex in nature seems attractive as it presents a physical picture explaining the integral nature of the spin and the statistics obeyed by the mesons.

As it is now generally admitted that the π-mesons are responsible for the nuclear forces and have the spin value one while the μ-mesons have the spin value $\frac{1}{2}$, we shall assume that the π-meson is a complex particle, composed of two μ-mesons, or rather of a charged μ-meson and a neutral anti-μ-meson bound together by strong attractive force. If π^+, π^-, and π^0 refer to the positively and negatively charged and neutral π-mesons, with similar notations for the μ-mesons, we represent the constituent particles for the π-mesons as follows:

$$\pi^+=\mu^++\text{anti-}\mu^0;\quad \pi^-=\mu^-+\text{anti-}\mu^0;\quad \pi^0=\mu^0+\text{anti-}\mu^0.$$

Since $m_\mu=(212\pm4)m_e$, and $m_\pi=(286\pm6)m_e$, we shall assume that the difference between twice the mass of the μ-meson and the π-meson is the mass equivalent of the binding energy of the π-meson. Taking for the binding potential, V, the step function:

$$V(r)=0 \text{ for } r>\hbar/m_\mu c,$$
$$V(r)=V_0=\text{constant, for } r<\hbar/m_\mu c,$$

and for the lowest eigenvalue $E=m_\pi c^2$, we have determined the depth V_0 of the assumed potential box. We found the following two solutions for V_0:

$$V_0=5.87m_\pi c^2=839.4 \text{ Mev} \quad \text{and} \quad V=3.03m_\pi c^2=433.3 \text{ Mev}.$$

The corresponding normalized solutions will be generally similar to those given by Fermi and Yang. The geometrical size of the meson in the present case will be of the order of $\hbar/m_\mu c$; i.e., the Compton wave-length for the μ-meson.

As regards the interpretations of the interactions between mesons and other particles we propose the following schemes:

(1) In collisions involving π^--mesons with different nuclei, the charged μ^--mesons (constituting the π^--meson) might be forced to occupy the hole representing the neutral anti-μ^0-meson, and thus the π^--meson will be annihilated, giving its energy and charge to the colliding nucleus. This might cause an explosion with the formation of a star.

(2) In certain cases, collisions could cause the disintegration of the π-meson itself, into its two constitutents. Thus we get:

$$\pi^+\rightarrow\mu^++\text{anti-}\mu^0 \text{ (a neutretto)},$$
$$\pi^-\rightarrow\mu^-+\text{anti-}\mu^0 \text{ (a neutretto)}.$$

(3) A free μ^0-meson, when colliding with a π-meson, could occupy the hole representing the anti-μ^0-meson and thus the charged μ-meson will be set free:

$$\mu^0+\pi^+\rightarrow\mu^++\text{two photons}.$$
$$\mu^0+\pi^-\rightarrow\mu^-+\text{two photons}.$$

These high energy gamma-photons will be of the type observed by Moyer, York, and Bjorklund.[3]

These photons could also result from the (self-) annihilation of the π^0-mesons caused by collisions with other particles.

(4) On the other hand, a free charged μ^--meson could be annihilated on collision with μ^+ or μ^0, giving rise to:

$$\mu^-+\mu^+\longrightarrow\text{two photons},$$
$$\mu^-+\mu^0\text{----an electron+a neutrino}.$$

This last reaction represents the decay of the μ-meson.

[1] E. Fermi and C. N. Yang, Phys. Rev. 76, 1739 (1949).
[2] L. de Broglie, *Une Nouvelle Theorie de la Lumiere* (Hermann & Cie, Paris, 1940); *La Theorie du Noyau* (Hermann & Cie, Paris, 1945).
[3] Moyer, York, and Bjorklund, Phys. Rev. 75, 1470 (1949).

On the Probability of Asymmetric and Symmetric Fission

T. YASAKI AND O. MIYATAKE
Physics Institute, Mathematics Institute, Yamanashi University, Kofu City, Japan
August 24, 1950

THIS paper explains the experimental facts that the symmetric fission becomes predominant compared to the asymmetric one, according as the velocity of the incident neutron increases, by the aid of assumptions about the structure of heavy nuclei. In this paper, we use the notation $\sigma(E)$, $T(E)$, and $R(E)$ as the cross section of a nucleon, the probability of free transmission through the nucleus, and the ratio of the symmetric to

that of the asymmetric fission yield respectively, when the energy of the incident neutron is E(Mev). The experimental results are:[1-4]

$$R(\text{thermal})\approx 0,\quad R(17)\approx 0.1,\quad R(45)\approx 0.8,\quad R(90)\approx 3.$$

According to the shell model of nuclei, the particles belonging to a smaller magic number spend relatively more time near the center of the nucleus than those belonging to a larger magic number. This circumstance is warranted by the oscillator potential[5] or by the potential which represents the surface tension.[6] We assume that the shells of magic numbers 2, 8, 20, 50, 82, and 126 are arranged concentrically from the center of the nucleus to its edge. As for proton density, we prefer Wigner's idea,[7] according to which the proton density is 17 percent higher than that of the central part. For simplicity, instead of the proton density gradually increasing, we assume that 27 protons are attached uniformly to the 50-shell (the neutron shell of the magic number 50). The radius of the core consisting of the neutron 50-shell and 27 protons is about 70 percent those of the nuclei U^{235}, Th^{232}, and Pu^{239}. The remaining protons are assumed to be distributed uniformly in the outer part of the nucleus.[8] These protons are assumed to have the same energy as those of the neutrons belonging to the same shell.

If we denote the energy difference between the n- and n'-shell as $E(n'-n)$, we obtain[9]

$$E(126\text{–}82)=5.8,\quad E(82\text{–}50)=5.2,\quad E(126\text{–}50)=11.1,$$
$$E(50\text{–}20)=8.6,\quad E(82\text{–}20)=13.8,\quad E(126-20)=19.6$$

in Mev. A shell is considered to become degenerate when one of its members is lost.[10] When a thermal neutron gets into the nucleus, owing to the binding energy of 6 Mev, the 82- and 126-shell may soon be degenerate, but the 50-shell remains undegenerate, and accordingly the fission is asymmetric. When the incident particle is of high energy,[11] it runs on straight and the particle struck by it, partaking of 25 Mev runs from this path perpendicularly. When one of these branches and trunk runs against a member of the core, the latter takes the energy sufficient to cause it to run away from the core, since $E(126\text{–}50)=11.1$, and the fission is nearly symmetric. To get the completely symmetric fission, the 20-shell must be destroyed, but we neglect this point.

We use the values $\sigma(100)=0.029$, $\sigma(50)=0.057$ in barns,[11] and $\sigma(25)=0.043$, which is smaller than that expected from the former two values, because the nucleus may be considered as a Fermi gas at 0°. Then we obtain

$$R(25)=0.15,\quad R(50)=0.54,\quad R(100)=4.6$$
and
$$T(25)=0.048,\quad R(50)=0.027,\quad T(100)=0.099.$$

From the above considerations, the following experimental facts will be clarified. The position of the foot of the yield curve is independent of the energy of the incident particle. This corresponds to the case in which the 50-shell remains undestroyed. When the 50-shell is destroyed but the 20-shell remains undestroyed, the two peaks of the yield curve approach each other. The fission becomes completely symmetric when the 20-shell is destroyed.

As a justification for our model we note that when the fission of U^{235} by the thermal neutron occurs, the proton density of the light fragment is computed to be 0.41, according to our model.[8] On the other hand, one of the two peaks of the experimental yield curve[1] is at Y^{95} whose proton density is also 0.41.

[1] Plutonium Project Report, Rev. Mod. Phys. **18**, 513 (1946).
[2] Nishina, Yasaki, Kimura, and Ikawa, Nature **146**, 24 (1940); Phys. Rev. **58**, 660 (1940); **59**, 323 (1941); **59**, 677 (1941); T. Yasaki, Sci. Pap. I. P. C. R. **37**, 457 (1940). A private answer concerning the yield was given to Professor G. T. Seaborg's question at the symposium of the University of California, when Yasaki visited there in September of 1940.
[3] E. Segrè and G. T. Seaborg, Phys. Rev. **59**, 212 (1941).
[4] J. Jungerman and S. C. Wright, Phys. Rev. **76**, 1112 (1949).
[5] H. A. Bethe and R. F. Bacher, Rev. Mod. Phys. **8**, 172 (1936).
[6] E. Fermi, *Nuclear Physics* (University of Chicago Press, Chicago, 1949), p. 169.
[7] E. Wigner, University of Pennsylvania Bicentennial Conference (1941).
[8] T. Yasaki and O. Miyatake, Phys. Rev. **79**, 740 (1950).
[9] E. Feenberg and K. C. Hammack, Phys. Rev. **75**, 1877 (1949).
[10] L. W. Nordheim, Phys. Rev. **75**, 1894 (1949).
[11] R. Serber, Phys. Rev. **72**, 1114 (1947).

On the General Motion of Matter at the Cosmological Scale

ANTONIO GIÃO
Lisbon, Portugal
December 1, 1949

WE have shown elsewhere[1] that the equations of Gauss of a hypersurface, which play a fundamental part in our unified field theory,[2] when combined with the equations of the gravitational field written as below [Eqs. (3)], lead to the conclusion that the cosmological constant λ_0 is necessarily positive and that space-time must be considered as a slightly deformed De Sitter hypersphere. Since the De Sitter-Lanczos ds^2 has the form[3]

$$ds^2=(dx^4)^2-P_S^2(x^4)\{(dx^1)^2+\sin^2x^1[(dx^2)^2+\sin^2x^2(dx^3)^2]\},\quad (1)$$

with $P_S=P_S^0\cosh(x^4/P_S^0)$, it is natural to consider a space-time such that

$$ds^2=(dx^4)^2-P^2(x^1,x^2,x^3,x^4)\times\{(dx^1)^2+\sin^2x^1[(dx^2)^2+\sin^2x^2(dx^3)^2]\},\quad (2)$$

the difference $P(x^1,x^2,x^3,x^4)-P_S(x^4)$ being a small quantity. The components of the energy-momentum density which correspond to this deformation of the empty De Sitter hypersphere can be deduced from the gravitational Einstein equations

$$R_k^i-\tfrac{1}{2}(R+\lambda_0)g_k^i=-(8\pi K/c^2)T_k^i,\quad (3)$$

where K is the Newtonian constant of gravitation. Let $\mathbf{T}_4$ denote the contravariant space vector of components (T_4^1, T_4^2, T_4^3), ∇ the space gradient operator, and Δ_s the space Laplacian operator. From Dingle's formulas[4] applied to (2) we then derive

$$(4\pi K/c^2)\mathbf{T}_4=(1/P^2)[P\nabla(\partial P/\partial x^4)-(\partial P/\partial x^4)\nabla P],\quad (4)$$

$$(8\pi K/c^2)T_4^4=\tfrac{1}{2}\lambda_0+(3/P^2)[(\partial P/\partial x^4)^2+1]-(2/P)\Delta_s P+(1/P^2)(\nabla P)^2-(4/P^3)[2\cot x^1(\partial P/\partial x^1)+(\cot x^2/\sin^2x^1)\partial P/\partial x^2].\quad (5)$$

The velocity $V^i\equiv cdx^i/ds$ of the general motion of matter at the cosmological scale which corresponds to these T_4^i $(i=1, 2, 3, 4)$ is given by $\mu V^iV_4\simeq c^2T_4^i$, μ denoting the density of rest mass. Hence: $V^j=T_4^jV_4/T_4^4$ (for $j=1, 2, 3$) and $\mu=c^2T_4^4/V_4^2$, since (2) gives $V_4=V^4$. The cosmological velocity of matter is small compared with c and we can write $V_4\simeq c$; consequently $\mathbf{V}=c\mathbf{T}_4/T_4^4$ and $\mu=T_4^4$. From (4) we then derive

$$\operatorname{curl}\mathbf{V}=[c^2/4\pi K(T_4^4)^2P^2][P\nabla(\partial P/\partial x^4)-(\partial P/\partial x^4)\nabla P]\times\nabla T_4^4=\mathbf{V}\times\nabla(\ln\mu).\quad (6)$$

We now consider a sub-class of small deformations of the De Sitter space-time by supposing that the matter of the universes with a ds^2 given by (2) corresponds exclusively to the difference between the expansion of these universes and the expansion of the De Sitter empty space-time. In other words, we are supposing now that the density of matter at an arbitrary point $A(x^1,x^2,x^3,x^4)$ of (2), where the radius has the value P, is the same as in the spatially isotropic universe of the same radius P. According to (5) this assumption is expressed by

$$(8\pi K/c^2)T_4^4=\tfrac{1}{2}\lambda_0+(3/P^2)[(\partial P/\partial x^4)^2+1].\quad (7)$$

Equation (6) then becomes

$$\operatorname{curl}\mathbf{V}=(3c^5/16\pi^2K^2\mu^2P^4)[\nabla(\partial P/\partial x^4)\times\nabla P].\quad (8)$$

From (4) and (8) we deduce: (1) that the matter corresponding to this sub-class of (2) is at rest (in the frame x^i) when $\nabla(\partial P/\partial x^4)=(\partial\ln P/\partial x^4)\nabla P$; (2) that the necessary and sufficient condition for the motion to be irrotational is expressed by $\nabla(\partial P/\partial x^4)=a\nabla P$, a denoting an arbitrary scalar. As these conditions are fulfilled only with very simple $P(x^i)$ functions, we can safely conclude that almost all deformations of the De Sitter hypersphere are accompanied by matter in a state of rotational motion. This result seems to be the relativistic explanation of the fundamental fact that all massive bodies (galaxies) are in a state of translatory and rotational motion. When the cosmological or quasi-cosmological

magnitudes $P \simeq 10^{28}$ cm, $\mu \simeq 10^{-27}$ g/cm³ are introduced in (8), we get Magn.$|\text{curl}\mathbf{V}| = 10^{7} \cdot$ Magn.$|\nabla(\partial P/\partial x^4) \times \nabla P|$. In order to derive a rough estimate of this magnitude we remark first that the expansive phase begun, as generally assumed,[5] 10^9 to 10^{10} years ago. Let us suppose that the temporal changes of ∇P for this period have the same order of magnitude as ∇P itself. From previous results[6] on the variations of the mean curvature of space-time we derive Magn.$\nabla P = 10^{-1}$ to 10^{-2}. We then get Magn.$|\text{curl}\mathbf{V}| = 10^{-12}$ to 10^{-14}/sec., which is the order of magnitude of the angular velocity of the galaxies.[7]

An important property of the cosmological motions analyzed here is that they are not caused by Newtonian gravitation, since $\partial g_{44}/\partial x^i = 0$ everywhere in the frame x^i of (2). According to (2) these motions arise from the non-Newtonian forces expressed by the derivatives $\partial \lg_{ij}/\partial x^k$ ($j = 1, 2, 3$; $k = 1, 2, 3, 4$) in the equations of the geodesic world lines. This result shows that the general motions of the galaxies are not necessarily controlled by Newtonian gravitation, which thus seems to be of decisive importance only for motions at a much smaller scale than the cosmological one.

[1] A. Gião, Comptes rendus **228**, 812 (1949).
[2] A. Gião, Portugaliae Physica **2**, 1–98 (1946); Portugaliae Mathematica **5**, 145–192 (1946); **6**, 67–114 (1947); **7**, 1–44 (1948); Phys. Rev. **76**, 764 (1949); J. de phys. et rad. **10**, 240–249 (1949).
[3] C. Lanczos, Physik. Zeits. **23**, 539 (1922).
[4] R. C. Tolman, *Relativity, Thermodynamics and Cosmology* (Oxford University Press, New York, 1934), pp. 253–257.
[5] A. Einstein, *The Meaning of Relativity* (Princeton University Press, Princeton, 1946), p. 120; McVittie, *Cosmological Theory*; R. C. Tolman, Rev. Mod. Phys. **21**, 374–378 (1949).
[6] A. Gião, Comptes Rendus **229**, 981 (1949).
[7] Bosler, *Astrophysique* (Hermann & Cie, Paris), p. 669; E. Hubble, Astrophys. J. **79**, 74 (1934); Russell, Dugan, and Stewart, Astronomy (II), pp. 943–945.

The Thermal Neutron Diffusion Length of Paraffin

C. W. TITTLE
North Texas State College, Denton, Texas
July 21, 1950

FOR the comparison of the theoretical and the experimental results concerning thermal neutron diffusion in paraffin, a precise value of the thermal neutron diffusion length L is frequently required. Such a value can be derived from some recently published data on the thermal neutron distribution in a paraffin slab, using pile neutrons.[1] The result of a least-squares analysis of this data is:

$$L(\text{paraffin}) = 2.42 \pm 0.04 \text{ cm},$$

the indicated error being statistical probable error. This compares with the older value[2] of $L = 2.1$ cm. It is now known that diffusion theory does not hold near a boundary,[3] and if the boundary point of the older determination is omitted, the two values are consistent.

The transport mean free path for thermal neutrons in paraffin can be derived from the diffusion length. From diffusion theory,

$$\lambda_{tr} = 3L^2/\lambda_a,$$

where λ_a is the absorption mean free path. If the absorption cross sections[4] of hydrogen and carbon at 0.025 ev are respectively 0.313 ± 0.013 and 0.0045 barn and the density of paraffin is 0.895 g/cm³, $\lambda_a = 44.9 \pm 1.9$ cm at the effective energy for absorption,[5] $(4/\pi)kT = 0.032$ ev. Then

$$\lambda_{tr}(\text{paraffin}) = 0.395 \pm 0.021 \text{ cm}.$$

These figures compare with the following for water at 20°C:

$$L(\text{water}) = 2.76 \text{ cm},^{6}$$
$$\lambda_{tr}(\text{water}) = 0.425 \pm 0.020 \text{ cm}.$$

The probable error of L(water) was assumed to be one percent.

[1] B. S. Smith and J. S. Tait, Nature **165**, 197 (1950).
[2] E. Amaldi and E. Fermi, Phys. Rev. **50**, 899 (1936).
[3] Auger, Munn, and Pontecorvo, Can. J. Research **25A**, 143 (1947).
[4] M. Ross and J. S. Story, *Reports on Progress in Physics* (Physical Society, 1948–49), Vol. XII, pp. 291–304.
[5] A. M. Weinberg, MDDC-1150, unpublished. A Maxwell-Boltzmann neutron speed distribution is assumed with effective temperature of 20°C.
[6] E. Fermi, AECD-2644, unpublished, p. 74.

Depression of the Thermal Neutron Density by a Detecting Foil*

C. W. TITTLE
North Texas State College, Denton, Texas
July 21, 1950

INTRODUCTION of a small absorber into a medium in which thermal neutrons are diffusing causes a depression of the neutron density in the vicinity of the absorber. This effect must often be known quantitatively for intercomparison of data on different media or with different detectors. The purpose of this paper is to describe a procedure whereby Bothe's[1] formulas for the factor f by which the neutron density is depressed by a disk-shaped foil can be used with an accuracy of two percent or better as determined by experiment. It has been found that if one uses the transport mean free path (λ_{tr}) where Bothe used the scattering mean free path, and if one uses Bothe's formula for a spherical shell of radius R without modification as applying to a disk of radius R, satisfactory agreement with experiment is obtained, although the uncertainties in the constants used in the theory introduce an error of the order of two percent in unfavorable cases, and the experiments are probably good to about one or two percent. Table I summarizes the comparison of theory with experiment. The experiments in the first six cases were performed by Bothe[1] with Dy_2O_3 detectors in paraffin, and in the last by Dacey, Paine, and Goodman[2] with In detectors in water.

TABLE I. Depression factor of a disk-shaped foil.

Foil No.	Foil radius	Foil thickness	α	Depression factor, f Expt.	Calc., Eq. (1)	Calc., Eq. (2)
1	1.40 cm	71 mg/cm²	0.339	0.72	0.71	0.71
2	1.40	36	0.197	0.82	0.81	0.81
3	1.40	6	0.038	0.98	0.96	0.96
4	0.70	69	0.332	0.84	0.85	0.83
5	0.70	35	0.193	0.91	0.91	0.90
6	0.70	6	0.038	0.96	0.98	0.98
7	1.51	58.8	0.0944	0.90±0.01	0.90	0.90

The effective energy of the thermal neutrons has been taken to be 0.032 ev for the purpose of determining the absorption cross sections to be used in the theory.[3] The absorption cross sections of Dy and In were taken to be 1040 and 170 barns, respectively.[4] It was assumed that the scattering cross section of Dy is negligible, and that that for In is 2 barns.[5]

The diffusion length L and transport mean free path λ_{tr} in the media have been taken to be:[6]

$$L(\text{paraffin}) = 2.42 \pm 0.04 \text{ cm},^{7} \quad \lambda_{tr}(\text{paraffin}) = 0.395 \pm 0.021 \text{ cm},^{8}$$
$$L(\text{water}) = 2.76 \pm 0.03 \text{ cm}, \quad \lambda_{tr}(\text{water}) = 0.425 \pm 0.020 \text{ cm}.$$

For purposes of reference, Bothe's sphere formulas are given here.

$$\frac{1}{f} = 1 + \frac{\alpha}{2}\left[\frac{3R}{2\lambda_{tr}}\frac{L}{R+L} - 1\right] \quad \text{if } R \gg \lambda_{tr} \cdots, \tag{1}$$

$$\frac{1}{f} = 1 + \frac{0.34\alpha R}{\lambda_{tr}} \quad \text{if } R \ll \lambda_{tr} \cdots. \tag{2}$$

In these equations the symbols have the meanings already ascribed, and α is the average probability that a neutron will be absorbed upon traversing the foil once, assuming an isotropic flux. Bothe gives the following expression for α:

$$\alpha = 1 - e^{-\mu d}(1 - \mu d) + \mu^2 d^2 Ei(-\mu d),$$

where μ is the neutron mass absorption coefficient of the foil material ($\mu = N_0\sigma_a/M$; N_0 = Avogadro's number, σ_a = absorption cross section per molecule, M = molecular weight), and d is the foil thickness expressed in g/cm². The exponential integral function $Ei(-x)$ is tabulated by Jahnke and Emde.[9]

In all the instances given, $R > \lambda_{tr}$. It is remarkable that both formulas give about the same result. It is not known whether this is fortuitous in the case of Eq. (2). It can be said, however,

that Eq. (1) is likely to break down when the first term in the bracket becomes 2 or smaller, and that Eq. (2) should not be used in media where absorption is much higher than it is in water, since Eq. (2) does not take absorption in the medium into account.

There appears to be an inversion of the experimental values for foils No. 3 and 6. Cases 1, 2, 4, 5, and 7 furnish the most severe tests of the formulas, however.

* This work was done with the Nuclear Shielding Project, Massachusetts Institute of Technology, Cambridge, Massachusetts, which is supported by a joint program of the ONR and the Bureau of Ships.

[1] W. Bothe, Zeits. f. Physik **120**, 437 (1943).

[2] Dacey, Paine, and Goodman, Mass. Inst. of Tech., Lab. for Nuclear Science and Engineering Tech. Report No. 23, October 20, 1949. The data have been reanalyzed.

[3] A. M. Weinberg, MDDC-1150, unpublished. The procedure applies to a Maxwellian neutron distribution in a weakly absorbing medium where the absorption cross section is proportional to $1/v$ (v=neutron speed).

[4] Goldsmith, Ibser, and Feld, *Neutron Cross Sections of the Elements* (Addison-Wesley Press, Cambridge, 1947).

[5] H. R. Kroeger, Nucleonics **5**, 51 (1949).

[6] C. W. Tittle, Phys. Rev. **80**, 758 (1950).

[7] Based on data by B. S. Smith and J. S. Tait, Nature **165**, 197 (1950). The paraffin density is not known but should introduce only negligible error.

[8] Based on a paraffin density of 0.895 g/cm³ (W. Bothe, personal communication).

[9] E. Jahnke and F. Emde, *Tables of Functions* (Dover Publishing Company, New York, or Teubner, Leipzig).

Scintillations Produced by Cosmic Rays*

C. G. MONTGOMERY AND D. D. MONTGOMERY
Sloane Physics Laboratory, Yale University, New Haven, Connecticut
September 22, 1950

THE recent interest in the use of scintillations for the detection of gamma-rays has led us to investigate the possibility of their application to cosmic-ray investigations. During the summer of 1949 some simple experiments were performed at Climax, Colorado, 3510 meters altitude, to detect cosmic-ray stars formed within the phosphor. To obtain a large area, a layer about 0.5-cm thick of the phosphor was placed in a glass dish 11 cm in diameter which was placed about 8 cm above the cathode of a 931A photomultiplier tube. The whole arrangement was placed in an insulated box with solid CO_2 for cooling. Three phosphors gave positive results: (1) commercial naphthalene flakes, (2) highly purified anthracene flakes, and (3) commercial naphthalene recrystallized from a CS_2 solution so as to form a solid compact mass of small crystals. The pulses from the photo-multiplier were amplified, presented on the screen of a Dumont type 248 oscilloscope and photographed. The background counts were taken by inserting a light shield between the dish of phosphor and the photo-multiplier. Without the shield the counting rate was between two and three times the background rate and approximately the same for each phosphor. The distribution in pulse sizes could be represented by a power law with an exponent of 3.2 in good agreement with the value obtained for stars measured in ionization chambers.[1] Negative results were obtained for a polystyrene phosphor and for a thin layer of Patterson type d phosphor covered by plates of various materials. This simple experimental arrangement suffers from the high background count and from the difficulty of obtaining an accurate measurement of the effective volume of the phosphor.

In order to reduce the background and to test the relative efficiencies of various phosphors, we have used two 1P21 photomultiplier tubes in coincidence with a single phosphor. To obtain a known energy loss in the crystal single cosmic-ray particles passing through the phosphor were selected by Geiger counters above and below the phosphor.[2] The pulse-size distribution for quadruple coincidences was measured for various phosphors. If the integral bias curves (bias changed equally in both channels) are plotted on double logarithmic paper, it is possible to make all curves coincide by a shift along the bias axis (multiplication of the bias voltage by a constant). In this way relative pulse sizes for a number of phosphors were determined and are given in Table I. A naphthalene crystal was chosen arbitrarily as the standard and assigned the value 100. The figures are probably accurate to within 10 percent. The solutions listed were contained in a thin Pyrex vessel and were saturated at room temperature.

TABLE I. Relative pulse sizes from various phosphors.

Phosphor	Pulse size
Single crystals	
Naphthalene	100
Anthracene	250
Calcium fluoride	40
Solutions	
Anthracene in benzene	10
Naphthalene in benzene	15
Terphenyl in xylene	75
Terphenyl in xylene plus 40 percent mineral oil	85
Stilbene in xylene plus 40 percent mineral oil	8
Anthracene in xylene plus 40 percent mineral oil	15

It was also found that relative pulse sizes could be determined by a similar procedure using a gamma-ray source and double coincidences between the photo-multiplier tubes with no Geiger counters. The values so obtained agreed well with those determined from cosmic rays.

In all cases the pulse-size distribution at large sizes appeared to be exponential, as would be expected if the distribution of size h of the pulses from a single photo-electron is given by $h^2dhe^{-h/\rho}/2\rho^3$ as assumed by Seitz and Mueller.[3]

* Assisted by the joint program of the ONR and AEC.

[1] C. G. Montgomery and D. D. Montgomery, Phys. Rev. **76**, 1482 (1949).

[2] A somewhat similar arrangement has been described by G. T. Reynolds, Proc. Echo Lake Cosmic Ray Symposium (June, 1949).

[3] F. Seitz and D. W. Mueller, Phys. Rev. **78**, 608 (1950).

Theory of Magnetic Properties of Anisotropic Permanent Magnet Alloys

K. HOSELITZ AND M. MCCAIG
Permanent Magnet Association, Central Research Laboratory, Sheffield, England
May 1, 1950

IN a recent letter Kittel, Nesbitt, and Shockley[1] suggest an explanation of the magnetic properties of Alnico V, based on the assumption that thermal nucleation in the form of plate-like aggregates, of volume 10^{-19} cm³, occurs during cooling between 900°3 and 800°C. If the magnetization of the nuclei differs from that of the matrix by 500 c.g.s. units, the presence of a magnetic field, H_i, influences the relative number of nuclei in planes parallel and perpendicular to the field direction. Plates in planes perpendicular to H_i require an additional energy of 1.5×10^{-13} erg, if they are magnetized in the field direction, on account of their high demagnetizing factor.

If the plates have the higher intensity of magnetization, the estimation of their demagnetization energy is irrelevant, since the plates, whatever their position, will be spontaneously magnetized in their plane, and if this is perpendicular to H_i, the maximum energy of interaction becomes $J_s\times v\times H_i=5\times10^{-14}$ erg.[2] If the energies of nuclei in different planes differ by that amount, the "suppression factor" is $e^{-\frac{1}{2}}$ and not e^{-1} as estimated by Kittel. It is believed that a factor of $e^{-\frac{1}{2}}$ could hardly lead to the strong anisotropy observed.

It may further be pointed out that our observations[3] on Alcomax II, which is an alloy very similar to Alnico V, are quite inconsistent with the kind of anisotropy to be expected from a system of oriented plates of magnetic material. In a properly heat-treated sample practically 100 percent of the magnetic constituent must consist of domains having one preferred axis of magnetization, but in the assembly of magnetic plates each domain would be expected to have two almost equivalent preferred directions. A system of oriented magnetic plates might explain some anisotropic magnetic properties, but it would not be of the degree observed in practice.

The alternative possibility of the plate-like precipitates being less magnetic than the matrix, avoids all these objections. The observed anisotropy and coercive force can be accounted for easily by a model in which the material consists of rod-shaped domains divided by plates. The above mechanism is not, however, the only possible one for producing the required heterogeneity.

One of us[4] has put forward an alternative theory in which the anisotropy is attributed to the relief of magnetostrictive stresses by gliding during the process of cooling in a magnetic field. According to this theory it is possible that the magnetic field influences embryos well below the critical size for stable nuclei. The presence of fully developed nuclei is improbable since most of the temperature range in which the field is effective lies in a single phase field.

Further work will be required to decide whether either or both of these processes occur.

[1] Kittel, Nesbitt, and Shockley, Phys. Rev. **77**, 839 (1950).
[2] At about 800°C, if there are two phases with a $\Delta J_s = 500$ c.g.s. units, one phase must be practically non-magnetic.
[3] K. Hoselitz and M. McCaig, Nature **164**, 581 (1949).
[4] M. McCaig, Nature **165**, 969 (1950).

Susceptibility and Magnetic Anisotropy of Indium Single Crystals

J. VERHAEGHE, G. VANDERMEERSSCHE,* AND G. LE COMPTE
Natuurkundig Laboratorium, Universiteit Gent, Gent, Belgium
September 25, 1950

IT is well known that small quantities of impurities have a great influence on the magnetic properties of metallic single crystals. Some interesting measurements have been made in this respect by Goetz and Focke,[1] Hart,[2] Rao and Sriraman,[3] Rao and Narayanaswami,[4] who investigated, respectively, single crystals of Bi, Sb, Cd, and Tl. For the same purpose we have made susceptibility measurements on indium single crystals.

Since no data of susceptibility of In have been published except those of Honda and Owen,[5] we want to give the results of our measurements on the susceptibility and anisotropy of that element.

The In, obtained from a Belgian firm, being impure, was purified several times by an electrolytic process. From the material obtained we made samples in the form of thin cylinders by melting in vacuum and molding in pure graphite. Following the Gouy method we determined the magnetic susceptibility by use of a microbalance. Since even after such a procedure the rods showed slight paramagnetism, we had to reheat them several times in their molds, bringing the temperature slightly below the melting point and etching their surfaces after each process. Thus we were able to remove almost all remaining impurities and we obtained reproducible results for the diamagnetic susceptibility.

A difficulty arose from the fact that we were unable to find the crystal axes by splitting the single crystals, owing to the softness of the metal, even after cooling in liquid air.

If ϕ represents the angle between the principal crystalline axis and the axis of the rod, θ the angle between the field and the vertical plane going through the principal crystalline axis, then the expression:

$$K_H = (K_{\parallel} \sin^2\phi + K_{\perp} \cos^2\phi) \cos^2\theta + K_{\perp} \sin^2\theta$$

enables us to find the value of $K_{\perp}$ by measurements on different samples. We also made polycrystalline samples and by measurement of their susceptibility, which is the same in all directions, we obtained $K_{\parallel}$ by using the formula:

$$K_H = \tfrac{1}{3}(2K_{\perp} + K_{\parallel}).$$

Our results are as follows:

Indium single crystals, density:	7.3082.
Polycrystalline material, density:	7.2985.
Principal susceptibilities:	$K_{\parallel} = -0.886 \times 10^{-6}$,
	$K_{\perp} = -0.398 \times 10^{-6}$.
Magnetic anisotropy:	$K_{\parallel} - K_{\perp} = -0.488 \times 10^{-6}$.

* Now at Rutgers University, New Brunswick, New Jersey.
[1] Goetz and Focke, Phys. Rev. **45**, 170 (1934).
[2] Hart, Proc. Roy. Soc. London **A156**, 687 (1936).
[3] Rao and Sriraman, Proc. Roy. Soc. London **A166**, 325 (1938).
[4] Rao and Narayanaswami, Phil. Mag. **26**, 1018 (1938).
[5] Honda and Owen, Ann. Physik **32**, 1027 (1910); **37**, 657 (1912).

The Ca^{45} Beta-Distribution Obtained in a Split Crystal Scintillation Spectrometer*

B. H. KETELLE
Chemistry Division, Oak Ridge National Laboratory, Oak Ridge, Tennessee
September 29, 1950

WITHIN the last year scintillation spectrometry has been improved to the point where it is possible to determine beta-distribution end points with fair precision, and when the maximum energy of the distribution is great, the high energy portion of the distribution appears to fit the shape of the theoretical curves. However, one always observes an excess of low energy betas relative to those of higher energy. This is presumably due to high energy betas giving up only part of their energy within the scintillation medium before being scattered out. Thus one not only observes a small light pulse but he fails to record one which should have been large. In spite of this difficulty, Bell *et al.*[1,2] have been able to obtain useful information concerning the beta-spectra of Be^{10} and K^{40}. However, as the maximum energy of the beta-distribution under study is reduced, the difficulties of studying its shape increase. Figure 1 shows an extreme example in the Kurie plot of Ca^{45} which was obtained using a detection arrangement shown in the insert. The source was mounted on a Formvar film 25 $\mu g/cm^2$ thick placed against the crystal with a 0.2 mg/cm^2 aluminum foil reflector surrounding the optical system. The electronic equipment is similar to that previously described.[3] In Fig. 1 the solid squares represent the original data and the solid circles are the results after correction for the resolution of the instrument, using the method of Owen and Primakoff.[4] Macklin *et al.*[5] have shown that the Ca^{45} disintegration gives an allowed beta-distribution with an end point at 254±3 kev. The straight line in Fig. 1 is drawn from this end point through the high energy experimental points. If the end point were not known, one would be unable to obtain a satisfactory value from this set of data. Also, the discrepancy between the experimental points and the straight line demonstrates the problem of studying the shape of the distribution of such a low energy beta.

Since the resolution correction is large only near the ends of the distribution, it would be desirable to utilize the data in the midregion for determining the end-point energy. Furthermore, these data can be obtained with better counting statistics. However, this can be done only if the extraneous low energy pulses can be eliminated. If the above explanation of their origin is correct, it should be possible to eliminate the difficulty by placing the source between two crystals in such a manner that the probability of observation of the scattered beta in the second crystal is great. Whereas this might be accomplished by using two crystals and two photo-multipliers, the arrangement shown in the insert of Fig. 2 has been used. The two anthracene crystals were matched to give equal pulse heights and resolution individually for the Cs^{137} conversion line. When this source was placed between the crystals, the observed number of pulses doubled, but the pulse height of the peak was unchanged and the resolution remained

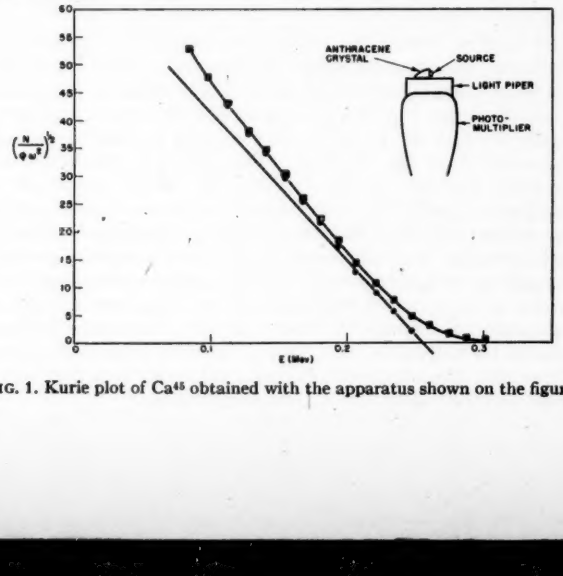

FIG. 1. Kurie plot of Ca^{45} obtained with the apparatus shown on the figure.

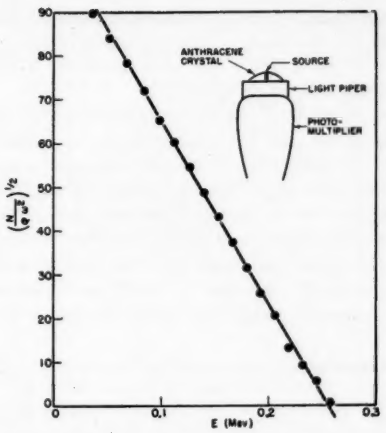

FIG. 2. Kurie plot of Ca^{45} obtained with the experimental arrangement shown on the figure.

equal to that of each crystal alone, 6.5 percent half-width at half-height. The Kurie plot of Ca^{45} shown in Fig. 2 was obtained with the source mounted between 25 $\mu g/cm^2$ Formvar films placed between the two crystals which were in contact. The resolution correction has been made. Since the plot is linear from 50 kev to the end point, one can now rely largely upon points obtained with good statistics to obtain the end point. The value obtained is 255±4 kev in good agreement with the value previously reported,[5] as is also the spectrum shape. Thus, it appears that this split crystal spectrometer can give reliable information about the shapes and maximum energies of low energy beta-emitters.

Credit for the success of this study is due in large part to helpful discussions with C. J. Borkowski, A. R. Brosi, and H. Zeldes and to R. A. Dandl and E. Fairstein who designed and calibrated the electronic circuits.

* This document is based on work performed for the AEC at the Oak Ridge National Laboratory.

[1] P. R. Bell and J. M. Cassidy, Phys. Rev. **77**, 301 (1950).
[2] Bell, Weaver, and Cassidy, Phys. Rev. **77**, 399 (1950).
[3] W. H. Jordon and P. B. Bell, Nucleonics **5**, 30 (1949).
[4] G. E. Owen and H. Primakoff, Phys. Rev. **74**, 1406 (1948).
[5] Macklin, Feldman, Lidolfsky, and Wu, Phys. Rev. **77**, 137 (1950).

Decay of Y^{87} and Sr^{87m}

L. G. MANN* AND PETER AXEL
University of Illinois,† Urbana, Illinois
September 27, 1950

Y^{87} and its daughter Sr^{87m} were investigated by using a double thin-lens beta-ray spectrometer, scintillation counters, and Geiger counters in coincidence. The activities were produced by bombarding strontium with deuterons. (The authors are indebted to the cyclotron staff at both the University of Washington in St. Louis and the University of Chicago for these bombardments.)

Decay of ground state of Y^{87}. The half-life of the ground state[1,2] was measured as 80.0±1 hours. At least 98 percent of the 80-hour Y^{87} decays to an excited state of Sr^{87} at 875 kev. This state immediately emits a 485±3-kev gamma-ray and leads to the 390±2-kev isomeric state. In addition to the predominant K-capture process, a very low intensity (less than one percent) positron spectrum exists. The low intensity of these positrons made an accurate energy determination impossible; the data are consistent with the value of 0.7 Mev reported by Robertson, Scott, and Pool.[2] Assuming this energy, the measured K-capture to positron ratio is much higher than the theoretically predicted value of 7 for an allowed transition. The value of $\log(f_K+f_\beta+)t=5.9$ and Mrs. Mayer's shell structure theory[3] indicates an allowed transition.

The K conversion coefficient of the 485-kev gamma-ray was measured by comparing the number of its conversion electrons to those of the 390-kev gamma-ray and using the measured K conversion coefficient (0.25) of the latter. The value of $3.3\pm0.5\times10^{-3}$ is consistent with the theoretical values only[4] for either electric quadrupole, magnetic dipole, or a mixture of both.

Upper state of Y^{87}. The upper isomeric state[1,2] of Y^{87} decays with a half-life of 14±1 hours. (When the details of its decay are completely investigated, a paper will be written on the entire decay scheme.) About 50 percent of the 14-hour activity leads to the 80-hour ground state. Although the growth of the 80-hour activity makes this certain, the radiation corresponding to this transition has not yet been identified. The remainder of the 14-hour activity has 374-kev conversion electrons associated with it. There are no 485-kev gamma-rays emitted by 14-hour Y^{87}. The 14-hour activity also has a low intensity positron spectrum whose maximum energy was measured as 1.1±0.1 Mev. The experimental K to positron ratio is 50 while the theoretical value for an allowed transition is 1.6. The log $(f_K+f_\beta+)t$ value is 5.5.

Decay of Sr^{87m}. The half-life[1,2,5] of Sr^{87m} was measured as 2.80 ±0.05 hours. This state emits a 390±2-kev gamma-ray which is partially converted. The K conversion coefficient was determined by using coincidence techniques and was found to be $N_e/N_\gamma=0.25\pm0.04$. This is consistent with the theoretical values only[4] for either magnetic 2^4 pole, electric 2^5 pole, or a mixture. The ratio of K- to L-conversion as determined in the spectrometer was 6.9±0.4.

The data on the excited states of Sr^{87} are consistent with internal conversion theory, nuclear isomeric theory,[6] and Mrs. Mayer's shell theory if the three energy levels are assigned as $g_{9/2}$, $P_{1/2}$, and $P_{3/2}$. (The spin of the ground state is known[7] to be 9/2.) The assignments of the Y^{87} states and a comparison with beta-decay theory cannot be made until the investigation of 14-hour Y^{87} is complete.

* Now at Stanford University.
† Supported by the joint program of the ONR and AEC.

[1] L. A. Dubridge and J. Marshall, Phys. Rev. **56**, 706 (1939) and Phys. Rev. **58**, 7 (1940).
[2] Robertson, Scott, and Pool, Phys. Rev. **78**, 318 (1950).
[3] M. G. Mayer, Phys. Rev. **78**, 16 (1950).
[4] Rose, Goertzel, Spinard, Harr, and Strong, report privately circulated.
[5] A. C. Helmholz, Phys. Rev. **60**, 415 (1941).
[6] P. Axel and S. M. Dancoff, Phys. Rev. **76**, 892 (1949).
[7] M. Heyden and H. Kopferman, Zeits. f. Physik **108**, 232 (1938).

Double Development of Nuclear Emulsions

Č. JECH
Department of Physics, State Radiotherapeutical Institute, Praha-Bulovka, Czechoslovakia
August 25, 1950

ONE of the most valuable features of the nuclear emulsion technique is the ability of a photographic emulsion to integrate the images of nuclear events which were registered by the emulsion before its development. Generally we have no means of determining at what time or in what order individual tracks were recorded, although this may be of interest in certain cases. Some information can be obtained on this subject from the study of the fading of the track images. The fading is dependent, however, on a number of factors and takes place only gradually and

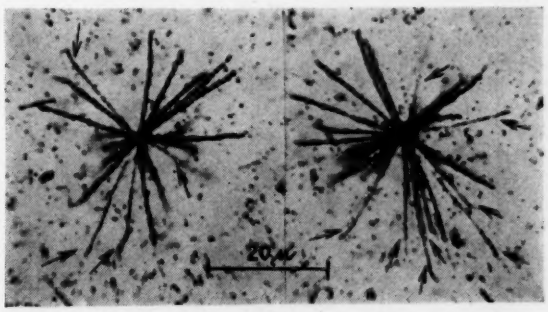

FIG. 1. Two microphotographs of Io (Th^{230}) stars showing distinctly two sorts of tracks registered during two successive one-day periods. The thin tracks registered during the second day are marked by arrows.

over a long period of time so that it is of little value for this purpose.

We have been able to differentiate between tracks emitted during separate time intervals (24 hours) using double development of the emulsion. This method enables us to distinguish according to the degree of development the heavy tracks of alpha-particles recorded before the first (full) development from the finer ones, which were emitted during the time elapsed between the first and second (partial) development.

In our experiments we deposited a fine suspension of Io (Th^{230}) in water on the surface of a Ilford C 2 emulsion. After 24 hours the plate was developed in the usual manner for ten minutes, washed, and dried without being fixed. After another 24 hours the plate was developed a second time but only for 2 minutes in the same (ID-19) developer and then treated with acetic acid and fixed. Many aggregates of alpha-tracks (such as those shown on Fig. 1) can be observed, in which two sorts (roughly equal in number) are clearly discernible. Heavy tracks in these aggregates were emitted during the first day and revealed by the first development. Thin tracks from the second development (recorded during the second day) appear to have smaller grain size but there is no reduced grain density along the tracks. We think that with proper procedures three or more developments could be used for various purposes and when temperature development is[1] applied, the time intervals between each development could be reduced, if desirable, to a few minutes.

[1] Dilworth, Occhialini, and Payne, Nature **162**, 102 (1948).

Internal Conversion Electrons and Other Radiations from Cl^{34}

LAWRENCE RUBY AND J. REGINALD RICHARDSON
Department of Physics, University of California, Los Angeles, California*
October 4, 1950

THE radiations emitted by Cl^{34} have been investigated in a large magnetic lens spectrometer similar to that of Hornyak *et al.*[1] The spectrometer has been calibrated with the 623.9-kev conversion electrons of Ba^{137} and its linearity checked with other sources.

The spectrum of the 33-min. Cl^{34} has been investigated by Zah Wei-Ho[2] using a cloud chamber. His results indicated a gamma-ray of 3.4 Mev and two groups of positrons with maximum energies of 5.1 and 2.4 Mev.

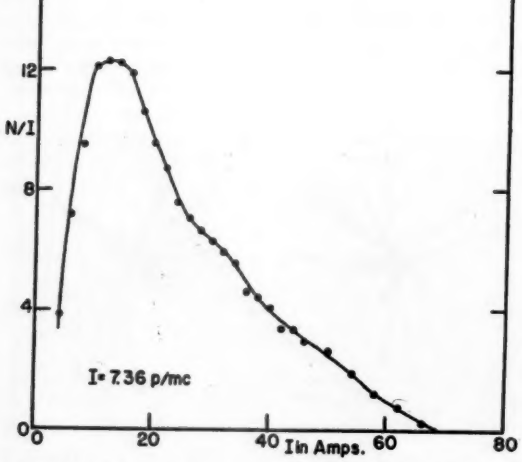

FIG. 1. The positron spectrum from Cl^{34}. The Kurie plot of this spectrum separates into three groups with upper limits at 4.55 Mev, 2.6 Mev, and 1.3 Mev.

We produced the Cl^{34} activity by bombarding NaCl with 18-Mev protons from the U.C.L.A. cyclotron according to the reaction $Cl^{35}(p,pn)Cl^{34}$. The activity was also produced by bombarding sulfur, giving the reaction $S^{34}(p,n)Cl^{34}$.

Our results on the positron spectrum indicate that it is complex (Fig. 1). The Kurie plot is consistent with the presence of three components. The end point of the most energetic component can easily be evaluated at 4.55±0.11 Mev. The other two components separate out of the Kurie plot at 2.58±0.26 Mev and 1.3±0.2 Mev. We tend to believe in the validity of this separation because of the supporting evidence of the gamma-radiation.

Internal conversion electrons at 142±3 kev from a previously unreported gamma-ray have been found as shown in Fig. 2. The

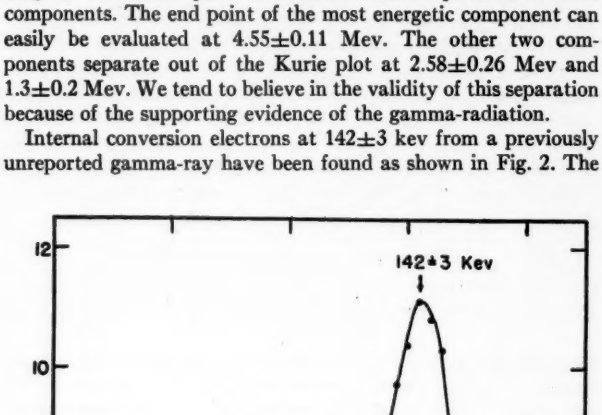

FIG. 2. The internal conversion electrons associated with Cl^{34}. This group corresponds to a gamma-ray of energy 0.145 Mev.

line is broadened by the size of the NaCl crystals. The decay of this line has been followed for three half-lives in the spectrometer to verify its origin in the Cl^{34} activity. The ratio of positrons to conversion electrons is 17 to 1. This gamma-ray is not entirely internally converted as seen from the appearance of an *L* conversion peak in the photo-electron spectrum from a thorium radiator. The energy of this peak is consistent with a gamma-ray of energy 145 kev.

The Cl^{34} high energy Compton spectrum has an inflection point at 3.06±0.13 Mev corresponding to a gamma-ray of energy 3.30±0.14 Mev and an inflection point at 1.90±0.12 corresponding to a gamma-ray of energy 2.13±0.12 Mev. The general features of the probable energy level diagram are obvious from the numbers involved, but they have not yet been verified by coincidence counting. The place of the 145-kev gamma-ray in the scheme has not been uniquely determined.

* This work was assisted by the joint program of the ONR and AEC.
[1] Hornyak, Lauritsen, and Rasmussen, Phys. Rev. **76**, 731 (1949).
[2] Zah Wei-Ho. Phys. Rev. **70**, 782 (1946).

Mass Dependence of the Superconducting Transition Temperature of Mercury*

B. SERIN, C. A. REYNOLDS, AND L. B. NESBITT
Rutgers University, New Brunswick, New Jersey
October 2, 1950

IN a recent communication,[1] Herzfeld, Maxwell, and Scott fitted the available data on the superconducting transition temperatures (T_c) of mercury isotopes of different mass (M), to a formula of the type $M^{\alpha}T_c=$const. by the method of least squares. The best fit to the[2] data was given by $\alpha=0.378$, whereas in an earlier communication,[3] we had proposed $\alpha=\frac{1}{2}$.

At the time of our communication, we did not feel that the accuracy of the data warranted a close scrutiny of the kind given to it by Herzfeld and co-authors; and the exponent $\frac{1}{2}$ was proposed as giving a good fit within the accuracy of the experimental values for the transition temperatures. The poor quality of the data is evident from the appreciable deviations of the experimental points from the relation, $M^{0.378}T_c=$const., derived by least squares.

Since our communication, the detailed theories of superconductivity of Bardeen[4] and Fröhlich[5] give the value $\frac{1}{2}$ for α.

Because of the importance of determining an accurate experimental value of α, in view of these theories, we have been engaged in an extensive investigation of the transition temperatures of mercury samples of different isotopic constitutions. We have found that the temperature spread of the transition from the superconducting to the normal state (and thus the accuracy with which the zero-field transition can be determined by extrapolation) is very sensitive to the way in which the samples are cooled to liquid air temperature, and also to the way in which liquid helium is admitted to the flask. The procedure finally adopted was to place a small amount of liquid air in the outer shield flask. The system was allowed to stand for about an hour, and then small amounts of liquid air were added over the course of another hour. It was possible to get an accurate idea of the temperature of the samples during cooling by measuring the change in resistance of pick-up coils surrounding them; and thus to bring the samples slowly through the freezing point of mercury. We found it equally important never to permit the initial blow-off of warm helium gas from the transfer tube to hit the samples; thus, we waited until liquid helium poured out of the transfer tube before placing the tube in the helium flask. This method of cooling clearly produces the minimum amount of strain in the samples.

Our most reliable data for our original samples and for a new set of three samples[6] of slightly different isotopic constitution (making a total of seven samples) are shown in Fig. 1, where $\log_{10}M$ is plotted *vs.* $\log_{10}T_c$. The measuring technique was the same as that described earlier,[7] except that the frequency of the alternating field was reduced to 20 c.p.s. The transition temperature for the sample of natural mercury is in good agreement with the value, 4.167°K, given by Misener.[8]

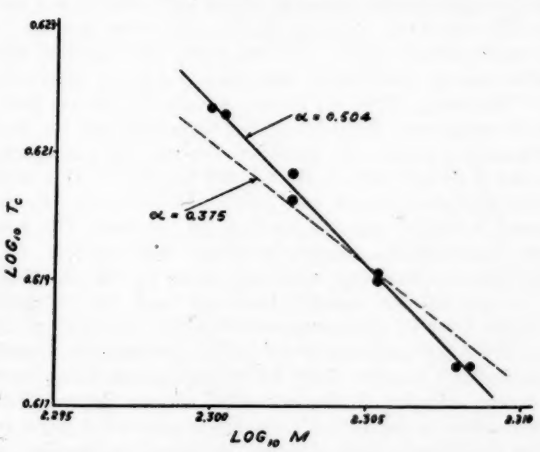

FIG. 1. Transition temperature as a function of the mass number.

The slope of the line as drawn in Fig. 1 is 0.504. For purposes of comparison a line of slope 0.375 is also drawn.

On the basis of these measurements, we feel that it is definitely established that in mercury, at least, the exponent α is certainly much closer to $\frac{1}{2}$ than to any other value having a simple physical interpretation. This result is in agreement with the predictions of the theories[4,5] mentioned above.

* This work was supported by the ONR, by the Research Corporation, by the Rutgers University Research Council, and by the Radio Corporation of America.
[1] Herzfeld, Maxwell, and Scott, Phys. Rev. **79**, 911 (1950).
[2] Herzfeld *et al.* conclude that the true value is $\alpha=3/8$, corresponding to constant thermal energy of the lattice.
[3] Serin, Reynolds, and Nesbitt, Phys. Rev. **78**, 813 (1950).
[4] J. Bardeen, Phys. Rev. **79**, 167 (1950).
[5] H. Fröhlich, Proc. Phys. Soc. London **63**, 778 (1950); Phys. Rev. **79**, 845 (1950).
[6] The isotopes were produced by Carbide and Carbon Chemical Division, Oak Ridge National Laboratory, Y-12 Area, Oak Ridge, Tennessee, and were obtained on allocation.
[7] Reynolds, Serin, Wright, and Nesbitt, Phys. Rev. **78**, 487 (1950).
[8] A. D. Misener, Proc. Roy. Soc. **174**, A, 262 (1940).

Temperature Effect in Geiger-Müller Counters

MOTOHARU KIMURA
Faculty of Science, Tohoku University, Sendai, Japan
July 10, 1950

THE temperature effect on the rate of spurious discharges in G-M counters (hard glass sealed-off type with out-gassed cathode of 2 cm diam. and 5 cm long) was observed when they were heated and cooled at constant rates. As is shown in Fig. 1, on the heating stage the rate of natural counts increased in various manners which depended on the filling gases and less markedly on the cathode material; it decreased rapidly on the cooling stage without exception. It was verified that these discharges were due to "Spontanentladung" and the occurrence of double or triple discharges ("Nachentladung") was very rare. The plateau curves were taken with a gamma-ray source and also without any source before and after each experiment, and we could not find marked changes in them, though those with natural counts were generally better after heating. The plateau lengths were generally between 150 and 500 v, with the slopes of 0.6 to 10 percent per 100 v. We observed the increases in spurious counts also when the counter voltage was applied intermittently, that is, for 20 sec. once every 3 min. The increased counting rate began to decrease again when the temperature rise was stopped and the counter was kept at a certain constant temperature near 100°C. The decrease was an almost exponential function of the time measured from the

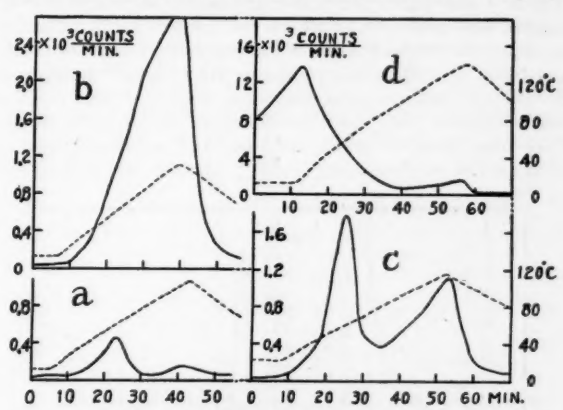

FIG. 1. Temperature effects on the rate of spontaneous discharges of the G-M counters. Full line: counts per min. The broken line gives the temperature. (a): A 76 mm, ethyl ether 9 mm. (b): A 95 mm, alcohol 10 mm. (c): A 98 mm, ethylene 10 mm. (d): A 90 mm, alcohol 10 mm, under visible light irradiation. All with Fe cathode and 0.1-mm W wire.

moment when the temperature rise was stopped. The above phenomena could not be attributed to the decrease of the work function of the cathode surfaces by heating, because (1) the counting rate was not a function of the temperature itself but of its sense and rate of change, and (2) the photo-sensitivity (by yellowish-red light from *W* filament lamp) decreased by heating as shown in Fig. 1a, though it increased gradually with time when the counter was kept at room temperature, as was found by Nonaka.[1] A tentative explanation can be given along the lines of adsorption and evaporation of the quenching gas molecules and the negative ions from the cathode surfaces.[2] A full account will appear in the *Journal of the Physical Society of Japan*.

[1] I. Nonaka, J. Phys. Soc. Japan **3**, 322 (1948).
[2] The author is indebted to Professor I. Nonaka for his kind discussion on these points.

The Gamma-Rays from Neutron-Activated Gold

R. W. Pringle and S. Standil
Physics Department, University of Manitoba, Winnipeg, Canada
September 29, 1950

With the advent of the study of photo-electron and pair production "lines" in the scintillation gamma-ray spectrometer,[1] there arise many fruitful applications of this new technique. Some new results in the low energy region, where the photoelectric effect predominates, have been obtained with neutron-activated gold and I^{131}. In the present spectrometer arrangement use is made of a small 1-cm cube crystal of NaI-Tl exposed to the uncollimated gamma-rays from the source, and an E.M.I. 5311 photo-multiplier operating at 1000 volts.

Figure 1 shows the differential pulse-height distribution curves obtained with a neutron-activated gold sample of 0.1 mC a few days after the irradiation. In *A* the features are the 69-kev Hg x-ray below 10 volts, the well-known 411-kev Au^{198} gamma-ray below 40 volts, and the unresolved hump between 10 and 20 volts. This is believed (see below) to correspond to the 159-kev and 209-kev lines known to belong to 3.3-day Au^{199}, which is formed by two successive (n,γ) reactions on Au^{197} during the irradiation,[2] and

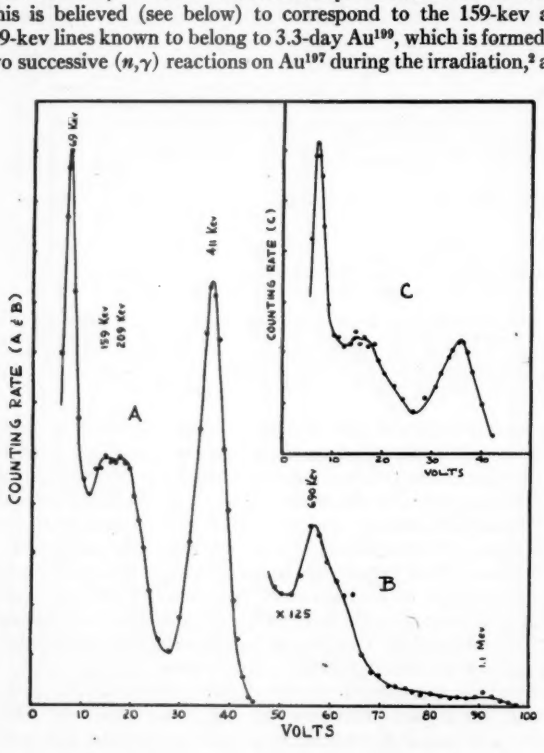

FIG. 1. Scintillation spectrometer pulse-height distributions for the gamma-rays from neutron-activated gold. *A*. Lower energy gamma-rays and x-ray. *B*. Counting rate scale ×125 to show new high energy components. *C*. Relative distribution of *A* after 11 half-lives of Au^{198}.

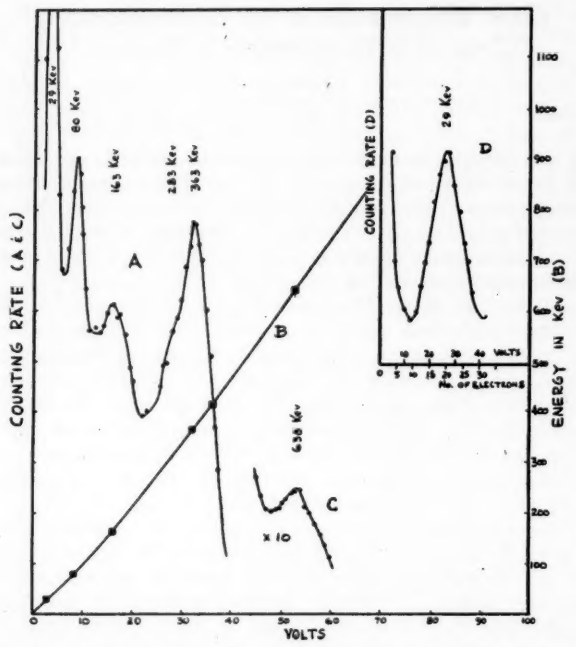

FIG. 2. Gamma-ray from I^{131}. *A*. Lower energy gamma-rays and x-ray. *B*. Energy-pulse-height relationship showing slight lack of linearity. *C*. Counting rate scale ×10 to show 638-kev component. *D*. X-ray at 29 kev shown on higher gain setting, with scale to show pulse heights estimated in terms of the number of electrons collected from the photo-multiplier cathode.

also to a contribution due to the Compton effect of the 411-kev gamma-ray. The lines occur at the full gamma-ray energies because of the trapping in the crystal of the low energy radiations and particles following the initial photoelectric effects. In *B* the counting rate scale has been magnified 125 times, and one can see clearly the presence of a new 690-kev gamma-ray below 60 volts and a new 1.1-Mev gamma-ray near 90 volts.[3] The calibration curve used to determine these energies is given in Fig. 2. In Fig. 1(*C*) the low energy region is given once again, this time after a lapse of 30 days from the observations of 1(*A*). The counting rate scale is given arbitrarily, but it is evident that the 2.7-day 411-kev component has decayed more rapidly than the rest of the curve. The decay rate for the curve below 20 volts agrees with that for a mixture of 3.3-day Au^{199} and 2.7-day Au^{198}. The relative sizes of the x-ray peaks in *A* and *C* suggest a large internal conversion coefficient for the Au^{199} 159-kev and 209-kev lines. Because of the much lower counting rates involved it has not been possible to follow the high energy components over more than 3 or 4 half-lives. The half-life of these appears, however, to be less than 3.0 days, and probably close to 2.7 days. One can therefore draw some interesting conclusions concerning the decay scheme for Au^{198}. The energy of the 411-kev line adds to the 690-kev line to give the component at 1.1 Mev, thus suggesting that the latter corresponds to a cross-over transition. We therefore visualize the existence of excited states in Hg^{198} at 411 kev and 1.1 Mev, and a complex beta-spectrum for Au^{198} which would consist of two components[4] of 960 kev and 270 kev (say two percent). This lower energy component has apparently not yet been detected.

The pulse-height-energy calibration curve for the scintillation spectrometer has been shown to be almost linear, but not exactly so. Figure 2 for I^{131} (gamma-rays 80 kev, 163 kev, 283 kev, 363 kev, and 638 kev, and x-ray 29 kev for Xe) illustrates the necessity of having such a curve (2(*B*)) for the instrument, using known gamma-ray energies. In the calibration curve a reference point corresponding to the Au^{198} 411-kev line is included. A slight curvature which is most marked below 150 kev may be observed, and thorough testing having shown that this curvature can only be

attributed to the photo-multiplier crystal combination, it may possibly represent a lack of exact linearity in the crystal light output-energy relationship for low energies.

In Fig. 2(*D*) is shown the 29-kev x-ray of Xe, obtained with a somewhat larger gain setting of the linear amplifier. From the resolution of this low energy line (50 percent), and other considerations, it has been possible to reconstruct approximately the pulse-height scale in terms of the numbers of electrons collected from the cathode. It is interesting to note that the noise level rises rapidly only below pulse heights corresponding to 3 or 4 electrons collected by the first dynode (or approximately 5 kev on the calibration curve[5]).

This project has been assisted by the National Research Council of Canada.

[1] R. W. Pringle, Nature **166**, 11 (1950). Pringle, Roulston, and Standil, Phys. Rev. **78**, 627 (1950). J. A. McIntyre and R. Hofstadter, Phys. Rev. **78**, 617 (1950). P. R. Bell and J. M. Cassidy, Phys. Rev. **79**, 173 (1950).
[2] R. D. Hill and J. W. Mihelich, Phys. Rev. **79**, 275 (1950).
[3] These results are in agreement with observations obtained recently by one of us (S.S.) with a beta-ray spectrometer in the laboratory of Dr. J. A. Gray.
[4] D. Saxon, Phys. Rev. **74**, 297 (1948).
[5] Pringle, Roulston, and Taylor, Rev. Sci. Inst. **21**, 216 (1950).

The Gamma-Radiation of Ba^{131}

E. B. Dale, E. D. Richert, T. A. Redfield, and J. D. Kurbatov
Department of Physics, Ohio State University, Columbus, Ohio
July 10, 1950

FOR determination of the energies of gamma-rays less abundant than the 496-kev gamma-ray of Ba^{131} barium nitrate was activated with the highest neutron flux available at the Oak Ridge National Laboratory. The gamma-radiation intensity of Ba^{131} received was about twice that of the previous activation. The barium was chemically purified and after disintegration of Ba^{133} was studied with a thin-lens spectrometer. A broad increase in the counting rate of photo-electrons was observed in the range corresponding to 180 to 220 kev indicating the presence of several gamma-rays. Only two peaks were sufficiently strong to define clearly the photo-electron energies. These peaks are shown in Fig. 1. The separation of peaks indicates that they are *K* and *L* peaks of a single gamma-ray of 213.5±2 kev. The energy values of this gamma-ray were calculated on the basis of averages, of several runs, for the *K* peak of 213.2±1 kev and for the *L* peak of 213.8±2 kev. The probable error was determined from the uncertainty in estimating exact peak positions. The 213.5-kev gamma-ray determined by the spectrometer probably corresponds to the previously reported gamma-ray of energy 220±10 kev found by absorption measurements.[1]

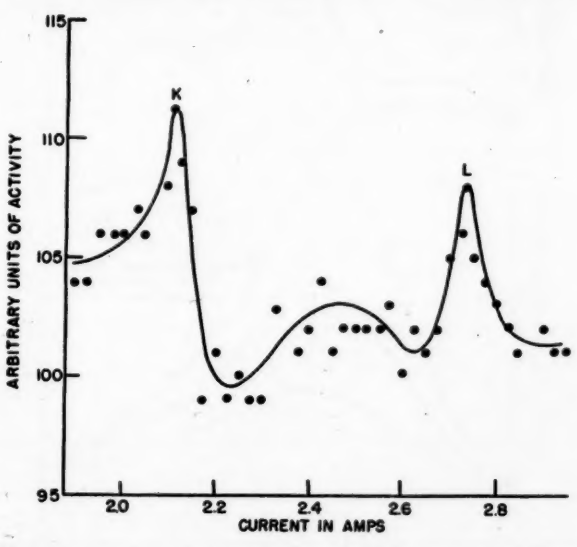

FIG. 1. Barium 131—*K* and *L* photo-electron peaks of 213.5±2-kev gamma-rays—lead radiator.

The authors sincerely appreciate the activation of the barium by the Oak Ridge National Laboratory.

The financial assistance given by the Graduate School and the Development Fund of The Ohio State University is gratefully acknowledged.

[1] Yu, Gideon, and Kurbatov, Phys. Rev. **71**, 382 (1947).

A Method for Measuring Paramagnetic Absorption on Small Samples

R. P. Lacroix, Ch. E. Ryter, and C. R. Extermann
University of Geneva, Geneva, Switzerland
October 2, 1950

WE have found it possible to make absorption measurements on very small samples of paramagnetic material.

In our apparatus, the two side arms of a magic tee are each terminated by a cavity. The cavity containing the sample is rectangular in shape and operates on the TE_{011} mode; the other one is a cylindrical TE_{011} resonator with means provided to vary its *Q*-factor within large limits, making it possible to set the resonance amplitude at the same value in both cavities. By tuning them to slightly different frequencies, and using a frequency sweep on the Klystron, we get the two resonance curves side by side on the oscilloscope. With a suitable vertical gain, amplitude comparison can thus be made quite accurately.

Using this apparatus, we found for the absorption of $MnSO_4 \cdot 4H_2O$ a value somewhat different from that given by Cummerow *et al.*[1] The shape of our curve (Fig. 1) seems to be closer to the theoretical curve of Frenkel; the normal paramagnetic susceptibility, χ, obtained from the integrated surface under the curve (0.25×10^{-25} cm³/ion) also fits better with direct measurement.

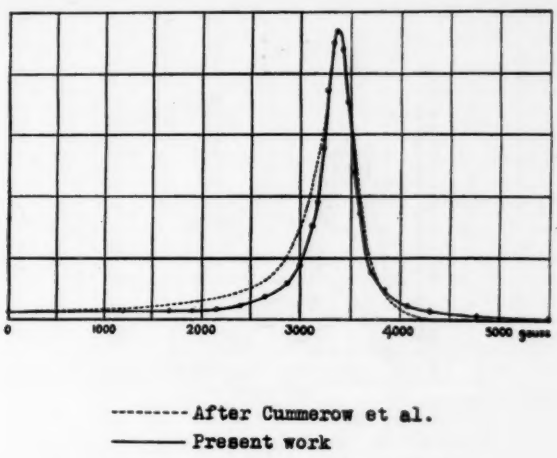

FIG. 1. Absorption curve of $MnSO_4 \cdot 4H_2O$.

We would suggest as a possible explanation for this discrepancy that the resonant rotation of the polarization plane[2] in the cavity when it is filled with a paramagnetic salt will tend to change the *Q*-factor. Our method seems to be free from this objection, as we used only thin samples in the vicinity of the walls.

[1] Cummerow, Halliday, and Moore, Phys. Rev. **72**, 1233 (1947).
[2] This phenomenon was predicted theoretically by Kastler (Comptes Rendus **228**, 1640 (1949)) and has been observed experimentally by Ryter *et al.* (Physica, Comptes Rendus de la Conférence sur le Magnétisme, Amsterdam, 1950).

Effect of Infra-Red on Emission and Trapping in ZnS:Cu Phosphors*†

RICHARD H. BUBE
Radio Corporation of America, RCA Laboratories Division, and Princeton University, Princeton, New Jersey
September 22, 1950

A STIMULATION band for ZnS:Cu phosphors has been found by Garlick and Mason,[1] and by the author, at about 1.2 to 1.3 microns. Daly[2] reported a stimulation band at 1.26 microns for a (Zn:Cd)S:Cu phosphor, as well as bands at 2.08 and 2.70 microns. Garlick and Mason attributed the band at 1.3 microns to the copper.

This letter reports the results obtained when a series[3] of hex.—ZnS:Cu(0.0–0.3), [NaCl(2)] phosphors[4] are stimulated by a broad band of infra-red, ranging in wave-length from approximately 0.8 to 3.0 microns. It is found that (1) there is a marked spectral shift to the blue in the stimulated emission, (2) the intensity of the stimulated emission does not depend simply on the number of electrons freed from traps by the infra-red, and (3) the extent of trap emptying by infra-red is a function of the temperature of stimulation.

The hex.—ZnS:Cu(0.0–0.03), [NaCl(2)] phosphor series has both blue and green emission bands. The variation of the spectral emission with copper proportions has been discussed elsewhere.[4] Pertinent for the discussion here is the fact that the blue band decreases in intensity, whereas the green band increases in intensity, for copper proportions between 0.0001 and 0.03 percent.

At room temperature, it was found that both the flash-up on application of the infra-red to a decaying phosphor (after an initial excitation by 3650A ultraviolet), and the phosphorescence emission during infra-red illumination were bluer than the unstimulated emission, for phosphors with 0.0001 to 0.003 percent Cu. A Wratten 47 filter was used to isolate the blue emission, and a Wratten 62 filter to isolate the green emission. Figure 1a shows the initial flash-up under infra-red for nine phosphors with increasing copper proportion, the infra-red being applied after one minute of decay. A complete decay cycle, before and during infra-red, is shown in Fig. 1b, for hex.—ZnS:Cu(0.001), [NaCl(2)].

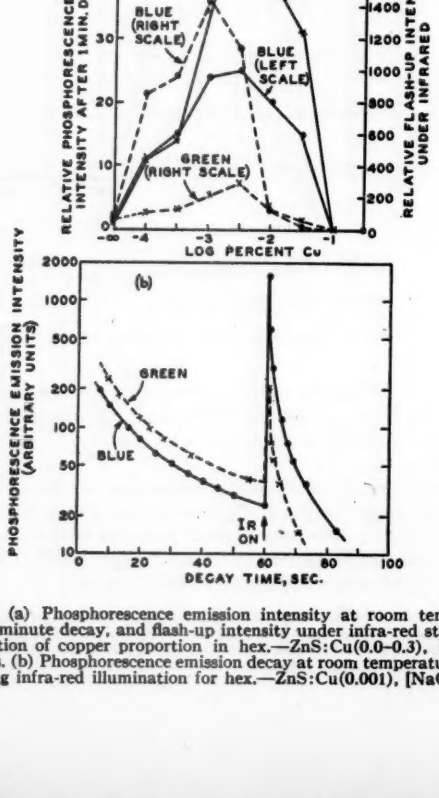

FIG. 1. (a) Phosphorescence emission intensity at room temperature after one minute decay, and flash-up intensity under infra-red stimulation as a function of copper proportion in hex.—ZnS:Cu(0.0–0.3), [NaCl(2)] phosphors. (b) Phosphorescence emission decay at room temperature before and during infra-red illumination for hex.—ZnS:Cu(0.001), [NaCl(2)].

TABLE I. Release of electrons from traps by infra-red.

Percent Cu	Relative no. of electrons freed by *IR* at −196°C in 18 min.	Relative no. of electrons freed by *IR* at 22°C in 4 min.
0.003	100	35
0.01	115	37
0.03	75	13
0.1	70	No traps present
0.3	40	No traps present

For no copper, the stimulation of blue and green emission as obtained from the filters is about the same, since the spectral emission consists only of a blue band with a long tail into the green. For 0.01 percent copper and above, little stimulation of any type occurs.

A study of the infra-red emptying of traps was made as a function of temperature using glow curve techniques. The phosphor is excited at temperature T, and is then allowed to decay at T for t minutes before a glow curve is run. The phosphor is then recooled to T, re-excited, and allowed to decay for t minutes with the infra-red on before a second glow curve is run. The difference between the area under the glow curve obtained after the t minutes of decay and infra-red, and the area obtained after t minutes of decay without infra-red, gives at least the minimum number of electrons freed from traps by the infra-red. Table I gives the results of such measurements. These results show that the decrease in the stimulation flash-up between 0.003 and 0.01 percent Cu is not caused by a decrease in the ability of the infra-red to empty traps.

The temperature dependence of the emptying of traps by infra-red is demonstrated by the glow curves of Fig. 2. Deep traps, rapidly emptied by infra-red at room temperature, are not emptied at all by infra-red at −196°C for comparable times of stimulation.

The energy corresponding to 1.3 microns is 0.95 ev, which is exactly the energy reported by Garlick and Gibson[5] for the difference between the conduction band and the excited state of the green-emitting center. The absorption of the 1.3-micron infra-red by the green-emitting center would decrease the probability of a transition giving green emission. This would result in a spectral

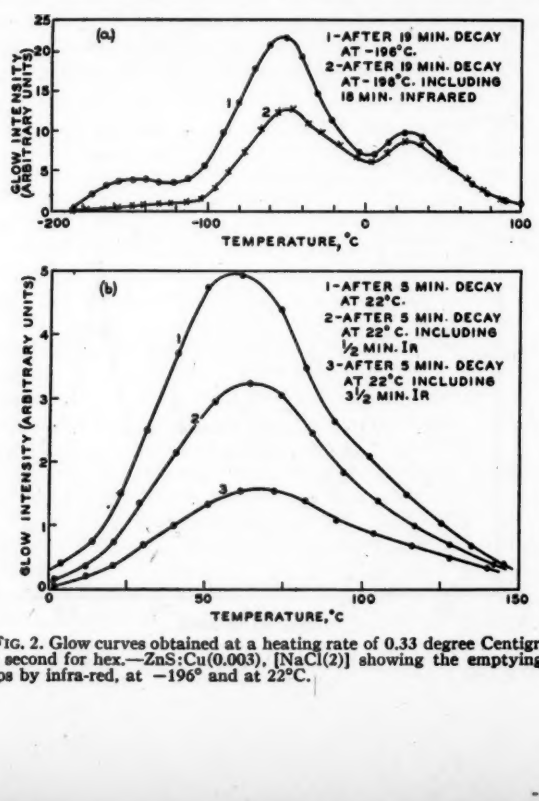
(a)
1-AFTER 19 MIN. DECAY AT −196°C.
2-AFTER 19 MIN. DECAY AT −196°C. INCLUDING 18 MIN. INFRARED
GLOW INTENSITY (ARBITRARY UNITS)
TEMPERATURE, °C
(b)
1-AFTER 5 MIN. DECAY AT 22°C.
2-AFTER 5 MIN. DECAY AT 22° C. INCLUDING ½ MIN. IR
3-AFTER 5 MIN. DECAY AT 22°C INCLUDING 3½ MIN. IR
GLOW INTENSITY (ARBITRARY UNITS)
TEMPERATURE, °C

FIG. 2. Glow curves obtained at a heating rate of 0.33 degree Centigrade per second for hex.—ZnS:Cu(0.003), [NaCl(2)] showing the emptying of traps by infra-red, at −196° and at 22°C.

shift to the blue under infra-red stimulation. The large decrease in stimulation between 0.003 and 0.01 percent Cu may be attributed to the large decrease in the number of effective blue-emitting centers (caused by an increase in the relative number of green-emitting centers and hence an increase in the rate of the process by which holes are transferred from blue-emitting to green-emitting centers) as shown by spectral curves.[4]

* This letter is part of a dissertation presented to the faculty of the Physics Department of Princeton University in May, 1950, as partial fulfillment for the requirements of the Ph.D. degree.
† This work was done under contract between ONR and RCA.
[1] G. F. J. Garlick and D. E. Mason, J. Electrochem. Soc. **96**, 90 (1949).
[2] E. F. Daly, Proc. Roy. Soc. **196**, 554 (1949).
[3] Proportions are given in weight percent.
[4] Full discussion of the preparation and luminescence characteristics of these phosphors is included in a paper by the author, R. H. Bube, Phys. Rev. **80**, 657 (1950).
[5] G. F. J. Garlick and A. F. Gibson, J. Opt. Soc. Am. **39**, 935 (1949).

Further Remarks on the Absorption of π^--Mesons in Hydrogen*

R. E. MARSHAK AND S. TAMOR
University of Rochester, Rochester, New York
AND
A. S. WIGHTMAN
Princeton University, Princeton, New Jersey
September 5, 1950

PANOFSKY, Aamodt, and York[1] have measured the γ-ray spectrum arising from the absorption of π^--mesons in hydrogen. As a result, it now appears fairly certain that the two processes hypothesized in an earlier paper,[2] namely: $\pi^-+P\rightarrow N+\gamma$ (radiative absorption) and $\pi^-+P\rightarrow N+\pi^0$ (mesic absorption) actually take place in nature.[3] Apart from the sensitive method which is furnished for the determination of the π^0-mass, the ratio of the mesic to radiative absorption probability determines the strength of the π^0-nucleon coupling. It is interesting to calculate[4] values of the π^0 coupling constant for various possible combinations of π^-- and π^0-fields and couplings.[5] The results are given in Table I. Column 1 contains expressions for the radiative absorption probability from the K-shell, while the remaining columns list expressions for the mesic absorption probability[6] and the values of the π^0-coupling constant (in units of $1/\hbar c$) which follow from the observed equality of radiative and mesic absorption.[7] The quantities g_P and g_N are the π^0-coupling constants with proton and neutron, respectively.

TABLE I. Absorption probabilities per sec.*

Radiative	Mesic		
$S(S)$	$S(S)-S(S)$	$S(S)-PS(PS)$	$S(S)-PS(PV)$
$2e^2\Gamma^2\delta^2$	$4\beta(\Delta g)^2$	$\beta^3\delta^2(\Delta g)^2$	$4\beta^3(\Delta g)^2$
	$(\Delta g)^2=0.008$	$(\Delta g)^2=27$	$(\Delta g)^2=0.15$
$PS(PS)$	$PS(PS)-S(S)$	$PS(PS)-PS(PS)$	$PS(PS)-PS(PV)$
$2e^2\delta^2$	$\frac{\beta^3}{4}\delta^4(\Delta g)^2$	$\beta\delta^2(\bar{g})^2$	$\beta\delta^2(\Delta g)^2$
	$(\Delta g)^2=210$	$(\bar{g})^2=0.06$	$(\Delta g)^2=0.06$
$PS(PV)$	$PS(PV)-S(S)$	$PS(PV)-PS(PS)$	$PS(PV)-PS(PV)$
$8e^2$	$\beta^3\delta^2(\Delta g)^2$	$\beta\delta^2(\Delta g)^2$	$\beta\delta^2(\bar{g})^2$
	$(\Delta g)^2=210$	$(\Delta g)^2=11$	$(\bar{g})^2=11$
$V(V)$	$V(V)-S(S)$	$V(V)-PS(PS)$	$V(V)-PS(PV)$
$(2/3)e^2$	$(4/3)\beta^3\delta^2 g_P^2$	$\beta\delta^2(\Delta g)^2$	$\beta\delta^2(\bar{g})^2$
	$g_P^2=13$	$(\Delta g)^2=0.93$	$(\bar{g})^2=0.93$
$PV(PV)$	$PV(PV)-S(S)$	$PV(PV)-PS(PS)$	$PV(PV)-PS(PV)$
$(2/3)e^2$	$4\beta(\Delta g)^2$	$\frac{\beta^3\delta^2}{3}[(\Delta g)^2+2(\bar{g})^2]$	$\frac{4\beta^3}{3}[(\Delta g)^2+2(\bar{g})^2]$
	$(\Delta g)^2=0.005$	$[(\Delta g)^2+2(\bar{g})^2=52$	$[(\Delta g)^2+2(\bar{g})^2]=0.3$

* The absorption probabilities per sec. are given in units of $\alpha^2\cdot g^4/\hbar c(\mu c^2/\hbar)\cdot(1/\hbar c)$, $\alpha=e^2/\hbar c$, g is the π^--coupling constant, μ is the π^--mass $\Gamma=4.71$ =difference between proton and neutron magnetic moments (in units of the nuclear magneton), $\delta=\mu/M$, $\beta=p_0/\mu c$, $\Delta g=g_P-g_N$, $\bar{g}=g_P+g_N$; in the first column, $PS(PV)$ means the absorption of a PS π^- with PV coupling; in column 3, for example, $PS(PV)-PS(PS)$ means the absorption of a PS π^- with PV coupling and the emission of a PS π^0 with PS coupling, etc.

Examination of Table I permits us to discard some of the theories when proper account is taken of other π-meson experiments; e.g., the upper limit of $5\cdot10^{-14}$ sec. on the lifetime[8] of π^0, the photon production[9] of $\pi^\pm$, π^0, etc. Since the very recent experiment on the π^--absorption in deuterium definitely excludes the scalar and vector fields for the charged π-meson,[9a] we shall pursue this analysis here only to the extent of pointing out that Table I provides evidence against a scalar field for π^0: the extremely large π^0-coupling constants predicted by combining a PS field for π^- with a S field for π^0 contradicts the assumption of weak coupling, whereas the extremely small π^0-coupling constants predicted by combining PV for π^- and S for π^0 leads to too long a lifetime for π^0-decay. Thus, the only consistent weak coupling theory which is possible is a PS field for π^0 and a PS or PV field for $\pi^\pm$. In order to decide between the PS and PV fields for the charged π-meson, it is necessary to invoke some other experiment; e.g. Brueckner[9] has concluded that the leveling off with energy of the cross section for photon production of π^+ is evidence for the PS field.

Even if we assume that both the charged and neutral π-mesons are pseudoscalar, neither the hydrogen nor the deuterium experiment fixes the nature of the coupling of the PS π-meson to the nucleon. In principle, a linear combination of PS and PV couplings is possible; the ratio, R, of the mesic to radiative absorption probabilities in hydrogen would then become (g_P, g_N, g, now refer to PS coupling while f, f_P, f_N refer to PV coupling):

$$R=\frac{\beta[g(\bar{g}+\Delta f)+f(\Delta g+\bar{f})]^2/\hbar c}{2\alpha(g-2/\delta f)^2}. \tag{1}$$

Equation (1) contains the dominant terms in an expansion in powers of δ; however, if a particular choice of g_P and g_N leads to a cancellation in the mesic absorption probability, the next term in δ has to be considered. For example, in the pure $PS(PS)-PS(PS)$ theory, R vanishes when $g_P=-g_N$; to the next order[10] in δ, $R=(\beta\delta^2/8\alpha)(\Delta g)^2/\hbar c$ so that the choice $g_P=-g_N$ leads to $g_P^2/\hbar c=g_N^2/\hbar c=2\alpha/\beta\delta^2=2.8$ (see Table I). A promising method for deciding between PS and PV coupling is to study the energy dependence of ordinary and charge exchange π-meson scattering by nucleons. PS coupling leads to a decreasing cross section with energy whereas PV coupling yields a rapidly increasing cross section.[11] For the meson energies produced by present accelerators (up to 150 Mev, say) the reaction of the meson field should not seriously modify the qualitative predictions of weak coupling theory.[12]

We are greatly indebted to Professor Panofsky for keeping us closely informed of experimental developments.

* This work is supported by the joint program of the ONR and AEC.
[1] Panofsky, Aamodt, and York, Phys. Rev. **78**, 825 (1950).
[2] R. Marshak and A. Wightman, Phys. Rev. **76**, 114 (1949); see also B. Bruno, Ark. f. Fysik 1, No. 2 (1949).
[3] A complete demonstration of the latter process would consist, of course, in measuring the two "low" energy γ-rays in coincidence.
[4] We use weak coupling theory; however, strong coupling theory yields similar results for some of the theories, according to a private communication from C. N. Yang.
[5] We have omitted the derivative couplings for the scalar, vector, and pseudovector theories since they do not lead to any essentially new results. Only spin zero theories are considered for π^0 since π^0 decays into two γ-rays.
[6] The $S(S)-S(S)$ expression given in Table I agrees with that given in reference 2 whereas the $PS(PS)-PS(PS)$ expression (Eq. (11)) is δ^2 times smaller. It is *not* true that the equivalence theorem holds for mesic absorption; as a matter of fact, the $PS(PS)-PS(PS)$ and $PS(PV)-PS(PV)$ expressions are *identical*. It is precisely this breakdown of the equivalence theorem for mesic absorption (in contrast to radiative absorption) which makes the hydrogen experiment so interesting and is responsible for some of the surprising numbers listed in Table I.
[7] Panofsky, Aamodt, and Hadley, private communication; $\beta=p_0/\mu c=0.23$ was used where μ_0 and p_0 are the π^0-mass and momentum respectively.
[8] A. Carlson, J. Hooper, and D. King, Phil. Mag. **41**, 701 (1950).
[9] J. Steinberger and A. Bishop, Phys. Rev. **78**, 494 (1950). Steinberger, Panofsky, and Stellar, Phys. Rev. **78**, 802 (1950). K. Brueckner, Phys. Rev. **79**, 641 (1950).

[9a] S. Tamor and R. E. Marshak, following letter.
[10] See Aidzu, Fujimoto, Fukuda, Hayakawa, Takayanagi, Takada, and Yamaguchi, Prog. Theor. Phys. (to be published).
[11] See Ashkin, Simon, and Marshak, Prog. Theor. Phys. (to be published); it is found that as the meson energy increases from 0 to $2\mu c^2$, the $PS(PS)$ scattering cross section decreases by a factor of 1.7 while the $PS(PV)$ cross section increases by a factor of 675.
[12] As is well known, strong coupling theory for PV coupling leads to the same rapid increase of cross section with energy.

On the Absorption of π^--Mesons in Deuterium*

S. TAMOR† AND R. E. MARSHAK
University of Rochester, Rochester, New York
September 5, 1950

SOME work on the absorption of π^--mesons by deuterons has already been published.[1,2] These papers do not consider the three possible modes of mesic disintegration of the deuteron. The π^--absorption may not only lead to the emission of two high energy neutrons (neutron absorption) but in analogy with the absorption in hydrogen,[3] absorption may also be accompanied by the emission of a γ-ray (radiative absorption) or a neutral meson (mesic absorption). A phenomenological treatment of these processes enables one to calculate the relative probabilities of neutron and radiative absorption independently of any detailed theory of nuclear forces and of the strength of the π^--meson-nucleon coupling; in fact, the ratio depends primarily upon the spin and parity of the π^--meson. The mesic absorption predictions depend to some extent on the π^0-nucleon coupling; even this arbitrariness is eliminated by making use of the hydrogen absorption experiment.

Wightman has shown[4] that most π^--mesons have moderation times down to the K shell of the mesic deuterium atom which are short compared to the lifetime for π–μ-decay. The neutron absorption of a π^--meson from the K shell is strongly affected by the requirements of the exclusion principle applied to the final two-neutron system. Thus, since the ground state of the deuteron is $^3S_1+{}^3D_1$ and the interaction of scalar mesons (with scalar coupling[5]) with nucleons does not lead to a spin flip, absorption of scalar mesons from states of even L are forbidden by parity conservation and the exclusion principle. Instead, absorption of a scalar meson will be accompanied by the emission of a photon in spite of the fact that the electromagnetic interaction is inherently weak. The other theories are also affected by the selection rules but in different ways.

The neutron and radiative absorption probabilities are listed in Table I, as is the ratio of the two. N is a normalization factor for the radial wave function of the deuteron and $\phi(0)$ is the amplitude of the meson wave function at the origin. We see that in view of the widely different theoretical predictions, the search for γ-rays from the absorption of π^--mesons in deuterium should yield fairly decisive information concerning the nature of the charged π-meson. The detection of appreciable numbers of γ-rays would exclude the vector charged π-meson. Furthermore, most scalar mesons which reach the K shell (absorption from the L shell is discussed below), should give rise to γ-rays in contrast to the other theories.

It should be mentioned that the distortion of the final state wave function by the neutron-neutron interaction (taken equal to the proton-proton interaction) affects the spectral distribution of the γ-rays. If one ignores this interaction, the γ-spectrum has a peak near 130 Mev and a width of about 12 Mev. The interaction sharpens the peak to a width of about 2 Mev and shifts the maximum to 134 Mev (assuming 140 Mev for the π^--mass); however, the total transition probability is affected only slightly.

The emission of a neutral meson is also possible if the $\pi^- - \pi^0$-mass difference exceeds[6] 3.55 Mev. Experiments at Berkeley indicate a mass difference of about 5 to 6 Mev. Using this mass difference and the coupling constants for π^0 obtained from the absorption in hydrogen[7] we can determine the competition from mesic absorption. For π^--mesons of spin 1, mesic absorption may be comparable to or even larger than radiative absorption, but both are dominated by neutron absorption. Assuming spin zero for π^- we find that mesic absorption is very improbable (down by a factor 10^4 compared to radiative absorption) for the same parity of π^- and π^0 because of the operation of the exclusion principle; for opposite parity, mesic absorption can compete with radiative absorption.

If the π^--meson is absorbed from a state of odd L, the selection rules are changed. However, absorption from P states is slower by a factor of 30 than the radiative transition to lower states (for scalar mesons). One can expect that about 95 percent of the π^--mesons will be absorbed from the $1S$ state.

While this letter was in preparation, Professor Panofsky very kindly informed us of the results of his experiment with Aamodt and Hadley on the π^--absorption in deuterium. Their observations are that about $\frac{1}{3}$ of the π^--mesons yield 130-Mev γ-rays while "low" energy γ-rays are absent. We believe that since the theory is phenomenological and is really quite insensitive to the more subtle properties of meson fields, it is difficult to escape the conclusion that the scalar and vector fields for the charged π-meson[8] are excluded by the results. There is further slight evidence that a pure $PS(PS)$ theory for the charged π-meson is ruled out. If the charge π-meson is pseudoscular, the absence of π^0 argues for equal parity[7] for π^0 and $\pi^\pm$.

A detailed paper will be published shortly by one of us (S.T.). We are indebted to Dr. Wightman for several helpful conversations.

TABLE I. Absorption probabilities per second from $1S$ state in units of $(N/3)\cdot(g^2/\hbar c)\cdot(\hbar/\mu c)^3\cdot\phi(0)^2\cdot c = 0.91\cdot10^{16}\cdot g^2/\hbar c$ sec.$^{-1}$. $S(S)$ means scalar mesons with scalar coupling, etc.

Meson theory	$S(S)$	$PS(PS)$	$PS(PV)$	$V(V)$	$PV(PV)$[d]
Neutron[a]	0[b]	$2.7\cdot10^{-3}$[c]	0.25	0.12	2.5 ($J=0$) 0 ($J=1$) 0.15 ($J=2$)
Radiative	0.012	$6.6\cdot10^{-4}$	0.12	$2.2\cdot10^{-3}$	$2.0\cdot10^{-2}$ ($J=1$) $2.4\cdot10^{-3}$ ($J=0$, 2)
Ratio	0	4.1	2.1	55	2

[a] These probabilities were obtained using the deuteron wave functions determined from the Hulthén potential; a change in the shape of the potential would not affect the ratios by more than a factor of 1.5.
[b] The zero result holds in the phenomenological approximation; a relativistic calculation leads to a transition probability of about $3\cdot10^{-4}$ (i.e., three percent of the radiative probability assuming that the latter receives contributions from the anomalous magnetic moments of proton and neutron).
[c] The neutron absorption for the $PS(PS)$ theory is about twice as great as the equivalence theorem would predict owing to the charge exchange in the nucleon-nucleon interaction [F. J. Dyson, Phys. Rev. 73, 929 (1948)]. The calculation was done using the Berkeley potential [R. S. Christian and E. W. Hart, Phys. Rev. 77, 441 (1950)].
[d] The ratio given here is not the ratio of the transition probabilities, but depends on the relative populations of the three states ($J=0$, 1, 2) of the meson-deuteron system. If the three states are populated according to their statistical weights, the ratio is 2:1. We are indebted to Dr. K. Brueckner for calling our attention to this point.

* This work is supported by the joint program of the ONR and AEC.
† AEC Predoctoral Fellow.
[1] B. Ferretti, Report on the International Conference on Low Temperatures and Fundamental Particles, Cambridge (1946), p. 75.
[2] C. Marty and J. Prentki, J. de phys. et rad. 10, 156 (1949).
[3] R. E. Marshak and A. Wightman, Phys. Rev. 76, 114 (1949) and preceding letter.
[4] A. Wightman, private communication.
[5] Scalar mesons with vector coupling do not lead to any essentially new results; actually, none of the derivative couplings lead to any qualitatively different results except possibly for the pseudoscalar theory (see Table I).
[6] Obtained from the deuteron binding energy of 2.24 Mev and the neutron-proton mass difference of 1.31 Mev [R. Bell and L. Elliot, Phys. Rev. 74, 1552 (1948)].
[7] Marshak, Tamor, and Wightman, preceding letter.
[8] This conclusion is in agreement with the one drawn from the angular distribution of photon-produced π^+-mesons [K. Brueckner, Phys. Rev. 79, 641 (1950)].

Comments on Truesdell's Paper on Bernoulli's Theorem for Viscous Compressible Fluids

BERNARD ETKIN
Department of Aeronautical Engineering, University of Toronto, Toronto, Canada
AND
VICTOR G. SZEBEHELY
Department of Applied Mechanics, Virginia Polytechnic Institute, Blacksburg, Virginia
September 11, 1950

1. The necessity[1] of the $\partial \mathbf{V}/\partial t = \mathbf{grad} U$ restriction is questionable since a Bernoulli theorem of the type defined by the author can be written even when the "local acceleration potential," U, does not exist. In that case Eq. (3) of reference 1 can be written as

$$\mathbf{w}\times\mathbf{v}+\mathbf{grad}\left(\frac{v^2}{2}+\frac{\lambda+2\mu}{\rho}\theta\right)=\bar{\mathbf{f}},$$

where

$$\bar{\mathbf{f}}=\mathbf{f}-\frac{1}{\rho}\mathbf{grad}\,p+(\lambda+2\mu)\frac{\theta}{\rho}\mathbf{grad}\log\rho-\frac{\mu}{\rho}\mathbf{curl}\,\mathbf{w}-\frac{\partial \mathbf{v}}{\partial t}.$$

Of course the additional generality obtained in this way increases the complexity of the definition of the curves $\mathcal{C}$ through the additional term $-\partial \mathbf{V}/\partial t$ in $\bar{\mathbf{f}}$.

2. In Eq. (2), and consequently in (3), there has been used the identity

$$\frac{\lambda+2\mu}{\rho}\mathbf{grad}\theta=\mathbf{grad}\left[(\lambda+2\mu)\frac{\theta}{\rho}\right]+(\lambda+2\mu)\frac{\theta}{\rho}\mathbf{grad}\log\rho,$$

presumably to introduce viscosity terms into the expression for the Bernoulli constant. Viscosity terms also appear, however, in the expression for $\bar{\mathbf{f}}$. It would seem preferable to put (3) in the form $\mathbf{w}\times\mathbf{v}+\mathbf{grad}(U+\frac{1}{2}v^2)=\bar{\mathbf{f}}$, where

$$\bar{\mathbf{f}}=\mathbf{f}-\frac{1}{\rho}\mathbf{grad}\,p+\frac{\lambda+2\mu}{\rho}\mathbf{grad}\theta-\frac{\mu}{\rho}\mathbf{curl}\,\mathbf{w}.$$

In this form both the Bernoulli constant and $\bar{\mathbf{f}}$ are simplified.

3. The utility of the classical Bernoulli theorems rests in the fact that they connect pressure with velocity. The author's grouping of the variables discards this feature except for incompressible flow. Thus the "generalized" Bernoulli theorem given in the paper does not reduce directly to the classical form when the appropriate simplifying assumptions are made.

A theorem which does contain the pressure, and which does reduce as desired is readily obtained. Assuming a conservative body force and a barotropic fluid, as well as steady vorticity, we have

$$\partial \mathbf{v}/\partial t=\mathbf{grad}U,\quad \mathbf{f}=-\mathbf{grad}\psi,\quad p=p(\rho).$$

Equation (3) of reference 1 can then be written as

$$\mathbf{w}+\mathbf{v}+\mathbf{grad}B=\bar{\mathbf{f}},$$

where

$$B\equiv U+\psi+\tfrac{1}{2}v^2+\int dp/\rho \text{ is the "Bernoulli constant,"}$$

and

$$\bar{\mathbf{f}}\equiv\frac{\lambda+2\mu}{\rho}\mathbf{grad}\theta-\frac{\mu}{\rho}\mathbf{curl}\,\mathbf{w}.$$

Here B resembles closely the classical form, and the definition of $\bar{\mathbf{f}}$ is simpler than the author's in that it does not contain either $\mathbf{f}$ or p. This is a matter of no small importance if the curves $\mathcal{C}$ are to be located in an actual flow problem.

4. In the special case $\mathbf{w}\times\mathbf{v}=0$, it follows at once from Eq. (3) that

$$\bar{\mathbf{f}}\cdot\mathbf{curl}\,\bar{\mathbf{f}}\equiv 0$$

since

$$\mathbf{curl}\,\bar{\mathbf{f}}=\mathbf{curl}\,\mathbf{grad}B\equiv 0.$$

Thus the condition on the existence of the surfaces is in this case automatically satisfied.

5. The application of the theorem to the solution of flow problems is difficult because of the complex definition of the curves $\mathcal{C}$. The writers regret that the author did not include some example of its use.

6. Finally, there are three typographical errors in Eq. (3), which should read:

$$\bar{\mathbf{f}}=\mathbf{f}-\frac{1}{\rho}\mathbf{grad}\,p+\frac{\lambda+2\mu}{\rho}\theta\,\mathbf{grad}\log\rho-\frac{\mu}{\rho}\mathbf{curl}\,\mathbf{w}.$$

[1] C. E. Truesdell, Phys. Rev. **77**, 535 (1950).

On Bailey's Theory of Growing Circularly Polarized Waves in a Sunspot

R. Q. TWISS
Royal Naval Scientific Services, Baldock, Hertsfordshire, England
September 11, 1950

IN a recent paper Bailey[1] developed a theory to show that circularly polarized waves in an ionized medium would be amplified, in certain frequency bands, if a d.c. axial magnetic field $\mathbf{B}_0$ was present and if the medium possessed a drift velocity $\mathbf{u}_0$ with a component parallel to the axial magnetic field. It was argued that the ordinary waves[2] would be amplified if

$$\mathbf{u}_0\cdot\mathbf{B}_0>0$$

and that the extraordinary waves would be amplified if

$$\mathbf{u}_0\cdot\mathbf{B}_0<0$$

the frequency bands in which amplification can take place being, for small u_0 just those bands that are attenuating when the ionosphere has zero drift velocity. Furthermore, the rate of growth of those amplified, or growing, waves is approximately independent of the magnitude of the drift velocity, being approximately equal to the rate of attenuation in a stationary ionosphere.

This result is so surprising that a detailed discussion both of the physical mechanism by which the energy amplification takes place and of the mechanism by which the growing wave is excited seems necessary before it can be accepted. Professor Bailey's theory is essentially mathematical in nature and his criterion for the existence of amplification is simply that the phase velocity of the growing wave

$$\exp(\alpha z)\cdot\exp[i(\beta z-wt)]$$

be positive. That is that

$$\alpha>0,\quad \beta>0.$$

If the phase velocity be positive it follows that the flow of energy associated with this wave is also positive, that is, out of the medium. Bailey concludes that, in this case, the growing wave is not a wave reflected from the far end of the medium but can be directly excited by an electromagnetic wave, of suitable polarization, incident in the initial surface of the medium. However, this conclusion is unjustified. If the transient response of the medium to a signal incident on the initial phase $z=0$ is analyzed, it can be shown that this growing wave will never be excited if the medium extends, without discontinuity, to infinity. If there is a surface of discontinuity at $z=d$, then the growing wave at z cannot be excited until a time greater than $(2d-z)/c$ has elapsed, where c is the velocity of light in vacuum.

Thus, despite the fact that it has a positive phase velocity, this growing wave must be regarded as a reflected wave, whose amplitude, at the surface of discontinuity, bears a relation to the amplitude at this point of the incident wave which is determined solely by the impedances of the true media on either side of the discontinuity.

Ideally, by suitable choice of this impedance, it should be possible to obtain power amplification in a laboratory device, but in the sun, where the change of space-charge density and magnetic

field with distance is presumably slow, it does not seem that Bailey's theory can account for the observed phenomenon.

It is hoped to publish elsewhere a detailed criticism of Bailey's theory, with particular attention to the physical aspects, together with an alternative explanation for the excess noise from sunspots.

[1] V. A. Bailey, Phys. Rev. **78**, 428 (1950).
[2] In the magneto-ionic theory ordinary waves have a sense of rotation of polarization opposite to that of a free electron under the action of the axial magnetic field while the reverse is true for the extraordinary waves.

Search for Be^7 States Using the Li^6 Technique*

GEORGE R. KEEPIN, JR.†
Radiation Laboratory, Department of Physics, University of California, Berkeley, California
October 2, 1950

IN Be^7, the mirrored counterpart of the single 480-kev excited state in Li^7 is now well established at 429 ± 15 kev by two independent methods.[1] However, two additional levels in Be^7 have been reported[2] in spectrum studies on neutrons from LiCl and LiF bombarded with 5.1-Mev (cyclotron) protons. Subsequently others[3] using similar techniques at lower proton energies have not found such levels. We have used the improved neutron energy resolution of the Li^6 technique[4] to measure $Li^7(p,n)Be^7$ neutron spectra in an extended search for any additional levels in Be^7. The possibility[2] of a proton energy threshold for excitation of these additional levels led us to extend E_p nearly 0.5 Mev above the maximum Van de Graaff beam energy previously employed.

The proton beam from the Berkeley electrostatic generator was deflected through a stationary 90°-analyzing magnet into a double slit system defining E_p to ±15 kev. A spectroscopically pure lithium target was used to eliminate extraneous (p,n) reactions from the negative radical of any Li compound. Metallic Li was evaporated onto a thin copper backing disk and transferred in an argon atmosphere to the target chamber. Target thickness measured less than 30 kev for all E_p. An oil-vapor trap was used to prevent carbon deposits on the target. Li^6 plates in Cd containers were mounted tangentially to neutron direction at radial angles $\eta=0$, 30, and 90° to the proton beam. Exposures were monitored by proton collection on the insulated target with a conventional current integrator to measure the charge. Exposed plates were faded, processed[5] and examined under 90× oil-immersion objectives and 8× oculars fitted with AO-1407 reticules. The sum of alpha- and triton ranges was measured to the nearest *RU* (Fig. 1); an eyepiece goniometer gave laboratory angles, ϕ, between neutron and triton, to the nearest degree. Details of data selection and analysis using the Li^6 technique for collimated and/or isotropic neutrons are available.[4,5]

Two separate runs were made at each $E_p=3.00$, 3.60, and 4.35 Mev. Approximately 10,000 disintegrations have been measured. Figure 1 shows measured histograms for $\eta=0°$. From mean energies of the resolved neutron groups in nine different spectra an average value of 433 ± 26 kev for the level excitation energy in Be^7 is obtained. It is noteworthy that this level was definitely excited even for the lowest $E_p=3.00$ Mev. Though some of the data suggest a level intermediate between 433 kev and the ground state, no single group corresponding to such a level was considered sufficiently resolved or sufficiently intense to be so identified with certainty. Spectra were corrected for the energy dependence of the geometrical selection criteria[5] but not for $\sigma_c(Li^6)$, since this is not established for $E_n>0.6$ Mev. Preliminary evidence[6] indicates a broad resonance near 2 Mev and probable $1/E$ flatness elsewhere. Applying this tentative σ-correction, no additional group is observed with more than 15 percent of ground-state intensity. In regions of large $d\sigma/dE_n$ (e.g., near 2 Mev) clearly there has been slight shifting and considerable spreading of the observed peaks. Most accurate comparison of relative group intensities and widths must await precison measurements, now underway, of $\sigma_c(Li^6)$ for $E_n>0.6$ Mev.

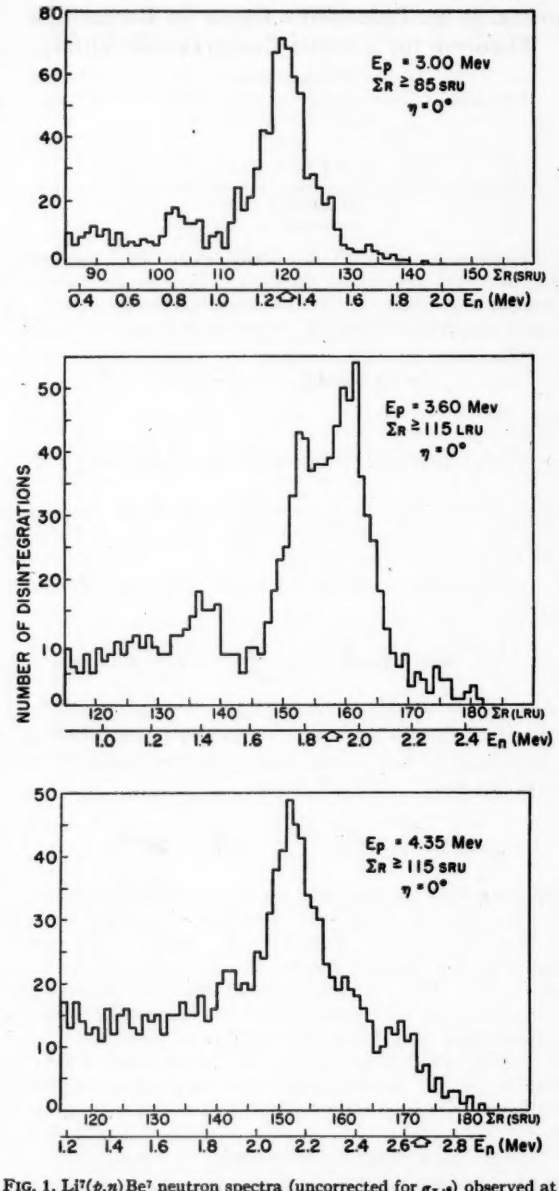

FIG. 1. $Li^7(p,n)Be^7$ neutron spectra (uncorrected for σ_{Li^6}) observed at 0° to the proton beam. Arrow indicates ground-state energy as calculated from E_p, η, and $Q=-1.63$ Mev. One $LRU=0.60\mu$; one $SRU=0.70\mu$.

Possible sources of error are considered in detail in the complete report of this work, UCRL-924; extraneous (p,n) reactions in the target assembly are shown to be negligible at these values of E_p, while any (n,p) reactions in the emulsion are readily distinguished from Li^6 disintegrations by track length or grain density variation. Li^6 monitor plates exposed near the target assembly indicated a less than one percent neutron background for all E_n.

I thank Professors L. W. Alvarez and E. Segrè for their advice and interest in this work, and Mr. F. C. Gilbert for his assistance in plate exposure and measurement.

* This work was performed under the auspices of the AEC.
† AEC Postdoctoral Fellow.
[1] Brown, Chao, Fowler, and Lauritsen, Phys. Rev. **78**, 88 (1950). T. Lauritsen and R. G. Thomas, Phys. Rev. **78**, 88 (1950).
[2] J. Grosskreutz and K. Mather, Phys. Rev. **77**, 580 (1950).
[3] Johnson, Laubenstein, and Richards, Phys. Rev. **77**, 413 (1950); Freier, Rosen, and Stratton, Phys. Rev. **79**, 721 (1950); B. Hammermesh and V. Hummel, Phys. Rev. **78**, 73 (1950).
[4] G. Keepin, Jr. and J. Roberts, Rev. Sci. Inst. **21**, 163 (1950); A. J. F. Siegert and G. Keepin, Jr., LAMS 937 (1950), unpublished.
[5] G. Keepin, Jr., UCRL 790 (1950), unpublished.

On the Magnetic Moments of the Proton and Neutron

ROALD K. WANGSNESS
University of Maryland, College Park, Maryland
September 14, 1950

ONE of the principal difficulties encountered by the theory of elementary particles is the explanation of the "anomalous" magnetic moments of the proton and neutron, for the moments are markedly different from the values of one nuclear magneton ($\mu_N = e\hbar/2Mc$) and zero, respectively, which would be expected from the Dirac equation. Current theories ascribe this difference to the effect of the circulation of mesons in the vicinity of a bare nucleon. All attempts at obtaining quantitative agreement between values calculated from this model and experiment seem to have been uniformly unsuccessful.[1] As a result, it may be of value to approach the problem from a somewhat different level of sophistication. In fact, as we shall see below, the most rudimentary semiclassical and dimensional considerations lead directly to extremely accurate formulas for the moments; in particular, the proton moment obtained in this way agrees *exactly* with the best available experimental value.

We begin by remembering that a characteristic length a which can be associated with the proton is the corresponding classical radius of a charged particle,[2] *viz.*, $a = 2e^2/3Mc^2$. In addition, we recall that the existence of an isolated magnetic pole has been shown by Dirac to be compatible with the requirements of quantum mechanics.[3] The magnitude of this pole is $g = \hbar c/2e$. Since the dimensions of magnetization are those of field, i.e., pole/(length)^2, it is natural to take $I_0 = g/a^2$ as the simplest formula for any magnetization which may be characteristic for this case. A sphere of radius a which is uniformly magnetized with magnetization I_0 has a magnetic moment

$$\mu_p = 4\pi a^3 I_0/3 = 4\pi a g/3 = (8\pi/9)\mu_N.$$

Identifying this moment with that of a proton, we see that its value in units of μ_N is $8\pi/9 = 2.79253$. Within the experimental uncertainty, this agrees exactly with the value 2.79255 ± 0.00010 given by Mack.[4]

Magnetization can also be expressed as pole/area, so one may wonder what the consequences may be of considering a circle of radius a to be the fundamental area; this leads to a characteristic magnetization $I_1 = g/\pi a^2$. Of more interest for us, however, is the difference, $\delta I = I_0 - I_1 = (\pi - 1)I_0/\pi$. For a sphere of radius a, the similar use of δI leads to a moment

$$|\mu_N| = 4(\pi - 1)a^3 I_0/3 = (8/9)(\pi - 1)\mu_N.$$

In this case $(8/9)(\pi - 1) = 1.90364$, while the neutron moment is 1.91280.[4] The discrepancy in the two values is less than ½ percent of the experimental value; this discrepancy may result from the necessity of using a radius for the neutron slightly different from that which is useful for the proton. From above, we immediately obtain the convenient formula: $|\mu_N|/\mu_p = (\pi - 1)/\pi$. This has the value 0.6817 as compared to the experimental value of 0.6850.

Although these models are suggestive and lead to the correct values for the moments, they are probably more of heuristic value than as a picture which can be taken literally. For example, the radius used is much smaller than that usually associated with nucleons, the latter being more of the order of the Compton wavelength, $h/Mc \approx e^2/mc^2 \approx$ range of nuclear forces. One would naturally prefer to obtain these numerical values directly from some general equation involving only e, $\hbar$, c, and m, say, rather than by invoking models of such specificity, but, in any case, the results obtained above are accurate and covenient formulas.

[1] For example: K. M. Case, Phys. Rev. **74**, 1884 (1948); J. M. Luttinger, Phys. Rev. **75**, 309, 1277 (1949); S. D. Drell, Phys. Rev. **76**, 427 (1949); S. Borowitz and W. Kohn, Phys. Rev. **76**, 818 (1949).
[2] M. Abraham and R. Becker, *Theorie der Elektrizität*, II, (Teubner, Leipzig, 1933), p. 43.
[3] P. A. M. Dirac, Phys. Rev. **74**, 817 (1948).
[4] J. E. Mack, Rev. Mod. Phys. **22**, 64 (1950).

Excited State of C^{14} from the $C^{13}(d, p)C^{14*}$ Reaction*

A. SPERDUTO, S. S. HOLLAND, JR., D. M. VAN PATTER, AND W. W. BUECHNER
Physics Department and Laboratory for Nuclear Science and Engineering, Massachusetts Institute of Technology, Cambridge, Massachusetts
October 2, 1950

AT present there is very little information concerning the excited states of C^{14}, and that which does exist has been confined to the $C^{13}(d,p)C^{14*}$ reaction. Bennett *et al.*,[1] using 1.0-Mev deuterons, found only the ground-state group with a Q-value of 6.09 ± 0.2 Mev. They concluded that there were probably no levels in C^{14} below 2.8 Mev. Humphreys and Watson,[2] using 3.8-Mev deuterons, reported two proton groups with Q-values of 5.82 ± 0.2 and 0.59 ± 0.3 Mev, which they assigned to the ground state of C^{14} and an excited level at 5.2 Mev. The increase in yield of the latter group with increased amount of C^{13} is not obvious from their published results. Recently, Curling and Newton,[3] using 0.93-Mev deuterons, measured a Q-value of 5.91 ± 0.03 Mev for the ground-state $C^{13}(d,p)C^{14}$ group. In addition, they observed a proton group, which, if assigned to the $C^{13}(d,p)C^{14*}$ reaction, would have a Q-value of 0.32 ± 0.03 Mev, corresponding to an excited state of C^{14} at 5.59 ± 0.04 Mev. This group occurred at the same range as a $N^{14}(d,p)N^{15*}$ group; however, they considered the group to be five times more intense than expected for the $N^{14}(d,p)N^{15*}$ group.

The gamma-radiations from $C^{13}+d$ have been measured by Thomas and Lauritsen.[4] They found a gamma-ray of 6.115 ± 0.030 Mev at 0.6-Mev bombarding energy which could only be assigned to the $C^{13}(d,p)C^{14*}$ reaction on the basis of energy considerations. In addition, they assigned a gamma-ray of 5.69 ± 0.05 Mev to the $C^{13}(d,p)C^{14*}$ reaction on the basis of the results of Curling and Newton.[3]

In view of the paucity of reported levels in C^{14} and also because C^{13} occurs as a contaminant on all targets (1.1 percent of natural carbon), it was decided to investigate the $C^{13}(d,p)$ reaction using the M.I.T. magnetic spectrometer. The targets used for this investigaton were prepared by allowing a few drops of a suspension of $BaCO_3$ in water to evaporate onto a thin film of Formvar stiffened by a thin layer of evaporated gold. By this method, targets were prepared of both normal $BaCO_3$ and $BaCO_3$ in which the C^{13} was enriched to 52 percent of the carbon content.[5] Direct evaporation of the $BaCO_3$ was not possible, inasmuch as it decomposes at high temperatures. The target thickness was estimated to be about 90 kev for the $C^{13}(d,p)C^{14}$ ground-state proton group. It was found that these targets survived long exposures to the bombarding deuterons, and their considerable thickness was not a disadvantage in the present work.

The lower curve in Fig. 1 indicates the results of a partial survey made at 1.507-Mev bombarding energy using an enriched $BaC^{13}O_3$

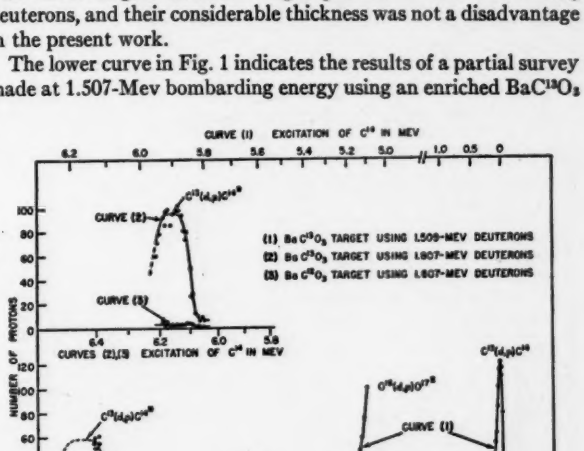

FIG. 1. Proton groups observed from targets of normal $BaCO_3$ and enriched $BaC^{13}O_3$ at bombarding energies of 1.509 and 1.807 Mev.

target. The observed $C^{13}(d,p)C^{14}$ ground-state group had a measured Q-value of 5.948 ± 0.014 Mev, in good agreement with Curling and Newton's value[3] of 5.91 ± 0.03 Mev. In addition, proton groups were investigated with energies between 2.0 and, 1.03 Mev, corresponding to a region of excitation of C^{14} from 5.1 to 6.14 Mev. One proton group was observed which, if assigned to the $C^{13}(d,p)C^{14*}$ reaction, had a Q-value of -0.148 ± 0.005 Mev, corresponding to an excited state of C^{14} at 6.096 ± 0.015 Mev. This group was estimated to be about three times more intense than the ground-state $C^{13}(d,p)C^{14}$ group. No additional proton groups were observed in this partial survey, except the low energy side of the $O^{16}(d,p)O^{17*}$ group with $Q=1.049$ Mev. The remainder of the $O^{16}(d,p)O^{17*}$ group was not observed because of the presence of a large background of deuterons elastically scattered from the target material.

The assignment of the previously unreported $C^{13}(d,p)C^{14*}$ group was verified in two ways. The yield of this group was observed at 1.807-Mev bombarding energy from both enriched $VaC^{13}O_3$ and normal $BaCO_3$ targets. The results shown in curves 2 and 3 indicated that this proton group should be attributed to the C^{13} isotope. In addition, a precise measurement was made of the change in energy of this proton group for a change in bombarding energy of 298 ± 2 kev. The expected shift in energy of a $C^{13}(d,p)$ group would be 238 ± 2 kev, while the shift for a $C^{12}(d,p)$ or $N^{14}(d,p)$ group would be 234 ± 2 kev or 242 ± 2 kev, respectively. The observed energy shift was 240 ± 2 kev, indicating that the target mass could not be different by more than one unit from 13. Since there are no known $C^{12}(d,p)$ or $N^{14}(d,p)$ groups in this region, the assignment of this group to the $C^{13}(d,p)C^{14*}$ reaction appears to be correct.

It is concluded that a level has been found in C^{14} at 6.095 ± 0.015 Mev, which is in excellent agreement with Thomas and Lauritsen's assignment[4] of a 6.115 ± 0.030-Mev gamma-ray to an excited state of C^{14}. No additional $C^{13}(d,p)C^{14*}$ groups were found in a region of excitation of C^{14} from 5.2 to 6.1 Mev with an intensity greater than 0.2 the intensity of the proton group corresponding to the 6.096-Mev level. Hence, there was no evidence for the proton group reported by Curling and Newton which would correspond to a level of C^{14} at 5.59 ± 0.04 Mev (indicated by region A in Fig. 1). Thomas and Lauritsen have assigned to this same level a gamma-ray of 5.69 ± 0.05 Mev which was 0.3 as intense as the 6.115-Mev gamma at 1.58-Mev bombarding energy. The present results indicate no corresponding proton group with this relative intensity at a bombarding energy of 1.51 Mev.

* This work has been assisted by the joint program of the ONR and AEC.
[1] Bennett, Bonner, Hudspeth, Richards, and Watt, Phys. Rev. **59**, 781 (1941).
[2] R. F. Humphreys and W. W. Watson, Phys. Rev. **60**, 542 (1941).
[3] C. D. Curling and J. O. Newton, Nature **165**, 609 (1950).
[4] R. G. Thomas and T. Lauritsen, Phys. Rev. **78**, 884 (1950).
[5] We are indebted to Professor J. D. Roberts of the M.I.T. Chemistry Department for the enriched $BaC^{13}O_3$.

Erratum: Scattering of Positrons and Electrons by Nuclei

[Phys. Rev. 79, 892 (1950)]

H. J. LIPKIN AND M. G. WHITE
Palmer Physical Laboratory, Princeton University, Princeton, New Jersey

October 6, 1950

THROUGH an editorial slip the errors in the figures given in Table I were indicated incorrectly. The correct form of Table I is as follows:

TABLE I. Ratio of e^-/e^+ scattering by platinum.

Kinetic energy (Mev)	e^-/e^+ (experimental)	e^-/e^+ (unscreened theory)
0.7	3.15 ± 0.15	2.74
1.0	3.13 ± 0.12	2.90
1.3	3.60 ± 0.36	2.98